

Von der Universität Bayreuth zur Erlangung des Grades eines
Doktors der Naturwissenschaften (Dr. rer. nat.)
genehmigte Abhandlung

From models to applications: Simulation of blood flow with an extended boundary integral method

von

Achim Guckenberger
Geboren in Würzburg

Tag der Einreichung: 14. Februar 2018

Tag des Kolloquiums: 27. April 2018

1. Gutachter: Prof. Dr. Stephan Gekle
2. Gutachter: Prof. Dr. Walter Zimmermann

Biofluid Simulation and Modeling
Fakultät für Mathematik, Physik und Informatik
Universität Bayreuth



UNIVERSITÄT
BAYREUTH

Document compiled on May 7, 2018, 8:37.

Created using pdf \LaTeX -1.40.17 (L \LaTeX 2 ϵ) with the help of KOMA-Script, microtype, tikz, pgfplots and many other packages.

Abstract

Deutsche Kurzzusammenfassung

Blut ist eine der wichtigsten Flüssigkeiten in unserem Leben. Doch trotz dessen Bedeutung sind wir noch immer weit von einem umfassenden Verständnis von dessen Eigenschaften entfernt. Dies kann auf das komplexe Verhalten dieses Fluids zurückgeführt werden. Die vorliegende Arbeit behandelt zwei spezifische Aspekte von Blutströmungen aus physikalischer Sicht mit Hilfe von dreidimensionalen numerischen Simulationen. Zum einen wird gezeigt, dass eine einzelne, in einem Mikrokanal fließende rote Blutzelle zwei unterschiedliche und stabile Formen annehmen kann, die „Croissant“ und „Slipper“ genannt werden. Insbesondere tritt eine Koexistenz beider Formen bei gleichen Parametern auf. Diese Bistabilität findet sich ebenso in entsprechenden Experimenten wieder, die von unseren wissenschaftlichen Partnern durchgeführt werden. Der detaillierte Vergleich der Ergebnisse zeigt eine quantitative Übereinstimmung. Zum anderen untersuchen wir mit Lipiden beschichtete Mikrobläschen in Zusammenhang mit gezielter Medikamentenzufuhr mittels Ultraschall. Wir zeigen, dass die speziellen Eigenschaften der Beschichtung der Bläschen, deren Schwingungen aufgrund des Ultraschalls und deren komplexe Interaktion mit den roten Blutzellen zu einem effizienten Protokoll für Medikamentenzufuhr führen. Dies lässt sich auf den sogenannten „Margination-Effekt“ zurückführen, welcher erst aufgrund der Wechselwirkung mit den roten Blutzellen auftritt. Falls die Zellen vernachlässigt werden, sind realistische Vorhersagen für solche Mikrobläschen in Blutströmungen nicht mehr möglich.

Bevor jedoch obige Forschungsprojekte durchgeführt werden können, müssen zunächst die zugrundeliegenden Methodiken untersucht und verbessert werden. Genauer gesagt besteht physikalische Forschung mittels numerischen Simulationen aus mehreren Ebenen, konkret den physikalischen Modellen, mathematischen Betrachtungen, Algorithmen, der numerischen Implementierung, der Validierung und zuletzt deren eigentlichen Anwendung. Die vorliegende Arbeit trägt zu all diesen Ebenen bei. Auf der ersten Ebene vergleichen wir sogenannte „lineare Biegemodelle“ mit dem weitverbreiteten Canham-Helfrich Modell. Beide stellen Modelle für die Biegesteifigkeit von deformierbaren Objekten wie rote Blutzellen dar. Von mathematischer Seite her wird daraufhin die normale Randintegralmethode in periodischen Systemen um volumenveränderliche Objekte erweitert, um die Untersuchung mit oszillierenden Mikrobläschen zu ermöglichen. In dem für uns wichtigen Fall eines periodischen Systems wird die Existenz und Eindeutigkeit der Lösung mathematisch bewiesen. Der Beweis enthält als Untermenge den üblichen Fall ohne volumenveränderliche Objekte (für den bisher kein Beweis in periodischen Systemen existierte). Auf algorithmischer Ebene vergleichen und bewerten wir bekannte Algorithmen für die Implementierung des Canham-Helfrich Modells. Es stellt sich heraus, dass keiner eine ordentliche Konvergenz aufweist und der Fehler einiger mit der Auflösung sogar anwächst. Nichtsdestotrotz sind sinnvolle Resultate in viskosen Strömungen möglich, auch wenn Ergebnisse aus der Literatur eine bemerkenswerte Streuung aufweisen. Der Methodenteil wird schließlich mit einem kurzen Abschnitt über die numerische Implementierung mittels MPI und der Validierung abgeschlossen. Im letzten Teil der Arbeit betrachten wir die Anwendung der Methode im Zuge obiger Studien.

English abstract

Blood is one of the most important fluids in our life. Despite its significance and because of its complex behavior, we are still far away from a comprehensive understanding of its properties. The present thesis elucidates two specific aspects of blood flow from a physical point of view using three-dimensional numerical simulations. First, we show that a single red blood cell flowing in a microchannel can assume two different major stable shapes, called “croissant” and “slipper”. Most importantly, both shapes can coexist, i.e. they are stable at the same parameters. This bistability is also observed in corresponding experimental investigations contributed by our collaborators. A detailed comparison uncovers quantitative agreement between both results. Second, we study lipid-coated microbubbles in the context of targeted drug delivery with ultrasound. We find that the special properties of the lipid coating, oscillations caused by the ultrasound and the complex interactions with the red blood cells lead to an effective drug delivery protocol. This is due to the effect of margination which hinges upon the presence of the red blood cells. If the cells are neglected, it becomes impossible to make realistic predictions for such bubbles in blood flow.

Before we are able to perform these two studies, however, we first need to advance the underlying methodology. More precisely, physical research via numerical simulations combines several layers: Physical models, mathematical examinations, algorithms, numerical implementation, validation of the tools and only then their application. The present work makes contributions to each of these layers. Regarding the first layer, we rigorously compare so-called “linear bending models” with the more common Canham-Helfrich model. Both are models for the bending rigidity of deformable objects such as red blood cells. On the mathematical side, we extend the standard periodic boundary integral method to include volume-changing objects in order to enable the study of oscillating microbubbles. For our important case of periodic domains, we provide a mathematical proof that it has exactly one solution. The proof contains as a subset the common boundary integral method without volume-changing objects (for which, so far, no proof in periodic domains existed). Algorithmically, a detailed evaluation of the available algorithms for the Canham-Helfrich model is performed. We uncover that no algorithm provides proper convergence and that some even show an increase of error with higher resolutions. Despite this, sensible results in viscous flows are possible, although existing references still show a remarkable scattering of results. We finish the methodological part with a short section on the numerical implementation with MPI and the validation. In the last part we consider the application of the method, resulting in the above studies.

Contents

Abstract	III
Deutsche Kurzzusammenfassung	III
English abstract	IV
I Extended abstract	1
1 Introduction	3
1.1 Motivation: Why and how to study blood flow	3
1.2 Scope & aim	4
1.3 Contributions and outline	4
2 Biology and models of blood flow	7
2.1 Structure and modeling of red blood cells	7
2.2 Modeling blood flow on the micro-scale	10
2.3 Capsules and vesicles	11
3 Describing volume-changing objects via an extended boundary integral equation	13
3.1 Introduction	13
3.2 General system description	13
3.3 The extended Fredholm boundary integral equation	14
3.4 Sketch of the proof	16
4 Algorithms for the surface forces	19
4.1 Surface discretization	19
4.2 In-plane elasticity	19
4.3 Helfrich bending forces	20
4.3.1 The model and the forces	20
4.3.2 Algorithms for the bending forces	21
4.3.2.1 Force formulation	21
4.3.2.2 Strong formulation	21
4.3.2.3 Weak formulation	22
4.3.3 Evaluation of the bending algorithms	22
4.3.3.1 Comparison with analytical results	22
4.3.3.2 A capsule in a linear shear flow	23
4.3.3.3 Conclusion	25
5 The boundary integral method: Algorithmic and numerical treatment of the boundary integral equation	27
5.1 Putting the boundary integral method into perspective	27
5.2 Algorithms	28
5.3 Implementation, optimization, parallelization and validation	29

6	Physical research projects	31
6.1	Bistability of red blood cells in microchannels	31
6.1.1	Motivation	31
6.1.2	Setup	32
6.1.3	Summary of our key results	33
6.2	Ultrasound-triggered margination of microbubbles	36
6.2.1	Motivation	36
6.2.2	Setup	37
6.2.3	Summary of our key results: Ultrasound-triggered margination	38
7	Conclusion & outlook	41
7.1	Conclusion	41
7.2	Outlook	42
7.2.1	Investigation of the stress-free shape of red blood cells	42
7.2.2	Further open questions	43
8	References	45
	Acknowledgments	71
II	Publications	73
9	The author's contributions	75
9.1	Major publications	75
9.2	Further publications	78
9.3	Presentations	78
10	Attached publications	79
	Publication 1: On the bending algorithms for soft objects in flows	
	Publication 2: Theory and algorithms to compute Helfrich bending forces: a review	
	Publication 3: A boundary integral method with volume-changing objects for ultrasound-triggered margination of microbubbles	
	Publication 4: 3D tomography of cells in micro-channels	
	Publication 5: Numerical-experimental observation of shape bistability of red blood cells flowing in a microchannel	

Part I

Extended abstract

1 Introduction

1.1 Motivation: Why and how to study blood flow

Blood is a core element for the functioning of mammalian bodies. It is responsible not only for delivering oxygen from the lungs to the remotest cells and carbon dioxide back to them, but also for transporting antibodies and phagocytes which are crucial for the immune system. Hence it is of no surprise that huge efforts were and are invested in the research of this fluid. One reason why blood is still an active research topic after all these decades is its complex nature, stemming from the interaction between the fluids and its particulate deformable constituents. New features and phenomena are thus still being uncovered regularly. The most prominent of its constituents are the red blood cells, also called erythrocytes, contributing approximately 40% to the total blood volume.

As such, an intricate knowledge on the micro-scale behavior of red blood cells (RBCs) and other particles in flows is imperative for advancements in many scientific fields. On a more basic level, it is required to understand how specific biological processes and organs work. As an example, it has been suggested that the spleen removes old and pathological RBCs from the vascular system due to decreased deformability of the cells, since they can no longer pass through very small slits [1]. Closely tied to this are medical diagnosis and treatments. A good comprehension of how various diseases affect the properties of the cells helps to guide the development of new drugs and therapies. Similarly, research on the flow behavior of the drugs themselves or on drug agents can guide the design of e.g. new administration protocols and the material selection (compare chapter 6.2). Furthermore, a good understanding is required for developing new blood analysis methods, especially in the promising and rapidly growing field of lab-on-a-chip devices [2, 3]. These small chips of sizes in the milli- to centimeter regime are cheap to manufacture and contain microfluidic channels. They exploit various properties of the immersed objects to achieve for example sorting into healthy and pathological components [4, 5]. Moreover, from a more academic point of view, the description of blood is an interesting problem due to the complex fluid-structure coupling, leading to a multitude of phenomena such as margination (stiff particles move to the outside of a blood stream) or the Fåhræus-Lindqvist effect (apparent viscosity decreases in smaller tubes) [6, 7]. Insights gained from this research together with the developed methodologies can also be used to analyze other subjects. An example here is the industrially relevant topic of microcapsule and bubble suspensions (e.g. in the context of food products [8]).

Three different fundamental paths exist to approach the topic of micro-scale blood flow: Via experiments, analytical theories or numerical simulations. While experiments are able to examine very large systems (e.g. a large part of a vascular system) and theories can provide deeper insights for special limiting cases (e.g. close-to-spherical vesicles), simulations have easy access to many observables (e.g. precise particle positions) and are able to consider nonlinear behavior (e.g. large deformations) in completely controlled environments. In the end, a combination of all three

methodologies is required to arrive at a deep understanding of the topic. But as time is finite, the present work concentrates on one methodology, namely numerical simulations. Experimental insights are contributed by the existing literature and our collaborators.

1.2 Scope & aim

Physical scope Blood flow is a highly complex and extremely large field. Thus, it is beyond the scope of a single or even multiple theses to research and describe blood flow in its entirety. Rather, one needs to make a selection. In the present case, we consider two major physical problems. The first one is the shapes assumed by isolated red blood cells flowing in microchannels. Hence, it is a problem of a more fundamental level, contributing to our comprehension of blood in a bottom-up approach. The second considered problem has a specific application as background, namely the targeted drug delivery by means of ultrasound contrast agents (coated microbubbles). It considers the question how the peculiarities of oscillating bubbles and red blood cell interactions can be exploited to attain an efficient drug delivery protocol.

Methodical scope A plethora of numerical techniques exist that are capable of simulating blood flow on the scale of individual cells. We provide a short overview in chapter 5.1. For the present work, we are using the boundary integral method (BIM) in 3D. Three properties are especially important for our research projects mentioned above, making this specific approach preferable to other methods: It is very efficient for a small number of particles, it can naturally handle objects with inner viscosities that are different to the ambient fluid viscosity and it allows for an extension to volume-changing objects. Further discussion of its advantages and disadvantages can be found in chapter 5.1. The fully three-dimensional treatment is important as non-axisymmetric behavior can emerge even in axisymmetric systems [9 – 11].

However, using simulations for physical research implies proper choices, methods and understanding of several underlying layers: The results depend on the chosen models, their correct translation into formulas, the selection of appropriate algorithms, an efficient implementation and the validation of the implementation. See figure 1.1 for a graphical illustration. It turned out that reaching our ultimate goal (studying blood flow via simulations) required contributions to each of these layers as outlined below. After all, a part of research in physics is also to know and build the necessary tools. In experiments this would be the experimental techniques, while here it means the models, mathematics, algorithms and numerics.

Aim The aim of this thesis is, therefore, to walk the path from the lowest to the highest layer appearing in blood flow simulations. Along the path we point out the standard elements and present in more details the encountered problems as well as our contributions to their solution.

1.3 Contributions and outline

We start by summarizing the state-of-the-art physical models employed in the description of blood flow in chapter 2, because the choices made here affect all higher levels. The models that are analyzed in-depth in this thesis are the Stokes equation (modeling the hydrodynamics) and the Helfrich model (for the bending resistance of red blood cells). Our contribution to the

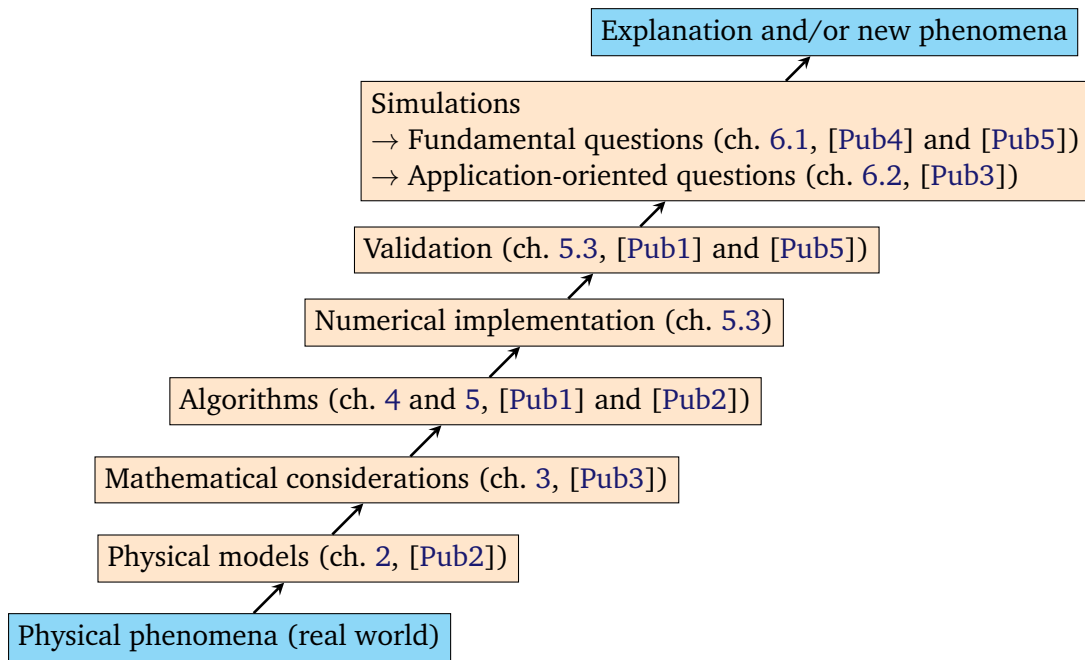


Fig. 1.1: The various layers when doing research via numerical simulations. The present thesis makes contributions to each one, located in the chapters listed within the diagram and further detailed in the dedicated publications.

model layer is a rigorous comparison between the common Canham-Helfrich bending model and so-called linear bending models [Pub2].¹

We then proceed in chapter 3 with presenting the mathematics of the hydrodynamic formulation, which is based on the Stokes equation. We extend the standard boundary integral equation to include volume-changing objects [Pub3]. The development of the extension was necessary in order to include oscillating and deformable microbubbles in blood flow. Existing simulation methods are not capable of handling red blood cells together with such bubbles.

On the algorithmic part, we shed for the first time light on the performance of various algorithms for the bending forces in chapter 4.3 ([Pub1] and [Pub2]¹). Bending forces are required here for the proper simulation of red blood cells, but are also very important for related fields of research (capsules, vesicles, etc.) and even unrelated ones (computer graphics etc.). An intermediate component (the mean curvature) is also necessary for the microbubbles.

Going one layer up to the actual implementation, the author wrote the base of the code for the boundary integral method already during his master thesis [12]. Creating a new code was necessary as no suitable and publicly available BIM code existed. During his doctorate, he implemented necessary extensions (such as for the bubbles) and several performance optimizations. He also implemented an MPI parallelization in the course of a KONWIHR research project, as outlined in chapter 5.2.

Continuing, the validation layer happened to some degree also during the author's master thesis. Nevertheless, our discussion on the bending algorithms in chapter 4.3.3 provides additional evidence for the correctness of the code [Pub1]. Most importantly, the research on the behavior of single RBCs and the comparison with new experiments by our collaborators (chapter 6.1) puts all layers to the test – successfully [Pub5].

¹Despite being a review to large extents, publication [Pub2] contains two novel contributions: First, the rigorous comparison between the linear bending models and the Canham-Helfrich model and second, the computation of the bending errors when using a spherical harmonics expansion.

Finally, we contribute to the highest layer and thus to the knowledge on blood flow by means of two studies. The first one is the just mentioned research, where we consider individual red blood cells flowing through a microchannel. Hence, it is important for the fundamental understanding of blood but also for certain applications. Our comparison between numerical and experimental measurements constitute the first of its kind with such details. We recover the two well-known common shapes assumed by the cells, croissants and slippers. Our most important finding is bistability and its systematic analysis, i.e. the coexistence of these shapes at the same set of parameters. It is presented in chapter 6.1 [Pub5]. The second study in chapter 6.2 [Pub3] considers lipid-coated microbubbles in blood flow. As such, it is more about a specific application rather than fundamental insights. We show that application of an ultrasound (causing the bubbles to oscillate) together with the special properties of the lipid coating and the interaction with the red blood cells causes the bubbles to migrate to the vessel wall (margination). Thus we can conclude that such bubbles constitute an efficient agent in targeted drug delivery protocols. The results also highlight that e.g. in-vitro experiments must take red blood cells into account in order to arrive at conclusions that can be translated to the in-vivo case.

Since the present thesis is in the format of a cumulative dissertation, the following chapters will serve as a guide along the path from the lowest to the highest layer, while providing context and summaries of our individual contributions. The full details can be found in the attached publications (part II).

2

Biology and models of blood flow

In order to capture the physical behavior of blood flow, the two most important components that need to be modeled are the red blood cells and the fluid inside and outside of the cells. The following sections will shortly outline the biology and the corresponding models.

2.1 Structure and modeling of red blood cells

Overview Red blood cells (erythrocytes) are created in the bone marrow and lack a nucleus, i.e. consist of only a membrane and an internal fluid (cytoplasm) [13]. The cytoplasm contains a high concentration of hemoglobin, a protein capable of binding oxygen molecules. It is therefore imperative for the cells in order to fulfill their main purpose, the delivery of oxygen from the lungs to the rest of the body. This inner fluid is Newtonian [14] and has a dynamic viscosity of $\mu_{\text{RBC}} = 5\text{--}15\text{ mPa s}$ for healthy human red blood cells at 37°C [13]. The precise value depends to a large extent on the hemoglobin concentration, with older cells exhibiting higher concentrations and, therefore, also higher viscosities [13].

The only structural part of the cell, its membrane, is formed by a lipid bilayer and an underlying cytoskeleton, both tethered together by several types of transmembrane proteins [13]. More precisely, the cytoskeleton consists of a complex and possibly dynamic [15] network of spectrin proteins which forms a triangular mesh when expanded [16]. This network is responsible for providing the membrane with its shear elasticity. The lipid bilayer, on the other hand, is composed of two layers of phospholipids and cholesterol. It endows the cell with some bending rigidity [17]. Furthermore, the area of the composite membrane stays nearly constant under deformations (at $\approx 140\ \mu\text{m}^2$ [18, 19]), i.e. it has a very high surface area dilatation modulus. This is to a large extent due to the lipid bilayer, while the cytoskeleton's dilatation resistance is notably smaller [17, 20]. Longer-lasting changes of the area above $\approx 4\%$ lead to cell rupturing [13, 21], while short lasting ($\approx 50\ \mu\text{s}$) changes of up to approximately 40% can be coped with [22].

Modeling the in-plane elasticity Since the membrane has a thickness of typically less than 100 nm [16] while the RBC in equilibrium has a typical diameter of $8\ \mu\text{m}$ [23], erythrocytes in flow simulations are usually modeled as inert objects having a homogeneous thin shell with zero thickness. Skalak et al. [24] introduced one of the most often used models for RBCs, the so-called Skalak model, which we will also employ in this thesis. It consists of a strain-hardening [25] component to model the shear elasticity with the corresponding shear modulus² $\kappa_S \approx 5 \times 10^{-6}\text{ N/m}$ [27, 28], and an area dilatation component with a modulus κ_A . As explained above, κ_A should be high enough to get an almost constant surface area, with appropriate values of around $\kappa_A = 10^3\kappa_S$ to $10^5\kappa_S$ [21, 24]. Such high moduli can impede a large performance penalty in numerical simulations, and hence smaller values are often chosen. Additional surface

²Note that different conventions exist for the definition of κ_S . Here we use the one by Krüger [26].

forces or constraints can be introduced to limit the surface deviations to large degrees [26, 29]. Naturally, the Skalak model is not the only possible choice [30, 31], with spring-network models having become another popular alternative [32–34].

Modeling the bending rigidity The bending rigidity of the RBC membrane is usually taken into account via the famous Helfrich (or Canham-Helfrich) model [35–37], which is prescribed in the form of a surface energy. A typical bending modulus is $\kappa_B \approx 3 \times 10^{-19}$ N m [28, 38]. The Helfrich model can be amended by an “area-difference elasticity” (ADE) term [21, 39], but it was apparently not used so far for RBCs in flow except in reference [40]. Bending forces are important to correctly capture equilibrium shapes when the shear stresses are nearly zero [21, 41] or to describe the wrinkles [42, 43] and shapes [11] that can appear during larger deformations. They can also improve the stability of numerical simulations [25]. Although the Helfrich model is used in a large part of the literature, a proper algorithm is still not established and different results are obtained in practice depending on the algorithm as we show in [Pub1].

Several publications [21, 42, 44–52] do not employ the Helfrich model but rather a so-called “linear bending model”. Different flavors exist. All of them have in common that the constitutive equation is not an energy, but rather the bending moments $M^{\alpha\beta}$ are prescribed directly. The reference state aside, this is either $M^{\alpha\beta} \sim H a^{\alpha\beta}$ or $M^{\alpha\beta} \sim b^{\alpha\beta}$ where $a^{\alpha\beta}$ is the metric tensor, $b^{\alpha\beta}$ the curvature tensor and H the mean curvature. Their relationship to the Helfrich model was so far not completely clear. Only Pozrikidis [46, p. 279] [48, ch. 2.8.2] made some rather cryptic statements, suggesting that some of them should be equivalent in the 2D case.

In publication [Pub2] we show mathematically that $M^{\alpha\beta} \sim H a^{\alpha\beta}$ and $M^{\alpha\beta} \sim b^{\alpha\beta}$ lead to the same traction jump (force per unit area) in 3D, but that this traction jump matches with the Helfrich result only to leading order, i.e. small deformations. Moreover, the higher orders lead to an additional qualitative difference in the tangential component of the traction jump: It is zero for the Helfrich model but non-zero for the linear bending models. Figure 2.1 exemplifies the traction jump as obtained from the Helfrich and the linear bending models for the biconcave discocyte shape, showing deviations of up to 35%. Linear bending models are only equivalent if they prescribe in-plane tensions correctly, something which is usually not the case.

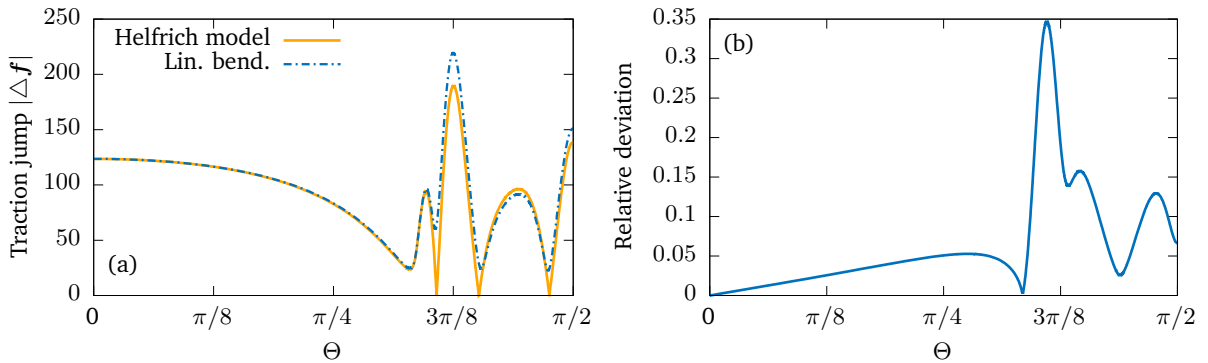


Fig. 2.1: (a) The traction jump $\Delta \mathbf{f}$ as obtained from the full Helfrich model in comparison with the linear bending models that neglect in-plane tensions for the discocyte shape (compare figure 2.2). Units measured in κ_B and the large radius of the discocyte. (b) Relative deviation between the data from (a). $\Theta := \arccos(x_3/\sqrt{x_1^2 + x_2^2 + x_3^2})$ is the polar angle as measured from the center of the discocyte. Reprinted from publication [Pub2] with permission from IOP Publishing.

Stress-free shape An open question in modeling the cell elasticity is that of the stress-free (or reference) shape. Due to the twofold nature of the RBC membrane, the question applies to both the lipid bilayer as well as the cytoskeleton. For the first, the reference shape is typically encoded in the Helfrich model via the so-called spontaneous (or reference) curvature c_0 (or H_0). The asymmetric distribution of the phospholipids between the two layers [13], which are themselves homogeneous on the μm -scale, indicates a non-zero value for c_0 that is spatially constant. Unfortunately, experimental values are non-existent so far. The most common choice is therefore $c_0 = 0$.

For the second constituent of the membrane, the cytoskeleton, a spatially inhomogeneous reference shape is required to explain results by Fischer [53]. He showed that the membrane is endowed with a “shape memory”: Membrane elements before a deformation and after equilibrating the deformed cell again are found at the same location. Two suggestions are currently discussed in the literature as possible candidates for the stress-free shape [41]: Either the discocyte equilibrium shape or an oblate spheroid that is nearly (but not completely) a sphere. So far the debate has not been settled, but more and more recent studies claim that the oblate shape is the correct one [54–61], although converse arguments also exist [62]. Analyses are made more complicated by the observation that both stress-free shapes result in distinct dynamics only for certain parameter ranges. If the ratio λ of the inner and outer viscosities is in the physiological range ($\lambda \approx 5$), the differences can be negligible [57]. In our studies in chapter 6 we use the discocyte reference state. We make a more in-depth comment on this issue in the outlook (chapter 7.2.1).

Further details The volume of the RBC is set by osmotic balance. Hence, it stays constant as long as the environment does not change [21, 63]. Simulations of cells in flow therefore assume a constant volume of around $\approx 100 \mu\text{m}^3$ [18, 19, 64]. Still, although the underlying equations already describe an impenetrable membrane, an artificial volume drift can occur in practice as a numerical artifact. It can be countered by introducing an additional ad-hoc volume force [26], exploiting the no-flux condition [29] or by a simple volume rescaling procedure [29].

In the absence of external forces, a healthy RBC equilibrates to a biconcave shape called discocyte with a diameter of approximately $8 \mu\text{m}$ and a thickness of $2.6 \mu\text{m}$ [23] as depicted in figure 2.2. A convenient mathematical formula to describe this geometry is given by Evans and Fung [23]. This shape is determined by the available excess area compared to a sphere with the same volume and the membrane forces [21]. In non-physiological environments [21, 54] or in case of diseases [65–67], other shapes such as stomatocytes or echinocytes are also possible. Application of external stresses (for example by placing the cells into a flow) leads to large reversible deformations as discussed in publication [Pub5] (chapter 6.1).

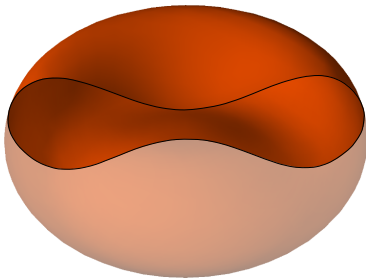


Fig. 2.2: The biconcave discocyte is the typical equilibrium shape of a healthy red blood cell. Half of it was made transparent for illustration purposes.

Red blood cells show additional features that were not mentioned so far and are not taken into account in the present work. The first one is membrane viscosity [7, 28, 38, 68–71], which is

often neglected in simulations [28] if the chosen method does not incorporate it as an intrinsic feature (such as in dissipative particle methods [33]). At least in some cases, the effect of membrane viscosity can also be modeled by a higher viscosity for the inner fluid [40, 60, 72]. Second, it was recently shown that the small fluctuations of the membrane cannot be explained only by the finite temperature of the environment, but rather that some part of it comes from active processes in the membrane [73]. The existence of fluctuations, active or passive, plays an important role in the determination of the elastic moduli [38]. For cells in flow they can, however, usually be neglected [28] except at very low flow rates where diffusion effects become important [11, 74] and near transition boundaries [75, 76]. As for the membrane viscosity, they are mostly (but not always [77, 78]) taken into account only if the method provides them naturally, although an actual comparison with and without fluctuations is missing so far. The third one is the ≈ 6 nm [79], i.e. very thin brush-like glycocalyx covering the membrane surface. Due to its thinness, it was not yet taken into account and is not expected to influence the dynamics of fast flowing cells, although it might play a role in the formation of rouleaux [80, 81].

We finally remark that the above given values are only *typical* values for *human healthy* red blood cells in *physiological* conditions. The values obtained from different experiments can scatter a lot (compare the overviews given in [19, 21, 26, 28]) and can also depend on the environment [21]. Pathological [3, 67, 82, 83], aged [13] and cells from other mammals [62, 84, 85] often have different properties.

2.2 Modeling blood flow on the micro-scale

The largest blood vessels in the human vascular system are the aorta, vena cava, arteries and veins with typical diameters in the $10^0 - 10^1$ mm range, the smallest the capillaries and venules that can become as small as $5 \mu\text{m}$ in diameter [3, 86, 87]. Depending on the target of the investigations, different methods are therefore appropriate. For vessels larger than $100 \mu\text{m}$ [88], continuum descriptions [89–91] of blood (that do not take into account the individual cells) can be appropriate. Including realistic, i.e. deformable RBCs at this level requires millions of cells and is therefore only possible with extreme efforts [34, 92–94]. On the other hand, an appropriate description of blood flow in microvessels must resolve the behavior of the individual cells. As system sizes are smaller, such systems are accessible with numerical simulations. Moreover, the Reynolds number in microvessels is often sufficiently small so that inertia effects can be neglected [6, 95]. In this thesis we concentrate on the description of systems in the $10 \mu\text{m}$ regime. This especially enables us to exploit the low Reynolds number to allow for a treatment of the problem with the boundary integral method (see chapter 3).

The volume percentage of red blood cells (hematocrit) is 45 % (male) and 40 % (female) in the largest vessels [87, 96]. In the microvascular system the hematocrit is notably reduced to below 20 % [97, 98]. Thus, simulations of blood flow in microvessels should not use the often cited value of 45 %. Other particulate constituents (white blood cells, platelets, von Willebrand factor, etc.) account for less than 1 % of the total blood volume [6, 18, 87]. They are therefore usually (but not always [99]) either neglected in biofluidic studies or – if not – they constitute the main target of the conducted research (e.g. regarding their margination behavior such as in references [100–105], [106–110] and [111], respectively). Appropriate modeling of the flow in capillary *networks* should take white blood cells into account as they can cause blockage of branches [112, 113].

The inner surface of the blood vessels is formed by endothelial cells and the glycocalyx (a brush-like covering) [114]. The effect of the glycocalyx on the dynamics of red blood cells

was barely considered so far [115–118] as the usual assumption is that its effects on the flow dynamics of RBCs can be described as an effective reduction of the vessel size [7, 119] (note, however, that this is not true for other constituents such as white blood cells [3, 6]). Instead, the vessel walls are typically modeled as stiff (no-slip condition) [120]. We also adapt this assumption in the present work.

The cells are flowing in blood plasma which consists of $\approx 90\%$ water, with the remaining volume containing several dissolved proteins and other substances [6, 87]. Of these constituents the protein fibrinogen has recently attracted increased attention in the biofluidics community, since it plays a primary role in RBC aggregation and clot formation [81, 86, 121–123]. For the purpose of describing blood flow under normal conditions (as is the case in the present work), blood plasma can be viewed as a Newtonian fluid with a dynamic viscosity of $\mu_{\text{Plasma}} \approx 1.2 \text{ mPa s}$ [7, 82, 124].

Of course, the goal of theoretical investigations is not necessarily to understand blood flow in vascular systems. Rather, other very important fields are in-vitro experiments and lab-on-a-chip devices [2, 3]. The latter are becoming more and more important as they promise effective and cheap analysis methods that currently require big and expensive machinery. In these cases, the red blood cells are facing completely different environments, e.g. with less or more obstacles (such as in deterministic lateral displacement devices [125–127]), different channel boundaries, higher velocities or other ambient viscosities. Simulation methods can usually handle these without major algorithmic changes by simply changing the input parameters appropriately.

2.3 Capsules and vesicles

The study of red blood cells and blood flow is closely related to the research of two other types of microparticles, namely capsules and vesicles [52]. One reason is that both share structural similarities with RBCs as they also consist of a thin membrane encapsulating some fluid. However, the composition of the membranes is quite different. On the one hand, capsules are made of polymers [52], leading to a constant volume but an extensible surface. Their dynamics is mostly governed by shear and area dilatation elasticity, although a small finite bending rigidity is also present that becomes important when the surface buckles [43]. Shear and area dilatation elasticity are often described with the Hookean or neo-Hookean constitutive models [25, 52]. Depending on the material, additional properties such as plasticity can be important [128].

Vesicles, on the other hand, consist of only a lipid bilayer [52]. They therefore exhibit bending rigidity (usually described by the Helfrich model), a very strong resistance against area dilatation and some surface viscosity, but no shear elasticity [129]. Their volume is conserved during reversible deformations.

From a mechanical point of view, red blood cells with their two-component structure can, therefore, be regarded as a combination of capsules and vesicles. Numerical codes that can simulate red blood cells thus also often support capsules and vesicles with no or only minor changes, although some numerical stability issues can arise for vesicles due to the missing shear elasticity. As an example, we consider a capsule in a linear shear flow in publication [Pub1] (section 4.3.3.2) with the same code that is used to describe RBCs.

Another reason for their frequent occurrence in blood flow related research is that especially vesicles are often used as model systems for red blood cells. Indeed, both share several qualitative similarities in their dynamic behavior [74, 130]. Moreover, in two-dimensional descriptions, shear elasticity is intrinsically absent and thus one is naturally restricted to vesicles.

3 Describing volume-changing objects via an extended boundary integral equation

The goal of this chapter is the mathematical description of the flow and the suspended objects. We introduce our core equation, a boundary integral equation, and especially its extension to support volume-changing objects such as oscillating microbubbles. The numerical discretization of the equation results in the boundary integral method, which we implement in code as described in chapter 5.

3.1 Introduction

We exploit the small Reynolds number in the microcirculation and base our studies on the Stokes equation, i.e. the Navier-Stokes equation at negligible Reynolds number [131]. Due to its linearity, the Stokes equation allows for a reformulation as boundary integral (BI) equations containing integrals over the surface of the suspended objects. Depending on the exact problem, different types of BI equations are obtained [131 – 133]. In this thesis we concentrate on a type that does not employ an auxiliary field and is appropriate for the description of deformable capsule-like objects such as capsules, vesicles, red blood cells or drops [134]. It will be extended below to also include deformable volume-changing objects such as bubbles.

The BI equations for the description of capsule-like objects in infinite and periodic domains has been extensively used in the past as the basis for numerical simulations, starting with Youngren and Acrivos [135] in 1975. However, a mathematical proof regarding existence and uniqueness of the solution is available only for the infinite [131, 132, 136, 137] but not for the periodic domain. Furthermore, volume-changing objects were barely considered so far [138 – 141], and especially lacked a formal proof. Such volume-changing objects are required e.g. for the study of oscillating microbubbles in chapter 6.2. We therefore first need to generalize the BI equation appropriately and prove its validity and consistency mathematically. This is done in the first part of publication [Pub3], with the basic ideas outlined below. It is important to note that the generalization and its proof also hold when no volume-changing objects are present, as employed in chapter 6.1 for the study of shapes assumed by RBCs flowing through microchannels. Such a proof was missing so far in periodic domains. Moreover, the proof holds not only for periodic but also for truly infinite domains by replacing the periodic Green’s functions with the appropriate free-space versions.

3.2 General system description

The very general system that we want to describe is illustrated in figure 3.1. As we employ periodic boundary conditions here, we define a unit cell $\Gamma \subset \mathbb{R}^3$ which, together with its content, is infinitely replicated in space. The Stokesian fluid outside of the immersed objects is denoted by $\Omega \subset \Gamma$ with a dynamic viscosity μ . An arbitrary number N_c of deformable capsule-like entities

\mathcal{C}_k can be suspended in Ω , each filled with a Stokesian fluid of viscosity $\mu\lambda_{\mathcal{C}_k}$, where $\lambda_{\mathcal{C}_k}$ is the viscosity ratio and k an index enumerating the particles. The volume flux $Q_{\mathcal{C}_k}$ out of or into the capsules is zero ($Q_{\mathcal{C}_k} = 0$), i.e. their volume is conserved. The actual particle type (RBC, vesicle, etc.) is defined by the constitutive models for the traction jump $\Delta \mathbf{f}$ (e.g. Helfrich model, Skalak law, etc.). Moreover, $N_{\mathcal{W}}$ open objects \mathcal{W}_k are possible. They can be either rigid or deformable. Finally, $N_{\mathcal{B}}$ volume-changing and deformable objects \mathcal{B}_k with volumes $V_{\mathcal{B}_k}$ are included that can model for example oscillating microbubbles. In contrast to capsules, we assume that their inside contains some compressible fluid with a very low viscosity that expands and contracts homogeneously, i.e.

$$\nabla \cdot \mathbf{u}(\mathbf{x}) = c_k, \quad \mathbf{x} \in \mathcal{B}_k. \quad (3.1)$$

The prescribed constant c_k can be related to the flux $Q_{\mathcal{B}_k}$ out of or into the object \mathcal{B}_k by $c_k = Q_{\mathcal{B}_k}/V_{\mathcal{B}_k}$ and is allowed to depend on time. However, the sum of all fluxes must be zero at all times to ensure conservation of the ambient fluid in Ω . $Q_{\mathcal{B}_k}$ together with a constitutive law for the traction jump (e.g. the Young-Laplace equation) determines the actual physical particle represented by \mathcal{B}_k .

To simplify the notation, we denote an arbitrary object by O_k , the total sets of objects by O and the total number of objects by N_O . Surfaces are represented by the symbol “ ∂ ”, such as in ∂O_k .

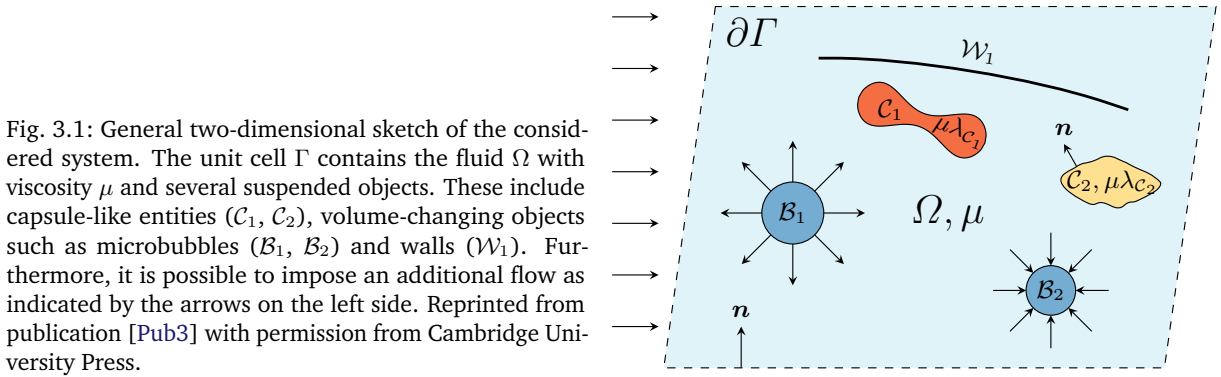


Fig. 3.1: General two-dimensional sketch of the considered system. The unit cell Γ contains the fluid Ω with viscosity μ and several suspended objects. These include capsule-like entities (\mathcal{C}_1 , \mathcal{C}_2), volume-changing objects such as microbubbles (\mathcal{B}_1 , \mathcal{B}_2) and walls (\mathcal{W}_1). Furthermore, it is possible to impose an additional flow as indicated by the arrows on the left side. Reprinted from publication [Pub3] with permission from Cambridge University Press.

3.3 The extended Fredholm boundary integral equation

The starting point of our development are two sets of equations. The first one is the ordinary Stokes equation:

$$-\nabla P(\mathbf{x}) + \mu \nabla^2 \mathbf{u}(\mathbf{x}) = 0, \quad \mathbf{x} \in \Omega. \quad (3.2)$$

Here, P is the pressure and \mathbf{u} the flow velocity. An identical equation holds for the inside of capsules except that the viscosity can be different. The Stokes equation is supplemented by the continuity equation. For the ambient fluid and the capsules, it is simply given by the incompressibility condition

$$\nabla \cdot \mathbf{u}(\mathbf{x}) = 0, \quad \mathbf{x} \in \Omega \cup \mathcal{C}. \quad (3.3)$$

The compressible fluid inside of volume-changing objects is assumed to have very low viscosity and thus the only model equation for this fluid is given by equation (3.1).

Using the reciprocal theorem for Stokes flow [131], one can then derive the boundary integral equation. This requires to integrate the reciprocal theorem over the volume Ω which, in periodic domains, is bounded by the surface $\partial\Gamma$ of the unit cell Γ . The key step is then to use the divergence theorem to convert the volume integral into integrals over the surfaces of all objects

and over $\partial\Gamma$. The integral over $\partial\Gamma$ can be simplified using equations (3.1) and (3.3) and, most importantly, gives a non-zero contribution. More precisely, the so-called double-layer integral $(\mathcal{K}_{\partial\Gamma}\mathbf{u})_j(\mathbf{x}_0) := \int_{\partial\Gamma} u_i(\mathbf{x})T_{ijl}(\mathbf{x}, \mathbf{x}_0)n_l(\mathbf{x}) dS(\mathbf{x})$ over $\partial\Gamma$ yields

$$(\mathcal{K}_{\partial\Gamma}\mathbf{u})_j(\mathbf{x}_0) = 8\pi \langle u_j \rangle_\Gamma + \frac{8\pi}{V_\Gamma} \sum_{k=1}^{N_B} Q_{\mathcal{B}_k} \chi_j^{(\mathcal{B}_k)}, \quad \mathbf{x}_0 \in \Omega, \quad j = 1, 2, 3. \quad (3.4)$$

Here, $\langle \mathbf{u} \rangle_\Gamma$ is the imposed average flow through the unit cell Γ with volume V_Γ , \mathbf{n} is the outer normal vector, T_{ijl} the periodic Green's function, $\chi^{(\mathcal{B}_k)}$ is the geometric centroid of \mathcal{B}_k and summation over repeated indices is implied. The last term containing the fluxes $Q_{\mathcal{B}_k}$ is the new one, being absent in the existing literature. Collecting all other integrals then leads to the boundary integral equation.

This equation allows one to compute a quantity (e.g. the velocity) everywhere *within* the fluid domain Ω as long as *all quantities on* the surfaces of the objects are known. Yet, one quantity on the surfaces is usually unknown. The standard procedure is now to move the evaluation point from the ambient domain onto the surfaces [131], thereby yielding a Fredholm boundary integral (FBI) equation. By solving the FBI equation, the unknown surface quantities are obtained (e.g. the velocities or the tractions). The fluid volume does not appear explicitly in this process, although the flow can still be computed in the whole domain as an optional post-processing step.

However, the solution of the Fredholm boundary integral equation is not unique. The physical interpretation is that the volume of the bubbles is not determined by the equation. This makes it necessary to add two additional terms to the equation in spirit of the so-called Wielandt deflation [133]. The final FBI equation forming the basis of our “volume-changing object boundary integral method” is then given by

$$\begin{aligned} u_j(\mathbf{x}_0) = & \frac{2}{1 + \lambda_{O_k}} \left[\langle u_j \rangle_\Gamma - \frac{1}{8\pi\mu} \sum_{q=1}^{N_O} (\mathcal{N}_{\partial O_q} \Delta \mathbf{f})_j(\mathbf{x}_0) \right. \\ & \left. + \frac{1}{8\pi} \sum_{q=1}^{N_O} (1 - \lambda_{O_q}) (\mathcal{K}_{\partial O_q} \mathbf{u})_j(\mathbf{x}_0) + \frac{1}{V_\Gamma} \sum_{q=1}^{N_B} Q_{\mathcal{B}_q} \chi_j^{(\mathcal{B}_q)} \right] \\ & - \frac{1 - \lambda_{O_k}}{1 + \lambda_{O_k}} z_j^{(k)}(\mathbf{x}_0) \left[\oint_{\partial O_k} u_l(\mathbf{x}) n_l(\mathbf{x}) dS(\mathbf{x}) - Q_{O_k} \right], \\ & \mathbf{x}_0 \in \partial O_k, \quad k = 1, \dots, N_O, \quad j = 1, 2, 3. \end{aligned} \quad (3.5)$$

As an example, given the imposed average flow $\langle \mathbf{u} \rangle_\Gamma$ through the unit cell Γ , the fluxes $Q_{\mathcal{B}_k}$ and the traction jumps $\Delta \mathbf{f}$ on all objects, this integral equation uniquely determines the velocity \mathbf{u} on the surface of all objects. The novel terms are the ones containing the fluxes $Q_{\mathcal{B}_q}$ and Q_{O_k} while the others are well known [42, 134]. Regarding the remaining symbols in equation (3.5), λ_{O_k} is simply the viscosity ratio λ_{C_k} in case of capsule-like objects, 1 in case of walls and 0 in case of volume-changing objects. Furthermore, we have $z^{(k)} := \mathbf{n}/S_{O_k}$ with the surface area S_{O_k} of object O_k . The single-layer integral over some surface ∂O_q is abbreviated as $(\mathcal{N}_S \Delta \mathbf{f})_j(\mathbf{x}_0) := \int_{\partial O_q} \Delta f_i(\mathbf{x}) G_{ij}(\mathbf{x}, \mathbf{x}_0) dS(\mathbf{x})$. For practical purposes, Green's functions G_{ij} and T_{ijl} need to be used that are adapted to the system, such as for an infinite [131] or periodic domain [42, 142]. The numerical procedure to solve equation (3.5) is outlined in chapter 5.

3.4 Sketch of the proof

That equation (3.5) has exactly one solution (existence and uniqueness) is non-trivial. Indeed, even if no volume-changing objects are present a proof is missing for the important case of periodic domains. Our approach as outlined below is based on the Fredholm theory [143]. A requirement is therefore that equation (3.5) is a Fredholm equation of the second kind. This implies that the traction jumps $\Delta \mathbf{f}$ need to be prescribed while the velocities \mathbf{u} are unknown, as is indeed the case in our applications (chapter 6).

To apply the theory, we first need to introduce the homogeneous equation corresponding to equation (3.5),

$$\begin{aligned}
 h_j(\mathbf{x}_0) = & \frac{1}{4\pi} \frac{1}{1 + \lambda_{O_k}} \sum_{q=1}^{N_O} (1 - \lambda_{O_q}) \oint_{\partial O_q} h_i(\mathbf{x}) T_{ijl}(\mathbf{x}, \mathbf{x}_0) n_l(\mathbf{x}) dS(\mathbf{x}) \\
 & - \frac{1 - \lambda_{O_k}}{1 + \lambda_{O_k}} z_j^{(k)}(\mathbf{x}_0) \oint_{\partial O_k} u_l(\mathbf{x}) n_l(\mathbf{x}) dS(\mathbf{x}), \\
 & \mathbf{x}_0 \in \partial O_k, \quad k = 1, \dots, N_O, \quad j = 1, 2, 3,
 \end{aligned} \tag{3.6}$$

as well as its adjoint,

$$\begin{aligned}
 a_j(\mathbf{x}_0) = & \frac{1 - \lambda_{O_k}}{4\pi} \sum_{q=1}^{N_O} \frac{1}{1 + \lambda_{O_q}} n_l(\mathbf{x}_0) \oint_{\partial O_q} a_i(\mathbf{x}) T_{jil}(\mathbf{x}_0, \mathbf{x}) dS(\mathbf{x}) \\
 & - \frac{1 - \lambda_{O_k}}{1 + \lambda_{O_k}} n_j(\mathbf{x}_0) \oint_{\partial O_k} z_l^{(k)}(\mathbf{x}) a_l(\mathbf{x}) dS(\mathbf{x}), \\
 & \mathbf{x}_0 \in \partial O_k, \quad k = 1, \dots, N_O, \quad j = 1, 2, 3,
 \end{aligned} \tag{3.7}$$

where \mathbf{h} and \mathbf{a} denote the respective solution fields. With this, the Fredholm alternative can be written as follows [143]:

Theorem 1 (Fredholm alternative)

1. The homogeneous and adjoint equations (3.6) and (3.7) have the same finite number of eigensolutions and complex conjugate eigenvalues.
2. If the homogeneous equation (3.6) has only the trivial solution $\mathbf{h} \equiv 0$, then the full equation (3.5) has exactly one solution (existence and uniqueness).
3. If the homogeneous equation (3.6) has a nontrivial solution, then the full equation (3.5) has solutions if and only if all eigensolutions \mathbf{a} of the adjoint equation (3.7) satisfy

$$\sum_{k=1}^{N_O} \oint_{\partial O_k} \mathbf{R}_j(\mathbf{x}) a_j(\mathbf{x}) dS(\mathbf{x}) = 0, \quad k = 1, \dots, N_O. \tag{3.8}$$

Here, \mathbf{R} contains all fully known terms (i.e. terms that are missing in the homogeneous equation).

The goal of the proof is thus to show that the adjoint equation has only the trivial solution, which automatically implies (due to the Fredholm alternative) that the homogeneous equation has also only the trivial solution and, ultimately, that there is exactly one solution to the full equation (3.5) (also due to the Fredholm alternative). The most difficult part is to show that the

adjoint has indeed only the trivial solution. We do this with a reductio ad absurdum argument. Hence, we assume that there exists a non-trivial solution ($\mathbf{a}(\mathbf{x}) \neq 0$) and show that this leads to a contradiction. More precisely, we show that *every* solution of the adjoint equation is of the form

$$\mathbf{a}(\mathbf{x}) \sim \mathbf{n}(\mathbf{x}). \quad (3.9)$$

The key to show this is to define an auxiliary field similar to Odqvist [136, §4] as

$$A_j(\mathbf{x}_0) := \sum_{q=1}^{N_O} \frac{1}{1 + \lambda_{O_q}} \oint_{\partial O_q} a_i(\mathbf{x}) G_{ij}(\mathbf{x}, \mathbf{x}_0) dS(\mathbf{x}), \quad \mathbf{x}_0 \in \mathbb{R}^3, \quad j = 1, 2, 3, \quad (3.10)$$

which turns out to be equivalent to a simple constant ($\mathbf{A} = \text{const}$) and which in turn implies $\mathbf{a}(\mathbf{x}) \sim \mathbf{n}(\mathbf{x})$. Finally, although every solution of the adjoint equation must be of the form (3.9), this form is actually no solution to the adjoint equation (3.7) except for $\mathbf{a}(\mathbf{x}) \equiv 0$. Hence, we arrive at the conclusion that the adjoint equation has only the trivial solution. This thereby completes the proof. The full details can be found in publication [Pub3].

4

Algorithms for the surface forces

Having shortly presented the models and basic hydrodynamic equations in the previous chapters, one needs to translate them into formulas and algorithms that can be implemented in code. After a short outline of the employed surface discretization and the computation of the in-plane elastic forces, we concentrate on an in-depth evaluation of algorithms for the Helfrich bending forces. The topics presented here are independent of the hydrodynamic solver which require the forces only as input. See chapter 5 for the algorithmic treatment of the boundary integral equation.

4.1 Surface discretization

In this work, the surfaces of suspended objects are represented by a set of points called nodes. This is common to many methodologies that assume infinitely thin surfaces (contrary to e.g. level-set [144–147] or phase-field [148, 149] methods). However, there exists a multitude of possibilities to interpolate the surface and quantities between the nodes which are all actively used in the biofluidic context, such as flat triangles (linear interpolation, e.g. [29, 131, 150–154]), curved triangles (quadratic interpolation) [46, 50, 131, 155, 156] or subdivision surface methods (quartic interpolation) [157–165], each with their own advantages and disadvantages. We present a short overview in publication [Pub2]. For simplicity, efficiency and flexibility we employ flat triangles in our studies. The other methods, for example, do not allow for straightforward *local* refinement as we use in [Pub3]. See figure 4.1 for an example of a mesh.

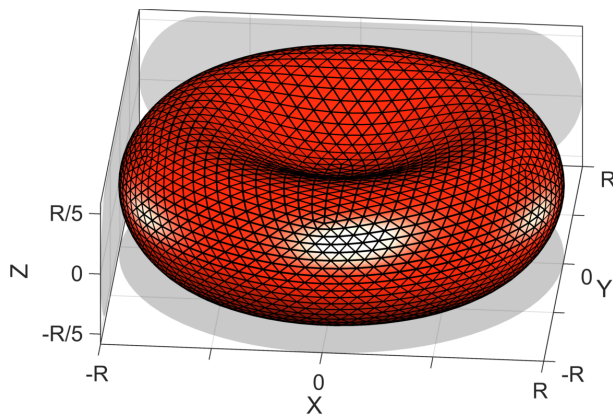


Fig. 4.1: Discretization of the discocyte shape with 5120 flat triangles. Reprinted from publication [Pub1] with permission from Elsevier.

4.2 In-plane elasticity

In case of capsule-like objects we prescribe certain models in order to determine the traction jump $\Delta \mathbf{f}$ (force per unit area) on their surface from the instantaneous deformation. $\Delta \mathbf{f}$ is required as input for the Fredholm boundary integral equation (3.5). In order to model the in-plane

elasticity of red blood cells and capsules, we typically employ the Skalak and neo-Hookean models, respectively, as outlined in chapter 2. They are specified in the form of a surface energy E_S . After discretization, E_S depends explicitly on the nodes $\mathbf{x}^{(i)}$. Hence, using the principal of virtual work, the force can then be computed via [73, 166–168]

$$\mathcal{F}(\mathbf{x}^{(i)}) = -\frac{\partial E_S}{\partial \mathbf{x}^{(i)}}, \quad i = 1, \dots, N, \quad (4.1)$$

where i enumerates all N nodes. It is often straightforward to compute the derivative analytically (compare [26]), making numerical differentiation obsolete. Note that \mathcal{F} has the dimension of a force (i.e. is measured in Newton), not of a force per unit area. Computation of the traction jump is then done via

$$\Delta \mathbf{f}(\mathbf{x}^{(i)}) = -\mathcal{F}(\mathbf{x}^{(i)})/A_i, \quad (4.2)$$

where A_i is the area “occupied” by the node. The most accurate choice for A_i is the “mixed area” introduced by Meyer et al. [169].

4.3 Helfrich bending forces

RBCs include some bending rigidity in addition to the in-plane elasticity, while vesicles are almost exclusively dominated by the bending forces. These forces are usually modeled according to the Canham-Helfrich model. Despite being the most common law used for this purpose, there is a striking vagueness in the literature about its numerical implementation, more specifically regarding the possible algorithms and their performance. This is all the more significant as most fluid-structure codes require the input of the bending component in the form of forces or forces per unit area similar to BIM, i.e. it is not a problem just tied to our method. Hence, we consider in details old and new algorithms for the bending forces in publications [Pub1] and [Pub2]. These will be outlined in the present section. Microbubbles use the Young-Laplace equation and thus require the mean curvature, which is also a component of the Canham-Helfrich model and is therefore automatically covered, too.

4.3.1 The model and the forces

The Canham-Helfrich model [35, 36] is given in terms of a total energy stored in a surface S as

$$E_B = \int_S 2\kappa_B (H - H_0)^2 dS + \int_S \kappa_K K dS. \quad (4.3)$$

Here, κ_B is the bending modulus, H the mean curvature, H_0 the reference (or spontaneous) curvature, K the Gaussian curvature and κ_K the Gaussian modulus. One possible way to express H is given by [170]

$$H(\mathbf{x}) = \frac{1}{2} \sum_{i=1}^3 (\Delta_S x_i) n_i(\mathbf{x}), \quad \mathbf{x} \in S, \quad (4.4)$$

where Δ_S is the Laplace-Beltrami operator [171] and \mathbf{n} the outer normalized normal vector. We employ the convention that H is positive for a sphere. The second integral in equation (4.3) is a simple constant as long as one considers a closed surface with constant topology [171], implying that it is irrelevant for the purpose of force computations and will be ignored in the following.

From equation (4.3) one can derive analytically the traction jump $\Delta \mathbf{f}$ (force per unit area

exerted by the fluid on the membrane) as

$$\Delta \mathbf{f}(\mathbf{x}) = -2\kappa_B [\Delta_S(H - H_0) + 2(H - H_0)(H^2 - K + H_0H)] \mathbf{n}, \quad (4.5)$$

constituting the Euler-Lagrange equation. There are two ways to derive it: Either via a variational derivative (e.g. [44, 171 – 173]) or by using the Kirchhoff-Love thin shell theory [174 – 177]. The latter calculation can also be found in details in publication [Pub2] where it was necessary for the comparison with the linear bending models (also compare section 2.1).

The major problem in designing algorithms for the implementation of equation (4.5) stems from the observation that a fourth order derivative is required: Two derivatives for the mean curvature H and another two derivatives for the Laplace-Beltrami operator $\Delta_S H$. A multitude of possible algorithms exist and are being used in the literature, but a systematic comparison was lacking so far. Hence, a well-informed implementation therefore required to perform exactly such a comparison, which was published in [Pub1] and [Pub2] and shall be shortly summarized next with the focus on flat triangles. For simplicity, we set $H_0 = 0$.

4.3.2 Algorithms for the bending forces

4.3.2.1 Force formulation

The numerical computation of the force is possible via three different paths. The first one is the application of the principle of virtual work as for the in-plane elasticity in section 4.2, except that E_S is now replaced with E_B . Because the nodal derivative in equation (4.1) yields a force rather than a force per unit area, we termed this method the “force formulation” in publication [Pub1]. Algorithms using this approach differ in the way they discretize the bending energy E_B .

One possibility is to exploit the Gauss-Bonnet theorem, leading to $E_B \sim \sum_{\langle i,j \rangle} (1 - \cos \theta_{ij})$, where the sum goes over each edge $\langle i, j \rangle$ once and θ_{ij} is the angle between the normal vectors of the two adjacent triangles. This is a very popular [11, 26, 32, 33, 56, 73, 103, 109, 110, 119, 127, 168, 178 – 192] approach and we named it Method A in [Pub1].³ Another method (Method B) uses a particular discretization (“cotangent scheme”) of the Laplace-Beltrami operator to compute H as described in reference [179] that is suitable for flat triangles.

In both cases the formula for \mathcal{F} can be derived analytically, making a numerical differentiation in equation (4.1) unnecessary. The formulas for Method A are given in detail in reference [26], while the ones for Method B are derived in publication [Pub1].

4.3.2.2 Strong formulation

The “strong formulation” uses the Euler-Lagrange equation (4.5) and discretizes all occurring quantities directly. In [Pub1] we called it the “variational formulation” which, in hindsight, can be misleading as this term is usually used synonymous with the “weak formulation” also introduced below.

The first method considered by us here, Method C, employs an almost identical discretization of the Laplace-Beltrami operator Δ_S [169] as Method B. Using this discretization, Method C computes first the mean curvature H at each node via equation (4.4) and in a second step the remaining quantities appearing in equation (4.5). This algorithm (or close variants of it) are often used in the biofluidic literature (e.g. [150, 151, 153, 193 – 198]). Yet another algorithm,

³The names of the methods were introduced by us to have a simple way of distinguishing the various algorithms. They are otherwise not common in the literature.

Method D, is similar to Method C but uses a new discretization of Δ_S that stems from the kernel of the heat equation [199]. So far it was not used in the biofluidic context. Method E uses least square fitting of parabolas onto the surface and appearing quantities in order to evaluate equation (4.5) [29].

Method SH is set apart from all other methods described here as it uses a spherical harmonics (SH) expansion rather than triangular elements to represent the surface and compute quantities on it. It is only used in the comparison with the analytical results for the traction jump but not for the capsule in a linear shear flow (which are the two test cases below). Method SH was implemented as an extension to the comparisons in [Pub1] and was considered only in [Pub2].

4.3.2.3 Weak formulation

The third big class is the weak formulation. In this approach, equation (4.5) is multiplied with an arbitrary trial function δx . The result is then integrated and the Laplace-Beltrami operator is moved from H to δx via two integrations by parts. Hence, the maximal total derivative appearing is of second order. The integral equation can then be discretized, leading to a linear system that can be solved numerically for the traction jump.

Method S in publication [Pub1] uses this approach together with Loop's subdivision scheme [200–202]. Our code does so far not yet include this algorithm. Rather, the results were contributed by our collaborators Paul G. Chen and Marc Leonetti [159, 165, 203].

4.3.3 Evaluation of the bending algorithms

Publications [Pub1] and [Pub2] present two different ways of evaluating the quality of the various methods: By comparing the various components (such as mean curvature or traction jump) to analytical results for a particular shape, and by considering the dynamics of a capsule in a linear shear flow. The first sheds light on their performance in a general context, while the second elucidates the differences in viscous flow applications where “a few” higher errors are found to be of minor influence.

4.3.3.1 Comparison with analytical results

Preliminaries All quantities appearing in equation (4.5) can be computed analytically for a fixed shape. We choose the typical discocyte shape as depicted in figure 4.1 (page 19) because it exhibits high curvatures on the rim and a change of the sign in the curvature near its center. Mathematically, the shape is given by

$$z = \pm \frac{R}{2} \sqrt{1 - \rho^2} (C_0 + C_1 \rho^2 + C_2 \rho^4), \quad (4.6)$$

where $\rho := \frac{1}{R} \sqrt{x^2 + y^2}$, $C_0 = 0.2072$, $C_1 = 2.0026$ and $C_2 = -1.1228$ [23, 158]. The large radius R is set to 1 here. We derive the analytical formulas by using Mathematica. Furthermore, we translate eq. (4.6) into a mesh by starting with an icosahedron or octahedron and refining it by placing new nodes on the center of the triangles' edges. Afterwards, the mesh is transformed to the discocyte by applying the mapping from equation (4.6).

The most important quantity for our simulations is the traction jump Δf . Hence, we will shortly present the corresponding results here. More details, also regarding the individual quantities in equation (4.5) can be found in [Pub1] and [Pub2]. Furthermore, as our hydrodynamic code

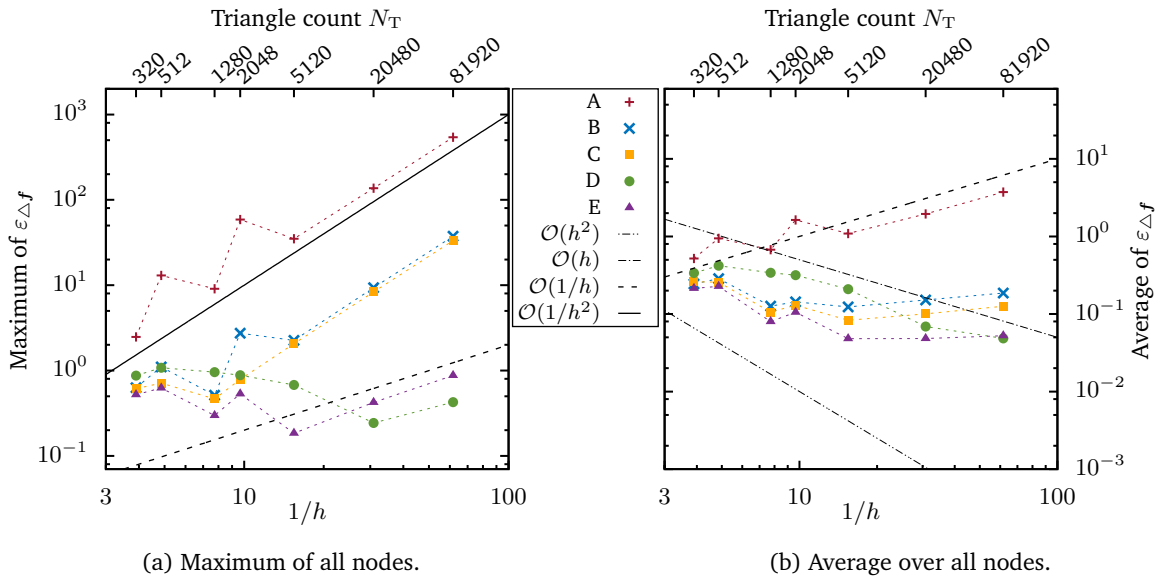


Fig. 4.2: Maximum and average relative errors of the bending traction jump Δf for the discocyte shape. Reprinted from publication [Pub1] with permission from Elsevier.

cannot employ the spherical harmonics approach (Method SH), we omit it here and refer the reader to the full publications.

Results for the traction jump The traction jump errors as produced by Methods A–E are depicted in figure 4.2. The left figure depicts the relative error ε in terms of the *maximum* taken over all nodes, while the right displays the *average* over all nodes. We show the behavior as a function of the resolution, expressed both in terms of the number of triangles (top axis) and inverse of the mean edge length h (bottom axis).

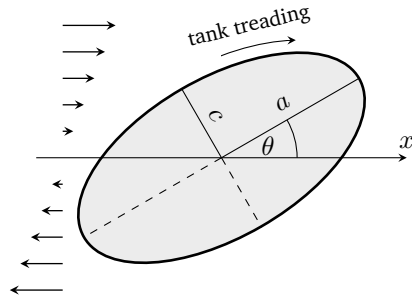
Regarding the maximal errors, all algorithms show diverging behavior except Method D which nevertheless fails to converge appropriately. For the average error, the picture looks not that devastating: Method A still clearly diverges, but Methods B, C and E do not diverge (although they retain a systematic error) and Method D appears to converge as $\mathcal{O}(h)$. Results for Method S are shown for a slightly different mesh in publication [Pub1]. It exhibits similar qualitative behavior as Method C, but at somewhat lower errors.

Obviously, these results with standard algorithms do not look very promising. Unfortunately, developing new algorithms for triangular meshes with higher accuracy at small to mediocre resolutions is an extremely difficult or even impossible task [204]: A few nodes are not sufficient to accurately represent the surface here, implying that more nodes (i.e. a larger support) need to be used. This, however, in turn is undesired as the Laplace-Beltrami operator should be only influenced by the nearest neighborhood. But for lower resolutions the nodes lie far apart from each other and hence parts of the geometry make contributions that represent completely different parts of the object.

4.3.3.2 A capsule in a linear shear flow

Preliminaries It has previously been reported that errors in the force computations at “some” nodes do not necessarily preclude accurate results for objects suspended in viscous flows [29]. Indeed, most of the algorithms introduced above are actively used by many research groups and

Fig. 4.3: Sketch of the ellipsoidal shape assumed by a capsule placed in a linear shear flow. a is the largest and c the smallest half axis, while θ is the inclination angle. The rotation of the membrane around the object’s centroid while the shape remains static is called “tank-treading”. Reprinted from publication [Pub1] with permission from Elsevier.



the many papers dealing with biofluidic questions show that they can indeed lead to correct physical results. Therefore, we will now consider their performance for a capsule in a linear shear flow. Due to its relative simplicity and long history, this system has often been employed for the validation of numerical methods by means of comparison with older publications.

The basic setup consists of an initially spherical capsule (also compare chapter 2.3) of radius R that is put into a linear shear flow with shear rate $\dot{\gamma}$ of infinite extent. The membrane not only includes resistance against bending but also some shear elasticity modeled by the neo-Hookean law with the shear modulus denoted by κ_S [25, 52]. The viscosity μ of the inner and outer fluids is identical. We solve the system by means of the boundary integral method (section 5), i.e. we assume small Reynolds numbers. Two dimensionless parameters define the behavior of the system [205]: The dimensionless shear rate (or capillary number) $G := \frac{\mu \dot{\gamma} R}{\kappa_S}$, and the dimensionless bending modulus $\hat{\kappa}_B := \frac{\kappa_B}{R^2 \kappa_S}$. After switching on the shear flow, the capsule deforms and becomes approximately ellipsoidal. Its deviation to a sphere can be described via the Taylor deformation parameter $D := \frac{a-c}{a+c}$, where a and c are the large and small half axes of the ellipsoid as depicted in figure 4.3.

Results We first note that without any bending forces ($\hat{\kappa}_B = 0$) the results produced with our BIM code agree very well with data from a multitude of references (e.g. [25, 46, 50, 51, 157, 160, 187, 195, 205]), i.e. our hydrodynamic code works as expected. The behavior of the capsule with added bending forces ($\kappa_B \neq 0$) is shown in figure 4.4. We see that the results of all bending algorithms nearly coincide with the exception of Method A. Hence, the extreme errors found for Method A in the analytical comparison really translate into different hydrodynamic behavior.

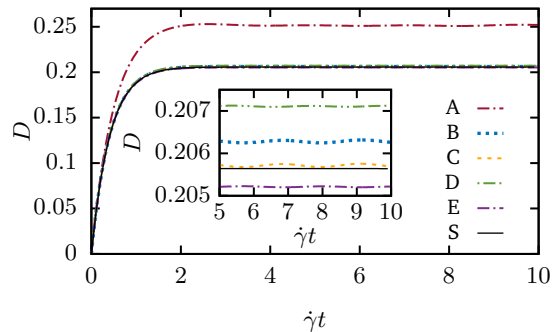


Fig. 4.4: Taylor deformation parameter as obtained via the various bending algorithms for $G = 0.2$ and $\hat{\kappa}_B = 0.15$. The inset shows a magnification of the steady state. Reprinted from publication [Pub1] with permission from Elsevier.

When comparing with results from the literature, however, a different picture emerges (see figure 4.5). Only a single reference [187] agrees with our deformation graphs (figure 4.5b) while all others show notable deviations (figure 4.5a). One possible source for some of the deviations might be the usage of slightly different constitutive equations. Pozrikidis [46] uses the Hookean

rather than the neo-Hookean model for the in-plane tension. Both lead to the same results only in the small deformation limit (which might not be valid here). Furthermore, Pozrikidis [46], Le et al. [50] and Zhu et al. [51] do not employ the Helfrich model but rather a linear bending model. As explained in section 2.1, both agree to leading order only, i.e. behave somewhat (but not entirely) different for larger deformations. Huang et al. [160] uses a model introduced by Zarda et al. [206] for which Pozrikidis [46] remarks that it is a generalization of a linear bending model. Nevertheless, one can clearly see that even if the physical models are perfectly the same, the various codes still produce different results (Method B–E/S vs. Le 2010; Le 2009 vs. Zhu 2015). A possible reason might be the different discretization schemes. This highlights the problematic nature of accurately computing the bending forces.

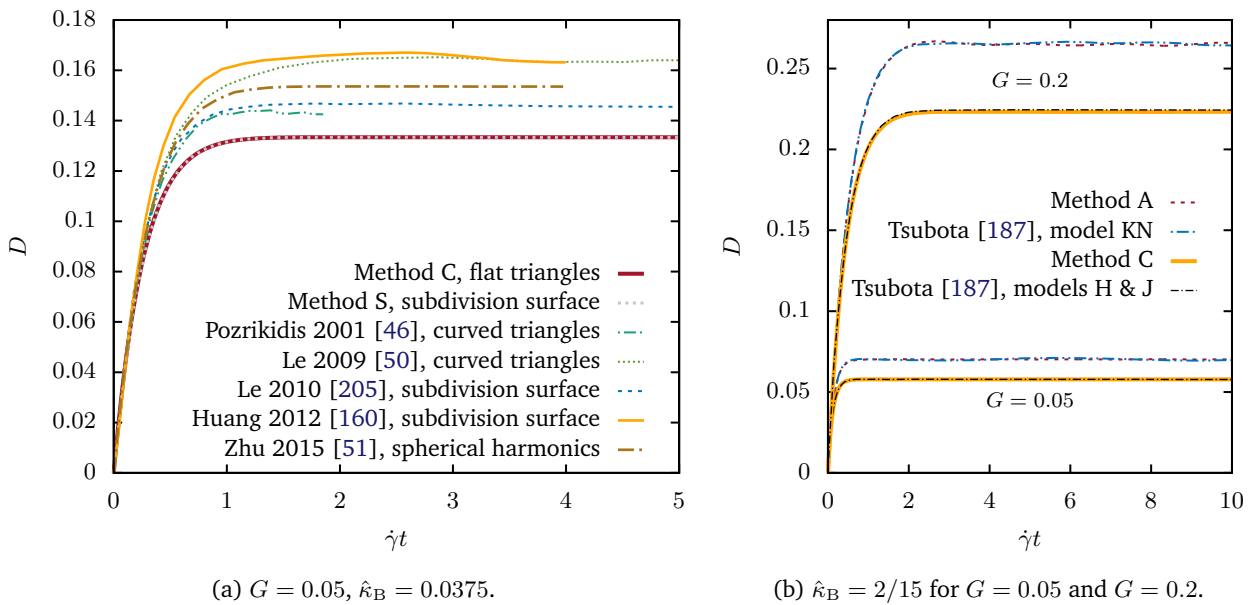


Fig. 4.5: Taylor deformation parameter computed via BIM in comparison to data from the literature. The result by our code is represented by Method A and C (the latter matches with B, D and E, compare figure 4.4). Reprinted from publication [Pub1] with permission from Elsevier.

4.3.3.3 Conclusion

In the end, the most practical and flexible algorithms for flat triangles appear to be Methods E and C. The first exhibits smaller errors while the latter was found to be more stable in dynamic simulations (which is the reason why we use it in our research projects in chapter 6). Compared to Method C, Method B gives slight worse results. Method D appears to be the most robust algorithm (i.e. it is only little affected by the homogeneity of the mesh) and has the best convergence properties, but unfortunately it reaches error levels comparable to the other methods only at very high and thus unpractical resolutions. Method A should not be used to represent the Helfrich model. Still, it might be sensible for stabilization purposes [207]. If the rest of the code (such as the computation of the boundary integrals) employ subdivision surface techniques, Method S can be used without much additional overhead. Hence, different algorithms work better in some contexts while others are preferable in other situations.

5 The boundary integral method: Algorithmic and numerical treatment of the boundary integral equation

5.1 Putting the boundary integral method into perspective

Other methods Boundary integral methods (BIM) are one of the oldest and most popular methods to study the dynamics of suspended objects in viscous flows [28, 42, 131, 134], starting with an article by Youngren and Acrivos [135] in 1975. But of course, it is not the only one. In recent years, the Lattice-Boltzmann [208–210] in conjunction with the immersed boundary method [26, 34, 77, 78, 167, 211–213] has also become an often used method owing to the comparably simple implementation, incorporation of inertia and the capability of straightforward large-scale parallelization. Alternative mesoscale approaches such as multiparticle collision dynamics [214–219] (also called stochastic rotation dynamics) and (smoothed [11, 61, 220–222]) dissipative particle dynamics [33, 94, 182, 185, 223–226] are also often and actively used in the biofluidic community. Other methods include the finite volume method [61, 99, 227–229], the immersed finite element method [230, 231], the moving particle semi-implicit method [232] and volume of fluid [233]. Also see recent reviews [28, 65, 234, 235].

Advantages of BIM Compared to other algorithms, the boundary integral method has various advantages and disadvantages. One of the most important general advantages is the fact that only the surfaces of the objects occur in the method. This means that the resolution of the surfaces is not tied to anything (such as a fluid grid), allowing for almost arbitrary geometries and straightforward global and local refinement, even during the course of a running simulation as used in publication [Pub3]. Indeed, also different discretization methodologies such as spherical harmonics are easily possible [42]. In the time domain, BIM exhibits similar freedoms, i.e. adaptive time integration schemes can be used straightforwardly.

Furthermore, an (intrinsic⁴) interpolation from the mesh to some grid is absent. As a consequence, the narrow space between close objects does not need to be resolved explicitly [28]. Moreover, truly infinite domains (along one, two or all three dimensions [142, 236–239] together with walls in the first two cases [240–248]) are possible. Infinite domains can be regarded as an extreme case where the fluid to particle volume ratio is zero. If it is only small (e.g. in low concentration suspensions), BIM can still have a significant performance and memory advantage over other methods (as the fluid domain is not explicitly resolved).

The boundary integral method also supports different viscosities at the inside and outside of objects without the need to keep track of internal points, which is different to e.g. Lattice-Boltzmann [212, 249]. No intrinsic non-physical parameters occur by default, and the parameters often correspond directly to the ones measured in experiments. Hence, some sort of fitting or

⁴The smooth particle mesh Ewald method (section 5.2) introduces a grid in the whole domain and a corresponding interpolation. However, this is a mere numerical trick to speed up the computation of long-range interactions rather than an intrinsic property of the method.

other conversion is not required in contrast to e.g. dissipative particle dynamics with spring-network models [33]. Finally, volume-changing objects (chapter 3) and truly solid objects (“completed double-layer boundary integral method” [132, 133, 168, 196, 197, 250]) can be supported by including additional terms.

Disadvantages of BIM On the downside, an absolutely fundamental restriction of BIM is its limitation to small Reynolds numbers as it is based on the Stokes equation, meaning that any fluid inertia is necessarily absent. Furthermore, thermal fluctuations are not an intrinsic ingredient and a method to incorporate them has been only recently presented [251].

Moreover, inclusion of channel boundaries can be a bit tricky: First, direct inclusion of the walls as mesh in periodic domains leads to some flow outside of the actual channel (as the channel is embedded in the unit cell) and consequently to a (slightly) varying mean flow within the channel. In our applications in chapter 6, however, we found that this is no issue. Second, for the direct method either the velocity or the traction jump can be prescribed on the wall surface. Stipulating the velocity leads to a proper no-slip condition but an ill-conditioned Fredholm equation of the first kind, while prescribing the traction jump implies a somewhat deformable wall but good natured numerical characteristics. We usually use the latter possibility. The alternative would be to include the walls directly in the Green’s functions via explicit but complicated expressions [240–248] or the “General Geometry Ewald like method” [195, 252–259].

In general, implementing boundary integral methods can be quite complicated which is at least in part due to the singular behavior of the Green’s functions, making special singularity removal procedures necessary [28, 29, 134, 260, 261]. This also applies to near-singular cases such as objects coming close to each other (which puts the above stated advantage of not having to resolve the fluid between objects somewhat into perspective).

Another undesirable property is the global aspect of the equations: Everything interacts with everything instantaneously. To prevent a quadratic scaling with the system size, advanced approaches such as the smooth particle mesh Ewald (SPME) [262] or the fast multipole method [92, 263–266] must be used. The latter can also fix the troublesome parallelization property of SPME (compare section 5.3).

5.2 Algorithms

Chapter 3 presented our boundary integral equation which forms the foundation of our simulation method. However, it is not directly amenable to an implementation. Rather we first need to apply appropriate algorithms, e.g. to discretize the integrals. These algorithms are known in the literature, and hence we only summarize here our choices concisely.

The first step is the discretization of the surfaces of the objects. We use flat triangles as we did for the computation of the surface forces (chapter 4.1). Using the same discrete elements for both the force calculation and the integrals suggests itself, but is not compulsory. The Fredholm boundary integral (FBI) equation requires the tractions or traction jumps as input, which we compute from the current geometry as explained in chapters 4.2 and 4.3. Afterwards, the integrals appearing in the FBI equation (3.5) are discretized using a standard Gaussian quadrature [267]. As is the nature of flat triangles, quantities within the elements are obtained by linear interpolation of the nodal values [131]. Special care is required at singular points, i.e. where the Green’s functions diverge. For the single-layer integral, we switch to polar coordinates to lift the singularity [268], while an analytic identity is used to subtract out the singularity in the double-layer integral [134]. The latter is also used to mitigate *nearly* singular behavior for

the double-layer which is necessary if objects come close to each other [269]. Moreover, a direct computation of the periodic Green's functions is impractically slow. Hence we use the Ewald decomposition as presented by Hasimoto [270] together with the smooth particle mesh Ewald method [262] to increase the performance considerably.

After discretizing the FBI equation, it turns into a dense and asymmetric linear system that we solve with GMRES [271] for the unknown quantity. As a consequence, the surface velocity \mathbf{u} is known on all surfaces and we can move the individual nodes \mathbf{x} in time according to the kinematic condition $\frac{d\mathbf{x}(t)}{dt} = \mathbf{u}(\mathbf{x}(t), t)$. This ODE is solved by a standard explicit ODE solver, for example Bogacki-Shampine [272] or Cash-Karp [273]. Artificial volume drifts due to the finite resolution of the discretization are countered by exploiting the no-flux condition as well as by rescaling the volume, similar to reference [29]. Moreover, additional stabilization schemes can be employed to keep the mesh of bubbles and vesicles from becoming inhomogeneous [29, 151, 269, 274], and the resolution can be increased locally via Rivara's longest-edge bisection algorithm [275].

5.3 Implementation, optimization, parallelization and validation

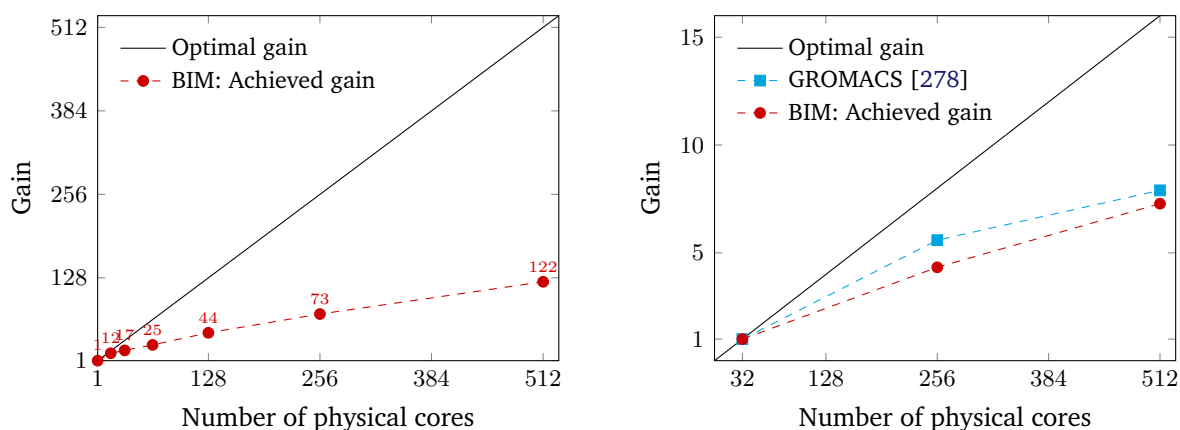
The basic code of the boundary integral method in infinite and periodic domains using most of the above algorithms and with OpenMP parallelization was written in C++ by the present author during his Master thesis. For the intricate details we therefore refer the reader to reference [12]. New developments made during his doctoral studies (such as the volume-changing objects in periodic domains or additional time integration algorithms) could be implemented in the existing code straightforwardly.

During his doctoral project, the author spent two months at the Leibniz-Rechenzentrum in Garching (Germany) in the framework of a KONWIHR project [276, 277]. The goal was to optimize the node-level performance (especially the OpenMP parallelization) and to parallelize the SPME code with MPI, allowing it to employ more than a single computing node. The implementation was successfully completed and is operational, but unfortunately the efficiency is hampered by the scaling behavior of the fast Fourier transform to several nodes (as implemented in `fftw` and Intel MKL). For example, a setup similar to the ones from publication [Pub3] but with approximately 10 times more RBCs showed a speed-up of 122 compared to a single core when using 512 cores (see figure 5.1a). Hence, the efficiency is only around 1/4. Note that going to significantly larger system sizes can improve the scaling behavior. Other software based on Fast Fourier transforms (FFTs) such as GROMACS also depicts similar behavior, as shown in figure 5.1b [278]. This is an intrinsic limitation of the FFT part of the algorithm. Efficient large-scale parallelization of long-range interactions could be achieved in the future by implementing the fast multipole method [92, 263–266], which however is a rather delicate task (which might be mitigated by suitable libraries [279, 280]). Furthermore, compared to SPME it comes with a higher constant in the complexity estimate [281] meaning that it will be faster only for very large systems.

After completing the KONWIHR project, the code was further optimized for node-level performance by several means. Most importantly, SIMD vectorization was implemented via the `Vc` library [282] in the core routines of the code. This resulted in performance gains of up to a factor of 2 on CPUs supporting the AVX extensions.

All in all, the size of the code base grew by a factor of approximately 1.6 during the author's doctorate when compared to the version at the end of his Master thesis. The total number of lines accumulates to almost 100 000 now.⁵

⁵Counting comments, blank lines and lines with code.



(a) Scaling behavior when the baseline (i.e. reference) is a single core. With 512 physical cores (1024 virtual cores, 32 nodes), a speedup of 122 is observed. The numbers above the data points indicate the gain.

(b) Scaling behavior when the baseline is 32 physical cores (2 nodes). Comparison with data for GROMACS 5 from reference [278, fig. 6] (32 physical Intel Haswell cores per node). The number of vertices in BIM was 107 279, the number of atoms in GROMACS was 142 000. I.e. the size of both systems is of the same order of magnitude.

Fig. 5.1: Scaling of our hybrid MPI-OpenMP boundary integral method code. The scaling is shown in terms of the number of physical cores, which are distributed over several computing nodes. Each node has two Intel SandyBridge Xeon E5-2680 CPUs, i.e. in total 16 physical and 32 virtual cores (“thin nodes” in the SuperMUC supercomputer at the Leibniz-Rechenzentrum in Garching). We use 32 OpenMP threads and 1 MPI process per node. Dashed lines are guides to the eyes.

The bulk of the main code validation was performed during the author’s master thesis [12]. New improvements (such as MPI or SIMDs) were carefully checked against a working version. Publication [Pub1] (section 4.3.3) and the supplementary information in publication [Pub3] show additional evidence regarding the correctness of the code. Publications [196] and [197] also employ parts of the code for the purpose of studying nanoparticle diffusion near deformable membranes, and found very good agreement with analytical computations. Furthermore, in publication [Pub5] (section 6.1) we compare our results successfully with experiments, indicating that not only the numerical implementation but also the *physical* modeling is suitable for the description of red blood cells in microchannel flows.

6

Physical research projects

After having selected appropriate models and algorithms, and having implemented them numerically, we can now turn towards applying the code. As already mentioned in the introduction (chapter 1.2), the field of blood flow is an extremely wide one with many unsolved questions remaining. Therefore, one must necessarily concentrate on a few specific problems.

In this thesis we are considering two different issues. The first is a more fundamental one, namely the shapes assumed by a single RBC in microchannel flows (section 6.1). The second is the behavior of oscillating ultrasound contrast agents (coated microbubbles) in blood flow, with special emphasis on targeted drug delivery (section 6.2).

6.1 Bistability of red blood cells in microchannels

6.1.1 Motivation

The analysis and prediction of shapes assumed by red blood cells flowing in micro-sized channels is a long-standing issue [283–285] with far-reaching consequences. For example, it is necessary for a better understanding of blood as a suspension [61, 119, 186, 286–288] and it is required to design more efficient and cheap analysis methods, e.g. in the form of lab-on-a-chip devices [2, 3, 5]. Despite its long history, we are still far away from a full comprehension owing to the complex interplay between the cell membranes and the fluid.

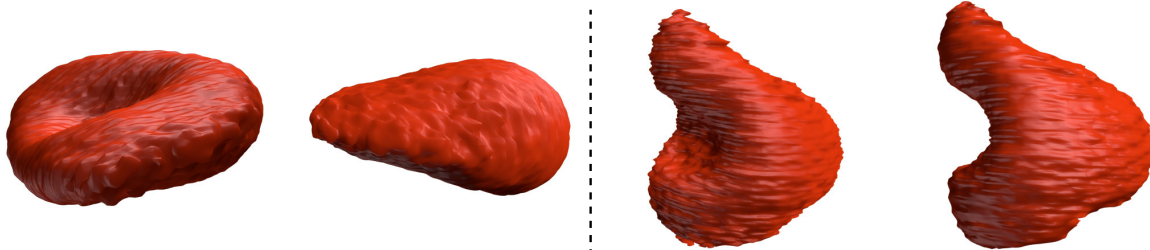
Qualitatively, experimental studies mostly observed two different shapes [285, 289–294]: croissants⁶ and slippers. Example images can be seen in figure 6.1. Yet, more detailed systematic experimental reports on the behavior of single RBCs are basically non-existent.

Numerically, this topic was often approached for simpler model systems such as vesicles in 2D [130, 296–302]. On the other hand, detailed investigations with realistic red blood cell models are rather scarce. Notable exceptions are three studies by the group of G. Gompper [11, 215, 217]: Two of these studies found discocytes below and parachutes above a certain velocity, depending on the elastic parameters [215] and the confinement [217]. Very detailed phase diagrams as functions of velocity and confinement were presented in the third paper [11].

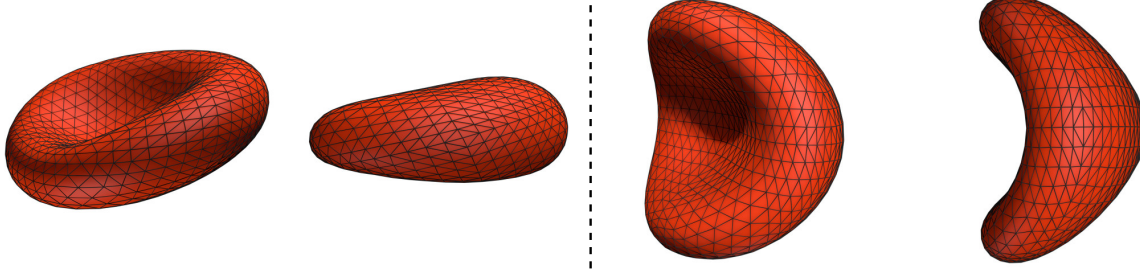
Yet, all these works on Poiseuille-like flows neglect or only shortly mention an important aspect of the problem, namely the influence of the initial condition. The only exception with a more detailed study regarding its influence considered a vesicle in an *unbounded* Poiseuille flow where a pronounced dependence on the initial position was found for higher viscosity ratios [295]. Moreover, most of the experimental and numerical studies (including references [11, 215, 217]) used viscosity ratios below or equal to one. This can insofar be criticized as recent works on 2D [298, 300] and 3D [295] vesicles found that the dynamics can change significantly when using e.g. the physiologically more relevant value of $\lambda = 5$ [14].

⁶Croissants are similar to parachutes. The difference is that the latter are perfectly rotationally symmetric while the first exhibit only two symmetry planes [295].

(a) 3D measurements



(b) Simulation results



slipper perspective

slipper side

croissant perspective

croissant side

Fig. 6.1: (a) Top row: Confocal microscope recordings of red blood cells flowing in a $25\ \mu\text{m} \times 10\ \mu\text{m}$ channel with velocities of $0.33\ \text{mm/s}$ (slipper) and $0.37\ \text{mm/s}$ (croissant). (b) Bottom row: Corresponding BIM simulations in the same geometry. Reprinted from publication [Pub4] with permission from AIP Publishing.

To enable more detailed future studies, publication [Pub4] presents a new confocal microscope technique developed in the group of Prof. C. Wagner which allows to record fully three-dimensional images of flowing RBCs. Croissants and slippers are observed. The author of the present thesis performed complementary BIM simulations and found slippers and metastable croissants that are very similar to the experimental recordings (see figure 6.1).

Publication [Pub5] comprises the first detailed and *systematic* study that combines both experiments and simulations of single RBCs in microchannel flows. The experiments were conducted by members of the group of Prof. C. Wagner. In contrast to the existing literature, we use $\lambda = 5$ and pay special attention to the initial condition in both methodologies, which enables us to make quantitative comparisons between the experimental and numerical results. We observe bistability: Croissants and slippers are found to be stable at the same set of parameters over a wide range of velocities. The results of [Pub5] are shortly summarized in the following.

6.1.2 Setup

The experiments in publication [Pub5] consider the behavior of individual healthy human red blood cells in a rectangular microchannel. The channel has a width of approximately $12\ \mu\text{m}$ and a height of around $10\ \mu\text{m}$. The viscosity of the fluid inside the cells is roughly five times higher than the viscosity of the ambient fluid. Experimental analysis of single cells is realized by using hematocrit values of less than 1% in the input reservoir and consideration of images showing only a single cell. Furthermore, as the 3D confocal microscopy from publication [Pub4] is limited to velocities below $1\ \text{mm/s}$, 2D images with standard bright-field microscopy are recorded. Shapes and positions of the cells are then extracted from these images. Cells at two locations in the channel are examined: at the channel entrance and $10\ \text{mm}$ downstream. The first location provides important information about the entry position, while the second shows the converged

shapes.

Our simulations mirror the experiments as close as possible. Hence we also use a rectangular $12\ \mu\text{m} \times 10\ \mu\text{m}$ channel (with slightly rounded corners to prevent numerical issues, compare figure 6.2) and a viscosity ratio of $\lambda = 5$. The fluid-structure problem is solved with the periodic boundary integral method (chapters 3 and 5). We employ the discocyte from equation (4.6) as the reference shape for the in-plane elasticity (Skalak model) and the spontaneous curvature is set to zero. The implementation of the RBC was already explained in chapters 2.1 and 4. We use Method C as bending algorithm as we found it to be the most stable one in the present setup.

In contrast to the experiments, we have full control over the initial condition. We therefore not only vary the initial position along a line that is close to the channel's diagonal (radial offset r_{init}), but also employ three different initial shapes. These include the typical discocyte, a croissant and a slipper. Also see figure 6.2 for an example setup.

The velocity is varied in the experiments and simulations in a range of approximately 0.1 mm/s to 10 mm/s. This completely covers the range of physiological velocities in vessels with diameters of the order of around $10\ \mu\text{m}$ [6, 86, 303].

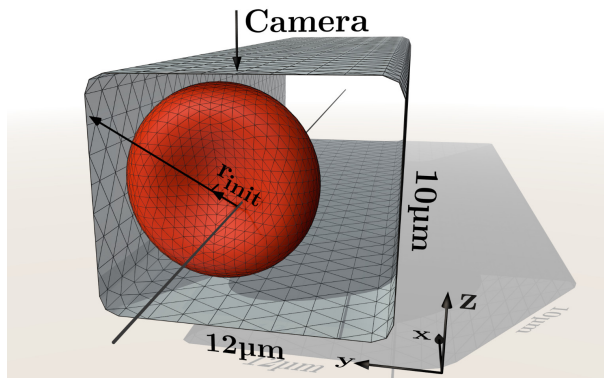


Fig. 6.2: Typical simulation setup used to study the behavior of a single red blood cell in a rectangular microchannel. The image shows an example when using a discocyte as the starting shape (other shapes are also used). Moreover, the cell is offset along the black arrow by an offset r_{init} . The arrow at the top illustrates the position of the camera in the experiments. Reproduced from publication [Pub5] with permission from the Royal Society of Chemistry.

6.1.3 Summary of our key results

Experiments We first consider the experimental observations 10 mm away from the channel entrance. Figure 6.3a shows the observed fraction of cell shapes as a function of the cell velocity. Cells that were not clearly classifiable as neither croissant nor slipper were termed as “others”. The diagram clearly shows that croissants dominate the picture at lower velocities, that croissants and slippers coexist at intermediate velocities (bistability) and that only slippers exist at higher velocities. Hence, it seems to be obvious that the velocity is the major parameter determining the shape. Yet, figure 6.3b shows that the offset distribution at the channel *entrance* widens with higher velocities, i.e. more cells are entering off-centered. This means that either the higher velocity or the larger offset at the entrance might be responsible for the observed fraction of shapes depicted in figure 6.3a. Unfortunately, the experimental data does not allow for a definite conclusion and numerical simulations are required.

Simulations By starting with the discocyte shape in the simulations and varying the initial radial position r_{init} as well as the velocity, we obtain the phase diagram shown in figure 6.4a. It depicts the shapes found in the steady state. As in the experiments, croissants and slippers are observed, with the result depending on the velocity. Most importantly, we also see a pronounced dependence on the initial position. Starting further off-centered tends to produce slippers while a

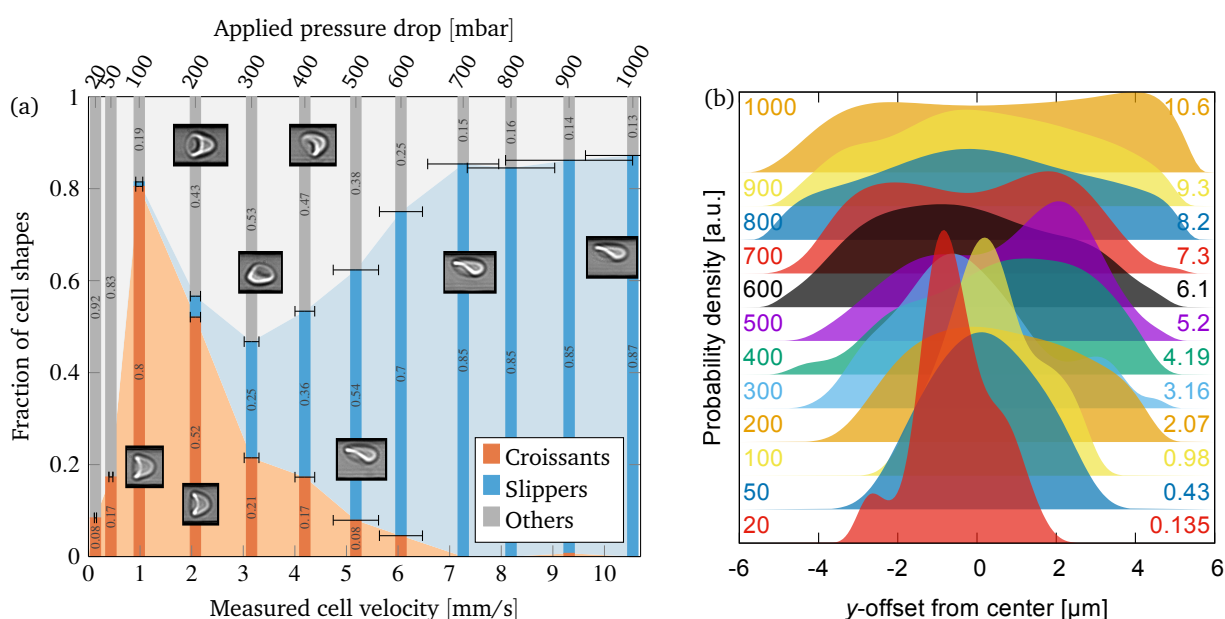


Fig. 6.3: Experimental results: (a) Observed cell shapes 10 mm away from the channel entrance as a function of cell velocity. The horizontal error bars show the standard deviation of the measured cell velocities. (b) Probability density function of the center-of-mass position of the cells at the channel entrance. The numbers on the left side depict the applied pressure drops in millibar, while the numbers on the right indicate the average cell velocity in mm/s. The curves are offset in the vertical direction to facilitate the illustration. Reproduced from publication [Pub5] with permission from the Royal Society of Chemistry.

starting position near the center yields croissants. As both are stable, we find bistability. There is one exception, namely only croissants are stable at velocities from around 2 to 3 mm/s.

Considering the observed shapes in more details (figure 6.4a), we can distinguish two different types of croissants and two different types of slippers. On the one hand, most of the croissants do not exhibit any relative movement and have two symmetry planes in the steady state (“non-TT croissants”). Yet, at higher velocities somewhat asymmetric shapes with pronounced tank-treading (TT) are found that are nevertheless very similar to croissants (see inset in figure 6.4b). On the other hand, the majority of slippers show tank-treading (“TT slippers”). At lower velocities, however, the tank-treading is suppressed and the object rotates similar to a rigid body (“tumbling”), with the shape still being reminiscent of a slipper (“non-TT slippers”). See the supplementary information of publication [Pub5] for some videos.

The dependence on the initial position also suggests a possible dependence on the initial shape. We therefore show in figure 6.4b the corresponding phase diagram when starting with a slipper.⁷ Compared to the first diagram, the “area” of croissants is reduced, i.e. slippers are found at smaller values of the initial radial offset. Apart from this, no qualitative differences are found. Especially the croissant-only region from 2 to 3 mm/s still exists.

Comparison Comparing the experimental (figure 6.3a) and numerical (figure 6.4) diagrams qualitatively, one can see that both are very similar: Croissants dominate at lower and slippers at higher velocities, with both coexisting at intermediate values. Making a quantitative comparison, however, is not immediately possible. Rather, we first need to use the results from the simulations

⁷In publication [Pub5] we also start with a croissant and rotated discocytes. The corresponding results are omitted here for brevity.

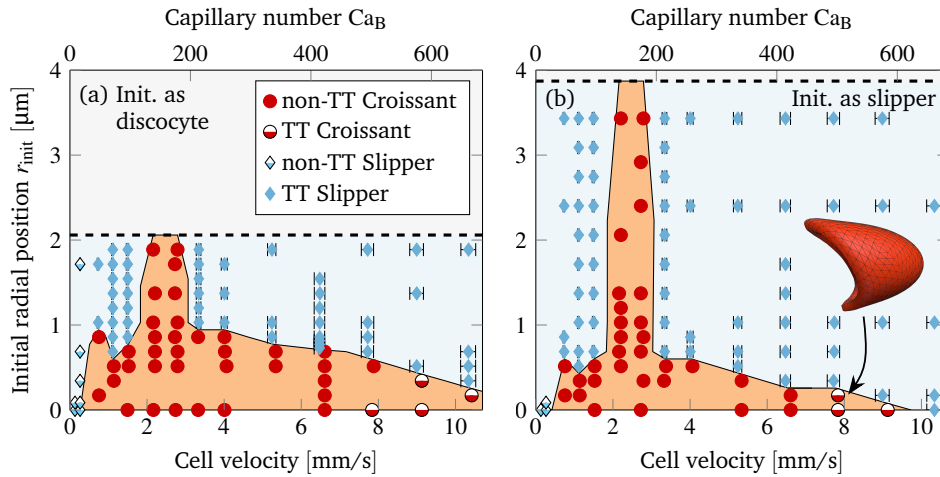


Fig. 6.4: Numerical results: Red blood cell shapes in the steady state as a function of velocity u and initial radial offset r_{init} . The top axis shows the results in terms of the capillary number $Ca_B := \mu u R_{\text{RBC}}^2 / \kappa_B$, where $\mu = 1.2 \text{ mPa s}$ is the ambient fluid viscosity and $R_{\text{RBC}} = 4 \mu\text{m}$ the large radius of the equilibrium discocyte shape. Each mark indicates one simulation, and the lines and shaded areas are guides to the eyes. Above the dashed line, the cell would overlap with the channel walls. The cell was started as a discocyte in figure (a) and as a slipper in figure (b). The inset in the right figure illustrates a tank-treading croissant. Reproduced from publication [Pub5] with permission from the Royal Society of Chemistry.

and make a prediction regarding the expected number of cell shapes. The idea to do this is the following. The simulations (figure 6.4) yield a critical value r_{trans} for the initial radial position below which croissants and above which slippers occur. Extracting the fraction of cells from figure 6.3b that enter the channel in the experiments with an offset⁸ below this particular value r_{trans} gives a certain value ϕ . Hence, the simulations predict that a fraction ϕ of the cells should become croissants. ϕ can therefore be directly compared with the experimental findings from figure 6.3a.

The result of this procedure can be seen in figure 6.5 where we show the prediction for both numerical phase diagrams (i.e. started with discocyte and slipper) in comparison with the experimental observations. Obviously, the prediction using the discocyte as starting shape shows somewhat more notable deviations. On the other hand, starting with the slipper gives very good agreement. This suggests that the cells are entering the channel in the experiments with rather asymmetric shapes because a slipper is less symmetric than a discocyte. Indeed, most of the cells observed at the channel entrance cannot be clearly classified (i.e. they are “others”).

Conclusion Due to the very good agreement, we can conclude that the physical models used in the simulations (chapter 2) can properly describe the dynamics of RBCs in microchannel flows. It also means that the chosen algorithms and their implementation is appropriate (chapters 4 and 5). Moreover, our experimental and numerical results clearly show that the initial condition has a decisive influence on the shapes assumed by red blood cells. This constitutes a fundamental finding. It also suggests that croissants and slippers occurring in-vivo are not just transients but rather intrinsically stable shapes. For more analyses and information we point the reader to publication [Pub5].

⁸Actually, we additionally take into account that the initial radial offset in the simulations is approximately along the diagonal while we only have the projection of the offset in the experiments.

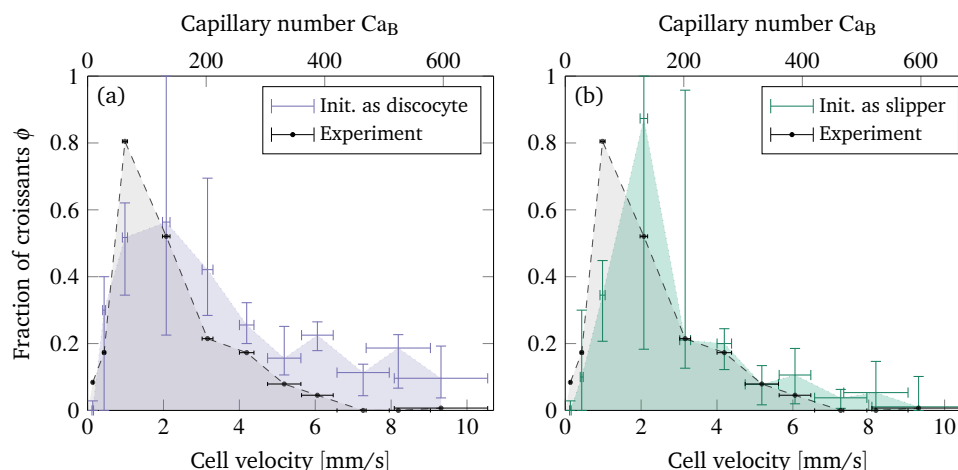


Fig. 6.5: Comparison between experimental and numerical results. The black dashed line is identical to the experimental findings depicted in figure 6.3a. The other points and lines show the fraction of croissants ϕ as predicted from the simulations and as explained in the main text. We show the standard deviation of the measured cell velocities as horizontal error bars, while the vertical error bars indicate the uncertainty in the prediction (see publication [Pub5]). Figure (a) shows the result when starting the simulations with the discocyte shape, figure (b) when starting with the slipper shape. Reproduced from publication [Pub5] with permission from the Royal Society of Chemistry.

6.2 Ultrasound-triggered margination of microbubbles

6.2.1 Motivation

Coated microbubbles, so-called ultrasound contrast agents, are nowadays used in medical ultrasound imaging regularly [304–308]. In the past years, a lot of research has been invested into making them usable as drug delivery agents [309–313], with first clinical studies having been conducted recently [313, 314]. The basic idea is to co-administer the bubbles together with the drug or, alternatively, to enrich the bubbles directly with the medical substance [313]. One then applies an ultrasound at the pathological region which causes the bubbles to oscillate, leading to an enhancement of the drug uptake due to their interactions with the vessel walls [312, 315]. Optimally, the bubbles should remain in the vessel center while flowing through the vascular system in order to prevent or delay their premature destruction as well as biochemical interactions with the endothelial cells. At the target site, however, they should be located near the vessel wall for direct interactions with the pathological cells [312, 313, 316].

We consider the issue of how to combine these two desired yet apparently contradictory properties in publication [Pub3]. Since no numerical method was available that could readily describe oscillating deformable microbubbles together with realistic deformable red blood cells, we first needed to extend the boundary integral method. This is done in the first part of publication [Pub3], as summarized in chapter 3. In the second part of publication [Pub3], which will be outlined below, we show that phospholipid-coated microbubbles [308, 309] stay in the vessel center if no ultrasound is applied. Application of an ultrasound leads to volume and thus to stiffness oscillations, where the latter is due to the special properties of the lipid coating. We show that this causes the bubbles to marginate, i.e. move to the vessel walls. Moreover, since margination only occurs in the presence of red blood cells (e.g. [7, 189, 191, 317]), this also highlights that in-vitro experiments have to take the cells into account in order to produce results that can be translated to the in-vivo case, contrary to the current practice where the bubbles are very often considered in isolation.

6.2.2 Setup

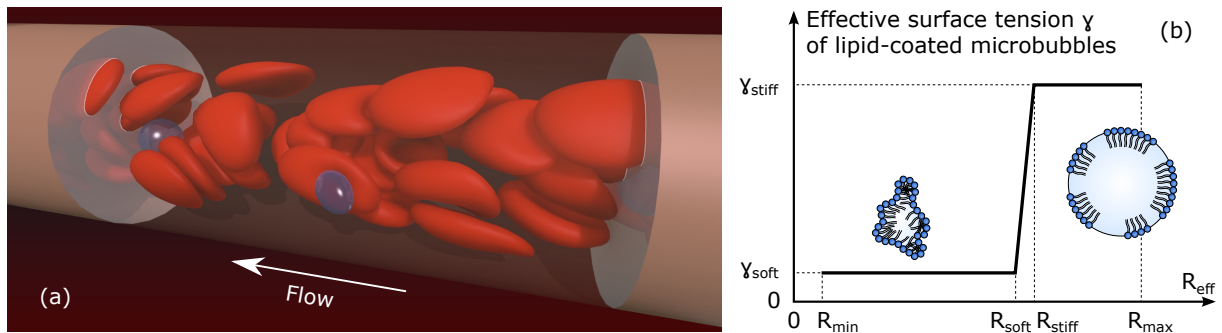


Fig. 6.6: System setup. (a) Example snapshot from the simulation for studying ultrasound-triggered margination of microbubbles. (b) Illustration of Marmottant et al.'s model for lipid coated microbubbles [318, 319]: Effective surface tension γ as a function of the effective bubble radius R_{eff} . The two insets show the sketches of a bubble in the buckled and in the ruptured state. Reprinted from publication [Pub3] with permission from Cambridge University Press.

The typical setup can be seen in figure 6.6a: Two bubbles are placed together with several red blood cells in a cylindrical microchannel of diameter $22 \mu\text{m}$. We employ periodic boundary conditions. The hematocrit (volume density of the RBCs) is set to the typical physiological value of 16% found in capillaries [97, 98]. We prescribe the average flow $\langle \mathbf{u} \rangle_{\Gamma}$ in equation (3.5) such that the maximal flow velocity is $u_{\text{max}} \approx 4.7 \text{ mm/s}$ in agreement with physiological velocities [6].

The bubbles are modeled according to Marmottant et al. [318]. Their model was shown to be suitable for lipid-coated microbubbles [308, 312, 319–322]. It is based on the observation that upon application of an ultrasound the bubbles oscillate between a compressed state (in which they are buckled [322] and very deformable [318, 323]) and an expanded state (in which their shell is ruptured and they are very stiff [318, 324]). This is captured by an effective surface tension γ as illustrated in figure 6.6b. Due to the smallness of the intermediate regime [319] between these two states, we approximate the overall behavior as a step-function, i.e.

$$\gamma(R_{\text{eff}}) = \begin{cases} \gamma_{\text{soft}} & \text{if } R_{\text{eff}} \leq R_{\text{soft}}, \\ \gamma_{\text{stiff}} & \text{if } R_{\text{eff}} > R_{\text{soft}}. \end{cases} \quad (6.1)$$

$R_{\text{eff}} := \sqrt[3]{3V/(4\pi)}$ is the effective radius and V the instantaneous bubble volume. The deformable state is characterized by an effective surface tension $\gamma_{\text{soft}} \approx 0$ [319], while the stiff state exhibits the high surface tension $\gamma_{\text{stiff}} = 7 \times 10^{-2} \text{ N/m}$ of an air-water interface. To ensure numerical stability, we mostly use $\gamma_{\text{soft}} = 0.5\kappa_S$ and $\gamma_{\text{stiff}} = 10\kappa_S$, where $\kappa_S = 5 \times 10^{-6} \text{ N/m}$ is the shear modulus of the red blood cells (compare section 2.1). The Young-Laplace equation $\Delta f = 2\gamma H \mathbf{n}$ is used to compute the traction jump Δf [134, 325, 326]. Note that it requires the mean curvature H , which is computed via Method C from chapter 4.

The equilibrium radius is chosen to be $2 \mu\text{m}$, which is a typical value for microbubbles [312, 319, 324]. This radius is set to be in the buckled state, meaning that by default the bubbles are deformable. Indeed, such an experimental preparation is possible e.g. by exposing them to a slight overpressure [320, 323, 324].

The effect of an acoustic source is modeled by prescribing a volume oscillation of

$$V_i(t) = V_i^{(0)} + A_i/(2\pi f)[1 - \cos(2\pi f t)] \quad (6.2)$$

or equivalently a flux of $Q_i(t) = A_i \sin(2\pi f t)$ for the i 'th bubble. The boundary integral method

requires the latter quantity as apparent from equation (3.5). $V_i^{(0)}$ is the initial volume, f the frequency and A_i the flux amplitude. We set $A_1 = -A_2$, i.e. the two bubbles are oscillating out-of-phase. This is required to conserve the ambient fluid volume (compare chapter 3). Since the interaction between the bubbles is screened due the RBCs and because margination depends on the stiffness oscillations rather than the phase, this restriction should not undermine the validity of our results. Also note that equation (6.2) fixes only the volume and that the bubbles can still deform.

Continuing, the stiff to soft duration ratio $\delta = T_+/T_-$ is the most important parameter. It describes the time T_+ spent in the stiff state ($R_{\text{eff}} > R_{\text{soft}}$) compared to the time T_- spent in the soft state ($R_{\text{eff}} \leq R_{\text{soft}}$). Furthermore, to prevent accumulation of the bubbles in small spots on the vessel wall [316, 327, 328], primary and secondary radiation forces [329, 330] should be minimized. Hence, we do not use frequencies in the lower megahertz range that are typical in current medical applications [312, 313], but smaller frequencies of $f \leq 10$ kHz. The margination effect presented below then leads to a homogeneous covering of the bubbles on the boundaries.

As the Stokes equation is the basis of our method, the Reynolds number should be small. On the one hand, for the translational motion we have $\text{Re}_T = 2R_{\text{RBC}} u_{\text{max}} \rho / \mu \approx 0.03 \ll 1$ with the dynamic viscosity $\mu = 1.2 \times 10^{-3}$ kg/(s m) and the density $\rho \approx 10^3$ kg/m³ of blood plasma [18]. On the other hand, the radial oscillations are characterized by $\text{Re}_R = (2R_0)^2 \rho f / \mu < 0.07 \ll 1$ for $f \leq 10$ kHz. As both values are much smaller than one, the Stokes equation is appropriate for the description of the dynamics.

The red blood cells were modeled as described in chapters 2.1 and 4. We employed Method C as bending algorithm as it showed the best stability. Also note that the above-mentioned parameters constitute the standard set that was used in the simulations. Several additional parameter variations are presented in publication [Pub3] and its supplementary information.

6.2.3 Summary of our key results: Ultrasound-triggered margination

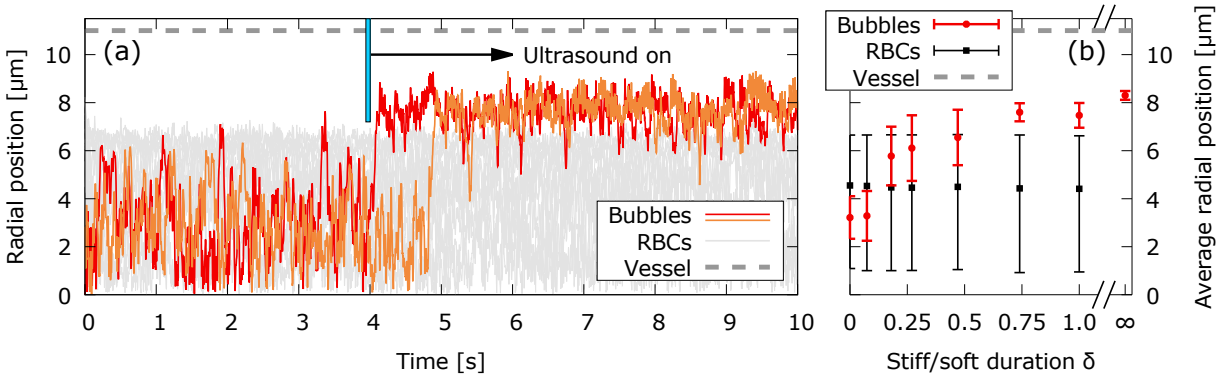


Fig. 6.7: Ultrasound triggered margination. (a) Radial position of two microbubbles and several red blood cells. The oscillations are off at the beginning and switched on after four seconds. $\delta = 1$. (b) Effect of different values for δ (i.e. different stiff to soft duration ratios). The error bars show the average minimal and maximal centroid positions. The rightmost value ($\delta \rightarrow \infty$) shows the result for bubbles that are always stiff. Reprinted from publication [Pub3] with permission from Cambridge University Press.

Our new discovery is concisely depicted in figure 6.7a for $\delta = 1$. In the first four seconds the volume oscillations are switched off. The bubbles are therefore in the soft state and flow with the red blood cells in the center of the channel in accordance with experimental observations [331]. After four seconds the oscillations are switched on, causing the bubbles to alternate periodically

between the soft and the stiff state, leading to their rapid and isotropic margination within less than one second. We termed this effect “ultrasound-triggered margination” (UTM).

UTM is a non-trivial discovery: It is well known that soft objects remain in the channel center while stiff ones migrate to the outside in blood flow [7, 189, 191, 317]. However, the bubbles continuously oscillate between a soft and a stiff state, making the result unclear a priori. The physical reason for their margination is that the deformation due to the flow and the interaction with the RBCs in the soft state happens on a much slower timescale ($\tau_{\text{deform}} \approx 2$ ms) than the relaxation into the nearly spherical shape at high surface tension in the stiff state ($\tau_{\text{stiff}} \approx 0.1$ ms). This means that the latter dominates the overall picture.

The large disparity of these two estimated timescales also indicates that it is a robust effect, i.e. also occurs for smaller values of δ when the bubbles spend more time in the soft state (which counteracts margination). Indeed, as figure 6.7b shows, we still observe margination for values as low as $\delta \approx 0.2$. It is also important to note that margination is an effect which comes from the interaction with the red blood cells. If they are removed, the bubbles will remain in the channel center, regardless of the value of δ .

Furthermore, figure 6.8 highlights that the migration is isotropic and leads to a homogeneous coverage of the vessel wall. This is a clear advantage over alternative approaches using e.g. radiation forces [329, 330] as already mentioned above. Moreover, once at the vessel wall, the bubbles will usually stay there, except for a few short-lived migrations to the inside.

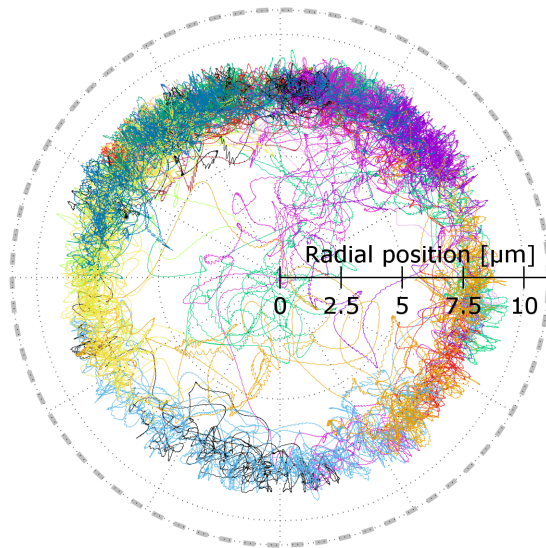


Fig. 6.8: Polar plot of bubble trajectories from several simulations with $\delta = 0.74$ and $\delta = 1$ after one second or after definite margination as seen from the outlet. The gray dashed line represents the vessel radius. Reprinted from publication [Pub3] with permission from Cambridge University Press.

These findings allow us to conclude that lipid-coated microbubbles allow for an efficient drug delivery protocol: They tend to remain in the channel center during their transport through the vascular system but migrate isotropically to the outside after applying an ultrasound. This margination is due to the interaction with the red blood cells. Removing the cells means that the effect disappears. Further results and analyses can be found in publication [Pub3].

7

Conclusion & outlook

7.1 Conclusion

In the present thesis we decided to study blood flow via simulations on two levels: First, on the level of a single cell (chapter 6.1) and second on the suspension level. In the latter case, we concentrated on the dynamics of lipid-coated microbubbles in blood flow subjected to ultrasound (chapter 6.2).

Yet, a requirement for numerical simulations is to have the necessary mathematics, algorithms and tools to do so. It turned out that a direct application of standard methods was not sufficient. A basic necessity is the description of the flow. While the standard boundary integral method (or many other methods in this regard) would be suitable for the simulation of single or multiple cells in channels, none so far could handle oscillating deformable microbubbles as required for our second research project. Thus, the latter made the development of our volume-changing object boundary integral method in chapter 3 necessary. Furthermore, an important component of red blood cells is their bending resistance. Implementing these seemed to be an easy task at first by simply taking a standard algorithm, but it became clear that something like a standard algorithm does not really exist. Rather, a multitude of models and methods are used in the literature without any available evaluation. A well-founded choice thus required an in-depth comparison first, implying chapters 2.1 (linear bending models) and 4.3 (bending algorithms) as necessary prerequisites to both of our research projects. Additional optimizations of the code as explained in chapter 5.3 reduced the often significant simulation times to manageable levels (usually in the 1 to 2 weeks regime). Only afterwards were we able to successfully complete them.

Our study on single-cell behavior (ch. 6.1) contributes to the fundamental understanding of blood flow by showing that the cells can have not only one intrinsically preferred shape in a given environment, but rather several shapes can coexist. The actually assumed shape depends on the history of the cell. Thus, this points out that the croissants and slippers observed in the microvascular system might not just be due to transient dynamics. Our results also put research on this topic into perspective where the initial condition is not considered.

The second study on oscillating microbubbles (ch. 6.2) contributes to the comprehension of blood flow in a specific application. Namely, researchers have been working on exploiting coated microbubbles for targeted drug delivery for several years. This is closely tied to the question of the behavior of these bubbles in ultrasound fields. Existing studies focused so far on an accurate description of isolated oscillating microbubbles, and on the behavior of such bubbles in flows, but in many cases without red blood cells. Our study presents the first simulation of coated microbubbles in a realistic blood flow. We showed that a lipid-coating can lead to a very effective drug delivery protocol. Moreover, our results indicate that future research on this topic (be it experimental or numerical) must incorporate red blood cells in order to arrive at conclusions meaningful for real-life applications.

Thus, all in all, we contributed and analyzed methodologies to study blood flow via numerical simulations, and we contributed the importance of shape-coexistence and the behavior of suspended lipid-coated microbubbles to the understanding of blood flow.

7.2 Outlook

7.2.1 Investigation of the stress-free shape of red blood cells

With a working and validated tool in hand, it can now be applied to answer a multitude of open questions. As already outlined in chapter 2.1, the form of the stress-free (or reference) shape of red blood cells still lacks a definite answer [41, 54–62]. For the in-plane elasticity, the historically more often used one is the equilibrium discocyte shape. It suggests itself as it means that the RBC’s membrane is actually stress-free in the equilibrium state. A different possibility is some oblate spheroid that is nearly a sphere. Depending on the elastic moduli and also the reference state for the bending forces, the equilibrium shape can still be a discocyte (but with a membrane that is no longer stress-free). In our studies in chapter 6, we have used the discocyte as stress-free shape. It would thus be highly interesting to see if changes occur when an oblate is used instead. This is especially true for the research on single RBCs from publication [Pub5] (chapter 6.1), as quantitative comparisons with experiments are possible.

After completing the work on [Pub5], the present author started to investigate this issue. Preliminary results shall be outlined in the following. Apart from the stress-free shape, the numerical setup is identical to the one from publication [Pub5]. The reference shape for the in-plane elasticity (Skalak law) is now however chosen to be an oblate spheroid with a reduced volume of $\tau = 0.995$, where $\tau := 6\sqrt{\pi}V/A^{3/2}$ (V is the spheroid’s volume that is larger than that of an RBC, while $A \approx 140 \mu\text{m}^2$ is its surface area that is identical to the RBC’s value). For the reference mean curvature, as appearing in equation (4.5), we use⁹ $H_0 = 0.705 \mu\text{m}^{-1}$. These values approximately match with the ones employed in references [58, 61]. We will call this particular stress-free shape configuration “OBL” in the following. The one from publication [Pub5] (discocyte for the in-plane elasticity and $H_0 = 0$) will be denoted by “DISC”.

The choice of the *starting* configuration and initial position r_{init} is unaffected by the choice of the stress-free shape. For simplicity, we concentrate here on the discocyte as the initial shape for both DISC and OBL. Figure 7.1a shows again the phase diagram for DISC from publication [Pub5]. In contrast, figure 7.1b depicts our preliminary results for OBL. Clearly, at cell velocities above 2 mm/s, no qualitative or even quantitative differences occur. However, at lower velocities DISC produces a significant amount of slippers while OBL only shows croissants. This is a striking difference. Very similar results are obtained for a slipper and a croissant starting shape.

Considering that no significant differences between DISC and OBL are observed for higher velocities, the agreement between the experimental measurements in publication [Pub5] and both phase diagrams remains unaffected in this velocity regime. At lower velocities, a more careful examination is required. The experimental results in figure 6.3a show mostly non-classifiable cells (“Others”) for velocities below 1 mm/s. Thus, no real statement can be made here using such 2D image microscopy (and we have not done so in [Pub5]). Rather, we need the full 3D shape information in order to classify the cells reliably.

The 3D confocal microscope technique presented in publication [Pub4] is suited perfectly for this task. Following the present author’s suggestion, Sina Kalweit and Dr. Stephan Quint (members of the group of Prof. Dr. C. Wagner) began to analyze the low velocity regime using

⁹The spontaneous curvature c_0 is sometimes defined as twice the value of H_0 , i.e. $c_0 = 2H_0 = 1.41 \mu\text{m}^{-1}$.

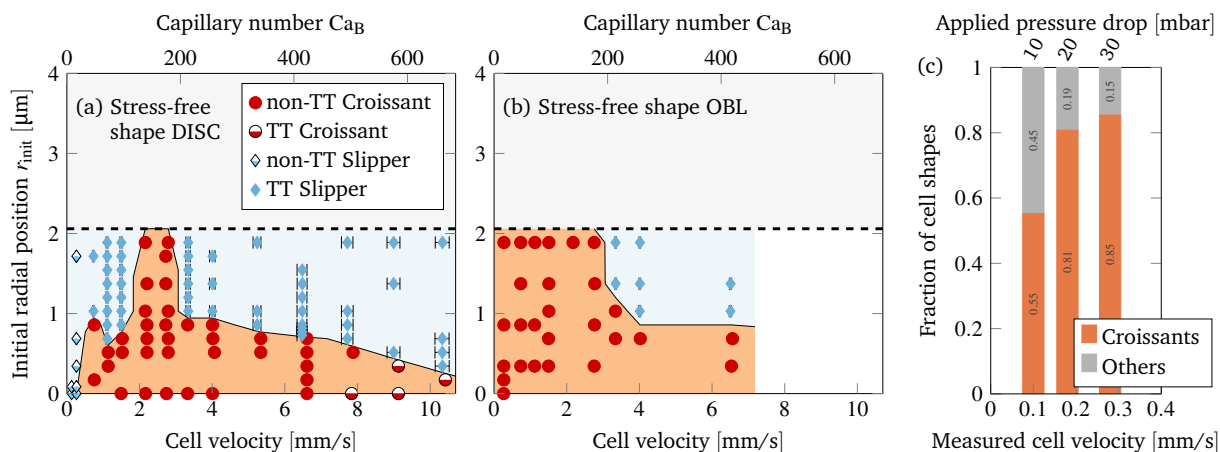


Fig. 7.1: (a) Numerical phase diagram for the DISC stress-free shape and the discocyte starting shape. The image is identical to figure 6.4a and is repeated here to allow a convenient comparison. Reproduced from publication [Pub5] with permission from the Royal Society of Chemistry. (b) Preliminary numerical results for the OBL stress-free shape and the discocyte starting shape. (c) Preliminary experimental results as obtained by 3D confocal imaging. Data provided by Sina Kalweit and Dr. Stephan Quint (members of the group of Prof. Dr. C. Wagner in Saarbrücken).

this method. The remaining parts of the experimental setup is identical to publication [Pub5]. Their new preliminary results can be seen in figure 7.1c. Clearly, the majority of the cells at low velocities have a croissant-like shape. Putting everything together we can therefore conclude that the stress-free shape of RBCs is most likely an oblate spheroid rather than a discocyte.

However, this statement should be taken with some care as the results are preliminary (and hence the present section is in the outlook chapter). Besides mapping out the phase diagram more carefully and for different starting configurations, one needs to take into account various possible stress-free shapes more systematically. This includes both the reference state for the in-plane elasticity (discocyte vs. oblate vs. prolate) and the spontaneous curvature c_0 (zero vs. positive vs. negative, also in light of reference [195]) as well as the precise values of τ and c_0 . Completely unrealistic values might be filtered out early by considering the equilibrium shape, which should be a discocyte close to equation (4.6). Furthermore, the question if a spatially inhomogeneous shear modulus can explain the results should be addressed. A detailed analysis of the actual shapes in the steady state would also be appropriate (e.g. regarding tank-treading or oscillatory behavior).

As a final note, it is also interesting that the stress-free shape appears to have significant influence only at low velocities (in this case below 2 mm/s), in agreement with [58, 62]. Therefore, we do not expect any differences in our microbubble study from publication [Pub3] where twice the velocity was used. Another reason is that the margination hinges upon the relative softness of the RBCs compared to the bubbles, and this is little affected by the stress-free shape.

7.2.2 Further open questions

Besides a continuation of the work on single cells with respect to the stress-free shape, further studies might shed some light on the influence of the viscosity ratio λ . 2D simulations with vesicles [300] indicate that significant changes are to be expected. Non-physiological values are also highly relevant for in-vitro experiments and medical analyses. Another possibility to continue would be to study the hydrodynamic clustering of cells (similar to the experiments in reference [122]), with special emphasis on different initial conditions. This could also pave

the way for a better understanding of dense suspensions. For example, a connection between the velocity-dependent bistability of single cells and suspension properties such as the effective viscosity might be uncovered.

Of course, a software package is never finished and new functionality can be implemented to study new systems. An ingredient missing so far in the modeling of RBCs is the membrane viscosity, which might be relevant in certain cases. A similar statement holds for thermal fluctuations (a possible methodology is presented in reference [251]). Furthermore, a more efficient parallelization would grant access to much larger systems such as microvascular networks. As explained in section 5.3, the current implementation is hampered by the Fast Fourier Transforms. Thus, improving the current situation is no straightforward task. As already mentioned, one possibility would be to use the fast multipole method that was demonstrated before to solve at least the scaling problem [92, 263 – 266]. Finally, more refined surface discretizations using e.g. spherical harmonics or subdivision surface methods could not only improve the accuracy of the bending computations but also of the solving of the boundary integral equation. This is necessary to study extremely confined systems such as the squeezing of cells through small slits [42].

8

References

- [1] I. V. Pivkin, Z. Peng, G. E. Karniadakis, P. A. Buffet, M. Dao, and S. Suresh (2016). Biomechanics of Red Blood Cells in Human Spleen and Consequences for Physiology and Disease. *Proceedings of the National Academy of Sciences* **113** (28), pp. 7804–7809. DOI: [10.1073/pnas.1606751113](https://doi.org/10.1073/pnas.1606751113) (cited on p. 3).
- [2] M. Toner and D. Irimia (2005). Blood-on-a-Chip. *Annual Review of Biomedical Engineering* **7** (1), pp. 77–103. DOI: [10.1146/annurev.bioeng.7.011205.135108](https://doi.org/10.1146/annurev.bioeng.7.011205.135108) (cited on pp. 3, 11, 31).
- [3] B. Sebastian and P. S. Dittrich (2018). Microfluidics to Mimic Blood Flow in Health and Disease. *Annual Review of Fluid Mechanics* **50** (1), pp. 483–504. DOI: [10.1146/annurev-fluid-010816-060246](https://doi.org/10.1146/annurev-fluid-010816-060246) (cited on pp. 3, 10, 11, 31).
- [4] T. M. Geislinger and T. Franke (2013). Sorting of Circulating Tumor Cells (MV3-Melanoma) and Red Blood Cells Using Non-Inertial Lift. *Biomicrofluidics* **7** (4), 044120. DOI: [10.1063/1.4818907](https://doi.org/10.1063/1.4818907) (cited on p. 3).
- [5] E. Henry, S. H. Holm, Z. Zhang, J. P. Beech, J. O. Tegenfeldt, D. A. Fedosov, and G. Gompper (2016). Sorting Cells by Their Dynamical Properties. *Scientific Reports* **6**, 34375. DOI: [10.1038/srep34375](https://doi.org/10.1038/srep34375) (cited on pp. 3, 31).
- [6] A. S. Popel and P. C. Johnson (2005). Microcirculation and Hemorheology. *Annual Review of Fluid Mechanics* **37** (1), pp. 43–69. DOI: [10.1146/annurev.fluid.37.042604.133933](https://doi.org/10.1146/annurev.fluid.37.042604.133933) (cited on pp. 3, 10, 11, 33, 37).
- [7] T. W. Secomb (2017). Blood Flow in the Microcirculation. *Annual Review of Fluid Mechanics* **49** (1), pp. 443–461. DOI: [10.1146/annurev-fluid-010816-060302](https://doi.org/10.1146/annurev-fluid-010816-060302) (cited on pp. 3, 9, 11, 36, 39).
- [8] J. M. Aguilera, P. J. Lillford, and G. V. Barbosa-Cánovas, eds. (2008). *Food Materials Science: Principles and Practice*. Food Engineering Series. New York: Springer. DOI: [10.1007/978-0-387-71947-4](https://doi.org/10.1007/978-0-387-71947-4) (cited on p. 3).
- [9] A. Farutin and C. Misbah (2013). Analytical and Numerical Study of Three Main Migration Laws for Vesicles Under Flow. *Physical Review Letters* **110** (10), 108104. DOI: [10.1103/PhysRevLett.110.108104](https://doi.org/10.1103/PhysRevLett.110.108104) (cited on p. 4).
- [10] J. L. McWhirter, H. Noguchi, and G. Gompper (2009). Flow-Induced Clustering and Alignment of Vesicles and Red Blood Cells in Microcapillaries. *Proceedings of the National Academy of Sciences* **106** (15), pp. 6039–6043. DOI: [10.1073/pnas.0811484106](https://doi.org/10.1073/pnas.0811484106) (cited on p. 4).
- [11] D. A. Fedosov, M. Peltomäki, and G. Gompper (2014). Deformation and Dynamics of Red Blood Cells in Flow through Cylindrical Microchannels. *Soft Matter* **10** (24), pp. 4258–4267. DOI: [10.1039/C4SM00248B](https://doi.org/10.1039/C4SM00248B) (cited on pp. 4, 8, 10, 21, 27, 31).

- [12] A. Guckenberger (2015). Simulation of Red Blood Cells and Microbubbles in Infinite and Periodic Stokes Flow. MA thesis. Universität Bayreuth (cited on pp. 5, 29, 30, 75, 76, 78).
- [13] N. Mohandas and P. G. Gallagher (2008). Red Cell Membrane: Past, Present, and Future. *Blood* **112** (10), pp. 3939–3948. DOI: [10.1182/blood-2008-07-161166](https://doi.org/10.1182/blood-2008-07-161166) (cited on pp. 7, 9, 10).
- [14] G. R. Cokelet and H. J. Meiselman (1968). Rheological Comparison of Hemoglobin Solutions and Erythrocyte Suspensions. *Science* **162** (3850), pp. 275–277. DOI: [10.1126/science.162.3850.275](https://doi.org/10.1126/science.162.3850.275) (cited on pp. 7, 31).
- [15] J. Li, G. Lykotrafitis, M. Dao, and S. Suresh (2007). Cytoskeletal Dynamics of Human Erythrocyte. *Proceedings of the National Academy of Sciences* **104** (12), pp. 4937–4942. DOI: [10.1073/pnas.0700257104](https://doi.org/10.1073/pnas.0700257104) (cited on p. 7).
- [16] A. Nans, N. Mohandas, and D. L. Stokes (2011). Native Ultrastructure of the Red Cell Cytoskeleton by Cryo-Electron Tomography. *Biophysical Journal* **101** (10), pp. 2341–2350. DOI: [10.1016/j.bpj.2011.09.050](https://doi.org/10.1016/j.bpj.2011.09.050) (cited on p. 7).
- [17] S. Svetina, D. Kuzman, R. E. Waugh, P. Ziherl, and B. Žekš (2004). The Cooperative Role of Membrane Skeleton and Bilayer in the Mechanical Behaviour of Red Blood Cells. *Bioelectrochemistry* **62** (2), pp. 107–113. DOI: [10.1016/j.bioelechem.2003.08.002](https://doi.org/10.1016/j.bioelechem.2003.08.002) (cited on p. 7).
- [18] R. Skalak, N. Ozkaya, and T. C. Skalak (1989). Biofluid Mechanics. *Annual Review of Fluid Mechanics* **21** (1), pp. 167–200. DOI: [10.1146/annurev.fl.21.010189.001123](https://doi.org/10.1146/annurev.fl.21.010189.001123) (cited on pp. 7, 9, 10, 38).
- [19] S. Guido and G. Tomaiuolo (2009). Microconfined Flow Behavior of Red Blood Cells in Vitro. *Comptes Rendus Physique* **10** (8), pp. 751–763. DOI: [10.1016/j.crhy.2009.10.002](https://doi.org/10.1016/j.crhy.2009.10.002) (cited on pp. 7, 9, 10).
- [20] D. E. Discher, N. Mohandas, and E. A. Evans (1994). Molecular Maps of Red Cell Deformation: Hidden Elasticity and in Situ Connectivity. *Science* **266** (5187), pp. 1032–1035. DOI: [10.1126/science.7973655](https://doi.org/10.1126/science.7973655) (cited on p. 7).
- [21] G. H. W. Lim, M. Wortis, and R. Mukhopadhyay. “Red Blood Cell Shapes and Shape Transformations: Newtonian Mechanics of a Composite Membrane.” In: *Soft Matter, Vol. 4: Lipid Bilayers and Red Blood Cells*. Ed. by G. Gompper and M. Schick. Soft Matter 4. Weinheim: Wiley-VCH, (2008), pp. 83–249. DOI: [10.1002/9783527623372](https://doi.org/10.1002/9783527623372) (cited on pp. 7–10).
- [22] F. Li, C. U. Chan, and C. D. Ohl (2013). Yield Strength of Human Erythrocyte Membranes to Impulsive Stretching. *Biophysical Journal* **105** (4), pp. 872–879. DOI: [10.1016/j.bpj.2013.06.045](https://doi.org/10.1016/j.bpj.2013.06.045) (cited on p. 7).
- [23] E. Evans and Y.-C. Fung (1972). Improved Measurements of the Erythrocyte Geometry. *Microvascular Research* **4** (4), pp. 335–347. DOI: [10.1016/0026-2862\(72\)90069-6](https://doi.org/10.1016/0026-2862(72)90069-6) (cited on pp. 7, 9, 22).
- [24] R. Skalak, A. Tozeren, R. P. Zarda, and S. Chien (1973). Strain Energy Function of Red Blood Cell Membranes. *Biophysical Journal* **13** (3), pp. 245–264. DOI: [10.1016/S0006-3495\(73\)85983-1](https://doi.org/10.1016/S0006-3495(73)85983-1) (cited on p. 7).

-
- [25] D. Barthès-Biesel, J. Walter, and A.-V. Salsac. “Flow-Induced Deformation of Artificial Capsules.” In: *Computational Hydrodynamics of Capsules and Biological Cells*. Ed. by C. Pozrikidis. Chapman & Hall/CRC Mathematical and Computational Biology Series. Boca Raton: CRC Press, (2010), pp. 35–70. DOI: [10.1201/EBK1439820056-c2](https://doi.org/10.1201/EBK1439820056-c2) (cited on pp. 7, 8, 11, 24).
- [26] T. Krüger (2012). *Computer Simulation Study of Collective Phenomena in Dense Suspensions of Red Blood Cells under Shear*. Wiesbaden: Vieweg+Teubner Verlag. DOI: [10.1007/978-3-8348-2376-2](https://doi.org/10.1007/978-3-8348-2376-2) (cited on pp. 7–10, 20, 21, 27).
- [27] Y.-Z. Yoon, J. Kotar, G. Yoon, and P. Cicuta (2008). The Nonlinear Mechanical Response of the Red Blood Cell. *Physical Biology* **5** (3), 036007. DOI: [10.1088/1478-3975/5/3/036007](https://doi.org/10.1088/1478-3975/5/3/036007) (cited on p. 7).
- [28] J. B. Freund (2014). Numerical Simulation of Flowing Blood Cells. *Annual Review of Fluid Mechanics* **46** (1), pp. 67–95. DOI: [10.1146/annurev-fluid-010313-141349](https://doi.org/10.1146/annurev-fluid-010313-141349) (cited on pp. 7–10, 27, 28).
- [29] A. Farutin, T. Biben, and C. Misbah (2014). 3D Numerical Simulations of Vesicle and Inextensible Capsule Dynamics. *Journal of Computational Physics* **275**, pp. 539–568. DOI: [10.1016/j.jcp.2014.07.008](https://doi.org/10.1016/j.jcp.2014.07.008) (cited on pp. 8, 9, 19, 22, 23, 28, 29).
- [30] P. Dimitrakopoulos (2012). Analysis of the Variation in the Determination of the Shear Modulus of the Erythrocyte Membrane: Effects of the Constitutive Law and Membrane Modeling. *Physical Review E* **85** (4), 041917. DOI: [10.1103/PhysRevE.85.041917](https://doi.org/10.1103/PhysRevE.85.041917) (cited on p. 8).
- [31] S. Svetina, G. Kokot, T. Š. Kebe, B. Žekš, and R. E. Waugh (2016). A Novel Strain Energy Relationship for Red Blood Cell Membrane Skeleton Based on Spectrin Stiffness and Its Application to Micropipette Deformation. *Biomechanics and Modeling in Mechanobiology* **15** (3), pp. 745–758. DOI: [10.1007/s10237-015-0721-x](https://doi.org/10.1007/s10237-015-0721-x) (cited on p. 8).
- [32] D. E. Discher, D. H. Boal, and S. K. Boey (1998). Simulations of the Erythrocyte Cytoskeleton at Large Deformation. II. Micropipette Aspiration. *Biophysical Journal* **75** (3), pp. 1584–1597. DOI: [10.1016/S0006-3495\(98\)74076-7](https://doi.org/10.1016/S0006-3495(98)74076-7) (cited on pp. 8, 21).
- [33] D. A. Fedosov, B. Caswell, and G. E. Karniadakis (2010). A Multiscale Red Blood Cell Model with Accurate Mechanics, Rheology, and Dynamics. *Biophysical Journal* **98** (10), pp. 2215–2225. DOI: [10.1016/j.bpj.2010.02.002](https://doi.org/10.1016/j.bpj.2010.02.002) (cited on pp. 8, 10, 21, 27, 28).
- [34] G. Závodszy, B. van Rooij, V. Azizi, and A. Hoekstra (2017). Cellular Level In-Silico Modeling of Blood Rheology with An Improved Material Model for Red Blood Cells. *Frontiers in Physiology* **8**, 563. DOI: [10.3389/fphys.2017.00563](https://doi.org/10.3389/fphys.2017.00563) (cited on pp. 8, 10, 27).
- [35] P. B. Canham (1970). The Minimum Energy of Bending as a Possible Explanation of the Biconcave Shape of the Human Red Blood Cell. *Journal of Theoretical Biology* **26** (1), pp. 61–81. DOI: [10.1016/S0022-5193\(70\)80032-7](https://doi.org/10.1016/S0022-5193(70)80032-7) (cited on pp. 8, 20).
- [36] W. Helfrich (1973). Elastic Properties of Lipid Bilayers: Theory and Possible Experiments. *Zeitschrift für Naturforschung. Teil C: Biochemie, Biophysik, Biologie, Virologie* **28** (11-12), pp. 693–703. DOI: [10.1515/znc-1973-11-1209](https://doi.org/10.1515/znc-1973-11-1209) (cited on pp. 8, 20).
- [37] E. A. Evans (1974). Bending Resistance and Chemically Induced Moments in Membrane Bilayers. *Biophysical Journal* **14** (12), pp. 923–931. DOI: [10.1016/S0006-3495\(74\)85959-X](https://doi.org/10.1016/S0006-3495(74)85959-X) (cited on p. 8).

- [38] Y. Park, C. A. Best, K. Badizadegan, R. R. Dasari, M. S. Feld, T. Kuriabova, M. L. Henle, A. J. Levine, and G. Popescu (2010). Measurement of Red Blood Cell Mechanics during Morphological Changes. *Proceedings of the National Academy of Sciences* **107** (15), pp. 6731–6736. DOI: [10.1073/pnas.0909533107](https://doi.org/10.1073/pnas.0909533107) (cited on pp. 8–10).
- [39] U. Seifert (1997). Configurations of Fluid Membranes and Vesicles. *Advances in Physics* **46** (1), pp. 13–137. DOI: [10.1080/00018739700101488](https://doi.org/10.1080/00018739700101488) (cited on p. 8).
- [40] J. W. Barrett, H. Garcke, and R. Nürnberg (2015). Numerical Computations of the Dynamics of Fluidic Membranes and Vesicles. *Physical Review E* **92** (5), 052704. DOI: [10.1103/PhysRevE.92.052704](https://doi.org/10.1103/PhysRevE.92.052704) (cited on pp. 8, 10).
- [41] D. Cordasco and P. Bagchi (2017). On the Shape Memory of Red Blood Cells. *Physics of Fluids* **29** (4), 041901. DOI: [10.1063/1.4979271](https://doi.org/10.1063/1.4979271) (cited on pp. 8, 9, 42).
- [42] H. Zhao, A. H. Isfahani, L. N. Olson, and J. B. Freund (2010). A Spectral Boundary Integral Method for Flowing Blood Cells. *Journal of Computational Physics* **229** (10), pp. 3726–3744. DOI: [10.1016/j.jcp.2010.01.024](https://doi.org/10.1016/j.jcp.2010.01.024) (cited on pp. 8, 15, 27, 44).
- [43] C. Dupont, A.-V. Salsac, D. Barthès-Biesel, M. Vidrascu, and P. L. Tallec (2015). Influence of Bending Resistance on the Dynamics of a Spherical Capsule in Shear Flow. *Physics of Fluids* **27** (5), 051902. DOI: [10.1063/1.4921247](https://doi.org/10.1063/1.4921247) (cited on pp. 8, 11).
- [44] J. T. Jenkins (1977). Static Equilibrium Configurations of a Model Red Blood Cell. *Journal of Mathematical Biology* **4** (2), pp. 149–169. DOI: [10.1007/BF00275981](https://doi.org/10.1007/BF00275981) (cited on pp. 8, 21).
- [45] T. W. Secomb (1988). Interaction between Bending and Tension Forces in Bilayer Membranes. *Biophysical Journal* **54** (4), pp. 743–746. DOI: [10.1016/S0006-3495\(88\)83010-8](https://doi.org/10.1016/S0006-3495(88)83010-8) (cited on p. 8).
- [46] C. Pozrikidis (2001). Effect of Membrane Bending Stiffness on the Deformation of Capsules in Simple Shear Flow. *Journal of Fluid Mechanics* **440**, pp. 269–291. DOI: [10.1017/S0022112001004657](https://doi.org/10.1017/S0022112001004657) (cited on pp. 8, 19, 24, 25, 75).
- [47] C. Pozrikidis (2003). Numerical Simulation of the Flow-Induced Deformation of Red Blood Cells. *Annals of Biomedical Engineering* **31** (10), pp. 1194–1205. DOI: [10.1114/1.1617985](https://doi.org/10.1114/1.1617985) (cited on p. 8).
- [48] C. Pozrikidis, ed. (2003). *Modeling and Simulation of Capsules and Biological Cells*. Chapman & Hall/CRC Mathematical Biology and Medicine Series. Boca Raton, FL: Chapman & Hall/CRC (cited on p. 8).
- [49] C. Pozrikidis (2005). Resting Shape and Spontaneous Membrane Curvature of Red Blood Cells. *Mathematical Medicine and Biology* **22** (1), pp. 34–52. DOI: [10.1093/imammb/dqh021](https://doi.org/10.1093/imammb/dqh021) (cited on p. 8).
- [50] D. V. Le, J. White, J. Peraire, K. M. Lim, and B. C. Khoo (2009). An Implicit Immersed Boundary Method for Three-Dimensional Fluid–membrane Interactions. *Journal of Computational Physics* **228** (22), pp. 8427–8445. DOI: [10.1016/j.jcp.2009.08.018](https://doi.org/10.1016/j.jcp.2009.08.018) (cited on pp. 8, 19, 24, 25).
- [51] L. Zhu and L. Brandt (2015). The Motion of a Deforming Capsule through a Corner. *Journal of Fluid Mechanics* **770**, pp. 374–397. DOI: [10.1017/jfm.2015.157](https://doi.org/10.1017/jfm.2015.157) (cited on pp. 8, 24, 25).

-
- [52] D. Barthès-Biesel (2016). Motion and Deformation of Elastic Capsules and Vesicles in Flow. *Annual Review of Fluid Mechanics* **48** (1), pp. 25–52. DOI: [10.1146/annurev-fluid-122414-034345](https://doi.org/10.1146/annurev-fluid-122414-034345) (cited on pp. 8, 11, 24).
- [53] T. M. Fischer (2004). Shape Memory of Human Red Blood Cells. *Biophysical Journal* **86** (5), pp. 3304–3313. DOI: [10.1016/S0006-3495\(04\)74378-7](https://doi.org/10.1016/S0006-3495(04)74378-7) (cited on p. 9).
- [54] G. H. W. Lim, M. Wortis, and R. Mukhopadhyay (2002). Stomatocyte – Discocyte – Echinocyte Sequence of the Human Red Blood Cell: Evidence for the Bilayer-Couple Hypothesis from Membrane Mechanics. *Proceedings of the National Academy of Sciences* **99** (26), pp. 16766–16769. DOI: [10.1073/pnas.202617299](https://doi.org/10.1073/pnas.202617299) (cited on pp. 9, 42).
- [55] J. Dupire, M. Socol, and A. Viallat (2012). Full Dynamics of a Red Blood Cell in Shear Flow. *Proceedings of the National Academy of Sciences* **109** (51), pp. 20808–20813. DOI: [10.1073/pnas.1210236109](https://doi.org/10.1073/pnas.1210236109) (cited on pp. 9, 42).
- [56] K.-i. Tsubota, S. Wada, and H. Liu (2014). Elastic Behavior of a Red Blood Cell with the Membrane’s Nonuniform Natural State: Equilibrium Shape, Motion Transition under Shear Flow, and Elongation during Tank-Treading Motion. *Biomechanics and Modeling in Mechanobiology* **13** (4), pp. 735–746. DOI: [10.1007/s10237-013-0530-z](https://doi.org/10.1007/s10237-013-0530-z) (cited on pp. 9, 21, 42).
- [57] D. Cordasco, A. Yazdani, and P. Bagchi (2014). Comparison of Erythrocyte Dynamics in Shear Flow under Different Stress-Free Configurations. *Physics of Fluids* **26** (4), 041902. DOI: [10.1063/1.4871300](https://doi.org/10.1063/1.4871300) (cited on pp. 9, 42).
- [58] Z. Peng, A. Mashayekh, and Q. Zhu (2014). Erythrocyte Responses in Low-Shear-Rate Flows: Effects of Non-Biconcave Stress-Free State in the Cytoskeleton. *Journal of Fluid Mechanics* **742**, pp. 96–118. DOI: [10.1017/jfm.2014.14](https://doi.org/10.1017/jfm.2014.14) (cited on pp. 9, 42, 43).
- [59] A. Viallat and M. Abkarian (2014). Red Blood Cell: From Its Mechanics to Its Motion in Shear Flow. *International Journal of Laboratory Hematology* **36** (3), pp. 237–243. DOI: [10.1111/ijlh.12233](https://doi.org/10.1111/ijlh.12233) (cited on pp. 9, 42).
- [60] J. Dupire, M. Abkarian, and A. Viallat (2015). A Simple Model to Understand the Effect of Membrane Shear Elasticity and Stress-Free Shape on the Motion of Red Blood Cells in Shear Flow. *Soft Matter* **11** (42), pp. 8372–8382. DOI: [10.1039/C5SM01407G](https://doi.org/10.1039/C5SM01407G) (cited on pp. 9, 10, 42).
- [61] L. Lanotte, J. Mauer, S. Mendez, D. A. Fedosov, J.-M. Fromental, V. Claveria, F. Nicoud, G. Gompper, and M. Abkarian (2016). Red Cells’ Dynamic Morphologies Govern Blood Shear Thinning under Microcirculatory Flow Conditions. *Proceedings of the National Academy of Sciences* **113** (47), pp. 13289–13294. DOI: [10.1073/pnas.1608074113](https://doi.org/10.1073/pnas.1608074113) (cited on pp. 9, 27, 31, 42).
- [62] M. Levant and V. Steinberg (2016). Intermediate Regime and a Phase Diagram of Red Blood Cell Dynamics in a Linear Flow. *Physical Review E* **94** (6), 062412. DOI: [10.1103/PhysRevE.94.062412](https://doi.org/10.1103/PhysRevE.94.062412) (cited on pp. 9, 10, 42, 43).
- [63] P. Janmey. “Cell Membranes and the Cytoskeleton.” In: *Structure and Dynamics of Membranes - Generic and Specific Interactions*. Ed. by R. Lipowsky and E. Sackmann. Vol. 1B. Handbook of Biological Physics 1. Amsterdam ; New York: North-Holland, (1995), pp. 805–849. DOI: [10.1016/S1383-8121\(06\)80010-2](https://doi.org/10.1016/S1383-8121(06)80010-2) (cited on p. 9).

- [64] Y. Kim, H. Shim, K. Kim, H. Park, S. Jang, and Y. Park (2014). Profiling Individual Human Red Blood Cells Using Common-Path Diffraction Optical Tomography. *Scientific Reports* **4**, 6659. DOI: [10.1038/srep06659](https://doi.org/10.1038/srep06659) (cited on p. 9).
- [65] X. Li, P. M. Vlahovska, and G. E. Karniadakis (2013). Continuum- and Particle-Based Modeling of Shapes and Dynamics of Red Blood Cells in Health and Disease. *Soft Matter* **9** (1), pp. 28–37. DOI: [10.1039/C2SM26891D](https://doi.org/10.1039/C2SM26891D) (cited on pp. 9, 27).
- [66] X. Li, M. Dao, G. Lykotrafitis, and G. E. Karniadakis (2017). Biomechanics and Biorheology of Red Blood Cells in Sickle Cell Anemia. *Journal of Biomechanics* **50** (Supplement C), pp. 34–41. DOI: [10.1016/j.jbiomech.2016.11.022](https://doi.org/10.1016/j.jbiomech.2016.11.022) (cited on p. 9).
- [67] J. Narla and N. Mohandas (2017). Red Cell Membrane Disorders. *International Journal of Laboratory Hematology* **39**, pp. 47–52. DOI: [10.1111/ijlh.12657](https://doi.org/10.1111/ijlh.12657) (cited on pp. 9, 10).
- [68] R. M. Hochmuth and R. E. Waugh (1987). Erythrocyte Membrane Elasticity and Viscosity. *Annual Review of Physiology* **49** (1), pp. 209–219. DOI: [10.1146/annurev.ph.49.030187.001233](https://doi.org/10.1146/annurev.ph.49.030187.001233) (cited on p. 9).
- [69] A. Diaz, D. Barthès-Biesel, and N. Pelekasis (2001). Effect of Membrane Viscosity on the Dynamic Response of an Axisymmetric Capsule. *Physics of Fluids* **13** (12), pp. 3835–3838. DOI: [10.1063/1.1403697](https://doi.org/10.1063/1.1403697) (cited on p. 9).
- [70] M. Dao, C. T. Lim, and S. Suresh (2003). Mechanics of the Human Red Blood Cell Deformed by Optical Tweezers. *Journal of the Mechanics and Physics of Solids* **51** (11), pp. 2259–2280. DOI: [10.1016/j.jmps.2003.09.019](https://doi.org/10.1016/j.jmps.2003.09.019) (cited on p. 9).
- [71] G. Prado, A. Farutin, C. Misbah, and L. Bureau (2015). Viscoelastic Transient of Confined Red Blood Cells. *Biophysical Journal* **108** (9), pp. 2126–2136. DOI: [10.1016/j.bpj.2015.03.046](https://doi.org/10.1016/j.bpj.2015.03.046) (cited on p. 9).
- [72] A. Yazdani and P. Bagchi (2013). Influence of Membrane Viscosity on Capsule Dynamics in Shear Flow. *Journal of Fluid Mechanics* **718**, pp. 569–595. DOI: [10.1017/jfm.2012.637](https://doi.org/10.1017/jfm.2012.637) (cited on p. 10).
- [73] H. Turlier, D. A. Fedosov, B. Audoly, T. Auth, N. S. Gov, C. Sykes, J.-F. Joanny, G. Gompper, and T. Betz (2016). Equilibrium Physics Breakdown Reveals the Active Nature of Red Blood Cell Flickering. *Nature Physics* **12** (5), pp. 513–519. DOI: [10.1038/nphys3621](https://doi.org/10.1038/nphys3621) (cited on pp. 10, 20, 21).
- [74] P. M. Vlahovska, T. Podgorski, and C. Misbah (2009). Vesicles and Red Blood Cells in Flow: From Individual Dynamics to Rheology. *Comptes Rendus Physique* **10** (8), pp. 775–789. DOI: [10.1016/j.crhy.2009.10.001](https://doi.org/10.1016/j.crhy.2009.10.001) (cited on pp. 10, 11).
- [75] M. Levant and V. Steinberg (2012). Amplification of Thermal Noise by Vesicle Dynamics. *Physical Review Letters* **109** (26), 268103. DOI: [10.1103/PhysRevLett.109.268103](https://doi.org/10.1103/PhysRevLett.109.268103) (cited on p. 10).
- [76] D. Abreu and U. Seifert (2013). Noisy Nonlinear Dynamics of Vesicles in Flow. *Physical Review Letters* **110** (23), 238103. DOI: [10.1103/PhysRevLett.110.238103](https://doi.org/10.1103/PhysRevLett.110.238103) (cited on p. 10).
- [77] S. Gekle (2016). Strongly Accelerated Margination of Active Particles in Blood Flow. *Biophysical Journal* **110** (2), pp. 514–520. DOI: [10.1016/j.bpj.2015.12.005](https://doi.org/10.1016/j.bpj.2015.12.005) (cited on pp. 10, 27).

-
- [78] C. Bächer, L. Schrack, and S. Gekle (2017). Clustering of Microscopic Particles in Constricted Blood Flow. *Physical Review Fluids* **2** (1), 013102. DOI: [10.1103/PhysRevFluids.2.013102](https://doi.org/10.1103/PhysRevFluids.2.013102) (cited on pp. 10, 27).
- [79] V. W. Linss, C. Pilgrim, and H. Feuerstein (1991). Wie Dick Ist Die Glykokalyx Des Menschlichen Erythrocyten? *Acta Histochemica* **91** (1), pp. 101–104. DOI: [10.1016/S0065-1281\(11\)80301-6](https://doi.org/10.1016/S0065-1281(11)80301-6) (cited on p. 10).
- [80] B. Neu and H. J. Meiselman (2002). Depletion-Mediated Red Blood Cell Aggregation in Polymer Solutions. *Biophysical Journal* **83** (5), pp. 2482–2490. DOI: [10.1016/S0006-3495\(02\)75259-4](https://doi.org/10.1016/S0006-3495(02)75259-4) (cited on p. 10).
- [81] C. Wagner, P. Steffen, and S. Svetina (2013). Aggregation of Red Blood Cells: From Rouleaux to Clot Formation. *Comptes Rendus Physique* **14** (6), pp. 459–469. DOI: [10.1016/j.crhy.2013.04.004](https://doi.org/10.1016/j.crhy.2013.04.004) (cited on pp. 10, 11).
- [82] O. K. Baskurt and H. J. Meiselman (2003). Blood Rheology and Hemodynamics. *Seminars in Thrombosis and Hemostasis* **29** (5), pp. 435–450. DOI: [10.1055/s-2003-44551](https://doi.org/10.1055/s-2003-44551) (cited on pp. 10, 11).
- [83] X. Li, H. Li, H.-Y. Chang, G. Lykotrafitis, and G. E. Karniadakis (2017). Computational Biomechanics of Human Red Blood Cells in Hematological Disorders. *Journal of Biomechanical Engineering* **139** (2), 021008. DOI: [10.1115/1.4035120](https://doi.org/10.1115/1.4035120) (cited on p. 10).
- [84] J. E. Smith, N. Mohandas, and S. B. Shohet (1979). Variability in Erythrocyte Deformability among Various Mammals. *American Journal of Physiology - Heart and Circulatory Physiology* **236** (5), H725–H730. DOI: [10.1152/ajpheart.1979.236.5.h725](https://doi.org/10.1152/ajpheart.1979.236.5.h725) (cited on p. 10).
- [85] O. K. Baskurt (1996). Deformability of Red Blood Cells from Different Species Studied by Resistive Pulse Shape Analysis Technique. *Biorheology* **33** (2), pp. 169–179. DOI: [10.1016/0006-355X\(96\)00014-5](https://doi.org/10.1016/0006-355X(96)00014-5) (cited on p. 10).
- [86] O. Baskurt, B. Neu, and H. Meiselman (2012). *Red Blood Cell Aggregation*. Boca Raton: CRC Press. DOI: [10.1201/b11221](https://doi.org/10.1201/b11221) (cited on pp. 10, 11, 33).
- [87] A. M. Robertson, A. Sequeira, and M. V. Kameneva. “Hemorheology.” In: *Hemodynamical Flows*. Oberwolfach Seminars 37. Birkhäuser Basel, (2008), pp. 63–120. DOI: [10.1007/978-3-7643-7806-6_2](https://doi.org/10.1007/978-3-7643-7806-6_2) (cited on pp. 10, 11).
- [88] H. Lei, D. A. Fedosov, B. Caswell, and G. E. Karniadakis (2013). Blood Flow in Small Tubes: Quantifying the Transition to the Non-Continuum Regime. *Journal of Fluid Mechanics* **722**, pp. 214–239. DOI: [10.1017/jfm.2013.91](https://doi.org/10.1017/jfm.2013.91) (cited on p. 10).
- [89] C. A. Taylor and D. A. Steinman (2010). Image-Based Modeling of Blood Flow and Vessel Wall Dynamics: Applications, Methods and Future Directions. *Annals of Biomedical Engineering* **38** (3), pp. 1188–1203. DOI: [10.1007/s10439-010-9901-0](https://doi.org/10.1007/s10439-010-9901-0) (cited on p. 10).
- [90] L. Campo-Deaño, M. S. N. Oliveira, and F. T. Pinho (2015). A Review of Computational Hemodynamics in Middle Cerebral Aneurysms and Rheological Models for Blood Flow. *Applied Mechanics Reviews* **67** (3), 030801. DOI: [10.1115/1.4028946](https://doi.org/10.1115/1.4028946) (cited on p. 10).
- [91] G. Gompper and D. A. Fedosov (2016). Modeling Microcirculatory Blood Flow: Current State and Future Perspectives. *Wiley Interdisciplinary Reviews: Systems Biology and Medicine* **8** (2), pp. 157–168. DOI: [10.1002/wsbm.1326](https://doi.org/10.1002/wsbm.1326) (cited on p. 10).

- [92] A. Rahimian, I. Lashuk, S. Veerapaneni, A. Chandramowlishwaran, D. Malhotra, L. Moon, R. Sampath, A. Shringarpure, J. Vetter, R. Vuduc, D. Zorin, and G. Biros (2010). Petascale Direct Numerical Simulation of Blood Flow on 200k Cores and Heterogeneous Architectures. In: *Proceedings of the 2010 ACM/IEEE International Conference for High Performance Computing, Networking, Storage and Analysis*. New Orleans: IEEE Computer Society. DOI: [10.1109/SC.2010.42](https://doi.org/10.1109/SC.2010.42) (cited on pp. 10, 28, 29, 44).
- [93] M. Bernaschi, M. Bisson, M. Fatica, S. Melchionna, and S. Succi (2013). Petaflop Hydrokinetic Simulations of Complex Flows on Massive GPU Clusters. *Computer Physics Communications* **184** (2), pp. 329–341. DOI: [10.1016/j.cpc.2012.09.016](https://doi.org/10.1016/j.cpc.2012.09.016) (cited on p. 10).
- [94] D. Rossinelli, Y.-H. Tang, K. Lykov, D. Alexeev, M. Bernaschi, P. Hadjidoukas, M. Bisson, W. Joubert, C. Conti, G. Karniadakis, M. Fatica, I. Pivkin, and P. Koumoutsakos (2015). The In-Silico Lab-on-a-Chip: Petascale and High-Throughput Simulations of Microfluidics at Cell Resolution. In: *Proceedings of the International Conference for High Performance Computing, Networking, Storage and Analysis*. SC '15. New York: ACM, 2:1–2:12. DOI: [10.1145/2807591.2807677](https://doi.org/10.1145/2807591.2807677) (cited on pp. 10, 27).
- [95] C. Misbah (2012). Vesicles, Capsules and Red Blood Cells under Flow. *Journal of Physics: Conference Series* **392**, 012005. DOI: [10.1088/1742-6596/392/1/012005](https://doi.org/10.1088/1742-6596/392/1/012005) (cited on p. 10).
- [96] M. V. Kameneva, M. J. Watach, and H. S. Borovetz (1999). Gender Difference in Rheologic Properties of Blood and Risk of Cardiovascular Diseases. *Clinical Hemorheology and Microcirculation* **21** (3,4), pp. 357–363 (cited on p. 10).
- [97] B. Klitzman and B. R. Duling (1979). Microvascular Hematocrit and Red Cell Flow in Resting and Contracting Striated Muscle. *American Journal of Physiology - Heart and Circulatory Physiology* **237** (4), H481–H490. DOI: [10.1152/ajpheart.1979.237.4.H481](https://doi.org/10.1152/ajpheart.1979.237.4.H481) (cited on pp. 10, 37).
- [98] S. D. House and H. H. Lipowsky (1987). Microvascular Hematocrit and Red Cell Flux in Rat Cremaster Muscle. *American Journal of Physiology - Heart and Circulatory Physiology* **252** (1), H211–H222. DOI: [10.1152/ajpheart.1987.252.1.H211](https://doi.org/10.1152/ajpheart.1987.252.1.H211) (cited on pp. 10, 37).
- [99] P. Balogh and P. Bagchi (2017). A Computational Approach to Modeling Cellular-Scale Blood Flow in Complex Geometry. *Journal of Computational Physics* **334**, pp. 280–307. DOI: [10.1016/j.jcp.2017.01.007](https://doi.org/10.1016/j.jcp.2017.01.007) (cited on pp. 10, 27).
- [100] J. B. Freund (2007). Leukocyte Margination in a Model Microvessel. *Physics of Fluids* **19** (2), 023301. DOI: [10.1063/1.2472479](https://doi.org/10.1063/1.2472479) (cited on p. 10).
- [101] A. H. G. Isfahani and J. B. Freund (2012). Forces on a Wall-Bound Leukocyte in a Small Vessel Due to Red Cells in the Blood Stream. *Biophysical Journal* **103** (7), pp. 1604–1615. DOI: [10.1016/j.bpj.2012.08.049](https://doi.org/10.1016/j.bpj.2012.08.049) (cited on p. 10).
- [102] D. A. Fedosov, J. Fornleitner, and G. Gompper (2012). Margination of White Blood Cells in Microcapillary Flow. *Physical Review Letters* **108** (2), 028104. DOI: [10.1103/PhysRevLett.108.028104](https://doi.org/10.1103/PhysRevLett.108.028104) (cited on p. 10).
- [103] D. A. Fedosov and G. Gompper (2014). White Blood Cell Margination in Microcirculation. *Soft Matter* **10** (17), pp. 2961–2970. DOI: [10.1039/C3SM52860J](https://doi.org/10.1039/C3SM52860J) (cited on pp. 10, 21).

-
- [104] N. Takeishi, Y. Imai, K. Nakaaki, T. Yamaguchi, and T. Ishikawa (2014). Leukocyte Margination at Arteriole Shear Rate. *Physiological Reports* **2** (6), e12037. DOI: [10.14814/phy2.12037](https://doi.org/10.14814/phy2.12037) (cited on p. 10).
- [105] W. Marth, S. Aland, and A. Voigt (2016). Margination of White Blood Cells: A Computational Approach by a Hydrodynamic Phase Field Model. *Journal of Fluid Mechanics* **790**, pp. 389–406. DOI: [10.1017/jfm.2016.15](https://doi.org/10.1017/jfm.2016.15) (cited on p. 10).
- [106] H. Zhao and E. S. G. Shaqfeh (2011). Shear-Induced Platelet Margination in a Microchannel. *Physical Review E* **83** (6), 061924. DOI: [10.1103/PhysRevE.83.061924](https://doi.org/10.1103/PhysRevE.83.061924) (cited on p. 10).
- [107] K. Vahidkhah, S. L. Diamond, and P. Bagchi (2014). Platelet Dynamics in Three-Dimensional Simulation of Whole Blood. *Biophysical Journal* **106** (11), pp. 2529–2540. DOI: [10.1016/j.bpj.2014.04.028](https://doi.org/10.1016/j.bpj.2014.04.028) (cited on p. 10).
- [108] T. Krüger (2016). Effect of Tube Diameter and Capillary Number on Platelet Margination and Near-Wall Dynamics. *Rheologica Acta* **55** (6), pp. 511–526. DOI: [10.1007/s00397-015-0891-6](https://doi.org/10.1007/s00397-015-0891-6) (cited on p. 10).
- [109] A. P. Spann, J. E. Campbell, S. R. Fitzgibbon, A. Rodriguez, A. P. Cap, L. H. Blackburne, and E. S. G. Shaqfeh (2016). The Effect of Hematocrit on Platelet Adhesion: Experiments and Simulations. *Biophysical Journal* **111** (3), pp. 577–588. DOI: [10.1016/j.bpj.2016.06.024](https://doi.org/10.1016/j.bpj.2016.06.024) (cited on pp. 10, 21).
- [110] A. Yazdani and G. E. Karniadakis (2016). Sub-Cellular Modeling of Platelet Transport in Blood Flow through Microchannels with Constriction. *Soft Matter* **12** (19), pp. 4339–4351. DOI: [10.1039/C6SM00154H](https://doi.org/10.1039/C6SM00154H) (cited on pp. 10, 21).
- [111] K. Rack, V. Huck, M. Hoore, D. A. Fedosov, S. W. Schneider, and G. Gompper (2017). Margination and Stretching of von Willebrand Factor in the Blood Stream Enable Adhesion. *Scientific Reports* **7** (1), 14278. DOI: [10.1038/s41598-017-14346-4](https://doi.org/10.1038/s41598-017-14346-4) (cited on p. 10).
- [112] O. Forouzan, X. Yang, J. M. Sosa, J. M. Burns, and S. S. Shevkoplyas (2012). Spontaneous Oscillations of Capillary Blood Flow in Artificial Microvascular Networks. *Microvascular Research* **84** (2), pp. 123–132. DOI: [10.1016/j.mvr.2012.06.006](https://doi.org/10.1016/j.mvr.2012.06.006) (cited on p. 10).
- [113] P. Balogh and P. Bagchi (2017). Direct Numerical Simulation of Cellular-Scale Blood Flow in 3D Microvascular Networks. *Biophysical Journal* **113** (12), pp. 2815–2826. DOI: [10.1016/j.bpj.2017.10.020](https://doi.org/10.1016/j.bpj.2017.10.020) (cited on p. 10).
- [114] S. Weinbaum, J. M. Tarbell, and E. R. Damiano (2007). The Structure and Function of the Endothelial Glycocalyx Layer. *Annual Review of Biomedical Engineering* **9** (1), pp. 121–167. DOI: [10.1146/annurev.bioeng.9.060906.151959](https://doi.org/10.1146/annurev.bioeng.9.060906.151959) (cited on p. 10).
- [115] T. W. Secomb, R. Hsu, and A. R. Pries (2001). Motion of Red Blood Cells in a Capillary with an Endothelial Surface Layer: Effect of Flow Velocity. *American Journal of Physiology - Heart and Circulatory Physiology* **281** (2), H629–H636. DOI: [10.1152/ajpheart.2001.281.2.h629](https://doi.org/10.1152/ajpheart.2001.281.2.h629) (cited on p. 11).
- [116] D. S. Hariprasad and T. W. Secomb (2012). Motion of Red Blood Cells near Microvessel Walls: Effects of a Porous Wall Layer. *Journal of Fluid Mechanics* **705**, pp. 195–212. DOI: [10.1017/jfm.2012.102](https://doi.org/10.1017/jfm.2012.102) (cited on p. 11).

- [117] L. Lanotte, G. Tomaiuolo, C. Misbah, L. Bureau, and S. Guido (2014). Red Blood Cell Dynamics in Polymer Brush-Coated Microcapillaries: A Model of Endothelial Glycocalyx in Vitro. *Biomicrofluidics* **8** (1), 014104. DOI: [10.1063/1.4863723](https://doi.org/10.1063/1.4863723) (cited on p. 11).
- [118] D. Tsvirkun, A. Grichine, A. Duperray, C. Misbah, and L. Bureau (2017). Microvasculature on a Chip: Study of the Endothelial Surface Layer and the Flow Structure of Red Blood Cells. *Scientific Reports* **7**, 45036. DOI: [10.1038/srep45036](https://doi.org/10.1038/srep45036) (cited on p. 11).
- [119] D. Katanov, G. Gompper, and D. A. Fedosov (2015). Microvascular Blood Flow Resistance: Role of Red Blood Cell Migration and Dispersion. *Microvascular Research* **99**, pp. 57–66. DOI: [10.1016/j.mvr.2015.02.006](https://doi.org/10.1016/j.mvr.2015.02.006) (cited on pp. 11, 21, 31).
- [120] J. B. Freund and J. Vermot (2014). The Wall-Stress Footprint of Blood Cells Flowing in Microvessels. *Biophysical Journal* **106** (3), pp. 752–762. DOI: [10.1016/j.bpj.2013.12.020](https://doi.org/10.1016/j.bpj.2013.12.020) (cited on p. 11).
- [121] M. Brust, O. Aouane, M. Thiébaud, D. Flormann, C. Verdier, L. Kaestner, M. W. Laschke, H. Selmi, A. Benyoussef, T. Podgorski, G. Coupier, C. Misbah, and C. Wagner (2014). The Plasma Protein Fibrinogen Stabilizes Clusters of Red Blood Cells in Microcapillary Flows. *Scientific Reports* **4**, 4348. DOI: [10.1038/srep04348](https://doi.org/10.1038/srep04348) (cited on p. 11).
- [122] V. Clavería, O. Aouane, M. Thiébaud, M. Abkarian, G. Coupier, C. Misbah, T. John, and C. Wagner (2016). Clusters of Red Blood Cells in Microcapillary Flow: Hydrodynamic versus Macromolecule Induced Interaction. *Soft Matter* **12**, pp. 8235–8245. DOI: [10.1039/C6SM01165A](https://doi.org/10.1039/C6SM01165A) (cited on pp. 11, 43).
- [123] D. Flormann, O. Aouane, L. Kaestner, C. Ruloff, C. Misbah, T. Podgorski, and C. Wagner (2017). The Buckling Instability of Aggregating Red Blood Cells. *Scientific Reports* **7** (1), 7928. DOI: [10.1038/s41598-017-07634-6](https://doi.org/10.1038/s41598-017-07634-6) (cited on p. 11).
- [124] S. Chien, S. Usami, H. M. Taylor, J. L. Lundberg, and M. I. Gregersen (1966). Effects of Hematocrit and Plasma Proteins on Human Blood Rheology at Low Shear Rates. *Journal of Applied Physiology* **21** (1), pp. 81–87. DOI: [10.1152/jappl.1966.21.1.81](https://doi.org/10.1152/jappl.1966.21.1.81) (cited on p. 11).
- [125] L. R. Huang, E. C. Cox, R. H. Austin, and J. C. Sturm (2004). Continuous Particle Separation Through Deterministic Lateral Displacement. *Science* **304** (5673), pp. 987–990. DOI: [10.1126/science.1094567](https://doi.org/10.1126/science.1094567) (cited on p. 11).
- [126] T. Krüger, D. Holmes, and P. V. Coveney (2014). Deformability-Based Red Blood Cell Separation in Deterministic Lateral Displacement Devices—A Simulation Study. *Biomicrofluidics* **8** (5), 054114. DOI: [10.1063/1.4897913](https://doi.org/10.1063/1.4897913) (cited on p. 11).
- [127] Z. Zhang, E. Henry, G. Gompper, and D. A. Fedosov (2015). Behavior of Rigid and Deformable Particles in Deterministic Lateral Displacement Devices with Different Post Shapes. *The Journal of Chemical Physics* **143** (24), 243145. DOI: [10.1063/1.4937171](https://doi.org/10.1063/1.4937171) (cited on pp. 11, 21).
- [128] A. Ghaemi, A. Philipp, A. Bauer, K. Last, A. Fery, and S. Gekle (2016). Mechanical Behaviour of Micro-Capsules and Their Rupture under Compression. *Chemical Engineering Science* **142**, pp. 236–243. DOI: [10.1016/j.ces.2015.11.002](https://doi.org/10.1016/j.ces.2015.11.002) (cited on p. 11).
- [129] D. Abreu, M. Levant, V. Steinberg, and U. Seifert (2014). Fluid Vesicles in Flow. *Advances in Colloid and Interface Science* **208**, pp. 129–141. DOI: [10.1016/j.cis.2014.02.004](https://doi.org/10.1016/j.cis.2014.02.004) (cited on p. 11).

-
- [130] B. Kaoui, G. Biroso, and C. Misbah (2009). Why Do Red Blood Cells Have Asymmetric Shapes Even in a Symmetric Flow? *Physical Review Letters* **103** (18), 188101. DOI: [10.1103/PhysRevLett.103.188101](https://doi.org/10.1103/PhysRevLett.103.188101) (cited on pp. 11, 31).
- [131] C. Pozrikidis (1992). *Boundary Integral and Singularity Methods for Linearized Viscous Flow*. Cambridge Texts in Applied Mathematics 8. New York: Cambridge University Press. DOI: [10.1017/CB09780511624124](https://doi.org/10.1017/CB09780511624124) (cited on pp. 13–15, 19, 27, 28).
- [132] M. Kohr and I. Pop (2004). *Viscous Incompressible Flow for Low Reynolds Numbers*. Ed. by C. A. Brebbia. Advances in Boundary Elements 16. Southampton: WIT Press (cited on pp. 13, 28).
- [133] S. Kim and S. J. Karrila (1991). *Microhydrodynamics: Principles and Selected Applications*. Boston: Butterworth-Heinemann (cited on pp. 13, 15, 28).
- [134] C. Pozrikidis (2001). Interfacial Dynamics for Stokes Flow. *Journal of Computational Physics* **169** (2), pp. 250–301. DOI: [10.1006/jcph.2000.6582](https://doi.org/10.1006/jcph.2000.6582) (cited on pp. 13, 15, 27, 28, 37).
- [135] G. K. Youngren and A. Acrivos (1975). Stokes Flow Past a Particle of Arbitrary Shape: A Numerical Method of Solution. *Journal of Fluid Mechanics* **69** (2), pp. 377–403. DOI: [10.1017/S0022112075001486](https://doi.org/10.1017/S0022112075001486) (cited on pp. 13, 27).
- [136] F. K. G. Odqvist (1930). Über die Randwertaufgaben der Hydrodynamik zäher Flüssigkeiten. *Mathematische Zeitschrift* **32** (1), pp. 329–375. DOI: [10.1007/BF01194638](https://doi.org/10.1007/BF01194638) (cited on pp. 13, 17).
- [137] O. A. Ladyzhenskaya (1969). *The Mathematical Theory of Viscous Incompressible Flow*. 2nd ed. New York: Gordon and Breach (cited on p. 13).
- [138] Q. Nie, S. Tanveer, T. F. Dupont, and X. Li (2002). Singularity Formation in Free-Surface Stokes Flows. In: *Recent Advances in Numerical Methods for Partial Differential Equations and Applications*. Ed. by X. Feng and T. P. Schulze. Vol. 306. Contemporary Mathematics. Knoxville, pp. 147–165. DOI: [10.1090/conm/306](https://doi.org/10.1090/conm/306) (cited on p. 13).
- [139] X. Sun and X. Li (2010). A Spectrally Accurate Boundary Integral Method for Interfacial Velocities in Two-Dimensional Stokes Flow. *Communications in Computational Physics* **8** (4), pp. 933–946. DOI: [10.4208/cicp.190909.090310a](https://doi.org/10.4208/cicp.190909.090310a) (cited on p. 13).
- [140] F. R. Cunha and M. Loewenberg (2003). A Study of Emulsion Expansion by a Boundary Integral Method. *Mechanics Research Communications* **30** (6), pp. 639–649. DOI: [10.1016/S0093-6413\(03\)00068-5](https://doi.org/10.1016/S0093-6413(03)00068-5) (cited on p. 13).
- [141] F. R. Cunha, A. J. DE Sousa, and M. Loewenberg (2003). A Mathematical Formulation of the Boundary Integral Equations for a Compressible Stokes Flow. *Computational and Applied Mathematics* **22** (1), pp. 53–73 (cited on p. 13).
- [142] C. Pozrikidis (1996). Computation of Periodic Green’s Functions of Stokes Flow. *Journal of Engineering Mathematics* **30** (1-2), pp. 79–96. DOI: [10.1007/BF00118824](https://doi.org/10.1007/BF00118824) (cited on pp. 15, 27).
- [143] R. Kress (2014). *Linear Integral Equations*. 3rd ed. Applied Mathematical Sciences 82. New York: Springer. DOI: [10.1007/978-1-4614-9593-2](https://doi.org/10.1007/978-1-4614-9593-2) (cited on p. 16).
- [144] Z. Y. Luo, F. Xu, T. J. Lu, and B. F. Bai (2010). Direct Numerical Simulation of Single Leukocyte Deformation in Microchannel Flow for Disease Diagnosis. *Journal of Medical Systems* **35** (5), pp. 869–876. DOI: [10.1007/s10916-010-9502-3](https://doi.org/10.1007/s10916-010-9502-3) (cited on p. 19).

- [145] D. Salac and M. Miksis (2011). A Level Set Projection Model of Lipid Vesicles in General Flows. *Journal of Computational Physics* **230** (22), pp. 8192–8215. DOI: [10.1016/j.jcp.2011.07.019](https://doi.org/10.1016/j.jcp.2011.07.019) (cited on p. 19).
- [146] A. Laadhari, P. Saramito, and C. Misbah (2012). Vesicle Tumbling Inhibited by Inertia. *Physics of Fluids* **24** (3), 031901. DOI: [10.1063/1.3690862](https://doi.org/10.1063/1.3690862) (cited on p. 19).
- [147] A. Laadhari, P. Saramito, C. Misbah, and G. Székely (2017). Fully Implicit Methodology for the Dynamics of Biomembranes and Capillary Interfaces by Combining the Level Set and Newton Methods. *Journal of Computational Physics* **343**, pp. 271–299. DOI: [10.1016/j.jcp.2017.04.019](https://doi.org/10.1016/j.jcp.2017.04.019) (cited on p. 19).
- [148] T. Biben, K. Kassner, and C. Misbah (2005). Phase-Field Approach to Three-Dimensional Vesicle Dynamics. *Physical Review E* **72** (4), 041921. DOI: [10.1103/PhysRevE.72.041921](https://doi.org/10.1103/PhysRevE.72.041921) (cited on p. 19).
- [149] Q. Du and J. Zhang (2008). Adaptive Finite Element Method for a Phase Field Bending Elasticity Model of Vesicle Membrane Deformations. *SIAM Journal on Scientific Computing* **30** (3), pp. 1634–1657. DOI: [10.1137/060656449](https://doi.org/10.1137/060656449) (cited on p. 19).
- [150] G. Boedec, M. Leonetti, and M. Jaeger (2011). 3D Vesicle Dynamics Simulations with a Linearly Triangulated Surface. *Journal of Computational Physics* **230** (4), pp. 1020–1034. DOI: [10.1016/j.jcp.2010.10.021](https://doi.org/10.1016/j.jcp.2010.10.021) (cited on pp. 19, 21).
- [151] T. Biben, A. Farutin, and C. Misbah (2011). Three-Dimensional Vesicles under Shear Flow: Numerical Study of Dynamics and Phase Diagram. *Physical Review E* **83** (3), 031921. DOI: [10.1103/PhysRevE.83.031921](https://doi.org/10.1103/PhysRevE.83.031921) (cited on pp. 19, 21, 29).
- [152] A. Yazdani and P. Bagchi (2012). Three-Dimensional Numerical Simulation of Vesicle Dynamics Using a Front-Tracking Method. *Physical Review E* **85** (5), 056308. DOI: [10.1103/PhysRevE.85.056308](https://doi.org/10.1103/PhysRevE.85.056308) (cited on p. 19).
- [153] I. R. Suárez, C. Leidy, G. Téllez, G. Gay, and A. Gonzalez-Mancera (2013). Slow Sedimentation and Deformability of Charged Lipid Vesicles. *PLoS ONE* **8** (7), e68309. Ed. by T. W. Secomb. DOI: [10.1371/journal.pone.0068309](https://doi.org/10.1371/journal.pone.0068309) (cited on pp. 19, 21).
- [154] Y. Seol, W.-F. Hu, Y. Kim, and M.-C. Lai (2016). An Immersed Boundary Method for Simulating Vesicle Dynamics in Three Dimensions. *Journal of Computational Physics* **322**, pp. 125–141. DOI: [10.1016/j.jcp.2016.06.035](https://doi.org/10.1016/j.jcp.2016.06.035) (cited on p. 19).
- [155] S. Ramanujan and C. Pozrikidis (1998). Deformation of Liquid Capsules Enclosed by Elastic Membranes in Simple Shear Flow: Large Deformations and the Effect of Fluid Viscosities. *Journal of Fluid Mechanics* **361**, pp. 117–143. DOI: [10.1017/S0022112098008714](https://doi.org/10.1017/S0022112098008714) (cited on p. 19).
- [156] J. Walter, A.-V. Salsac, D. Barthès-Biesel, and P. Le Tallec (2010). Coupling of Finite Element and Boundary Integral Methods for a Capsule in a Stokes Flow. *International Journal for Numerical Methods in Engineering* **83** (7), pp. 829–850. DOI: [10.1002/nme.2859](https://doi.org/10.1002/nme.2859) (cited on p. 19).
- [157] D.-V. Le and S. T. Wong (2011). A Front-Tracking Method with Catmull–Clark Subdivision Surfaces for Studying Liquid Capsules Enclosed by Thin Shells in Shear Flow. *Journal of Computational Physics* **230** (9), pp. 3538–3555. DOI: [10.1016/j.jcp.2011.01.047](https://doi.org/10.1016/j.jcp.2011.01.047) (cited on pp. 19, 24).

-
- [158] D.-V. Le (2010). Subdivision Elements for Large Deformation of Liquid Capsules Enclosed by Thin Shells. *Computer Methods in Applied Mechanics and Engineering* **199** (37-40), pp. 2622–2632. DOI: [10.1016/j.cma.2010.04.014](https://doi.org/10.1016/j.cma.2010.04.014) (cited on pp. 19, 22).
- [159] J. Gounley, G. Boedec, M. Jaeger, and M. Leonetti (2016). Influence of Surface Viscosity on Droplets in Shear Flow. *Journal of Fluid Mechanics* **791**, pp. 464–494. DOI: [10.1017/jfm.2016.39](https://doi.org/10.1017/jfm.2016.39) (cited on pp. 19, 22).
- [160] W.-X. Huang, C. B. Chang, and H. J. Sung (2012). Three-Dimensional Simulation of Elastic Capsules in Shear Flow by the Penalty Immersed Boundary Method. *Journal of Computational Physics* **231** (8), pp. 3340–3364. DOI: [10.1016/j.jcp.2012.01.006](https://doi.org/10.1016/j.jcp.2012.01.006) (cited on pp. 19, 24, 25).
- [161] F. Feng and W. S. Klug (2006). Finite Element Modeling of Lipid Bilayer Membranes. *Journal of Computational Physics* **220** (1), pp. 394–408. DOI: [10.1016/j.jcp.2006.05.023](https://doi.org/10.1016/j.jcp.2006.05.023) (cited on p. 19).
- [162] A. P. Spann, H. Zhao, and E. S. G. Shaqfeh (2014). Loop Subdivision Surface Boundary Integral Method Simulations of Vesicles at Low Reduced Volume Ratio in Shear and Extensional Flow. *Physics of Fluids* **26** (3), 031902. DOI: [10.1063/1.4869307](https://doi.org/10.1063/1.4869307) (cited on p. 19).
- [163] H. Zhao, A. P. Spann, and E. S. G. Shaqfeh (2011). The Dynamics of a Vesicle in a Wall-Bound Shear Flow. *Physics of Fluids* **23** (12), 121901. DOI: [10.1063/1.3669440](https://doi.org/10.1063/1.3669440) (cited on p. 19).
- [164] H. Zhao and E. S. G. Shaqfeh (2013). The Dynamics of a Non-Dilute Vesicle Suspension in a Simple Shear Flow. *Journal of Fluid Mechanics* **725**, pp. 709–731. DOI: [10.1017/jfm.2013.207](https://doi.org/10.1017/jfm.2013.207) (cited on p. 19).
- [165] G. Boedec, M. Leonetti, and M. Jaeger (2017). Isogeometric FEM-BEM Simulations of Drop, Capsule and Vesicle Dynamics in Stokes Flow. *Journal of Computational Physics* **342**, pp. 117–138. DOI: [10.1016/j.jcp.2017.04.024](https://doi.org/10.1016/j.jcp.2017.04.024) (cited on pp. 19, 22).
- [166] M. Kraus, W. Wintz, U. Seifert, and R. Lipowsky (1996). Fluid Vesicles in Shear Flow. *Physical Review Letters* **77** (17), pp. 3685–3688. DOI: [10.1103/PhysRevLett.77.3685](https://doi.org/10.1103/PhysRevLett.77.3685) (cited on p. 20).
- [167] T. Krüger, F. Varnik, and D. Raabe (2011). Efficient and Accurate Simulations of Deformable Particles Immersed in a Fluid Using a Combined Immersed Boundary Lattice Boltzmann Finite Element Method. *Computers & Mathematics with Applications* **61** (12), pp. 3485–3505. DOI: [10.1016/j.camwa.2010.03.057](https://doi.org/10.1016/j.camwa.2010.03.057) (cited on pp. 20, 27).
- [168] H. Zhao, E. S. G. Shaqfeh, and V. Narsimhan (2012). Shear-Induced Particle Migration and Margination in a Cellular Suspension. *Physics of Fluids* **24** (1), 011902. DOI: [10.1063/1.3677935](https://doi.org/10.1063/1.3677935) (cited on pp. 20, 21, 28).
- [169] M. Meyer, M. Desbrun, P. Schröder, and A. H. Barr. “Discrete Differential-Geometry Operators for Triangulated 2-Manifolds.” In: *Visualization and Mathematics III*. Ed. by H.-C. Hege and K. Polthier. Mathematics and Visualization 3. Berlin, Heidelberg: Springer, (2003), pp. 35–57. DOI: [10.1007/978-3-662-05105-4_2](https://doi.org/10.1007/978-3-662-05105-4_2) (cited on pp. 20, 21).
- [170] G. Xu (2004). Discrete Laplace–Beltrami Operators and Their Convergence. *Computer Aided Geometric Design* **21** (8), pp. 767–784. DOI: [10.1016/j.cagd.2004.07.007](https://doi.org/10.1016/j.cagd.2004.07.007) (cited on p. 20).

- [171] M. Deserno (2015). Fluid Lipid Membranes: From Differential Geometry to Curvature Stresses. *Chemistry and Physics of Lipids* **185**, pp. 11–45. DOI: [10.1016/j.chemphyslip.2014.05.001](https://doi.org/10.1016/j.chemphyslip.2014.05.001) (cited on pp. 20, 21).
- [172] O.-Y. Zhong-Can and W. Helfrich (1989). Bending Energy of Vesicle Membranes: General Expressions for the First, Second, and Third Variation of the Shape Energy and Applications to Spheres and Cylinders. *Physical Review A* **39** (10), pp. 5280–5288. DOI: [10.1103/PhysRevA.39.5280](https://doi.org/10.1103/PhysRevA.39.5280) (cited on p. 21).
- [173] A. Laadhari, C. Misbah, and P. Saramito (2010). On the Equilibrium Equation for a Generalized Biological Membrane Energy by Using a Shape Optimization Approach. *Physica D: Nonlinear Phenomena* **239** (16), pp. 1567–1572. DOI: [10.1016/j.physd.2010.04.001](https://doi.org/10.1016/j.physd.2010.04.001) (cited on p. 21).
- [174] J. T. Jenkins (1977). The Equations of Mechanical Equilibrium of a Model Membrane. *SIAM Journal on Applied Mathematics* **32** (4), pp. 755–764. DOI: [10.1137/0132063](https://doi.org/10.1137/0132063) (cited on p. 21).
- [175] D. J. Steigmann (1999). Fluid Films with Curvature Elasticity. *Archive for Rational Mechanics and Analysis* **150** (2), pp. 127–152. DOI: [10.1007/s002050050183](https://doi.org/10.1007/s002050050183) (cited on p. 21).
- [176] R. A. Sauer, T. X. Duong, K. K. Mandadapu, and D. J. Steigmann (2017). A Stabilized Finite Element Formulation for Liquid Shells and Its Application to Lipid Bilayers. *Journal of Computational Physics* **330**, pp. 436–466. DOI: [10.1016/j.jcp.2016.11.004](https://doi.org/10.1016/j.jcp.2016.11.004) (cited on p. 21).
- [177] P. M. Naghdi. “The Theory of Shells and Plates.” In: *Linear Theories of Elasticity and Thermoelasticity: Linear and Nonlinear Theories of Rods, Plates, and Shells*. Ed. by C. Truesdell. Mechanics of Solids 2. Springer Berlin Heidelberg, (1973), pp. 425–640. DOI: [10.1007/978-3-662-39776-3_5](https://doi.org/10.1007/978-3-662-39776-3_5) (cited on p. 21).
- [178] Y. Kantor and D. R. Nelson (1987). Phase Transitions in Flexible Polymeric Surfaces. *Physical Review A* **36** (8), pp. 4020–4032. DOI: [10.1103/PhysRevA.36.4020](https://doi.org/10.1103/PhysRevA.36.4020) (cited on p. 21).
- [179] G. Gompper and D. M. Kroll (1996). Random Surface Discretizations and the Renormalization of the Bending Rigidity. *Journal de Physique I France* **6** (10), pp. 1305–1320. DOI: [10.1051/jp1:1996246](https://doi.org/10.1051/jp1:1996246) (cited on p. 21).
- [180] S. Komura, K. Tamura, and T. Kato (2005). Buckling of Spherical Shells Adhering onto a Rigid Substrate. *The European Physical Journal E* **18** (3), pp. 343–358. DOI: [10.1140/epje/e2005-00038-5](https://doi.org/10.1140/epje/e2005-00038-5) (cited on p. 21).
- [181] J. Li, M. Dao, C. T. Lim, and S. Suresh (2005). Spectrin-Level Modeling of the Cytoskeleton and Optical Tweezers Stretching of the Erythrocyte. *Biophysical Journal* **88** (5), pp. 3707–3719. DOI: [10.1529/biophysj.104.047332](https://doi.org/10.1529/biophysj.104.047332) (cited on p. 21).
- [182] I. V. Pivkin and G. E. Karniadakis (2008). Accurate Coarse-Grained Modeling of Red Blood Cells. *Physical Review Letters* **101** (11), 118105. DOI: [10.1103/PhysRevLett.101.118105](https://doi.org/10.1103/PhysRevLett.101.118105) (cited on pp. 21, 27).
- [183] W. Pan, B. Caswell, and G. E. Karniadakis (2010). A Low-Dimensional Model for the Red Blood Cell. *Soft Matter* **6** (18), pp. 4366–4376. DOI: [10.1039/C0SM00183J](https://doi.org/10.1039/C0SM00183J) (cited on p. 21).

-
- [184] W. Pan, D. A. Fedosov, B. Caswell, and G. E. Karniadakis (2011). Predicting Dynamics and Rheology of Blood Flow: A Comparative Study of Multiscale and Low-Dimensional Models of Red Blood Cells. *Microvascular Research* **82** (2), pp. 163–170. DOI: [10.1016/j.mvr.2011.05.006](https://doi.org/10.1016/j.mvr.2011.05.006) (cited on p. 21).
- [185] D. A. Fedosov, B. Caswell, and G. E. Karniadakis. “Dissipative Particle Dynamics Modeling of Red Blood Cells.” In: *Computational Hydrodynamics of Capsules and Biological Cells*. Chapman & Hall/CRC Mathematical and Computational Biology Series. CRC Press, (2010), pp. 183–218. DOI: [10.1201/EBK1439820056-c6](https://doi.org/10.1201/EBK1439820056-c6) (cited on pp. 21, 27).
- [186] D. A. Fedosov, W. Pan, B. Caswell, G. Gompper, and G. E. Karniadakis (2011). Predicting Human Blood Viscosity in Silico. *Proceedings of the National Academy of Sciences* **108** (29), pp. 11772–11777. DOI: [10.1073/pnas.1101210108](https://doi.org/10.1073/pnas.1101210108) (cited on pp. 21, 31).
- [187] K.-i. Tsubota (2014). Short Note on the Bending Models for a Membrane in Capsule Mechanics: Comparison between Continuum and Discrete Models. *Journal of Computational Physics* **277**, pp. 320–328. DOI: [10.1016/j.jcp.2014.08.007](https://doi.org/10.1016/j.jcp.2014.08.007) (cited on pp. 21, 24, 25).
- [188] R. Kusters, T. van der Heijden, B. Kaoui, J. Harting, and C. Storm (2014). Forced Transport of Deformable Containers through Narrow Constrictions. *Physical Review E* **90** (3), 033006. DOI: [10.1103/PhysRevE.90.033006](https://doi.org/10.1103/PhysRevE.90.033006) (cited on p. 21).
- [189] K. Müller, D. A. Fedosov, and G. Gompper (2014). Margination of Micro- and Nano-Particles in Blood Flow and Its Effect on Drug Delivery. *Scientific Reports* **4**, 4871. DOI: [10.1038/srep04871](https://doi.org/10.1038/srep04871) (cited on pp. 21, 36, 39).
- [190] K. Lykov, X. Li, H. Lei, I. V. Pivkin, and G. E. Karniadakis (2015). Inflow/Outflow Boundary Conditions for Particle-Based Blood Flow Simulations: Application to Arterial Bifurcations and Trees. *PLOS Computational Biology* **11** (8), e1004410. DOI: [10.1371/journal.pcbi.1004410](https://doi.org/10.1371/journal.pcbi.1004410) (cited on p. 21).
- [191] K. Müller, D. A. Fedosov, and G. Gompper (2016). Understanding Particle Margination in Blood Flow – A Step toward Optimized Drug Delivery Systems. *Medical Engineering and Physics* **38** (1), pp. 2–10. DOI: [10.1016/j.medengphy.2015.08.009](https://doi.org/10.1016/j.medengphy.2015.08.009) (cited on pp. 21, 36, 39).
- [192] M. Mehrabadi, D. N. Ku, and C. K. Aidun (2016). Effects of Shear Rate, Confinement, and Particle Parameters on Margination in Blood Flow. *Physical Review E* **93** (2), 023109. DOI: [10.1103/PhysRevE.93.023109](https://doi.org/10.1103/PhysRevE.93.023109) (cited on p. 21).
- [193] G. Boedec, M. Jaeger, and M. Leonetti (2012). Settling of a Vesicle in the Limit of Quasispherical Shapes. *Journal of Fluid Mechanics* **690**, pp. 227–261. DOI: [10.1017/jfm.2011.427](https://doi.org/10.1017/jfm.2011.427) (cited on p. 21).
- [194] A. Farutin and C. Misbah (2012). Squaring, Parity Breaking, and S Tumbling of Vesicles under Shear Flow. *Physical Review Letters* **109** (24), 248106. DOI: [10.1103/PhysRevLett.109.248106](https://doi.org/10.1103/PhysRevLett.109.248106) (cited on p. 21).
- [195] K. Sinha and M. D. Graham (2015). Dynamics of a Single Red Blood Cell in Simple Shear Flow. *Physical Review E* **92** (4), 042710. DOI: [10.1103/PhysRevE.92.042710](https://doi.org/10.1103/PhysRevE.92.042710) (cited on pp. 21, 24, 28, 43).
- [196] A. Daddi-Moussa-Ider, A. Guckenberger, and S. Gekle (2016). Long-Lived Anomalous Thermal Diffusion Induced by Elastic Cell Membranes on Nearby Particles. *Physical Review E* **93** (1), 012612. DOI: [10.1103/PhysRevE.93.012612](https://doi.org/10.1103/PhysRevE.93.012612) (cited on pp. 21, 28, 30, 78).

- [197] A. Daddi-Moussa-Ider, A. Guckenberger, and S. Gekle (2016). Particle Mobility between Two Planar Elastic Membranes: Brownian Motion and Membrane Deformation. *Physics of Fluids* **28** (7), 071903. DOI: [10.1063/1.4955013](https://doi.org/10.1063/1.4955013) (cited on pp. 21, 28, 30, 78).
- [198] S. Bogner, U. Rüde, and J. Harting (2016). Curvature Estimation from a Volume-of-Fluid Indicator Function for the Simulation of Surface Tension and Wetting with a Free-Surface Lattice Boltzmann Method. *Physical Review E* **93** (4), 043302. DOI: [10.1103/PhysRevE.93.043302](https://doi.org/10.1103/PhysRevE.93.043302) (cited on p. 21).
- [199] M. Belkin, J. Sun, and Y. Wang (2008). Discrete Laplace Operator on Meshed Surfaces. In: *SCG '08: Proceedings of the Twenty-Fourth Annual Symposium on Computational Geometry*. Maryland: ACM, pp. 278–287. DOI: [10.1145/1377676.1377725](https://doi.org/10.1145/1377676.1377725) (cited on p. 22).
- [200] C. T. Loop (1987). Smooth Subdivision Surfaces Based on Triangles. Master thesis. Utah, USA: University of Utah (cited on p. 22).
- [201] F. Cirak, M. Ortiz, and P. Schröder (2000). Subdivision Surfaces: A New Paradigm for Thin-Shell Finite-Element Analysis. *International Journal for Numerical Methods in Engineering* **47** (12), pp. 2039–2072. DOI: [10.1002/\(SICI\)1097-0207\(20000430\)47:12<2039::AID-NME872>3.0.CO;2-1](https://doi.org/10.1002/(SICI)1097-0207(20000430)47:12<2039::AID-NME872>3.0.CO;2-1) (cited on p. 22).
- [202] P.-O. Persson, M. J. Aftosmis, and R. Haimes. “On the Use of Loop Subdivision Surfaces for Surrogate Geometry.” In: *Proceedings of the 15th International Meshing Roundtable*. Ed. by P. P. Pébay. Springer Berlin Heidelberg, (2006), pp. 375–392. DOI: [10.1007/978-3-540-34958-7_22](https://doi.org/10.1007/978-3-540-34958-7_22) (cited on p. 22).
- [203] C. de Loubens, J. Deschamps, G. Boedec, and M. Leonetti (2015). Stretching of Capsules in an Elongation Flow, a Route to Constitutive Law. *Journal of Fluid Mechanics* **767** (R3). DOI: [10.1017/jfm.2015.69](https://doi.org/10.1017/jfm.2015.69) (cited on p. 22).
- [204] M. Wardetzky, S. Mathur, F. Kälberer, and E. Grinspun (2007). Discrete Laplace Operators: No Free Lunch. In: *SGP '07 Proceedings of the Fifth Eurographics Symposium on Geometry Processing*. Ed. by A. Belyaev and M. Garland. SGP '07. Barcelona: Eurographics Association, pp. 33–37 (cited on p. 23).
- [205] D. V. Le (2010). Effect of Bending Stiffness on the Deformation of Liquid Capsules Enclosed by Thin Shells in Shear Flow. *Physical Review E* **82** (1), 016318. DOI: [10.1103/PhysRevE.82.016318](https://doi.org/10.1103/PhysRevE.82.016318) (cited on pp. 24, 25, 75).
- [206] P. R. Zarda, S. Chien, and R. Skalak (1977). Elastic Deformations of Red Blood Cells. *Journal of Biomechanics* **10** (4), pp. 211–221. DOI: [10.1016/0021-9290\(77\)90044-6](https://doi.org/10.1016/0021-9290(77)90044-6) (cited on p. 25).
- [207] T. Krüger, B. Kaoui, and J. Harting (2014). Interplay of Inertia and Deformability on Rheological Properties of a Suspension of Capsules. *Journal of Fluid Mechanics* **751**, pp. 725–745. DOI: [10.1017/jfm.2014.315](https://doi.org/10.1017/jfm.2014.315) (cited on p. 25).
- [208] S. Succi (2001). *The Lattice Boltzmann Equation for Fluid Dynamics and Beyond*. Ed. by G. H. Golub, R. Jeltsch, W. A. Light, and E. Süli. Numerical Mathematics and Scientific Computation. Oxford: Clarendon Press (cited on p. 27).
- [209] B. Dünweg and A. J. C. Ladd. “Lattice Boltzmann Simulations of Soft Matter Systems.” In: *Advanced Computer Simulation Approaches for Soft Matter Sciences III*. Ed. by P. C. Holm and P. K. Kremer. Advances in Polymer Science 221. Springer Berlin Heidelberg, (2009), pp. 89–166. DOI: [10.1007/978-3-540-87706-6_2](https://doi.org/10.1007/978-3-540-87706-6_2) (cited on p. 27).

-
- [210] A. Arnold, O. Lenz, S. Kesselheim, R. Weeber, F. Fahrenberger, D. Roehm, P. Košovan, and C. Holm. “ESPResSo 3.1: Molecular Dynamics Software for Coarse-Grained Models.” In: *Meshfree Methods for Partial Differential Equations VI*. Ed. by M. Griebel and M. A. Schweitzer. Lecture Notes in Computational Science and Engineering 89. Berlin, Heidelberg: Springer, (2013), pp. 1–23. DOI: [10.1007/978-3-642-32979-1_1](https://doi.org/10.1007/978-3-642-32979-1_1) (cited on p. 27).
- [211] D. A. Reasor, J. R. Clausen, and C. K. Aidun (2012). Coupling the Lattice-Boltzmann and Spectrin-Link Methods for the Direct Numerical Simulation of Cellular Blood Flow. *International Journal for Numerical Methods in Fluids* **68** (6), pp. 767–781. DOI: [10.1002/flid.2534](https://doi.org/10.1002/flid.2534) (cited on p. 27).
- [212] B. Kaoui and J. Harting (2016). Two-Dimensional Lattice Boltzmann Simulations of Vesicles with Viscosity Contrast. *Rheologica Acta* **55** (6), pp. 465–475. DOI: [10.1007/s00397-015-0867-6](https://doi.org/10.1007/s00397-015-0867-6) (cited on p. 27).
- [213] T. Krüger, H. Kusumaatmaja, A. Kuzmin, O. Shardt, G. Silva, and E. M. Viggien (2017). *The Lattice Boltzmann Method - Principles and Practice*. Graduate Texts in Physics. Springer. DOI: [10.1007/978-3-319-44649-3](https://doi.org/10.1007/978-3-319-44649-3) (cited on p. 27).
- [214] H. Noguchi and G. Gompper (2004). Fluid Vesicles with Viscous Membranes in Shear Flow. *Physical Review Letters* **93** (25), 258102. DOI: [10.1103/PhysRevLett.93.258102](https://doi.org/10.1103/PhysRevLett.93.258102) (cited on p. 27).
- [215] H. Noguchi and G. Gompper (2005). Shape Transitions of Fluid Vesicles and Red Blood Cells in Capillary Flows. *Proceedings of the National Academy of Sciences* **102** (40), pp. 14159–14164. DOI: [10.1073/pnas.0504243102](https://doi.org/10.1073/pnas.0504243102) (cited on pp. 27, 31).
- [216] G. Gompper, T. Ihle, D. M. Kroll, and R. G. Winkler. “Multi-Particle Collision Dynamics: A Particle-Based Mesoscale Simulation Approach to the Hydrodynamics of Complex Fluids.” In: *Advanced Computer Simulation Approaches for Soft Matter Sciences III*. Ed. by C. Holm and K. Kremer. Advances in Polymer Science 221. Berlin, Heidelberg: Springer, (2009), pp. 1–87. DOI: [10.1007/978-3-540-87706-6_1](https://doi.org/10.1007/978-3-540-87706-6_1) (cited on p. 27).
- [217] J. L. McWhirter, H. Noguchi, and G. Gompper (2011). Deformation and Clustering of Red Blood Cells in Microcapillary Flows. *Soft Matter* **7** (22), pp. 10967–10977. DOI: [10.1039/C1SM05794D](https://doi.org/10.1039/C1SM05794D) (cited on pp. 27, 31).
- [218] E. Westphal, S. P. Singh, C. C. Huang, G. Gompper, and R. G. Winkler (2014). Multi-particle Collision Dynamics: GPU Accelerated Particle-Based Mesoscale Hydrodynamic Simulations. *Computer Physics Communications* **185** (2), pp. 495–503. DOI: [10.1016/j.cpc.2013.10.004](https://doi.org/10.1016/j.cpc.2013.10.004) (cited on p. 27).
- [219] J. Mauer, M. Peltomäki, S. Poblete, G. Gompper, and D. A. Fedosov (2017). Static and Dynamic Light Scattering by Red Blood Cells: A Numerical Study. *PLOS ONE* **12** (5), e0176799. DOI: [10.1371/journal.pone.0176799](https://doi.org/10.1371/journal.pone.0176799) (cited on p. 27).
- [220] P. Español and M. Revenga (2003). Smoothed Dissipative Particle Dynamics. *Physical Review E* **67** (2), 026705. DOI: [10.1103/PhysRevE.67.026705](https://doi.org/10.1103/PhysRevE.67.026705) (cited on p. 27).
- [221] K. Müller, D. A. Fedosov, and G. Gompper (2015). Smoothed Dissipative Particle Dynamics with Angular Momentum Conservation. *Journal of Computational Physics* **281**, pp. 301–315. DOI: [10.1016/j.jcp.2014.10.017](https://doi.org/10.1016/j.jcp.2014.10.017) (cited on p. 27).

- [222] T. Ye, N. Phan-Thien, C. T. Lim, L. Peng, and H. Shi (2017). Hybrid Smoothed Dissipative Particle Dynamics and Immersed Boundary Method for Simulation of Red Blood Cells in Flows. *Physical Review E* **95** (6), 063314. DOI: [10.1103/PhysRevE.95.063314](https://doi.org/10.1103/PhysRevE.95.063314) (cited on p. 27).
- [223] P. J. Hoogerbrugge and J. M.V. A. Koelman (1992). Simulating Microscopic Hydrodynamic Phenomena with Dissipative Particle Dynamics. *EPL (Europhysics Letters)* **19** (3), pp. 155 – 160. DOI: [10.1209/0295-5075/19/3/001](https://doi.org/10.1209/0295-5075/19/3/001) (cited on p. 27).
- [224] A. L. Blumers, Y.-H. Tang, Z. Li, X. Li, and G. E. Karniadakis (2017). GPU-Accelerated Red Blood Cells Simulations with Transport Dissipative Particle Dynamics. *Computer Physics Communications* **217** (Supplement C), pp. 171 – 179. DOI: [10.1016/j.cpc.2017.03.016](https://doi.org/10.1016/j.cpc.2017.03.016) (cited on p. 27).
- [225] C. Gao, P. Zhang, G. Marom, Y. Deng, and D. Bluestein (2017). Reducing the Effects of Compressibility in DPD-Based Blood Flow Simulations through Severe Stenotic Microchannels. *Journal of Computational Physics* **335**, pp. 812 – 827. DOI: [10.1016/j.jcp.2017.01.062](https://doi.org/10.1016/j.jcp.2017.01.062) (cited on p. 27).
- [226] Z. Li, X. Bian, X. Li, M. Deng, Y.-H. Tang, B. Caswell, and G. E. Karniadakis. “Dissipative Particle Dynamics: Foundation, Evolution, Implementation, and Applications.” In: *Particles in Flows*. Advances in Mathematical Fluid Mechanics. Birkhäuser, Cham, (2017), pp. 255 – 326. DOI: [10.1007/978-3-319-60282-0_5](https://doi.org/10.1007/978-3-319-60282-0_5) (cited on p. 27).
- [227] S. Yon and C. Pozrikidis (1998). A Finite-Volume/Boundary-Element Method for Flow Past Interfaces in the Presence of Surfactants, with Application to Shear Flow Past a Viscous Drop. *Computers & Fluids* **27** (8), pp. 879 – 902. DOI: [10.1016/S0045-7930\(98\)00013-9](https://doi.org/10.1016/S0045-7930(98)00013-9) (cited on p. 27).
- [228] G. Tryggvason, B. Bunner, A. Esmaeeli, D. Juric, N. Al-Rawahi, W. Tauber, J. Han, S. Nas, and Y. J. Jan (2001). A Front-Tracking Method for the Computations of Multiphase Flow. *Journal of Computational Physics* **169** (2), pp. 708 – 759. DOI: [10.1006/jcph.2001.6726](https://doi.org/10.1006/jcph.2001.6726) (cited on p. 27).
- [229] S. Krishnan, E. S. G. Shaqfeh, and G. Iaccarino (2017). Fully Resolved Viscoelastic Particulate Simulations Using Unstructured Grids. *Journal of Computational Physics* **338**, pp. 313 – 338. DOI: [10.1016/j.jcp.2017.02.068](https://doi.org/10.1016/j.jcp.2017.02.068) (cited on p. 27).
- [230] Y. Liu, L. Zhang, X. Wang, and W. K. Liu (2004). Coupling of Navier–Stokes Equations with Protein Molecular Dynamics and Its Application to Hemodynamics. *International Journal for Numerical Methods in Fluids* **46** (12), pp. 1237 – 1252. DOI: [10.1002/flid.798](https://doi.org/10.1002/flid.798) (cited on p. 27).
- [231] Y. Liu and W. K. Liu (2006). Rheology of Red Blood Cell Aggregation by Computer Simulation. *Journal of Computational Physics* **220** (1), pp. 139 – 154. DOI: [10.1016/j.jcp.2006.05.010](https://doi.org/10.1016/j.jcp.2006.05.010) (cited on p. 27).
- [232] A. M. Gambaruto (2015). Computational Haemodynamics of Small Vessels Using the Moving Particle Semi-Implicit (MPS) Method. *Journal of Computational Physics* **302**, pp. 68 – 96. DOI: [10.1016/j.jcp.2015.08.039](https://doi.org/10.1016/j.jcp.2015.08.039) (cited on p. 27).
- [233] A. Jafari, P. Zamankhan, S. M. Mousavi, and P. Kolari (2009). Numerical Investigation of Blood Flow. Part II: In Capillaries. *Communications in Nonlinear Science and Numerical Simulation* **14** (4), pp. 1396 – 1402. DOI: [10.1016/j.cnsns.2008.04.007](https://doi.org/10.1016/j.cnsns.2008.04.007) (cited on p. 27).

-
- [234] D. A. Fedosov, H. Noguchi, and G. Gompper (2014). Multiscale Modeling of Blood Flow: From Single Cells to Blood Rheology. *Biomechanics and Modeling in Mechanobiology* **13** (2), pp. 239–258. DOI: [10.1007/s10237-013-0497-9](https://doi.org/10.1007/s10237-013-0497-9) (cited on p. 27).
- [235] T. Ye, N. Phan-Thien, and C. T. Lim (2016). Particle-Based Simulations of Red Blood Cells—A Review. *Journal of Biomechanics* **49** (11), pp. 2255–2266. DOI: [10.1016/j.jbiomech.2015.11.050](https://doi.org/10.1016/j.jbiomech.2015.11.050) (cited on p. 27).
- [236] D. Lindbo and A.-K. Tornberg (2011). Fast and Spectrally Accurate Summation of 2-Periodic Stokes Potentials. arXiv: [1111.1815](https://arxiv.org/abs/1111.1815) [[physics.flu-dyn](https://arxiv.org/abs/1111.1815)] (cited on p. 27).
- [237] O. Marin, K. Gustavsson, and A.-K. Tornberg (2012). A Highly Accurate Boundary Treatment for Confined Stokes Flow. *Computers & Fluids* **66**, pp. 215–230. DOI: [10.1016/j.compfluid.2012.06.008](https://doi.org/10.1016/j.compfluid.2012.06.008) (cited on p. 27).
- [238] R. Cortez and F. Hoffmann (2014). A Fast Numerical Method for Computing Doubly-Periodic Regularized Stokes Flow in 3D. *Journal of Computational Physics* **258**, pp. 1–14. DOI: [10.1016/j.jcp.2013.10.032](https://doi.org/10.1016/j.jcp.2013.10.032) (cited on p. 27).
- [239] L. Greengard and M. C. Kropinski (2004). Integral Equation Methods for Stokes Flow in Doubly-Periodic Domains. *Journal of Engineering Mathematics* **48** (2), pp. 157–170. DOI: [10.1023/B:ENGI.0000011923.59797.92](https://doi.org/10.1023/B:ENGI.0000011923.59797.92) (cited on p. 27).
- [240] J. R. Blake (1971). A Note on the Image System for a Stokeslet in a No-Slip Boundary. *Mathematical Proceedings of the Cambridge Philosophical Society* **70** (2), pp. 303–310. DOI: [10.1017/S0305004100049902](https://doi.org/10.1017/S0305004100049902) (cited on pp. 27, 28).
- [241] N. Liron and S. Mochon (1976). Stokes Flow for a Stokeslet between Two Parallel Flat Plates. *Journal of Engineering Mathematics* **10** (4), pp. 287–303. DOI: [10.1007/BF01535565](https://doi.org/10.1007/BF01535565) (cited on pp. 27, 28).
- [242] M. E. Staben, A. Z. Zinchenko, and R. H. Davis (2003). Motion of a Particle between Two Parallel Plane Walls in Low-Reynolds-Number Poiseuille Flow. *Physics of Fluids* **15** (6), pp. 1711–1733. DOI: [10.1063/1.1568341](https://doi.org/10.1063/1.1568341) (cited on pp. 27, 28).
- [243] R. B. Jones (2004). Spherical Particle in Poiseuille Flow between Planar Walls. *The Journal of Chemical Physics* **121** (1), pp. 483–500. DOI: [10.1063/1.1738637](https://doi.org/10.1063/1.1738637) (cited on pp. 27, 28).
- [244] B. U. Felderhof (2005). Effect of the Wall on the Velocity Autocorrelation Function and Long-Time Tail of Brownian Motion. *The Journal of Physical Chemistry B* **109** (45), pp. 21406–21412. DOI: [10.1021/jp051335b](https://doi.org/10.1021/jp051335b) (cited on pp. 27, 28).
- [245] B. U. Felderhof (2005). Effect of the Wall on the Velocity Autocorrelation Function and Long-Time Tail of Brownian Motion in a Viscous Compressible Fluid. *The Journal of Chemical Physics* **123** (18), 184903. DOI: [10.1063/1.2084948](https://doi.org/10.1063/1.2084948) (cited on pp. 27, 28).
- [246] B. U. Felderhof (2006). Diffusion and Velocity Relaxation of a Brownian Particle Immersed in a Viscous Compressible Fluid Confined between Two Parallel Plane Walls. *The Journal of Chemical Physics* **124** (5), 054111. DOI: [10.1063/1.2165199](https://doi.org/10.1063/1.2165199) (cited on pp. 27, 28).
- [247] P. Janssen and P. Anderson (2008). A Boundary-Integral Model for Drop Deformation between Two Parallel Plates with Non-Unit Viscosity Ratio Drops. *Journal of Computational Physics* **227** (20), pp. 8807–8819. DOI: [10.1016/j.jcp.2008.06.027](https://doi.org/10.1016/j.jcp.2008.06.027) (cited on pp. 27, 28).

- [248] Z. Gimbutas, L. Greengard, and S. Veerapaneni (2015). Simple and Efficient Representations for the Fundamental Solutions of Stokes Flow in a Half-Space. *Journal of Fluid Mechanics* **776** (R1). DOI: [10.1017/jfm.2015.302](https://doi.org/10.1017/jfm.2015.302) (cited on pp. 27, 28).
- [249] S. Frijters, T. Krüger, and J. Harting (2015). Parallelised Hoshen–Kopelman Algorithm for Lattice-Boltzmann Simulations. *Computer Physics Communications* **189**, pp. 92–98. DOI: [10.1016/j.cpc.2014.12.014](https://doi.org/10.1016/j.cpc.2014.12.014) (cited on p. 27).
- [250] S. J. Karrila and S. Kim (1989). Integral Equations of the Second Kind for Stokes Flow: Direct Solution for Physical Variables and Removal of Inherent Accuracy Limitations. *Chemical Engineering Communications* **82** (1), pp. 123–161. DOI: [10.1080/00986448908940638](https://doi.org/10.1080/00986448908940638) (cited on p. 28).
- [251] Y. Bao, M. Rachh, E. Keaveny, L. Greengard, and A. Donev (2017). A Fluctuating Boundary Integral Method for Brownian Suspensions. *arXiv:1709.01480 [math]*. arXiv: [1709.01480 \[math\]](https://arxiv.org/abs/1709.01480) (cited on pp. 28, 44).
- [252] J. P. Hernández-Ortiz, J. J. de Pablo, and M. D. Graham (2007). Fast Computation of Many-Particle Hydrodynamic and Electrostatic Interactions in a Confined Geometry. *Physical Review Letters* **98** (14), 140602. DOI: [10.1103/PhysRevLett.98.140602](https://doi.org/10.1103/PhysRevLett.98.140602) (cited on p. 28).
- [253] P. Pranay, S. G. Anekal, J. P. Hernandez-Ortiz, and M. D. Graham (2010). Pair Collisions of Fluid-Filled Elastic Capsules in Shear Flow: Effects of Membrane Properties and Polymer Additives. *Physics of Fluids* **22** (12), 123103. DOI: [10.1063/1.3524531](https://doi.org/10.1063/1.3524531) (cited on p. 28).
- [254] A. Kumar and M. D. Graham (2011). Segregation by Membrane Rigidity in Flowing Binary Suspensions of Elastic Capsules. *Physical Review E* **84** (6), 066316. DOI: [10.1103/PhysRevE.84.066316](https://doi.org/10.1103/PhysRevE.84.066316) (cited on p. 28).
- [255] A. Kumar and M. D. Graham (2012). Accelerated Boundary Integral Method for Multiphase Flow in Non-Periodic Geometries. *Journal of Computational Physics* **231** (20), pp. 6682–6713. DOI: [10.1016/j.jcp.2012.05.035](https://doi.org/10.1016/j.jcp.2012.05.035) (cited on p. 28).
- [256] A. Kumar, R. G. Henríquez Rivera, and M. D. Graham (2014). Flow-Induced Segregation in Confined Multicomponent Suspensions: Effects of Particle Size and Rigidity. *Journal of Fluid Mechanics* **738**, pp. 423–462. DOI: [10.1017/jfm.2013.592](https://doi.org/10.1017/jfm.2013.592) (cited on p. 28).
- [257] L. Zhu, J. Rabault, and L. Brandt (2015). The Dynamics of a Capsule in a Wall-Bounded Oscillating Shear Flow. *Physics of Fluids* **27** (7), 071902. DOI: [10.1063/1.4926675](https://doi.org/10.1063/1.4926675) (cited on p. 28).
- [258] K. Sinha and M. D. Graham (2016). Shape-Mediated Margination and Demargination in Flowing Multicomponent Suspensions of Deformable Capsules. *Soft Matter* **12** (6), pp. 1683–1700. DOI: [10.1039/C5SM02196K](https://doi.org/10.1039/C5SM02196K) (cited on p. 28).
- [259] X. Zhao, J. Li, X. Jiang, D. Karpeev, O. Heinonen, B. Smith, J. P. Hernandez-Ortiz, and J. J. de Pablo (2017). Parallel O(N) Stokes’ Solver towards Scalable Brownian Dynamics of Hydrodynamically Interacting Objects in General Geometries. *The Journal of Chemical Physics* **146** (24), 244114. DOI: [10.1063/1.4989545](https://doi.org/10.1063/1.4989545) (cited on p. 28).
- [260] I. B. Bazhlekov, P. D. Anderson, and H. E. H. Meijer (2004). Nonsingular Boundary Integral Method for Deformable Drops in Viscous Flows. *Physics of Fluids* **16** (4), pp. 1064–1081. DOI: [10.1063/1.1648639](https://doi.org/10.1063/1.1648639) (cited on p. 28).

-
- [261] R. Cortez, L. Fauci, and A. Medovikov (2005). The Method of Regularized Stokeslets in Three Dimensions: Analysis, Validation, and Application to Helical Swimming. *Physics of Fluids* **17** (3), 031504. DOI: [10.1063/1.1830486](https://doi.org/10.1063/1.1830486) (cited on p. 28).
- [262] D. Saintillan, E. Darve, and E. S. G. Shaqfeh (2005). A Smooth Particle-Mesh Ewald Algorithm for Stokes Suspension Simulations: The Sedimentation of Fibers. *Physics of Fluids* **17** (3), 033301. DOI: [10.1063/1.1862262](https://doi.org/10.1063/1.1862262) (cited on pp. 28, 29).
- [263] Y. J. Liu and N. Nishimura (2006). The Fast Multipole Boundary Element Method for Potential Problems: A Tutorial. *Engineering Analysis with Boundary Elements* **30** (5), pp. 371–381. DOI: [10.1016/j.enganabound.2005.11.006](https://doi.org/10.1016/j.enganabound.2005.11.006) (cited on pp. 28, 29, 44).
- [264] H. Wang, T. Lei, J. Li, J. Huang, and Z. Yao (2007). A Parallel Fast Multipole Accelerated Integral Equation Scheme for 3D Stokes Equations. *International Journal for Numerical Methods in Engineering* **70** (7), pp. 812–839. DOI: [10.1002/nme.1910](https://doi.org/10.1002/nme.1910) (cited on pp. 28, 29, 44).
- [265] A.-K. Tornberg and L. Greengard (2008). A Fast Multipole Method for the Three-Dimensional Stokes Equations. *Journal of Computational Physics* **227** (3), pp. 1613–1619. DOI: [10.1016/j.jcp.2007.06.029](https://doi.org/10.1016/j.jcp.2007.06.029) (cited on pp. 28, 29, 44).
- [266] S. K. Veerapaneni, A. Rahimian, G. Biros, and D. Zorin (2011). A Fast Algorithm for Simulating Vesicle Flows in Three Dimensions. *Journal of Computational Physics* **230** (14), pp. 5610–5634. DOI: [10.1016/j.jcp.2011.03.045](https://doi.org/10.1016/j.jcp.2011.03.045) (cited on pp. 28, 29, 44).
- [267] G. R. Cowper (1973). Gaussian Quadrature Formulas for Triangles. *International Journal for Numerical Methods in Engineering* **7** (3), pp. 405–408. DOI: [10.1002/nme.1620070316](https://doi.org/10.1002/nme.1620070316) (cited on p. 28).
- [268] C. Pozrikidis (1995). Finite Deformation of Liquid Capsules Enclosed by Elastic Membranes in Simple Shear Flow. *Journal of Fluid Mechanics* **297**, pp. 123–152. DOI: [10.1017/S002211209500303X](https://doi.org/10.1017/S002211209500303X) (cited on p. 28).
- [269] M. Loewenberg and E. J. Hinch (1996). Numerical Simulation of a Concentrated Emulsion in Shear Flow. *Journal of Fluid Mechanics* **321**, pp. 395–419. DOI: [10.1017/S002211209600777X](https://doi.org/10.1017/S002211209600777X) (cited on p. 29).
- [270] H. Hasimoto (1959). On the Periodic Fundamental Solutions of the Stokes Equations and Their Application to Viscous Flow Past a Cubic Array of Spheres. *Journal of Fluid Mechanics* **5** (2), pp. 317–328. DOI: [10.1017/S0022112059000222](https://doi.org/10.1017/S0022112059000222) (cited on p. 29).
- [271] Y. Saad and M. Schultz (1986). GMRES: A Generalized Minimal Residual Algorithm for Solving Nonsymmetric Linear Systems. *SIAM Journal on Scientific and Statistical Computing* **7** (3), pp. 856–869. DOI: [10.1137/0907058](https://doi.org/10.1137/0907058) (cited on p. 29).
- [272] P. Bogacki and L. F. Shampine (1989). A 3(2) Pair of Runge - Kutta Formulas. *Applied Mathematics Letters* **2** (4), pp. 321–325. DOI: [10.1016/0893-9659\(89\)90079-7](https://doi.org/10.1016/0893-9659(89)90079-7) (cited on p. 29).
- [273] J. R. Cash and A. H. Karp (1990). A Variable Order Runge-Kutta Method for Initial Value Problems with Rapidly Varying Right-Hand Sides. *ACM Transactions on Mathematical Software* **16** (3), pp. 201–222. DOI: [10.1145/79505.79507](https://doi.org/10.1145/79505.79507) (cited on p. 29).
- [274] A. Z. Zinchenko, M. A. Rother, and R. H. Davis (1997). A Novel Boundary-Integral Algorithm for Viscous Interaction of Deformable Drops. *Physics of Fluids* **9** (6), pp. 1493–1511. DOI: [10.1063/1.869275](https://doi.org/10.1063/1.869275) (cited on p. 29).

- [275] M. C. Rivara (1984). Algorithms for Refining Triangular Grids Suitable for Adaptive and Multigrid Techniques. *International Journal for Numerical Methods in Engineering* **20** (4), pp. 745–756. DOI: [10.1002/nme.1620200412](https://doi.org/10.1002/nme.1620200412) (cited on p. 29).
- [276] Bayerisches Staatsministerium für Wissenschaft, Forschung und Kunst. *KONWIHR*. URL: <http://www.konwihr.uni-erlangen.de/> (accessed on 16.01.2018) (cited on p. 29).
- [277] A. Guckenberger and S. Gekle (2016). *A Highly-Parallelized Boundary Integral Implementation for Blood Flow Simulations*. URL: <https://www.lrz.de/services/compute/labs/cfdlab/Project3/> (accessed on 16.01.2018) (cited on p. 29).
- [278] M. J. Abraham, T. Murtola, R. Schulz, S. Páll, J. C. Smith, B. Hess, and E. Lindahl (2015). GROMACS: High Performance Molecular Simulations through Multi-Level Parallelism from Laptops to Supercomputers. *SoftwareX* **1–2**, pp. 19–25. DOI: [10.1016/j.softx.2015.06.001](https://doi.org/10.1016/j.softx.2015.06.001) (cited on pp. 29, 30).
- [279] D. Malhotra and G. Biros (2015). PVFMM: A Parallel Kernel Independent FMM for Particle and Volume Potentials. *Communications in Computational Physics* **18** (3), pp. 808–830. DOI: [10.4208/cicp.020215.150515sw](https://doi.org/10.4208/cicp.020215.150515sw) (cited on p. 29).
- [280] W. B. March, B. Xiao, S. Tharakan, C. D. Yu, and G. Biros (2015). A Kernel-Independent FMM in General Dimensions. In: *Proceedings of the International Conference for High Performance Computing, Networking, Storage and Analysis*. SC '15. New York: ACM, 24:1–24:12. DOI: [10.1145/2807591.2807647](https://doi.org/10.1145/2807591.2807647) (cited on p. 29).
- [281] A. Gholami, D. Malhotra, H. Sundar, and G. Biros (2014). FFT, FMM, or Multigrid? A Comparative Study of State-of-the-Art Poisson Solvers in the Unit Cube. *arXiv:1408.6497 [cs, math]*. arXiv: [1408.6497 \[cs, math\]](https://arxiv.org/abs/1408.6497) (cited on p. 29).
- [282] M. Kretz and V. Lindenstruth (2012). Vc: A C++ Library for Explicit Vectorization. *Software: Practice and Experience* **42** (11), pp. 1409–1430. DOI: [10.1002/spe.1149](https://doi.org/10.1002/spe.1149) (cited on p. 29).
- [283] R. Skalak and P. I. Branemark (1969). Deformation of Red Blood Cells in Capillaries. *Science* **164** (3880), pp. 717–719. DOI: [10.1126/science.164.3880.717](https://doi.org/10.1126/science.164.3880.717) (cited on p. 31).
- [284] R. M. Hochmuth, R. N. Marple, and S. P. Sutera (1970). Capillary Blood Flow: I. Erythrocyte Deformation in Glass Capillaries. *Microvascular Research* **2** (4), pp. 409–419. DOI: [10.1016/0026-2862\(70\)90034-8](https://doi.org/10.1016/0026-2862(70)90034-8) (cited on p. 31).
- [285] P. Gaehtgens, C. Dührssen, and K. H. Albrecht (1980). Motion, Deformation, and Interaction of Blood Cells and Plasma during Flow through Narrow Capillary Tubes. *Blood Cells* **6** (4), pp. 799–817 (cited on p. 31).
- [286] V. Vitkova, M.-A. Mader, B. Polack, C. Misbah, and T. Podgorski (2008). Micro-Macro Link in Rheology of Erythrocyte and Vesicle Suspensions. *Biophysical Journal* **95** (6), pp. L33–L35. DOI: [10.1529/biophysj.108.138826](https://doi.org/10.1529/biophysj.108.138826) (cited on p. 31).
- [287] T. Krüger, M. Gross, D. Raabe, and F. Varnik (2013). Crossover from Tumbling to Tank-Treading-like Motion in Dense Simulated Suspensions of Red Blood Cells. *Soft Matter* **9** (37), pp. 9008–9015. DOI: [10.1039/C3SM51645H](https://doi.org/10.1039/C3SM51645H) (cited on p. 31).
- [288] M. Thiébaud, Z. Shen, J. Harting, and C. Misbah (2014). Prediction of Anomalous Blood Viscosity in Confined Shear Flow. *Physical Review Letters* **112** (23), 238304. DOI: [10.1103/PhysRevLett.112.238304](https://doi.org/10.1103/PhysRevLett.112.238304) (cited on p. 31).

-
- [289] Y. Suzuki, N. Tateishi, M. Soutani, and N. Maeda (1996). Deformation of Erythrocytes in Microvessels and Glass Capillaries: Effects of Erythrocyte Deformability. *Microcirculation* **3** (1), pp. 49–57. DOI: [10.3109/10739689609146782](https://doi.org/10.3109/10739689609146782) (cited on p. 31).
- [290] T. W. Secomb, B. Styp-Rekowska, and A. R. Pries (2007). Two-Dimensional Simulation of Red Blood Cell Deformation and Lateral Migration in Microvessels. *Annals of Biomedical Engineering* **35** (5), pp. 755–765. DOI: [10.1007/s10439-007-9275-0](https://doi.org/10.1007/s10439-007-9275-0) (cited on p. 31).
- [291] M. Faivre (2006). Drops, Vesicles and Red Blood Cells: Deformability and Behavior under Flow. PhD thesis. Grenoble: Université Joseph-Fourier - Grenoble I (cited on p. 31).
- [292] M. Abkarian, M. Faivre, R. Horton, K. Smistrup, C. A. Best-Popescu, and H. A. Stone (2008). Cellular-Scale Hydrodynamics. *Biomedical Materials* **3** (3), 034011. DOI: [10.1088/1748-6041/3/3/034011](https://doi.org/10.1088/1748-6041/3/3/034011) (cited on p. 31).
- [293] G. Tomaiuolo, M. Simeone, V. Martinelli, B. Rotoli, and S. Guido (2009). Red Blood Cell Deformation in Microconfined Flow. *Soft Matter* **5** (19), pp. 3736–3740. DOI: [10.1039/B904584H](https://doi.org/10.1039/B904584H) (cited on p. 31).
- [294] J. C. A. Cluitmans, V. Chokkalingam, A. M. Janssen, R. Brock, W. T. S. Huck, and G. J.C.G. M. Bosman (2014). Alterations in Red Blood Cell Deformability during Storage: A Microfluidic Approach. *BioMed Research International* **2014**, 764268. DOI: [10.1155/2014/764268](https://doi.org/10.1155/2014/764268) (cited on p. 31).
- [295] A. Farutin and C. Misbah (2014). Symmetry Breaking and Cross-Streamline Migration of Three-Dimensional Vesicles in an Axial Poiseuille Flow. *Physical Review E* **89** (4), p. 042709. DOI: [10.1103/PhysRevE.89.042709](https://doi.org/10.1103/PhysRevE.89.042709) (cited on p. 31).
- [296] T. W. Secomb and R. Skalak (1982). A Two-Dimensional Model for Capillary Flow of an Asymmetric Cell. *Microvascular Research* **24** (2), pp. 194–203. DOI: [10.1016/0026-2862\(82\)90056-5](https://doi.org/10.1016/0026-2862(82)90056-5) (cited on p. 31).
- [297] B. Kaoui, N. Tahiri, T. Biben, H. Ez-Zahraouy, A. Benyoussef, G. Biros, and C. Misbah (2011). Complexity of Vesicle Microcirculation. *Physical Review E* **84** (4), 041906. DOI: [10.1103/PhysRevE.84.041906](https://doi.org/10.1103/PhysRevE.84.041906) (cited on p. 31).
- [298] B. Kaoui, T. Krüger, and J. Harting (2012). How Does Confinement Affect the Dynamics of Viscous Vesicles and Red Blood Cells? *Soft Matter* **8** (35), pp. 9246–9252. DOI: [10.1039/C2SM26289D](https://doi.org/10.1039/C2SM26289D) (cited on p. 31).
- [299] L. Shi, T.-W. Pan, and R. Glowinski (2012). Deformation of a Single Red Blood Cell in Bounded Poiseuille Flows. *Physical Review E* **85** (1), 016307. DOI: [10.1103/PhysRevE.85.016307](https://doi.org/10.1103/PhysRevE.85.016307) (cited on p. 31).
- [300] N. Tahiri, T. Biben, H. Ez-Zahraouy, A. Benyoussef, and C. Misbah (2013). On the Problem of Slipper Shapes of Red Blood Cells in the Microvasculature. *Microvascular Research* **85**, pp. 40–45. DOI: [10.1016/j.mvr.2012.10.001](https://doi.org/10.1016/j.mvr.2012.10.001) (cited on pp. 31, 43).
- [301] G. R. Lázaro, A. Hernández-Machado, and I. Pagonabarraga (2014). Rheology of Red Blood Cells under Flow in Highly Confined Microchannels: I. Effect of Elasticity. *Soft Matter* **10** (37), pp. 7195–7206. DOI: [10.1039/C4SM00894D](https://doi.org/10.1039/C4SM00894D) (cited on p. 31).
- [302] O. Aouane, M. Thiébaud, A. Benyoussef, C. Wagner, and C. Misbah (2014). Vesicle Dynamics in a Confined Poiseuille Flow: From Steady State to Chaos. *Physical Review E* **90** (3), 033011. DOI: [10.1103/PhysRevE.90.033011](https://doi.org/10.1103/PhysRevE.90.033011) (cited on p. 31).

- [303] A. R. Pries, T. W. Secomb, and P. Gaehtgens (1995). Structure and Hemodynamics of Microvascular Networks: Heterogeneity and Correlations. *American Journal of Physiology - Heart and Circulatory Physiology* **269** (5), H1713–H1722. DOI: [10.1152/ajpheart.1995.269.5.h1713](https://doi.org/10.1152/ajpheart.1995.269.5.h1713) (cited on p. 33).
- [304] A. L. Klibanov. “Ultrasound Contrast Agents: Development of the Field and Current Status.” In: *Contrast Agents II*. Ed. by W. Krause. Topics in Current Chemistry 222. Springer Berlin Heidelberg, (2002), pp. 73–106. DOI: [10.1007/3-540-46009-8_3](https://doi.org/10.1007/3-540-46009-8_3) (cited on p. 36).
- [305] J. R. Lindner (2004). Microbubbles in Medical Imaging: Current Applications and Future Directions. *Nature Reviews Drug Discovery* **3** (6), pp. 527–533. DOI: [10.1038/nrd1417](https://doi.org/10.1038/nrd1417) (cited on p. 36).
- [306] E. Stride (2009). Physical Principles of Microbubbles for Ultrasound Imaging and Therapy. *Cerebrovascular Diseases* **27** (2), pp. 1–13. DOI: [10.1159/000203122](https://doi.org/10.1159/000203122) (cited on p. 36).
- [307] S. Unnikrishnan and A. L. Klibanov (2012). Microbubbles as Ultrasound Contrast Agents for Molecular Imaging: Preparation and Application. *American Journal of Roentgenology* **199** (2), pp. 292–299. DOI: [10.2214/AJR.12.8826](https://doi.org/10.2214/AJR.12.8826) (cited on p. 36).
- [308] T. Faez, M. Emmer, K. Kooiman, M. Versluis, A. van der Steen, and N. de Jong (2013). 20 Years of Ultrasound Contrast Agent Modeling. *IEEE Transactions on Ultrasonics, Ferroelectrics, and Frequency Control* **60** (1), pp. 7–20. DOI: [10.1109/TUFFC.2013.2533](https://doi.org/10.1109/TUFFC.2013.2533) (cited on pp. 36, 37).
- [309] K. Ferrara, R. Pollard, and M. Borden (2007). Ultrasound Microbubble Contrast Agents: Fundamentals and Application to Gene and Drug Delivery. *Annual Review of Biomedical Engineering* **9** (1), pp. 415–447. DOI: [10.1146/annurev.bioeng.8.061505.095852](https://doi.org/10.1146/annurev.bioeng.8.061505.095852) (cited on p. 36).
- [310] O. Couture, J. Foley, N. F. Kassell, B. Larrat, and J.-F. Aubry (2014). Review of Ultrasound Mediated Drug Delivery for Cancer Treatment: Updates from Pre-Clinical Studies. *Translational Cancer Research* **3** (5), pp. 494–511. DOI: [10.3978/j.issn.2218-676X.2014.10.01](https://doi.org/10.3978/j.issn.2218-676X.2014.10.01) (cited on p. 36).
- [311] E. Unger, T. Porter, J. Lindner, and P. Grayburn (2014). Cardiovascular Drug Delivery with Ultrasound and Microbubbles. *Advanced Drug Delivery Reviews* **72**, pp. 110–126. DOI: [10.1016/j.addr.2014.01.012](https://doi.org/10.1016/j.addr.2014.01.012) (cited on p. 36).
- [312] K. Kooiman, H. J. Vos, M. Versluis, and N. de Jong (2014). Acoustic Behavior of Microbubbles and Implications for Drug Delivery. *Advanced Drug Delivery Reviews*. Ultrasound triggered drug delivery **72**, pp. 28–48. DOI: [10.1016/j.addr.2014.03.003](https://doi.org/10.1016/j.addr.2014.03.003) (cited on pp. 36–38).
- [313] B. H. A. Lammertink, C. Bos, R. Deckers, G. Storm, C. T. W. Moonen, and J.-M. Escoffre (2015). Sonochemotherapy: From Bench to Bedside. *Experimental Pharmacology and Drug Discovery* **6**, 138. DOI: [10.3389/fphar.2015.00138](https://doi.org/10.3389/fphar.2015.00138) (cited on pp. 36, 38).
- [314] S. Kotopoulis, G. Dimcevski, E. M. Cormack, M. Postema, B. T. Gjertsen, and O. H. Gilja (2016). Ultrasound- and Microbubble-Enhanced Chemotherapy for Treating Pancreatic Cancer: A Phase I Clinical Trial. *The Journal of the Acoustical Society of America* **139** (4), pp. 2092–2092. DOI: [10.1121/1.4950209](https://doi.org/10.1121/1.4950209) (cited on p. 36).

-
- [315] I. Lentacker, I. De Cock, R. Deckers, S. C. De Smedt, and C. T. W. Moonen (2014). Understanding Ultrasound Induced Sonoporation: Definitions and Underlying Mechanisms. *Advanced Drug Delivery Reviews*. Ultrasound triggered drug delivery **72**, pp. 49–64. DOI: [10.1016/j.addr.2013.11.008](https://doi.org/10.1016/j.addr.2013.11.008) (cited on p. 36).
- [316] J. J. Rychak, A. L. Klibanov, K. F. Ley, and J. A. Hossack (2007). Enhanced Targeting of Ultrasound Contrast Agents Using Acoustic Radiation Force. *Ultrasound in Medicine & Biology* **33** (7), pp. 1132–1139. DOI: [10.1016/j.ultrasmedbio.2007.01.005](https://doi.org/10.1016/j.ultrasmedbio.2007.01.005) (cited on pp. 36, 38).
- [317] R. D’Apolito, G. Tomaiuolo, F. Taraballi, S. Minardi, D. Kirui, X. Liu, A. Cevenini, R. Palomba, M. Ferrari, F. Salvatore, E. Tasciotti, and S. Guido (2015). Red Blood Cells Affect the Margination of Microparticles in Synthetic Microcapillaries and Intravital Microcirculation as a Function of Their Size and Shape. *Journal of Controlled Release* **217**, pp. 263–272. DOI: [10.1016/j.jconrel.2015.09.013](https://doi.org/10.1016/j.jconrel.2015.09.013) (cited on pp. 36, 39).
- [318] P. Marmottant, S. van der Meer, M. Emmer, M. Versluis, N. DE Jong, S. Hilgenfeldt, and D. Lohse (2005). A Model for Large Amplitude Oscillations of Coated Bubbles Accounting for Buckling and Rupture. *The Journal of the Acoustical Society of America* **118** (6), pp. 3499–3505. DOI: [10.1121/1.2109427](https://doi.org/10.1121/1.2109427) (cited on p. 37).
- [319] M. Overvelde, V. Garbin, J. Sijl, B. Dollet, N. de Jong, D. Lohse, and M. Versluis (2010). Nonlinear Shell Behavior of Phospholipid-Coated Microbubbles. *Ultrasound in Medicine & Biology* **36** (12), pp. 2080–2092. DOI: [10.1016/j.ultrasmedbio.2010.08.015](https://doi.org/10.1016/j.ultrasmedbio.2010.08.015) (cited on p. 37).
- [320] P. J. A. Frinking, E. Gaud, J. Brochot, and M. Arditi (2010). Subharmonic Scattering of Phospholipid-Shell Microbubbles at Low Acoustic Pressure Amplitudes. *IEEE Transactions on Ultrasonics, Ferroelectrics, and Frequency Control* **57** (8), pp. 1762–1771. DOI: [10.1109/TUFFC.2010.1614](https://doi.org/10.1109/TUFFC.2010.1614) (cited on p. 37).
- [321] A. Doinikov and A. Bouakaz (2011). Review of Shell Models for Contrast Agent Microbubbles. *IEEE Transactions on Ultrasonics, Ferroelectrics and Frequency Control* **58** (5), pp. 981–993. DOI: [10.1109/TUFFC.2011.1899](https://doi.org/10.1109/TUFFC.2011.1899) (cited on p. 37).
- [322] J. Sijl, M. Overvelde, B. Dollet, V. Garbin, N. DE Jong, D. Lohse, and M. Versluis (2011). “Compression-Only” Behavior: A Second-Order Nonlinear Response of Ultrasound Contrast Agent Microbubbles. *The Journal of the Acoustical Society of America* **129** (4), pp. 1729–1739. DOI: [10.1121/1.3505116](https://doi.org/10.1121/1.3505116) (cited on p. 37).
- [323] J. J. Rychak, J. R. Lindner, K. Ley, and A. L. Klibanov (2006). Deformable Gas-Filled Microbubbles Targeted to P-Selectin. *Journal of Controlled Release* **114** (3), pp. 288–299. DOI: [10.1016/j.jconrel.2006.06.008](https://doi.org/10.1016/j.jconrel.2006.06.008) (cited on p. 37).
- [324] M. A. Borden, D. E. Kruse, C. F. Caskey, S. Zhao, P. A. Dayton, and K. W. Ferrara (2005). Influence of Lipid Shell Physicochemical Properties on Ultrasound-Induced Microbubble Destruction. *IEEE Transactions on Ultrasonics, Ferroelectrics, and Frequency Control* **52** (11), pp. 1992–2002. DOI: [10.1109/TUFFC.2005.1561668](https://doi.org/10.1109/TUFFC.2005.1561668) (cited on p. 37).
- [325] G. K. Youngren and A. Acrivos (1976). On the Shape of a Gas Bubble in a Viscous Extensional Flow. *Journal of Fluid Mechanics* **76** (3), pp. 433–442. DOI: [10.1017/S0022112076000724](https://doi.org/10.1017/S0022112076000724) (cited on p. 37).
- [326] H. Power (1992). The Low Reynolds Number Deformation of a Gas Bubble in Shear Flow: A General Approach via Integral Equations. *Engineering Analysis with Boundary Elements* **9** (1), pp. 31–37. DOI: [10.1016/0955-7997\(92\)90122-N](https://doi.org/10.1016/0955-7997(92)90122-N) (cited on p. 37).

- [327] P. Dayton, A. Klibanov, G. Brandenburger, and K. Ferrara (1999). Acoustic Radiation Force in Vivo: A Mechanism to Assist Targeting of Microbubbles. *Ultrasound in Medicine & Biology* **25** (8), pp. 1195–1201. DOI: [10.1016/S0301-5629\(99\)00062-9](https://doi.org/10.1016/S0301-5629(99)00062-9) (cited on p. 38).
- [328] J. P. Kilroy, A. L. Klibanov, B. R. Wamhoff, D. K. Bowles, and J. A. Hossack (2014). Localized in Vivo Model Drug Delivery with Intravascular Ultrasound and Microbubbles. *Ultrasound in Medicine & Biology* **40** (10), pp. 2458–2467. DOI: [10.1016/j.ultrasmedbio.2014.04.007](https://doi.org/10.1016/j.ultrasmedbio.2014.04.007) (cited on p. 38).
- [329] J. J. Rychak, A. L. Klibanov, and J. A. Hossack (2005). Acoustic Radiation Force Enhances Targeted Delivery of Ultrasound Contrast Microbubbles: In Vitro Verification. *IEEE Transactions on Ultrasonics, Ferroelectrics, and Frequency Control* **52** (3), pp. 421–433. DOI: [10.1109/TUFFC.2005.1417264](https://doi.org/10.1109/TUFFC.2005.1417264) (cited on pp. 38, 39).
- [330] K. A. Johnson, H. R. Vormohr, A. A. Doinikov, A. Bouakaz, C. W. Shields, G. P. López, and P. A. Dayton (2016). Experimental Verification of Theoretical Equations for Acoustic Radiation Force on Compressible Spherical Particles in Traveling Waves. *Physical Review E* **93** (5), 053109. DOI: [10.1103/PhysRevE.93.053109](https://doi.org/10.1103/PhysRevE.93.053109) (cited on pp. 38, 39).
- [331] J. R. Lindner, J. Song, A. R. Jayaweera, J. Sklenar, and S. Kaul (2002). Microvascular Rheology of Definity Microbubbles after Intra-Arterial and Intravenous Administration. *Journal of the American Society of Echocardiography* **15** (5), pp. 396–403. DOI: [10.1067/mje.2002.117290](https://doi.org/10.1067/mje.2002.117290) (cited on p. 38).
- [332] M. Schraml (2015). Implementation of an Advanced Bending Model for Red Blood Cells with Application to Stokes Flow. Bachelor’s thesis. Universität Bayreuth (cited on p. 75).

Acknowledgments

First and foremost, I want to express my gratitude to my supervisor Prof. Dr. Stephan Gekle for his guidance, project suggestions, initiation of the collaboration with Prof. Dr. Christian Wagner's group as well as the KONWIHR project, enabling visits to many a conference and his help with and contributions to the publications.

Of course, the publications would have also been impossible without my collaborators. Thus, many thanks go to Alexander Kihm and Dr. Stephan Quint (for performing the experiments), Dr. Thomas John for helpful discussions, Prof. Dr. Christian Wagner for assigning them to the suggested projects, Prof. Dr. Marc Leonetti and Dr. Paul G. Chen for contributing the subdivision surface results to our bending evaluation, and Marcel P. Schraml for implementing the fitting method.

I also give my thanks to Abdallah Daddi-Moussa-Ider for putting the BIM code to good use, and for accompanying me to many of the conferences. Thanks also go to Christian Schaaf for our delightful shoptalks and many good drinks shared. I also say thank you to Ali Ghaemi for many interesting discussions and in general the whole workgroup for the many enjoyable meetings. Awesome technical support was provided by Markus Hilt: Thank you for all the quick responses to technical difficulties! Claudia Brandt also has my thanks for her fast and flawless administration work. My thanks also go to the staff at the Leibniz-Rechenzentrum, especially to Momme Allalen, Luigi Iapichino and Igor Pasichnyk for their support during the KONWIHR project.

My eternal gratitude goes to Bernd Feist, Dominik Sieder and Julian Kahle for all the exhilarating gaming nights and trips. I would also like to highlight the staff at the Kletterzentrum Bayreuth for providing such an awesome bouldering and climbing facility. And finally, I would also like to express my gratitude toward my family for their continuing aid.

Part II

Publications

9

The author's contributions

9.1 Major publications

[Pub1] A. Guckenberger, M. P. Schraml, P. G. Chen, M. Leonetti and S. Gekle (2016). On the bending algorithms for soft objects in flows. *Computer Physics Communications* **207**, pp. 1–23. DOI: [10.1016/j.cpc.2016.04.018](https://doi.org/10.1016/j.cpc.2016.04.018)

Relevant chapter in this thesis: 4.3.

Breakdown of the individual contributions:

- A. Guckenberger during his doctorate helped to develop the concept of the paper, developed the Mathematica code based on M. P. Schraml's code for the computation of the analytical results, improved and fixed the implementation of Method E and enhanced Method A, initiated and handled the collaboration with P. G. Chen and M. Leonetti, helped to supervise M. P. Schraml, performed the whole comparison with the analytical results, performed the BIM simulations of the capsule in a shear flow (except for Method S), made the corresponding comparisons with the literature and, finally, wrote most of the manuscript.
- A. Guckenberger implemented during his Master thesis [12] Method A (only the small-angle approximation), Method B (including the derivation of the necessary formulas in the appendix of [Pub1]), Method C and Method D. He also performed a comparison of the shear flow results obtained with these methods with (only) two references from the literature (namely [46, 205]).
- The Lattice-Boltzmann (LBM) simulations were contributed by S. Gekle. He supervised and helped to develop the concept of the paper, contributed to the discussion of the results and participated in the writing of the manuscript.
- The raw data for Method S was contributed by P. G. Chen and M. Leonetti, as was the explanation of Method S.
- During his Bachelor thesis [332], M. P. Schraml implemented a first version of the Mathematica code to compute the analytical results for the discocyte shape. He also implemented a first version of Method E in the BIM code. M. P. Schraml also made first comparisons of Method E with the analytical data and with shear flow results from the other methods. The author of the present thesis helped to supervise M. P. Schraml and debugged and enhanced the codes afterwards as necessary.

[Pub2] A. Guckenberger and S. Gekle (2017). Theory and algorithms to compute Helfrich bending forces: a review. *Journal of Physics: Condensed Matter* **29** (20), 203001. DOI: [10.1088/1361-648X/aa6313](https://doi.org/10.1088/1361-648X/aa6313)

Relevant chapters in this thesis: 2.1 and 4.3.

Breakdown of the individual contributions:

- The author of the present thesis (during his doctorate) wrote large portions of the manuscript and contributed a large part of the references. He also built the spherical harmonics code and made the comparison with the analytical results. He developed the concept of and carried out the analytical computations in the appendix (derivation of the traction jump), including the comparison between the Canham-Helfrich and the linear bending models.
- S. Gekle supervised and developed the concept of the paper, helped to write the manuscript and contributed many of the references.

Note: Despite being a review to large extents, publication [Pub2] contains two novel contributions: First, the rigorous comparison between the linear bending models and the Canham-Helfrich model and second, the computation of the bending errors when using a spherical harmonics expansion.

[Pub3] A. Guckenberger and S. Gekle (2018). A boundary integral method with volume-changing objects for ultrasound-triggered margination of microbubbles. *Journal of Fluid Mechanics* **836**, pp. 952–997. DOI: [10.1017/jfm.2017.836](https://doi.org/10.1017/jfm.2017.836)

Relevant chapters in this thesis: 3 and 6.2.

Breakdown of the individual contributions:

- The author of the present thesis (during his doctorate) helped to develop the concept of the paper, derived the presented equations, developed the mathematical proof, made the necessary numerical implementations, performed the simulations, analyzed the results and wrote most parts of the text.
- A. Guckenberger during his Master thesis [12] started to develop the extended boundary integral equation for volume-changing objects. However, the equation together with the proof was only valid in infinite domains. Periodic domains were not yet possible.
- S. Gekle designed and supervised the research, checked the validity of the proof, helped with the discussion of the results and contributed to the writing of the manuscript.

[Pub4] S. Quint, A. F. Christ, A. Guckenberger, S. Himbert, L. Kaestner, S. Gekle and C. Wagner (2017). 3D tomography of cells in micro-channels. *Applied Physics Letters* **111** (10), 103701. DOI: [10.1063/1.4986392](https://doi.org/10.1063/1.4986392)

Relevant chapter in this thesis: 6.1.

A. Guckenberger (during his doctorate) performed and analyzed the numerical simulations, rendered all shapes (including the experimental ones) in figure 2 and contributed to the discussion as well as the manuscript.

The remainder of the work was done by the coauthors. In particular, the 3D confocal microscope technique was designed, implemented and used by the coauthors from Saarbrücken.

[Pub5] A. Guckenberger, A. Kihm, T. John, C. Wagner and S. Gekle (2018). Numerical-experimental observation of shape bistability of red blood cells flowing in a microchannel. *Soft Matter* **14** (11), pp. 2032–2043. DOI: [10.1039/C7SM02272G](https://doi.org/10.1039/C7SM02272G)

Relevant chapter in this thesis: 6.1.

Breakdown of the individual contributions:

- A. Guckenberger (during his doctorate) helped to develop the concept of the paper, managed the collaboration, performed and analyzed the numerical simulations and prepared most of the manuscript, including the design and creation of the figures and videos.
- A. Kihm performed the experiments, analyzed the experimental data, helped in the discussion and contributed to the manuscript.
- T. John helped in the discussion and contributed to the manuscript.
- C. Wagner helped to supervise the project, helped in the discussion and contributed to the manuscript.
- S. Gekle designed and supervised the research, initiated the collaboration, helped in the discussion and contributed to the manuscript.

9.2 Further publications

The author of the present thesis wrote the basis of the boundary integral method code during his Master thesis [12] as used in the following two publications. He also contributed to the discussion and the proofreading of the manuscripts during his doctorate.

- [196] A. Daddi-Moussa-Ider, A. Guckenberger, and S. Gekle (2016). Long-Lived Anomalous Thermal Diffusion Induced by Elastic Cell Membranes on Nearby Particles. *Physical Review E* **93**(1), 012612. DOI: [10.1103/PhysRevE.93.012612](https://doi.org/10.1103/PhysRevE.93.012612)
- [197] A. Daddi-Moussa-Ider, A. Guckenberger, and S. Gekle (2016). Particle Mobility between Two Planar Elastic Membranes: Brownian Motion and Membrane Deformation. *Physics of Fluids* **28**(7), 071903. DOI: [10.1063/1.4955013](https://doi.org/10.1063/1.4955013)

9.3 Presentations

The author of the present thesis presented the work to the scientific community at the following conferences, summer schools and workshops during his doctorate:

Talks:

- 13. March 2015 DPG Spring Meeting (Berlin, Germany)
- 29. July 2015 KONWIHR Kick-Off Workshop (Garching, Germany)
- 17. Sept. 2015 Workshop "Living Fluids" (Saarbrücken, Germany)
- 25. Feb. 2016 KONWIHR Results Workshop (Garching, Germany)
- 08. March 2016 DPG Spring Meeting (Regensburg, Germany)
- 26. Jan. 2017 Conference "Flowing Matter" (Porto, Portugal)
- 20. March 2017 DPG Spring Meeting (Dresden, Germany)
- 13. July 2017 Conference "DSFD" (Erlangen, Germany)
- 09. Oct. 2017 Conference "Blood Flow" (Paris, France)
- 06. Dec. 2017 Evaluation symposium (Bayreuth, Germany)

Poster presentations:

- 19. June 2016 Workshop "Hybrid Simulation Methods in Fluid Dynamics" (Garching, Germany)
- 12. July 2016 Summer School "Active Complex Matter" (Cargèse, Corsica)
- 9. Oct. 2016 Conference "Patterns in Nature" (Bayreuth, Germany)
- 25. Sept. 2017 Summer School "Complex Motion in Fluids" (Cambridge, UK)

Publication 1

On the bending algorithms for soft objects in flows

by

A. Guckenberger, M. P. Schraml, P. G. Chen, M. Leonetti and
S. Gekle

Computer Physics Communications **207**, pp. 1 – 23 (2016)

DOI: [10.1016/j.cpc.2016.04.018](https://doi.org/10.1016/j.cpc.2016.04.018)

Reproduced with permission from Elsevier.



On the bending algorithms for soft objects in flows



Achim Guckenberger^{a,*}, Marcel P. Schraml^a, Paul G. Chen^b, Marc Leonetti^c,
Stephan Gekle^a

^a Biofluid Simulation and Modeling, Fachbereich Physik, Universität Bayreuth, Bayreuth, Germany

^b Aix-Marseille Université, CNRS, Centrale Marseille, M2P2, UMR7340, Marseille, France

^c Aix-Marseille Université, CNRS, Centrale Marseille, IRPHE, UMR7342, Marseille, France

ARTICLE INFO

Article history:

Received 1 March 2016

Received in revised form

27 April 2016

Accepted 30 April 2016

Available online 11 May 2016

Keywords:

Helfrich bending

Laplace–Beltrami operator

Mean curvature

Capsule deformation in shear flow

ABSTRACT

One of the most challenging aspects in the accurate simulation of three-dimensional soft objects such as vesicles or biological cells is the computation of membrane bending forces. The origin of this difficulty stems from the need to numerically evaluate a fourth order derivative on the discretized surface geometry. Here we investigate six different algorithms to compute membrane bending forces, including regularly used methods as well as novel ones. All are based on the same physical model (due to Canham and Helfrich) and start from a surface discretization with flat triangles. At the same time, they differ substantially in their numerical approach. We start by comparing the numerically obtained mean curvature, the Laplace–Beltrami operator of the mean curvature and finally the surface force density to analytical results for the discocyte resting shape of a red blood cell. We find that *none* of the considered algorithms converges to zero error at all nodes and that for some algorithms the error even diverges. There is furthermore a pronounced influence of the mesh structure: Discretizations with more irregular triangles and node connectivity present serious difficulties for most investigated methods.

To assess the behavior of the algorithms in a realistic physical application, we investigate the deformation of an initially spherical capsule in a linear shear flow at small Reynolds numbers. To exclude any influence of the flow solver, two conceptually very different solvers are employed: the Lattice–Boltzmann and the Boundary Integral Method. Despite the largely different quality of the bending algorithms when applied to the static red blood cell, we find that in the actual flow situation most algorithms give consistent results for both hydrodynamic solvers. Even so, a short review of earlier works reveals a wide scattering of reported results for, e.g., the Taylor deformation parameter.

Besides the presented application to biofluidic systems, the investigated algorithms are also of high relevance to the computer graphics and numerical mathematics communities.

© 2016 Elsevier B.V. All rights reserved.

1. Introduction

The computer simulation of soft deformable objects such as cells, synthetic capsules or vesicles in three-dimensional (3D) hydrodynamic flows is a rapidly increasing field in computational physics. The smallest investigated systems consider the dynamic motion of a single object in shear or channel flow [1–15], in a gravitational field [16–19], through narrow constrictions [20–22], or the diffusion of small particles near elastic membranes [23]. On a larger scale, a number of studies focus on the effective viscosity of dense suspensions [24–29] which is closely connected to the

formation of cell-free layers near the channel walls in case of blood flow [30–33]. The investigation of suspensions containing two or more types of particles is another important field in which usually one focuses on the cross-streamline migration of the particles [30, 32, 34–41]. From a computational perspective, an adequate method for the above problems requires two ingredients: Solution of a hydrodynamic problem for the flow for which a variety of methods such as Boundary Integral [42–44], Lattice–Boltzmann [28, 45–48] or particle methods [49–52] are available, and solution of a solid mechanics problem for the objects' interfaces.

The investigated objects are filled with fluid, separated from the outside by a membrane which is typically modeled as an infinitely thin elastic sheet. Forces originating from the linearized deformation of such a sheet can be split into in-plane elasticity (shear and area dilatation) and out-of-plane (bending)

* Corresponding author.

E-mail address: achim.guckenberger@uni-bayreuth.de (A. Guckenberger).

components. For the former a number of elastic laws such as neo-Hookean (e.g. [3,53]) or Skalak [54] have been proposed, depending on the physical properties of the studied object, and recently different numerical modeling approaches have been compared [55]. Bending contributions are very often described via a simple law proposed by Canham and Helfrich [56,57], stating that the local bending energy density is proportional to the square of the local mean curvature. Depending on the type of object, different contributions may dominate the total force. Vesicles, for example, lack shear elasticity and are thus entirely dominated by bending forces [5–7,11,58]. For elastic capsules, on the other hand, the elasticity governs most of the behavior, with bending causing mostly secondary effects [3,28,53,58]. However, in certain situations it can become the dominating factor. For instance, it defines the wavelength of local wrinkles appearing for capsules especially at low shear rates due to local compressive forces [3,53,59–63]. Neglecting the bending rigidity in this case reduces not only the numerical stability but also the physical reliance greatly, making realistic simulations practically impossible [3,28,53,61,64]. For red blood cells, both elasticity and bending are relevant, where the latter determines the equilibrium shape [65]. Hence, the accuracy of the employed bending algorithm is of major concern.

To compute the mechanics of the membrane, it is typically discretized via a set of marker points whose positions are advected with the hydrodynamic flow. The most flexible, most easy-to-implement and therefore also one of the most widely used methods to interpolate between the nodes is a discretization via flat triangles [18,43,58,63,66–69]. Recently, subdivision surface methods [4,70–74] are becoming increasingly popular, too. Other methods include curved triangles [2,75,76], B-Splines [3], or global approaches such as spherical harmonics [10,20,77]. The latter are most efficient for not too large deformations. Bending forces are computed as the derivative of the out-of-plane stress which, by the principle of virtual work, is the variational derivative of the bending energy [78,79]. Since the mean curvature already contains the second derivative, in total the fourth derivative of the surface geometry is required. This poses a severe algorithmic and numerical challenge because the surface discretizations are often not \mathcal{C}^4 smooth.

Here we study a set of six algorithms to compute the bending forces for the most common case of a membrane discretized via flat triangles. A major difference between the algorithms is their approach on the Laplace–Beltrami operator, a key component of the bending forces. Note that its discretization is subject to active research [80–87]. For this work, we employ methods that are devised by or based on principles of Kantor and Nelson [88, hereafter called Method A], Gompper and Kroll [89, Method B], Meyer et al. [90, Method C], Belkin et al. [84, Method D], Farutin et al. [68, Method E] and Loop and Cirak et al. [73,74, Method S]. The latter, albeit being a subdivision method, also departs from flat triangles. To the best of our knowledge, no publication has so far used Belkin et al.’s discretization (Method D) for the computation of bending forces. In a recent work, Tsubota [69] compared three different algorithms akin to Methods A and C. He considered a shear flow setup and the equilibrium shape of a red blood cell (RBC), finding that Method A shows notable deviations to C. No comparison with an analytically solvable reference shape or earlier simulation work was attempted.

As a start we calculate the discretization error for the analytically known surface of an RBC. We find a strong difference in the quality and robustness of the algorithms: Most are very sensitive to the surface discretization and *none* converge at all nodes as the resolution is increased. The results are summarized in Tables 2 and 3. To assess the performance of the bending algorithms in a typical flow setup, we then investigate the deformation of an initially spherical capsule in a viscous shear

flow. The capsule is endowed with both shear and bending rigidity. To exclude any artifacts possibly arising from the flow solver, we use the Boundary Integral (BIM) as well as the Lattice–Boltzmann method (LBM). In general we find a very good agreement between both approaches. The deviations between the six bending algorithms are much less pronounced in this setup than in the analytical part. A comparison with the literature, however, reveals a wide scattering of reported values for the Taylor deformation parameter.

We finally note that our study may also be relevant in other areas where the numerical evaluation of the Laplace–Beltrami operator, which is a main focus of this work, plays an important role. In geometry processing, for example, it is often used for the visualization of high-curvature regimes, highlighting of surface details, or surface smoothing and reconstruction [81,84,90,91].

2. Computation of bending forces

2.1. The physical model of the bending energy

All bending algorithms used in the present work and in the majority of the literature depart from the seminal works of Canham [56] and Helfrich [57]. They considered a three-dimensional soft object with an infinitely thin interface endowed with bending resistance. They then proposed the following constitutive law for the bending energy:

$$E_B = 2\kappa_B \int_S [H(\mathbf{x})]^2 dS(\mathbf{x}). \quad (1)$$

Henceforth, S is the instantaneous smooth surface of the object and κ_B is the bending modulus. The local mean curvature is given by $H = \frac{1}{2}(c_1 + c_2)$, where c_1 and c_2 are the local principal curvatures. H is taken to be positive for a sphere. In principle an additional term dependent on the Gaussian curvature appears in the bending energy. Fortunately, this term is constant if the topology of the object does not change [57,89]. Thus it is negligible for the purpose of force computations. A spontaneous (or reference) curvature can be included in Eq. (1) [65], but for simplicity we take the minimum energy reference state as a flat sheet.

For later convenience, we introduce an alternative expression for H [81]:

$$H(\mathbf{x}) = \frac{1}{2} \sum_{i=1}^3 (\Delta_S x_i) n_i(\mathbf{x}), \quad \mathbf{x} \in S. \quad (2)$$

$\mathbf{n}(\mathbf{x})$ is the outer normal vector of the membrane surface S at position \mathbf{x} and $\Delta_S = \nabla^S \cdot \nabla^S$ denotes the Laplace–Beltrami operator with ∇^S being the surface gradient. Subscripts indicate vector components.

2.2. Principles for the computation of bending forces

The general goal is to compute the forces from the bending energy (1) while using an approximation for the surface S . As outlined in the introduction, we approximate S via flat triangles, i.e. each surface element consists of three nodes (vertices) and three straight edges. The force is then required at each node $\mathbf{x}^{(i)}$ with $i = 1, \dots, N$. We denote by N the number of nodes and by N_T the number of triangles.

To be more precise, the hydrodynamic simulations performed in Section 4 require either the force $\mathbf{F}^h(\mathbf{x}^{(i)})$ (LBM) or the traction jump $\Delta \mathbf{f}^h(\mathbf{x}^{(i)}) := (\sigma_+ - \sigma_-) \cdot \mathbf{n}$ (BIM). σ_+ and σ_- are the stress tensors at the outside and inside of S , respectively, and \mathbf{n} again the outer normal vector. The force equilibrium conditions read [53,58]

$$\mathbf{F}^h = -\mathbf{F} \quad \text{and} \quad (3)$$

$$\Delta \mathbf{f}^h = -\mathbf{f}. \quad (4)$$

Table 1
Overview of the six methods A–E and S employed in this work.

Method	A	B	C	D	E	S
Basic ingredient from	Kantor [88]	Gompper [89]	Meyer [90]	Belkin [84]	Farutin [68]	Cirak [74]
Result	Force	Force	Force density	Force density	Force density	Force density
Derivative	Nodal	Nodal	Variational	Variational	Variational	FEM
Basic idea	Normal vector discretization	Δ_S via co-tangent scheme	Δ_S via co-tangent scheme	Δ_S via heat equation	Parabolic fitting	Subdivision surface

Depending on the employed bending algorithm, either the force \mathbf{F} or the surface force density \mathbf{f} is obtained. Conversion between both is thus necessary and will be described in Section 2.6.

Computation of \mathbf{F} or \mathbf{f} means to perform a variational derivative of Eq. (1) with respect to small deformations of the surface. The six algorithms considered in this work (named A–E and S) effectively calculate this derivative and are summarized in Table 1. From a conceptual standpoint, there is a major difference between the methods. The first two algorithms (Methods A and B) first discretize the surface and then perform the variational derivative by means of a direct differentiation with respect to the nodes' positions (termed "force formulation" below). This yields the force \mathbf{F} . The three methods C–E perform the discretization after the variational derivative (termed "variational formulation" by us) and thus provide the force density \mathbf{f} . The last method S is similar to the force formulation as it introduces the discretization beforehand. However, it uses the weak formulation, solving a linear system of discretized integral equations by means of the finite element method (FEM). This leads again to the force density \mathbf{f} .

2.3. Force formulation

The first two Methods A and B first discretize the integral and the mean curvature from Eq. (1). The energy E_B then depends on the node coordinates $\mathbf{x}^{(i)}$ explicitly. By the principle of virtual work, they subsequently derive the force according to

$$\mathbf{F}(\mathbf{x}^{(i)}) = -\frac{\partial E_B}{\partial \mathbf{x}^{(i)}}, \quad i = 1, \dots, N. \quad (5)$$

This derivative can often be performed analytically.

2.3.1. Method A

Method A starts with the expression $\int_S (H^2 - 2K) dS = \int_S (\partial_\alpha \mathbf{n}) \cdot (\partial_\alpha \mathbf{n}) dS$ [89]. The integral with the Gaussian curvature K remains constant due to the Gauss–Bonnet theorem if the topology does not change and hence plays no role for the force calculation. The mean curvature part can be identified with Eq. (1). A direct discretization of the integral together with the approximation of equilateral triangles [89] then leads to the often employed expression (e.g. [9, 22, 27, 28, 32, 33, 36, 37, 40, 41, 52, 69, 88, 89, 92–95])

$$E_B \approx 2\tilde{\kappa}_B \sum_{(i,j)} (1 - \cos \theta_{ij}), \quad (6)$$

where the sum runs once over all edges (i, j) . θ_{ij} is the angle between the normal vectors of the two triangles that contain edge (i, j) .

One critical issue with this formula is the value of $\tilde{\kappa}_B$. It is usually not identical to the physical κ_B appearing in Eq. (1). In case of a sphere approximated by equilateral triangles it is simply $\tilde{\kappa}_B = \sqrt{3} \kappa_B$. But in general the value depends on the shape of the object [89]. Nevertheless, one usually finds this value also being used for non-spherical shapes. Here we set $\tilde{\kappa}_B = \sqrt{3} \kappa_B$, too. We remark that one could use Eq. (6) as the model equation directly, i.e. to take it not as an approximation of the Helfrich law in the first place. In this case our analysis must be viewed as addressing the question

"how near or far away" it is from the Helfrich model rather than "how well of an approximation" it is.

A further simplification encountered from time to time is the usage of the small angle approximation $\cos \theta_{ij} \approx 1 - \frac{1}{2} \theta_{ij}^2$ [28, 29, 39, 52]. Its advantage is that it does not require the computation of a sine. We also tested this alternative and found a slight increase of the errors presented below. But because the error increase remained below 5% and because the hydrodynamic simulations turned out to be insensitive to it, we restrict ourselves to the more common equation (6).

The analytic formulas for the derivative in Eq. (5) are presented in great detail in [28, ch. C.2] for the small angle approximation. Apart from the occurrence of an additional sine (stemming from the above cosine), they can be also used unchanged for Eq. (6) and will therefore not be repeated here.¹ After knowing the force \mathbf{F} at each node, the force density can be computed as outlined in Section 2.6 below. This method is identical to "model KN" from Tsubota [69].

2.3.2. Method B

Gompper and Kroll [89] approximated the Laplace–Beltrami operator in the expression for the mean curvature from Eq. (2) by a variant of the so-called cotangent scheme, namely

$$\Delta_S x_l^{(i)} \approx \frac{\sum_{j^{(i)}} (\cot \vartheta_1^{(ij)} + \cot \vartheta_2^{(ij)}) (x_l^{(i)} - x_l^{(j)})}{2A_{\text{Voronoi}}^{(i)}}, \quad i = 1, \dots, N, \quad l = 1, 2, 3, \quad (7)$$

where the sum runs over the first ring of neighbor nodes of $\mathbf{x}^{(i)}$. The integral from Eq. (1) is then discretized as

$$E_B \approx \frac{\kappa_B}{2} \sum_{i=1}^N (2H(\mathbf{x}^{(i)}))^2 A_{\text{Voronoi}}^{(i)}, \quad (8)$$

with N denoting the total number of nodes. $\vartheta_1^{(ij)}$ and $\vartheta_2^{(ij)}$ are the angles opposite to the edge (i, j) in the triangles which contain nodes $\mathbf{x}^{(j-1)}$ and $\mathbf{x}^{(j+1)}$, respectively. See Fig. 1 for a sketch. $A_{\text{Voronoi}}^{(i)}$ is the Voronoi area of node $\mathbf{x}^{(i)}$, defined by

$$A_{\text{Voronoi}}^{(i)} := \frac{1}{8} \sum_{j^{(i)}} (\cot \vartheta_1^{(ij)} + \cot \vartheta_2^{(ij)}) |\mathbf{x}^{(i)} - \mathbf{x}^{(j)}|^2, \quad i = 1, \dots, N. \quad (9)$$

The area is geometrically contoured by connecting the circumcenter points of the triangles. It must be noted that this Voronoi area

¹ For the sake of completeness we note that for a non-zero reference state the formula $\theta_{ij} = \arccos(\mathbf{n}_i \cdot \mathbf{n}_j)$ as given in [28, ch. C.2] is only valid for convex parts of the surface. Otherwise, the value needs to be multiplied with -1 to correctly capture the reference shape. Here, \mathbf{n}_i (\mathbf{n}_j) is the normal vector of the i 'th (j 'th) triangle. Furthermore, care must be taken if $\sqrt{1 - (\mathbf{n}_i \cdot \mathbf{n}_j)^2} \approx 0$, because then divisions through zero would occur. In this case the correct resulting force is simply zero for zero reference states. For non-zero reference states one needs to compute the correct value by an analytic limiting procedure.

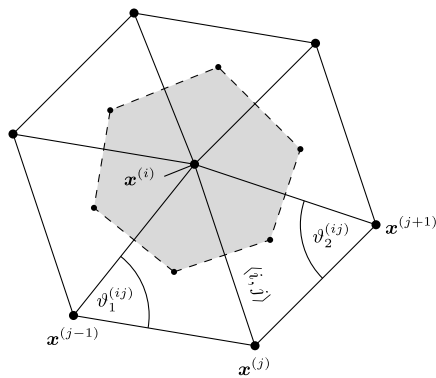


Fig. 1. Ring-1 neighbors of some node $\mathbf{x}^{(i)}$. We marked one of the neighbors arbitrarily as $\mathbf{x}^{(j)}$. The shaded region depicts the Voronoi area $A_{\text{Voronoi}}^{(i)}$.

does not lead to an exact covering of the surface if non-obtuse triangles occur [90], as outlined in the description of Method C below. Nevertheless, similar to Gompper and Kroll we use it for all triangles, no matter if obtuse or not.

The publication by Gompper and Kroll only provides the discretizations outlined above. To arrive at the force at node $\mathbf{x}^{(i)}$, we compute the gradient in Eq. (5) with the energy from Eq. (8) analytically, as explained in the Appendix A. Finally, the approach from Section 2.6 is used to obtain the force density.

The solver presented in Refs. [49,50] and subsequent publications [96–100] is based on Eq. (8). “Model J” from Tsubota [69] is somewhat similar in spirit, but more simplistic.

2.4. Variational formulations

The three Methods C–E depart from an analytical and exact expression for the surface force density. It follows from the first variation of the bending energy $\delta E_B = -\int_S \mathbf{f} \cdot \delta \mathbf{x} \, dS$ as [8,78,79]

$$\mathbf{f}(\mathbf{x}) = 2\kappa_B (2H(H^2 - K) + \Delta_S H) \mathbf{n}, \quad \mathbf{x} \in S. \quad (10)$$

Here, $K = c_1 c_2$ is the Gaussian curvature with c_1 and c_2 being again the principal curvatures. \mathbf{n} is the outer normal vector at \mathbf{x} whose numerical computation also depends on the employed method. Similar expressions are obtained when a spontaneous or reference curvature is included [79]. The methods presented hereafter differ by how they compute the different quantities appearing in Eq. (10).

2.4.1. Method C

Meyer et al. [90] derive the following discretization for the Laplace–Beltrami operator on triangulated meshes from a contour integral around node $\mathbf{x}^{(i)}$ (also see Refs. [58,81]):

$$\Delta_S w(\mathbf{x}^{(i)}) \approx \frac{\sum_{j^{(i)}} (\cot \vartheta_1^{(ij)} + \cot \vartheta_2^{(ij)}) (w(\mathbf{x}^{(i)}) - w(\mathbf{x}^{(j)}))}{2A_{\text{mixed}}^{(i)}}, \quad (11)$$

$$i = 1, \dots, N.$$

w is an arbitrary two-times continuously differentiable function on S . The notation is otherwise identical to Section 2.3.2. Obviously, it is another variant of the cotangent scheme. Comparing this equation with Eq. (7), we immediately see that they are almost the same with the sole difference being that the “mixed area” $A_{\text{mixed}}^{(i)}$ rather than the Voronoi area $A_{\text{Voronoi}}^{(i)}$ is used. For rings with non-obtuse triangles, one simply has $A_{\text{Voronoi}}^{(i)} = A_{\text{mixed}}^{(i)}$. However, using the Voronoi area for obtuse triangles leads to an incomplete tiling of the surface area, i.e. the sum of all Voronoi areas is not necessarily the same as the total surface area. For this reason, Meyer et al. introduced the mixed area: Rather than forming the

area by all circumcenter points of all triangles, it uses the point in the middle of edges that are opposite of obtuse angles. Its precise definition and algorithm can be found in [90].

The mixed area aside, the second major difference compared to Method B is that Eq. (10) is being evaluated directly. Hence, after the mean curvature has been computed via Eqs. (11) and (2), the Laplace–Beltrami operator of the mean curvature, $\Delta_S H$, is calculated by applying formula (11) again on H [58].

For the Gaussian curvature K , Meyer et al. give the following simple expression [90]:

$$K(\mathbf{x}^{(i)}) = \frac{1}{A_{\text{mixed}}^{(i)}} \left(2\pi - \sum_t \theta_t^{(i)} \right), \quad i = 1, \dots, N. \quad (12)$$

This is a discretization of the Gauss–Bonnet theorem. The sum runs over all triangles t sharing node $\mathbf{x}^{(i)}$, and $\theta_t^{(i)}$ is the angle in triangle t at node $\mathbf{x}^{(i)}$.

The last ingredient is the normal vector $\mathbf{n}(\mathbf{x}^{(i)})$. Several approaches exist to derive its value from the well-defined normal vectors of the triangles. Jin et al. [101] compared several often used methods. They concluded that summing the normal vectors of the triangles containing node $\mathbf{x}^{(i)}$ and weighting them with the angle $\theta_t^{(i)}$ gives the best results in many cases (“mean weighted by angle” approach, MWA). An often used alternative is to normalize the result of $\Delta_S \mathbf{x}$. However, we found that the MWA algorithm provides superior results and thus we will adopt it in this work.

We finally remark that e.g. Refs. [8,12,16,18,23,35,58,66,67,80,81,102] and [44,103–105] use the same or similar algorithms (where the latter refer to it as contour integral based method and only employ it for H). Method C is “model H” from Tsubota [69].

2.4.2. Method D

Method D differs from Method C by the discretization of the Laplace–Beltrami operator. It is based on a kernel of the diffusion or heat equation, and reads [84]

$$\Delta_S w(\mathbf{x}^{(i)}) \approx \frac{1}{4\pi a_i^2} \sum_{t=1}^{N_T} \frac{A_t}{3} \sum_{\mathbf{p} \in V(t)} \exp\left(-\frac{1}{4a_i} |\mathbf{p} - \mathbf{x}^{(i)}|^2\right) \times (w(\mathbf{x}^{(i)}) - w(\mathbf{p})), \quad i = 1, \dots, N. \quad (13)$$

N_T denotes the number of triangles, $V(t)$ is the set of vertices of triangle t , and A_t its area. Furthermore, a_i is some free parameter that represents the neighborhood of node $\mathbf{x}^{(i)}$. Because it has the dimension of a squared length, we use $a_i = A_{\text{mixed}}^{(i)}$ in the following. Other choices lead to very similar results.

Obviously, a single evaluation of the operator has a complexity of $\mathcal{O}(N_T) \approx \mathcal{O}(N)$, where N is the number of nodes. Since we need to compute the bending forces at all vertices, Method D has an overall complexity of $\mathcal{O}(N^2)$ which can become prohibitively slow for larger meshes. On the other hand, the large supports leads to an insensitivity regarding noise [84], a fact which we also find reflected in our results below.

In practice we have slightly modified the above algorithm: Imagine a plane that goes through the centroid [106] of the object and with its normal vector pointing from the centroid to node $\mathbf{x}^{(i)}$. Then we only take into account points that lie above this plane. Otherwise, nodes that lie close in 3D space but are located far apart when measured along the surface (geodesic distance) would lead to large errors. This is the usual case for the dimples of red blood cells studied below.

Apart from the discretization of Δ_S , the remaining parts of the algorithm are identical to Method C. Especially note that the Gaussian curvature is still computed with Meyer et al.’s discretization given by Eq. (12) (because Ref. [84] does not provide an alternative), and the normal vector algorithm remains MWA. To

the best of our knowledge, no publication so far used Belkin et al.'s discretization in the context of bending models.

It is also worth noticing that Li et al. [87] developed a similar formulation in a recent paper. Rather than using the *Euclidean* distance $|\mathbf{p} - \mathbf{x}^{(i)}|$ in the exponential function, they employ the *geodesic* distance between these points. Furthermore they do not take into account all triangles but only those within a certain cutoff (measured, again, via the geodesic distance). For most cases with mediocre resolution they report slightly better results for the mean curvature than for Belkin et al.'s discretization, becoming (mostly) better with increasing resolutions. Because of the only small advantage at practical resolutions and because it is non-trivial and often expensive to compute the geodesic distance between points on general triangular meshes [107], we have not yet attempted its implementation.

2.4.3. Method E

Instead of using a direct finite-differences like approach, Farutin et al. [68] employ a least square fitting procedure. The algorithm consists of three steps: In the first step, a local coordinate system at each node is created. Two axes are arbitrarily chosen to be parallel to the approximated tangential plane, while the third axis is parallel to the approximated normal vector. We estimate the normal vector again via the MWA algorithm. Next, one paraboloid is fitted to *each* of the three components of all the ring-1 nodes around each vertex. This involves the solution of three 5×5 linear systems per node. The fitting coefficients can be identified with local derivatives. They therefore provide a direct method to compute the mean and Gaussian curvature, the metric tensor and a refined approximation for the normal vector via standard differential geometry [68]. The final step fits a paraboloid to the mean curvature, yielding the coefficients required to evaluate $\Delta_S H$. Putting everything together, the force density can then be computed via formula (10).

We remark that this algorithm requires each node to have at least five neighbors. Otherwise, the paraboloid would not be uniquely defined. For nodes with less than five neighbors, we extend the mean square fitting to include the ring-2. This leads to a well-defined problem for general meshes. Furthermore, in principle more rings can always be included as shortly discussed in Section 3.5. An efficient algorithm for higher ring orders is breadth-first search.

Besides [68], publications that use the same basic idea to obtain the mean curvature include e.g. Refs. [67,81,104,108], although they fit a single paraboloid onto the surface itself (rather than to the components of the coordinates).

2.5. Method S

Method S is somewhat set apart from the previous five algorithms. Departing from the usual mesh with flat triangles, the subdivision scheme of Loop [73,74] is applied to refine and average the surface. The method converges to a smooth limit surface which is \mathcal{C}^2 almost everywhere, corresponding to quartic box-splines. An exception are vertices that do not have six neighbors. There it is reduced to \mathcal{C}^1 . With this method, the displacement field of an element depends on the (usually 12) neighboring triangles. In addition to being a versatile geometrical representation useful in computer aided design, the Loop subdivision is particularly well adapted to physical problems involving first and second-order derivatives such as infinitely thin shells described by a Kirchhoff-Love energy functional. Indeed, the nodal forces at the membrane are determined by using the virtual work principle in its weak formulation, taking into account the membrane and bending strains [74]. This leads to a linear system of discretized integral equations that is treated with the finite element method.

It means notably that neither Gaussian and mean curvatures nor the Laplace–Beltrami operator of the mean curvature need to be calculated explicitly. Still, the Gaussian and the mean curvature can be obtained from byproducts of the result, and we show them in Section 3. We use GMRES [109] with a residuum of 10^{-9} to solve the linear system. The complexity in general is therefore $\mathcal{O}(N^2)$. This method has already been applied to capsules without bending resistance in a planar elongation flow [13] and droplets with dilational and shear surface viscosities [70] with a full validation section in each case. See Ref. [70] for further details.

Refs. [4,13,70–72] also use similar subdivision surfaces in the biofluid context.

2.6. Conversion from forces to surface force densities

As already mentioned above, the quantity that is required to couple the membrane bending mechanics to the hydrodynamic flow depends on the employed flow solver. For our chosen LBM implementation one needs the force \mathbf{F} at each surface node $\mathbf{x}^{(i)}$, while for BIM the surface force density \mathbf{f} is required. By designating a certain area surrounding each node as the “node area” one can interconvert between both quantities by simply multiplying (dividing) the force density (force) by the respective node area [32,69,72]. This interconversion is necessary for a comparison of all six algorithms with a single flow solver, as Methods A and B yield the force \mathbf{F} while C, D, E and S yield the force density \mathbf{f} .

We use Meyer et al.'s mixed area A_{mixed} already introduced in Section 2.4.1 because of its perfect surface tiling property. Hence, the conversion is performed by the formula

$$\mathbf{f}(\mathbf{x}^{(i)}) \approx \frac{1}{A_{\text{mixed}}^{(i)}} \mathbf{F}(\mathbf{x}^{(i)}), \quad i = 1, \dots, N. \quad (14)$$

3. Benchmarking against analytical results for a static red blood cell

3.1. Red blood cell shape and methodology

RBC shape and discretizations. To quantitatively assess the quality and differences between the six bending approaches presented in the previous section, we consider the typical RBC shape as shown in Fig. 2.

We choose this shape for two reasons: Firstly, it is simple enough to allow derivations of analytical expressions for all relevant quantities, including the force density itself, by means of differential geometry and standard computer algebra software. Secondly, it is a realistic shape which has regions where the mean curvature has different signs (i.e. turning points) and is thus complex enough to serve as a reasonable test subject. An oblate spheroid, for example, would be simpler to handle, but is a lot farther away from real-world situations in case of blood flow.

The considered shape can be described by the formula

$$z = \pm \frac{R}{2} \sqrt{1 - \rho^2} (C_0 + C_1 \rho^2 + C_2 \rho^4) \quad (15)$$

with $\rho := \frac{1}{R} \sqrt{x^2 + y^2}$ and the constants $C_0 = 0.2072$, $C_1 = 2.0026$ and $C_2 = -1.1228$ [110,111]. R is the length of the large half-axis of the RBC, and is often taken to be $R \approx 4 \mu\text{m}$. In this section we use $R = 1$, effectively non-dimensionalizing all lengths by the RBC radius.

The discretization as shown in Fig. 2(a) is derived by successively refining a regular icosahedron via division of each triangle into four new elements according to Loop's subdivision scheme [73,74]. The z -coordinates of the nodes are afterwards

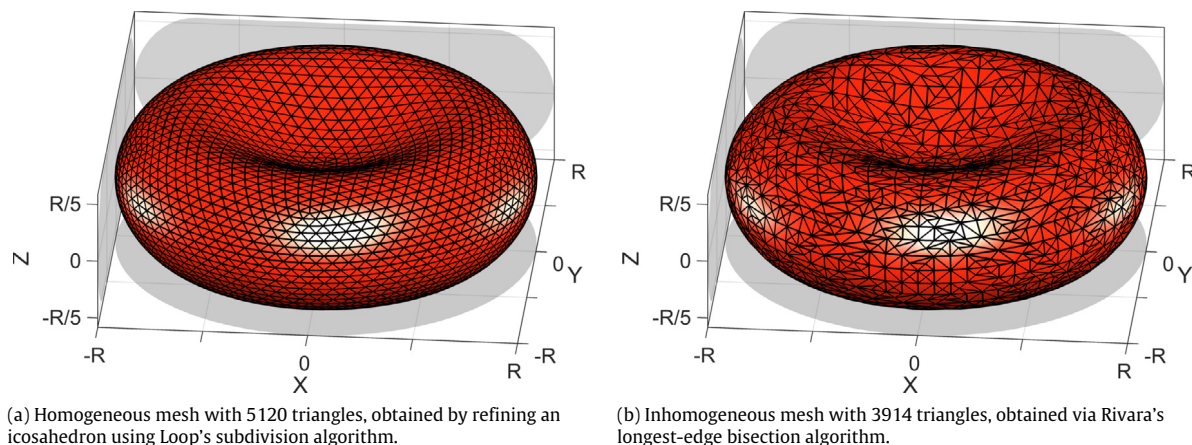


Fig. 2. Illustrations of the typical red blood cell shape discretized with the two different MT1 methods as described in the main text. Meshes of type MT2 look very similar (see Fig. B.18), except that the triangles around nodes with five neighbors are somewhat larger.

modified via application of formula (15). This leads to the very homogeneous meshes with 320, 1280, 5120, 20,480 and 81,920 triangles considered below. All of the nodes have six neighbors, with the exception of exactly twelve vertices retaining only five neighbors for any N . The meshes with 512 and 2048 triangles are based on a regular octahedron, leading to four or six neighbors. We call discretizations based on Loop's refinement “MT1”.

We also assess the behavior on three other mesh types for Methods A–E. The first is the inhomogeneous one shown in Fig. 2(b). This mesh with 3914 triangles is obtained by starting from an icosahedron refined to 320 triangles via Loop's scheme (MT1). We then apply Rivara's longest-edge bisection algorithm [112] three times and transform the result via Eq. (15) to the RBC. Each node has four to ten neighbors. The second additional mesh is very similar to the homogeneous geometries described above, except that new nodes introduced during the refinement are simply placed at the middle of edges rather than according to Loop's algorithm. This is an often used scheme, and results in a slightly different structure. We will refer to it as “MT2” and outline observed differences in the main text where appropriate. The actual data can be found in Appendix B. As a third mesh we consider the application of Rivara's algorithm to an MT2 object with 320 elements, resulting in 3848 triangles. See the supplementary information (SI) for a collection of mesh properties such as typical edge lengths (Appendix C).

Evaluation and error measures. All numerical results were obtained using double precision arithmetic. They are plotted as functions of the polar angle θ_i , computed via

$$\theta_i = \arccos \left(\frac{z_i}{\sqrt{x_i^2 + y_i^2 + z_i^2}} \right), \quad (16)$$

where x_i , y_i and z_i are the Cartesian coordinates of node $\mathbf{x}^{(i)}$, $i = 1, \dots, N$. The RBC described by Eq. (15) is axisymmetric and hence the results at each position will be plotted as a function of the polar angle only. This corresponds to a projection of the azimuthal direction into a single plane. We do not just compute the data at some cross section because the *mesh* is non-axisymmetric and hence results do vary with the azimuthal angle.

The relative errors of the normal vector, the mean curvature and the force density are computed as normalized Euclidean norms:

$$\begin{aligned} \varepsilon_{\mathbf{n}}(\theta_i) &:= |\mathbf{n}^a(\mathbf{x}^{(i)}) - \mathbf{n}^n(\mathbf{x}^{(i)})|, \\ \varepsilon_H(\theta_i) &:= \frac{|H^a(\mathbf{x}^{(i)}) - H^n(\mathbf{x}^{(i)})|}{\max |H^a|}, \\ \varepsilon_{\mathbf{f}}(\theta_i) &:= \frac{|\mathbf{f}^a(\mathbf{x}^{(i)}) - \mathbf{f}^n(\mathbf{x}^{(i)})|}{\max |\mathbf{f}^a|}, \end{aligned} \quad (17)$$

where the superscripts a and n denote the analytical and the numerical value, respectively. Errors for the Gaussian curvature, ε_K , and the Laplace–Beltrami operator of H , $\varepsilon_{\Delta_S H}$, are handled the same way as ε_H . Note that ε_n is the error relative to the length of the normal vector $|\mathbf{n}^a| = 1$. Furthermore, we compute the errors relative to the maximal analytic values because transitions through zero exist. Using the local analytic results as the reference would lead to greatly exaggerated error values: The numeric algorithms never produce zero values at precisely the same positions as the analytics. Approximately, one has for $R = 1$ and $\kappa_B = 1$: $\max |H^a| \approx 2.20098$, $\max |K^a| \approx 3.60620$, $\max |\Delta_S H^a| \approx 109.095$ and $\max |\mathbf{f}^a| \approx 189.457$.

Continuing, the tables and graphics presented in this work show two different measures for the total error. The maximum error of all the nodes is calculated as $\max_i \varepsilon_{\bullet}(\theta_i)$ and represents the local worst case result. On the other hand, the average error is computed as $\sum_{i=1}^N \varepsilon_{\bullet}(\theta_i)/N$ with N being the number of nodes on the RBC. It measures the overall performance of the algorithm for viscous flows. More precisely speaking, the average can be interpreted as a discretization of a continuous error measure, for example $\sum_{i=1}^N \varepsilon_{\mathbf{f}}(\theta_i)/N \sim \int_S |\mathbf{f} - \mathbf{f}^a| dS$, because $1/N \sim h^2 \sim dS$ where h is the mean edge length. Similar integrals determine the flow in the Stokes regime, compare Section 4.3.1. The average measure is therefore the more meaningful quantity in this particular application. Indeed, previous studies reported that a few problematic nodes do not affect the overall hydrodynamic results significantly [68]. We confirm this in Section 4.

Below we show the numerical results as a function of θ . Corresponding images of the errors can be found in the supplementary material (see Appendix C). Furthermore, we display the two error measures (maximum and average) as a function of the inverse of the *mean* edge length h or, equivalently, as a function of triangle count N_T .

We start by considering the normal vector, the mean curvature and the Laplace–Beltrami operator of the mean curvature. These are required for the evaluation of Eq. (10) in the variational formulation. The Gaussian curvature is considered in the supplementary information (see Appendix C). As a last step we combine the results to get the force density \mathbf{f} , where we also include the two algorithms based on the force formulation. Tables 2 and 3 at the end of this section summarize all results.

3.2. Normal vector

As outlined in Section 2.4, we use the MWA algorithm to compute the normal vector for Methods C and D. In case of

Method E, the MWA normal vector is taken as the input and the fit procedure yields a new result. Farutin et al. [68] stated a convergence rate for E of $\mathcal{O}(h^2)$.

Fig. 3 shows the maximum and average of the relative error ε_n of the normal vector for the MT1 based meshes.

Obviously, E as well as MWA converge roughly with $\mathcal{O}(h^2)$ in both error measures at the beginning. For E this is in line with the report of Farutin et al. At larger resolutions MWA appears to decay as $\mathcal{O}(h)$ for the maximum error. We remark that the computation of \mathbf{n} by normalization of $\Delta_S \mathbf{x}$ for Methods C and D often leads to errors that are an order of magnitude larger.

The subdivision based Method S is a bit different. Its maximal error tends to behave first as $\mathcal{O}(h^2)$ and then as $\mathcal{O}(h)$, similar to MWA, although the absolute values are roughly one order of magnitude smaller. The major error source are nodes that are members of the ring-1 neighborhood of vertices that have only five neighbors, i.e. where the surface is only \mathcal{C}^1 smooth. On the other hand, the majority of the surface is \mathcal{C}^2 which leads to the observed $\mathcal{O}(h^3)$ convergence of the average error.

Considering the inhomogeneous mesh with 3914 triangles, both MWA and Method E are found to be sensitive to irregularities, albeit E is a bit less affected. Furthermore, both show similar behavior on the second mesh type MT2, except that MWA decays as $\mathcal{O}(h)$ starting with 5120 elements (see Fig. B.19 in Appendix B).

3.3. Mean curvature

The mean curvature H is one of the central ingredients for the computation of the bending energy (cf. Eq. (1)) and, subsequently, the bending forces. However, it is explicitly required only for Methods C, D and E. Method S yields it as a byproduct. The mean curvature from these four approaches is shown in Fig. 4 in comparison to the analytical result. Correspondingly, Fig. 5 presents the maximal and average errors.

Method C seems to retain a systematic maximal error because the results at a few nodes slightly above $\theta = 3\pi/8$ do not converge to the correct result (identical to the highlighted nodes in Fig. 9(c)). These nodes have six neighbors, just like most of the other vertices and thus are not very “special” at first sight. For further analysis we turn to Xu [80] who gives a *sufficient* condition for convergence: Firstly, the node must have six neighbors. Secondly, there must exist a local parametric representation $q \in \mathbb{R}^2$ of the surface such that $q_j = q_{j-1} + q_{j+1} - q_i$ where i indicates some node and j enumerates its six neighbors. If we choose at each node a coordinate system with two axes in the tangential plane and the last axis along the (analytic) normal vector, we find that this condition is most severely violated at precisely the non-converging points. This suggests why we find a systematic error. Note, however, that this is merely a sufficient rather than a necessary condition for convergence. As such, convergence can and is observed at other nodes although they also violate this condition or do not even have six neighbors. The same is observed for the MT2 meshes (Fig. B.20 in Appendix B).

Both Method D's and E's approaches lead to convergent results regarding the maximum error. The rate is roughly $\mathcal{O}(h)$ for Method E which is consistent with Ref. [68]. Hence we find that algorithm E is superior to C as also noticed by Zinchenko et al. [104] for two variants of the methods. For D the rate seems to be $\approx \mathcal{O}(h^2)$, albeit it has error levels that are typically half to one order of magnitude larger than E for the present case. Notice that D's operator can actually be proven to converge point-wise for arbitrary meshes and hence also in the here employed Euclidean norm [84], a fact which is reflected in our results. Method S has problems with the \mathcal{C}^1 regions as error levels quickly stagnate. The absolute values are still comparably small.

With respect to the average errors, algorithms C–E display the same behavior: they converge as $\mathcal{O}(h^2)$. Method D is still the one with the largest errors. E and C are alike, with E having a slight edge. The subdivision scheme S appears to converge faster at first. At higher resolutions, the rate reduces to $\mathcal{O}(h^2)$.

Finally, we consider the inhomogeneous mesh with 3914 triangles. Algorithm E shows a serious increase of the error while it is tremendous for Method C. The largest errors for C come from nodes with only four neighbors, although some of them show smaller deviations (also note that the meshes with $N_T = 512$ and $N_T = 2048$ have vertices with four adjacent nodes). On the other hand, Method D is largely unaffected by the irregularities. This indicates that it is more robust than the other algorithms, an observation which can be attributed to the larger support [84].

We remark that the MT2 meshes lead to the same conclusions, except that the error magnitudes can be significantly larger (cf. Appendix B). The Gaussian curvature is analyzed in the supplementary material, revealing similar results (see Appendix C).

3.4. Laplace–Beltrami operator of the mean curvature

The remaining quantity that needs to be computed for Eq. (10) is the Laplace–Beltrami operator of the mean curvature, $\Delta_S H$. As described in Section 2.4, it is calculated by applying the Laplace discretization idea again to H for C, D and E. Method S does not easily allow the computation of $\Delta_S H$. Considering the results from the previous Section 3.3, we do not expect Method C to converge. Our findings are shown in Figs. 6 and 7.

Obviously, the expectation is met: Method C fails to converge entirely. The maximum of the error even diverges quickly as $\mathcal{O}(1/h^2)$ because of the troublesome points already identified for the mean curvature. Algorithm E at first appears to become more precise with higher resolutions in the maximum error measure, but then appears to diverge with a rate of $\approx \mathcal{O}(1/h)$ for $N_T \geq 5120$. Indeed, Farutin et al. report the same trend. In the context of Stokes flow, however, they found that it can still provide very good results [68] (also see the average error and Section 4). Even the deviations for the rather lenient Method D fail to decay with resolutions beyond 20,480 triangles.

Regarding the average error measure, Method C retains a systematic deviation. Methods D and E both converge with roughly $\mathcal{O}(h^2)$ in the presented case. Unfortunately, for meshes of type MT2 we observe an entirely different behavior (see Fig. B.21 in Appendix B): The rate for D is reduced to $\mathcal{O}(h)$, and E fails to converge (although it does not diverge). Hence, D is again much more robust with respect to different triangulations than E.

This is also reflected in the results for the inhomogeneous mesh with 3914 triangles (see Fig. 7). Method E and especially C depict severe difficulties for both the maximal and average errors, yielding values that are mostly one to two orders of magnitude larger than for 1280 triangles. In contrast to the previous sections, Method D also shows some problems for the maximal error, although it can keep the average error on an adequate level.

3.5. Force density

Finally, we combine all the quantities via Eq. (10) and get the force density \mathbf{f} for Methods C, D and E. Additionally, Methods A, B and S are applied as described in Sections 2.3, 2.5 and 2.6. We plot the results in Figs. 8–10. The bending modulus has been set to $\kappa_B = 1$ in all cases.

Variational formulation. Since the value of $\Delta_S H$ dominates Eq. (10), it is of no surprise that the errors ε_f for C, D and E are very similar to $\varepsilon_{\Delta_S H}$. Notably, Method D appears to converge with $\mathcal{O}(h)$ only for

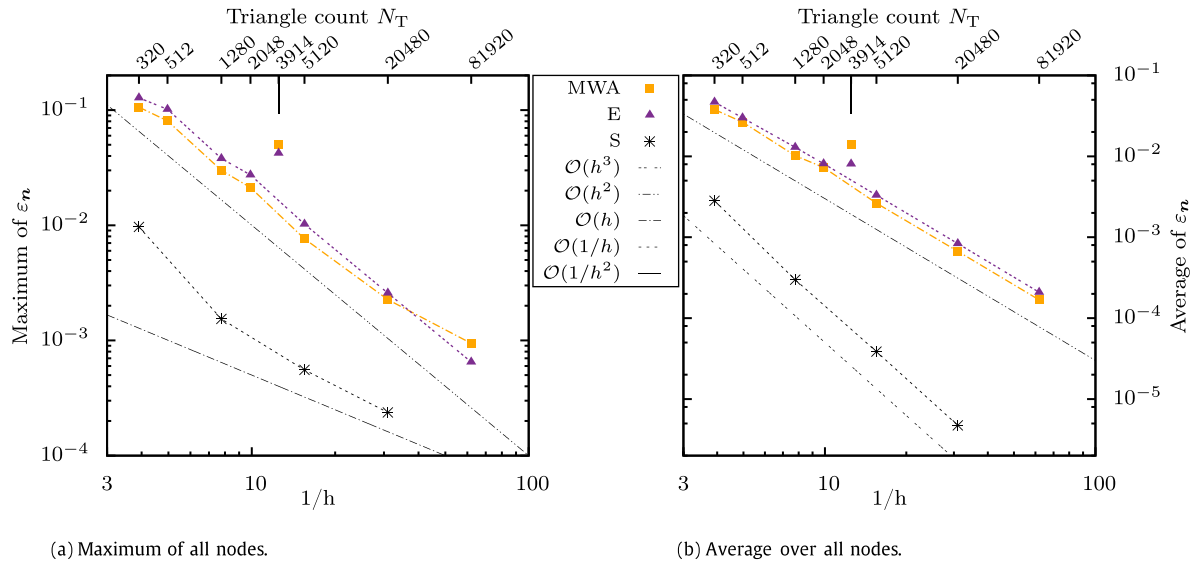


Fig. 3. The maximum and average of the relative error ε_n of the normal vector as a function of resolution N_T or, equivalently, as a function of the inverse of the mean edge length h for the RBC shape MT1. MWA is the “mean weighted by angle” algorithm from [101]. Black lines without symbols depict typical scaling behaviors. Results for the inhomogeneous mesh with 3914 triangles are highlighted by the small vertical line at the top. The numerical values and a breakdown per node as a function of the polar angle θ can be found in the supplementary material. The results for the MT2 mesh types are in Fig. B.19.

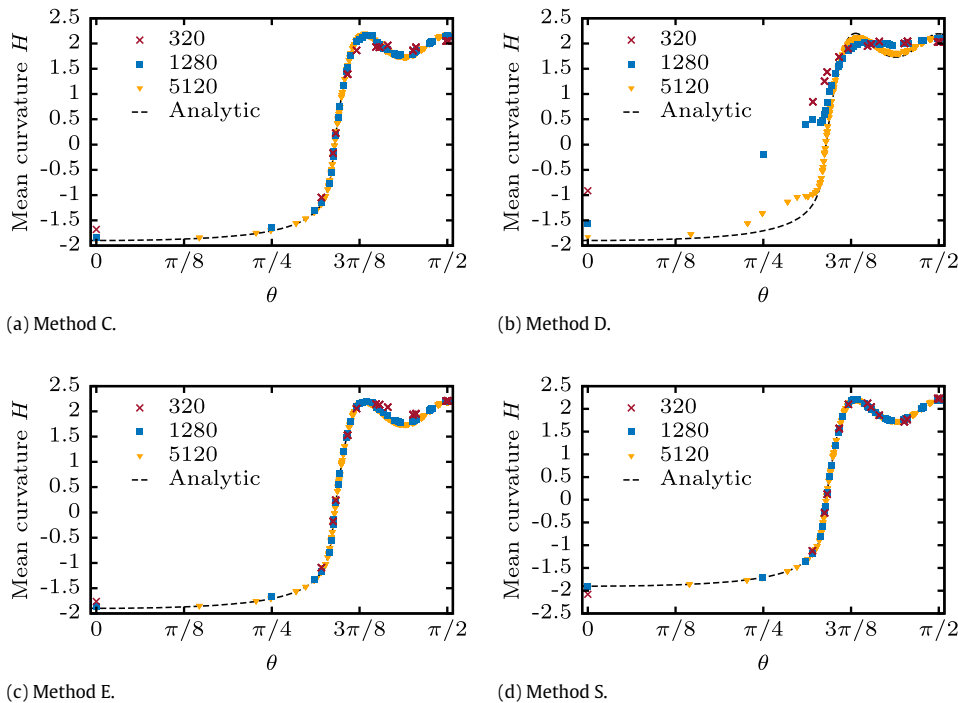


Fig. 4. The mean curvature H of a MT1 RBC obtained from the four different algorithms (symbols) and compared to the analytical result (dashed line) as a function of the polar angle θ . The errors at each node can be found in the supplementary information (see Appendix C).

the MT2 average error measure but not for the maximal, retaining a systematic deviation there. The maximal errors for E and C diverge with $\mathcal{O}(1/h)$ and $\mathcal{O}(1/h^2)$, respectively. The averaged error remains roughly constant for C, but decays as $\mathcal{O}(h^2)$ for E. As noted above, this last rate does not carry over to the MT2 meshes in Appendix B (Fig. B.23) where E behaves similar to C. To this end, the error pattern on the surface differs notably between MT1 (Fig. 9(e)) and MT2 (Fig. 22(e)).

Force formulation. Regarding the force formulation, Method B is alike to C regarding the general behavior. However, the latter has a notable edge over the first. C is also less (but still a lot) affected by more irregular triangulations. The same holds for MT2 meshes,

too. There are only two possible sources for these deviations, since both use virtually the same discretization of the Laplace–Beltrami operator as outlined in Section 2.4.1. The first reason could be the imperfect surface tiling used for Method B (Voronoi rather than mixed area). Secondly, the differing approach for the variational derivative (before and after discretization). A quick check where we replaced $A_{\text{mixed}}^{(i)}$ with $A_{\text{Voronoi}}^{(i)}$ in Method C (Eq. (11)) leads to almost identical values as B (except for the inhomogeneous mesh where the errors are even more extreme). Therefore we conclude that at least for meshes with mediocre homogeneity the choice of either force or variational formulation has only a minor influence, in agreement with [69]. On the other hand, a proper surface tiling

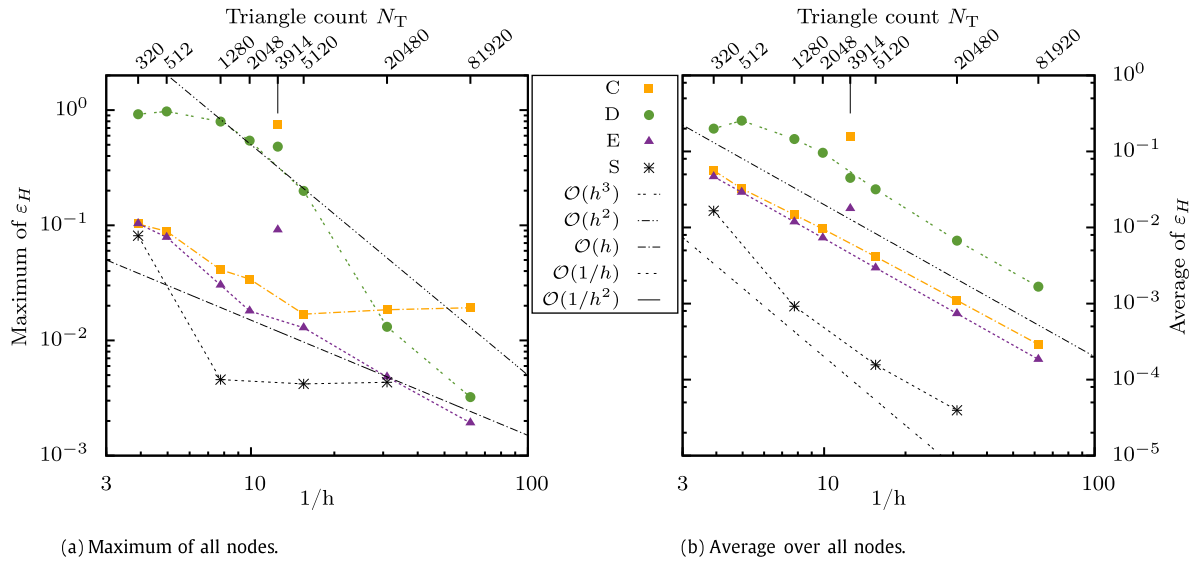


Fig. 5. The maximum and average of the relative error ϵ_H of the mean curvature (MT1). For the numeric values, see the supplementary information (Appendix C). The results for MT2 are in Fig. B.20.

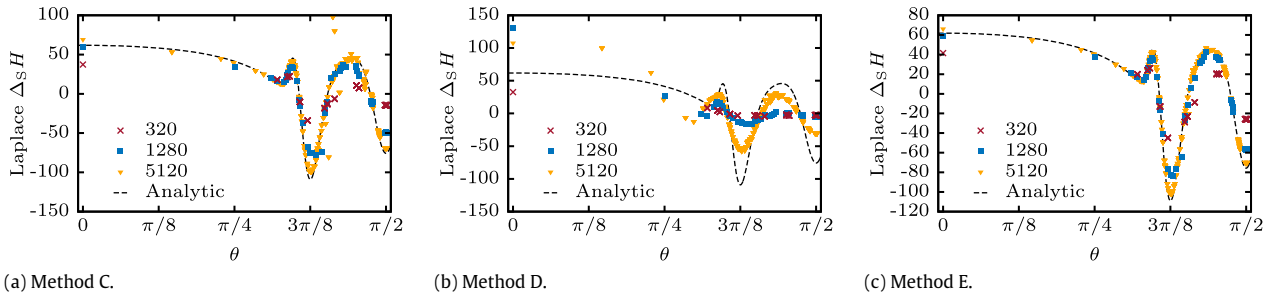


Fig. 6. The result of evaluating the Laplace–Beltrami operator on the mean curvature, $\Delta_S H$. MT1 meshes. Figures with the corresponding errors can be found in the supplementary information (see Appendix C).

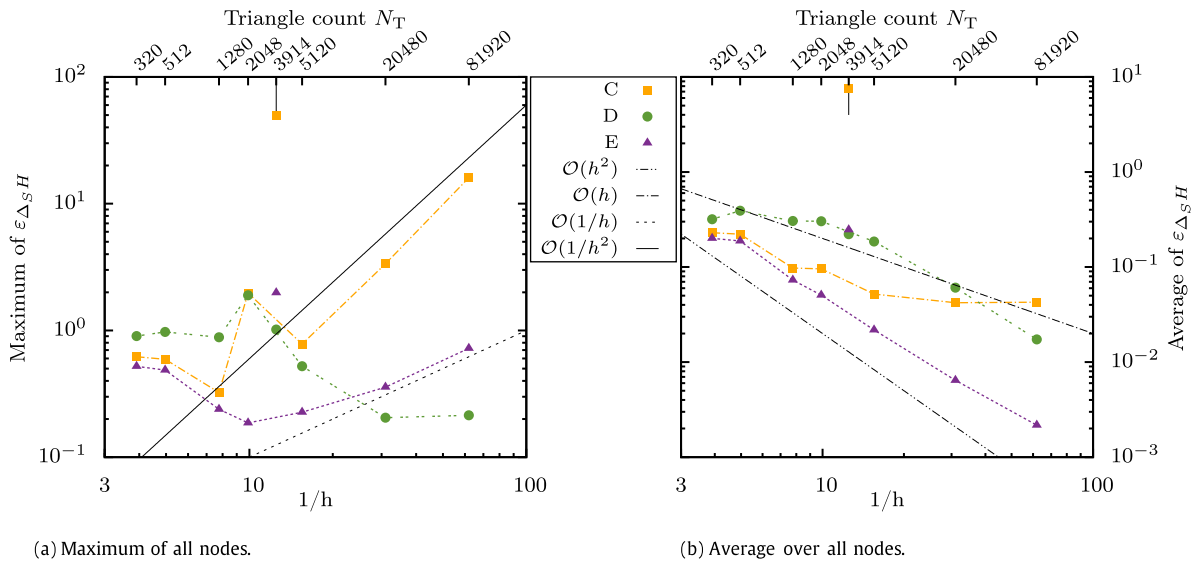


Fig. 7. The maximum and average of the relative error of the Laplace–Beltrami operator applied to H . MT1 meshes. The results for MT2 are in Fig. B.21. The numeric values are in the supplementary information (see Appendix C).

turns out to be important. Nevertheless, we remark again that both methods still exhibit very high sensitivity to the mesh regularity, and both do not converge.

Method A always shows extreme errors: Not only are the absolute values orders of magnitude larger than for the other

methods and its maximal error diverges as $\mathcal{O}(1/h^2)$, but even the average error increases with the resolution at a rate of $\mathcal{O}(1/h)$ for MT2 meshes (see Fig. B.23 in Appendix B). The major problems originate from nodes with a different number of neighbors than six (see Fig. 9(a)).

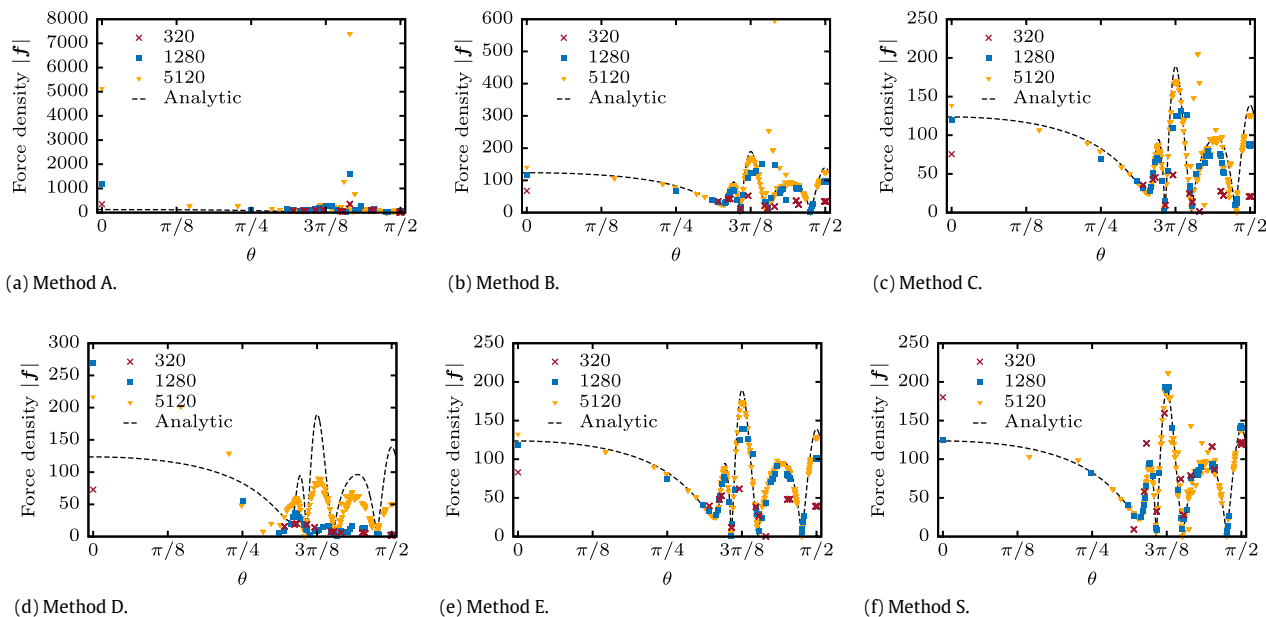


Fig. 8. The magnitude of the force density f computed via the six different bending algorithms and compared to the analytical result. MT1 meshes and $\hat{\kappa}_B = 1$. The errors are displayed in Fig. 9.

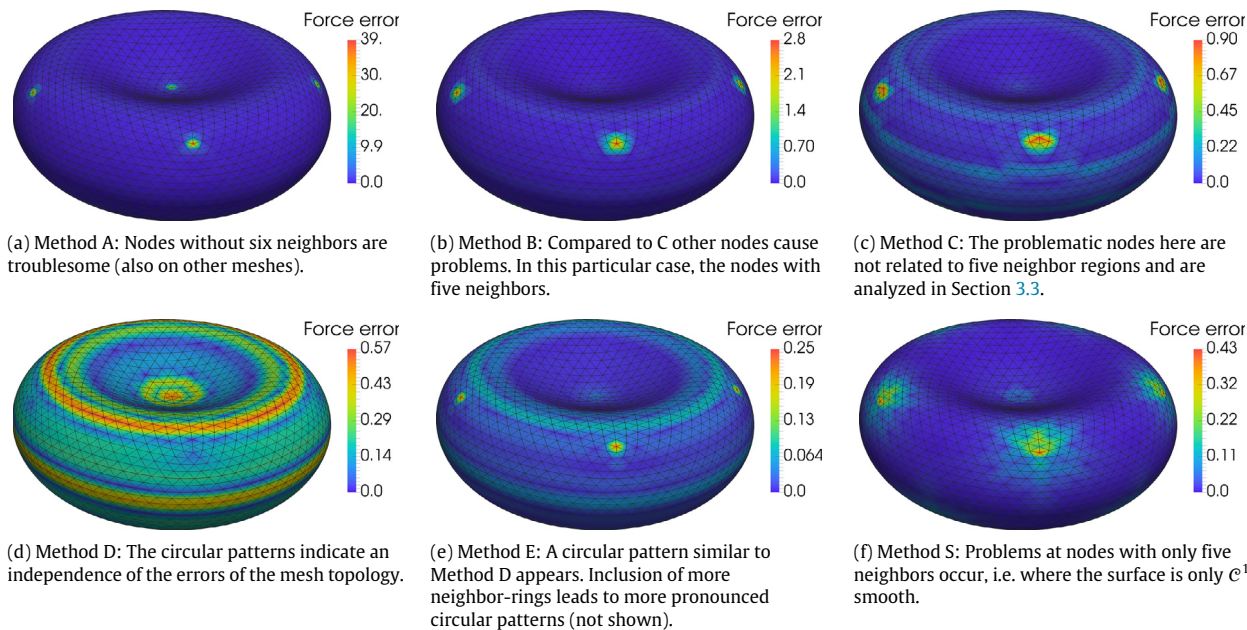


Fig. 9. 3D illustration of the errors ε_f of the force density from Fig. 8 for 5120 triangles. MT1 meshes. The results for MT2 are in Fig. B.22. Note the scales of the color bars (for interpretation of the scales, the reader is referred to the web version of this article). A projection of the azimuthal direction onto a single plane can be found in the supplementary information (see Appendix C).

Method S. The subdivision surface algorithm, Method S, exhibits a $\mathcal{O}(1/h^2)$ divergence of the maximal error, just like A, B and C. The average error also saturates, although with a significantly smaller value than the others. As noted before and as clearly visible in Fig. 9(f), the five neighbor regions contain the biggest troublemakers, most likely because the surface is only C^1 smooth there.

Method E with a larger support. We also tested a slight modification of Method E that takes into account not just the first ring of neighbors for the fitting procedure, but also the second and third rings. The values are included in the tables in the supplementary material (see Appendix C). In general we found three differences: First of all, for smaller resolutions ($N_T \leq 5120$) the errors are larger for higher ring orders. Second, the start of the $\mathcal{O}(1/h)$ section

in the maximal error measure is postponed to higher resolutions, but it still exists. Third, they can handle the inhomogeneous mesh far better but still not as good as approach D. Therefore, we conclude that taking into account more neighbors benefits the overall robustness of the fitting method (as reported in [82]), albeit leading to larger errors at mediocre (and thus often practical) resolutions. This is in line with Method D, which is an extreme case, having all nodes as support. Indeed, the 3D error pattern of E (Fig. 9(e)) becomes more similar to that of algorithm D (Fig. 9(d)). But note that the underlying discretization idea of the latter is completely different.

Final notes. One also has to emphasize the absolute value of the errors: No method yields relative maximal errors below 10% for all considered resolution, and they are often in the $>200\%$ regime for

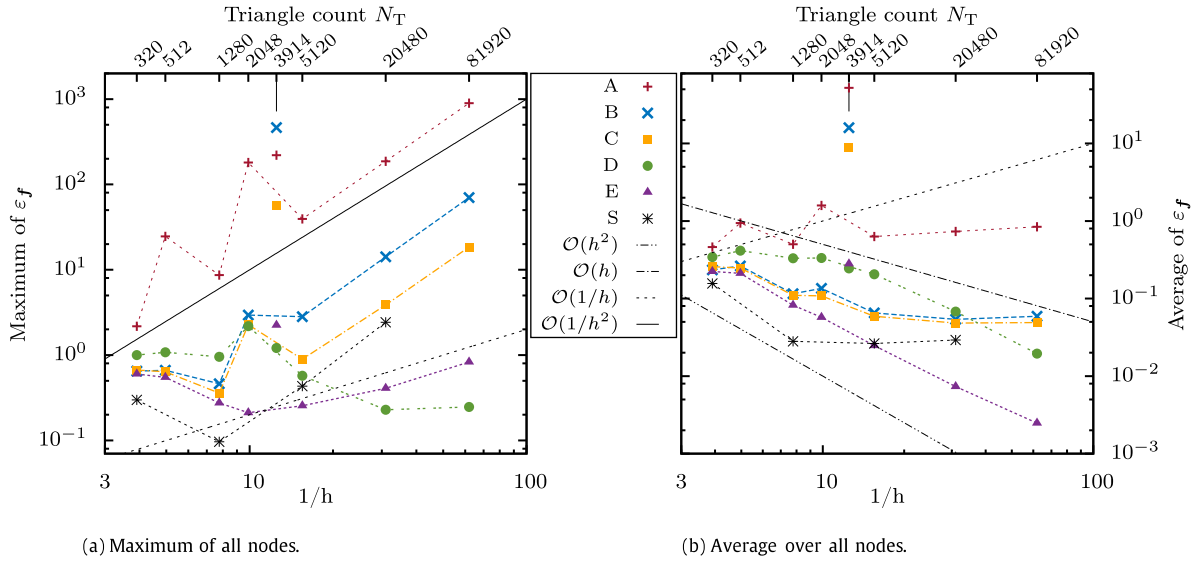


Fig. 10. The maximum and average of the relative error of the force density. MT1 meshes. The results for MT2 are in Fig. B.23. For the numerical values see the supplementary information (Appendix C).

irregular meshes. This illustrates the basic difficulty of computing a fourth order derivative on triangulated meshes. We remark that it is theoretically impossible to construct a discrete Laplace–Beltrami operator that satisfies all expected properties simultaneously [83].

A concise summary of all the results can be found in Tables 2 and 3 using the MT2 meshes for Methods A–E (MT1 is the same or better) and MT1 for Method S. Due to the revealed mesh dependencies, the exact quality of the algorithms highly depends on the individual case. Still we are positive that the tables can serve as a general guideline.

4. An elastic capsule in shear flow

4.1. Basic setup

We now analyze the performance of the bending algorithms in the context of Stokes flow. Despite the sometimes very large deviations compared to the analytics as presented in the previous section, one can expect a better performance in such an application [68,69]. As already noted above, viscous flows lead to an averaging of the errors.

We consider an initially spherical capsule of radius R placed in a linear shear flow with shear rate $\dot{\gamma}$ as illustrated in Fig. 11. The Reynolds number is much smaller than one. This is an often studied system and performance test case in the recent literature [1–4,8,10,55,62,69,71,75,102,113,114], also motivated by several experiments that displayed varying results [14,59,115].

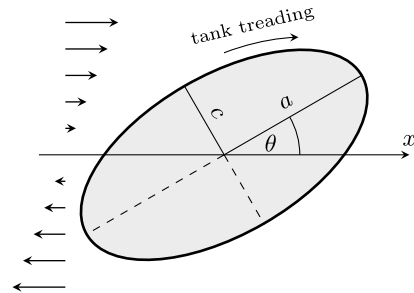


Fig. 11. 2D illustration of the linear shear system. The actual simulation is three-dimensional. The spherical capsule deforms to an ellipsoid-like shape. a is the largest and c the smallest half-axis, while θ is the inclination angle. The membrane rotates around the object’s centroid (the so-called “tank-treading” motion).

The infinitely thin capsule surface is endowed not just with a bending rigidity, but additionally with a shear elasticity as described in the next Section 4.2. Its inside is filled with a Newtonian fluid having the same viscosity as the ambient flow. It is well known that for not too large shear rates the shape of such an object becomes approximately an ellipsoid. This state is usually described by the Taylor deformation parameter $D := \frac{a-c}{a+c}$ with the largest and smallest semi axes a and c , respectively, and the inclination angle θ between the x -axis and a . We extract D and θ at each time step from an ellipsoid with the same inertia tensor [48, 116].

Table 2

Summary of the convergence results for the RBC. The symbol ● indicates convergence to zero errors, ○ convergence with a systematic error and ■ divergence as the resolution is increased. K is the Gaussian curvature, H the mean curvature and f the force density. Note that only in D the average errors of the force density seem to converge to zero, while no algorithm shows convergence of the maximum error.

Method	A	B	C	D	E	S
K			○	○	●	○
H			○	●	●	○
$\Delta_s H$			■	○	■	■
f	■	■	○	○	○	■

(a) Maximum errors.

Table 3

Summary of problematic behavior for the inhomogeneous mesh. ● means no troubles, ○ labels problems only in the maximal but not in the average error measure and ■ indicates a significant increase of the deviations in both error measures.

Method	A	B	C	D	E
K			■	■	■
H			■	●	■
$\Delta_s H$			■	○	■
f	■	■	■	○	■

(b) Average errors.

The system parameters can be cast into two dimensionless values [113]: the dimensionless shear rate (or elastic capillary number) $G := \frac{\mu \dot{\gamma} R}{\kappa_S}$ and the dimensionless ratio between shear and bending resistance $\hat{\kappa}_B := \frac{\kappa_B}{R^2 \kappa_S}$. κ_S is the shear modulus for the in-plane tensions (compare the next section). Note that different conventions exist in the literature. Furthermore, the reference state for these in-plane tensions is taken to be the initial sphere, whereas the bending reference state is a flat sheet (also see Section 2). Numerically, the sphere is constructed using Loop's subdivision as presented in Section 3.1 (MT1), just without the final transformation to the RBC shape. We consider 320, 1280 and 5120 triangles as well as the inhomogeneous 3914 triangle mesh. The results with MT2 meshes are practically identical and will therefore not be discussed any further.

4.2. In-plane forces

Apart from the bending forces, we additionally take into account elastic in-plane tensions to allow for comparisons with the existing literature. We choose the widely used neo-Hookean law (e.g. [3,53]) whose in-plane energy density due to stretching can be written as

$$\epsilon_S = \frac{\kappa_S}{6} \left(I_1 + \frac{1}{I_2 + 1} - 1 \right). \quad (18)$$

Other forms exist in the literature. I_1 and I_2 are the strain invariants. They are related to the principal in-plane stretch ratios λ_1 and λ_2 via

$$I_1 = \lambda_1^2 + \lambda_2^2 - 2 \quad \text{and} \quad (19a)$$

$$I_2 = \lambda_1^2 \lambda_2^2 - 1. \quad (19b)$$

The total energy is given by the surface integration

$$E_S = \oint_{S_0} \epsilon_S dS_0, \quad (20)$$

where the surface S_0 denotes the surface in the *reference* (i.e. initial) state.

Assuming that the deformation varies linearly over the triangles, the force is then obtained via the finite element method by performing the derivative of Eq. (20) with respect to the node positions $\mathbf{x}^{(i)}$

$$\mathbf{F}(\mathbf{x}^{(i)}) = - \frac{\partial E_S}{\partial \mathbf{x}^{(i)}} \quad (21)$$

analytically, just like it was done for the bending forces in Section 2.3. Section 2.6 is used to arrive at the force density. The details are elaborated in Refs. [1,28] and will not be repeated here. We remark that this method gives very good results when compared with the literature, as shown below in Section 4.4.

4.3. Flow solvers

We now describe the two employed flow solvers: The Boundary Integral method (BIM) and the Immersed–Boundary Lattice–Boltzmann method (LBM). As the main focus of this article is on the computation of bending forces, we will keep the description fairly brief.

4.3.1. Boundary Integral method

The Boundary Integral method was first applied in the context of Stokes flow by Youngren and Acrivos in 1975 [42]. Its basic assumption is that the Reynolds number is much smaller than

unity. The method then exploits the fact that the Stokes equation is linear, and can therefore be rewritten as an integral equation [43, 44]:

$$u_j(\mathbf{x}) = u_j^\infty(\mathbf{x}) - \frac{1}{8\pi\mu} \oint_S \sum_{i=1}^3 \Delta f_i^h(\mathbf{y}) G_{ij}(\mathbf{y}, \mathbf{x}) dS(\mathbf{y}), \quad (22)$$

$$\mathbf{x} \in S, \quad j = 1, 2, 3.$$

\mathbf{x} is a point on the surface S of the capsule that is suspended in the infinite fluid domain, \mathbf{u} is the surface velocity and μ the dynamic viscosity of the inner and outer fluids. $\mathbf{u}^\infty(\mathbf{x}) = \dot{\gamma} x_3 \hat{\mathbf{e}}_x$ is the imposed shear flow with the shear rate $\dot{\gamma}$ and the shear plane perpendicular to the z -direction. $\hat{\mathbf{e}}_x$ denotes the unit vector along the x -axis. Finally, $G_{ij}(\mathbf{y}, \mathbf{x}) := \delta_{ij}/r + r_i r_j / r^3$ is the free-space Green's function, whereas $\mathbf{r} := \mathbf{y} - \mathbf{x}$ and $r := |\mathbf{r}|$. Thus, given the traction jump $\Delta \mathbf{f}^h$ via formula (4), this integral equation allows us to compute the velocity at each node of the capsule's surface. Afterwards, they are moved with the flow according to the kinematic (no-slip) condition [44]

$$\frac{d\mathbf{x}}{dt} = \mathbf{u}(\mathbf{x}), \quad \mathbf{x} \in S, \quad (23)$$

where t denotes the time.

Methods A–E. The first five Methods A–E directly use the discretization of the surface S with flat triangles. Integrals are performed by a Gaussian quadrature with 7 points per triangle [117]. Necessary quantities at these points are obtained via linear interpolation from the nodes [43]. The polar integration rule is used for singular triangles [118]. The ordinary differential equation (23) is solved using the Cash–Karp method [119] which is an explicit embedded Runge–Kutta scheme of order four and five, i.e. an adaptive step size algorithm. Its relative tolerance is fixed to 10^{-7} while the absolute tolerance is $10^{-6}R$. Decreasing both by a factor of 10 did not change the results significantly. Note that the mesh remains very homogeneous throughout the whole simulation thanks to the elastic forces acting between the nodes; no additional mesh control scheme was necessary.

Solving Eq. (22) can lead to a volume drift (a mere discretization artifact). To counter it, we first rotate the $3N$ -dimensional solution vector onto the hyperplane defined by the discretized version of the no-flux condition $\oint_S \mathbf{u} \cdot \mathbf{n} dS = 0$, similar to the approach employed in Ref. [68]. This reduces the drift but cannot eliminate it completely. Hence, after each time step we additionally rescale the object as described in [68]. This leads to a perfect conservation of volume.

Method S. Method S uses a completely different code basis and is entirely based on Loop's subdivision surface algorithm (cf. Section 2.5). I.e. Eq. (22) is computed using the smooth limit surface. Triangles, where the Green's function has a singularity, are treated as in Ref. [68]. The time evolution (23) is solved using the trapezoidal rule, a fully implicit scheme. The time step size is fixed to $\dot{\gamma} \Delta t = 10^{-4}$. No remeshing was performed during the simulations. Furthermore, the volume drift remained below 0.005% (320 triangles) and 0.0002% (≥ 1280 triangles) during all simulations. See Ref. [70] for more details.

4.3.2. Lattice–Boltzmann

The Lattice–Boltzmann method is a mesoscopic method for solving fluid problems which is based on a discretization of space and velocities. Over the last couple of years it has become a well-established method. We omit the details here. They can be found for example in Refs. [45–47]. We use the D3Q19 scheme as provided by the ESPResSo package [120,121].

For the capsule we implemented the Immersed Boundary Method (IBM) into ESPResSo [120], following mostly the works of

Krüger [28,48]. Besides the elastic and bending forces, we add an additional force to minimize deviations from the initial volume as in [28], controlled by the modulus κ_V . The source code is publicly available in the current development branch of ESPResSo.

To solve the dynamics, the explicit Euler scheme with the time step set to $\dot{\gamma}\Delta t = 2.5 \times 10^{-5}$ and the LBM grid size to $13.5/R \equiv 1$ are used. Contrary to BIM, periodic boundary conditions are (necessarily) employed. The simulation box size is set to $9.5R \times 9.5R$ in the lateral direction and $19.0R$ in height (changing it does not alter the results significantly). The shear flow is realized by placing two plane parallel walls moving in opposite directions at the top and bottom of the simulation box, implemented with the bounce-back boundary condition. Before inserting the sphere in the center of the box, we wait until the shear flow is fully developed. The Reynolds number $Re = Rv/\nu$, with ν the velocity of the walls and ν the kinematic viscosity, is always smaller than 0.3. The lattice Mach number is always smaller than 0.01. Finally, the modulus of the volume conservation force is fixed to $\kappa_V = 100\kappa_S$ (in simulation units), leading to a maximal volume drift of less than 0.1% in the presented simulations.

4.4. Verification of the codes

Extensive tests were carried out to ensure the correctness of our three simulation codes. An example for $\hat{\kappa}_B = 0$ (i.e. without any bending) can be found in Fig. 12 that compares the BIM code of Methods A–E with several references found in the literature. Some of them use vastly different simulation methodologies. Notice that the simulations remain stable despite the occurrence of buckling thanks to the small effective bending rigidity inherent to finite element methods [3,55,76]. A comparison with the LBM code can be found in Fig. 12(a). For $\hat{\kappa}_B \neq 0$ consider Fig. 17. Method S can be seen to produce identical results in Fig. 14.

All in all, the images show very good agreement, both between BIM and LBM as well as with the literature. The results were checked to be well converged, as also shown in the next section. We remark that the data in Section 3 was produced using the code basis of the two BIM implementations.

4.5. Analysis of the different bending algorithms

4.5.1. Convergence with resolution

We now compare the performance of the different bending algorithms for the capsule with both shear and bending resistance. As a starting point we investigate the convergence of each method with respect to the number of triangles used to discretize the surface. Choosing $G = 0.2$ and $\hat{\kappa}_B = 0.15$, the results in Fig. 13 are obtained.

Method A appears to be rather insensitive to the resolution which is somewhat surprising considering the increase of its error with the number of triangles (Fig. 10). However, it has serious troubles with the inhomogeneous mesh, just like in the analytic comparison, leading to an oscillatory graph. In 3D this is notable as a surface with slight “bumps”. On the other hand, Method C and especially S are the fastest converging algorithms, giving similar results as the other approaches but already at 320 triangles. This observation fits well with the average error in Fig. 10(b) which roughly remained constant. Furthermore, this also indicates that indeed the average rather than the maximum error is the more meaningful measure for the present setup. After all, the maximum error diverged as seen in Fig. 10(a), but this behavior is not reflected here. However, C obtained very high errors for the inhomogeneous triangulation even in the average measure, although in shear flow no effect is observed (Fig. 13(c)). Method B is slightly inferior regarding convergence compared to C, but otherwise identical.

E reaches its limit at $N_T = 1280$. The slowest convergence is exhibited by Method D.

We finally note that very similar observations are made for $G = 0.05$ and $\hat{\kappa}_B = 0.0375$ and for the inclination angles as depicted in the supplementary information (see Appendix C). The same holds for meshes of type MT2.

4.5.2. Direct comparison of the methods

A direct comparison of the six algorithms for a resolution of 5120 triangles using BIM is shown in Fig. 14. For the small shear rate and bending modulus in Fig. 14(a) only minor differences are observed. This shows that for small deformations the actual method plays only a secondary role, at least for sufficiently homogeneous meshes. However, larger deviations are seen if the parameters are increased to $G = 0.2$ and $\hat{\kappa}_B = 0.15$ as shown in Fig. 14(b). Most notably, Method A deviates strongly from the other five methods. This might be understandable from the large errors that were observed in Section 3 for this algorithm. Tsubota [69] also noticed major differences between Methods A and C. Furthermore, B–E and S coincide almost perfectly, with deviations in the $<1\%$ regime. For these we observed average errors that differ by approximately one order of magnitude (Fig. 10(b)), so this is somewhat surprising. We conclude that all methods except A are roughly equally well suited for this setup.

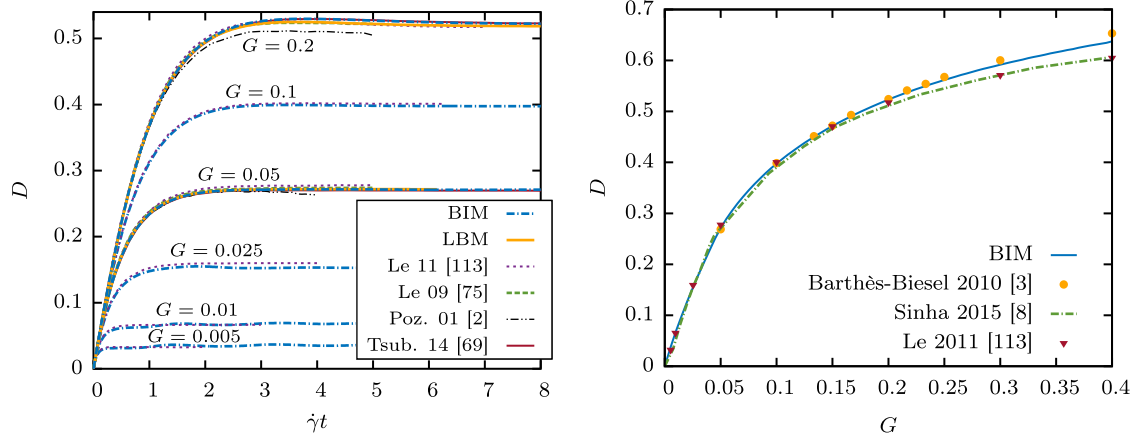
To assess a possible influence of the flow solver, we also simulate the system with Lattice–Boltzmann, restricting ourselves here to Methods A and B which directly yield the nodal forces \mathbf{F} as required by our LBM implementation. The results in Fig. 15 show very good agreement with the BIM data, proving that the observed differences are inherent to the bending algorithms themselves and largely independent of the flow solver.

4.5.3. Performance considerations

An important criterion in the selection of the most suitable bending algorithm for a given problem will be its execution speed. The approaches examined in the present work exhibit significantly different performance characteristics. Most notably the computational complexity of Method D and S are $\mathcal{O}(N^2)$ while the remaining algorithms are $\mathcal{O}(N)$. Indeed, all methods except D and S require (mostly) only the first ring of neighbors. We refrain here from comparing absolute execution times as varying degrees of optimization levels (caching of quantities, parallelization, SIMD vectorization, etc.) and the hardware may strongly influence these times. But in most cases one expects to find that *one* evaluation of Method D or S is the slowest (due to the inferior scaling), followed by Method E (because the fitting procedure involves solving several small linear systems), and the remaining algorithms being the fastest.

Instead, we employ an implementation-independent indicator, namely the required time step Δt to remain in the stable region. In general, stiffer systems require smaller time steps if explicit integrators are used. Since we use an explicit adaptive time stepping algorithm for the BIM implementation of Methods A–E, the automatically chosen values for Δt can serve as an indicator for the stiffness and the overall performance of dynamic simulations. Table 4 shows the corresponding data for two different shear rates and bending moduli.

We first note that an increase of triangle count by a factor of four leads to a decrease of the step size by roughly one order of magnitude for all algorithms—except for Method D. This algorithm also exhibits the largest of all time steps. This can be attributed to its already mentioned robustness which in turn originates from its large support (cf. Sections 2.4.2 and 3.5). The smallest time step is required by Method A, being roughly a factor of 3 smaller than for B, C and E (which all have approximately the same Δt). Moreover, the inhomogeneous mesh takes its toll for Methods A, C and especially



(a) Time evolution of the Taylor deformation parameter D for various dimensionless shear rates G . Results by Huang et al., 2012 [71], Le, 2010 [4] and Zhu 2015 [10] are not included for clarity but match well with our BIM.

(b) Stationary value of the deformation parameter as a function of the shear rate. The stationary value is computed by averaging the deformation parameter for $\dot{\gamma}t \in [5; 10]$.

Fig. 12. Time evolution and stationary values of the Taylor deformation parameter D for a spherical capsule without bending resistance ($\hat{\kappa}_B = 0$) and 5120 triangles in shear flow. We checked that the inhomogeneous mesh with 3914 triangles leads to similar results for $G = 0.05$ and $G = 0.2$. Comparison with the values of Le and Wong, 2011 [113] (projection method & IBM, subdivision surface), Le et al., 2009 [75] (projection method & IBM, curved triangles), Pozrikidis, 2001 [2] (BIM, curved triangles), Tsubota, 2014 [69] (BIM, flat triangles), Barthès-Biesel et al., 2010 [3] (BIM, B-Splines) and Sinha and Graham, 2015 [8] (BIM, flat triangles).

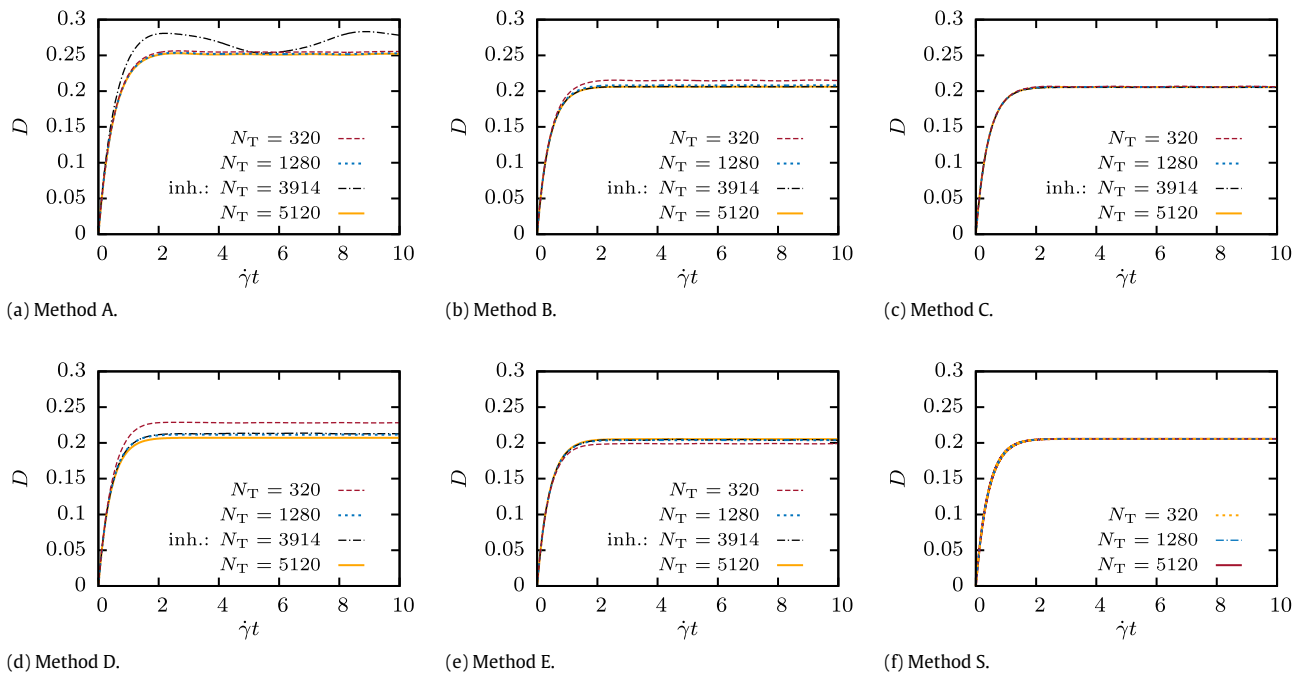


Fig. 13. Taylor deformation parameter as a function of time after turning on the shear flow for BIM. $G = 0.2$ and $\hat{\kappa}_B = 0.15$. We find that for almost all algorithms 320 triangles are too coarse to obtain converged results, whereas the curves for 1280 and 5120 triangles are almost indistinguishable. Method A shows significant changes for the inhomogeneous mesh with 3914 triangles. Graphs of the inclination angle and results for a different shear rate can be found in the supplementary material (see Appendix C).

B, leading to step sizes even below or equal to the one for 5120 triangles. Out of the three, C performs the best but cannot compete with E or even D.

The general effect of decreasing step sizes with resolution is explained by Boedec et al. [58]: More triangles imply that oscillatory modes with shorter wavelengths are resolved, but shorter wavelengths in turn mean faster typical time scales for the bending forces. Hence, the more triangles, the smaller the shortest occurring time scales and thus the smaller the necessary Δt .

Furthermore, considering the data without any bending ($\hat{\kappa}_B = 0$), one notices the tremendous effect the inclusion of bending effects has on the step size and thus on the overall performance. For mediocre resolutions, Δt is often two orders of magnitude

larger than with bending. This relates to the general stiffness of the appearing fourth derivative. A usual remedy is to work with an implicit or semi-implicit time stepping scheme, as we did in Method S. See for example Refs. [58,77].

4.5.4. Comparison with the literature

Before we can compare our simulations with the literature, we comment on the constitutive bending law. Namely, some references use the linear relation [2,10,20,75]

$$\mathbf{m} = \kappa_B \mathbf{B} \quad (24)$$

for the bending moment \mathbf{m} , where \mathbf{B} is the Cartesian curvature tensor. Pozrikidis [2] showed that this model is equivalent to

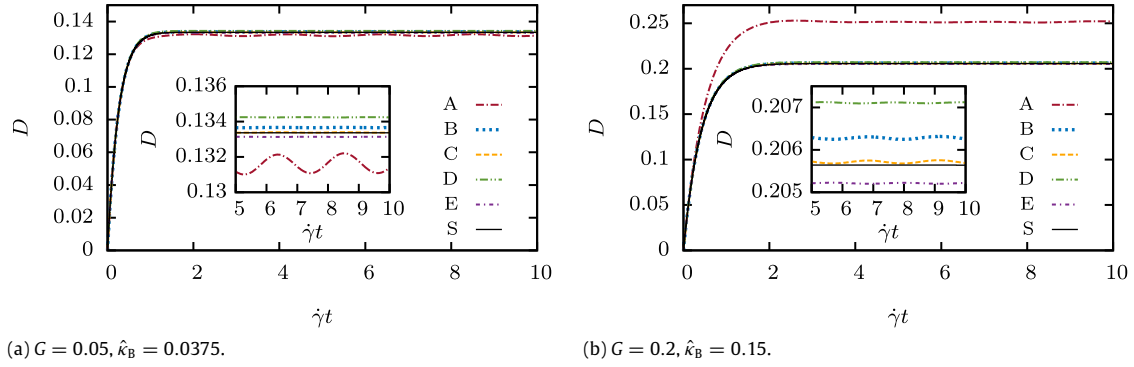


Fig. 14. Direct comparison of all bending algorithms for BIM and 5120 triangles. Insets: Magnification of $\dot{\gamma}t \in [5; 10]$.

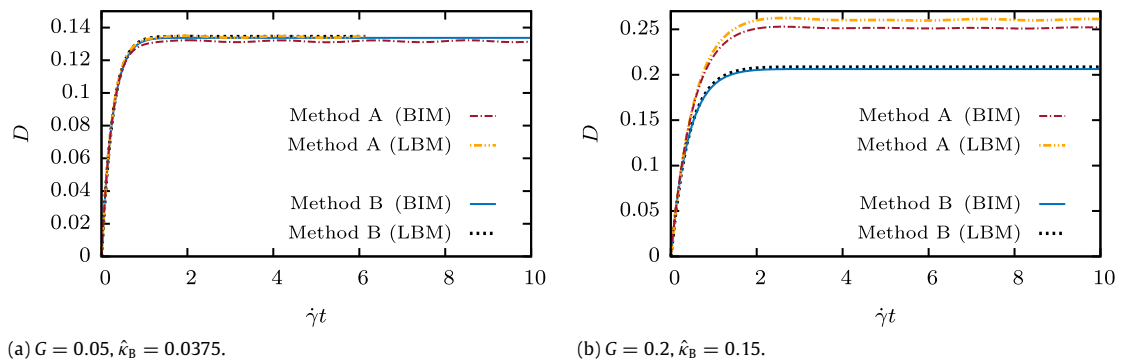


Fig. 15. Comparison of the LBM results with BIM for two different shear rates and bending moduli. In both cases 5120 triangles were used.

Table 4

Average dimensionless time step size $\dot{\gamma} \Delta t$ for the different bending algorithms and resolutions as chosen by the Cash-Karp algorithm for BIM. The relative tolerance of the time stepping scheme is 10^{-7} and the absolute tolerance is $10^{-6}R$. We also included the data without any bending ($\hat{\kappa}_B = 0$ column). The corresponding deformations can be seen in Figs. 12(a), 13 and the supplementary information (see Appendix C). The average is performed over Δt in the range $\dot{\gamma}t \in [5; 10]$.

Triangles	$\hat{\kappa}_B = 0$	A	B	C	D	E
320	0.081	0.016	0.060	0.057	0.085	0.057
1280	0.064	0.0015	0.0057	0.0056	0.063	0.0060
5120	0.029	0.00014	0.00053	0.00052	0.0085	0.00056
3914 (inh.)	0.023	0.00014	0.00014	0.00040	0.013	0.0017

(a) Average $\dot{\gamma} \Delta t$ for $G = 0.05, \hat{\kappa}_B = 0.0375$.

Triangles	$\hat{\kappa}_B = 0$	A	B	C	D	E
320	0.20	0.013	0.052	0.050	0.15	0.048
1280	0.16	0.0012	0.0050	0.0049	0.078	0.0051
5120	0.13	0.00011	0.00046	0.00046	0.0076	0.00048
3914 (inh.)	0.11	0.00012	0.000023	0.00035	0.011	0.0013

(b) Average $\dot{\gamma} \Delta t$ for $G = 0.2, \hat{\kappa}_B = 0.15$.

the Helfrich law from Eq. (1) (also see [53]). Similar, he remarks that for zero reference curvatures the model introduced by Zarda et al. [122] is the same, too.

Keeping this in mind, we compare the results from the literature in Figs. 16 and 17. The data obtained using Method C (BIM with flat triangles) and Method S (BIM with subdivision surfaces) is also included. Both are representative for the remaining algorithms as well as the LBM flow solver as has been shown in Fig. 14, with the sole exception of Method A.

Observing Fig. 16, we note that the values scatter a lot ($\lesssim 20\%$). The source is not easily identified. The algorithm for the shear

elasticity and the flow solver should have no influence, as we observe good agreement between our BIM and LBM (Fig. 15) and with the literature for $\hat{\kappa}_B = 0$ (Fig. 12) for all references. We also rule out errors in our implementation of the bending for Methods A and C: Tsubota [69] employs virtually the same algorithms and discretizations as we do, and his results agree with ours extremely well (Fig. 17). Also Method S, which uses a completely different code basis and, additionally, subdivision surfaces, matches almost perfectly with the remaining methods except A. Furthermore, we carefully checked that (apart from the explicitly mentioned differences) all references use the same physical laws.

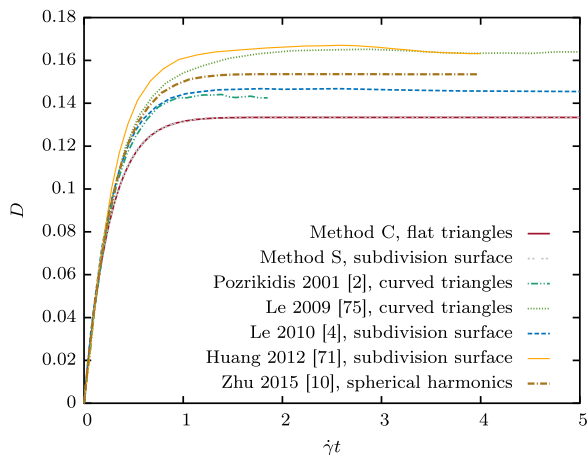


Fig. 16. Comparison of the deformation parameter for $G = 0.05$ and $\hat{\kappa}_B = 0.0375$ from the recent literature with Method C (BIM, 5120 flat triangles) and Method S (BIM, subdivision surface with 5120 elements). All references use the same physical parameters, except for Pozrikidis [2] who used a Hookean elastic law. All use the Helfrich or the equivalent linear bending model from Eq. (24), except Huang et al. [71] who employs the also equivalent bending model introduced by Zarda et al. [122] (see main text). However, the employed flow and discretization algorithms vary greatly. We note that our LBM simulations give the same results as Method C (Fig. 15) and that both BIM and LBM agree well without bending with the literature as shown in Section 4.4.

Considering the agreement for $\hat{\kappa}_B = 0$, this once again emphasizes the huge difficulty inherent in the computation of the bending forces.

5. Conclusion

To summarize, we presented six different algorithms to compute the bending forces on 3D meshes discretized with flat triangles. They are all based on the famous Canham–Helfrich constitutive law for the bending energy, but differ in their numerical implementation, using well-known ingredients and new developments. The methods, denoted by A–E and S, can be sorted into three different categories, depending on the variational derivative being performed before (“force formulation”) or after (“variational formulation”) the surface discretization. Method S is somewhat set apart from the others because it uses the finite element method to obtain the force density. Their characteristics were collected in Table 1 (Section 2.2). In short: Method A contains a sum over all angles between the triangles’ normal vectors, whereas Method B uses a variant of the cotangent scheme. The same holds for Method C, except that it employs the variational formulation and a slightly different measure for the area per node. Moreover, Method D is based on a kernel of the heat equation, Method E fits multiple parabolas onto the surface components, and Method S uses a subdivision scheme.

We then analyzed the behavior of the algorithms quantitatively by comparing their various components such as the mean curvature H or the Laplace–Beltrami operator of H (essentially a fourth order derivative) and finally the bending force itself with analytic results obtained for the typical red blood cell shape. A concise overview of the results was given in Tables 2 and 3 (Section 4.1). Regarding the maximum error, only Method D provides an acceptable approximation, being also the most robust on inhomogeneous meshes. No method converged at all nodes. If the errors are averaged over the entire mesh, Methods B–E and

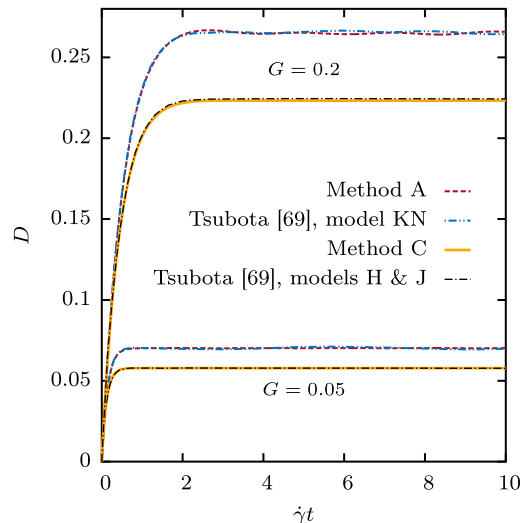


Fig. 17. Comparison of the deformation parameter for $\hat{\kappa}_B = 2/15$ (once for $G = 0.05$ and once for $G = 0.2$) for Methods A and C with Tsubota, 2014 [69]. 5120 triangles. Method A is virtually identical to model KN from [69], Method C is essentially alike to model H. Note that Tsubota uses BIM, 4604 flat triangles and the same physical conditions.

S give acceptable errors, but only D actually shows convergence. In general we found that the more vertices an algorithm takes into account to compute the values at a single node, the better the overall robustness. Hence, all Methods except D depict high sensitivity to the regularity of the mesh. No major quality differences regarding the underlying principle of force and variational formulations (before and after discretization) were observed.

As a physical application we considered an elastic capsule in a viscous shear flow. All approaches gave similar results with the exception of Method A which showed significant deviations. Still this illustrates that the behavior of some single individual points is of only minor concern for the purpose of hydrodynamics in the small Reynolds number regime. Furthermore, a small review of the existing literature employing different surface discretizations revealed large deviations for the hydrodynamic results, illustrating again the tremendous difficulty inherent with computing a fourth order derivative even on higher order surface approximations.

The results for the individual methods can be summarized as follows:

- Method A showed the largest errors of all the methods for the force density, quickly diverging in both the maximal and sometimes even the average error measure. The hydrodynamics were noticeably different compared to the other algorithms, especially for the inhomogeneous mesh. Hence it is very sensitive to irregularities. Furthermore, it often required the smallest step size in order to remain in the stable region. Even the theoretical relationship to Helfrich’s law is somewhat “blurred” because of the shape-dependent relationship between the numerical parameter $\tilde{\kappa}_B$ from Eq. (6) and the physical bending modulus κ_B . On the other hand, it is the most easily implemented method.
- Method B turned out to be similar to Method C for homogeneous meshes, but is somewhat worse for inhomogeneous triangulations regarding errors and required step size.

- Method C depicted diverging behavior for the maximal error measure of the force density \mathbf{f} , while the deviations stayed roughly constant in the average measure. However, the algorithm displayed troubles with the inhomogeneous mesh. The hydrodynamical results were very similar to Methods B–E and S, and the required step size was comparable to B and E.
- Method D was by far the most robust, showing convergence for \mathbf{f} on the regular meshes (albeit with a systematic deviation in the maximal error measure) and working reasonably well on the inhomogeneous one. It also leads to the largest step sizes. Unfortunately, one evaluation is very expensive since it scales as $\mathcal{O}(N^2)$ where N are the number of nodes.
- Method E is similar to C as the maximal errors for \mathbf{f} diverged and the average remained roughly constant. However, it handled the irregular mesh better than Methods A–C but still worse than D. The required step size was comparable to Methods B and C.
- Method S in general showed behavior alike to Method C. However, it provided errors that were significantly smaller. The complexity is $\mathcal{O}(N^2)$.

When taking the results for the systems investigated here as general guidelines, we make the following recommendations if one wishes to implement the Helfrich law for bending forces on triangulated meshes:

- Method D is in principle the best algorithm due to its robustness and often acceptable convergence properties. It should be chosen if performance is no issue and the resolution is sufficiently high. Therefore it is currently the best choice for computer graphics applications. Unfortunately, it is most likely too slow for dynamic simulations, which also often need to work with relatively coarse meshes where it performed below average.
- Method S is a good choice for homogeneous meshes due to the comparably small errors, although it does not provide proper convergence. It should especially be chosen over E if other parts of the numerical algorithm (such as surface integrals) can benefit from the subdivision surface representation. The $\mathcal{O}(N^2)$ scaling has a small prefactor, which means that it is no bottleneck for practical resolutions. The major error source were nodes without six neighbors, indicating that it is not well suited for more irregular meshes.
- Method E is the second best choice if one wishes to stay with flat triangles in all parts of the numeric implementation. The reason is that it is also relatively robust, but has worse convergence properties than D (similar to S). Compared to e.g. algorithm C, the errors for \mathbf{f} were always smaller. Furthermore, it has a much better computational complexity than Method D, making it suitable for larger simulations.
- Method C is inferior to Method E and S regarding absolute errors, and hence E or S are usually preferable. The exception might be if performance issues arise: C can be implemented more efficiently since it does not involve solving linear systems. We remark that it provides very good results for the shear flow setup, even for more irregular triangulations.
- Method B has similar stiffness and implementation characteristics as Method C, but performs worse especially for the inhomogeneous mesh. Depending on the application, the only advantage compared to C might be that it directly yields a force rather than a force density.
- Method A can be used if the goal is not to approximate the Helfrich model but to just include “some” bending resistance, i.e. in case Method A is taken as the *model itself*. Another useful application would be to prevent the mesh from buckling e.g. in shear flow simulations (i.e. for the purpose of numerical stability [29]). In this case we suggest to use the small angle

approximation from Section 2.3.1 for efficiency reasons. Note that the bending modulus must be chosen sufficiently small in order to keep the required step size large and the physical impact as small as possible. In any other case, one of the other algorithms should be preferred.

As a future research direction, a promising approach would be to mix the algorithms. For example, Method E often showed the smallest errors for the mean curvature H , while Method D is the most robust. Hence it might be worthwhile to use approach E for H and D for the Laplace–Beltrami operator of H .

Acknowledgments

We would like to thank G. Boedec, A. Farutin and M. Jaeger for helpful discussions. Funding from the Volkswagen Foundation and computing time granted by the Leibniz-Rechenzentrum on SuperMUC is gratefully acknowledged by A. Guckenberger, M.P. Schraml and S. Gekle. Funding and support from the KONWIHR network is appreciated by A. Guckenberger and S. Gekle. A. Guckenberger thanks the Elitenetzwerk Bayern (ENB), Macromolecular Science, for their support. P. G. Chen and M. Leonetti have benefited from financial support from the ANR Polytransflow (Grant No. 13-BS09-0015-01), from Labex MEC (Grant No. ANR-11-LABX-0092), from A*MIDEX (Grant No. ANR-11-IDEX-0001-02), and from CNES. This work was granted access to the HPC resources of Aix-Marseille Université financed by the project Equip@Meso (ANR-10-EQPX-29-01).

Appendix A. Derivation of the force for Method B

In this section we provide the derivation of the force $\mathbf{F}(\mathbf{x}^{(l)})$ at some node $\mathbf{x}^{(l)}$, $l = 1, \dots, N$ via Method B from Section 2.3.2. N is the number of surface nodes. We start by writing Eq. (8) as

$$E_B \approx \frac{\kappa_B}{2} \sum_{i=1}^N \tilde{E}_B^{(i)}, \quad (\text{A.1})$$

where

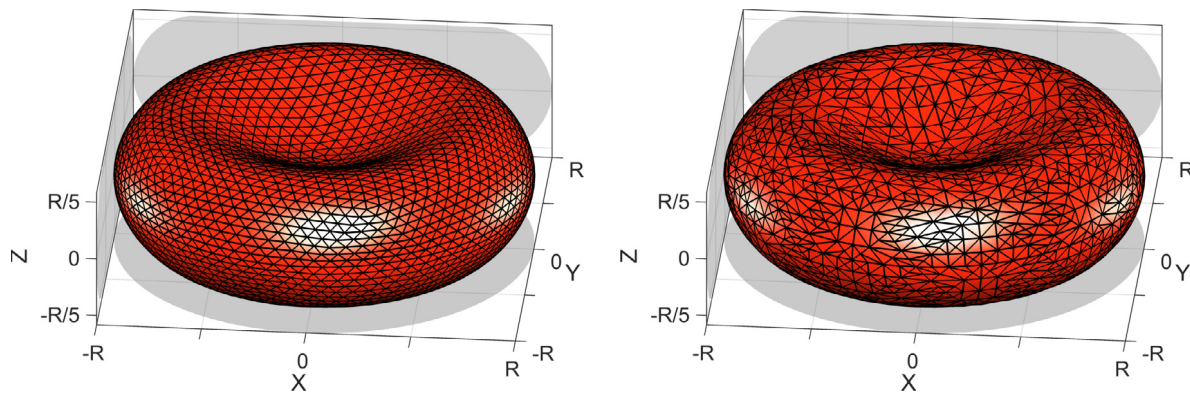
$$\tilde{E}_B^{(i)} := 2 \frac{\left[\sum_{j(i)} (\mathbf{x}^{(i)} - \mathbf{x}^{(j)}) T_{ij} \right]^2}{\sum_{j(i)} l_{ij}^2 T_{ij}}, \quad i = 1, \dots, N, \quad (\text{A.2})$$

the sums with $j(i)$ are sums over all neighbors j of node i , and

$$T_{ij} := \cot \vartheta_1^{(ij)} + \cot \vartheta_2^{(ij)}, \quad l_{ij} := |\mathbf{x}^{(i)} - \mathbf{x}^{(j)}|. \quad (\text{A.3})$$

The angles $\vartheta_1^{(ij)}$ and $\vartheta_2^{(ij)}$ were already defined in Section 2.3.2. See Fig. 1 for a sketch. We now require an analytic expression for the force $\mathbf{F}(\mathbf{x}^{(l)})$ from Eq. (5) at each node $\mathbf{x}^{(l)}$, with the energy from Eq. (A.1). For this, we compute the k 'th component of the gradient of $\tilde{E}_B^{(i)}$ with respect to the vertex $\mathbf{x}^{(l)}$:

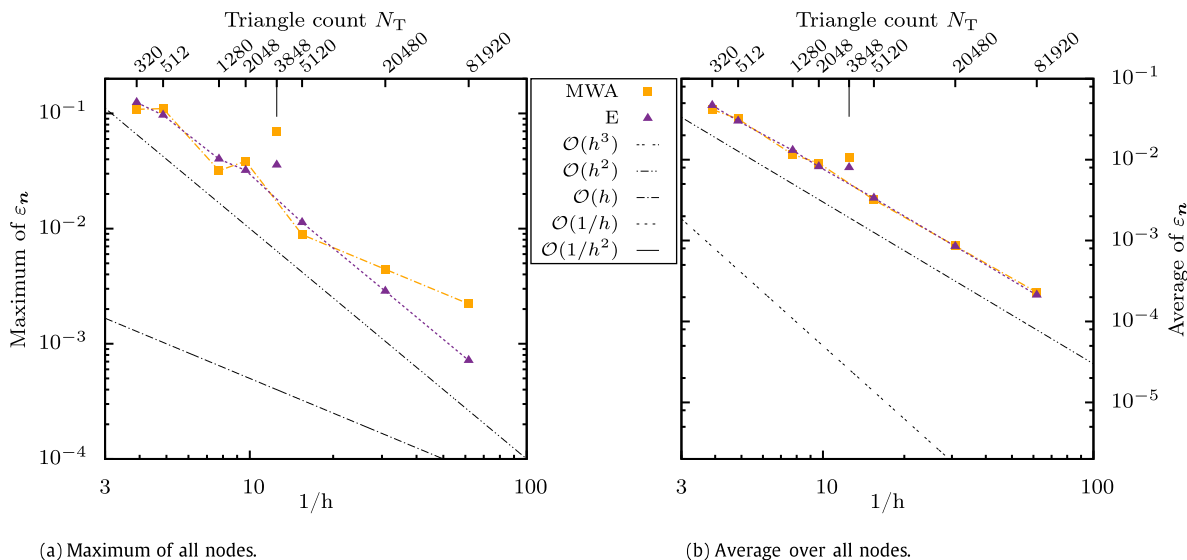
$$\begin{aligned} \frac{\partial \tilde{E}_B^{(i)}}{\partial x_k^{(l)}} &= 4 \frac{\sum_{j(i)} (\mathbf{x}^{(i)} - \mathbf{x}^{(j)}) T_{ij}}{\sum_{j(i)} l_{ij}^2 T_{ij}} \\ &\quad \cdot \sum_{j(i)} \left[(\mathbf{x}^{(i)} - \mathbf{x}^{(j)}) \frac{\partial T_{ij}}{\partial x_k^{(l)}} + T_{ij} \hat{\mathbf{e}}_k (\delta_{il} - \delta_{jl}) \right] \\ &\quad - 2 \frac{\left[\sum_{j(i)} (\mathbf{x}^{(i)} - \mathbf{x}^{(j)}) T_{ij} \right]^2}{\left(\sum_{j(i)} l_{ij}^2 T_{ij} \right)^2} \sum_{j(i)} \left[T_{ij} \frac{\partial (l_{ij}^2)}{\partial x_k^{(l)}} + l_{ij}^2 \frac{\partial T_{ij}}{\partial x_k^{(l)}} \right]. \quad (\text{A.4}) \end{aligned}$$



(a) Homogeneous mesh MT2 with 5120 triangles, obtained by refining an icosahedron by placing new nodes in the middle of edges and moving them out onto the sphere.

(b) Inhomogeneous mesh with 3848 triangles derived from MT2, obtained via Rivara's longest-edge bisection algorithm.

Fig. B.18. Illustrations of the typical RBC shape discretized with the MT2 approach. See Fig. 2 for the MT1 meshes.



(a) Maximum of all nodes.

(b) Average over all nodes.

Fig. B.19. The maximum and average of the relative error ε_n of the normal vector for the MT2 mesh. The version with the MT1 mesh can be found in Fig. 3, and the numerical values in the SI (see Appendix C).

Here, $\hat{\mathbf{e}}_k$ is the k 'th canonical unit vector and δ_{il} the Kronecker symbol. Continuing, we find

$$\frac{\partial(l_{ij}^2)}{\partial \mathbf{x}^{(l)}} = 2(\mathbf{x}^{(i)} - \mathbf{x}^{(j)})(\delta_{il} - \delta_{jl}). \quad (\text{A.5})$$

Next, we need to express T_{ij} and therefore the angles $\vartheta_{1,2}^{(ij)}$ through the nodes' positions. Thus, we define

$$\chi_{i,j,j-1} := \cos \vartheta_1^{(ij)} = \frac{(\mathbf{x}^{(i)} - \mathbf{x}^{(j-1)}) \cdot (\mathbf{x}^{(j)} - \mathbf{x}^{(j-1)})}{l_{i,j-1} l_{j,j-1}} \quad \text{and} \quad (\text{A.6a})$$

$$\chi_{i,j,j+1} := \cos \vartheta_2^{(ij)} = \frac{(\mathbf{x}^{(i)} - \mathbf{x}^{(j+1)}) \cdot (\mathbf{x}^{(j)} - \mathbf{x}^{(j+1)})}{l_{i,j+1} l_{j,j+1}}, \quad (\text{A.6b})$$

where $j-1$ specifies the “previous” and $j+1$ the “next” node relative to node j of the ring-1 neighbors of vertex i , as seen in Fig. 1. Circular enumeration is implied. We can now exploit $\vartheta_{1,2}^{(ij)} \in]0, \pi[$ and write

$$T_{ij} = \frac{\chi_{i,j,j-1}}{\sqrt{1 - \chi_{i,j,j-1}^2}} + \frac{\chi_{i,j,j+1}}{\sqrt{1 - \chi_{i,j,j+1}^2}}. \quad (\text{A.7})$$

This leads to

$$\frac{\partial T_{ij}}{\partial \mathbf{x}^{(l)}} = \frac{1}{(1 - \chi_{i,j,j-1}^2)^{3/2}} \frac{\partial \chi_{i,j,j-1}}{\partial \mathbf{x}^{(l)}} + \frac{1}{(1 - \chi_{i,j,j+1}^2)^{3/2}} \frac{\partial \chi_{i,j,j+1}}{\partial \mathbf{x}^{(l)}}, \quad (\text{A.8})$$

whereas for $m = j-1$ or $m = j+1$ we find

$$\begin{aligned} \frac{\partial \chi_{i,j,m}}{\partial \mathbf{x}^{(l)}} &= \frac{1}{l_{im} l_{jm}} \left[(\delta_{il} - \delta_{ml}) (\mathbf{x}^{(j)} - \mathbf{x}^{(m)}) \right. \\ &\quad + (\delta_{jl} - \delta_{ml}) (\mathbf{x}^{(i)} - \mathbf{x}^{(m)}) - \frac{l_{jm}}{l_{im}} \chi_{ijm} (\delta_{il} - \delta_{ml}) (\mathbf{x}^{(i)} - \mathbf{x}^{(m)}) \\ &\quad \left. - \frac{l_{im}}{l_{jm}} \chi_{ijm} (\delta_{jl} - \delta_{ml}) (\mathbf{x}^{(j)} - \mathbf{x}^{(m)}) \right]. \end{aligned} \quad (\text{A.9})$$

Substituting Eq. (A.9) into (A.8), and then (A.8) and (A.5) into (A.4) gives the contribution of node $\mathbf{x}^{(i)}$ (and its neighbors) to the force acting on node $\mathbf{x}^{(l)}$. The total force $\mathbf{F}(\mathbf{x}^{(l)})$ then follows from summing over all these contributions and multiplying the result with $-\frac{\kappa_B}{2}$. Obtaining the force density \mathbf{f} from \mathbf{F} was explained in Section 2.6.

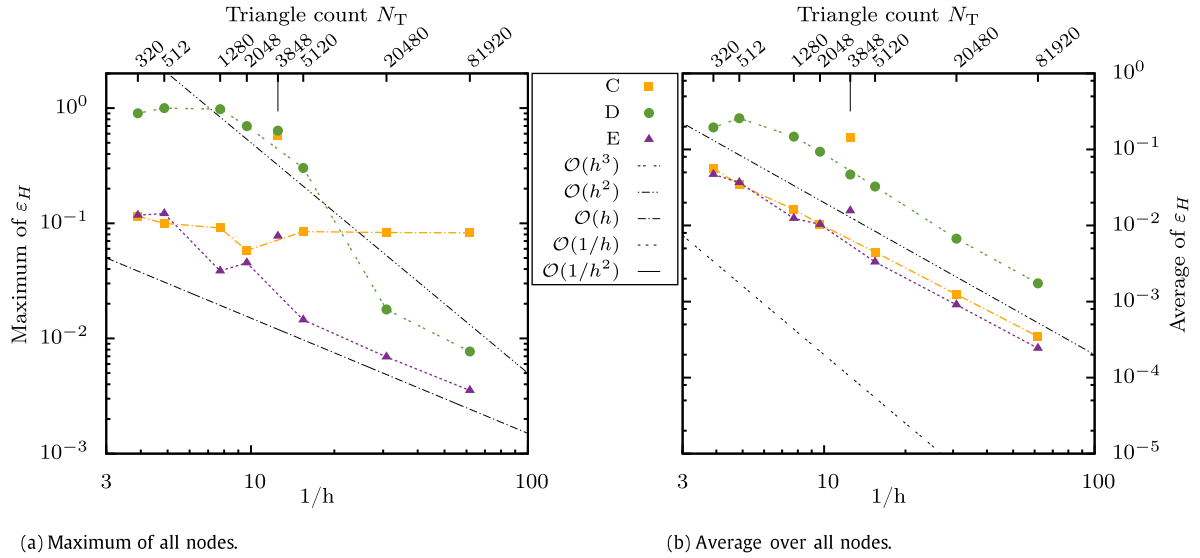


Fig. B.20. The maximum and average of the relative error ε_H of the mean curvature for the MT2 mesh. The version with the MT1 mesh can be found in Fig. 5, and the numeric values in the SI (see Appendix C).

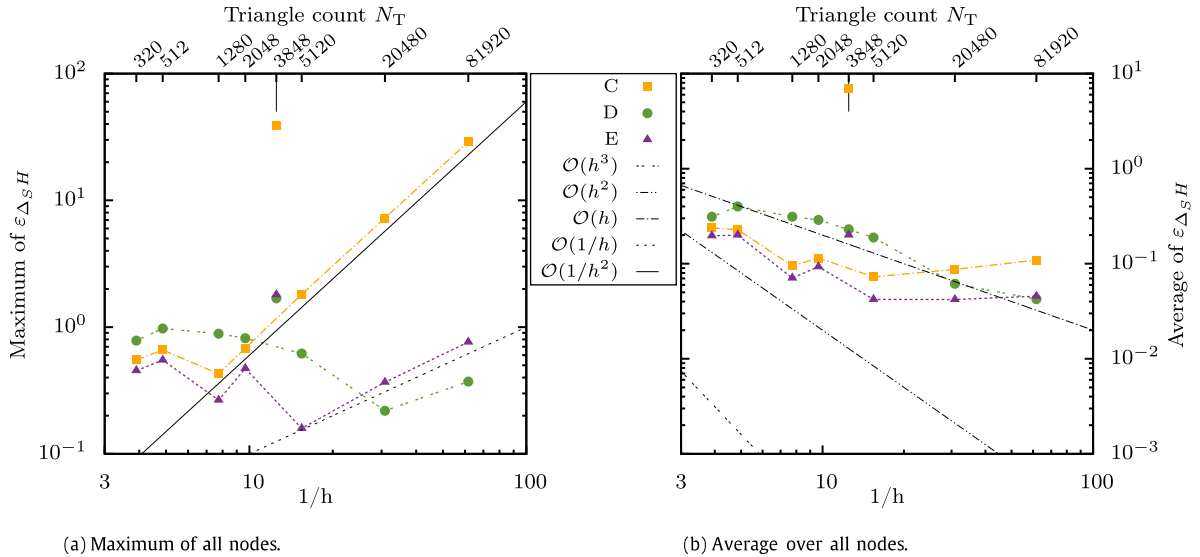


Fig. B.21. The maximum and average of the relative error of the Laplace–Beltrami operator applied to H for the MT2 mesh. The version with the MT1 mesh can be found in Fig. 7, and the numeric values in the SI (see Appendix C).

Appendix B. MT2 mesh

Section 3 from the main text presented the maximal and average errors for the various Methods for the typical RBC shape using MT1 meshes. Here we provide the same figures as in Section 3 for Methods A–E with the MT2 mesh. We highlight the major differences below.

As a start, Fig. B.18 shows 3D images of the homogeneous and inhomogeneous MT2 discretizations. Compared to the MT1 versions from Fig. 2, the triangles around nodes with only five neighbors are somewhat larger. Note that the inhomogeneous mesh (Fig. 18(b)) has 3848 rather than 3914 triangles because the edge lengths are different. Hence, the splitting order of the edges in Rivara’s algorithm is different, and therefore also the final mesh.

The errors for the normal vector are depicted in Fig. B.19. We remark that the MT2 mesh reduces the convergence rate of the maximal error for the MWA algorithm to $\mathcal{O}(h)$ at smaller resolutions than the MT1 mesh.

The results for the mean curvature in Fig. B.20 do not differ largely in the convergence rates compared to MT1, but in the

absolute value of the maximal errors. Notably, Method C is almost up to one order of magnitude larger.

For the Laplace of the mean curvature, $\Delta_S H$, see Fig. B.21. Here, the maximal error for the otherwise very robust Method D starts to increase with resolutions beyond 20,480 triangles (contrary to the MT1 version, where it stays constant). The rate for the average error is reduced from $\mathcal{O}(h^2)$ to $\mathcal{O}(h)$. Method E shows qualitatively different behavior for the average error, too: Rather than decreasing with $\approx \mathcal{O}(h^2)$, it remains constant beyond 5120 triangles, i.e. does not converge properly. Furthermore, the absolute values for Method C are often more than a factor of two larger.

We finally consider the force density in Fig. B.23. Of course, the same observation as for $\Delta_S H$ hold for Methods C–E. Method B behaves the same as Method C. Moreover, Method A shows divergence with a rate of roughly $\mathcal{O}(h)$ for the average error, whereas in the MT1 version it stays approximately constant. Regarding the 3D patterns in Fig. B.22, the most notable change occurs for Method E. Rather than regular circles, more random

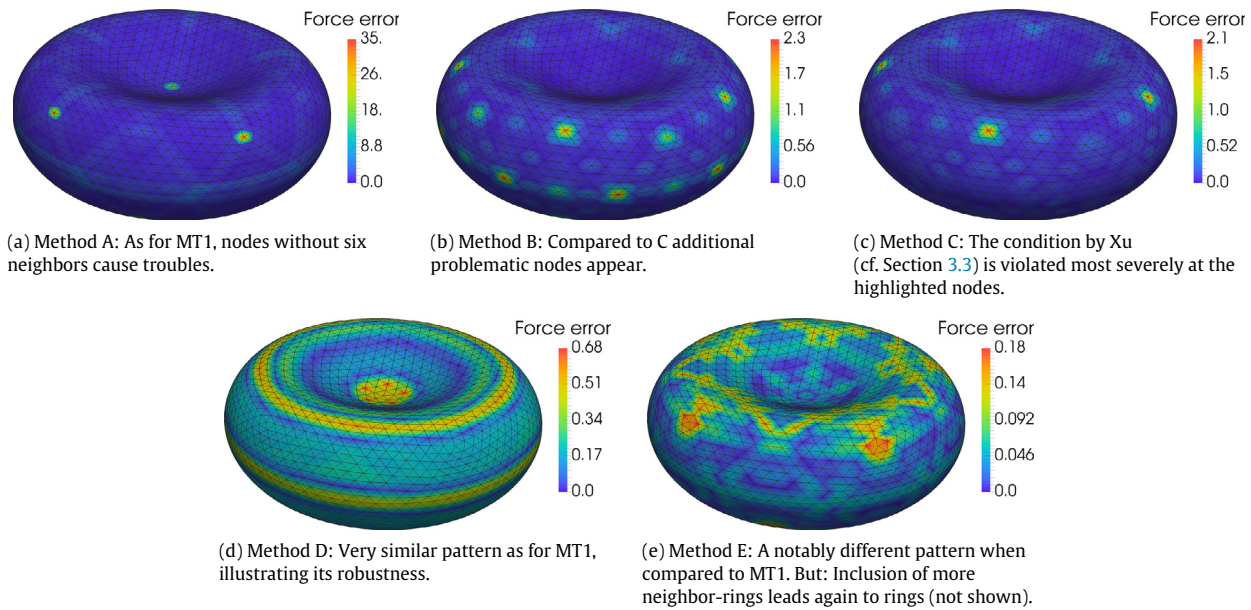


Fig. B.22. 3D illustration of the errors ϵ_f of the force density for 5120 triangles with the MT2 meshes. Note the scales of the color bars (for interpretation of the scales, the reader is referred to the web version of this article). The MT1 meshes were displayed in Fig. 9.

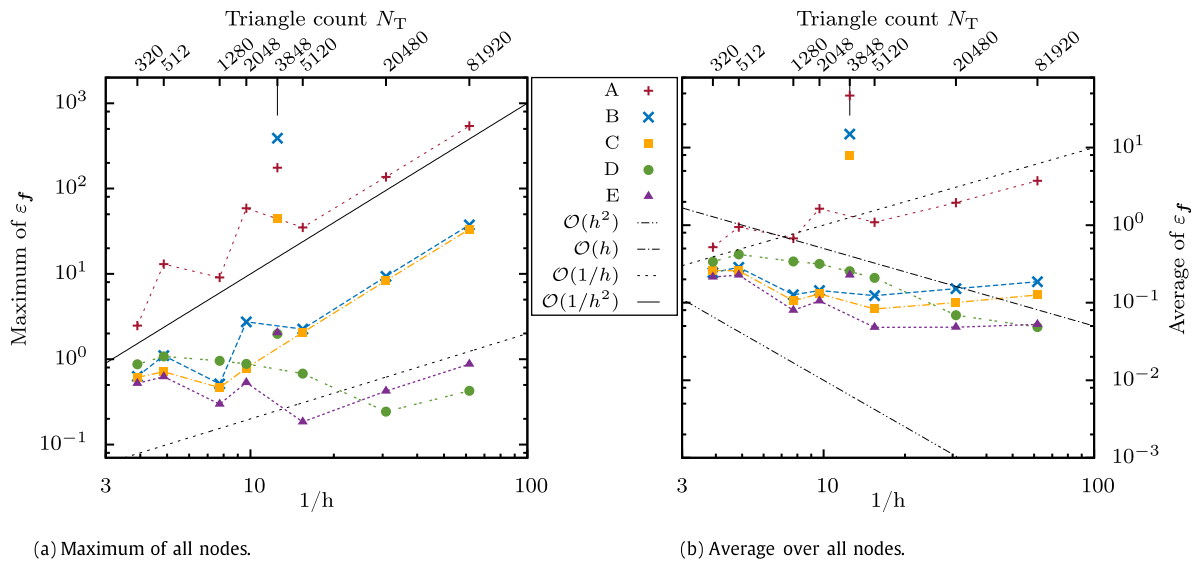


Fig. B.23. The maximum and average of the relative error of the force density for the MT2 mesh. The version with the MT1 mesh can be found in Fig. 10, and the numerical values in the SI (see Appendix C).

patterns emerge. Inclusion of more rings, however, recovers circular patterns similar to Method D.

Appendix C. Supplementary data

Supplementary material related to this article can be found online at <http://dx.doi.org/10.1016/j.cpc.2016.04.018>.

References

[1] M. Kraus, W. Wintz, U. Seifert, R. Lipowsky, Fluid vesicles in shear flow, *Phys. Rev. Lett.* 77 (17) (1996) 3685–3688. <http://dx.doi.org/10.1103/PhysRevLett.77.3685>.

[2] C. Pozrikidis, Effect of membrane bending stiffness on the deformation of capsules in simple shear flow, *J. Fluid Mech.* 440 (2001) 269–291. <http://dx.doi.org/10.1017/S0022112001004657>.

[3] D. Barthès-Biesel, J. Walter, A.-V. Salsac, Flow-induced deformation of artificial capsules, in: C. Pozrikidis (Ed.), *Computational Hydrodynamics of Capsules and Biological Cells*, in: Chapman & Hall/CRC Mathematical and

Computational Biology Series, CRC Press, Boca Raton, 2010, pp. 35–70. <http://dx.doi.org/10.1201/EBK1439820056-c2>.

[4] D.V. Le, Effect of bending stiffness on the deformation of liquid capsules enclosed by thin shells in shear flow, *Phys. Rev. E* 82 (1) (2010) 016318. <http://dx.doi.org/10.1103/PhysRevE.82.016318>.

[5] B. Kaoui, G. Birocs, C. Misbah, Why do red blood cells have asymmetric shapes even in a symmetric flow? *Phys. Rev. Lett.* 103 (18) (2009) 188101. <http://dx.doi.org/10.1103/PhysRevLett.103.188101>.

[6] O. Aouane, M. Thiébaud, A. Benyoussef, C. Wagner, C. Misbah, Vesicle dynamics in a confined Poiseuille flow: From steady state to chaos, *Phys. Rev. E* 90 (3) (2014) 033011. <http://dx.doi.org/10.1103/PhysRevE.90.033011>.

[7] C. Misbah, Vacillating breathing and tumbling of vesicles under shear flow, *Phys. Rev. Lett.* 96 (2) (2006) 028104. <http://dx.doi.org/10.1103/PhysRevLett.96.028104>.

[8] K. Sinha, M.D. Graham, Dynamics of a single red blood cell in simple shear flow, *Phys. Rev. E* 92 (4) (2015) 042710. <http://dx.doi.org/10.1103/PhysRevE.92.042710>.

[9] D.A. Fedosov, M. Peltomäki, G. Gompper, Deformation and dynamics of red blood cells in flow through cylindrical microchannels, *Soft Matter* 10 (24) (2014) 4258–4267. <http://dx.doi.org/10.1039/C4SM00248B>.

[10] L. Zhu, L. Brandt, The motion of a deforming capsule through a corner, *J. Fluid Mech.* 770 (2015) 374–397. <http://dx.doi.org/10.1017/jfm.2015.157>.

- [11] D. Abreu, M. Levant, V. Steinberg, U. Seifert, Fluid vesicles in flow, *Adv. Colloid Interface Sci.* 208 (2014) 129–141. <http://dx.doi.org/10.1016/j.cis.2014.02.004>.
- [12] A. Farutin, C. Misbah, Squaring, parity breaking, and S tumbling of vesicles under shear flow, *Phys. Rev. Lett.* 109 (24) (2012) 248106. <http://dx.doi.org/10.1103/PhysRevLett.109.248106>.
- [13] C. de Loubens, J. Deschamps, G. Boedec, M. Leonetti, Stretching of capsules in an elongation flow, a route to constitutive law, *J. Fluid Mech.* 767 (R3) (2015) <http://dx.doi.org/10.1017/jfm.2015.69>.
- [14] C. de Loubens, J. Deschamps, F. Edwards-Levy, M. Leonetti, Tank-treading of microcapsules in shear flow, *J. Fluid Mech.* 789 (2016) 750–767. <http://dx.doi.org/10.1017/jfm.2015.758>.
- [15] T. Omori, T. Ishikawa, D. Barthès-Biesel, A.-V. Salsac, Y. Imai, T. Yamaguchi, Tension of red blood cell membrane in simple shear flow, *Phys. Rev. E* 86 (5) (2012) 056321. <http://dx.doi.org/10.1103/PhysRevE.86.056321>.
- [16] G. Boedec, M. Jaeger, M. Leonetti, Settling of a vesicle in the limit of quasispherical shapes, *J. Fluid Mech.* 690 (2012) 227–261. <http://dx.doi.org/10.1017/jfm.2011.427>.
- [17] G. Boedec, M. Jaeger, M. Leonetti, Sedimentation-induced tether on a settling vesicle, *Phys. Rev. E* 88 (1) (2013) 010702. <http://dx.doi.org/10.1103/PhysRevE.88.010702>.
- [18] I.R. Suárez, C. Leidy, G. Téllez, G. Gay, A. Gonzalez-Mancera, Slow sedimentation and deformability of charged lipid vesicles, *PLoS One* 8 (7) (2013) e68309. <http://dx.doi.org/10.1371/journal.pone.0068309>.
- [19] H.-H. Boltz, J. Kierfeld, Shapes of sedimenting soft elastic capsules in a viscous fluid, *Phys. Rev. E* 92 (3) (2015) 033003. <http://dx.doi.org/10.1103/PhysRevE.92.033003>.
- [20] H. Zhao, A.H. Isfahani, L.N. Olson, J.B. Freund, A spectral boundary integral method for flowing blood cells, *J. Comput. Phys.* 229 (10) (2010) 3726–3744. <http://dx.doi.org/10.1016/j.jcp.2010.01.024>.
- [21] J.B. Freund, The flow of red blood cells through a narrow spleen-like slit, *Phys. Fluids* 1994–Present 25 (11) (2013) 110807. <http://dx.doi.org/10.1063/1.4819341>.
- [22] R. Kusters, T. van der Heijden, B. Kaoui, J. Harting, C. Storm, Forced transport of deformable containers through narrow constrictions, *Phys. Rev. E* 90 (3) (2014) 033006. <http://dx.doi.org/10.1103/PhysRevE.90.033006>.
- [23] A. Daddi-Moussa-Ider, A. Guckenberger, S. Gekle, Long-lived anomalous thermal diffusion induced by elastic cell membranes on nearby particles, *Phys. Rev. E* 93 (1) (2016) 012612. <http://dx.doi.org/10.1103/PhysRevE.93.012612>.
- [24] R. Fåhræus, T. Lindqvist, The viscosity of the blood in narrow capillary tubes, *Am. J. Physiol.* 96 (3) (1931) 562–568.
- [25] A.R. Pries, T.W. Secomb, T. Gessner, M.B. Sperandio, J.F. Gross, P. Gaetgens, Resistance to blood flow in microvessels in vivo, *Circ. Res.* 75 (5) (1994) 904–915. <http://dx.doi.org/10.1161/01.RES.75.5.904>.
- [26] A.R. Pries, T.W. Secomb, P. Gaetgens, Biophysical aspects of blood flow in the microvasculature, *Cardiovasc. Res.* 32 (4) (1996) 654–667. [http://dx.doi.org/10.1016/S0008-6363\(96\)00065-X](http://dx.doi.org/10.1016/S0008-6363(96)00065-X).
- [27] D.A. Fedosov, W. Pan, B. Caswell, G. Gompper, G.E. Karniadakis, Predicting human blood viscosity in silico, *Proc. Natl. Acad. Sci.* 108 (29) (2011) 11772–11777. <http://dx.doi.org/10.1073/pnas.1101210108>.
- [28] T. Krüger, Computer simulation study of collective phenomena in dense suspensions of red blood cells under shear (Ph.D. thesis), Ruhr-Universität Bochum, 2012. <http://dx.doi.org/10.1007/978-3-8348-2376-2>.
- [29] T. Krüger, B. Kaoui, J. Harting, Interplay of inertia and deformability on rheological properties of a suspension of capsules, *J. Fluid Mech.* 751 (2014) 725–745. <http://dx.doi.org/10.1017/jfm.2014.315>.
- [30] P.A. Aarts, S.A. van den Broek, G.W. Prins, G.D. Kuiken, J.J. Sixma, R.M. Heethaar, Blood platelets are concentrated near the wall and red blood cells, in the center in flowing blood, *Arterioscler. Thromb. Vasc. Biol.* 8 (6) (1988) 819–824. <http://dx.doi.org/10.1161/01.ATV.8.6.819>.
- [31] J.B. Freund, M.M. Orescanin, Cellular flow in a small blood vessel, *J. Fluid Mech.* 671 (2011) 466–490. <http://dx.doi.org/10.1017/S0022112010005835>.
- [32] H. Zhao, E.S.G. Shaqfeh, V. Narsimhan, Shear-induced particle migration and margination in a cellular suspension, *Phys. Fluids* 1994–Present 24 (1) (2012) 011902. <http://dx.doi.org/10.1063/1.3677935>.
- [33] D. Katanov, G. Gompper, D.A. Fedosov, Microvascular blood flow resistance: Role of red blood cell migration and dispersion, *Microvasc. Res.* 99 (2015) 57–66. <http://dx.doi.org/10.1016/j.mvr.2015.02.006>.
- [34] J.B. Freund, Leukocyte margination in a model microvessel, *Phys. Fluids* 1994–Present 19 (2) (2007) 023301. <http://dx.doi.org/10.1063/1.2472479>.
- [35] K. Vahidkhal, S.L. Diamond, P. Bagchi, Platelet dynamics in three-dimensional simulation of whole blood, *Biophys. J.* 106 (11) (2014) 2529–2540. <http://dx.doi.org/10.1016/j.bpj.2014.04.028>.
- [36] K. Müller, D.A. Fedosov, G. Gompper, Margination of micro- and nanoparticles in blood flow and its effect on drug delivery, *Sci. Rep.* 4 (2014) <http://dx.doi.org/10.1038/srep04871>.
- [37] D.A. Fedosov, G. Gompper, White blood cell margination in microcirculation, *Soft Matter* 10 (17) (2014) 2961–2970. <http://dx.doi.org/10.1039/C3SM52860J>.
- [38] S. Fitzgibbon, A.P. Spann, Q.M. Qi, E.S.G. Shaqfeh, In vitro measurement of particle margination in the microchannel flow: Effect of varying hematocrit, *Biophys. J.* 108 (10) (2015) 2601–2608. <http://dx.doi.org/10.1016/j.bpj.2015.04.013>.
- [39] S. Gekle, Strongly accelerated margination of active particles in blood flow, *Biophys. J.* 110 (2) (2016) 514–520. <http://dx.doi.org/10.1016/j.bpj.2015.12.005>.
- [40] K. Müller, D.A. Fedosov, G. Gompper, Understanding particle margination in blood flow—A step toward optimized drug delivery systems, *Med. Eng. Phys.* 38 (1) (2016) 2–10. <http://dx.doi.org/10.1016/j.medengphy.2015.08.009>.
- [41] M. Mehrabadi, D.N. Ku, C.K. Aidun, Effects of shear rate, confinement, and particle parameters on margination in blood flow, *Phys. Rev. E* 93 (2) (2016) 023109. <http://dx.doi.org/10.1103/PhysRevE.93.023109>.
- [42] G.K. Youngren, A. Acrivos, Stokes flow past a particle of arbitrary shape: a numerical method of solution, *J. Fluid Mech.* 69 (2) (1975) 377–403. <http://dx.doi.org/10.1017/S0022112075001486>.
- [43] C. Pozrikidis, Boundary integral and singularity methods for linearized viscous flow, in: *Cambridge Texts in Applied Mathematics*, vol. 8, Cambridge University Press, New York, 1992. <http://dx.doi.org/10.1017/CBO9780511624124>.
- [44] C. Pozrikidis, Interfacial dynamics for Stokes flow, *J. Comput. Phys.* 169 (2) (2001) 250–301. <http://dx.doi.org/10.1006/jcp.2000.6582>.
- [45] S. Succi, *The lattice Boltzmann equation for fluid dynamics and beyond*, in: *Numerical Mathematics and Scientific Computation*, Clarendon Press, Oxford, 2001.
- [46] B. Dünweg, A.J.C. Ladd, Lattice Boltzmann simulations of soft matter systems, in: P.C. Holm, P.K. Kremer (Eds.), *Advanced Computer Simulation Approaches for Soft Matter Sciences III*, in: *Advances in Polymer Science*, vol. 221, Springer, Berlin, Heidelberg, 2009, pp. 89–166. http://dx.doi.org/10.1007/978-3-540-87706-6_2.
- [47] C.K. Aidun, J.R. Clausen, Lattice-Boltzmann method for Complex Flows, *Annu. Rev. Fluid Mech.* 42 (1) (2010) 439–472. <http://dx.doi.org/10.1146/annurev-fluid-121108-145519>.
- [48] T. Krüger, F. Varnik, D. Raabe, Efficient and accurate simulations of deformable particles immersed in a fluid using a combined immersed boundary lattice Boltzmann finite element method, *Comput. Math. Appl.* 61 (12) (2011) 3485–3505. <http://dx.doi.org/10.1016/j.camwa.2010.03.057>.
- [49] H. Noguchi, G. Gompper, Fluid vesicles with viscous membranes in shear flow, *Phys. Rev. Lett.* 93 (25) (2004) 258102. <http://dx.doi.org/10.1103/PhysRevLett.93.258102>.
- [50] H. Noguchi, G. Gompper, Dynamics of fluid vesicles in shear flow: Effect of membrane viscosity and thermal fluctuations, *Phys. Rev. E* 72 (1) (2005) 011901. <http://dx.doi.org/10.1103/PhysRevE.72.011901>.
- [51] G. Gompper, T. Ihle, D.M. Kroll, R.G. Winkler, Multi-particle collision dynamics: A particle-based mesoscale simulation approach to the hydrodynamics of complex fluids, in: C. Holm, K. Kremer (Eds.), *Advanced Computer Simulation Approaches for Soft Matter Sciences III*, in: *Advances in Polymer Science*, vol. 221, Springer, Berlin, Heidelberg, 2009, pp. 1–87. http://dx.doi.org/10.1007/978-3-540-87706-6_1.
- [52] D.A. Fedosov, B. Caswell, G.E. Karniadakis, Dissipative particle dynamics modeling of red blood cells, in: *Chapman & Hall/CRC Mathematical and Computational Biology Series*, CRC Press, 2010, pp. 183–218. <http://dx.doi.org/10.1201/EBK1439820056-c6>.
- [53] D. Barthès-Biesel, Motion and deformation of elastic capsules and vesicles in flow, *Annu. Rev. Fluid Mech.* 48 (1) (2016) 25–52. <http://dx.doi.org/10.1146/annurev-fluid-122414-034345>.
- [54] R. Skalak, A. Tozeren, R.P. Zarda, S. Chien, Strain energy function of red blood cell membranes, *Biophys. J.* 13 (3) (1973) 245–264. [http://dx.doi.org/10.1016/S0006-3495\(73\)85938-1](http://dx.doi.org/10.1016/S0006-3495(73)85938-1).
- [55] T. Omori, T. Ishikawa, D. Barthès-Biesel, A.-V. Salsac, J. Walter, Y. Imai, T. Yamaguchi, Comparison between spring network models and continuum constitutive laws: Application to the large deformation of a capsule in shear flow, *Phys. Rev. E* 83 (4) (2011) 041918. <http://dx.doi.org/10.1103/PhysRevE.83.041918>.
- [56] P.B. Canham, The minimum energy of bending as a possible explanation of the biconcave shape of the human red blood cell, *J. Theoret. Biol.* 26 (1) (1970) 61–81. [http://dx.doi.org/10.1016/S0022-5193\(70\)80032-7](http://dx.doi.org/10.1016/S0022-5193(70)80032-7).
- [57] W. Helfrich, Elastic properties of lipid bilayers: theory and possible experiments, *Z. Naturforsch. C* 28 (1973) 693–703.
- [58] G. Boedec, M. Leonetti, M. Jaeger, 3D vesicle dynamics simulations with a linearly triangulated surface, *J. Comput. Phys.* 230 (4) (2011) 1020–1034. <http://dx.doi.org/10.1016/j.jcp.2010.10.021>.
- [59] A. Walter, H. Rehage, H. Leonhard, Shear induced deformation of microcapsules: shape oscillations and membrane folding, *Colloids Surf. A* 183–185 (2001) 123–132. [http://dx.doi.org/10.1016/S0927-7757\(01\)00564-7](http://dx.doi.org/10.1016/S0927-7757(01)00564-7).
- [60] H. Luo, C. Pozrikidis, Buckling of a pre-compressed or pre-stretched membrane in shear flow, *Int. J. Solids Struct.* 44 (24) (2007) 8074–8085. <http://dx.doi.org/10.1016/j.ijsolstr.2007.05.027>.
- [61] X. Li, K. Sarkar, Front tracking simulation of deformation and buckling instability of a liquid capsule enclosed by an elastic membrane, *J. Comput. Phys.* 227 (10) (2008) 4998–5018. <http://dx.doi.org/10.1016/j.jcp.2008.01.034>.
- [62] R. Finken, S. Kessler, U. Seifert, Micro-capsules in shear flow, *J. Phys.: Condens. Matter* 23 (18) (2011) 184113. <http://dx.doi.org/10.1088/0953-8984/23/18/184113>.
- [63] C. Dupont, A.-V. Salsac, D. Barthès-Biesel, M. Vidrascu, P.L. Tallec, Influence of bending resistance on the dynamics of a spherical capsule in shear flow, *Phys. Fluids* 1994–Present 27 (5) (2015) 051902. <http://dx.doi.org/10.1063/1.4921247>.
- [64] E. Lac, D. Barthès-Biesel, N.A. Pelekasis, J. Tsamopoulos, Spherical capsules in three-dimensional unbounded Stokes flows: effect of the membrane constitutive law and onset of buckling, *J. Fluid Mech.* 516 (2004) 303–334. <http://dx.doi.org/10.1017/S002211200400062X>.

- [65] C. Pozrikidis, Resting shape and spontaneous membrane curvature of red blood cells, *Math. Med. Biol.* 22 (1) (2005) 34–52. <http://dx.doi.org/10.1093/imammb/dqh021>.
- [66] T. Biben, A. Farutin, C. Misbah, Three-dimensional vesicles under shear flow: Numerical study of dynamics and phase diagram, *Phys. Rev. E* 83 (3) (2011) 031921. <http://dx.doi.org/10.1103/PhysRevE.83.031921>.
- [67] A. Yazdani, P. Bagchi, Three-dimensional numerical simulation of vesicle dynamics using a front-tracking method, *Phys. Rev. E* 85 (5) (2012) 056308. <http://dx.doi.org/10.1103/PhysRevE.85.056308>.
- [68] A. Farutin, T. Biben, C. Misbah, 3D numerical simulations of vesicle and inextensible capsule dynamics, *J. Comput. Phys.* 275 (2014) 539–568. <http://dx.doi.org/10.1016/j.jcp.2014.07.008>.
- [69] K. Tsubota, Short note on the bending models for a membrane in capsule mechanics: Comparison between continuum and discrete models, *J. Comput. Phys.* 277 (2014) 320–328. <http://dx.doi.org/10.1016/j.jcp.2014.08.007>.
- [70] J. Gounley, G. Boedec, M. Jaeger, M. Leonetti, Influence of surface viscosity on droplets in shear flow, *J. Fluid Mech.* 791 (2016) 464–494. <http://dx.doi.org/10.1017/jfm.2016.39>.
- [71] W.-X. Huang, C.B. Chang, H.J. Sung, Three-dimensional simulation of elastic capsules in shear flow by the penalty immersed boundary method, *J. Comput. Phys.* 231 (8) (2012) 3340–3364. <http://dx.doi.org/10.1016/j.jcp.2012.01.006>.
- [72] A.P. Spann, H. Zhao, E.S.G. Shaqfeh, Loop subdivision surface boundary integral method simulations of vesicles at low reduced volume ratio in shear and extensional flow, *Phys. Fluids* 1994–Present 26 (3) (2014) 031902. <http://dx.doi.org/10.1063/1.4869307>.
- [73] C.T. Loop, Smooth subdivision surfaces based on triangles (Master thesis), University of Utah, Utah, USA, 1987.
- [74] F. Cirak, M. Ortiz, P. Schröder, Subdivision surfaces: a new paradigm for thin-shell finite-element analysis, *Internat. J. Numer. Methods Engrg.* 47 (12) (2000) 2039–2072. <http://dx.doi.org/10.1002/%28SICI%291097-0207%2820000430%2947%3A12%3C2039%3A%3AAID-NME87%3E3.0.CO%3B2-1>.
- [75] D.V. Le, J. White, J. Peiraire, K.M. Lim, B.C. Khoo, An implicit immersed boundary method for three-dimensional fluid-membrane interactions, *J. Comput. Phys.* 228 (22) (2009) 8427–8445. <http://dx.doi.org/10.1016/j.jcp.2009.08.018>.
- [76] J. Walter, A.-V. Salsac, D. Barthès-Biesel, P. Le Tallec, Coupling of finite element and boundary integral methods for a capsule in a Stokes flow, *Internat. J. Numer. Methods Engrg.* 83 (7) (2010) 829–850. <http://dx.doi.org/10.1002/nme.2859>.
- [77] S.K. Veerapaneni, A. Rahimian, G. Biros, D. Zorin, A fast algorithm for simulating vesicle flows in three dimensions, *J. Comput. Phys.* 230 (14) (2011) 5610–5634. <http://dx.doi.org/10.1016/j.jcp.2011.03.045>.
- [78] O.-Y. Zhong-Can, W. Helfrich, Bending energy of vesicle membranes: General expressions for the first, second, and third variation of the shape energy and applications to spheres and cylinders, *Phys. Rev. A* 39 (10) (1989) 5280–5288. <http://dx.doi.org/10.1103/PhysRevA.39.5280>.
- [79] A. Laadhari, C. Misbah, P. Saramito, On the equilibrium equation for a generalized biological membrane energy by using a shape optimization approach, *Phys. D* 239 (16) (2010) 1567–1572. <http://dx.doi.org/10.1016/j.physd.2010.04.001>.
- [80] G. Xu, Convergence of discrete Laplace–Beltrami operators over surfaces, *Comput. Math. Appl.* 48 (3–4) (2004) 347–360. <http://dx.doi.org/10.1016/j.camwa.2004.05.001>.
- [81] G. Xu, Discrete Laplace–Beltrami operators and their convergence, *Comput. Aided Geom. Design* 21 (8) (2004) 767–784. <http://dx.doi.org/10.1016/j.cagd.2004.07.007>.
- [82] T.D. Gatzke, C.M. Grimm, Estimating curvature on triangular meshes, *Int. J. Shape Model.* 12 (01) (2006) 1–28. <http://dx.doi.org/10.1142/S0218654306000810>.
- [83] M. Wardetzky, S. Mathur, F. Kälberer, E. Grinspun, Discrete Laplace operators: No free lunch, in: A. Belyaev, M. Garland (Eds.), SGP’07 Proceedings of the Fifth Eurographics Symposium on Geometry Processing, SGP’07, Eurographics Association, Barcelona, 2007, pp. 33–37.
- [84] M. Belkin, J. Sun, Y. Wang, Discrete Laplace operator on meshed surfaces, in: SCG’08: Proceedings of the Twenty-Fourth Annual Symposium on Computational Geometry, ACM, Maryland, 2008, pp. 278–287. <http://dx.doi.org/10.1145/1377676.1377725>.
- [85] M. Alexa, M. Wardetzky, Discrete Laplacians on General Polygonal Meshes, in: SIGGRAPH’11, ACM, New York, 2011, pp. 102:1–102:10. <http://dx.doi.org/10.1145/1964921.1964997>.
- [86] M.M. Mesmoudi, L.D. Floriani, P. Magillo, Concentrated curvature for mean curvature estimation in triangulated surfaces, in: M. Ferri, P. Frosini, C. Landi, A. Cerri, B.D. Fabio (Eds.), Computational Topology in Image Context, in: Lecture Notes in Computer Science, vol. 7309, Springer, Berlin, Heidelberg, 2012, pp. 79–87. http://dx.doi.org/10.1007/978-3-642-30238-1_9.
- [87] X. Li, G. Xu, Y.J. Zhang, Localized discrete Laplace–Beltrami operator over triangular mesh, *Comput. Aided Geom. Design* 39 (2015) 67–82. <http://dx.doi.org/10.1016/j.cagd.2015.09.001>.
- [88] Y. Kantor, D.R. Nelson, Phase transitions in flexible polymeric surfaces, *Phys. Rev. A* 36 (8) (1987) 4020–4032. <http://dx.doi.org/10.1103/PhysRevA.36.4020>.
- [89] G. Gompper, D.M. Kroll, Random surface discretizations and the renormalization of the bending rigidity, *J. Phys. Fr.* 6 (10) (1996) 1305–1320. <http://dx.doi.org/10.1051/jp1:1996246>.
- [90] M. Meyer, M. Desbrun, P. Schröder, A.H. Barr, Discrete differential-geometry operators for triangulated 2-manifolds, in: H.-C. Hege, K. Polthier (Eds.), Visualization and Mathematics III, in: Mathematics and Visualization, vol. III, Springer, Berlin, Heidelberg, 2003, pp. 35–57. http://dx.doi.org/10.1007/978-3-662-05105-4_2.
- [91] B. Lévy, Laplace–Beltrami Eigenfunctions towards an algorithm that “understands” geometry, in: Proceedings of the IEEE International Conference on Shape Modeling and Applications 2006, SMI’06, IEEE Computer Society, Washington, DC, USA, 2006. <http://dx.doi.org/10.1109/SMI.2006.21>.
- [92] S. Komura, K. Tamura, T. Kato, Buckling of spherical shells adhering onto a rigid substrate, *Eur. Phys. J. E* 18 (3) (2005) 343–358. <http://dx.doi.org/10.1140/epje/e2005-00038-5>.
- [93] J. Li, M. Dao, C.T. Lim, S. Suresh, Spectrin-level modeling of the cytoskeleton and optical tweezers stretching of the erythrocyte, *Biophys. J.* 88 (5) (2005) 3707–3719. <http://dx.doi.org/10.1529/biophysj.104.047332>.
- [94] I.V. Pivkin, G.E. Karniadakis, Accurate coarse-grained modeling of red blood cells, *Phys. Rev. Lett.* 101 (11) (2008) 118105. <http://dx.doi.org/10.1103/PhysRevLett.101.118105>.
- [95] D.A. Fedosov, B. Caswell, G.E. Karniadakis, A multiscale red blood cell model with accurate mechanics, rheology, and dynamics, *Biophys. J.* 98 (10) (2010) 2215–2225. <http://dx.doi.org/10.1016/j.bpj.2010.02.002>.
- [96] H. Noguchi, G. Gompper, Shape transitions of fluid vesicles and red blood cells in capillary flows, *Proc. Natl. Acad. Sci.* 102 (40) (2005) 14159–14164. <http://dx.doi.org/10.1073/pnas.0504243102>.
- [97] H. Noguchi, G. Gompper, Swinging and tumbling of fluid vesicles in shear flow, *Phys. Rev. Lett.* 98 (12) (2007) 128103. <http://dx.doi.org/10.1103/PhysRevLett.98.128103>.
- [98] J.L. McWhirter, H. Noguchi, G. Gompper, Flow-induced clustering and alignment of vesicles and red blood cells in microcapillaries, *Proc. Natl. Acad. Sci.* 106 (15) (2009) 6039–6043. <http://dx.doi.org/10.1073/pnas.0811484106>.
- [99] J.L. McWhirter, H. Noguchi, G. Gompper, Deformation and clustering of red blood cells in microcapillary flows, *Soft Matter* 7 (22) (2011) 10967–10977. <http://dx.doi.org/10.1039/C1SM05794D>.
- [100] J.L. McWhirter, H. Noguchi, G. Gompper, Ordering and arrangement of deformed red blood cells in flow through microcapillaries, *New J. Phys.* 14 (8) (2012) 085026. <http://dx.doi.org/10.1088/1367-2630/14/8/085026>.
- [101] S. Jin, R.R. Lewis, D. West, A comparison of algorithms for vertex normal computation, *Vis. Comput.* 21 (1–2) (2005) 71–82. <http://dx.doi.org/10.1007/s00371-004-0271-1>.
- [102] A. Yazdani, P. Bagchi, Influence of membrane viscosity on capsule dynamics in shear flow, *J. Fluid Mech.* 718 (2013) 569–595. <http://dx.doi.org/10.1017/jfm.2012.637>.
- [103] M. Loewenberg, E.J. Hinch, Numerical simulation of a concentrated emulsion in shear flow, *J. Fluid Mech.* 321 (1996) 395–419. <http://dx.doi.org/10.1017/S002211209600777X>.
- [104] A.Z. Zinchenko, M.A. Rother, R.H. Davis, A novel boundary-integral algorithm for viscous interaction of deformable drops, *Phys. Fluids* 1994–Present 9 (6) (1997) 1493–1511. <http://dx.doi.org/10.1063/1.869275>.
- [105] I.B. Bazhlekov, P.D. Anderson, H.E.H. Meijer, Nonsingular boundary integral method for deformable drops in viscous flows, *Phys. Fluids* 1994–Present 16 (4) (2004) 1064–1081. <http://dx.doi.org/10.1063/1.1648639>.
- [106] C. Zhang, T. Chen, Efficient feature extraction for 2D/3D objects in mesh representation, in: Proceedings ICIP 2001, vol. 3, IEEE Signal Processing Society, Thessaloniki, 2001, pp. 935–938. <http://dx.doi.org/10.1109/ICIP.2001.958278>.
- [107] R. Aiello, F. Banterle, N. Pietroni, L. Malomo, P. Cignoni, R. Scopigno, Compression and querying of arbitrary geodesic distances, in: V. Murino, E. Puppo (Eds.), Image Analysis and Processing—ICIAIP 2015, in: Lecture Notes in Computer Science, vol. 9279, Springer International Publishing, 2015, pp. 282–293. http://dx.doi.org/10.1007/978-3-319-23231-7_26.
- [108] F.R. Cunha, M. Loewenberg, A study of emulsion expansion by a boundary integral method, *Mech. Res. Commun.* 30 (6) (2003) 639–649. [http://dx.doi.org/10.1016/S0093-6413\(03\)00068-5](http://dx.doi.org/10.1016/S0093-6413(03)00068-5).
- [109] Y. Saad, M. Schultz, GMRES: A generalized minimal residual algorithm for solving nonsymmetric linear systems, *SIAM J. Sci. Stat. Comput.* 7 (3) (1986) 856–869. <http://dx.doi.org/10.1137/0907058>.
- [110] E. Evans, Y.-C. Fung, Improved measurements of the erythrocyte geometry, *Microvasc. Res.* 4 (4) (1972) 335–347. [http://dx.doi.org/10.1016/0026-2862\(72\)90069-6](http://dx.doi.org/10.1016/0026-2862(72)90069-6).
- [111] D.-V. Le, Subdivision elements for large deformation of liquid capsules enclosed by thin shells, *Comput. Methods Appl. Mech. Engrg.* 199 (37–40) (2010) 2622–2632. <http://dx.doi.org/10.1016/j.cma.2010.04.014>.
- [112] M.C. Rivara, Algorithms for refining triangular grids suitable for adaptive and multigrid techniques, *Internat. J. Numer. Methods Engrg.* 20 (4) (1984) 745–756. <http://dx.doi.org/10.1002/nme.1620200412>.
- [113] D.-V. Le, S.T. Wong, A front-tracking method with Catmull–Clark subdivision surfaces for studying liquid capsules enclosed by thin shells in shear flow, *J. Comput. Phys.* 230 (9) (2011) 3538–3555. <http://dx.doi.org/10.1016/j.jcp.2011.01.047>.
- [114] Z.Y. Luo, S.Q. Wang, L. He, F. Xu, B.F. Bai, Inertia-dependent dynamics of three-dimensional vesicles and red blood cells in shear flow, *Soft Matter* 9 (40) (2013) 9651–9660. <http://dx.doi.org/10.1039/C3SM51823J>.
- [115] K.S. Chang, W.L. Olbricht, Experimental studies of the deformation and breakup of a synthetic capsule in steady and unsteady simple shear flow, *J. Fluid Mech.* 250 (1993) 609–633. <http://dx.doi.org/10.1017/S0022112093001582>.

- [116] S. Ramanujan, C. Pozrikidis, Deformation of liquid capsules enclosed by elastic membranes in simple shear flow: large deformations and the effect of fluid viscosities, *J. Fluid Mech.* 361 (1998) 117–143. <http://dx.doi.org/10.1017/S0022112098008714>.
- [117] G.R. Cowper, Gaussian quadrature formulas for triangles, *Internat. J. Numer. Methods Engrg.* 7 (3) (1973) 405–408. <http://dx.doi.org/10.1002/nme.1620070316>.
- [118] C. Pozrikidis, Finite deformation of liquid capsules enclosed by elastic membranes in simple shear flow, *J. Fluid Mech.* 297 (1995) 123–152. <http://dx.doi.org/10.1017/S002211209500303X>.
- [119] W.H. Press, S.A. Teukolsky, W.T. Vetterling, B.P. Flannery, *Numerical Recipes in C: The Art of Scientific Computing*, second ed., Cambridge University Press, Cambridge, 2002.
- [120] A. Arnold, O. Lenz, S. Kesselheim, R. Weeber, F. Fahrenberger, D. Roehm, P. Košovan, C. Holm, ESPResSo 3.1: Molecular dynamics software for coarse-grained models, in: M. Griebel, M.A. Schweitzer (Eds.), *Meshfree Methods for Partial Differential Equations VI*, in: *Lecture Notes in Computational Science and Engineering*, vol. 89, Springer, Berlin, Heidelberg, 2013, pp. 1–23. http://dx.doi.org/10.1007/978-3-642-32979-1_1.
- [121] H.J. Limbach, A. Arnold, B.A. Mann, C. Holm, ESPResSo—an extensible simulation package for research on soft matter systems, *Comput. Phys. Comm.* 174 (9)(2006) 704–727. <http://dx.doi.org/10.1016/j.cpc.2005.10.005>.
- [122] P.R. Zarda, S. Chien, R. Skalak, Elastic deformations of red blood cells, *J. Biomech.* 10 (4) (1977) 211–221. [http://dx.doi.org/10.1016/0021-9290\(77\)90044-6](http://dx.doi.org/10.1016/0021-9290(77)90044-6).

Supplementary information for “On the bending algorithms for soft objects in flows”

Achim Guckenberg^{*}, Marcel P. Schraml^{*}, Paul G. Chen[†], Marc Leonetti[‡], Stephan Gekle^{*}

Date: April 27, 2016

Contents

S1 Supplementary information for the comparison with analytical results	1
S1.1 Normal vector	1
S1.2 Mean curvature	4
S1.3 Gaussian curvature	4
S1.4 Laplace-Beltrami operator of the mean curvature	8
S1.5 Force density	8
S2 Additional shear flow data: Deformation and inclination angle figures	11

S1 Supplementary information for the comparison with analytical results

In this section we present additional information, supplementing the results from section 3 and Appendix B from the main text where we compared the analytical results for an RBC with the numerics. Namely, we provide plots of the errors as a function of the polar angle θ and numeric tables of the maximal and average errors. The tables include the various homogeneous meshes MT1 and MT2 as well as the inhomogeneous ones with 3914 and 3848 triangles. See tables [S1](#) and [S2](#) for their properties, and section 3.1 for the underlying difference between MT1 and MT2. Additionally, they list the values for a regular mesh with 5120 triangles whose nodes were shifted randomly by white noise with amplitude $0.01\% \times R$, where R is the RBC radius. The observed behavior is very similar to the inhomogeneous mesh. The columns labeled E2 and E3 contain the results for Method E if the ring-2 and ring-3 of neighbors, respectively, are taken into account. Finally, we also discuss the Gaussian curvature.

S1.1 Normal vector

The main part can be found in section 3.2 in the main text. Figure [S1](#) depicts the relative error for the MWA, E and S algorithms, and tables [S3](#) (MT1) and [S4](#) (MT2) the maximum and average errors, respectively.

^{*}Biofluid Simulation and Modeling, Fachbereich Physik, Universität Bayreuth, Bayreuth

[†]Aix-Marseille Université, CNRS, Centrale Marseille, M2P2, UMR7340, Marseille, France

[‡]Aix-Marseille Université, CNRS, Centrale Marseille, IRPHE, UMR7342, Marseille, France

Number of			Edge lengths/ R			Edge angles [$^\circ$]		Neighbors		Constructed from
Triangles N_T	Nodes N	Edges	Min.	Mean h	Max.	Min.	Max.	Min.	Max.	
320	162	480	0.163	0.256	0.313	37.3	100	5	6	Icosahedron
512	258	768	0.0660	0.202	0.269	28.8	91.3	4	6	Octahedron
1280	642	1920	0.0744	0.129	0.157	36.8	99.0	5	6	Icosahedron
2048	1026	3072	0.0246	0.101	0.135	28.6	92.4	4	6	Octahedron
5120	2562	7680	0.0336	0.0645	0.0788	36.6	98.3	5	6	Icosahedron
20480	10242	30720	0.0152	0.0323	0.0394	36.5	98.0	5	6	Icosahedron
81920	40962	122880	0.00687	0.0161	0.0197	36.5	97.8	5	6	Icosahedron
3914 (inh.)	1959	5871	0.0407	0.0800	0.159	17.3	139	4	10	320 + Ref.
5120 ($\pm 0.01\%$)	2562	7680	0.0335	0.0645	0.0789	36.4	98.4	5	6	5120 + noise

Table S1: Statistics of the various employed MT1 meshes for the red blood cell shape from section 3.1 of the main text: Number of triangles, vertices (nodes) and edges; minimum, average and maximum edge lengths (in units of the large radius R); minimum and maximum angles between the edges within each triangle; minimum and maximum number of ring-1 neighbors; construction basis. In this work we use the mean edge length h as the characteristic edge length. The homogeneous meshes are constructed by refining an icosahedron or octahedron using Loop's subdivision scheme. The inhomogeneous mesh with 3914 triangles is constructed from the mesh with 320 triangles and successive longest bisection refinement. For the MT2 meshes, see table S2.

Number of			Edge lengths/ R			Edge angles [$^\circ$]		Neighbors		Constructed from
Triangles N_T	Nodes N	Edges	Min.	Mean h	Max.	Min.	Max.	Min.	Max.	
320	162	480	0.176	0.256	0.325	37.4	101	5	6	Icosahedron
512	258	768	0.108	0.206	0.302	29.2	102	4	6	Octahedron
1280	642	1920	0.0882	0.129	0.165	36.9	103	5	6	Icosahedron
2048	1026	3072	0.0536	0.104	0.152	28.7	104	4	6	Octahedron
5120	2562	7680	0.0441	0.0648	0.0826	36.7	103	5	6	Icosahedron
20480	10242	30720	0.0220	0.0324	0.0413	36.6	104	5	6	Icosahedron
81920	40962	122880	0.0110	0.0162	0.0207	36.5	104	5	6	Icosahedron
3848 (inh.)	1926	5772	0.0439	0.0800	0.165	18.3	134	4	10	320 + Ref.
5120 ($\pm 0.01\%$)	2562	7680	0.0440	0.0648	0.0828	36.6	104	5	6	5120 + noise

Table S2: Statistics of the various employed meshes for the red blood cell shape similar to table S1, but now for the MT2 mesh type.

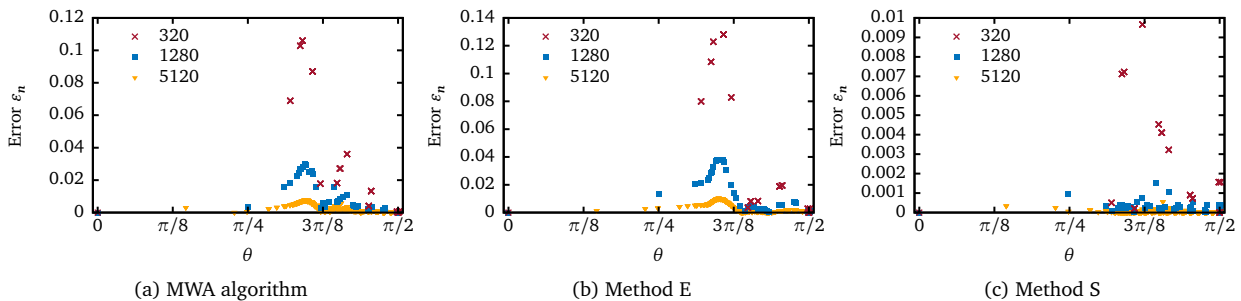


Figure S1: The relative error ϵ_n of the normal vector as defined in equation (17) (in the main text) of a RBC, obtained via the three different algorithms. MT1 meshes.

Triangles	MWA	E	E2	E3	S
320	0.11	0.13	0.34	0.51	0.0097
512	0.081	0.10	0.28	0.45	
1280	0.030	0.038	0.12	0.22	0.0015
2048	0.021	0.027	0.085	0.16	
5120	0.0076	0.010	0.033	0.065	0.00056
20480	0.0023	0.0026	0.0084	0.017	0.00024
81920	0.00094	0.00065	0.0021	0.0043	
3914 (inh.)	0.050	0.042	0.095	0.16	
5120 ($\pm 0.01\%$)	0.0091	0.012	0.033	0.065	

(a) Maximum of all nodes.

Triangles	MWA	E	E2	E3	S
320	0.038	0.047	0.13	0.24	0.0028
512	0.026	0.030	0.088	0.16	
1280	0.010	0.013	0.040	0.075	0.00030
2048	0.0073	0.0081	0.025	0.049	
5120	0.0026	0.0033	0.011	0.021	0.000039
20480	0.00067	0.00083	0.0027	0.0055	0.0000047
81920	0.00017	0.00021	0.00068	0.0014	
3914 (inh.)	0.014	0.0080	0.018	0.037	
5120 ($\pm 0.01\%$)	0.0028	0.0035	0.011	0.021	

(b) Average over all nodes.

Table S3: The maximum and average of the normal vector error ϵ_n . MT1 meshes; the MT2 data is in table S4. The row with 3914 triangles is for the inhomogeneous mesh, and the one labeled “5120 ($\pm 0.01\%$)” is for a mesh with 5120 triangles whose nodes were shifted randomly by white noise. Columns E2 and E3 depict Method E with the second and third ring of neighbors taken into account, respectively. A graphical representation of part of the data was given in figure 3 in the main text. The breakdown as a function of θ can be found in figure S1.

Triangles	MWA	E	E2	E3
320	0.11	0.12	0.34	0.50
512	0.11	0.097	0.29	0.46
1280	0.032	0.040	0.11	0.22
2048	0.038	0.032	0.091	0.17
5120	0.0089	0.011	0.035	0.068
20480	0.0044	0.0029	0.0092	0.018
81920	0.0022	0.00072	0.0023	0.0047
3848 (inh.)	0.070	0.036	0.097	0.17
5120 ($\pm 0.01\%$)	0.011	0.012	0.036	0.068

(a) Maximum of all nodes.

Triangles	MWA	E	E2	E3
320	0.042	0.047	0.13	0.24
512	0.032	0.030	0.092	0.16
1280	0.012	0.013	0.040	0.075
2048	0.0091	0.0082	0.026	0.051
5120	0.0032	0.0034	0.011	0.021
20480	0.00086	0.00085	0.0027	0.0055
81920	0.00023	0.00021	0.00069	0.0014
3848 (inh.)	0.011	0.0080	0.018	0.038
5120 ($\pm 0.01\%$)	0.0033	0.0035	0.011	0.021

(b) Average over all nodes.

Table S4: The maximum and average of the normal vector error ϵ_n . MT2 meshes. See table S3 for the MT1 version. A graphical representation was given in figure B.19 in the main text.

S1.2 Mean curvature

The analysis can be found in section 3.3 in the main text. In figure S2 we show the relative errors for the Methods C, D, E and S as a function of the polar angle θ . Tables S5 (MT1) and S6 (MT2) collect the maximal and average errors.

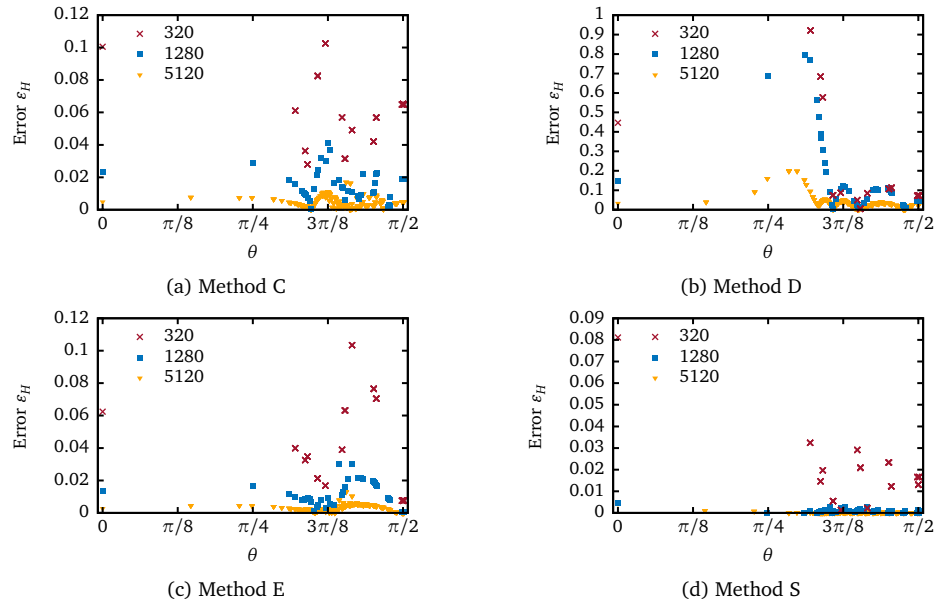


Figure S2: Relative errors ε_H for the mean curvature as defined in equation (17) in the main text. MT1 meshes. Figure 4 shows the actually obtained values for H . Note that Method C retains high errors especially at a few nodes around $\theta = 3\pi/8$, as analyzed in section 3.3.

S1.3 Gaussian curvature

Here we consider the Gaussian curvature similar to our investigations on the mean curvature from section 3.3 in the main text. As noted in the methods section 2.4.2, algorithms C and D both use the same approach while E and S differ. A and B do not provide it. Figure S3 compares the numerical with the analytical results, figure S4 depicts the corresponding errors and figures S5 (MT1) and S6 (MT2) as well as tables S7 (MT1) and S8 (MT2) summarize them. All in all, the behavior is similar to the mean curvature. Notably, Method C fails to converge in the maximal error measure. The reason are again the points already identified in section 3.3 in the main text. Algorithm E, on the other hand, converges as $\mathcal{O}(h)$ at higher resolutions, while Method S does not converge. Using the average

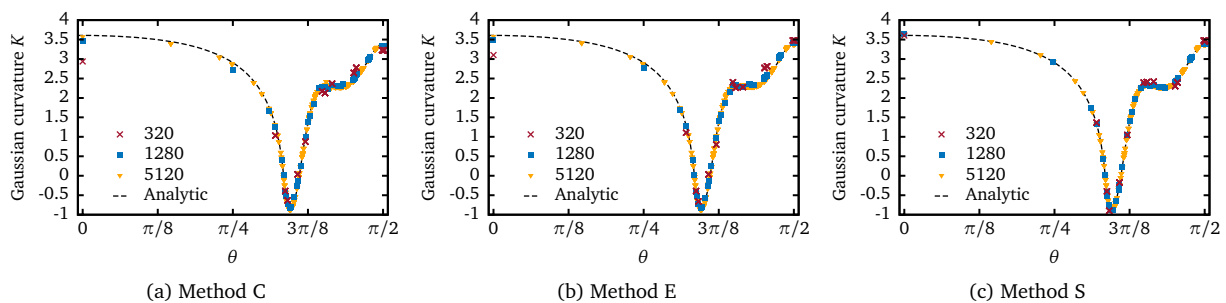


Figure S3: The Gaussian curvature of a RBC obtained from the three different algorithms and compared to the analytical result. MT1 meshes. Note that Method D uses the same approach as C.

Triangles	C	D	E	E2	E3	S
320	0.10	0.92	0.10	0.27	0.51	0.081
512	0.089	0.97	0.079	0.19	0.36	
1280	0.041	0.80	0.030	0.078	0.15	0.0046
2048	0.034	0.54	0.018	0.055	0.11	
5120	0.017	0.20	0.013	0.027	0.042	0.0042
20480	0.018	0.013	0.0048	0.0095	0.015	0.0043
81920	0.019	0.0032	0.0019	0.0036	0.0054	
3914 (inh.)	0.75	0.48	0.091	0.18	0.20	
5120 ($\pm 0.01\%$)	0.088	0.20	0.085	0.040	0.047	

(a) Maximum of all nodes.

Triangles	C	D	E	E2	E3	S
320	0.056	0.20	0.047	0.17	0.29	0.017
512	0.032	0.25	0.029	0.10	0.21	
1280	0.015	0.15	0.012	0.041	0.086	0.00092
2048	0.0096	0.096	0.0073	0.025	0.053	
5120	0.0041	0.032	0.0029	0.010	0.021	0.00016
20480	0.0011	0.0067	0.00074	0.0025	0.0052	0.000039
81920	0.00029	0.0017	0.00018	0.00063	0.0013	
3914 (inh.)	0.16	0.045	0.018	0.031	0.057	
5120 ($\pm 0.01\%$)	0.015	0.032	0.014	0.011	0.021	

(b) Average over all nodes.

Table S5: The maximum and average of the mean curvature error. MT1 meshes. The corresponding image is figure 5 from the main text, and the breakdown is picture S2; the MT2 data is in table S6.

Triangles	C	D	E	E2	E3
320	0.12	0.90	0.12	0.27	0.51
512	0.100	1.00	0.12	0.21	0.37
1280	0.091	0.98	0.039	0.078	0.15
2048	0.058	0.70	0.045	0.089	0.12
5120	0.085	0.30	0.015	0.025	0.044
20480	0.083	0.018	0.0069	0.0092	0.015
81920	0.083	0.0077	0.0035	0.0046	0.0068
3848 (inh.)	0.58	0.64	0.077	0.13	0.21
5120 ($\pm 0.01\%$)	0.096	0.31	0.064	0.040	0.052

(a) Maximum of all nodes.

Triangles	C	D	E	E2	E3
320	0.056	0.19	0.047	0.16	0.29
512	0.034	0.26	0.037	0.10	0.20
1280	0.016	0.15	0.012	0.040	0.083
2048	0.010	0.094	0.010	0.030	0.055
5120	0.0045	0.033	0.0033	0.010	0.021
20480	0.0012	0.0067	0.00091	0.0028	0.0056
81920	0.00035	0.0017	0.00024	0.00078	0.0015
3848 (inh.)	0.14	0.047	0.016	0.027	0.052
5120 ($\pm 0.01\%$)	0.015	0.033	0.014	0.011	0.021

(b) Average over all nodes.

Table S6: The maximum and average of the mean curvature error. MT2 meshes. The corresponding image is figure B.20 from the main text. See table S5 for the MT1 version.

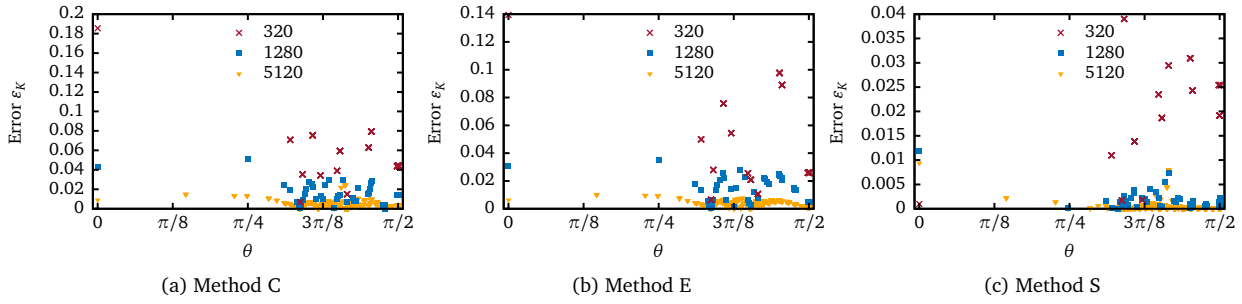


Figure S4: Relative error for the Gaussian curvatures in figure S3 (MT1 meshes).

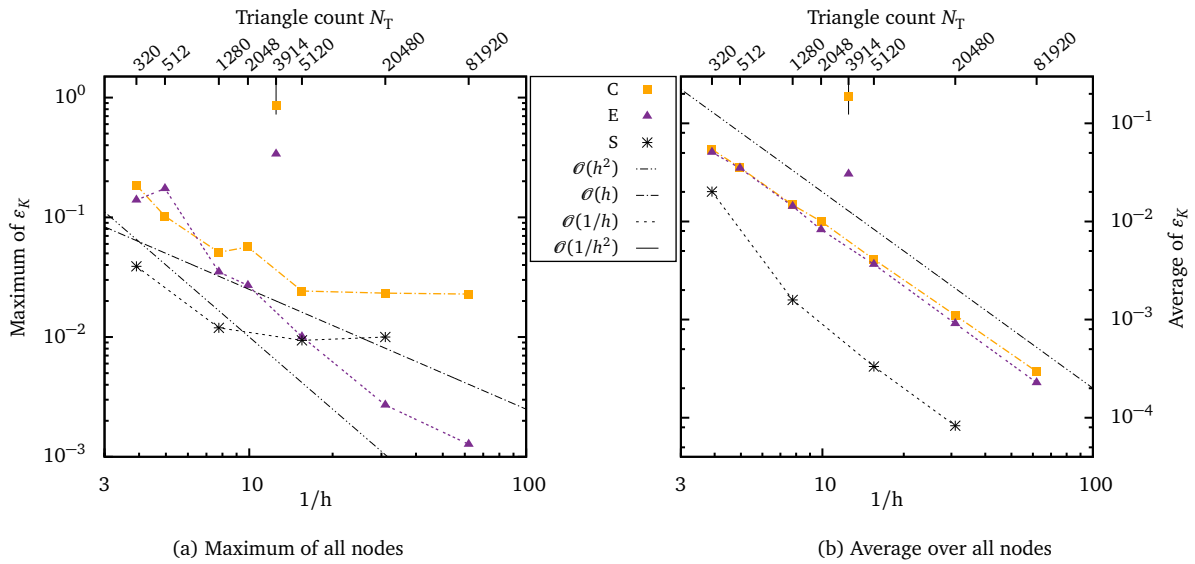


Figure S5: The maximum and average of the relative error ϵ_K of the Gaussian curvature. MT1 meshes. For the MT2 version see figure S6, for the numeric values see table S7.

Triangles	C	E	E2	E3	S
320	0.19	0.14	0.46	0.75	0.039
512	0.10	0.17	0.22	0.44	
1280	0.051	0.035	0.12	0.26	0.012
2048	0.057	0.027	0.070	0.14	
5120	0.024	0.010	0.034	0.069	0.0094
20480	0.023	0.0027	0.0093	0.019	0.010
81920	0.023	0.0013	0.0024	0.0050	
3914 (inh.)	0.86	0.34	0.19	0.22	
5120 ($\pm 0.01\%$)	0.13	0.12	0.053	0.076	

(a) Maximum of all nodes

Triangles	C	E	E2	E3	S
320	0.054	0.051	0.16	0.33	0.020
512	0.035	0.035	0.11	0.22	0.0016
1280	0.015	0.014	0.047	0.094	0.00033
2048	0.010	0.0082	0.029	0.059	0.000083
5120	0.0041	0.0037	0.012	0.025	0.00033
20480	0.0011	0.00091	0.0031	0.0064	0.000083
81920	0.00030	0.00023	0.00077	0.0016	
3914 (inh.)	0.19	0.030	0.039	0.068	
5120 ($\pm 0.01\%$)	0.023	0.023	0.014	0.025	

(b) Average over all nodes

Table S7: The maximum and average of the Gaussian curvature error for the MT1 meshes, as shown in figure S5. The MT2 data is in table S8.

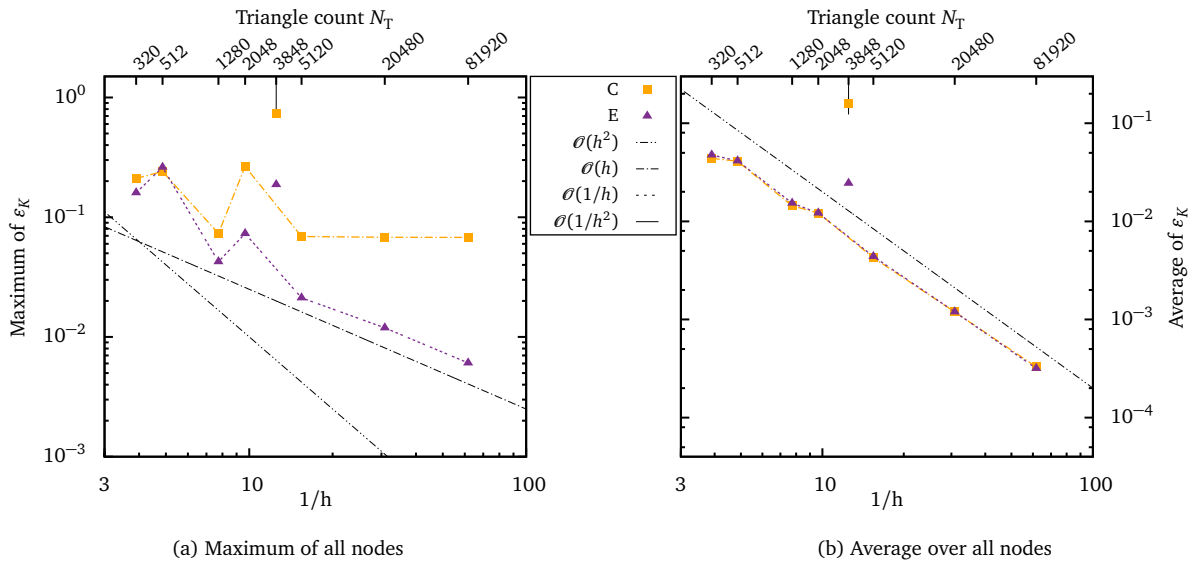


Figure S6: The maximum and average of the relative error ϵ_K of the Gaussian curvature for the MT2 mesh types. For the MT1 version see figure S5, for the numeric values see table S8.

Triangles	C	E	E2	E3
320	0.21	0.16	0.46	0.74
512	0.24	0.26	0.26	0.46
1280	0.073	0.043	0.14	0.27
2048	0.27	0.073	0.12	0.14
5120	0.069	0.021	0.044	0.076
20480	0.068	0.012	0.023	0.032
81920	0.068	0.0061	0.013	0.018
3848 (inh.)	0.74	0.19	0.24	0.24
5120 ($\pm 0.01\%$)	0.11	0.098	0.061	0.080

(a) Maximum of all nodes

Triangles	C	E	E2	E3
320	0.044	0.047	0.16	0.33
512	0.041	0.041	0.11	0.21
1280	0.014	0.015	0.045	0.090
2048	0.012	0.012	0.031	0.058
5120	0.0043	0.0044	0.013	0.025
20480	0.0012	0.0012	0.0038	0.0074
81920	0.00033	0.00032	0.0011	0.0021
3848 (inh.)	0.16	0.024	0.035	0.070
5120 ($\pm 0.01\%$)	0.023	0.023	0.015	0.025

(b) Average over all nodes

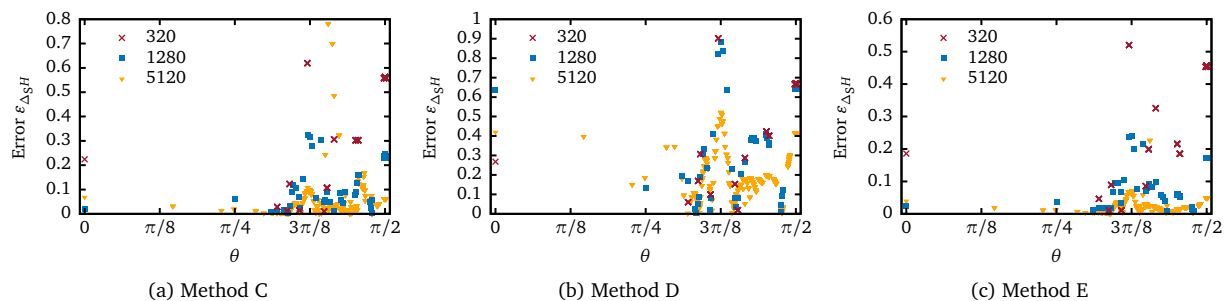
Table S8: The maximum and average of the Gaussian curvature error for the MT2 meshes, as shown in figure S6. The MT1 data is in table S7.

measure, all three show a decay of the error as $\mathcal{O}(h^2)$. Note that C and E still exhibit the same problems on the inhomogeneous mesh. On MT2 meshes, no qualitative differences are observed for C and E, but the maximal errors are up to half an order of magnitude larger.

Because Method D uses the Gaussian curvature K from Method C, one might expect that its error of the total bending force \mathbf{f} is being hampered by the systematic error retained for C. However, the total error is dominated by the Laplace-Beltrami operator $\Delta_S H$ rather than K . This can be seen by comparing the corresponding errors depicted in figures 7 and 10 from the main text.

S1.4 Laplace-Beltrami operator of the mean curvature

Most of the analysis is located in section 3.4 in the main text. Figure S7 depicts the relative errors as a function of θ , while tables S9 (MT1) and S10 (MT2) list the maximal and average errors.

Figure S7: The numerical error $\varepsilon_{\Delta_S H}$ upon evaluating the Laplace-Beltrami operator on the mean curvature. MT1 meshes. The graphs for $\Delta_S H$ can be found in figure 6 in the main text.

S1.5 Force density

The major part of the analysis can be found in section 3.5 in the main text. In figure S8 we show the errors as a function of θ . Tables S11 (MT1) and S12 (MT2) display the numerical values for the maximal and average errors.

Triangles	C	D	E	E2	E3
320	0.62	0.90	0.52	0.88	1.0
512	0.59	0.97	0.49	0.84	0.99
1280	0.32	0.88	0.24	0.56	0.77
2048	2.0	1.9	0.19	0.47	0.68
5120	0.78	0.52	0.23	0.25	0.38
20480	3.4	0.20	0.36	0.29	0.23
81920	16	0.21	0.72	0.56	0.34
3914 (inh.)	50	1.0	2.0	0.92	0.95
5120 ($\pm 0.01\%$)	5.1	0.55	4.7	0.40	0.39

(a) Maximum of all nodes.

Triangles	C	D	E	E2	E3
320	0.23	0.32	0.20	0.35	0.35
512	0.22	0.39	0.19	0.36	0.41
1280	0.098	0.31	0.073	0.19	0.28
2048	0.096	0.30	0.051	0.14	0.24
5120	0.052	0.19	0.022	0.066	0.12
20480	0.042	0.061	0.0064	0.019	0.037
81920	0.043	0.017	0.0022	0.0054	0.010
3914 (inh.)	7.6	0.22	0.25	0.17	0.21
5120 ($\pm 0.01\%$)	0.51	0.19	0.51	0.077	0.12

(b) Average over all nodes.

Table S9: The maximum and average of the relative error $\varepsilon_{\Delta_S H}$ of the Laplace-Beltrami operator of the mean curvature. MT1 meshes; the MT2 data is in table S10. A graphical representation is figure 7 from the main text, and the breakdown is image S7.

Triangles	C	D	E	E2	E3
320	0.55	0.78	0.45	0.76	0.88
512	0.66	0.98	0.55	0.84	1.00
1280	0.43	0.89	0.27	0.57	0.78
2048	0.68	0.82	0.47	0.54	0.71
5120	1.8	0.62	0.16	0.24	0.39
20480	7.2	0.22	0.37	0.16	0.17
81920	29	0.37	0.76	0.35	0.22
3848 (inh.)	39	1.7	1.8	0.76	0.75
5120 ($\pm 0.01\%$)	3.4	0.63	3.4	0.32	0.40

(a) Maximum of all nodes.

Triangles	C	D	E	E2	E3
320	0.24	0.31	0.20	0.34	0.35
512	0.23	0.40	0.20	0.38	0.42
1280	0.095	0.31	0.071	0.19	0.29
2048	0.11	0.29	0.093	0.16	0.24
5120	0.073	0.19	0.042	0.065	0.12
20480	0.087	0.062	0.042	0.034	0.042
81920	0.11	0.042	0.046	0.033	0.031
3848 (inh.)	7.0	0.23	0.20	0.15	0.21
5120 ($\pm 0.01\%$)	0.49	0.19	0.49	0.076	0.12

(b) Average over all nodes.

Table S10: The maximum and average of the relative error $\varepsilon_{\Delta_S H}$ of the Laplace-Beltrami operator of the mean curvature. MT2 meshes. See table S9 for the MT1 version. A graphical representation is figure B.21 from the main text.

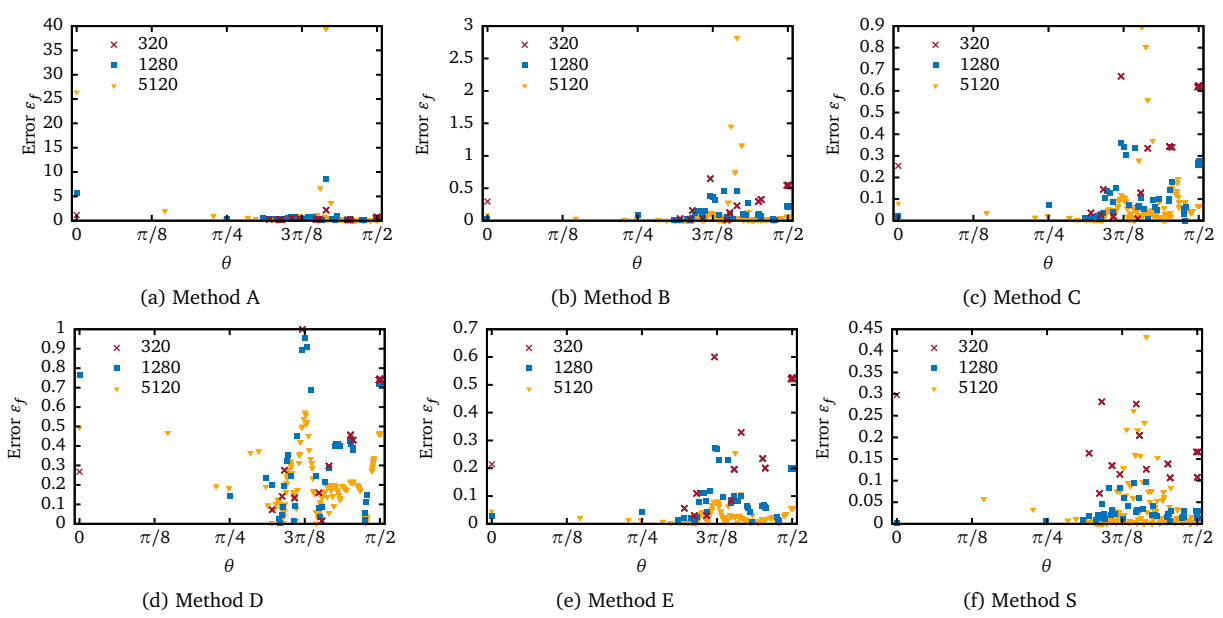


Figure S8: The numerical error ε_f upon evaluating the force density. MT1 meshes. Corresponding graphs for $|f|$ are located in figure 8 in the main text.

Triangles	A	B	C	D	E	E2	E3	S
320	2.2	0.65	0.67	1.00	0.60	0.93	1.0	0.30
512	25	0.66	0.64	1.1	0.55	0.92	1.0	
1280	8.7	0.46	0.36	0.95	0.27	0.62	0.85	0.096
2048	181	2.9	2.3	2.2	0.21	0.53	0.76	
5120	39	2.8	0.90	0.57	0.25	0.27	0.43	0.43
20480	186	14	3.9	0.23	0.41	0.33	0.26	2.4
81920	897	70	18	0.25	0.83	0.65	0.39	
3914 (inh.)	220	464	57	1.2	2.2	1.00	1.0	
5120 ($\pm 0.01\%$)	55	6.7	5.8	0.61	5.4	0.45	0.44	

(a) Maximum of all nodes.

Triangles	A	B	C	D	E	E2	E3	S
320	0.46	0.23	0.26	0.34	0.22	0.36	0.35	0.16
512	0.94	0.26	0.25	0.41	0.21	0.40	0.43	
1280	0.50	0.12	0.11	0.33	0.082	0.21	0.31	0.028
2048	1.6	0.14	0.11	0.33	0.057	0.16	0.26	
5120	0.63	0.065	0.059	0.21	0.025	0.075	0.14	0.026
20480	0.73	0.054	0.048	0.068	0.0073	0.022	0.042	0.029
81920	0.84	0.059	0.049	0.020	0.0025	0.0062	0.012	
3914 (inh.)	52	16	8.7	0.24	0.28	0.19	0.24	
5120 ($\pm 0.01\%$)	1.9	0.58	0.58	0.21	0.59	0.088	0.14	

(b) Average over all nodes.

Table S11: The maximum and average of the relative error ε_f of the force density. MT1 meshes. See figure 10 in the main text for the corresponding picture and figure S8 for the breakdown. The MT2 data is in table S12.

Triangles	A	B	C	D	E	E2	E3
320	2.5	0.63	0.61	0.87	0.52	0.80	0.87
512	13	1.1	0.71	1.1	0.62	0.91	1.0
1280	9.1	0.51	0.46	0.96	0.30	0.64	0.86
2048	59	2.7	0.79	0.88	0.53	0.61	0.78
5120	35	2.3	2.1	0.68	0.18	0.27	0.44
20480	137	9.3	8.3	0.24	0.42	0.18	0.19
81920	542	38	33	0.43	0.88	0.41	0.25
3848 (inh.)	175	389	45	2.0	2.0	0.85	0.82
5120 ($\pm 0.01\%$)	40	3.9	3.9	0.70	3.9	0.36	0.45

(a) Maximum of all nodes.

Triangles	A	B	C	D	E	E2	E3
320	0.52	0.24	0.26	0.34	0.21	0.35	0.34
512	0.94	0.29	0.26	0.42	0.23	0.41	0.44
1280	0.68	0.13	0.11	0.34	0.080	0.21	0.32
2048	1.6	0.14	0.13	0.32	0.11	0.18	0.27
5120	1.1	0.12	0.083	0.21	0.048	0.073	0.13
20480	2.0	0.15	0.10	0.069	0.048	0.039	0.048
81920	3.7	0.19	0.13	0.049	0.052	0.037	0.036
3848 (inh.)	47	15	8.0	0.25	0.23	0.17	0.24
5120 ($\pm 0.01\%$)	2.0	0.58	0.56	0.21	0.56	0.086	0.13

(b) Average over all nodes.

Table S12: The maximum and average of the relative error ε_f of the force density. MT2 meshes. See figure B.23 in the main text for the corresponding picture. See table S11 for the MT1 version.

S2 Additional shear flow data: Deformation and inclination angle figures

Here we supplement the information provided in section 4.5.1 from the main text for the elastic capsule in a viscous shear flow. Figure S9 depicts the deformation parameter for $G = 0.05$ and $\hat{\kappa}_B = 0.0375$ for all algorithms and various resolutions using MT1 meshes. Additionally, figure S10 shows the corresponding inclination angle θ as a function of time. Finally, image S11 displays θ for the larger shear rate $G = 0.2$ and bending modulus $\hat{\kappa}_B = 0.15$. All in all, the qualitative behavior is identical to the one analyzed in the main text for the deformation parameter at $G = 0.2$ and $\hat{\kappa}_B = 0.15$ (section 4.5.1), except that the inclination angle appears to be a bit more sensitive to the resolution and the mesh regularity.

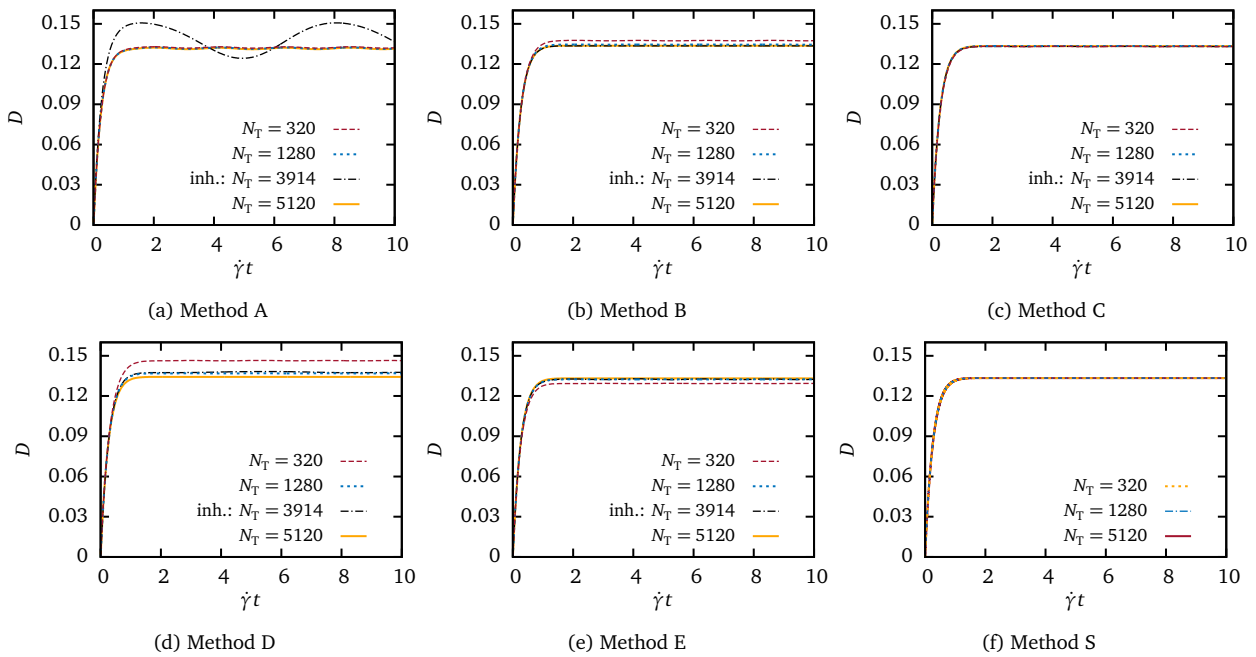


Figure S9: Taylor deformation parameter as a function of time after turning on the shear flow for BIM. Similar to figure 13 from the main text, except for $G = 0.05$ and $\hat{\kappa}_B = 0.0375$. The behavior of the inclination angle for the same set of parameters is displayed in figure S10.

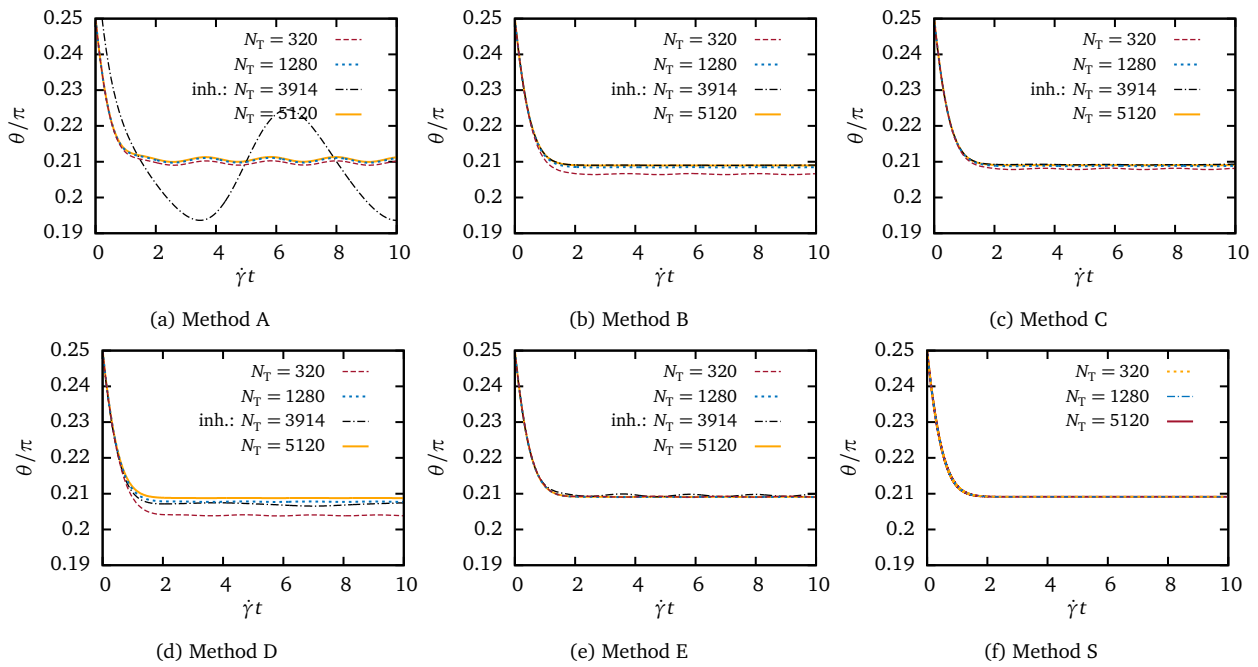


Figure S10: Inclination angle as a function of time for BIM. $G = 0.05$ and $\hat{\kappa}_B = 0.0375$. The deformation parameter is shown in figure S9.

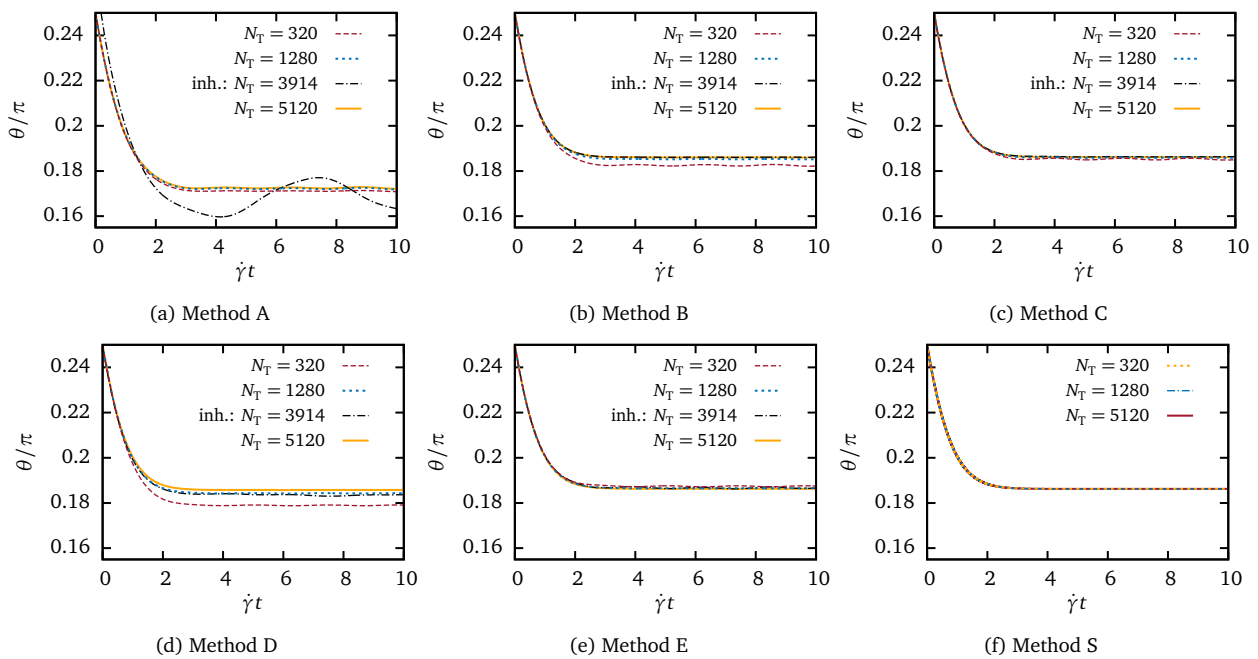


Figure S11: Inclination angle for BIM for $G = 0.2$ and $\hat{\kappa}_B = 0.15$. The deformation parameter can be found in figure 13 in the main text.

Publication 2

Theory and algorithms to compute Helfrich bending forces: a review

by

A. Guckenberger and S. Gekle

Journal of Physics: Condensed Matter **29** (20), 203001 (2017)

DOI: [10.1088/1361-648X/aa6313](https://doi.org/10.1088/1361-648X/aa6313)

Reproduced with permission from IOP Publishing.

Topical Review

Theory and algorithms to compute Helfrich bending forces: a review

Achim Guckenberger and Stephan Gekle

Biofluid Simulation and Modeling, Fachbereich Physik, Universität Bayreuth, Germany

E-mail: achim.guckenberger@uni-bayreuth.de

Received 9 August 2016, revised 23 February 2017

Accepted for publication 27 February 2017

Published 13 April 2017



CrossMark

Abstract

Cell membranes are vital to shield a cell's interior from the environment. At the same time they determine to a large extent the cell's mechanical resistance to external forces. In recent years there has been considerable interest in the accurate computational modeling of such membranes, driven mainly by the amazing variety of shapes that red blood cells and model systems such as vesicles can assume in external flows. Given that the typical height of a membrane is only a few nanometers while the surface of the cell extends over many micrometers, physical modeling approaches mostly consider the interface as a two-dimensional elastic continuum.

Here we review recent modeling efforts focusing on one of the computationally most intricate components, namely the membrane's bending resistance. We start with a short background on the most widely used bending model due to Helfrich. While the Helfrich bending energy by itself is an extremely simple model equation, the computation of the resulting forces is far from trivial. At the heart of these difficulties lies the fact that the forces involve second order derivatives of the local surface curvature which by itself is the second derivative of the membrane geometry. We systematically derive and compare the different routes to obtain bending forces from the Helfrich energy, namely the variational approach and the thin-shell theory. While both routes lead to mathematically identical expressions, so-called linear bending models are shown to reproduce only the leading order term while higher orders differ. The main part of the review contains a description of various computational strategies which we classify into three categories: the *force*, the *strong* and the *weak* formulation. We finally give some examples for the application of these strategies in actual simulations.

Keywords: Helfrich bending, red blood cells, vesicles and capsules, biofluid simulations, elastic membranes, spherical harmonics, subdivision surface methods

(Some figures may appear in colour only in the online journal)

1. Introduction

When immersed into an external flow, even such simple soft objects as vesicles or red blood cells (RBCs) deform into an amazing variety of dynamically moving shapes including slippers, parachutes or tumbling discocytes [1–5]. These arise from the complex interplay between the external and internal flow and the mechanical stiffness of the membrane. In the case

of red blood cells the membrane consists of four components [6, 7]: shear resistance due to the network of cross-linked spectrin proteins (cytoskeleton) and bending rigidity as well as area inextensibility and surface viscosity due to the lipid bilayer. Omitting the lipid bilayer leads to objects which have no or very little bending resistance and which are commonly denoted as capsules [5]. Removal of the spectrin network eliminates shear resistance leading to what is called a vesicle

[4]. For theoretical or computational modeling, membranes are typically considered as two-dimensional elastic sheets and their physical complexity is lumped into effective moduli for shear resistance, bending rigidity, area dilatation and sometimes surface viscosity [2, 8].

The study of soft object dynamics in flows is a serious challenge. Being deprived of a minimum energy principle in this non-equilibrium situation, the analytical prediction of cell and vesicle dynamics represents a formidable task. Experimentally, a full appreciation of the dynamics would require three-dimensional recordings combined with time-resolved tracking of the membrane while usually one is restricted to two-dimensional microscopic imaging. Although considerable progress has been achieved to overcome these theoretical [2, 9] and experimental [10–14] difficulties, in many situations one currently depends on numerical simulations to gain further insight into the physical phenomena and mechanisms governing the objects' behavior in external flows. An accordingly large interest exists in the development and validation of accurate and efficient numerical techniques [1, 8, 15–20].

In this review, we focus on one specific aspect of these numerical simulations, namely the bending forces originating from the lipid bilayer. Bending forces are important for the accurate modeling of vesicles, red blood cells and sometimes even capsules [1, 4, 5]. The typical starting point for their computation is an energy functional that provides the bending energy density for a given membrane geometry. In its most simple and, at the same time, most commonly used form the local bending energy density is proportional to the square of the local surface curvature. Variants of this form have been postulated by Canham [21], Helfrich [22] and Evans [23] in the early 1970s, but can also be derived from classical elasticity or by taking the continuum limit of models that explicitly consider the interaction between individual lipid molecules. In the mathematics community the bending functional is known under the term 'Willmore surface/energy' [24–26].

Our goal is to summarize the origins of this energy, to outline different derivations of the ensuing bending forces and finally to give an account of available numerical algorithms together with an overview of recent applications. A detailed assessment of the quality of a variety of methods can be found in two recent papers [27, 28]. We do not cover other aspects such as shear elasticity or flow solvers. For these we refer the reader to recent reviews [8, 15, 17, 19] and books [16, 29]. Other related reviews [2, 4, 5, 18, 30] also include experimental observations. Collective behavior of many soft objects with a focus on blood flow is reviewed in [20, 31–33].

The organization of the paper is as follows. In section 2.1 we introduce the physical motivation of the Helfrich bending energy and outline how to derive the bending forces via a variational derivative as well as thin shell theory. The latter is given in detail in appendix A, which allows us to draw a connection to so-called 'linear bending models'. In sections 2.2 and 2.3 we briefly touch upon the still open question of the spontaneous curvature and introduce some experimental techniques to measure the bending modulus. Section 3.1 discusses various possibilities to represent the membrane shape in a

discretized fashion for use in computer algorithms. Based on these, section 3.2 focuses on a classification of different computational methods according to their conceptual similarities and differences. In section 3.3 we briefly summarize results of a recent comparison regarding the quality of different algorithms [27] and extend the comparison to the important case of spherical harmonics, with details provided in appendix B. Finally, in section 4 we describe some recent applications of the computational algorithms.

2. Physical model of membrane bending

2.1. The Helfrich model

2.1.1. Bending energy. Vesicle walls and red blood cell membranes contain a lipid bilayer which leads to the membrane's resistance against bending as well as its rather strict area inextensibility [4, 6, 7]. The bilayer consists of two neighboring sheets of elongated lipid molecules whose axes are oriented perpendicular to the membrane surface. Their hydrophilic heads point outwards towards the aqueous surrounding while the hydrophobic tails are buried in the membrane interior. Different forms of the bending energy have been proposed in the past, with the common denominator that they all depend on the square of the mean curvature [21–24]. One of the most popular models for the energy per unit deformed area ϵ_B dates back to Helfrich [22], who introduced it as

$$\epsilon_B(\mathbf{x}) = 2\kappa_B(H - H_0)^2 + \kappa_K K, \quad \mathbf{x} \in S. \quad (1)$$

This constitutive law has later been called the spontaneous curvature model [34], also compare section 2.2. All appearing quantities might in principle depend on \mathbf{x} . The total bending energy stored in the infinitesimally thin interface S is then

$$E_B = \int_S 2\kappa_B(H - H_0)^2 dS + \int_S \kappa_K K dS. \quad (2)$$

Here, κ_B is the usually constant bending modulus (having unit of energy) and $H(\mathbf{x})$ is the local mean curvature which is defined by

$$H(\mathbf{x}) = \frac{1}{2}(\kappa_1 + \kappa_2), \quad \mathbf{x} \in S, \quad (3)$$

i.e. the average of the principal curvatures κ_1 and κ_2 [35, 36]. Note that the sign of H can be defined such that it is either positive or negative for a sphere. We adopt the convention that H shall be positive for a sphere. An alternative but equivalent expression is given by [37]

$$H(\mathbf{x}) = \frac{1}{2} \sum_{i=1}^3 (\Delta_S x_i) n_i(\mathbf{x}), \quad \mathbf{x} \in S, \quad (4)$$

where \mathbf{n} is the outer normalized normal vector and Δ_S is the so-called Laplace–Beltrami operator [36, equation (33)]. This form reveals more clearly that the bending energy already involves a second order derivative of the surface. This can be contrasted with the surface tension of a liquid–liquid interface whose energy involves only the area itself.

The Gaussian curvature is $K(\mathbf{x}) = \kappa_1 \kappa_2$ and its associated Gaussian (or saddle splay) modulus is κ_K . Both moduli κ_B and

κ_K are often similar in magnitude [36]. However, the Gauss–Bonnet theorem [36, equation (70)] states that the integral of K over a closed (but not an open [36, 38–42]) surface is a topological invariant, i.e. it is a constant as long as the topology for a closed object does not change. Hence, it can often be discarded from the very beginning. H_0 is the spontaneous curvature which will be discussed further in section 2.2 below. We point the reader to [36] for an excellent overview of the required math and the Helfrich Hamiltonian in general.

Equation (1) can be obtained via three different routes. In the original work [22] the form of the energy functional (1) has been phenomenologically proposed. It can also be justified by the observation that the energy density for fluid membranes can only depend on the local area stretch and the mean and Gaussian curvatures. Taylor expansion to second order then leads to an expression of the form (1) [36, 43, 44]. In light of this it is somewhat surprising that it remains valid even when $1/H$ is of the same order of magnitude as the bilayer thickness [45].

Secondly, equation (1) can also be derived from a continuum mechanics perspective¹. Here, one starts by considering the membrane as a three-dimensional isotropic and linear (i.e. Hookean) elastic material. In the limit of thin and inextensible shells, a careful derivation of the elastic stresses and the resulting elastic energy for a given deformation then leads to an expression equivalent to the first and most important term in equation (1) (compare [44, equation (24)] [46, equation (1.132)] [35, equation (4.52)] [48, equation (7)]). The bending modulus κ_B can then be calculated explicitly as a function of the membrane thickness h and the elastic parameters (e.g. Young’s modulus E) of the material [5, 36, 44, 48]. Given the complex molecular structure of RBCs [6], the assumption of isotropic and homogeneous elastic properties of the lipid bilayer may however be called into question for cells and an empirical approach to the value of κ_B might be a better choice.

In the third method, the form of equation (1) is derived from microscopic models that consider individual lipid molecules. Assuming an interaction potential between the molecules and taking the limit of an infinite amount of molecules, one arrives at equation (1) [49, 50]. Molecular scale models can be combined with the continuum mechanics approach given in the previous paragraph by assuming spatial variability of the elastic parameters [51] which to lowest order again leads to equation (1).

2.1.2. Bending forces. The term ‘bending force’ in the present context needs to be understood in the following way: consider a deformed membrane S whose shape is known. The deformation results in forces $\mathbf{f}_B(\mathbf{x})$ driving the interface back to equilibrium. At the same time, flows on the outside and inside of the membrane result in tractions (forces per unit area), whose difference across the surface provides a traction jump $\Delta\mathbf{f}_B(\mathbf{x})$. Assuming negligible membrane inertia, the internal membrane bending forces must be in local equilibrium with the external fluid traction jump at each point in time, implying [5, 35, 52]

$$\Delta\mathbf{f}_B(\mathbf{x}) = -\mathbf{f}_B(\mathbf{x}), \quad \mathbf{x} \in S. \quad (5)$$

The goal now is to compute the bending forces \mathbf{f}_B or equivalently the traction jump $\Delta\mathbf{f}_B$ from the current deformation if the energy stored in the surface is given by equation (2). Analytically, this goal is commonly achieved by one of two possibilities.

Variational formulation. In the first approach one performs a variational derivative of equation (2) while applying some external force such that the membrane is in equilibrium. Consider arbitrary infinitesimal and virtual displacements $\delta\mathbf{x}$ (but which adhere to possible constraints) of the vector \mathbf{x} that maps the deformed surface. The virtual work performed by the forces when some membrane point is displaced is thus given by $\Delta\mathbf{f}_B \cdot \delta\mathbf{x}$, and for the whole membrane by $\delta W_{\text{ext}} := \int_S \Delta\mathbf{f}_B(\mathbf{x}) \cdot \delta\mathbf{x} \, dS(\mathbf{x})$. Hence, the membrane is in equilibrium for [53–57]

$$\begin{aligned} \delta\mathcal{E} &:= \delta E_B - \delta W_{\text{ext}} \\ &= \delta E_B - \int_S \Delta\mathbf{f}_B(\mathbf{x}) \cdot \delta\mathbf{x} \, dS(\mathbf{x}) \stackrel{!}{=} 0. \end{aligned} \quad (6)$$

Explicitly evaluating δE_B from equation (2) for variations in the normal direction and evoking the arbitrariness of $\delta\mathbf{x}$ eventually leads to the Euler–Lagrange equation [24, 36, 41, 57–66]

$$\begin{aligned} \Delta\mathbf{f}_B &= -2\kappa_B[\Delta_S(H - H_0) \\ &\quad + 2(H - H_0)(H^2 - K + H_0H)]\mathbf{n}. \end{aligned} \quad (7)$$

H_0 , H , K and \mathbf{n} may depend on the position $\mathbf{x} \in S$. κ_B and κ_K , on the other hand, are assumed to be constant. If they were not, an additional tangential term would arise [67]. Note that for constant moduli without additional constraints and for closed objects tangential variations only represent a reparameterization of the surface and provide no further information [61], i.e. the traction jump consists of only the above normal component.

Equation (7) and variations thereof can be used to determine the equilibrium shapes of vesicles for $\Delta\mathbf{f}_B = 0$ [17, 21, 34, 58, 68–70]. In the context of hydrodynamic simulations, the reverse problem is considered and the traction jump $\Delta\mathbf{f}_B$ is determined from the instantaneous deformation. $\Delta\mathbf{f}_B$ is exerted by the fluid on the membrane and is the central quantity which couples the solid and the fluid mechanics part of the problem [35, 71, 72]. Explicit expressions for the stress tensor also exist (equation (A.43) in the appendix), representing a first integral of equation (7) [2, 36, 57, 61, 65, 70, 73].

Note that the Euler–Lagrange equation (7) also remains valid if the surface is not closed: the first normal variation of the second term in equation (2) that contains the (constant) saddle splay modulus κ_K still drops out [36, 38, 41]. Yet, contrary to the case of closed objects without constraints, demanding that the first *tangential* variation of \mathcal{E} vanishes now provides additional information, namely boundary conditions for the shape at the borders that actually do depend on κ_K [38–40, 74]. I.e. although equation (7) remains valid in the interior of the surface, additional conditions arise at the borders that determine the possible shapes in agreement with recent experiments on vesicles [42].

¹ Note that in engineering solid mechanics the term ‘membrane theory’ actually refers to thin shells *without* bending resistance [46, 47].

Shell formulation. The second approach to derive equation (7) uses thin shell theory [35, 70, 75–78]. Tension tensor and bending moments can be obtained by computing appropriate derivatives of the energy density with respect to the metric and curvature tensors, respectively. Balancing these by the externally imposed traction jump Δf_B invokes first a local torque and subsequently a local force balance. Yet, in the end equation (7) is obtained [76, equation (6.19)]. We explicitly perform this calculation and show the equivalence of the two approaches in appendix A.

Linear bending models. Sometimes one directly starts with a constitutive linear model [70, 79–82] for the bending moments $M_{\alpha\beta}$ on S , such as

$$M_{\alpha\beta} = -2\kappa_B(H - H_0)a_{\alpha\beta}, \quad \alpha, \beta = 1, 2, \quad (8)$$

where $a_{\alpha\beta}$ is the metric tensor (the coefficients of the first fundamental form) and Greek indices denote curvilinear components. This ansatz leads to equation (7) only if additional contributions to the tension tensor are appropriately accounted for. However, deviant forms of equation (8) (often involving the curvature tensor [54, 80, 81, 83–86]) and/or neglecting the tension tensor contributions are commonly used and usually yield only the leading order term ($\Delta_S H$) from equation (7) when considering small deviations from a plane as shown in appendix A.5. Higher orders may differ [48, 58, 79]. Since the relations between these various approaches are not clearly established in the present literature, we derive and compare the traction jumps for these models in some detail in appendix A.5.

Constraints. Many derivations of equation (7) enforce additional constraints, such as constant volume (for closed particles) or conserved surface area which mimic the balance of osmotic pressure and the large area dilatation modulus, respectively, of vesicles [4, 34] and red blood cells [1, 6, 87]. These lead to additional terms containing Lagrange multipliers that are added to \mathcal{E} and also modify the Euler–Lagrange equation. For the volume conservation, \mathcal{E} is complemented by $\Delta p V$, where V is the particle’s volume and the Lagrange multiplier Δp represents a pressure difference [39, 41, 59–61, 64]. Equation (7) receives an additional $\Delta p \mathbf{n}$.

Furthermore, two possibilities exist to enforce a constant surface area: either a local or a total area constraint. The total surface area constraint is implemented by adding $\sigma \int_S dS$ to \mathcal{E} , with the Lagrange multiplier σ being a constant effective tension [36, 38, 39, 59, 60, 64, 88]. This leads to the supplement $2\sigma H \mathbf{n}$ in equation (7).

The local surface area constraint, on the other hand, is enforced by adding $\int \tilde{\sigma}(\mathbf{x}) dS$ to \mathcal{E} , where the Lagrange multiplier $\tilde{\sigma}(\mathbf{x})$ is a non-constant effective tension [2, 13, 52, 55, 58, 61, 88–98, 99]. A *tangential* first variation of the total energy \mathcal{E} then leads to an equation involving $\tilde{\sigma}$, whereas the normal first variation gives the Euler–Lagrange equation. Combining both effectively means to amend equation (7) with the term $2\tilde{\sigma} H \mathbf{n} - \nabla_S \tilde{\sigma}$, where ∇_S denotes the surface gradient [52] equation (60)]. We explicitly derive this term in appendix A.6. Now, if one solves the Euler–Lagrange equation for the shape,

$\tilde{\sigma}$ is fixed by the tangential equation. Since we prescribe the surface and solve for Δf_B , $\tilde{\sigma}$ is determined from the incompressibility of the lipid bilayer fluid flow, $\nabla_S \cdot \mathbf{u} = 0$ [52]. This is equivalent to stipulating that the area of a small surface patch should remain constant [100] chapter 1.7.2]. We also note that $\tilde{\sigma}$ must be necessarily constant for closed objects without external forces, meaning that both the local and global models often predict the same equilibrium behavior [41, 55].

Directly solving for the Lagrange multipliers is possible [52, 77, 88, 92, 101–103]. For simplicity, constraints are also often implemented approximately using penalty methods. For example, one may introduce appropriate *ad-hoc* potential energies to penalize deviations from the desired values [55, 72, 93, 104–107]. In the case of area inextensibility it is also possible to use suitable in-plane elasticity models (such as the Skalak constitutive law [108]) to replace [94, 109] or supplement [72, 110] other area constraints.

Membrane inertia. Equation (5) implies that the fluid and the membrane are always in local equilibrium. This means that the inertia of the membrane itself is neglected (otherwise an additional acceleration term would appear [78, 111, 112]). This is common even for those methods where the *fluid* inertia is included such as Lattice–Boltzmann [72, 113]. Thus, the motion of the membrane is determined by the no-slip condition, i.e. the local membrane velocity is taken equal to the local fluid velocity.

An alternative approach is to endow the membrane itself with a mass and to obtain its motion by integration of Newton’s third law (force formulation, see section 3.2.2) which is common practice in particle methods such as multiparticle collision dynamics (MPCD) [114–116] or (smoothed) dissipative particle dynamics [18, 117–126].

Finite thickness and other models. Some simulations incorporate a membrane with a finite thickness. This effectively means to drop some simplifying assumptions that ultimately lead to the Helfrich model [127–133]. Explicitly taking into account the two leaflets for bilayer membranes has also been done [134]. Finally, ad-hoc models are sometimes used that have no (or at least no obvious) connection to the Helfrich law [135–137].

2.2. Area-difference model and spontaneous curvature

In many situations, especially for closed objects such as cells [6] or vesicles [34], the two sheets composing the lipid bilayer are not identical. For example, the inner layer may possess less or different lipids than the outer one. The minimum energy state is then no longer a flat sheet, but a curved shape with a prescribed difference ΔA_0 between the areas occupied by the two sheets. Such a situation can be modeled by including an additional contribution to the energy in equation (2), leading to the area-difference elasticity (ADE) model [34, 70, 138–140]:

$$E_B = \int_S \epsilon_B dS + \kappa_\Delta (\Delta A - \Delta A_0)^2. \quad (9)$$

κ_Δ is the area difference elastic modulus and ΔA is the instantaneous area difference expressible by the distance h between the neutral surfaces of the lipid monolayers as $\Delta A = 2h \int_S H \, dS$ [36, equation (77)]. For $\kappa_\Delta \rightarrow \infty$ the area difference becomes a hard constraint and the so-called bilayer coupling model is obtained [34, 138, 141]. The contributions of H , H_0 , ΔA and ΔA_0 to the traction jump differ from each other in general, i.e. cannot be merged. Nevertheless, when solving for the stationary shapes, the *total set* of solutions is the same when using either H_0 or κ_Δ or both [138, 142]. Yet, the full ADE model has apparently not been used to study soft objects in flows where the instantaneous shape is given as input, with the exception of [143]. This might therefore be a promising task for the future, but for the remainder of this paper we will restrict ourselves to H_0 , i.e. to the Helfrich model (1).

A slightly more complicated situation arises when molecules other than lipids, e.g. transmembrane proteins, are present in the bilayer. These usually extend across both monolayers and may occupy a different area at one end than at the other, resulting again in an area difference. However, in contrast to a simple difference in the number of lipids, membrane proteins can often form clusters and/or are chemically attached to other parts of the cell membrane such as the spectrin network [6], leading to a spatially inhomogeneous spontaneous curvature $H_0(\mathbf{x})$.

While it is possible to obtain experimental values for H_0 for vesicles [56, 144], there currently exist no direct measurements of the spontaneous curvature (or area difference) of red blood cells, although the asymmetric distribution of the phospholipid types between the two leaflets of the bilayer [6] suggests a non-zero spontaneous curvature. Indeed, not even the stress-free shape for the in-plane shear elasticity could be determined unambiguously so far [145–147]. All in all, this lack of knowledge represents a certain hindrance to accurate red blood cell simulations. Different ways to overcome it have been suggested [66, 82, 139], although a consensus has yet to be reached.

The area-difference and bilayer-coupling models have been extensively used to compute vesicle equilibrium shapes (see section 4.1). For cells or vesicles in external flows, the spontaneous curvature model following equation (1) is more popular and most (but not all) numerical algorithms for bending forces described in the following section can relatively easily incorporate an arbitrary $H_0(\mathbf{x})$. Due to the experimental uncertainty, however, many red blood cell simulations are conducted with $H_0 = 0$. Yet, some researchers [82, 109, 148] choose a constant $H_0 \neq 0$ while others [72, 84, 85, 149] set $H_0(\mathbf{x}) = H_R(\mathbf{x})$ where $H_R(\mathbf{x})$ is the curvature of the resting shape, i.e. the shape that the object assumes in the absence of any external forces or flows. For red blood cells $H_R(\mathbf{x})$ corresponds to the discocyte shape (see figure 2). A recent careful analysis [66] suggested the spontaneous curvature of an oblate spheroid as a viable alternative for red blood cells.

2.3. Experimental determination of bending moduli

The bending modulus κ_B is a simulation parameter which needs to be determined by experiments. Various experimental setups exist for this task (see e.g. the reviews [144, 150–152]

for vesicles and [7, 153] for red blood cells). Each experimental setup can be modeled either analytically or numerically with κ_B as a free parameter whose value is then adjusted until agreement between the model and the experimental data is obtained.

In the first and most classical approach for cells, the membrane is sucked into a micropipette while the shape is recorded with a microscope as a function of the pressure difference [154–157]. The deformed shape sensitively depends on the elastic parameters of the cell and can be used to determine the bending modulus κ_B . Besides that, the shapes obtained by micropipette aspiration simulations can be directly compared to experiments which serves as a validation for the entire RBC model including, but not limited to, the bending algorithm [158, 159].

Secondly, the bending modulus can be computed from the wavelength of wrinkles at low flow strength as has been done for elastic capsules [131, 160], but has also been proposed for lipid membranes [161, 162].

Finally, the fluctuations of the cell membrane in thermal equilibrium (e.g. [163–168]) can be used to measure the bending modulus or to validate simulation models [105], although some complications may arise due to active processes in the cell membrane [169].

In principle, the above techniques can also be used to retrieve the bending modulus from molecular dynamics simulations. This has indeed been done for vesicles (see e.g. [45, 152, 170–173]), but apparently no one has attempted it so far for realistic RBCs.

The popular approach to measure elasticity constants by the stretching of cells via tweezers [174, 175] or atomic force microscopes [176] is unfortunately rather insensitive to the bending rigidity and can consequently not be used to obtain accurate information about that particular component [66, figure 6] [105]. Nevertheless, these experiments have often been used to validate other parts of computational models [66, 105, 107, 135, 177–182].

In the end, measured values for κ_B of healthy human red blood cells scatter rather widely in the range of $0.2\text{--}9 \times 10^{-19}$ J [8, 153, 155]. Most simulations are being conducted with values between 2 and 4×10^{-19} J.

3. Numerical approaches

3.1. Surface discretizations

As already noted in the previous sections, cells, capsules and vesicles are typically modeled with infinitely thin surfaces. The finite (albeit very small) thickness is effectively taken into account via constitutive laws, for example the Helfrich model from equation (1). Such 2D manifolds embedded into the 3D space are usually implemented numerically by representing the surface with a distribution of points (nodes). Integration and differentiation operations are then calculated via some interpolation or approximation of the surface between these nodes. These discretizations form the basis for the computation of bending forces and we therefore describe some commonly used approaches in the following:

Flat triangles. The simplest method uses linear interpolation between 3 nodes together with an unstructured mesh, leading to a representation with flat triangles. It is one of the most often used approaches owing to its simplicity and versatility ([52, 71, 93, 94, 98, 107, 183] among many others). For example, a local increase of resolution (refinement) is easily possible and was used in the biofluidic context e.g. in [15, 110, 184–186] (see [187] for a recent overview of refinement methodologies). However, since it leads to a C^0 surface, computation of higher derivatives such as curvatures even within the elements requires the inclusion of several neighbors. Moreover, the results are often sensitive to the mesh regularity [27].

Spring network models [17, 18, 105, 135, 136, 158, 177, 188, 189] can also be classified into this category (although one could imagine spring networks containing quadrilaterals and other elements in principle, in practice they appear to be only used with triangles)². The major difference between these models and the continuum models emerges in the computation of in-plane elasticities [191], where their merit lies in the simplicity of implementation. Expressions for the bending resistance, on the other hand, usually assume the same form as in the continuum descriptions and follow the same methodologies as in the ‘force formulation’ (see section 3.2.2 below).

Higher order elements. Quadratic interpolation between 6 nodes leads to curved triangles [54, 71, 83, 192, 193]. They have the advantage that second order properties (such as the curvatures) within an element can be computed by direct differentiation. Nevertheless, even first order derivatives at the nodes or element borders remain ambiguous, requiring some averaging of the surrounding values [192]. It is also possible to increase the interpolation order by including more nodes within each element, leading to spectral element methods with exponential convergence properties as the order increases [194–197], although global surface smoothness is still not automatically ensured [195].

Subdivision methods. Subdivision surface methods are becoming increasingly popular. They constitute a generalization of spline based approaches. Starting from a coarse unstructured control mesh of quadrilaterals or flat triangles, one successively introduces new nodes and elements according to certain predefined rules. A key observation is that any point on the limit surface obtained by an infinite number of refinements can be directly evaluated via some closed analytical formula. This enables easy and efficient computations of derivatives. Different variations of this idea exist. One needs to distinguish between interpolating (the original nodes are

members of the limit surface) and approximating schemes (the original nodes are not necessarily located on the limit surface). The first ones have the advantage that the limit surface is more directly connected to the control mesh. However, the latter have the big advantage of being C^1 smooth everywhere (even C^2 at regular nodes³), whereas in the first case the curvatures are not always bounded [198]. This makes approximating approaches the dominant choice for dynamic simulations of soft objects. Two popular schemes are the Catmull–Clark (quadrilateral based) [199, 200] and especially the Loop (based on flat triangles) [55, 91, 96, 102, 198, 201–205] subdivision methods. We remark again that both reduce to C^1 smoothness near irregular nodes. Hence, good mesh regularity is a requirement for accurate derivatives [27].

Spectral methods. Another class are spectral methods where functions are expanded using some basis functions whose support extends over the whole domain (this is not to be confused with spectral element methods [194, 195], where the support of the individual high-order polynomials extend only over the elements). In the present biofluidic context, the surface itself and functions defined on it are usually expanded using spherical harmonics [84, 85, 92, 101, 103, 206–209]. They work best for nearly spherical shapes and can result in spectral accuracy (i.e. the error decays exponentially fast). Instead of spherical harmonics a simple Fourier series expansion is also possible, albeit rarely used [210].

Other methodologies. An (almost) completely two times continuously differentiable surface may be constructed by using cubic B-Splines together with a structured mesh [211–213]. Unfortunately, for closed objects two singular poles occur where the derivatives are not well defined, requiring e.g. extrapolation of quantities [214] or the usage of a second (rotated [212] or unstructured [191]) mesh. Finally, NURBS [77] and fully three-dimensional phase field models have also been employed [215, 216].

3.2. Computation of bending forces

The surface discretizations described above can be combined with different methods to compute the actual bending forces, which we describe in this section. For the sake of completeness, we shortly mention in section 3.2.1 the computation of bending forces in the computationally much simpler case of two-dimensional and axisymmetric geometries. In full 3D, the wealth of available methods can be sorted into three categories: the *force formulation* (section 3.2.2) starts from the energy equation (2) and yields a force at each node. The *strong formulation* (section 3.2.3) and the *weak formulation* (section 3.2.4) on the other hand depart from the Euler–Lagrange equation (7) and yield a surface force density. Approaches based on the thin-shell formalism (including the linear bending models) are often implemented by means of the strong formulation. All methods have their advantages and disadvantages and there

²Spring network models start from the basic assumption that the cytoskeleton of red blood cells can be appropriately modeled by not discretizing any continuum descriptions, but rather by mimicking the spectrin proteins *directly* with a, possibly coarser, triangulated mesh [158]. This idea originates from the observation that the expanded cytoskeleton forms a lattice-like network [190]. The actual membrane properties are implemented via appropriate potentials acting between the nodes, stemming from coarse-grained molecular or from reasonable ad-hoc models [158]. Connections of the associated potential strengths (spring constants) with continuum properties (elastic moduli) are then usually established by considering special cases of the mesh, such as regular hexagonal networks [189, 191].

³Regular nodes are defined by having 4 (quadrilaterals) or 6 (triangles) neighbor nodes.

is currently no consensus on which one is the best for a specific application.

3.2.1. Two-dimensional and axisymmetric models. In two dimensions, the Helfrich bending energy (with zero reference curvature) is simply $E_B = \frac{1}{2} \int H^2 ds$, where s denotes a coordinate along the contour and the integration goes over the full perimeter of the particle. A variational derivative leads to [89, 90, 217]

$$\Delta f_B = \kappa_B \left(\frac{\partial^2 H}{\partial s^2} + \frac{1}{2} H^3 \right) \mathbf{n} \quad (10)$$

in analogy to equation (7). Different equivalent expressions are possible if the particle is locally inextensible [217]. The interface can be discretized by using for example straight lines [89, 90, 119, 218], level-set [219–223], phase field [88, 224, 225], spline [226] or Fourier methods [217, 227–229].

Axisymmetric algorithms start from the full 3D equations and reduce them by one dimension via the assumption of rotational symmetry. Differentiation and integration on the surfaces thus reduce to 1D problems. Approximations of the interfaces employ e.g. straight lines [230, 231], Fourier expansions [95, 232, 233], B-Splines [134], level-set [223] or phase field models [234–236].

3.2.2. Direct application of the principle of virtual work (force formulation). In full 3D, the first possibility to numerically compute the forces from the bending energy E_B is to directly discretize the integral as well as the mean curvature appearing in equation (2). Thereafter, E_B depends explicitly on the node positions \mathbf{x}^i with $i = 1, \dots, N$, i.e. $E_B = E_B(\{\mathbf{x}^i\})$, where $\{\mathbf{x}^i\}$ means the collection of all N nodes. Contrary to the approaches presented in the following sections, this effectively makes the force formulation a discrete model. By the principle of virtual work, the force (in Newton) acted upon the membrane node \mathbf{x}^i by the fluid is given by the gradient [109, 169, 237, 238]

$$\mathbf{F}(\mathbf{x}^i) = \frac{\partial E_B(\{\mathbf{x}^i\})}{\partial \mathbf{x}^i}, \quad i = 1, \dots, N. \quad (11)$$

Roughly speaking, this is a discretized version of the variational derivative leading to equation (7) [81, p 93]. For many surface discretizations, the gradient can be computed analytically using the explicit expression for the discretized bending energy [27, 72]. Guckenberger *et al* [27] named this method ‘force formulation’ because it yields a force (rather than a force density) at each node.

Some flow solvers, e.g. boundary integral methods, require the force per unit area (traction jump) instead of the force. In this case, one divides by the area A_i associated with or ‘occupied’ by the node:

$$\Delta f_B(\mathbf{x}^i) \approx \mathbf{F}(\mathbf{x}^i)/A_i, \quad i = 1, \dots, N. \quad (12)$$

Using flat triangles, typical choices for A_i are 1/3 of the total area of the triangles surrounding \mathbf{x}^i [86, 93, 98, 109] or Meyer’s mixed area [27, 239]. The results presented in [27] suggest that the latter gives superior results since it leads to a perfect tiling of the surface (i.e. $\sum_{i=1}^N A_i = A$, where A is the total surface area).

We remark that although computationally convenient, the force formulation as a discrete model is observed to be more sensitive to the mesh regularity (i.e. to element area and connectivity variances) than the continuum approaches presented in sections 3.2.3 and 3.2.4 [81, p 93] [27, chapter 3.5]. For sufficiently regular meshes, however, similar results can be achieved [27, chapter 3.5]. Also note that ‘pure’ spring network models necessarily use the force formulation idea as they start with a discrete model in the first place.

Out of the various available surface discretizations described in section 3.1, the force formulation has thus far been used only with flat triangles and subdivision surface schemes.

Flat triangles. Depending on the surface approximation, discretizing the integral and the mean curvature H in equation (2) within the force formulation can be done in different ways. Here we describe the two most often used possibilities for flat triangles (termed Method A and B in [27]).

Method A starts from an often used expression [28, 72, 105, 109, 117, 121–126, 147, 158, 169, 189, 240–250, 251] similar to an angle-potential:

$$E_B = 2\tilde{\kappa}_B \sum_{\langle i,j \rangle} [1 - \cos(\theta_{ij} - \theta_{ij}^0)]. \quad (13)$$

Here, the sum runs over all edges $\langle i,j \rangle$ once, θ_{ij} is the angle between the normal vectors of the adjacent triangles with edge $\langle i,j \rangle$, θ_{ij}^0 indicates the reference (or spontaneous) angle and $\tilde{\kappa}_B$ is an effective bending modulus. This formula can be connected to the Helfrich model from equation (2) for special cases, such as a sphere approximated by equilateral triangles and zero reference curvature. In this case the effective and physical bending moduli are related by [241]

$$\tilde{\kappa}_B = \sqrt{3} \kappa_B. \quad (14)$$

Despite being rigorously valid only for this special mesh topology and geometry, the relation (14) is often also used in the general case.

Method B is based on a finite difference cotangent scheme for the Laplace–Beltrami operator (and thus also of the mean curvature H according to equation (4)). Note that different variants of this scheme can be found in the literature, obtainable e.g. by evaluating a contour integral [52, 98, 239]. Method B uses the discretization described in [241]:

$$\Delta_S w(\mathbf{x}^i) \approx \frac{\sum_{j(i)} (\cot \vartheta_1^{ij} + \cot \vartheta_2^{ij}) (w(\mathbf{x}^i) - w(\mathbf{x}^j))}{2A_V^i}, \quad i = 1, \dots, N. \quad (15)$$

w is some arbitrary function on the surface S , the sum goes over the next neighbors of node \mathbf{x}^i , A_V^i denotes its Voronoi area [239], and ϑ_1^{ij} and ϑ_2^{ij} are the angles opposite to the edge $\langle i,j \rangle$ in the triangles which contain nodes \mathbf{x}^{j-1} and \mathbf{x}^{j+1} . See figure 1 for a sketch. This scheme is used in [98] as well as [106, 252] and subsequent publications [114, 115, 188, 253, 254].

Besides methods A and B, many other possibilities exist such as including triangle areas as weights in equation (13) [243] or using some other discretizations of the mean curvature [28, 237],

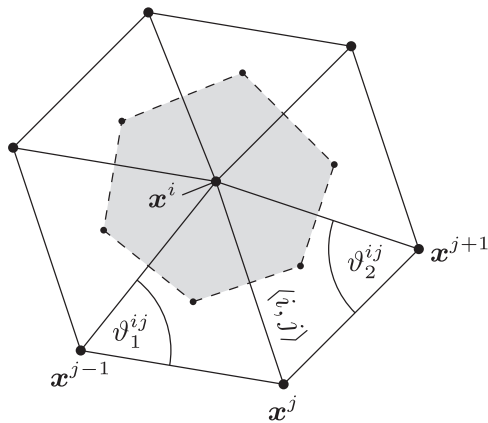


Figure 1. The first ring of neighbors around some node x^i . The shaded region marks the Voronoi area A_v^i . Modified from [27] with permission from Elsevier.

also including the ones presented in the next section 3.2.3. The underlying problem of finding appropriate discretizations for the curvatures and the Laplace–Beltrami operator on triangulated meshes has attracted a lot of researchers from the mathematics and computer science communities since it is also of high relevance for other fields such as computer graphics or surface reconstruction. See for example the recent [37, 239, 255–269]. Yet, one has to acknowledge that no perfect discretization of the Laplace–Beltrami operator can exist [260].

Subdivision schemes. The ‘force formulation’ is also compatible with other surface representations. For example, [91, 96, 102] employed Loop’s subdivision surface method and obtained the mean curvature within elements by means of direct differentiation. Nodal values were computed by subsequent averaging.

3.2.3. Computation by means of the Euler–Lagrange equation (strong formulation). Another possibility is to evaluate the Euler–Lagrange equation (7) or the equations from thin shell theory (see appendix A) directly. This requires as the most intricate ingredient an approximation for the Laplace–Beltrami operator of the mean curvature, $\Delta_S H$, i.e. a fourth order derivative. We note that Guckenberger *et al* [27] termed this idea ‘variational formulation’ because it uses the expression (7) which is obtained by variational calculus. Since, however, this term is also often used in connection with the finite element method (see section 3.2.4), we will denote it here as the ‘strong formulation’. As in the previous section, the implementation details of the strong formulation depend on the underlying surface discretization.

Flat triangles. One basic idea is to apply the same procedure that was used to compute the mean curvature H via equation (4) again to $\Delta_S H$. For example, if H was computed with a cotangent scheme at all nodes, then $\Delta_S H$ can be approximated by applying the cotangent scheme to H itself. This is Method C in [27]. To be more precise, the authors employed equation (15) except that the Voronoi area in the denominator was

replaced with Meyer’s mixed area [239] leading to a perfect tiling of the surface and thus to superior results when compared with Method B [27]. This approach (sometimes with slight changes) has often been used by other researchers (e.g. [37, 52, 66, 86, 93, 183, 255, 270–272]).

A second possibility for flat triangles is based on a kernel of the heat equation (Method D in [27]), and essentially consists of computing the sum of the distances between the evaluation point and *all* other vertices of the mesh weighted with an exponential decay [261]. Due to the global support, the convergence properties were found to be the best of all the considered methods, but at the price of a large performance impact [27]. This is most likely the reason why it has not been used in the biofluidic context before. We remark that a cut-off can be applied to increase performance, and that employing the geodesic distance (the distance along the surface) improves results further [269].

A third possibility uses parabolic fitting of the surface components and of the mean curvature around the evaluation point [107] (Method E in [27]). The robustness of this algorithm can be easily tuned by including more neighbors. Other fitting polynomials are also possible [273], with fourth or higher order polynomials allowing for a direct computation of $\Delta_S H$ in one go. Otherwise, several successive fits are necessary. Method E was used (sometimes in modified form) e.g. in [37, 99, 107, 186, 272, 274–277]. References [94, 104, 146, 148, 278–285] use a combination of parabolic fitting for H and a direct discretization of the Laplace–Beltrami operator of H in the spirit of Method C. Moreover, as already mentioned in the force formulation section, countless other ways to discretize the Laplace–Beltrami operator on triangulated meshes exist (see section 3.2.2 and the provided therein).

So far we have only discussed approaches to compute the mean curvature H and its Laplace–Beltrami operator $\Delta_S H$. Yet, equation (7) also sports the Gaussian curvature K as well as the normal vector \mathbf{n} . Fortunately, since $\Delta_S H$ is often the dominating term (see appendix A.4.4) and they only contain second and first order derivatives, respectively, their approximations usually introduce only negligible errors [27]. If the parabolic fitting idea is used, both can be computed naturally from the fitted surface [107]. In case of the other two schemes (methods C and D), it is convenient and quite accurate [27] to compute K by means of a discretized version of the Gauss–Bonnet theorem [239], and \mathbf{n} via the ‘mean weighted by angle’ algorithm [286].

Higher order elements. Curved triangles allow the direct computation of the curvatures and normal vectors within the elements since all quantities are assumed to vary quadratically inside of them. Nevertheless, discontinuities arise at the nodes. As a solution, the resulting quantities are averaged. Afterwards, assuming that they vary quadratically, too, the final traction jump is computed for example by performing one derivative explicitly and the other by means of a contour integral [54, 83]. Spectral element methods have apparently not been used to compute equation (7).

Subdivision surfaces. To the best of our knowledge, subdivision surface methods were not yet used to evaluate the local equilibrium condition (7) directly. This probably stems from the fact that they are mostly used together with the finite element method (section 3.2.4) in the general field of thin-shell analysis [198].

Spectral methods. Here, the surface components [84, 101, 103, 207, 208] or sometimes only the radius [91, 92] are expanded into a spherical harmonics series. Evaluation of equation (7) or of the thin shell theory equations from appendix A is then in principle straightforward since the derivatives act on the basis functions and are well-defined everywhere [287]. We provide more details in appendix B. However, because the mean curvature H decays only slowly in the spectral space, a comparably high number of modes must be used. This in turn often results in prohibitively slow performance in the evaluation of the hydrodynamics. The typical remedy is a procedure called de-aliasing: generally speaking, one can use a relatively low resolution for the hydrodynamics, but upsample the grid (via spherical harmonics interpolation) for the purpose of computing the bending forces [84, 101, 103, 207]. A possible alternative might be to bypass the transformation of H and directly compute $\Delta_S H$ from the surface components, as remarked in the appendix.

Other spectral methods besides spherical harmonics were apparently not used so far for the purpose of 3D bending computations.

Other discretizations. It is also possible to employ a level set [288] or combined level set method and essentially non-oscillatory (ENO) reconstruction [182] to directly evaluate equation (7). Using three-dimensional phase-field models is another possibility [215].

3.2.4. Finite element method (weak formulation). In the third possibility to compute the bending forces, equation (7) is multiplied with an arbitrary trial function (typically denoted $\delta\mathbf{x}$) and integrated over the membrane surface. Then the fourth order derivative of \mathbf{x} is reduced to a second order derivative by means of two successive integrations by parts. These effectively move the derivatives to the trial functions $\delta\mathbf{x}$. Thus we find an integral equation constituting the so-called weak formulation of equation (7) which can be solved by a finite element method (FEM) for $\Delta\mathbf{f}_B$ [55, 149, 193, 198, 204, 289]. The basic idea here is to discretize the surface with some elements and expand the surface \mathbf{x} as well as the trial functions $\delta\mathbf{x}$ in terms of a finite number of shape functions having local support on the elements. After substituting them into the integral equation, evoking the arbitrariness of $\delta\mathbf{x}$ and also discretizing the integral via some numerical quadrature, one ends up with a sparse linear system of equations that determines $\Delta\mathbf{f}_B$ [55, 131]⁴. Alternatively, the value of $\Delta\mathbf{f}_B$ at some node can be *approximated* via the mean value theorem, dodging the explicit solution of the linear system [133, equation (62)] [149].

⁴In typical engineering applications the finite element method is applied the other way round, i.e. one usually solves for the expansion coefficients of the surface \mathbf{x} while the traction is prescribed [193].

Proper convergence requires that if the integrand contains an r 'th derivative, then the elements must approximate the surface such that it is C^r within the elements and C^{r-1} at the element borders [289, chapter 3.6]. Hence, since the bending energy contains a second order derivative, the elements themselves should be C^2 , and C^1 at their borders. This is similar to the force formulation (section 3.2.2) which also requires only a second order derivative, but is in stark contrast to the strong formulation (section 3.2.3) which requires that the surface is at least C^3 (otherwise the fourth order derivative would not be well defined). Despite having similar requirements as the force formulation, so far it remains unclear whether the force or the weak formulation performs better with respect to *accuracy* if the same surface elements are employed. Overall, the major advantage of FEM seems to lie in its *stability* [193, 290], although rigorous comparisons with the other two alternatives are apparently missing.

Considering the differentiability requirements, subdivision surface methods are often used for this approach [55, 149, 198, 200], as for Method S in [27]. Splines [213, 291], NURBS [77] or mixed phase field models are also possible [216].

The C^1 requirement can be bypassed by introducing the mean curvature H as an additional independent variable [26, 292]. Hence, the overall system to be solved for $\Delta\mathbf{f}_B$ and H consists not only of the weak form of the Euler–Lagrange equation, but also of an additional equation (also in weak form) for the mean curvature. This system contains only first order derivatives and is thus amenable to discretizations with flat triangles, resulting in a stable scheme [26, equations (4.3) and (4.4)] [290, equations (3.4f) or (4.15f)] [143, 292–294]. An alternative is to use curved triangles (which also form a C^0 surface, as mentioned above) [295, 296].

As a side note, [206] employs the weak formulation similar to FEM, but together with spherical harmonics (which have global support and thus the method cannot be really classified as FEM). By choosing a particular trial function $\delta\mathbf{x}$, they obtain an equation with the expansion coefficients for the traction jump on the one side, and an expression involving the known derivatives of $\delta\mathbf{x}$ on the other side. The traction jump in the spatial domain is then obtained by a simple backward transformation.

3.3. Comparison of a selection of methods

An easy way to analyze the performance of bending algorithms is to consider shapes for which analytical formulas for the traction jumps can be derived. Guckenberger *et al* [27] studied methods originating from flat triangles (methods A–E and S mentioned above) for the typical equilibrium shape of a red blood cell, see figure 2. Methods A and B use the force formulation, C–E the strong formulation, and Method S the finite element method. They computed the maximal and average errors of the numerically obtained traction jump with respect to the analytical result in all cases. The spontaneous curvature was set to zero.

Their results for a certain type of mesh (called MT1 in [27]) is shown in figure 3 for the mean curvature H , and in figure 4 for the traction jump $\Delta\mathbf{f}_B$. Regarding the maximal

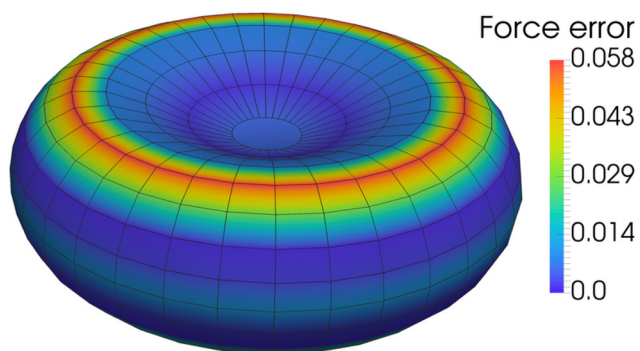


Figure 2. The typical shape of a red blood cell, as described by equations (B.14a–B.14c). Intersections of the grid lines indicate the nodes used for the spherical harmonics expansion of order 16, and the color depicts the nodal errors of evaluating the traction jump (the maximum and average is shown in figure 4). Most other expansion orders show similar error patterns.

error, none of the algorithms converge properly. Moreover, Method D, which appears to converge at least with a systematic error, also begins to diverge beyond a certain resolution when the mesh topology is slightly changed (mesh MT2 in [27], not repeated here).

For the average error, which is more relevant in Stokes flow applications, Method D appears to show proper convergence. Taking the MT2 mesh into account, all other algorithms roughly converge with a systematic error, except Method A which clearly diverges.

The authors of [27] concluded that in principle the best scheme is Method D, although it is too slow for practical uses because it requires sufficiently high resolutions and scales as $\mathcal{O}(N^2)$ where N is the number of nodes. Hence, Method S or Method E are usually better choices. But note that the quality of the subdivision surface method S highly depends on the mesh regularity. See [27] for more details and an in-depth discussion together with some guidelines.

Here we additionally include results obtained using the strong formulation with a spherical harmonics expansion of order p as described in appendix B. Figure 2 shows a typical error distribution for Δf_B on the surface for $p = 16$. The errors for the mean curvature H drop to machine precision beyond an order $p \geq 5$, see figure 3. In this case the RBC surface is exactly representable by a spherical harmonics series of order 5. The mean curvature itself, on the other hand, cannot be expressed by just a few terms of the expansion owing to its highly nonlinear dependency on the surface geometry. As we compute the Laplace–Beltrami operator of H by expanding H again into spherical harmonics, the error decay of the traction jump in figure 4 occurs roughly exponentially (as is typical for spectral methods). If we computed the fourth order derivatives directly as remarked in the appendix, we would expect a jump to machine precision as for H . Hence we conclude that for spherical harmonics a somewhat more practical test would consider some non-exactly representable surface and assess its performance there. However, the main problem is to obtain precise reference results for such an object and we therefore leave this task for future work.

4. Applications

We will now summarize some important applications and provide an overview of the contexts in which the individual methods are being used.

4.1. Membranes in the absence of an externally imposed flow

The computation of equilibrium shapes of vesicles and red blood cells is a problem with a long history [17, 21, 34, 58, 68–70]. The goal is to find the minimum of the surface’s energy under appropriate constraints. In case of vesicles this usually means to minimize the bending energy from equation (2) or the extended version from equation (9) (which includes the area-difference) under the constraints of constant surface area and volume. For red blood cells additional terms are needed to take the finite shear elasticities into account, although early works have neglected them.

To this end, it would in principle be possible to use the Euler–Lagrange equation (equation (7) with $\Delta f_B = 0$ and appropriate amendments for the constraints) and solve it for the unknown shape directly. However, since it constitutes a 4th order nonlinear PDE, this is a formidable numerical task and was only attempted under the assumption of axisymmetry [58, 68–70, 142, 231, 297, 298]. Alternatively, the bending forces can be used to solve a damped equation of motion where the mass and the damping coefficients only influence the speed of convergence but do not modify the final equilibrium shapes. For example, Tsubota *et al* [28, 147] used this approach together with flat triangles. A third and the most popular possibility is to perform a direct minimization of the energy via methods such as Monte Carlo [70, 139] or quadratic programming [141, 299]. This has been done for axisymmetric [223, 234] but also fully three-dimensional shapes. Employed discretizations include for example flat triangles (e.g. [70, 139, 243, 296, 299], and publications using Brakke’s surface evolver [300] such as [301, 302]). Moreover, spherical harmonics [141, 303], subdivision surface methods [55] or B-Splines [213] have been used, sometimes in the framework of the finite element method [55, 213, 216].

In the related context of membrane thermal fluctuations, adequate simulations also require the inclusion of bending resistance. For example, [140, 304, 305] used spherical harmonics and [169] used a spring network model. Bending must also be included when considering the diffusion of nanoparticles near realistic red blood cells which was done in [86, 306–309] via flat triangles and Method C from section 3.2.3.

In table 1 we list an overview of all works simulating isolated soft objects with or without an external flow together with the employed bending algorithms.

4.2. A single object in flow

The behavior of even a single soft object such as a vesicle, capsule or red blood cell in simple flows can be amazingly complex [1–5, 97], even bearing the possibility for deterministic chaos [310, 311]. For vesicles the dynamics is mostly determined

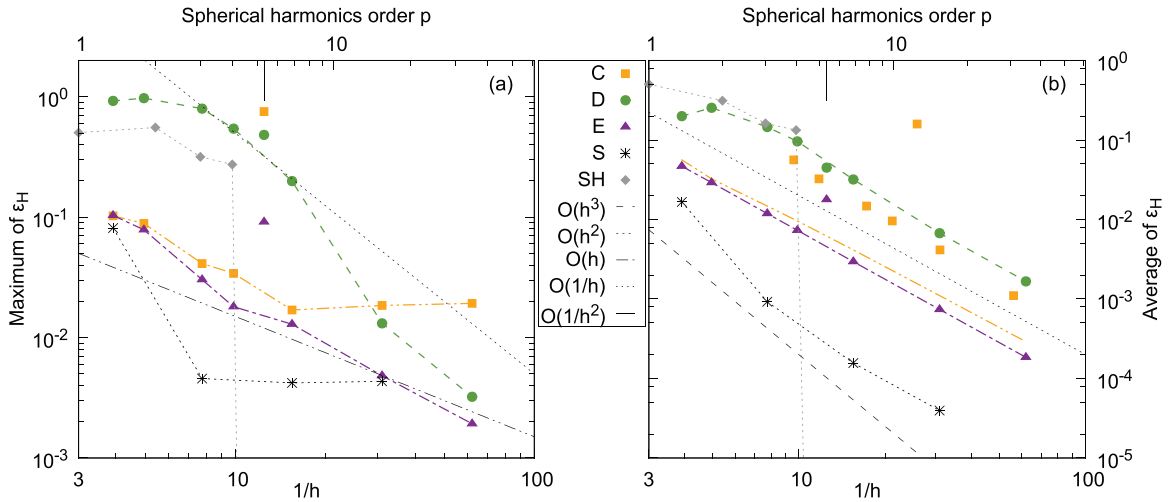


Figure 3. (a) Maximal and (b) average errors of the mean curvature H for the discocyte shape from figure 2. Methods C–E and S use flat triangles with a mean edge length of h (inverse on the lower x -axis). The lines are meant as guides to the eye to assess the typical convergence behavior. The vertical line at the top indicates results for an inhomogeneous triangulated mesh. Data for methods A–E and S from [27] (MT1 mesh). The result for the spherical harmonics method SH is shown as a function of the truncation order p (upper x -axis, *no correlation* with the lower axis exists). Note that the error drops to machine precision ($\approx 10^{-14}$ for double precision arithmetic) for $p \geq 5$. Errors for the Gaussian curvature K are very similar.

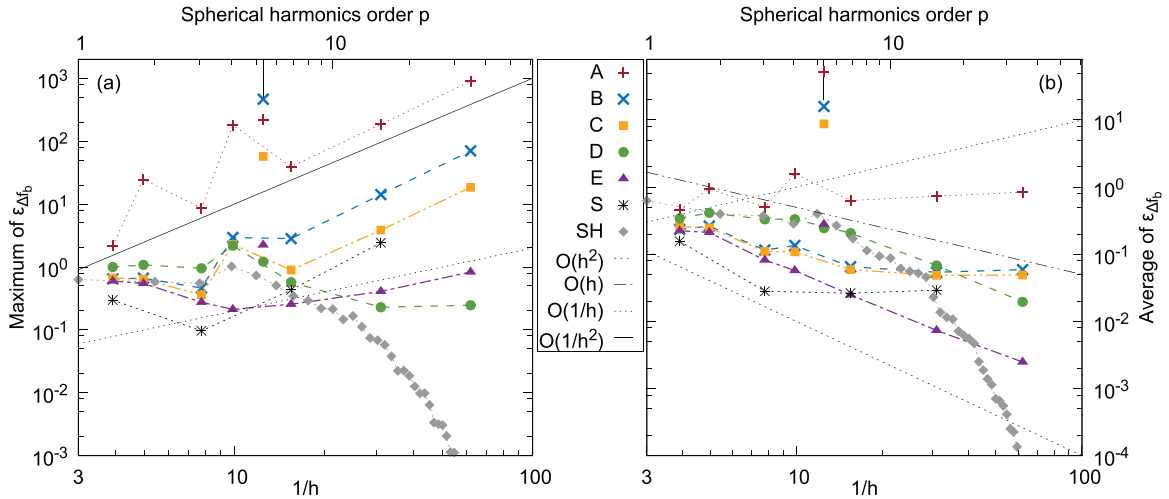


Figure 4. (a) Maximal and (b) average errors of the traction jump Δf_B for the discocyte shape from figure 2. Setup and symbols similar to figure 3. Data for methods A–E and S from [27] (MT1 mesh). Errors for $\Delta_S H$ look very similar.

Table 1. Overview of recent numerical works for a single object with or without external flow that compute the bending forces using full 3D methodologies. We only list publications that use the Helfrich bending law or a linear bending model (see section 2.1.2). Methods A–E have been shortly described in section 3.2 and in detail in [27]. Note that the discretizations only refer to the computation of the bending forces (other components of the solvers might use different approaches).

Discretization	Force formulation	Strong formulation (Euler–Lagrange)	Weak formulation (FEM)
Flat triangles	A [18, 27, 28, 105, 123, 147, 169, 180, 189, 243, 244, 247–249] B [27, 98, 106, 115, 188, 252, 253]	C [27, 52, 66, 86, 93, 183, 270, 271, 279, 306–309, 320, 321] D [27] E [27, 99, 107, 275–277] C + E [94, 104, 146, 148, 278–282]	[143, 293]
Higher order elements (curved triangles)		[54, 83]	[296]
Subdivision methods	[91, 102]		[27, 55, 149, 200, 204, 205]
Spectral methods (spherical harmonics)		[84, 85, 91, 92, 207, 209, 322, 323]	[206]*
Other methods		[182, 215]	

*Reference [206] uses the weak formulation but not the FEM, as explained in section 3.2.4.

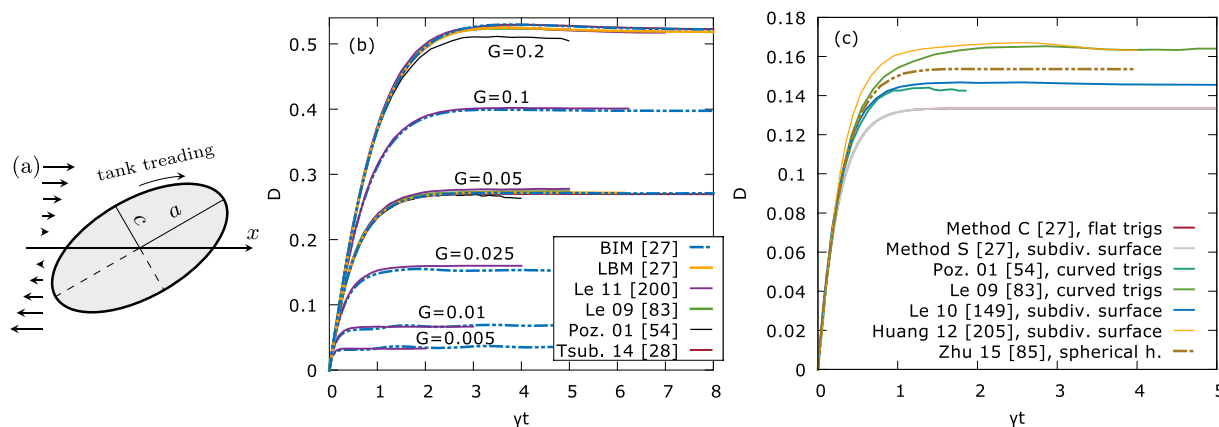


Figure 5. Results from 3D simulations of an initially spherical capsule under the influence of a linear shear flow. (a) 2D sketch. a is the largest and c the smallest half axis. ‘Tank treading’ refers to the rotation of the membrane around the object’s centroid while the shape remains constant. (b) Time evolution of the Taylor deformation parameter D for various dimensionless shear rates G without bending resistance as a function of the dimensionless time γt . Viscosity ratio $\lambda = 1$. Results by Huang *et al* [205], Le [149] and Zhu and Brandt [85] are not included for clarity but match well with BIM. (c) Comparison of the recent literature for $G = 0.05$ and $\hat{\kappa}_B = 0.0375$, i.e. with some bending resistance included. Viscosity ratio $\lambda = 1$. Method C was introduced in section 3.2.3, Method S in section 3.2.4. All references use the same physical models and parameters, except for Pozrikidis [54] who used a Hookean elastic law. All use the Helfrich or a linear bending model (see section 2.1.2), except Huang *et al* [205] who employ the bending model introduced by Zarda *et al* [324]. However, the employed flow and discretization algorithms vary greatly. (a)–(c) Modified from [27] with permission from Elsevier.

by bending forces in connection with area inextensibility and volume conservation. Red blood cells are mostly dominated by shear elasticity, although the maximal deformation can be notably reduced by the bending resistance [54] and it prevents the formation of sharp cusps [312]. For very thin-shelled capsules, bending forces are often assumed to be negligible [5]. They only manifest in zones of negative stress where they define the wavelength of the emerging wrinkles [5, 72, 211, 212, 313, 314]. Recent works in this category are also collected in table 1.

Two prototypical flows are commonly used: linear shear flows and Poiseuille flows. The former is somewhat simpler as the incoming flow far away from the object possesses a spatially constant shear rate while the latter is somewhat more relevant for applications in micro- or biofluidics. Occasionally, also time-dependent flows have been investigated [280, 315–319].

4.2.1. Linear shear flows

Spherical capsules. The influence of bending resistance has been systematically studied almost only for an initially spherical elastic capsule endowed with additional bending rigidity in linear shear flows. The capsule at low shear rates deforms into an approximate ellipsoid and performs a tank-treading motion, i.e. the membrane rotates around the stationary shape. This is illustrated in figure 5(a). The system parameters can be cast into three dimensionless values: the dimensionless shear rate (or elastic capillary number) $G = \mu\gamma R/\kappa_S$, the dimensionless ratio between shear and bending resistance $\hat{\kappa}_B = \kappa_B/(R^2\kappa_S)$ and the viscosity ratio $\lambda = \mu_C/\mu$. Here, κ_S is the shear modulus for the in-plane tensions (usually modeled by the neo-Hookean law [5, 27]), R the initial radius, μ the dynamic viscosity of the ambient fluid, μ_C the dynamic viscosity of the internal fluid, and γ the shear rate. Note that different conventions for the moduli exist in

the literature. The reference state for the in-plane tensions is taken to be the initial sphere and the bending reference state is usually a flat sheet ($H_0 = 0$).

The shape is typically described by the Taylor deformation parameter $D = \frac{a-c}{a+c}$ with the largest and smallest semi axes a and c , respectively, and the inclination angle θ between the x -axis and a . D and θ can be extracted from an ellipsoid with the same inertia tensor [192, 238]. Without bending forces, ample data is available because this setup is very often used for the verification of hydrodynamic simulation codes. There is very good agreement across a wide range of surface discretizations and flow solvers as shown in figure 5(b).

Once bending forces are included, however, one observes a surprisingly large spread of the values reported in the literature as shown in figure 5(c). Since all simulations are intended to model the same physical situation, this spread is somewhat unexpected. Given the excellent agreement without bending forces in figure 5(b), a decisive influence of the flow solver is unlikely. The fact that some of the references use a linear bending model is also most likely not the reason as the curves in question do not match among themselves and because the $\Delta_S H$ term (which is common to all) should dominate the behavior (compare appendix A.5). Moreover, not even results using the same surface discretization methodologies agree with each other. This spread thus clearly exemplifies the difficulty of accurately computing the bending forces. In the future, it would be interesting to conduct similar studies including a non-zero spontaneous curvature.

Non-spherical objects. Vesicles typically obey strict area and volume conservation and thus, for any deformation to be possible, the initial shape must not be a sphere. This adds an additional dimensionless parameter called the reduced volume $\nu = 6\sqrt{\pi}V/S^{3/2} \leq 1$ [325], where $\nu = 1$ corresponds to

Table 2. Overview of recent numerical works using full 3D methodologies similar to table 1, but for the interaction of several particles (≥ 2) in external flows.

Discretization	Force formulation	Strong formulation (Euler–Lagrange)	Weak formulation (FEM)
Flat triangles	A [18, 72, 109, 117, 118, 121–126, 245, 246, 250, 251, 340, 342, 344–350, 359, 366, 367] B [114, 115, 254]	C [110] E (only H) [186, 274] C + E [283–285]	[293]
Subdivision methods	[96]		[358]
Spectral methods (spherical harmonics)		[84, 101, 103, 207, 208, 341, 343, 368, 369]	

a sphere. Owing to the excess area, additional phenomena such as vacillating-breathing, tumbling or kayaking motions arise (see [9, 92, 93, 102, 143, 253, 271, 325] and the reviews [4, 97]). Similar features are shown by capsules [206, 326, 327]. The dynamics of red blood cells ($\nu \approx 0.6$ [1, 271]) can be even richer, adding states like breathing or tilted tank-treading [3, 10, 32, 66, 146, 181, 248, 278, 281, 328–331]. Finally, spatial variations of the bending modulus can lead to self-propelled [67] or migrating [332] particles.

4.2.2. Poiseuille flows. Studies of vesicles in bounded or unbounded Poiseuille flows are scarcer than for linear shear flows. Known shapes for vesicles include bullets, parachutes, croissants and static slippers [275, 333–335]. Red blood cells add states known from linear shear flows (e.g. tumbling), but also novel ones such as snaking or ‘dynamic’ slippers [18, 97, 153, 188, 248, 336]. Moreover, the transition from the discocyte to the parachute shape was shown to depend on the bending modulus for vesicles as well as cells [188, 248].

4.3. Several particles under flow

In many real-world situations, soft objects are not isolated but occur in suspensions. Numerical studies on very diluted [13, 18, 114, 115, 337–339] and medium to dense [72, 109, 110, 117, 121–123, 125, 126, 250, 251, 283–285, 340–350] RBC suspensions are relatively abundant. Also see [8, 18, 20, 32, 33, 351] for recent reviews. On the other hand, 3D simulations of interacting vesicles or capsules are quite rare. For example, two or more capsules have been simulated without [214, 352–357] and sometimes with [129, 358, 359] some bending rigidity in 3D. Numerical studies of interacting vesicles were mostly limited to 2D so far (e.g. [13, 217, 337, 360–365]), with the notable exception of [96]. Also note that [101, 103, 208, 293] touched the subject but focused on the development of the numerical method rather than on physical results.

In table 2 we give an overview of recent works in conjunction with the employed bending algorithm. Interestingly, most simulations are based on flat triangles and very often use Method A from equation (13). The most likely reason for this is the algorithm’s simplicity and efficiency in terms of the number of arithmetic operations, although [27] found that it requires comparably small time steps. Its lack of high fidelity seems to be of only minor concern for red blood cell suspension simulations given the relative smallness of and

uncertainty in experimentally determined bending moduli (and spontaneous curvature), the variation of RBC properties with age [153, 163, 370–372], and the routinely neglected influence of the vessel wall’s glycocalyx [373, 374]. Hence, effects that are also observed *in vivo* must have a certain robustness and low-accuracy bending methods may be acceptable for these applications, although systematic studies have not been conducted so far.

5. Summary and future perspectives

Bending forces are an integral component of many simulation codes for the study of natural or artificial soft particle suspensions. While the complexity of solving the Navier-Stokes equations for the hydrodynamic flow has long been recognized, the computational difficulties of computing bending forces have not always been fully appreciated.

In this review, we attempted to give an overview of the various approaches for bending forces developed during the last decades. We focused on membranes whose bending energy can be described by the famous Helfrich model. The described methods can be classified into three broad categories which are termed the *force*, the *strong* (or Euler–Lagrange) and the *weak* formulation. In addition, bending algorithms can be combined with different ways to discretize the surface itself. *Flat triangles*, *spherical harmonics* and *subdivision* schemes are the most widely used methods. Almost all of the described bending algorithms are currently being used in modern simulations of soft objects in flows. Yet, the simple case of a capsule in a linear shear flow clearly shows that the numerically predicted dynamics are in fairly good agreement with each other only if bending effects are neglected. As soon as bending forces are included, the various implementations start to scatter rather widely.

For future research, both numerical and physical issues come to mind. Numerically, an important task would be a systematic study on how the different bending algorithms behave when combined with different surface discretizations. While such a comparison has been attempted for flat triangles and spherical harmonics in section 3.3, it does not yet provide a clear and systematic distinction between the force, strong and weak formulations. It would certainly be worthwhile to study the advantages and disadvantages of the three methodologies more systematically, which would require to use the same surface discretization in all three cases. The ultimate goal would be to establish a definite reference algorithm that is proven to

provide correct and especially robust results and at the same time has practical performance for dynamic simulations with many particles. Furthermore, it is at present also unclear if and how the quality of the various algorithms would change once a spontaneous curvature is included.

On the more physical side it would be interesting to systematically assess the influence of the bending rigidity and/or spontaneous curvature for the practically relevant case of a soft object in Poiseuille flow similar to what has been done in shear flow. Moreover, the effect of the bending resistance on the behavior of dense suspensions (speed of margination, formation and thickness of the cell-free layer, etc) appears to not have been systematically considered so far.

The final issue concerns the spontaneous curvature H_0 . Although a noticeable influence of H_0 on the behavior of a single cell in flow has been found in a recent simulation study [66], a consensus on whether a spontaneous curvature should be included e.g. for red blood cells, and, if so, what its value should be, seems currently not in sight. Presumably, only novel sophisticated experiments can help to fully settle this question.

Acknowledgments

The authors would like to thank A Daddi-Moussa-Ider for helpful discussions. Funding from the Volkswagen Foundation and computing time granted by the Leibniz-Rechenzentrum on SuperMUC are gratefully acknowledged by A Guckenberger and S Gekle. A Guckenberger additionally thanks the Elitenetzwerk Bayern (ENB), Macromolecular Science, for their support.

Appendix A. Derivation of the Euler–Lagrange equation via thin shell theory

While abundant literature on the derivation of the Euler–Lagrange equation (7) via the variational principle is available [24, 36, 41, 57–61, 63–66, 75], completely worked out derivations by means of the Kirchhoff–Love thin shell theory are much harder to find. This theory is based upon the assumptions that deformations do not change the thickness and that normals to the mid-surface remain normal after deformation [78, 111]. Here we provide such a full derivation, with two major purposes in mind: first, to demonstrate clearly and in a consistent framework the equivalence of the variational and the thin shell approach. Second, to obtain the precise relationship between the often used linear bending models mentioned in section 2.1.2 and the Helfrich model. We show that these linear bending models lead to a traction jump whose leading order term is equivalent to the leading order term from the full Helfrich equation (7). Higher order terms usually differ. To this end, it will not suffice to use equations that only hold for small deformations as employed e.g. by Pozrikidis [35, p 272] [54, p 277]. Steigmann [76] and Naghdi [78] provide an appropriate formalism for finite deformations which we are going to adopt in the present work. Also see Sauer and Duong for a concise overview [112].

A.1. Differential geometry

We will use the formalism of differential geometry to describe the surface. A very good introduction can be found in the recent review by Deserno [36], and we will only summarize the required notations and results below.

As a start, we introduce two curvilinear coordinates θ^1 and θ^2 and the chart $\mathbf{x}(\theta^1, \theta^2)$ that describes the deformed surface⁵. The (in general non-unit) tangent vectors are given by [36, equation (4)]

$$\mathbf{a}_\alpha := \mathbf{x}_{,\alpha} \equiv \frac{\partial \mathbf{x}}{\partial \theta^\alpha}, \quad (\text{A.1})$$

where Greek indices assume the values 1 and 2, and the comma denotes the partial derivative with respect to θ^α acting on each Cartesian component. We further introduce the normalized normal vector

$$\mathbf{n} := \frac{\mathbf{a}_1 \times \mathbf{a}_2}{|\mathbf{a}_1 \times \mathbf{a}_2|}, \quad (\text{A.2})$$

the symmetric metric tensor (coefficients of the first fundamental form) [36, equation (8)]

$$a_{\alpha\beta} := \mathbf{a}_\alpha \cdot \mathbf{a}_\beta, \quad (\text{A.3})$$

its determinant [36, equation (13)]

$$a := \det a_{\alpha\beta} = a_{11}a_{22} - a_{12}a_{21} \quad (\text{A.4})$$

and the symmetric curvature tensor (coefficients of the second fundamental form) [36, equation (15)]

$$b_{\alpha\beta} := -\mathbf{a}_{\alpha,\beta} \cdot \mathbf{n} = \mathbf{a}_\alpha \cdot \mathbf{n}_{,\beta}. \quad (\text{A.5})$$

Note that here we use the convention of Deserno regarding the sign, meaning that the mean curvature of a sphere will be positive. Steigmann [76] uses the opposite sign.

The mean curvature is given by [76, equation (3.8)] [78, equation (A.2.28)]

$$H := \frac{1}{2} \text{trace}(b_\beta^\alpha) = \frac{1}{2} b_\alpha^\alpha = \frac{1}{2} a^{\alpha\beta} b_{\alpha\beta}, \quad (\text{A.6})$$

and the Gaussian curvature by [76, equation (3.8)] [78, equation (A.2.29)]

$$K := \det b_\beta^\alpha = b_1^1 b_2^2 - b_2^1 b_1^2 = \frac{1}{2} \hat{\varepsilon}^{\alpha\beta} \hat{\varepsilon}^{\lambda\mu} b_{\alpha\lambda} b_{\beta\mu}. \quad (\text{A.7})$$

Here, $\hat{\varepsilon}^{\alpha\beta} := \mathbf{e}^{\alpha\beta} / \sqrt{a}$, with the antisymmetric tensor $\mathbf{e}^{\alpha\beta}$ defined by $e^{11} = e^{22} = 0$, $e^{12} = 1$ and $e^{21} = -1$. Summation over repeated indices is implied.

We will need a few more results from differential geometry. To this end, we first introduce the tensor [76, equation (6.7)]

$$\tilde{b}^{\alpha\beta} := 2H a^{\alpha\beta} - b^{\alpha\beta}. \quad (\text{A.8})$$

With this, we summarize the following relations:

$$\mathbf{n}_{;\alpha} = b_\alpha^\beta \mathbf{a}_\beta, \quad (\text{Weingarten}) [36, \text{equation (37a)}] \quad (\text{A.9a})$$

$$\mathbf{a}_{\alpha;\beta} = -b_{\alpha\beta} \mathbf{n}, \quad (\text{Gauss}) [36, \text{equation (37b)}] \quad (\text{A.9b})$$

$$a_{;\gamma}^{\alpha\beta} = 0, \quad [36, \text{equation (27)}] \quad (\text{A.9c})$$

⁵In general, several charts will be required [36].

$$\tilde{b}_{;\alpha}^{\alpha\beta} = 0, \quad [76, \text{equation (6.6)}] \quad (\text{A.9d})$$

$$a^{\alpha\beta} b_{\alpha\beta} = 2H, \quad [36, \text{equation (17)}] \quad (\text{A.9e})$$

$$b_{\mu}^{\alpha} \tilde{b}^{\mu\beta} = K a^{\alpha\beta}, \quad [76, \text{equation (6.14)}] \quad (\text{A.9f})$$

$$\phi_{;\alpha} = \phi_{,\alpha}, \quad [36, \text{below equation (26)}] \quad (\text{A.9g})$$

$$\phi_{;\beta;\alpha} a^{\alpha\beta} = \Delta_S \phi, \quad [36, \text{equation (32)}] \quad (\text{A.9h})$$

where ϕ is some scalar valued function and Δ_S the Laplace–Beltrami operator. The semicolon denotes the *covariant* derivative defined with respect to $a^{\alpha\beta}$ [36, equation (24a)]. Note that covariant derivatives do not commute in general [36, equation (34)], and that equation (A.9g) does not hold if ϕ is a tensor density with non-zero weight such as a [36, footnote 9]. Another relation that will be needed is

$$\tilde{b}^{\alpha\gamma} b_{\gamma\beta} = a_{\beta\lambda} b_{\gamma}^{\lambda} \tilde{b}^{\alpha\gamma} = K a_{\beta\lambda} a^{\lambda\alpha} = K \delta_{\beta}^{\alpha}, \quad (\text{A.10})$$

where the usual rising operation [36, equation (10)] was used for the first equal sign, then equation (A.9f), and finally the Kronecker-delta δ_{γ}^{α} [36, equation (9)]. Also remember that the metric and curvature tensors are symmetric. This leads to

$$\tilde{b}^{\alpha\beta} b_{\alpha\beta} = K \delta_{\alpha}^{\alpha} = 2K. \quad (\text{A.11})$$

Combination with equation (A.8) gives [58, equation (2.34)]

$$b^{\alpha\gamma} b_{\gamma\beta} = 2H b_{\beta}^{\alpha} - K \delta_{\beta}^{\alpha} \quad (\text{A.12})$$

and

$$b^{\alpha\beta} b_{\alpha\beta} = 4H^2 - 2K. \quad (\text{A.13})$$

Moreover, using equations (A.8), (A.9c), (A.9d) and (A.9g) we can also derive

$$b_{;\alpha}^{\alpha\beta} = 2H_{,\alpha} a^{\alpha\beta}. \quad (\text{A.14})$$

A.2. Thin shell theory

Performing a force balance for a small patch of the surface [35, 111], one can derive the local equilibrium balance from equation (5) as [76, equation (2.1)] [78, equation (9.13)]

$$\mathbf{T}_{;\alpha}^{\alpha} + \Delta \mathbf{f}_B = 0. \quad (\text{A.15})$$

$\Delta \mathbf{f}_B$ is the traction jump due to the flows (as in equation (5)) and \mathbf{T}^{α} are two stress vectors⁶. If inertia plays a role, an additional term would need to be taken into account [78, 111, 112]. For simplicity we will restrict ourselves to the interior of the surfaces, i.e. we will not consider the boundaries of open objects.

To continue, we separate \mathbf{T}^{α} into tangential and normal components:

$$\mathbf{T}^{\alpha} = N^{\alpha} + S^{\alpha} \mathbf{n}, \quad (\text{A.16})$$

⁶ Deserno [36] calls $-\mathbf{T}^{\alpha}$ the surface stress tensor and denotes it by ‘ \mathbf{f}^{α} ’.

with [76, equation (2.4)]

$$N^{\alpha} := N^{\beta\alpha} \mathbf{a}_{\beta}, \quad (\text{A.17})$$

where $N^{\alpha\beta}$ is an in-plane tension tensor and S^{α} represents the transverse shear tension [35]. Note that $N^{\alpha\beta}$ is in general not symmetric [112]. Furthermore, we introduce a tension tensor $\sigma^{\alpha\beta}$ via [76, equation (2.5)]

$$N^{\alpha\beta} = \sigma^{\alpha\beta} + b_{\mu}^{\alpha} M^{\mu\beta}, \quad (\text{A.18})$$

where $M^{\alpha\beta}$ are bending moments [35]. Finally, we have from a local torque balance⁷ [76, equation (2.9)] [35, chapter 4.2]

$$S^{\alpha} = -M_{;\beta}^{\alpha\beta}. \quad (\text{A.19})$$

$\sigma^{\alpha\beta}$ (or equivalently $N^{\alpha\beta}$) and $M^{\alpha\beta}$ are determined from appropriate constitutive laws. One possibility is to specify them directly [54, 58, 79–81, 83–85]. Alternatively, they may be derived from a postulated energy density function. To this end, we introduce the energy per unit undeformed area ε . Assuming a homogeneous mass density, $\sigma^{\alpha\beta}$ and $M^{\alpha\beta}$ are then determined by

$$\sigma^{\alpha\beta} = \frac{1}{J} \left(\frac{\partial \varepsilon}{\partial a_{\alpha\beta}} + \frac{\partial \varepsilon}{\partial a_{\beta\alpha}} \right), \quad (\text{A.20a})$$

$$M^{\alpha\beta} = \frac{1}{2J} \left(\frac{\partial \varepsilon}{\partial b_{\alpha\beta}} + \frac{\partial \varepsilon}{\partial b_{\beta\alpha}} \right) \quad (\text{A.20b})$$

(compare [77, equation (25)] [76, equation (2.6), [111, equation (4.9)] and [78, equation (15.15)] with the help of footnote 7). Note that for example $(\frac{\partial \varepsilon}{\partial a_{\alpha\beta}} + \frac{\partial \varepsilon}{\partial a_{\beta\alpha}})/2$ is sometimes simply written as $\frac{\partial \varepsilon}{\partial a_{\alpha\beta}}$ [78, p 537] [375, equation (3.16)]. The local area dilation is given by [76, equation (2.7)] [77]

$$J := \sqrt{aA}. \quad (\text{A.21})$$

Here, A is the determinant of the metric tensor of the reference surface.

To be more precise, the energy density ε only determines the *symmetric* parts of $\sigma^{\alpha\beta}$ and $M^{\alpha\beta}$ because the right-hand side in equations (A.20) only contains symmetric expressions. The skew (or antisymmetric) parts are undetermined at first [78, p 537 and p 551]. However, the skew part of the bending moments $M^{\alpha\beta}$ plays no role in this case and can be set to zero [78, equation (15.17)] without loss of generality [111, p 285], making $M^{\alpha\beta}$ symmetric. Moreover, a local torque balance can be used to derive (compare [112] [78, equation (10.21)] [111,

⁷ Note that for most of the quantities different conventions exist; here we follow reference [76]. Most importantly, $N^{\alpha\beta}$ from equation (A.17) might be defined transposed as $N^{\alpha} = N^{\alpha\beta} \mathbf{a}_{\beta}$ [78, equation (9.40)], and $M^{\alpha\beta}$ might be obtained from a derivative with respect to $-b_{\alpha\beta}$ in equation (A.20b) [78, equations (5.61) and (15.15)] [111, equation (4.9)]. If only the $-b_{\alpha\beta}$ derivative convention is used, equation (A.18) becomes $N^{\alpha\beta} = \sigma^{\alpha\beta} - b_{\mu}^{\alpha} M^{\mu\beta}$ [111, equation (4.9)] and equation (A.19) becomes $S^{\alpha} = M_{;\beta}^{\alpha\beta}$ [111, equation (5.3)] [84, equation (22a)] [58, equation (A.7)] [35, equation (4.14)]. If additionally the transposed convention is employed, we have $N^{\alpha\beta} = \sigma^{\alpha\beta} - b_{\mu}^{\beta} M^{\mu\alpha}$ [78, equation (10.26)]. Naturally, these two conventions also change equation (A.22). We also remark that the sign convention for the curvature tensor (A.5) is independent of this.

equation (6.1)] [35, equation (4.14)] [84, equation (22b)] [58, equation (A.8)] while keeping footnote 7 in mind)

$$e_{\alpha\beta}(N^{\alpha\beta} - b_{\mu}^{\alpha}M^{\mu\beta}) = 0. \quad (\text{A.22})$$

The antisymmetric tensor $e_{\alpha\beta}$ has been introduced above. This equation fixes the skew part of $N^{\alpha\beta}$ [78, equation (15.18)] by implying that the skew part of $\sigma^{\alpha\beta}$ should be zero, i.e. that $\sigma^{\alpha\beta}$ must be symmetric [112, equation (71)]. Thus, in short, one can take equations (A.20) to define $\sigma^{\alpha\beta}$ and $M^{\alpha\beta}$ completely, and equation (A.22) will be satisfied automatically [111]⁸.

Before we continue, we derive explicit expressions for the tangential (f^{β}) and normal (f^3) components of the traction jump

$$\Delta \mathbf{f}_{\mathbf{B}} = f^{\beta} \mathbf{a}_{\beta} + f^3 \mathbf{n}. \quad (\text{A.23})$$

To this end, rewrite

$$\begin{aligned} \mathbf{T}_{;\alpha}^{\alpha} &= (N^{\beta\alpha} \mathbf{a}_{\beta})_{;\alpha} + (S^{\alpha} \mathbf{n})_{;\alpha} \\ &= N^{\beta\alpha}_{;\alpha} \mathbf{a}_{\beta} + N^{\beta\alpha} \mathbf{a}_{\beta;\alpha} + S^{\alpha}_{;\alpha} \mathbf{n} + S^{\alpha} \mathbf{n}_{;\alpha}. \end{aligned}$$

Using equations (A.9a) and (A.9b), we find

$$\mathbf{T}_{;\alpha}^{\alpha} = (S^{\alpha} b_{\alpha}^{\beta} + N^{\beta\alpha}) \mathbf{a}_{\beta} + (S^{\alpha}_{;\alpha} - N^{\beta\alpha} b_{\beta\alpha}) \mathbf{n}. \quad (\text{A.24})$$

Hence, equation (A.15) can be written as

$$f^{\beta} = -S^{\alpha} b_{\alpha}^{\beta} - N^{\beta\alpha}_{;\alpha}, \quad (\text{A.25a})$$

$$f^3 = -S^{\alpha}_{;\alpha} + N^{\alpha\beta} b_{\alpha\beta}. \quad (\text{A.25b})$$

These equations match with [76, equation (6.17)] (mind the H sign convention), [78, equation (15.20)] [58, equations (A9) and (A10)] (mind footnote 7) as well as with [84, equation (23)] [86, equations (A18) and (A19)] [35, equation (4.13)] (mind footnote 7 and the H sign).

Given an energy density ε , equations (A.15)–(A.20) fully determine the traction jump $\Delta \mathbf{f}_{\mathbf{B}}$. Hence, the goal will be to apply this formalism to the Helfrich model from equation (1). To this end, note again that ε is the energy per unit *undeformed* area [77], i.e. the total energy of some surface patch is given by $\int \varepsilon dS_0$ where the integration goes over the undeformed surface (compare [111, equation (2.19)] and [43, 77]). The Helfrich energy density $\varepsilon_{\mathbf{B}}$ as in the main text, however, is usually specified per unit *deformed* area, i.e. the total energy is $\int \varepsilon_{\mathbf{B}} dS$. Considering that $dS_0 = \sqrt{A} d\theta^1 d\theta^2$ and $dS = \sqrt{a} d\theta^1 d\theta^2$ [36, equation (84)], and furthermore demanding that $\varepsilon dS_0 \stackrel{!}{=} \varepsilon_{\mathbf{B}} dS$, we find with equation (A.21) [77]

$$\varepsilon = J \varepsilon_{\mathbf{B}}. \quad (\text{A.26})$$

Thus, for the Helfrich model from equation (1) [76, equation (7.17)]:

$$\varepsilon = J [2\kappa_{\mathbf{B}}(H - H_0)^2 + \kappa_{\mathbf{K}}K]. \quad (\text{A.27})$$

⁸ Note, that if some constitutive laws for $N^{\alpha\beta}$ and $M^{\alpha\beta}$ are provided directly rather than via some energy density (as is done for some of the linear bending models of appendix A.5), equation (A.22) constitutes a restriction for the possible laws [376, chapter 4].

A.3. Derivation of the traction jump for a general energy functional

A.3.1. Intermediary results. To start the derivation of general formulas, we use that the bending contribution to ε for fluid membranes can only depend on J , H and K [43]:

$$\varepsilon = \varepsilon(J, H, K). \quad (\text{A.28})$$

The Helfrich model is contained as a special case. Using the chain rule, we find for equations (A.20) [76, equation (6.13)]

$$\begin{aligned} \sigma^{\alpha\beta} &= -\frac{1}{J}(-J\varepsilon_{,J} + 2K\varepsilon_{,K} + 2H\varepsilon_{,H})a^{\alpha\beta} \\ &\quad + \varepsilon_{,H} \tilde{b}^{\alpha\beta} / J, \end{aligned} \quad (\text{A.29a})$$

$$M^{\alpha\beta} = -\frac{1}{J} \left(\frac{1}{2} \varepsilon_{,H} a^{\alpha\beta} + \varepsilon_{,K} \tilde{b}^{\alpha\beta} \right), \quad (\text{A.29b})$$

where $\tilde{b}^{\alpha\beta}$ was defined in equation (A.8). Furthermore, using equations (A.9c) and (A.9d), we obtain for the transverse shear tension in equation (A.19) [76, equation (6.18)]

$$S^{\alpha} = \frac{1}{2}(\varepsilon_{,H}/J)_{;\beta} a^{\alpha\beta} + (\varepsilon_{,K}/J)_{;\beta} \tilde{b}^{\alpha\beta}. \quad (\text{A.30})$$

The next step is to compute $N^{\alpha\beta}$ from equation (A.18). In order to facilitate the connection with the linear bending models later on, we separate the contributions by introducing two *artificial* parameters ζ and ξ :

$$N^{\alpha\beta} = \zeta \sigma^{\alpha\beta} + \xi b_{\mu}^{\alpha} M^{\mu\beta}. \quad (\text{A.31})$$

Setting $\zeta = \xi = 1$ recovers the full equations. Next, compute

$$b_{\mu}^{\alpha} M^{\mu\beta} = \frac{1}{2J} \varepsilon_{,H} b^{\alpha\beta} + \frac{\varepsilon_{,K}}{J} K a^{\alpha\beta}, \quad (\text{A.32})$$

where equation (A.9f) and the usual rising operations [36, equation (10)] have been used. Using the definition of $\tilde{b}^{\alpha\beta}$, equation (A.31) assumes the form

$$\begin{aligned} N^{\alpha\beta} &= -\frac{1}{J} [-J\zeta\varepsilon_{,J} + (2\zeta - \xi)K\varepsilon_{,K}] a^{\alpha\beta} \\ &\quad - \frac{1}{2J} (2\zeta - \xi) \varepsilon_{,H} b^{\alpha\beta}. \end{aligned} \quad (\text{A.33})$$

A.3.2. Tangential component. The tangential components of the traction jump are given via equation (A.25a). Using equations (A.9c), (A.9f) and (A.14), we find

$$\begin{aligned} f^{\beta} &= \frac{1}{2} (2\zeta - \xi - 1) (\varepsilon_{,H}/J)_{;\alpha} b^{\alpha\beta} \\ &\quad + [(-\zeta\varepsilon_{,J} + (2\zeta - \xi)K\varepsilon_{,K}/J)_{;\alpha} \\ &\quad - (\varepsilon_{,K}/J)_{;\alpha} K \\ &\quad + (2\zeta - \xi) H_{, \alpha} \varepsilon_{,H} / J] a^{\alpha\beta}, \end{aligned} \quad (\text{A.34})$$

or for the true values $\xi = \zeta = 1$

$$\begin{aligned} f^{\beta} &= [(-\varepsilon_{,J} + K\varepsilon_{,K}/J)_{;\alpha} - (\varepsilon_{,K}/J)_{;\alpha} K \\ &\quad + H_{, \alpha} \varepsilon_{,H} / J] a^{\alpha\beta}. \end{aligned} \quad (\text{A.35})$$

A.3.3. Normal component. To evaluate equation (A.25b), first calculate

$$S_{;\alpha}^{\alpha} = \frac{1}{2}\Delta_S(\varepsilon_{,H}/J) + (\varepsilon_{,K}/J)_{;\alpha;\beta}\tilde{b}^{\alpha\beta}, \quad (\text{A.36})$$

where we used equations (A.9c), (A.9d), (A.9g) and (A.9h) and the symmetry of $\tilde{b}^{\alpha\beta}$ to exchange the covariant derivatives. Using equations (A.9e), (A.8) and (A.13), we obtain the general result for arbitrary ζ , ξ and $\varepsilon(J, H, K)$

$$\begin{aligned} f^3 = & -\frac{1}{2}\Delta_S(\varepsilon_{,H}/J) - (\varepsilon_{,K}/J)_{;\alpha;\beta}\tilde{b}^{\alpha\beta} \\ & - \frac{2H}{J}[-\zeta J\varepsilon_{,J} + (2\zeta - \xi)K\varepsilon_{,K}] \\ & - \frac{2\zeta - \xi}{J}(2H^2 - K)\varepsilon_{,H}, \end{aligned} \quad (\text{A.37})$$

or for the true values $\xi = \zeta = 1$

$$\begin{aligned} f^3 = & -\frac{1}{2}\Delta_S(\varepsilon_{,H}/J) - (\varepsilon_{,K}/J)_{;\alpha;\beta}\tilde{b}^{\alpha\beta} \\ & - \frac{2H}{J}[-J\varepsilon_{,J} + K\varepsilon_{,K}] \\ & - \frac{1}{J}(2H^2 - K)\varepsilon_{,H}. \end{aligned} \quad (\text{A.38})$$

This is the final general formula for the normal component of the traction jump.

A.4. Derivation of the traction jump for the Helfrich model

We will now specialize the above relations for the Helfrich model from equation (A.27) for constant κ_B and κ_K . For convenient comparison with the literature, we will also provide intermediary results.

A.4.1. Intermediary results. First of all, from equations (A.29) we find the symmetric tension tensor $\sigma^{\alpha\beta}$ and the bending moments as [77, equation (28)]

$$\begin{aligned} \sigma^{\alpha\beta} = & [2\kappa_B(H - H_0)^2 - \kappa_K K] a^{\alpha\beta} \\ & - 4\kappa_B(H - H_0)b^{\alpha\beta}, \end{aligned} \quad (\text{A.39a})$$

$$M^{\alpha\beta} = -2\kappa_B(H - H_0)a^{\alpha\beta} - \kappa_K\tilde{b}^{\alpha\beta}. \quad (\text{A.39b})$$

Hence, the transverse shear tension (A.30) is given by

$$S^\alpha = 2\kappa_B(H - H_0)_{;\beta} a^{\alpha\beta}, \quad (\text{A.40})$$

and the full in-plane tension tensor (A.33) is

$$\begin{aligned} N^{\alpha\beta} = & [2\kappa_B\zeta(H - H_0)^2 - (\zeta - \xi)\kappa_K K] a^{\alpha\beta} \\ & - 2\kappa_B(2\zeta - \xi)(H - H_0)b^{\alpha\beta}. \end{aligned} \quad (\text{A.41})$$

Also note that for $\xi = \zeta = 1$ (the correct values), one directly finds [77, equation (28)]

$$N^{\alpha\beta} = 2\kappa_B(H - H_0)^2 a^{\alpha\beta} - 2\kappa_B(H - H_0)b^{\alpha\beta}, \quad (\text{A.42})$$

i.e. the result is independent of the saddle-splay modulus κ_K .

We shortly stop at this point and actually compute the stress vectors T^α from equation (A.16). A short computation shows for $\zeta = \xi = 1$:

$$\begin{aligned} T^\alpha = & 2\kappa_B(H - H_0)^2 a^{\alpha\beta} a_\beta \\ & - 2\kappa_B(H - H_0)b^{\alpha\beta} a_\beta \\ & + 2\kappa_B(H - H_0)_{;\beta} a^{\alpha\beta} n. \end{aligned} \quad (\text{A.43})$$

This expression for the stress vectors matches with the surface stress tensor from [36, equation (96)] for a constant H_0 and [61, equation (51)] [62, equation (14)] for $H_0 = 0$ up to a definition-implied global sign. It also agrees with [70, equation (2.64)] and [57, equation (128)]. As explained in [36], T^α represent a first integral of the Euler–Lagrange equation.

A.4.2. Tangential component. Substituting equation (A.27) into equation (A.34) gives the following tangential components of the traction jump:

$$\begin{aligned} f^\beta = & 2\kappa_B(2\zeta - \xi - 1)(H - H_0)_\alpha b^{\alpha\beta} \\ & + [4\kappa_B(H - H_0)H_{,\alpha} + \kappa_K K_{,\alpha}](\zeta - \xi)a^{\alpha\beta}. \end{aligned} \quad (\text{A.44})$$

For $\zeta = \xi = 1$ this obviously reduces to

$$f^\beta = 0. \quad (\text{A.45})$$

Thus, for the actual Helfrich model the tangential tractions vanish in the interior of the surface if no additional constraints are used.

A.4.3. Normal component. It is straightforward to evaluate equation (A.37) with ε from equation (A.27). The result is

$$\begin{aligned} f^3 = & -2\kappa_B\{\Delta_S(H - H_0) \\ & + 2(H - H_0)[(2\zeta - \xi)(2H^2 - K) - \zeta H(H - H_0)]\} \\ & - 2\kappa_K(\zeta - \xi)HK, \end{aligned} \quad (\text{A.46})$$

or for $\xi = \zeta = 1$

$$\begin{aligned} f^3 = & -2\kappa_B[\Delta_S(H - H_0) \\ & + 2(H - H_0)(H^2 - K + H_0H)]. \end{aligned} \quad (\text{A.47})$$

Taking equation (A.23) into account, the results (A.45) and (A.47) match *exactly* with the one from equation (7) obtained via a variational derivative. Thus, the variational and the shell theory approaches are compatible with each other and lead to the same results. Also note that the κ_K term drops out, as required by the Gauss–Bonnet theorem. We further remark that the Laplace–Beltrami term in equation (A.46) is always there, regardless of the values of κ_K , ξ and ζ .

A.4.4. Order of the individual terms. In view of the linear bending models presented in the next section, it is of some interest to know the importance of the individual terms occurring in equation (A.47). To this end, consider a general surface in the Monge gauge [36]: at least locally, the surface can be described by the vector $\tilde{\mathbf{x}}(x, y) := (x, y, h(x, y)) \in \mathbb{R}^3$ with the height function h . We assume that the deviations from a plane are of order $\psi > 0$, i.e. $h_{,x} \sim \mathcal{O}(\psi)$ and $h_{,y} \sim \mathcal{O}(\psi)$. Next, a deformation $\mathbf{u} \in \mathbb{R}^3$ leads to the deformed surface $\mathbf{x}(x, y) := \tilde{\mathbf{x}}(x, y) + \mathbf{u}(x, y)$. The deformation shall be of order $\chi > 0$, i.e. $\mathbf{u}_{,x} \sim \mathcal{O}(\chi)$ and $\mathbf{u}_{,y} \sim \mathcal{O}(\chi)$. Furthermore, we set the reference shape (but not the undeformed state $\tilde{\mathbf{x}}$) to be a flat plane ($H_0 = 0$).

With this we can compute the various geometric quantities for the deformed surface \mathbf{x} to leading orders, similar to [86]. In the end, we obtain

$$\Delta_S H \sim \mathcal{O}(\psi) + \mathcal{O}(\chi) + \mathcal{O}(\psi\chi) + \text{h.o.}, \quad (\text{A.48a})$$

$$H(H^2 - K) \sim \mathcal{O}(\chi\psi^2) + \text{h.o.}, \quad (\text{A.48b})$$

and for the full normal component

$$f^3 \mathbf{n} \sim \mathcal{O}(\psi) + \mathcal{O}(\chi) + \mathcal{O}(\psi\chi) + \text{h.o.}, \quad (\text{A.48c})$$

where ‘h.o.’ stands for ‘higher orders’. Hence, at least for small deviations from a plane ($\psi, \chi \ll 1$) we have $|\Delta_S H| \gg |H(H^2 - K)|$, which is consistent with [86, equation (A20)].

This also seems to hold for larger deviations from a plane. For example, for the typical RBC shape from equations (B.14a–B.14c) and figure 2, $\Delta_S H$ is found to be up to almost one order of magnitude larger than the others, i.e. [27]

$$\max|2\Delta_S H| \approx 218, \quad (\text{A.49a})$$

$$\max|4H(H^2 - K)| \approx 28.8, \quad (\text{A.49b})$$

$$\max|f^3 \mathbf{n}| \approx 189 \quad (\text{A.49c})$$

(units chosen such, that the large RBC radius is 1 and $\kappa_B = 1$).

A.5. Linear bending models

Some authors use a so-called ‘linear bending model’ instead of the Helfrich model as already described in section 2.1.2 of the main text. The purpose of this section is to shed some light on the relationship between these two types. In linear bending models, the bending moments and in-plane tensions are not derived from an energy functional as in equations (A.20a) and (A.20b). Instead, their form is given by postulated constitutive laws. A common assumption of such models is that the saddle splay modulus κ_K plays no role (which is always true for closed objects with constant topology).

In the following we will consider four such models (a–d) which are similar, but not identical.

A.5.1. Model a. The first constitutive law we consider is the ‘linear isotropic model’ presented e.g. by Pozrikidis [80, equation (10)] [81, equation (2.5.11)]

$$M^{\alpha\beta} = -2\kappa_B(H - H_0)a^{\alpha\beta}. \quad (\text{A.50})$$

It is further assumed [54, p 277] that only the *antisymmetric* components of the in-plane tension tensor $N^{\alpha\beta}$ are affected by the bending rigidity, namely via equation (A.22). Due to the particular form of $M^{\alpha\beta}$, this contribution however amounts to zero, i.e. we have in total

$$N^{\alpha\beta} = 0. \quad (\text{A.51})$$

Note that additional material properties (such as resistance against shearing) might still lead to a non-zero total $N^{\alpha\beta}$. The two equations (A.50) and (A.51) are captured by $\kappa_K = 0$ and

$\zeta = \eta = 0$ in our general framework presented above (see equations (A.31) and (A.39b)). The resulting traction jump is therefore obtained via equations (A.46) and (A.44) as

$$f^\beta = -2\kappa_B(H - H_0)_{,\alpha} b^{\alpha\beta}, \quad (\text{A.52a})$$

$$f^3 = -2\kappa_B \Delta_S(H - H_0). \quad (\text{A.52b})$$

Considering expressions (A.48), the normal component matches to leading orders with the result (A.47) for the Helfrich model. Interestingly, an additional tangential component arises. For the series expansion similar to equations (A.48) we find $f^\beta a_\beta \sim \mathcal{O}(\psi\chi) + \text{h.o.}$, and so the normal component dominates at least for $\psi, \chi \ll 1$. This is affirmed for the typical RBC shape, where $\max|f^\beta a_\beta| \approx 62.7$ which is less than one third of the value for the normal component (A.52b) (see equation (A.49a)). Moreover, figure A1 depicts the complete traction jumps and the relative deviation to the Helfrich model for the RBC shape. In the rather flat dimple regions, the deviations are small ($\lesssim 5\%$) which is in agreement with the series expansion; they only become larger in the high curvature regime. Thus, all in all, the complete traction jump $\Delta \mathbf{f}_B$ of model a matches with the Helfrich model to leading order $\mathcal{O}(\psi) + \mathcal{O}(\chi)$.

A.5.2. Model b. Another model that has sometimes been used [80, equation (8)] [81, equation (2.5.9)] [83, equation (25)] [54, equation (4.6)] [5, equation (23)] is given by

$$M^{\alpha\beta} = -\kappa_B(b^{\alpha\beta} - 2H_0 a^{\alpha\beta}). \quad (\text{A.53})$$

$N^{\alpha\beta}$ is once again determined via equation (A.22) (assumption of no symmetric components), and once again the skew part and hence the full $N^{\alpha\beta}$ can be shown to be zero, too. Using equations (A.19), (A.9c) and (A.14), we find

$$S^\alpha = 2\kappa_B(H - H_0)_{,\beta} a^{\alpha\beta}, \quad (\text{A.54})$$

which matches exactly with expression (A.40) for the Helfrich model. Considering that $N^{\alpha\beta} = 0$, the traction jump is thus given by equations (A.46) and (A.44) with $\zeta = \eta = 0$:

$$f^\beta = -2\kappa_B(H - H_0)_{,\alpha} b^{\alpha\beta}, \quad (\text{A.55a})$$

$$f^3 = -2\kappa_B \Delta_S(H - H_0). \quad (\text{A.55b})$$

Thus, at least from the viewpoint of the traction jump, models a and b can be considered to be equivalent.

A.5.3. Model c. Yet another constitutive equation is the one employed by Zhao *et al* and others [84, equation (21)] [85, p 382] [86, equation (A12)]. Although it is also called ‘linear isotropic model’ in [84], its form is slightly different from Pozrikidis’s version (equation (A.50)). It is given by

$$M_{\beta}^{\alpha} = -\kappa_B(b_{\beta}^{\alpha} - B_{\beta}^{\alpha}). \quad (\text{A.56})$$

Equation (A.22) determines the skew components of $N^{\alpha\beta}$ and the symmetric components of $N^{\alpha\beta}$ are assumed to be independent of the bending rigidity. $B_{\alpha\beta} = -\mathbf{X}_{,\alpha\beta} \cdot \mathbf{N}$ is the curvature tensor of the reference surface $\mathbf{X}(\theta^1, \theta^2)$ (see

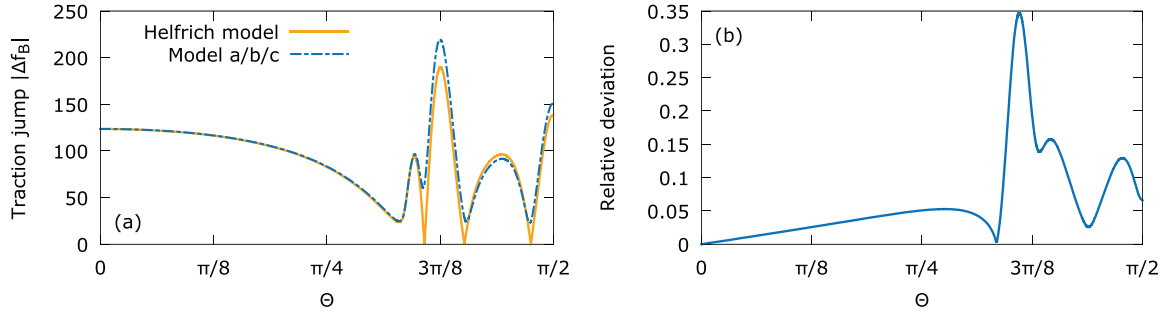


Figure A1. Comparison between the traction jumps of the Helfrich model and the linear bending models for the typical red blood cell shape from figure 2. The spontaneous curvature is set to zero ($H_0 = 0$), in which case linear bending models a, b and c are equivalent. Analytic computations via equations (B.14a–B.14c), and the polar angle is defined as $\Theta := \arccos(x_3/\sqrt{x_1^2 + x_2^2 + x_3^2})$ with the Cartesian coordinates x_1, x_2 and x_3 . Note that the shape is axisymmetric, and thus the results are independent of the azimuthal angle. (a) The magnitude of the full traction jump $|\Delta f_B|$ (units chosen such, that $\kappa_B = 1$ and the large RBC radius is 1). (b) Relative deviation $|\Delta f_B^H - \Delta f_B^L|/\max|\Delta f_B^H|$, where the upper indices H and L denote the Helfrich and linear bending models, respectively, and $\max|\Delta f_B^H| \approx 189$. Only minor deviations are observed in the rather flat dimple regions ($\Theta \lesssim 5\pi/16$), in agreement with the series expansion from the main text.

equation (A.5) and [77, equation (11)]) and N the corresponding normal vector. Furthermore, we have $B_\beta^\alpha = A^{\alpha\gamma} B_{\gamma\beta}$ with the metric tensor $A^{\alpha\beta}$ of the reference state [77]. The in-plane tension tensor is according to equation (A.22) and [78, equation (15.18)]

$$N^{\alpha\beta} = \frac{1}{2} \kappa_B B_{\gamma\lambda}^\mu b_{\lambda\mu} (a^{\alpha\lambda} a^{\gamma\beta} - a^{\alpha\gamma} a^{\lambda\beta}), \quad (\text{A.57})$$

because its symmetric components are assumed to be zero (if no additional elasticities exist). This expression is non-zero for *general* reference states X although some authors assume otherwise [84, 85]. As an example, taking a unit sphere [36, equation (2b)] for the deformed geometry $\mathbf{x}(\theta^1, \theta^2)$ leads to $(N^{\alpha\beta}) = \frac{1}{2} \kappa_B (B_1^2 - B_2^2 / \sin^2 \theta^1) \begin{pmatrix} 0 & -1 \\ 1 & 0 \end{pmatrix}$ in spherical coordinates, where $\theta^1 \in [0; \pi]$ is the polar angle. Continuing, the components of the traction jump follow from equations (A.25) as

$$f^\beta = -2\kappa_B H_{,\alpha} b^{\alpha\beta} + \kappa_B B_{\gamma;\lambda}^\alpha a^{\gamma\lambda} b_\alpha^\beta + \frac{1}{2} \kappa_B (B_{\gamma\lambda}^\mu b_{\lambda\mu};_\alpha (a^{\alpha\lambda} a^{\gamma\beta} - a^{\alpha\gamma} a^{\lambda\beta})), \quad (\text{A.58a})$$

$$f^3 = -2\kappa_B \Delta_S H + \kappa_B B_{\gamma;\beta;\alpha}^\alpha a^{\gamma\beta}. \quad (\text{A.58b})$$

The second line for f^β is absent if we assume $N^{\alpha\beta} = 0$. Interestingly, f^β is always independent of $N^{\alpha\beta}$ for the expression from equation (A.57). In any case, the result matches with the previous two models for a flat reference state, but differs for general B_β^α . A precise and concise relationship is unfortunately not easily established. We further remark that application of equations (A.58) to small axisymmetric deformations of a spherical membrane recovers the expressions from [309, equation (A19)] to leading order.

A.5.4. Model d. Jenkins [58] focuses on the derivation of the Euler–Lagrange equation for the Helfrich model for $H_0 = 0$

via the variational approach. Later on, he postulates some constitutive equations to make the connection between the variational and the thin shell formulation, namely [58, equations (A.11) and (A.12)]

$$M^{\alpha\beta} = -2\kappa_B H a^{\alpha\beta}, \quad (\text{A.59a})$$

$$N^{\alpha\beta} = -2\kappa_B H b^{\alpha\beta} \quad (\text{A.59b})$$

(plus some inextensibility contribution). Most notably there is a non-zero bending contribution to $N^{\alpha\beta}$, contrary to the previous models. He shows that these equations lead to the same Euler–Lagrange equation.

Unfortunately, he made a mistake during his variational derivative. Namely, he forgot to vary the surface element or equivalently $\delta\sqrt{a}$ in [58, equation (2.18)]⁹. This results in $2H^2$ instead of the correct H^2 in the Euler–Lagrange equation (A.47). Another consequence is that it leads him to propose an incorrect constitutive law for $N^{\alpha\beta}$. Taking this into account, he would have probably specified the constitutive equations as

$$M^{\alpha\beta} = -2\kappa_B H a^{\alpha\beta}, \quad (\text{A.60a})$$

$$N^{\alpha\beta} = 2\kappa_B H^2 a^{\alpha\beta} - 2\kappa_B H b^{\alpha\beta}. \quad (\text{A.60b})$$

Comparing with equations (A.39b) and (A.42), these equations reproduce the traction jump of the Helfrich model (for $H_0 = 0$) exactly.

A.5.5. Summary. To summarize, the traction jump derived from the linear bending models a and b agree with each other, and with model c at least for zero reference curvatures. Furthermore, all three agree to leading order (i.e. for small deviations from a plane) in the traction jump with the Helfrich

⁹ Jenkins additionally integrates over the deformed rather than the undeformed surface for the γ term in [58, equation (2.18)], leading to an incorrect equation for the surface inextensibility. Otherwise, he would have obtained the correct equation (A.65). Nevertheless, this does not affect the bending traction jump itself.

law for a flat reference state, where the leading order term is given by $\sim \Delta_S H$. Perfect agreement with the Helfrich model, however, requires to take into account the non-zero bending contributions to the symmetric part of the in-plane tension tensor $N^{\alpha\beta}$ (model d). These are often neglected, inducing additional tangential components.

A.6. Inextensibility constraint

Similar to the variational derivative formalism, it is also possible to include the local area incompressibility constraint in the thin-shell derivation. This can be done by adding the term $\int_S \tilde{\sigma} dS$ to the total energy (see section 2.1.2). This is equivalent to adding $\tilde{\sigma} J$ to equation (A.27), i.e. [76, equation (2.8)] [112]

$$\varepsilon \rightarrow \varepsilon + \tilde{\sigma} J, \quad (\text{A.61})$$

Here, $\tilde{\sigma} = \tilde{\sigma}(\theta^1, \theta^2)$ is the local Lagrange multiplier. Taking into account that $\tilde{\sigma}$ does not depend on the surface (i.e. neither on J , H or K) but only on the curvilinear coordinates, equation (A.38) then provides the normal contribution

$$f^3 \rightarrow f^3 + 2H\tilde{\sigma} \quad (\text{A.62})$$

for $\zeta = 1$. On the other hand, the tangential equation (A.35) gives

$$f^\beta \rightarrow f^\beta - \tilde{\sigma}_{,\alpha} a^{\alpha\beta}, \quad (\text{A.63})$$

i.e. a non-zero additional term. Using the definition of the surface gradient [52, equation (60)] given by

$$\nabla_S \tilde{\sigma} = \tilde{\sigma}_{,\alpha} a^\alpha = \tilde{\sigma}_{,\alpha} a^{\alpha\beta} a_\beta, \quad (\text{A.64})$$

as well as equation (A.23), the total traction jump thus receives the additional term

$$\Delta f_B \rightarrow \Delta f_B + 2H\tilde{\sigma} \mathbf{n} - \nabla_S \tilde{\sigma} \quad (\text{A.65})$$

due to the inextensibility. Its significance has already been explained in section 2.1.2.

Appendix B. Using spherical harmonics to compute the bending forces

We detail here the direct computation of the traction jump from equation (7) (strong formulation) using spherical harmonics. The methodology closely follows [101, 103].

A square-integrable function $f(\vartheta, \varphi)$ with $\vartheta \in [0; \pi]$ and $\varphi \in [0; 2\pi]$ can be expanded into a spherical harmonics series:

$$f(\vartheta, \varphi) = \sum_{l=0}^{\infty} \sum_{m=-l}^l \hat{f}_l^m Y_l^m(\vartheta, \varphi). \quad (\text{B.1})$$

The coefficients $\hat{f}_l^m \in \mathbb{C}$ are given by an integration over the unit sphere,

$$\hat{f}_l^m = \int_0^\pi \int_0^{2\pi} f(\vartheta, \varphi) \bar{Y}_l^m(\vartheta, \varphi) \sin \vartheta d\varphi d\vartheta. \quad (\text{B.2})$$

\bar{Y}_l^m is the complex conjugate of the spherical harmonic Y_l^m defined by

$$Y_l^m(\vartheta, \varphi) := \sqrt{\frac{2l+1}{4\pi} \frac{(l-m)!}{(l+m)!}} \tilde{P}_l^m(\vartheta) e^{im\varphi}, \quad (\text{B.3})$$

with i being the imaginary unit, $\tilde{P}_l^m(\vartheta) := P_l^m(\cos \vartheta)$ and the associated Legendre polynomials

$$P_l^m(x) := \frac{(-1)^m}{2^l l!} (1-x^2)^{m/2} \frac{d^{l+m}}{dx^{l+m}} [(x^2-1)^l]. \quad (\text{B.4})$$

Note that the Condon–Shortley phase $(-1)^m$ is included here. We compute the spherical harmonic Y_l^m via the C++ `boost` library.

Let p be the truncation order for the spherical harmonics expansion. The latitude direction is covered by $p+1$ points $\vartheta_i = \arccos z_i$, $i = 0, \dots, p$, where z_i are the Gauss–Legendre nodes with corresponding weights ν_i (computable e.g. via the `gauleg` routine from [377]). Integrations are done using the Gauss–Legendre quadrature. Furthermore, we distribute $2p+2$ points equidistantly in the longitudinal direction, i.e. $\varphi_j = \pi j / (p+1)$, $j = 0, \dots, 2p+1$. Integration in this direction is performed by means of the trapezoidal rule with weights $\mu_j = \pi / (p+1)$, $j = 0, \dots, 2p+1$ (i.e. every point has the same weight). Hence, equation (B.2) is approximated by

$$\hat{f}_l^m \approx \sum_{i=0}^p \sum_{j=0}^{2p+1} \nu_i \mu_j f(\vartheta_i, \varphi_j) \bar{Y}_l^m(\vartheta_i, \varphi_j). \quad (\text{B.5})$$

These algorithms and integration points are chosen because equation (B.5) is then superalgebraically = exponentially = spectrally convergent with the order p for smooth functions [101]. Note that due to the truncation, we have $l = 0, \dots, p$ and $m = -l, \dots, l$. This also implies

$$f(\vartheta_i, \varphi_j) \approx \sum_{l=0}^p \sum_{m=-l}^l \hat{f}_l^m Y_l^m(\vartheta_i, \varphi_j). \quad (\text{B.6})$$

We remark that the forward and backward transformations can be done using the fast Fourier transform (FFT) for the longitude and the fast Legendre transform (FLT) for the latitude direction. In practice FLTs are rarely used. For simplicity we also abstain from using FFTs, as they would make the computation of higher order derivatives much more complex.

Derivatives of $f(\vartheta, \varphi)$ can now be rolled off onto the spherical harmonics Y_l^m . The most problematic ones are derivatives with respect to ϑ , where one of several recurrence relations for the Legendre polynomials should be used. One possible choice that comes without issues at the poles $\vartheta = 0, \pi$ is presented in [287]. Taking into account the Condon–Shortley phase and using the chain rule, we find

$$\begin{aligned} \frac{\partial}{\partial \vartheta} Y_l^m(\vartheta, \varphi) &= -\frac{1}{2} \sqrt{(l+m)(l-m+1)} Y_l^{m-1}(\vartheta, \varphi) e^{i\varphi} \\ &\quad + \frac{1}{2} \sqrt{(l-m)(l+m+1)} Y_l^{m+1}(\vartheta, \varphi) e^{-i\varphi}, \end{aligned} \quad (\text{B.7a})$$

$$\begin{aligned}
& \frac{\partial^2}{\partial \vartheta^2} Y_l^m(\vartheta, \varphi) \\
&= \frac{1}{4} \sqrt{(l+m)(l+m-1)(l-m+1)(l-m+2)} e^{2i\varphi} Y_l^{m-2}(\vartheta, \varphi) \\
&- \frac{1}{4} [(l-m+1)(l+m) + (l-m)(l+m+1)] Y_l^m(\vartheta, \varphi) \\
&+ \frac{1}{4} \sqrt{(l-m)(l-m-1)(l+m+1)(l+m+2)} e^{-2i\varphi} Y_l^{m+2}(\vartheta, \varphi).
\end{aligned} \tag{B.7b}$$

In equation (B.7a), the full Y_l^{m-1} term is missing for $m = -l$ and the full Y_l^{m+1} term is missing for $m = l$ (so the result is simply zero for $m = l = 0$). Similar for equation (B.7b), the term containing Y_l^{m-2} is absent for $m \leq -l + 1$ and the full Y_l^{m+2} term must be omitted for $m \geq l - 1$. Fortunately, φ derivatives are simpler: the k 'th derivative is obviously given by

$$\frac{\partial^k}{\partial \varphi^k} Y_l^m(\vartheta, \varphi) = (im)^k Y_l^m(\vartheta, \varphi), \quad k \in \mathbb{N}. \tag{B.8}$$

We use these formulas to compute derivatives of f by substituting them into equation (B.6), e.g.

$$\frac{\partial}{\partial \vartheta} f(\vartheta_i, \varphi_j) \approx \sum_{l=0}^p \sum_{m=-l}^l \hat{f}_l^m \left[\frac{\partial}{\partial \vartheta} Y_l^m(\vartheta, \varphi) \right] \Bigg|_{\substack{\vartheta=\vartheta_i \\ \varphi=\varphi_j}}. \tag{B.9}$$

We note that second order derivatives should not be computed by two successive first order derivatives involving one back and forward transformation, because not every first order derivative results in a smooth function on the surface. As an example take the z -component of the unit sphere, $z(\vartheta, \varphi) = \cos \vartheta$. Its first order derivative is $\partial_{\vartheta} z(\vartheta, \varphi) = -\sin \vartheta$, which is not smooth at $\vartheta = 0, \pi$ when considered on the sphere (compare e.g. $\varphi = 0$ and $\varphi = \pi$). Thus, its series expansion converges only very slowly. Direct computation of the second order derivative via equation (B.7b) circumvents this particular problem. The same holds for derivatives with respect to φ and mixed derivatives.

With this setup in place, calculating the traction jump from equation (7) is more or less straightforward. We employ the definitions and results of differential geometry from section A.1 with $\theta^1 = \vartheta$ and $\theta^2 = \varphi$. However, for notational convenience we will use the alternative names

$$E := a_{11}, \quad F := a_{12} = a_{21}, \quad G := a_{22}, \tag{B.10a}$$

$$L := b_{11}, \quad M := b_{12} = b_{21}, \quad N := b_{22}. \tag{B.10b}$$

With $W^2 := EG - F^2$, the mean curvature is then given by [101]

$$H = \frac{EN - 2FM + GL}{2W^2} \tag{B.11}$$

and the Gaussian curvature by

$$K = \frac{LN - M^2}{W^2}. \tag{B.12}$$

The Laplace–Beltrami operator of some function f is [101]

$$\begin{aligned}
\Delta_S f &= \frac{1}{W} \frac{\partial}{\partial \varphi} \left(\frac{E \partial_{\varphi} f - F \partial_{\vartheta} f}{W} \right) \\
&+ \frac{1}{W} \frac{\partial}{\partial \vartheta} \left(\frac{G \partial_{\vartheta} f - F \partial_{\varphi} f}{W} \right),
\end{aligned} \tag{B.13}$$

which in the present context is of course only really applied to H .

In practice, we start by computing the grid (ϑ_i, φ_j) for a given order p with $i = 0, \dots, p$ and $j = 0, \dots, 2p + 1$ as explained above. The surface nodes $\mathbf{x}(\vartheta_i, \varphi_j)$ for the RBC shape are then obtained by setting [27]

$$x_1(\vartheta_i, \varphi_j) = R \sin \vartheta_i \cos \varphi_j, \tag{B.14a}$$

$$x_2(\vartheta_i, \varphi_j) = R \sin \vartheta_i \sin \varphi_j, \tag{B.14b}$$

$$x_3(\vartheta_i, \varphi_j) = \pm \frac{R}{2} \sqrt{1 - \rho^2} (C_0 + C_1 \rho^2 + C_2 \rho^4), \tag{B.14c}$$

where R is the given length of the large half-axis, $\rho^2 := (x^2 + y^2)/R^2$, $C_0 = 0.2072$, $C_1 = 2.0026$ and $C_2 = -1.1228$ [203, 378]. The plus sign is used for $\vartheta \leq \pi/2$, the minus sign otherwise.

Next, each individual Cartesian component of \mathbf{x} is transformed via equation (B.5) to provide the representation in the spectral domain. First and second order derivatives (in the spatial domain) are then obtained by means of equations (B.7a), (B.7b) and (B.8) in conjunction with backward transforms as in equation (B.9). This allows us to calculate H and K at each grid point (ϑ_i, φ_j) .

For $\Delta_S H$, equation (B.13) as well as W are first expanded by hand via the chain rule. Derivatives of E, F, G are obtained directly from the spectral coefficients of \mathbf{x} as before. To get the derivatives of H , we first transform H into spectral space (equation (B.5)) and then apply again the derivative formulas (B.7). Afterwards, the traction jump from equation (7) is obtained by combining all temporary results.

We emphasize again that the transform (B.5) is only applied to the components of \mathbf{x} and once for H , but not to any other intermediate quantity such as $a_{\alpha\beta}$ or $b_{\alpha\beta}$. In principle, it would be possible to bypass the transform of H by expanding $\Delta_S H$ via the chain rule until only derivatives of \mathbf{x} (up to fourth order) remain, which can then be evaluated directly using formulas similar to equation (B.7a) [287]. We speculate that it would boost algorithmic precision because the only case where aliasing can then occur is in the transform of \mathbf{x} . This should make de-aliasing procedures as used in [84, 101, 103, 207] obsolete. Considering the results presented in section 3.3, we would then expect a similar drop to machine precision for the traction jump in figure 4 as seen for the mean curvature in figure 3. However, deriving the necessary formulas is quite cumbersome and therefore has not been attempted so far.

On a related note, the de-aliasing rules mentioned in [84, 101, 103, 207] are only required in the first place if other formulas need to be evaluated that are content with smaller orders of p . In this case, the smaller order can be upsampled by means of interpolation (i.e. evaluating equation (B.6) also at intermediary points) for the sake of computing the bending forces with a higher resolution.

References

- [1] Misbah C 2012 Vesicles, capsules and red blood cells under flow *J. Phys.: Conf. Ser.* **392** 012005
- [2] Vlahovska P M, Barthes-Biesel D and Misbah C 2013 Flow dynamics of red blood cells and their biomimetic counterparts *C. R. Phys.* **14** 451–8
- [3] Viallat A and Abkarian M 2014 Red blood cell: from its mechanics to its motion in shear flow *Int. J. Lab. Hematol.* **36** 237–43
- [4] Abreu D, Levant M, Steinberg V and Seifert U 2014 Fluid vesicles in flow *Adv. Colloid Interface Sci.* **208** 129–41
- [5] Barthès-Biesel D 2016 Motion and deformation of elastic capsules and vesicles in flow *Annu. Rev. Fluid Mech.* **48** 25–52
- [6] Mohandas N and Gallagher P G 2008 Red cell membrane: past, present and future *Blood* **112** 3939–48
- [7] Kim Y, Kim K and Park Y 2012 Measurement techniques for red blood cell deformability: recent advances *Blood Cell - An Overview of Studies in Hematology* ed T Moschandreu (Rijeka: InTech) pp 167–94
- [8] Freund J B 2014 Numerical simulation of flowing blood cells *Annu. Rev. Fluid Mech.* **46** 67–95
- [9] Guedda M, Abaidi M, Benlahsen M and Misbah C 2012 Dynamic modes of quasispherical vesicles: exact analytical solutions *Phys. Rev. E* **86** 051915
- [10] Dupire J, Socol M and Viallat A 2012 Full dynamics of a red blood cell in shear flow *Proc. Natl Acad. Sci.* **109** 20808–13
- [11] Minetti C, Podgorski T, Coupier G and Dubois F 2014 Fully automated digital holographic processing for monitoring the dynamics of a vesicle suspension under shear flow *Biomed. Opt. Express* **5** 1554
- [12] Choi Y-S and Lee S-J 2009 Three-dimensional volumetric measurement of red blood cell motion using digital holographic microscopy *Appl. Opt.* **48** 2983
- [13] Clavería V, Aouane O, Thiébaud M, Abkarian M, Coupier G, Misbah C, John T and Wagner C 2016 Clusters of red blood cells in microcapillary flow: hydrodynamic versus macromolecule induced interaction *Soft Matter* **12** 8235–45
- [14] Merola F *et al* 2017 Tomographic flow cytometry by digital holography *Light Sci. Appl.* **6** e16241
- [15] Cristini V and Kassab G S 2005 Computer modeling of red blood cell rheology in the microcirculation: a brief overview *Ann. Biomed. Eng.* **33** 1724–7
- [16] Pozrikidis C 2010 *Computational Hydrodynamics of Capsules and Biological Cells (Chapman and Hall/CRC Mathematical and Computational Biology Series)* (Boca Raton, FL: CRC Press) (<https://doi.org/10.1201/EBK1439820056>)
- [17] Li X, Vlahovska P M and Karniadakis G E 2013 Continuum- and particle-based modeling of shapes and dynamics of red blood cells in health and disease *Soft Matter* **9** 28–37
- [18] Fedosov D A, Noguchi H and Gompper G 2014 Multiscale modeling of blood flow: from single cells to blood rheology *Biomech. Model. Mechanobiol.* **13** 239–58
- [19] Ju M, Ye S S, Namgung B, Cho S, Low H T, Leo H L and Kim S 2015 A review of numerical methods for red blood cell flow simulation *Comput. methods Biomech. Biomed. Eng.* **18** 130–40
- [20] Gompper G and Fedosov D A 2016 Modeling microcirculatory blood flow: current state and future perspectives *WIREs Syst. Biol. Med.* **8** 157–68
- [21] Canham P B 1970 The minimum energy of bending as a possible explanation of the biconcave shape of the human red blood cell *J. Theor. Biol.* **26** 61–81
- [22] Helfrich W 1973 Elastic properties of lipid bilayers: theory and possible experiments *Z. Naturforsch. C* **28** 693–703
- [23] Evans E A 1974 Bending resistance and chemically induced moments in membrane bilayers *Biophys. J.* **14** 923–31
- [24] Weiner J L 1978 On a problem of chen, Willmore *et al Indiana Univ. Math. J.* **27** 19–35
- [25] Deckelnick K, Dziuk G and Elliott C M 2005 Computation of geometric partial differential equations and mean curvature flow *Acta Numer.* **14** 139–232
- [26] Dziuk G 2008 Computational parametric Willmore flow *Numer. Math.* **111** 55
- [27] Guckenberger A, Schraml M P, Chen P G, Leonetti M and Gekle S 2016 On the bending algorithms for soft objects in flows *Comput. Phys. Commun.* **207** 1–23
- [28] Tsubota K-I 2014 Short note on the bending models for a membrane in capsule mechanics: comparison between continuum and discrete models *J. Comput. Phys.* **277** 320–8
- [29] Prosperetti A and Tryggvason G (ed) 2007 *Computational methods for Multiphase Flow* (Cambridge: Cambridge University Press) (<https://doi.org/10.1017/CBO9780511607486>)
- [30] Brown F L H 2008 Elastic modeling of biomembranes and lipid bilayers *Annu. Rev. Phys. Chem.* **59** 685–712
- [31] Popel A S and Johnson P C 2005 Microcirculation and hemorheology *Annu. Rev. Fluid Mech.* **37** 43–69
- [32] Omori T, Imai Y, Kikuchi K, Ishikawa T and Yamaguchi T 2014 Hemodynamics in the microcirculation and in microfluidics *Ann. Biomed. Eng.* **43** 238–57
- [33] Fogelson A L and Neeves K B 2015 Fluid mechanics of blood clot formation *Annu. Rev. Fluid Mech.* **47** 377–403
- [34] Seifert U 1997 Configurations of fluid membranes and vesicles *Adv. Phys.* **46** 13–137
- [35] Pozrikidis C 2001 Interfacial dynamics for Stokes flow *J. Comput. Phys.* **169** 250–301
- [36] Deserno M 2015 Fluid lipid membranes: from differential geometry to curvature stresses *Chem. Phys. Lipids* **185** 11–45
- [37] Xu G 2004 Discrete Laplace–Beltrami operators and their convergence *Comput. Aided Geom. Des.* **21** 767–84
- [38] Capovilla R, Guven J and Santiago J A 2002 Lipid membranes with an edge *Phys. Rev. E* **66** 021607
- [39] Capovilla R, Guven J and Santiago J A 2003 Deformations of the geometry of lipid vesicles *J. Phys. A: Math. Gen.* **36** 6281
- [40] Tu Z C and Ou-Yang Z C 2003 Lipid membranes with free edges *Phys. Rev. E* **68** 061915
- [41] Steigmann D, Baesu E, Rudd R, Belak J and McElfresh M 2003 On the variational theory of cell-membrane equilibria *Interfaces Free Boundaries* **5** 357–66
- [42] Yao Z, Sknepnek R, Thomas C K and de la Cruz M O 2012 Shapes of pored membranes *Soft Matter* **8** 11613–9
- [43] Baesu E, Rudd E R, Belak J and McElfresh M 2004 Continuum modeling of cell membranes *Int. J. Non-Linear Mech.* **39** 369–77
- [44] Fogden A, Hyde S T and Lundberg G 1991 Bending energy of surfactant films *J. Chem. Soc. Faraday Trans.* **87** 949–55
- [45] Harmandaris V A and Deserno M 2006 A novel method for measuring the bending rigidity of model lipid membranes by simulating tethers *J. Chem. Phys.* **125** 204905
- [46] Møllmann H 1981 *Introduction to the Theory of Thin Shells* (New York: Wiley)

- [47] Ventsel E and Krauthammer T 2001 *Thin Plates and Shells: Theory, Analysis and Applications* (New York: CRC Press)
- [48] Knoche S and Kierfeld J 2011 Buckling of spherical capsules *Phys. Rev. E* **84** 046608
- [49] Seguin B and Fried E 2013 Microphysical derivation of the Canham–Helfrich free-energy density *J. Math. Biol.* **68** 647–65
- [50] Kheyfets B, Galimzyanov T, Drozdova A and Mukhin S 2016 Analytical calculation of the lipid bilayer bending modulus *Phys. Rev. E* **94** 042415
- [51] Campelo F, Arnarez C, Marrink S J and Kozlov M M 2014 Helfrich model of membrane bending: from Gibbs theory of liquid interfaces to membranes as thick anisotropic elastic layers *Adv. Colloid Interface Sci.* **208** 25–33
- [52] Boedec G, Leonetti M and Jaeger M 2011 3D vesicle dynamics simulations with a linearly triangulated surface *J. Comput. Phys.* **230** 1020–34
- [53] Landau L D and Lifshitz E M 1986 *Theory of Elasticity Course of Theoretical Physics* vol 7, 3rd edn (Oxford: Pergamon)
- [54] Pozrikidis C 2001 Effect of membrane bending stiffness on the deformation of capsules in simple shear flow *J. Fluid Mech.* **440** 269–91
- [55] Feng F and Klug W S 2006 Finite element modeling of lipid bilayer membranes *J. Comput. Phys.* **220** 394–408
- [56] Lee H J, Peterson E L, Phillips R, Klug W S and Wiggins P A 2008 Membrane shape as a reporter for applied forces *Proc. Natl Acad. Sci.* **105** 19253–7
- [57] Powers T R 2010 Dynamics of filaments and membranes in a viscous fluid *Rev. Mod. Phys.* **82** 1607–31
- [58] Jenkins J T 1977 Static equilibrium configurations of a model red blood cell *J. Math. Biol.* **4** 149–69
- [59] Zhong-Can O-Y and Helfrich W 1987 Instability and deformation of a spherical vesicle by pressure *Phys. Rev. Lett.* **59** 2486–8
- [60] Zhong-Can O-Y and Helfrich W 1989 Bending energy of vesicle membranes: general expressions for the first, second and third variation of the shape energy and applications to spheres and cylinders *Phys. Rev. A* **39** 5280–8
- [61] Capovilla R and Guven J 2002 Stresses in lipid membranes *J. Phys. A: Math. Gen.* **35** 6233
- [62] Guven J 2004 Membrane geometry with auxiliary variables and quadratic constraints *J. Phys. A: Math. Gen.* **37** L313
- [63] Lomholt M A and Miao L 2006 Descriptions of membrane mechanics from microscopic and effective two-dimensional perspectives *J. Phys. A: Math. Gen.* **39** 10323
- [64] Laadhari A, Misbah C and Saramito P 2010 On the equilibrium equation for a generalized biological membrane energy by using a shape optimization approach *Phys. Nonlinear Phenom.* **239** 1567–72
- [65] Napoli G and Vergori L 2010 Equilibrium of nematic vesicles *J. Phys. A: Math. Theor.* **43** 445207
- [66] Sinha K and Graham M D 2015 Dynamics of a single red blood cell in simple shear flow *Phys. Rev. E* **92** 042710
- [67] Olla P 2011 Tank-treading as a means of propulsion in viscous shear flows *J. Fluid Mech.* **680** 265–86
- [68] Helfrich W and Deuling H J 1975 Some theoretical shapes of red blood cells *J. Phys. Colloques* **36** C1–327
- [69] Seifert U, Berndl K and Lipowsky R 1991 Shape transformations of vesicles: phase diagram for spontaneous-curvature and bilayer-coupling models *Phys. Rev. A* **44** 1182–202
- [70] Lim G H W, Wortis M and Mukhopadhyay R 2008 Red blood cell shapes and shape transformations: Newtonian mechanics of a composite membrane *Soft Matter, Volume 4: Lipid Bilayers and Red Blood Cells* ed G Gompper and M Schick (Weinheim: Wiley) pp 83–249
- [71] Pozrikidis C 1992 *Boundary Integral and Singularity methods for Linearized Viscous Flow* (Cambridge Texts in Applied Mathematics vol 8) (New York: Cambridge University Press) (<https://doi.org/10.1017/CBO9780511624124>)
- [72] Krüger T 2012 *Computer Simulation Study of Collective Phenomena in Dense Suspensions of Red Blood Cells Under Shear* (New York: Springer) (<https://doi.org/10.1007/978-3-8348-2376-2>)
- [73] Fournier J-B 2007 On the stress and torque tensors in fluid membranes *Soft Matter* **3** 883–8
- [74] Arroyo M and De Simone A 2009 Relaxation dynamics of fluid membranes *Phys. Rev. E* **79** 031915
- [75] Jenkins J T 1977 The equations of mechanical equilibrium of a model membrane *SIAM J. Appl. Math.* **32** 755–64
- [76] Steigmann D J 1999 Fluid films with curvature elasticity *Arch. Ration. Mech. Anal.* **150** 127–52
- [77] Sauer R A, Duong T X, Mandadapu K K and Steigmann D J 2017 A stabilized finite element formulation for liquid shells and its application to lipid bilayers *J. Comput. Phys.* **330** 436–66
- [78] Naghdi P M 1973 *The theory of shells and plates Linear Theories of Elasticity and Thermoelasticity: Linear and Nonlinear Theories of Rods, Plates, and Shells (Mechanics of Solids No. 2)* ed C Truesdell (Berlin: Springer) pp 425–640
- [79] Secomb T W 1988 Interaction between bending and tension forces in bilayer membranes *Biophys. J.* **54** 743–6
- [80] Pozrikidis C 2003 Numerical simulation of the flow-induced deformation of red blood cells *Ann. Biomed. Eng.* **31** 1194–205
- [81] Pozrikidis C 2003 *Modeling and Simulation of Capsules and Biological Cells (Chapman and Hall/CRC Mathematical Biology, Medicine Series)* (London: Chapman and Hall)
- [82] Pozrikidis C 2005 Resting shape and spontaneous membrane curvature of red blood cells *Math. Med. Biol.* **22** 34–52
- [83] Le D V, White J, Peraire J, Lim K M and Khoo B C 2009 An implicit immersed boundary method for three-dimensional fluid-membrane interactions *J. Comput. Phys.* **228** 8427–45
- [84] Zhao H, Isfahani A H G, Olson L N and Freund J B 2010 A spectral boundary integral method for flowing blood cells *J. Comput. Phys.* **229** 3726–44
- [85] Zhu L and Brandt L 2015 The motion of a deforming capsule through a corner *J. Fluid Mech.* **770** 374–97
- [86] Daddi-Moussa-Ider A, Guckenberger A and Gekle S 2016 Long-lived anomalous thermal diffusion induced by elastic cell membranes on nearby particles *Phys. Rev. E* **93** 012612
- [87] Skalak R, Ozkaya N and Skalak T C 1989 Biofluid mechanics *Annu. Rev. Fluid Mech.* **21** 167–200
- [88] Aland S, Egerer S, Lowengrub J and Voigt A 2014 Diffuse interface models of locally inextensible vesicles in a viscous fluid *J. Comput. Phys.* **277** 32–47
- [89] Cantat I and Misbah C 1999 Vesicle dynamics in chemotaxis, haptotaxis, under shear flow *Transport and Structure* ed S C Müller *et al (Lecture Notes in Physics* vol 532–2) (Berlin: Springer) pp 93–136
- [90] Kaoui B, Ristow G, Cantat I, Misbah C and Zimmermann W 2008 Lateral migration of a two-dimensional vesicle in unbounded Poiseuille flow *Phys. Rev. E* **77** 021903
- [91] Zhao H, Spann A P and Shaqfeh E S G 2011 The dynamics of a vesicle in a wall-bound shear flow *Phys. Fluids* **23** 121901
- [92] Zhao H and Shaqfeh E S G 2011 The dynamics of a vesicle in simple shear flow *J. Fluid Mech.* **674** 578–604
- [93] Biben T, Farutin A and Misbah C 2011 Three-dimensional vesicles under shear flow: numerical study of dynamics and phase diagram *Phys. Rev. E* **83** 031921
- [94] Yazdani A and Bagchi P 2012 Three-dimensional numerical simulation of vesicle dynamics using a front-tracking method *Phys. Rev. E* **85** 056308

- [95] Zhao H and Shaqfeh E S G 2013 The shape stability of a lipid vesicle in a uniaxial extensional flow *J. Fluid Mech.* **719** 345–61
- [96] Zhao H and Shaqfeh E S G 2013 The dynamics of a non-dilute vesicle suspension in a simple shear flow *J. Fluid Mech.* **725** 709–31
- [97] Vlahovska P M, Podgorski T and Misbah C 2009 Vesicles and red blood cells in flow: from individual dynamics to rheology *C. R. Phys.* **10** 775–89
- [98] Seol Y, Hu W-F, Kim Y and Lai M-C 2016 An immersed boundary method for simulating vesicle dynamics in three dimensions *J. Comput. Phys.* **322** 125–41
- [99] Farutin A, Piasecki T, Słowicka A M, Misbah C, Wajnryb E and Ekiel-Jeżewska M L 2016 Dynamics of flexible fibers and vesicles in Poiseuille flow at low Reynolds number *Soft Matter* **12** 7307–23
- [100] Pozrikidis C 2011 *Introduction to Theoretical and Computational Fluid Dynamics* 2nd edn (New York: Oxford University Press)
- [101] Veerapaneni S K, Rahimian A, Biros G and Zorin D 2011 A fast algorithm for simulating vesicle flows in three dimensions *J. Comput. Phys.* **230** 5610–34
- [102] Spann A P, Zhao H and Shaqfeh E S G 2014 Loop subdivision surface boundary integral method simulations of vesicles at low reduced volume ratio in shear and extensional flow *Phys. Fluids* **26** 031902
- [103] Rahimian A, Veerapaneni S K, Zorin D and Biros G 2015 Boundary integral method for the flow of vesicles with viscosity contrast in three dimensions *J. Comput. Phys.* **298** 766–86
- [104] Bagchi P 2010 Front-tracking methods for capsules, vesicles and blood cells *Computational Hydrodynamics of Capsules and Biological Cells (Chapman & Hall/CRC Mathematical and Computational Biology Series)* ed C Pozrikidis (Boca Raton, FL: CRC Press) pp 35–70
- [105] Fedosov D A, Caswell B and Karniadakis G E 2010 A multiscale red blood cell model with accurate mechanics, rheology and dynamics *Biophys. J.* **98** 2215–25
- [106] Noguchi H and Gompper G 2005 Dynamics of fluid vesicles in shear flow: effect of membrane viscosity and thermal fluctuations *Phys. Rev. E* **72** 011901
- [107] Farutin A, Biben T and Misbah C 2014 3D numerical simulations of vesicle and inextensible capsule dynamics *J. Comput. Phys.* **275** 539–68
- [108] Skalak R, Tozeren A, Zarda R P and Chien S 1973 Strain energy function of red blood cell membranes *Biophys. J.* **13** 245–64
- [109] Zhao H, Shaqfeh E S G and Narsimhan V 2012 Shear-induced particle migration and margination in a cellular suspension *Phys. Fluids* **24** 011902
- [110] Guckenberger A and Gekle S 2017 A boundary integral method with volume-changing objects for ultrasound-triggered margination of microbubbles (arXiv:1608.05196)
- [111] Steigmann D J 1999 On the relationship between the Cosserat and Kirchhoff–Love theories of elastic shells *Math. Mech. Solids* **4** 275–88
- [112] Sauer R A and Duong T X 2015 On the theoretical foundations of thin solid and liquid shells *Math. Mech. Solids* **1** (<https://doi.org/10.1177/1081286515594656>)
- [113] Aidun C K and Clausen J R 2010 Lattice-Boltzmann method for complex flows *Annu. Rev. Fluid Mech.* **42** 439–72
- [114] McWhirter J L, Noguchi H and Gompper G 2009 Flow-induced clustering and alignment of vesicles and red blood cells in microcapillaries *Proc. Natl Acad. Sci.* **106** 6039–43
- [115] McWhirter J L, Noguchi H and Gompper G 2011 Deformation and clustering of red blood cells in microcapillary flows *Soft Matter* **7** 10967–77
- [116] Lamura A and Gompper G 2013 Dynamics and rheology of vesicle suspensions in wall-bounded shear flow *Europhys. Lett.* **102** 28004
- [117] Fedosov D A, Pan W, Caswell B, Gompper G and Karniadakis G E 2011 Predicting human blood viscosity in silico *Proc. Natl Acad. Sci.* **108** 11772–7
- [118] Fedosov D A, Caswell B, Suresh S and Karniadakis G E 2011 Quantifying the biophysical characteristics of Plasmodium-falciparum-parasitized red blood cells in microcirculation *Proc. Natl Acad. Sci.* **108** 35–9
- [119] Fedosov D A, Fornleitner J and Gompper G 2012 Margination of white blood cells in microcapillary flow *Phys. Rev. Lett.* **108** 028104
- [120] Li X, Popel A S and Karniadakis G E 2012 Blood-plasma separation in Y-shaped bifurcating microfluidic channels: a dissipative particle dynamics simulation study *Phys. Biol.* **9** 026010
- [121] Fedosov D A and Gompper G 2014 White blood cell margination in microcirculation *Soft Matter* **10** 2961–70
- [122] Müller K, Fedosov D A and Gompper G 2014 Margination of micro- and nano-particles in blood flow and its effect on drug delivery *Sci. Rep.* **4** 4871
- [123] Katanov D, Gompper G and Fedosov D A 2015 Microvascular blood flow resistance: role of red blood cell migration and dispersion *Microvasc. Res.* **99** 57–66
- [124] Lykov K, Li X, Lei H, Pivkin I V and Karniadakis G E 2015 Inflow/outflow boundary conditions for particle-based blood flow simulations: application to arterial bifurcations and trees *PLOS Comput. Biol.* **11** e1004410
- [125] Müller K, Fedosov D A and Gompper G 2016 Understanding particle margination in blood flow—a step toward optimized drug delivery systems *Med. Eng. Phys.* **38** 2–10
- [126] Yazdani A and Karniadakis G E 2016 Sub-cellular modeling of platelet transport in blood flow through microchannels with constriction *Soft Matter* **12** 4339–51
- [127] MacMeccan R M, Clausen J R, Neitzel G P and Aidun C K 2009 Simulating deformable particle suspensions using a coupled lattice-Boltzmann and finite-element method *J. Fluid Mech.* **618** 13–39
- [128] Clausen J R and Aidun C K 2010 Capsule dynamics and rheology in shear flow: particle pressure and normal stress *Phys. Fluids* **22** 123302
- [129] Clausen J R, Reasor D A and Aidun C K 2011 The rheology and microstructure of concentrated non-colloidal suspensions of deformable capsules *J. Fluid Mech.* **685** 202–34
- [130] Peng Z, Asaro R J and Zhu Q 2011 Multiscale modelling of erythrocytes in Stokes flow *J. Fluid Mech.* **686** 299–337
- [131] Dupont C, Salsac A-V, Barthès-Biesel D, Vidrascu M and Le Tallec P 2015 Influence of bending resistance on the dynamics of a spherical capsule in shear flow *Phys. Fluids* **27** 051902
- [132] Sigüenza J, Mendez S, Ambard D, Dubois F, Jourdan F, Mozul R and Nicoud F 2016 Validation of an immersed thick boundary method for simulating fluid-structure interactions of deformable membranes *J. Comput. Phys.* **322** 723–46
- [133] Le D-V and Tan Z 2010 Large deformation of liquid capsules enclosed by thin shells immersed in the fluid *J. Comput. Phys.* **229** 4097–116
- [134] Rahimi M and Arroyo M 2012 Shape dynamics, lipid hydrodynamics and the complex viscoelasticity of bilayer membranes *Phys. Rev. E* **86** 011932
- [135] Dupin M M, Halliday I, Care C M, Alboul L and Munn L L 2007 Modeling the flow of dense suspensions of deformable particles in three dimensions *Phys. Rev. E* **75** 066707

- [136] Dupin M M, Halliday I, Care C M and Munn L L 2008 Lattice Boltzmann modelling of blood cell dynamics *Int. J. Comput. Fluid Dyn.* **22** 481–92
- [137] Cimrák I, Gusenbauer M and Schrefl T 2012 Modelling and simulation of processes in microfluidic devices for biomedical applications *Comput. Math. Appl.* **64** 278–88
- [138] Seifert U 1995 The concept of effective tension for fluctuating vesicles *Z. Phys. B* **97** 299–309
- [139] Lim G H W, Wortis M and Mukhopadhyay R 2002 Stomatocyte-discocyte-echinocyte sequence of the human red blood cell: evidence for the bilayer couple hypothesis from membrane mechanics *Proc. Natl Acad. Sci.* **99** 16766–9
- [140] Jaric M N 2008 Gaussian fluctuations of lipid bilayer vesicles: a numerical study *PhD Thesis*, Simon Fraser University Burnaby
- [141] Khairy K and Howard J 2011 Minimum-energy vesicle and cell shapes calculated using spherical harmonics parameterization *Soft Matter* **7** 2138–43
- [142] Mukhopadhyay R, Gerald Lim H W and Wortis M 2002 Echinocyte shapes: bending, stretching and shear determine spicule shape and spacing *Biophys. J.* **82** 1756–72
- [143] Barrett J W, Garcke H and Nürnberg R 2015 Numerical computations of the dynamics of fluidic membranes and vesicles *Phys. Rev. E* **92** 052704
- [144] Bassereau P, Sorre B and Lévy A 2014 Bending lipid membranes: experiments after W. Helfrich's model *Adv. Colloid Interface Sci.* **208** 47–57
- [145] Li J, Lykotrafitis G, Dao M and Suresh S 2007 Cytoskeletal dynamics of human erythrocyte *Proc. Natl Acad. Sci.* **104** 4937–42
- [146] Cordasco D, Yazdani A and Bagchi P 2014 Comparison of erythrocyte dynamics in shear flow under different stress-free configurations *Phys. Fluids* **26** 041902
- [147] Tsubota K-I, Wada S and Liu H 2014 Elastic behavior of a red blood cell with the membrane's nonuniform natural state: equilibrium shape, motion transition under shear flow and elongation during tank-treading motion *Biomech. Model. Mechanobiol.* **13** 735–46
- [148] Cordasco D and Bagchi P 2016 Dynamics of red blood cells in oscillating shear flow *J. Fluid Mech.* **800** 484–516
- [149] Le D V 2010 Effect of bending stiffness on the deformation of liquid capsules enclosed by thin shells in shear flow *Phys. Rev. E* **82** 016318
- [150] Dimova R 2014 Recent developments in the field of bending rigidity measurements on membranes *Adv. Colloid Interface Sci.* **208** 225–34
- [151] Nagle J F, Jablin M S, Tristram-Nagle S and Akabori K 2015 What are the true values of the bending modulus of simple lipid bilayers? *Chem. Phys. Lipids* **185** 3–10
- [152] Bochicchio D and Monticelli L 2016 The membrane bending modulus in experiments and simulations: a puzzling picture *Advances in Biomembranes and Lipid Self-Assembly* vol 23, ed A Iglíč, C V Kulkarni and M Rappolt (Cambridge: Academic) pp 117–43
- [153] Guido S and Tomaiuolo G 2009 Microconfined flow behavior of red blood cells *in vitro* *C. R. Phys.* **10** 751–63
- [154] Evans E A 1983 Bending elastic modulus of red blood cell membrane derived from buckling instability in micropipet aspiration tests *Biophys. J.* **43** 27–30
- [155] Mohandas N and Evans E 1994 Mechanical properties of the red cell membrane in relation to molecular structure and genetic defects *Annu. Rev. Biophys. Biomol. Struct.* **23** 787–818
- [156] Byfield F J, Aranda-Espinoza H, Romanenko V G, Rothblat G H and Levitan I 2004 Cholesterol depletion increases membrane stiffness of aortic endothelial cells *Biophys. J.* **87** 3336–43
- [157] Fournier J-B and Galatola P 2008 Corrections to the Laplace law for vesicle aspiration in micropipettes and other confined geometries *Soft Matter* **4** 2463–70
- [158] Discher D E, Boal D H and Boey S K 1998 Simulations of the erythrocyte cytoskeleton at large deformation. II. Micropipette aspiration *Biophys. J.* **75** 1584–97
- [159] Peng Z, Asaro R J and Zhu Q 2010 Multiscale simulation of erythrocyte membranes *Phys. Rev. E* **81** 031904
- [160] Dupont C, Le Tallec P, Barthès-Biesel D, Vidrascu M and Salsac A V 2015 Dynamics of a spherical capsule in a planar hyperbolic flow: influence of bending resistance *Proc. IUTAM* **16** 70–9
- [161] Noguchi H 2011 Anisotropic surface tension of buckled fluid membranes *Phys. Rev. E* **83** 061919
- [162] Hu M, Iv P D and Deserno M 2013 Determining the bending modulus of a lipid membrane by simulating buckling *J. Chem. Phys.* **138** 214110
- [163] Costa M, Ghiran I, Peng C-K, Nicholson-Weller A and Goldberger A L 2008 Complex dynamics of human red blood cell flickering: alterations with *in vivo* aging *Phys. Rev. E* **78** 020901
- [164] Betz T, Lenz M, Joanny J-F and Sykes C 2009 ATP-dependent mechanics of red blood cells *Proc. Natl Acad. Sci.* **106** 15320–5
- [165] Park Y K, Best C A, Badizadegan K, Dasari R R, Feld M S, Kuriabova T, Henle M L, Levine A J and Popescu G 2010 Measurement of red blood cell mechanics during morphological changes *Proc. Natl Acad. Sci.* **107** 6731–6
- [166] Byun H S, Hillman T R, Higgins J M, Diez-Silva M, Peng Z, Dao M, Dasari R R, Suresh S and Park Y K 2012 Optical measurement of biomechanical properties of individual erythrocytes from a sickle cell patient *Acta Biomater.* **8** 4130–8
- [167] Wennerström H and Olsson U 2014 The undulation force; theoretical results versus experimental demonstrations *Adv. Colloid Interface Sci.* **208** 10–3
- [168] Minetti C, Vitkova V, Dubois F and Bivas I 2016 Digital holographic microscopy as a tool to study the thermal shape fluctuations of lipid vesicles *Opt. Lett.* **41** 1833
- [169] Turlier H, Fedosov D A, Audoly B, Auth T, Gov N S, Sykes C, Joanny J-F, Gompper G and Betz T 2016 Equilibrium physics breakdown reveals the active nature of red blood cell flickering *Nat. Phys.* **12** 513–9
- [170] Watson M C, Brandt E G, Welch P M and Brown F L H 2012 Determining biomembrane bending rigidities from simulations of modest size *Phys. Rev. Lett.* **109** 028102
- [171] Deserno M, Kremer K, Paulsen H, Peter C and Schmid F 2013 Computational studies of biomembrane systems: theoretical considerations, simulation models, and applications *From Single Molecules to Nanoscopically Structured Materials (Advances in Polymer Science vol 206)* ed T Basché, K Müllen and M Schmidt (New York: Springer) pp 237–83
- [172] Tarazona P, Chacón E and Bresme F 2013 Thermal fluctuations and bending rigidity of bilayer membranes *J. Chem. Phys.* **139** 094902
- [173] Sodt A J, Venable R M, Lyman E and Pastor R W 2016 Nonadditive compositional curvature energetics of lipid bilayers *Phys. Rev. Lett.* **117** 138104
- [174] Mills J P, Qie L, Dao M, Lim C T and Suresh S 2004 Nonlinear elastic and viscoelastic deformation of the human red blood cell with optical tweezers *Mol. Cell. Biomech.* **1** 169–80
- [175] Suresh S, Spatz J, Mills J P, Micoulet A, Dao M, Lim C T, Beil M and Seufferlein T 2005 Connections between single-cell biomechanics and human disease states:

- gastrointestinal cancer and malaria *Acta Biomater.* **1** 15–30
- [176] Scheffer L, Bitler A, Ben-Jacob E and Korenstein R 2001 Atomic force pulling: probing the local elasticity of the cell membrane *Eur. Biophys. J.* **30** 83–90
- [177] Dao M, Li J and Suresh S 2006 Molecularly based analysis of deformation of spectrin network and human erythrocyte *Mater. Sci. Eng. C* **26** 1232–44
- [178] Fedosov D A, Caswell B and Karniadakis G E 2010 Systematic coarse-graining of spectrin-level red blood cell models *Comput. Methods Appl. Mech. Eng.* **199** 1937–48
- [179] Reasor D A, Clausen J R and Aidun C K 2012 Coupling the lattice-Boltzmann and spectrin-link methods for the direct numerical simulation of cellular blood flow *Int. J. Numer. methods Fluids* **68** 767–81
- [180] Krüger T, Holmes D and Coveney P V 2014 Deformability-based red blood cell separation in deterministic lateral displacement devices—a simulation study *Biomicrofluidics* **8** 054114
- [181] Luo Z Y and Bai B F 2015 Dynamics of biconcave vesicles in a confined shear flow *Chem. Eng. Sci.* **137** 548–55
- [182] Hao W, Xu Z, Liu C and Lin G 2015 A fictitious domain method with a hybrid cell model for simulating motion of cells in fluid flow *J. Comput. Phys.* **280** 345–62
- [183] Suárez I R, Leidy C, Téllez G, Gay G and Gonzalez-Mancera A 2013 Slow sedimentation and deformability of charged lipid vesicles *PLoS One* **8** e68309
- [184] Cristini V, Bławdziewicz J and Loewenberg M 2001 An adaptive mesh algorithm for evolving surfaces: simulations of drop breakup and coalescence *J. Comput. Phys.* **168** 445–63
- [185] Bazhlekov I B, Anderson P D and Meijer H E H 2004 Nonsingular boundary integral method for deformable drops in viscous flows *Phys. Fluids* **16** 1064–81
- [186] Cunha F R and Loewenberg M 2003 A study of emulsion expansion by a boundary integral method *Mech. Res. Commun.* **30** 639–49
- [187] de Oliveira S L G 2012 An overview of procedures for refining triangulations *Computational Science and Its Applications - ICCSA 2012 (Lecture Notes in Computer Science No. 7333)* ed B Murgante et al (Berlin: Springer) pp 198–213
- [188] Noguchi H and Gompper G 2005 Shape transitions of fluid vesicles and red blood cells in capillary flows *Proc. Natl Acad. Sci. USA* **102** 14159–64
- [189] Fedosov D A, Caswell B and Karniadakis G E 2010 Dissipative particle dynamics modeling of red blood cells *Computational Hydrodynamics of Capsules and Biological Cells (Chapman & Hall/CRC Mathematical and Computational Biology Series)* ed C Pozrikidis (Boca Raton, FL: CRC Press) pp 183–218
- [190] Nans A, Mohandas N and Stokes D L 2011 Native ultrastructure of the red cell cytoskeleton by cryo-electron tomography *Biophys. J.* **101** 2341–50
- [191] Omori T, Ishikawa T, Barthès-Biesel D, Salsac A-V, Walter J, Imai Y and Yamaguchi T 2011 Comparison between spring network models and continuum constitutive laws: application to the large deformation of a capsule in shear flow *Phys. Rev. E* **83** 041918
- [192] Ramanujan S and Pozrikidis C 1998 Deformation of liquid capsules enclosed by elastic membranes in simple shear flow: large deformations and the effect of fluid viscosities *J. Fluid Mech.* **361** 117–43
- [193] Walter J, Salsac A-V, Barthès-Biesel D and Le Tallec P 2010 Coupling of finite element and boundary integral methods for a capsule in a Stokes flow *Int. J. Numer. Methods Eng.* **83** 829–50
- [194] Pozrikidis C 2006 A spectral collocation method with triangular boundary elements *Eng. Anal. Bound. Elem.* **30** 315–24
- [195] Wang Y and Dimitrakopoulos P 2006 A three-dimensional spectral boundary element algorithm for interfacial dynamics in Stokes flow *Phys. Fluids* **18** 082106
- [196] Dodson W R III and Dimitrakopoulos P 2008 Spindles, cusps and bifurcation for capsules in Stokes flow *Phys. Rev. Lett.* **101** 208102
- [197] Dodson W R III and Dimitrakopoulos P 2009 Dynamics of strain-hardening and strain-softening capsules in strong planar extensional flows via an interfacial spectral boundary element algorithm for elastic membranes *J. Fluid Mech.* **641** 263–96
- [198] Cirak F, Ortiz M and Schröder P 2000 Subdivision surfaces: a new paradigm for thin-shell finite-element analysis *Int. J. Numer. Methods Eng.* **47** 2039–72
- [199] Catmull E and Clark J 1978 Recursively generated B-spline surfaces on arbitrary topological meshes *Comput. Aided Des.* **10** 350–5
- [200] Le D-V and Wong S T 2011 A front-tracking method with Catmull–Clark subdivision surfaces for studying liquid capsules enclosed by thin shells in shear flow *J. Comput. Phys.* **230** 3538–55
- [201] Loop C T 1987 Smooth subdivision surfaces based on triangles *Master Thesis*, University of Utah Utah, USA
- [202] Persson P-O, Aftosmis M J and Haimes R 2006 On the use of loop subdivision surfaces for surrogate geometry *Proc. 15th Int. Meshing Roundtable* ed P P Pébay (Berlin: Springer) pp 375–92
- [203] Le D-V 2010 Subdivision elements for large deformation of liquid capsules enclosed by thin shells *Comput. Methods Appl. Mech. Eng.* **199** 2622–32
- [204] Gounley J, Boedec G, Jaeger M and Leonetti M 2016 Influence of surface viscosity on droplets in shear flow *J. Fluid Mech.* **791** 464–94
- [205] Huang W-X, Chang C B and Sung H J 2012 Three-dimensional simulation of elastic capsules in shear flow by the penalty immersed boundary method *J. Comput. Phys.* **231** 3340–64
- [206] Kessler S, Finken R and Seifert U 2008 Swinging and tumbling of elastic capsules in shear flow *J. Fluid Mech.* **605** 207–26
- [207] Freund J B and Zhao H 2010 A high-resolution fast boundary-integral method for multiple interacting blood cells *Computational Hydrodynamics of Capsules and Biological Cells (Chapman & Hall/CRC Mathematical and Computational Biology Series)* ed C Pozrikidis (Boca Raton, FL: CRC Press) pp 71–111
- [208] Rahimian A et al 2010 Petascale direct numerical simulation of blood flow on 200K cores and heterogeneous architectures *Proc. 2010 ACM/IEEE Int. Conference for High Performance Computing, Networking, Storage and Analysis (New Orleans)* (IEEE Computer Society) (<https://doi.org/10.1109/SC.2010.42>)
- [209] Veerapaneni S 2016 Integral equation methods for vesicle electrohydrodynamics in three dimensions *J. Comput. Phys.* **326** 278–89
- [210] Zhou H and Pozrikidis C 1995 Deformation of liquid capsules with incompressible interfaces in simple shear flow *J. Fluid Mech.* **283** 175–200
- [211] Lac E, Barthès-Biesel D, Pelekasis N A and Tsamopoulos J 2004 Spherical capsules in three-dimensional unbounded Stokes flows: effect of the membrane constitutive law and onset of buckling *J. Fluid Mech.* **516** 303–34
- [212] Barthès-Biesel D, Walter J and Salsac A-V 2010 Flow-induced deformation of artificial capsules *Computational Hydrodynamics of Capsules and Biological Cells (Chapman & Hall/CRC Mathematical and Computational Biology Series)* ed C Pozrikidis (Boca Raton, FL: CRC Press) pp 35–70
- [213] Rangarajan R and Gao H 2015 A finite element method to compute three-dimensional equilibrium configurations of

- fluid membranes: optimal parameterization, variational formulation and applications *J. Comput. Phys.* **297** 266–94
- [214] Lac E, Morel A and Barthès-Biesel D 2007 Hydrodynamic interaction between two identical capsules in simple shear flow *J. Fluid Mech.* **573** 149
- [215] Biben T, Kassner K and Misbah C 2005 Phase-field approach to three-dimensional vesicle dynamics *Phys. Rev. E* **72** 041921
- [216] Du Q and Zhang J 2008 Adaptive finite element method for a phase field bending elasticity model of vesicle membrane deformations *SIAM J. Sci. Comput.* **30** 1634–57
- [217] Veerapaneni S K, Gueyffier D, Zorin D and Biros G 2009 A boundary integral method for simulating the dynamics of inextensible vesicles suspended in a viscous fluid in 2D *J. Comput. Phys.* **228** 2334–53
- [218] Kaoui B, Biros G and Misbah C 2009 Why do red blood cells have asymmetric shapes even in a symmetric flow? *Phys. Rev. Lett.* **103** 188101
- [219] Luo Z Y, Xu F, Lu T J and Bai B F 2010 Direct numerical simulation of single leukocyte deformation in microchannel flow for disease diagnosis *J. Med. Syst.* **35** 869–76
- [220] Salac D and Miksis M 2011 A level set projection model of lipid vesicles in general flows *J. Comput. Phys.* **230** 8192–215
- [221] Laadhari A, Saramito P and Misbah C 2012 Vesicle tumbling inhibited by inertia *Phys. Fluids* **24** 031901
- [222] Laadhari A, Saramito P and Misbah C 2014 Computing the dynamics of biomembranes by combining conservative level set and adaptive finite element methods *J. Comput. Phys.* **263** 328–52
- [223] Laadhari A, Saramito P and Misbah C 2016 An adaptive finite element method for the modeling of the equilibrium of red blood cells *Int. J. Numer. Meth. Fluids* **80** 397–428
- [224] Marth W, Aland S and Voigt A 2016 Margination of white blood cells: a computational approach by a hydrodynamic phase field model *J. Fluid Mech.* **790** 389–406
- [225] Ghigliotti G, Biben T and Misbah C 2010 Rheology of a dilute two-dimensional suspension of vesicles *J. Fluid Mech.* **653** 489–518
- [226] Sui Y, Chew Y, Roy P, Chen X and Low H 2007 Transient deformation of elastic capsules in shear flow: effect of membrane bending stiffness *Phys. Rev. E* **75** 066301
- [227] Freund J B 2007 Leukocyte margination in a model microvessel *Phys. Fluids* **19** 023301
- [228] Sohn J S, Tseng Y-H, Li S, Voigt A and Lowengrub J S 2010 Dynamics of multicomponent vesicles in a viscous fluid *J. Comput. Phys.* **229** 119–44
- [229] Rahimian A, Veerapaneni S K and Biros G 2010 Dynamic simulation of locally inextensible vesicles suspended in an arbitrary two-dimensional domain, a boundary integral method *J. Comput. Phys.* **229** 6466–84
- [230] Trozzo R, Boedec G, Leonetti M and Jaeger M 2015 Axisymmetric boundary element method for vesicles in a capillary *J. Comput. Phys.* **289** 62–82
- [231] Boltz H-H and Kierfeld J 2015 Shapes of sedimenting soft elastic capsules in a viscous fluid *Phys. Rev. E* **92** 033003
- [232] Veerapaneni S K, Gueyffier D, Biros G and Zorin D 2009 A numerical method for simulating the dynamics of 3D axisymmetric vesicles suspended in viscous flows *J. Comput. Phys.* **228** 7233–49
- [233] Sohn J, Li S, Li X and Lowengrub J S 2012 Axisymmetric multicomponent vesicles: a comparison of hydrodynamic and geometric models *Int. J. Numer. Meth. Biomed. Engng.* **28** 346–68
- [234] Du Q, Liu C and Wang X 2004 A phase field approach in the numerical study of the elastic bending energy for vesicle membranes *J. Comput. Phys.* **198** 450–68
- [235] Rosolen A, Peco C and Arroyo M 2013 An adaptive meshfree method for phase-field models of biomembranes. Part I: approximation with maximum-entropy basis functions *J. Comput. Phys.* **249** 303–19
- [236] Lowengrub J, Allard J and Aland S 2016 Numerical simulation of endocytosis: viscous flow driven by membranes with non-uniformly distributed curvature-inducing molecules *J. Comput. Phys.* **309** 112–28
- [237] Kraus M, Wintz W, Seifert U and Lipowsky R 1996 Fluid vesicles in shear flow *Phys. Rev. Lett.* **77** 3685–8
- [238] Krüger T, Varnik F and Raabe D 2011 Efficient and accurate simulations of deformable particles immersed in a fluid using a combined immersed boundary lattice Boltzmann finite element method *Comput. Math. Appl.* **61** 3485–505
- [239] Meyer M, Desbrun M, Schröder P and Barr A H 2003 Discrete differential-geometry operators for triangulated 2-manifolds *Visualization and Mathematics III (Mathematics and Visualization No. 3)* ed H-C Hege and K Polthier (Berlin: Springer) pp 35–57
- [240] Kantor Y and Nelson D R 1987 Phase transitions in flexible polymeric surfaces *Phys. Rev. A* **36** 4020–32
- [241] Gompper G and Kroll D M 1996 Random surface discretizations and the renormalization of the bending rigidity *J. Phys. I France* **6** 1305–20
- [242] Komura S, Tamura K and Kato T 2005 Buckling of spherical shells adhering onto a rigid substrate *Eur. Phys. J. E* **18** 343–58
- [243] Li J, Dao M, Lim C T and Suresh S 2005 Spectrin-level modeling of the cytoskeleton and optical tweezers stretching of the erythrocyte *Biophys. J.* **88** 3707–19
- [244] Pivkin I V and Karniadakis G E 2008 Accurate coarse-grained modeling of red blood cells *Phys. Rev. Lett.* **101** 118105
- [245] Pan W, Caswell B and Karniadakis G E 2010 A low-dimensional model for the red blood cell *Soft Matter* **6** 4366–76
- [246] Pan W, Fedosov D A, Caswell B and Karniadakis G E 2011 Predicting dynamics and rheology of blood flow: a comparative study of multiscale and low-dimensional models of red blood cells *Microvasc. Res.* **82** 163–70
- [247] Kusters R, van der Heijden T, Kaoui B, Harting J and Storm C 2014 Forced transport of deformable containers through narrow constrictions *Phys. Rev. E* **90** 033006
- [248] Fedosov D A, Peltomäki M and Gompper G 2014 Deformation and dynamics of red blood cells in flow through cylindrical microchannels *Blood Matter* **10** 4258–67
- [249] Zhang Z, Henry E, Gompper G and Fedosov D A 2015 Behavior of rigid and deformable particles in deterministic lateral displacement devices with different post shapes *J. Chem. Phys.* **143** 243145
- [250] Mehrabadi M, Ku D N and Aidun C K 2016 Effects of shear rate, confinement and particle parameters on margination in blood flow *Phys. Rev. E* **93** 023109
- [251] Spann A P, Campbell J E, Fitzgibbon S R, Rodriguez A, Cap A P, Blackburne L H and Shaqfeh E S G 2016 The effect of hematocrit on platelet adhesion: experiments and simulations *Biophys. J.* **111** 577–88
- [252] Noguchi H and Gompper G 2004 Fluid vesicles with viscous membranes in shear flow *Phys. Rev. Lett.* **93** 258102
- [253] Noguchi H and Gompper G 2007 Swinging and tumbling of fluid vesicles in shear flow *Phys. Rev. Lett.* **98** 128103
- [254] McWhirter L J, Noguchi H and Gompper G 2012 Ordering and arrangement of deformed red blood cells in flow through microcapillaries *New J. Phys.* **14** 085026

- [255] Xu G 2004 Convergence of discrete Laplace–Beltrami operators over surfaces *Comput. Math. Appl.* **48** 347–60
- [256] Botsch M, Pauly M, Rossli C, Bischoff S and Kobbelt L 2006 Geometric modeling based on triangle meshes *ACM SIGGRAPH 2006 Courses* (New York: ACM) (<https://doi.org/10.1145/1185657.1185839>)
- [257] Gatzke T D and Grimm C M 2006 Estimating curvature on triangular meshes *Int. J. Shape Model.* **12** 1–28
- [258] Sorkine O 2006 Differential representations for mesh processing *Comput. Graph. Forum* **25** 789–807
- [259] Hildebrandt K, Polthier K and Wardetzky M 2007 On the convergence of metric and geometric properties of polyhedral surfaces *Geom. Dedicata* **123** 89–112
- [260] Wardetzky M, Mathur S, Kälberer F and Grinspun E 2007 Discrete Laplace operators: no free lunch *Proc. Fifth Eurographics Symp. on Geometry Processing* ed A Belyaev and M Garland (Barcelona: Eurographics Association) pp 33–7
- [261] Belkin M, Sun J and Wang Y 2008 Discrete Laplace operator on meshed surfaces *Proc. Twenty-Fourth Annual Symp. on Computational Geometry* (ACM: Maryland) pp 278–87
- [262] Sullivan J M 2008 Curvatures of smooth and discrete surfaces *Discrete Differential Geometry (Oberwolfach Seminars vol 38)* ed A I Bobenko *et al* (Basel: Birkhäuser) pp 175–88
- [263] Wardetzky M 2008 Convergence of the cotangent formula: an overview *Discrete Differential Geometry (Oberwolfach Seminars vol 38)* ed A I Bobenko *et al* (Basel: Birkhäuser) pp 275–86
- [264] Reuter M, Biasotti S, Giorgi D, Giuseppe Patanè and Spagnuolo M 2009 Discrete Laplace–Beltrami operators for shape analysis and segmentation *Comput. Graph.* **33** 381–90
- [265] Wu J-Y, Chi M-H and Chen S-G 2010 A local tangential lifting differential method for triangular meshes *Math. Comput. Simul.* **80** 2386–402
- [266] Alexa M and Wardetzky M 2011 Discrete Laplacians on general polygonal meshes *SIGGRAPH* (New York: ACM) pp 102:1–10
- [267] Yang X and Zheng J 2013 Curvature tensor computation by piecewise surface interpolation *Comput. Aided Des.* **45** 1639–50
- [268] Chen S-G, Chi M-H and Wu J-Y 2015 High-order algorithms for Laplace–Beltrami operators and geometric invariants over curved surfaces *J. Sci. Comput.* **65** 839–65
- [269] Li X, Xu G and Zhang Y J 2015 Localized discrete Laplace–Beltrami operator over triangular mesh *Comput. Aided Geom. Des.* **39** 67–82
- [270] Boedec G, Jaeger M and Leonetti M 2012 Settling of a vesicle in the limit of quasispherical shapes *J. Fluid Mech.* **690** 227–61
- [271] Farutin A and Misbah C 2012 Squaring, parity breaking and S tumbling of vesicles under shear flow *Phys. Rev. Lett.* **109** 248106
- [272] Bogner S, Råde U and Harting J 2016 Curvature estimation from a volume-of-fluid indicator function for the simulation of surface tension and wetting with a free-surface lattice Boltzmann method *Phys. Rev. E* **93** 043302
- [273] Fraternali F, Farina I and Carpentieri G 2014 A discrete-to-continuum approach to the curvatures of membrane networks and parametric surfaces *Mech. Res. Commun.* **56** 18–25
- [274] Zinchenko A Z, Rother M A and Davis R H 1997 A novel boundary-integral algorithm for viscous interaction of deformable drops *Phys. Fluids* **9** 1493–511
- [275] Farutin A and Misbah C 2014 Symmetry breaking and cross-streamline migration of three-dimensional vesicles in an axial poiseuille flow *Phys. Rev. E* **89** 042709
- [276] Farutin A and Misbah C 2013 Analytical and numerical study of three main migration laws for vesicles under flow *Phys. Rev. Lett.* **110** 108104
- [277] Prado G, Farutin A, Misbah C and Bureau L 2015 Viscoelastic transient of confined Red blood cells *Biophys. J.* **108** 2126–36
- [278] Yazdani A Z K, Kalluri M R and Bagchi P 2011 Tank-treading and tumbling frequencies of capsules and red blood cells *Phys. Rev. E* **83** 046305
- [279] Yazdani A and Bagchi P 2013 Influence of membrane viscosity on capsule dynamics in shear flow *J. Fluid Mech.* **718** 569–95
- [280] Zhao M and Bagchi P 2011 Dynamics of microcapsules in oscillating shear flow *Phys. Fluids* **23** 111901
- [281] Cordasco D and Bagchi P 2013 Orbital drift of capsules and red blood cells in shear flow *Phys. Fluids* **25** 091902
- [282] Cordasco D and Bagchi P 2014 Intermittency and synchronized motion of red blood cell dynamics in shear flow *J. Fluid Mech.* **759** 472–88
- [283] Vahidkhah K, Diamond S L and Bagchi P 2014 Platelet dynamics in three-dimensional simulation of whole blood *Biophys. J.* **106** 2529–40
- [284] Vahidkhah K and Bagchi P 2015 Microparticle shape effects on margination, near-wall dynamics and adhesion in a three-dimensional simulation of red blood cell suspension *Soft Matter* **11** 2097–109
- [285] Vahidkhah K, Balogh P and Bagchi P 2016 Flow of red blood cells in stenosed microvessels *Sci. Rep.* **6** 28194
- [286] Jin S, Lewis R R and West D 2005 A comparison of algorithms for vertex normal computation *Vis. Comput.* **21** 71–82
- [287] Bosch W 2000 On the computation of derivatives of Legendre functions *Phys. Chem. Earth Part Solid Earth Geod.* **25** 655–9
- [288] Kolahdouz E and Salac D 2015 Electrohydrodynamics of three-dimensional vesicles: a numerical approach *SIAM J. Sci. Comput.* **37** B473–94
- [289] Rao S S 2005 *The Finite Element Method in Engineering* 4th edn (Boston: Butterworth-Heinemann) (<https://doi.org/10.1016/B978-075067828-5/50004-4>)
- [290] Barrett J, Garcke H and Nürnberg R 2016 Finite element approximation for the dynamics of asymmetric fluidic biomembranes *Math. Comput.* **86** 1037–69
- [291] Deckelnick K, Katz J and Schieweck F 2015 A C^1 -finite element method for the Willmore flow of two-dimensional graphs *Math. Comput.* **84** 2617–43
- [292] Rusu R E 2005 An algorithm for the elastic flow of surfaces *Interfaces Free Boundaries* **7** 229–39
- [293] Barrett J W, Garcke H and Nürnberg R 2016 A stable numerical method for the dynamics of fluidic membranes *Numer. Math.* **134** 783–822
- [294] Rodrigues D S, Ausas R F, Mut F and Buscaglia G C 2015 A semi-implicit finite element method for viscous lipid membranes *J. Comput. Phys.* **298** 565–84
- [295] Bonito A, Nochetto R H and Sebastian Pauletti M 2010 Parametric FEM for geometric biomembranes *J. Comput. Phys.* **229** 3171–88
- [296] Bonito A, Nochetto R H and Pauletti M S 2011 Dynamics of biomembranes: effect of the bulk fluid *Math. Model. Nat. Phenom.* **6** 25–43
- [297] Deuling H J and Helfrich W 1976 Red blood cell shapes as explained on the basis of curvature elasticity *Biophys. J.* **16** 861–8
- [298] Blyth M G and Pozrikidis C 2004 Solution space of axisymmetric capsules enclosed by elastic membranes *Eur. J. Mech. A* **23** 877–92
- [299] Khairy K, JiFoo J and Howard J 2008 Shapes of red blood cells: comparison of 3D confocal images with the bilayer-couple model *Cell. Bioeng.* **1** 173
- [300] Brakke K A 1992 The surface evolver *Exp. Math.* **1** 141–65
- [301] Zihlerl P and Svetina S 2005 Nonaxisymmetric phospholipid vesicles: rackets, boomerangs and starfish *Europhys. Lett.* **70** 690–6

- [302] Sakashita A, Urakami N, Zihelr P and Imai M 2012 Three-dimensional analysis of lipid vesicle transformations *Soft Matter* **8** 8569–81
- [303] Heinrich V, Svetina S and Žekš B 1993 Nonaxisymmetric vesicle shapes in a generalized bilayer-couple model and the transition between oblate and prolate axisymmetric shapes *Phys. Rev. E* **48** 3112–23
- [304] Seifert U 1999 Fluid membranes in hydrodynamic flow fields: formalism and an application to fluctuating quasispherical vesicles in shear flow *Eur. Phys. J. B* **8** 405–15
- [305] Miao L, Lomholt M A and Kleis J 2002 Dynamics of shape fluctuations of quasi-spherical vesicles revisited *Eur. Phys. J. E* **9** 143–60
- [306] Daddi-Moussa-Ider A, Guckenberger A and Gekle S 2016 Particle mobility between two planar elastic membranes: Brownian motion and membrane deformation *Phys. Fluids* **28** 071903
- [307] Daddi-Moussa-Ider A and Gekle S 2016 Hydrodynamic interaction between particles near elastic interfaces *J. Chem. Phys.* **145** 014905
- [308] Daddi-Moussa-Ider A, Lisicki M and Gekle S 2017 Mobility of an axisymmetric particle near an elastic interface *J. Fluid Mech.* **811** 210–33
- [309] Daddi-Moussa-Ider A and Gekle S 2017 Hydrodynamic mobility of a solid particle near a spherical elastic membrane: axisymmetric motion *Phys. Rev. E* **95** 013108
- [310] Dupire J, Abkarian M and Viallat A 2010 Chaotic dynamics of red blood cells in a sinusoidal flow *Phys. Rev. Lett.* **104** 168101
- [311] Aouane O, Thiébaud M, Benyoussef A, Wagner C and Misbah C 2014 Vesicle dynamics in a confined Poiseuille flow: from steady state to chaos *Phys. Rev. E* **90** 033011
- [312] Secomb T W, Skalak R, Özkaya N and Gross J F 1986 Flow of axisymmetric red blood cells in narrow capillaries *J. Fluid Mech.* **163** 405–23
- [313] Li X and Sarkar K 2008 Front tracking simulation of deformation and buckling instability of a liquid capsule enclosed by an elastic membrane *J. Comput. Phys.* **227** 4998–5018
- [314] Bryngelson S H and Freund J B 2016 Buckling and its effect on the confined flow of a model capsule suspension *Rheol. Acta* **55** 451–64
- [315] Kessler S, Finken R and Seifert U 2009 Elastic capsules in shear flow: analytical solutions for constant and time-dependent shear rates *Eur. Phys. J. E* **29** 399–413
- [316] Noguchi H 2010 Dynamic modes of red blood cells in oscillatory shear flow *Phys. Rev. E* **81** 061920
- [317] Farutin A and Misbah C 2012 Rheology of vesicle suspensions under combined steady and oscillating shear flows *J. Fluid Mech.* **700** 362–81
- [318] Matsunaga D, Imai Y, Yamaguchi T and Ishikawa T 2015 Deformation of a spherical capsule under oscillating shear flow *J. Fluid Mech.* **762** 288–301
- [319] Zhu L L, Rabault J and Brandt L 2015 The dynamics of a capsule in a wall-bounded oscillating shear flow *Phys. Fluids* **27** 071902
- [320] Boedec G, Jaeger M and Leonetti M 2013 Sedimentation-induced tether on a settling vesicle *Phys. Rev. E* **88** 010702
- [321] Gounley J and Peng Y 2015 Response and recovery times of elastic and viscoelastic capsules in shear flow *Commun. Comput. Phys.* **17** 1151–68
- [322] Freund J B 2013 The flow of red blood cells through a narrow spleen-like slit *Phys. Fluids* **25** 110807
- [323] Zhu L, Rorai C, Mitra D and Brandt L 2014 A microfluidic device to sort capsules by deformability: a numerical study *Soft Matter* **10** 7705–11
- [324] Zarda P R, Chien S and Skalak R 1977 Elastic deformations of red blood cells *J. Biomech.* **10** 211–21
- [325] Misbah C 2006 Vacillating breathing and tumbling of vesicles under shear flow *Phys. Rev. Lett.* **96** 028104
- [326] Finken R, Kessler S and Seifert U 2011 Micro-capsules in shear flow *J. Phys.: Condens. Matter* **23** 184113
- [327] Vlahovska P M, Young Y-N, Danker G and Misbah C 2011 Dynamics of a non-spherical microcapsule with incompressible interface in shear flow *J. Fluid Mech.* **678** 221–47
- [328] Tran-Son-Tay R, Sutura S P and Rao P R 1984 Determination of red blood cell membrane viscosity from rheoscopic observations of tank-treading motion *Biophys. J.* **46** 65–72
- [329] Abkarian M, Faivre M and Viallat A 2007 Swinging of red blood cells under shear flow *Phys. Rev. Lett.* **98** 188302
- [330] Yazdani A Z K and Bagchi P 2011 Phase diagram and breathing dynamics of a single red blood cell and a biconcave capsule in dilute shear flow *Phys. Rev. E* **84** 026314
- [331] Fischer T M and Korzeniewski R 2015 Angle of inclination of tank-treading red cells: dependence on shear rate and suspending medium *Biophys. J.* **108** 1352–60
- [332] Laumann M, Bauknecht P, Gekle S, Kienle D and Zimmermann W 2016 Cross-stream migration of asymmetric particles driven by oscillating shear *Europhys. Lett.* **117** 44001
- [333] Farutin A and Misbah C 2011 Symmetry breaking of vesicle shapes in Poiseuille flow *Phys. Rev. E* **84** 011902
- [334] Danker G, Vlahovska P M and Misbah C 2009 Vesicles in Poiseuille flow *Phys. Rev. Lett.* **102** 148102
- [335] Coupier G, Farutin A, Minetti C, Podgorski T and Misbah C 2012 Shape diagram of vesicles in Poiseuille flow *Phys. Rev. Lett.* **108** 178106
- [336] Abkarian M, Faivre M, Horton R, Smistrup K, Best-Popescu C A and Stone H A 2008 Cellular-scale hydrodynamics *Biomed. Mater.* **3** 034011
- [337] Tomaiuolo G, Lanotte L, Ghigliotti G, Misbah C and Guido S 2012 Red blood cell clustering in Poiseuille microcapillary flow *Phys. Fluids* **24** 051903
- [338] Brust M *et al* 2014 The plasma protein fibrinogen stabilizes clusters of red blood cells in microcapillary flows *Sci. Rep.* **4** 4348
- [339] Bryngelson S H and Freund J B 2016 Capsule-train stability *Phys. Rev. Fluids* **1** 033201
- [340] Fedosov D A, Caswell B, Popel A S and Karniadakis G E 2010 Blood flow and cell-free layer in microvessels *Microcirculation* **17** 615–28
- [341] Freund J B and Orescanin M M 2011 Cellular flow in a small blood vessel *J. Fluid Mech.* **671** 466–90
- [342] Lei H, Fedosov D A, Caswell B and Karniadakis G E 2013 Blood flow in small tubes: quantifying the transition to the non-continuum regime *J. Fluid Mech.* **722** 214–39
- [343] Freund J B and Shapiro B 2012 Transport of particles by magnetic forces and cellular blood flow in a model microvessel *Phys. Fluids* **24** 051904
- [344] Zhao H and Shaqfeh E S G 2011 Shear-induced platelet margination in a microchannel *Phys. Rev. E* **83** 061924
- [345] Reasor D A, Mehrabadi M, Ku D N and Aidun C K 2012 Determination of critical parameters in platelet margination *Ann. Biomed. Eng.* **41** 238–49
- [346] Takeishi N, Imai Y, Nakaaki K, Yamaguchi T and Ishikawa T 2014 Leukocyte margination at arteriole shear rate *Physiol. Rep.* **2** e12037
- [347] Fitzgibbon S, Spann A P, Qi Q M and Shaqfeh E S G 2015 *In vitro* measurement of particle margination in the microchannel flow: effect of varying hematocrit *Biophys. J.* **108** 2601–8
- [348] Gekle S 2016 Strongly accelerated margination of active particles in blood flow *Biophys. J.* **110** 514–20

- [349] Krüger T 2016 Effect of tube diameter and capillary number on platelet margination and near-wall dynamics *Rheol. Acta* **55** 511–26
- [350] Bächer C, Schrack L and Gekle S 2017 Clustering of microscopic particles in constricted blood flow *Phys. Rev. Fluids* **2** 013102
- [351] Lipowsky H H 2013 *In vivo* studies of blood rheology in the microcirculation in an *in vitro* world: past, present and future *Biorheology* **50** 3–16
- [352] Kumar A and Graham M D 2011 Segregation by membrane rigidity in flowing binary suspensions of elastic capsules *Phys. Rev. E* **84** 066316
- [353] Kumar A and Graham M D 2012 Mechanism of margination in confined flows of blood and other multicomponent suspensions *Phys. Rev. Lett.* **109** 108102
- [354] Kumar A, Henríquez Rivera R G and Graham M D 2014 Flow-induced segregation in confined multicomponent suspensions: effects of particle size and rigidity *J. Fluid Mech.* **738** 423–62
- [355] Matsunaga D, Imai Y, Omori T, Ishikawa T and Yamaguchi T 2014 A full GPU implementation of a numerical method for simulating capsule suspensions *J. Biomech. Sci. Eng.* **9** 14-00039
- [356] Lac E and Barthès-Biesel D 2008 Pairwise interaction of capsules in simple shear flow: three-dimensional effects *Phys. Fluids* **20** 040801
- [357] Doddi S K and Bagchi P 2008 Effect of inertia on the hydrodynamic interaction between two liquid capsules in simple shear flow *Int. J. Multiph. Flow* **34** 375–92
- [358] Le D-V and Chiam K-H 2011 Hydrodynamic interaction between two nonspherical capsules in shear flow *Phys. Rev. E* **84** 056322
- [359] Püger B, Kaoui B and Harting J 2014 Interplay of inertia and deformability on rheological properties of a suspension of capsules *J. Fluid Mech.* **751** 725–45
- [360] Ghigliotti G, Selmi H, Asmi L E and Misbah C 2012 Why and how does collective red blood cells motion occur in the blood microcirculation? *Phys. Fluids* **24** 101901
- [361] Shen Z, Coupier G, Kaoui B, Polack B, Harting J, Misbah C and Podgorski T 2016 Inversion of hematocrit partition at microfluidic bifurcations *Microvasc. Res.* **105** 40–6
- [362] Thiébaud M and Misbah C 2013 Rheology of a vesicle suspension with finite concentration: a numerical study *Phys. Rev. E* **88** 062707
- [363] Thiébaud M, Shen Z, Harting J and Misbah C 2014 Prediction of anomalous blood viscosity in confined shear flow *Phys. Rev. Lett.* **112** 238304
- [364] Quaife B and Biros G 2015 High-order adaptive time stepping for vesicle suspensions with viscosity contrast *Proc. IUTAM* **16** 89–98
- [365] Quaife B and Biros G 2016 Adaptive time stepping for vesicle suspensions *J. Comput. Phys.* **306** 478–99
- [366] Krüger T, Gross M, Raabe D and Varnik F 2013 Crossover from tumbling to tank-treading-like motion in dense simulated suspensions of red blood cells *Soft Matter* **9** 9008–15
- [367] Takeishi N, Imai Y, Yamaguchi T and Ishikawa T 2015 Flow of a circulating tumor cell and red blood cells in microvessels *Phys. Rev. E* **92** 063011
- [368] Wang W, Diacovo T G, Chen J, Freund J B and King M R 2013 Simulation of platelet, thrombus and erythrocyte hydrodynamic interactions in a 3D arteriole with *in vivo* comparison *PLoS One* **8** e76949
- [369] Freund J B and Vermot J 2014 The Wall-stress footprint of blood cells flowing in microvessels *Biophys. J.* **106** 752–62
- [370] Bransky A, Korin N, Nemirovski Y and Dinnar U 2007 Correlation between erythrocytes deformability and size: a study using a microchannel based cell analyzer *Microvasc. Res.* **73** 7–13
- [371] Franco R S, Estela Puchulu-Campanella M, Barber L A, Palascak M B, Joiner C H, Low P S and Cohen R M 2013 Changes in the properties of normal human red blood cells during *in vivo* aging *Am. J. Hematol.* **88** 44–51
- [372] Malka R, Delgado F F, Manalis S R and Higgins J M 2014 *In vivo* volume and hemoglobin dynamics of human red blood cells *PLoS Comput. Biol.* **10** e1003839
- [373] Weinbaum S, Tarbell J M and Damiano E R 2007 The structure and function of the endothelial glycocalyx layer *Annu. Rev. Biomed. Eng.* **9** 121–67
- [374] Alphonsus C S and Rodseth R N 2014 The endothelial glycocalyx: a review of the vascular barrier *Anaesthesia* **69** 777–84
- [375] Steigmann D J and Ogden R W 1999 Elastic surface—substrate interactions *Proc. R. Soc.* **455** 437–74
- [376] Simo J C and Fox D D 1989 On a stress resultant geometrically exact shell model. Part I: formulation and optimal parametrization *Comput. Methods Appl. Mech. Eng.* **72** 267–304
- [377] Press W H, Teukolsky S A, Vetterling W T and Flannery B P 2007 *Numerical Recipes 3rd Edition: The Art of Scientific Computing* 3rd edn (New York: Cambridge University Press)
- [378] Evans E and Fung Y-C 1972 Improved measurements of the erythrocyte geometry *Microvasc. Res.* **4** 335–47

Publication 3

**A boundary integral method with volume-changing
objects for ultrasound-triggered margination of
microbubbles**

by

A. Guckenberger and S. Gekle

Journal of Fluid Mechanics **836**, pp. 952–997 (2018)

DOI: [10.1017/jfm.2017.836](https://doi.org/10.1017/jfm.2017.836)

Copyright by Cambridge University Press. Reprinted with permission.

A boundary integral method with volume-changing objects for ultrasound-triggered margination of microbubbles

Achim Guckenberg^{1,†} and Stephan Gekle¹

¹Biofluid Simulation and Modeling, Fachbereich Physik, Universität Bayreuth, 95440 Bayreuth, Germany

(Received 1 February 2017; revised 11 August 2017; accepted 14 November 2017)

A variety of numerical methods exist for the study of deformable particles in dense suspensions. None of the standard tools, however, currently include volume-changing objects such as oscillating microbubbles in three-dimensional periodic domains. In the first part of this work, we develop a novel method to include such entities based on the boundary integral method. We show that the well-known boundary integral equation must be amended with two additional terms containing the volume flux through the bubble surface. We rigorously prove the existence and uniqueness of the solution. Our proof contains as a subset the simpler boundary integral equation without volume-changing objects (such as red blood cell or capsule suspensions) which is widely used but for which a formal proof in periodic domains has not been published to date. In the second part, we apply our method to study microbubbles for targeted drug delivery. The ideal drug delivery agent should stay away from the biochemically active vessel walls during circulation. However, upon reaching its target it should attain a near-wall position for efficient drug uptake. Though seemingly contradictory, we show that lipid-coated microbubbles in conjunction with a localized ultrasound pulse possess precisely these two properties. This ultrasound-triggered margination is due to hydrodynamic interactions between the red blood cells and the oscillating lipid-coated microbubbles which alternate between a soft and a stiff state. We find that the effect is very robust, existing even if the duration in the stiff state is more than three times lower than the opposing time in the soft state.

Key words: blood flow, boundary integral methods, capsule/cell dynamics

1. Introduction

Margination refers to the effect that stiff objects such as platelets, leucocyte or stiff synthetic microparticles preferentially travel along the walls in suspension flows, e.g. in the vascular system (Freund 2007; Freund & Shapiro 2012; Namdee *et al.* 2013; Fedosov & Gompper 2014; Kumar, Henríquez Rivera & Graham 2014; D’Apolito *et al.* 2015; Fitzgibbon *et al.* 2015; Müller, Fedosov & Gompper 2015;

[†] Email address for correspondence: achim.guckenberger@uni-bayreuth.de

Vahidkhan & Bagchi 2015; Gekle 2016; Mehrabadi, Ku & Aidun 2016; Müller, Fedosov & Gompper 2016; Bächer, Schrack & Gekle 2017). This is a result of softer particles such as red blood cells (RBCs), drops or capsules migrating towards the centre away from the boundaries (Aarts *et al.* 1988; Fedosov *et al.* 2011; Farutin & Misbah 2013; Mukherjee & Sarkar 2014; Singh, Li & Sarkar 2014; Katanov, Gompper & Fedosov 2015; Qi & Shaqfeh 2017). A similar effect occurs not only in Poiseuille but also in bounded shear flow due to the image stresslet generated by the presence of the wall (Smart & Leighton 1991; Mukherjee & Sarkar 2013; Singh *et al.* 2014). Migration behaviour has implications for targeted drug delivery as efficient drug uptake is only possible if the drug delivery agents are positioned close to the walls of the blood vessels near the target organ (Rychak *et al.* 2007; Kooiman *et al.* 2014; Lammertink *et al.* 2015). Accordingly, it advocates the use of stiff particles as drug delivery agents. Yet, during the transport phase towards the target the agents should remain buried in the vessel interior to avoid high shear stress and premature biochemical interaction with the endothelial wall. This would speak in favour of using soft particles. Being able to combine both seemingly contradicting properties might lead to a very effective drug administration protocol.

One of the most promising approaches for targeted drug delivery is the use of coated microbubbles (ultrasound contrast agents, see e.g. Klibanov 2002; Lindner 2004; Unnikrishnan & Klibanov 2012; Faez *et al.* 2013) to actively and selectively enhance drug uptake (Ferrara, Pollard & Borden 2007; Couture *et al.* 2014; Kooiman *et al.* 2014; Owen *et al.* 2014; Unger *et al.* 2014; Lammertink *et al.* 2015; Kotopoulos *et al.* 2016). In the simplest scenario, microbubbles are injected together with the actual drug suspension and an ultrasound pulse is applied at the target organ which makes the bubbles oscillate periodically. This strongly enhances drug uptake due to the forces that the oscillating microbubbles exert on nearby endothelial cells (Kooiman *et al.* 2014). More recently, there have also been numerous attempts to use the bubbles themselves as drug carriers by biochemically attaching active drug substances e.g. on the bubble surface which are released due to an ultrasound pulse at the target organ (Couture *et al.* 2014; Kooiman *et al.* 2014; Unger *et al.* 2014).

Microbubbles coated with a phospholipid layer (Ferrara *et al.* 2007; Faez *et al.* 2013) are usually rather soft deformable objects in the absence of ultrasound (Marmottant *et al.* 2005; Overvelde *et al.* 2010). They would therefore be expected to be buried inside the blood stream akin to RBCs, as also concluded from *in vivo* experiments (Lindner *et al.* 2002). This allows for their safe transport, but makes them at first sight unsuitable candidates for drug delivery. Yet, during ultrasound exposure bubble expansion beyond a critical radius R_{soft} in the low-pressure phase causes stiffening of the bubble shell (Marmottant *et al.* 2005; Rychak *et al.* 2006; Overvelde *et al.* 2010) which might induce margination. On the other hand, shrinking in the high-pressure phase leads to buckling (softening) of the phospholipid shell (Sijl *et al.* 2011). Since the bubbles thus rapidly oscillate between a soft and a stiff state, it is *a priori* unclear if and to what extent such objects would show margination.

We study this question by means of three-dimensional (3-D) numerical simulations. Many methodologies are available for computing flows with hard or deformable particles, provided that the volume of each particle remains unchanged. These methods are able to accurately reproduce the margination of stiff particles which originates from their hydrodynamic interaction with the surrounding RBCs. Here however, we require a method that can handle deformable volume-changing microbubbles together with RBCs in a periodic channel. Such a method is currently not available. The first part of our paper therefore deals with the development of our volume-changing object boundary integral method (VCO-BIM) in periodic domains. Compared

to existing boundary integral formulations we find that additional terms occur which account for the volume fluxes across the bubble surfaces. We prove mathematically that the resulting Fredholm integral equation has exactly one solution. The proof and the method hold for an arbitrary amount of volume-changing objects and capsule-like entities (RBCs, vesicles, drops, etc.) with arbitrary viscosity ratios. We give the proof in some detail and generality since a number of recent publications (e.g. Loewenberg & Hinch 1996; Zinchenko & Davis 2000; Lindbo & Tornberg 2010; Zhao *et al.* 2010) derive and use boundary integral equations in periodic domains (without bubbles), but a proof of uniqueness and existence of their solution has not been established to date. We also note that very occasionally boundary integral methods have been used with expanding bubbles (Power 1992, 1996; Power & de Power 1992; Nie *et al.* 2002), but these attempts have been restricted to infinite domains, making them unsuitable for blood flow simulations.

In the second part we use our VCO-BIM to find that microbubbles indeed show what we call ultrasound-triggered margination (UTM): Ultrasound exposure causes rapid and reliable margination of otherwise soft microbubbles. UTM is caused by the special properties of the lipid bubble shell and their interaction with the red blood cells. The effect is robust and rapidly drives microbubbles towards the endothelial wall even if the ‘stiff time’ (i.e. the time during which the bubble size is larger than the critical radius R_{soft}) is more than three times smaller than the opposing ‘soft time’. Phospholipid-coated microbubbles are thus shown to simultaneously possess two highly desirable, but seemingly contradicting properties: safe passage in the low shear zones of the vessel interior and near-endothelial position at the target organ, the latter being easily controllable by ultrasound exposure.

2. The volume-changing object boundary integral method

Obtaining numerical solutions of the Stokes equation via boundary integral methods has a long history starting with the publication by Youngren & Acrivos (1975). Well established is the direct method that is suitable for the simulation of incompressible deformable particles with viscosity ratios $\lambda \neq 0, \infty$ in an infinite domain (Pozrikidis 2001). Rigorous proofs of existence and uniqueness of the solution exist (e.g. Odqvist 1930; Ladyzhenskaya 1969; Pozrikidis 1992; Kohr & Pop 2004). They are enabled by the fact that the equation is a Fredholm integral equation of the second kind, allowing for the application of the Fredholm theory (e.g. Kress 2014). If deformable bubbles ($\lambda = 0$) with volume changes are included, only the method in an infinite domain but no complete proof exists (Nie *et al.* 2002).

Indirect boundary integral methods solve a (typically second kind) equation for an auxiliary field, from which the physical velocity can be computed afterwards. Such a formulation has been used to model expanding bubbles in an infinite domain with established existence and uniqueness results for the solution (Power 1992; Power & de Power 1992; Power 1996). Another indirect variant is the completed double-layer boundary integral method (CDLBIEM) tailored for simulating rigid objects ($\lambda = \infty$), with proofs in infinite domains being well established (e.g. Power & Miranda 1987; Karrila & Kim 1989; Kim & Karrila 1991; Kohr & Pop 2004).

Without bubbles, equations in periodic domains for direct (e.g. Hasimoto 1959; Zick & Homsy 1982; Loewenberg & Hinch 1996; Zinchenko & Davis 2000; Zhao *et al.* 2010; Freund & Orescanin 2011; Freund 2013; Freund & Vermot 2014) and indirect methods (e.g. Fan, Phan-Thien & Zheng 1998; Lindbo & Tornberg 2010; Zhao &

Shaqfeh 2011; Freund & Shapiro 2012; Zhao, Shaqfeh & Narsimhan 2012; Wang *et al.* 2013; af Klinteberg & Tornberg 2014, 2016; Fitzgibbon *et al.* 2015; Spann *et al.* 2016) are well known. The general geometry Ewald-like method (GGEM) also uses an indirect formulation to make the equations amenable to an accelerated computation. This was mostly used for problems where two of the three spatial directions are periodic (Hernández-Ortiz, de Pablo & Graham 2007; Pranay *et al.* 2010; Kumar & Graham 2011, 2012; Kumar *et al.* 2014; Zhu, Rabault & Brandt 2015; Sinha & Graham 2015, 2016; Zhao *et al.* 2017). Yet, statements regarding existence and uniqueness of the solution are lacking so far. This may be of some concern since some well-known proofs for the infinite domain (e.g. Pozrikidis 1992, chap. 4.5) require an auxiliary field that would violate the conservation of the ambient fluid if applied to periodic domains, even if all individual objects are volume conserving.

The purpose of the present section is thus twofold. First, we show that the presence of volume-changing objects in periodic domains leads to new non-trivial terms in the equation for the direct boundary integral method. Second, we rigorously prove the existence and uniqueness of the solution of this periodic boundary integral equation employed in the present work and in other publications as listed above.

For this, we start by deriving the Fredholm boundary integral (FBI) equation for 3-D periodic domains with deformable capsule-like ($\lambda \neq 0, \infty$) volume-conserving particles and deformable volume-changing objects such as bubbles. The final result for N_O objects O_k in a periodic domain with unit cell Γ of volume V_Γ is

$$\begin{aligned}
 u_j(\mathbf{x}_0) = & \frac{2}{1 + \lambda_{O_k}} \left[\langle u_j \rangle_\Gamma - \frac{1}{8\pi\mu} \sum_{q=1}^{N_O} (\mathcal{N}_{\partial O_q} \mathbf{F})_j(\mathbf{x}_0) \right. \\
 & + \frac{1}{8\pi} \sum_{q=1}^{N_O} (1 - \lambda_{O_q}) (\mathcal{K}_{\partial O_q} \mathbf{u})_j(\mathbf{x}_0) + \frac{1}{V_\Gamma} \sum_{q=1}^{N_B} Q_{B_q} \chi_j^{(B_q)} \left. \right] \\
 & - \frac{1 - \lambda_{O_k}}{1 + \lambda_{O_k}} z_j^{(k)}(\mathbf{x}_0) \left[\oint_{\partial O_k} u_l(\mathbf{x}) n_l(\mathbf{x}) \, dS(\mathbf{x}) - Q_{O_k} \right], \\
 & \mathbf{x}_0 \in \partial O_k, \quad k = 1, \dots, N_O, \quad j = 1, 2, 3.
 \end{aligned} \tag{2.1}$$

This equation forms the basis of our VCO-BIM. Here, k is the index of the object on whose surface the evaluation point \mathbf{x}_0 is located. Moreover, \mathbf{u} on the left-hand side is the velocity on the surface ∂O_k of the k th object, $\langle u_j \rangle_\Gamma$ the prescribed average flow through Γ and μ the dynamic viscosity. λ_{O_k} is an effective viscosity ratio for the k th object defined in (2.13) below. Furthermore, \mathbf{F} is the outer traction in the case of bubbles and otherwise the jump of the traction across the interfaces. $\mathcal{N}_{\partial O_q} \mathbf{F}$ and $\mathcal{K}_{\partial O_q} \mathbf{u}$ are the usual single- and double-layer integrals, respectively, evaluated with the Green's functions for a 3-D periodic domain (given by (2.11) and (2.12)). The second term on the second line is the first novel contribution from the N_B volume-changing bubbles and contains the centroid $\chi^{(B_q)}$ as well as the volume flux Q_{B_q} into or out of the bubble. The latter is a possibly time-dependent, prescribed quantity chosen such that the sum of all fluxes is zero. Finally, the last line is essentially a part of the so-called Wielandt deflation (Kim & Karrila 1991) where z^k is a known function. Again, for bubbles a new term due to the flux Q_{O_k} appears. As we will show, the last line is imperative for bubbles ($\lambda_{O_k} = 0$) as it ensures uniqueness, contrary to objects with $\lambda_{O_k} \neq 0$ where it is merely an optional accelerator for the numerical procedure.

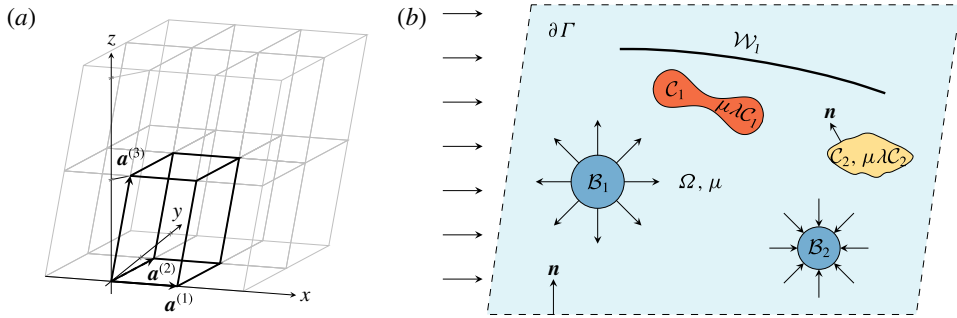


FIGURE 1. (Colour online) (a) Example of a triclinic unit cell Γ (thick lines), together with 11 replicas (thin grey lines). In this example, the two basis vectors $\mathbf{a}^{(1)}$ and $\mathbf{a}^{(2)}$ lie in the x - y -plane, but $\mathbf{a}^{(2)}$ is not parallel to the y -axis. (b) Two-dimensional sketch of the general three-dimensional problem. $\Gamma \subset \mathbb{R}^3$ contains the whole unit cell (everything within the dashed border $\partial\Gamma$). $\Omega \subset \Gamma$ is the ambient fluid with dynamic viscosity μ (light blue). As an example, two capsule-like entities ($\mathcal{C}_1, \mathcal{C}_2$), two volume-changing bubbles ($\mathcal{B}_1, \mathcal{B}_2$) and a wall \mathcal{W}_1 are shown. The normal vectors always point into Ω . The arrows on the left represent an imposed flow.

After introducing the system components in § 2.1, we use § 2.2 to derive the general boundary integral equation including volume-changing bubbles in periodic domains. Section 2.3 then turns the boundary integral equation into the numerically solvable Fredholm boundary integral equation (2.1) and, most importantly, rigorously proves existence and uniqueness of the solution. This proof includes the periodic BIM equation without bubbles which is solved numerically by a number of existing codes (e.g. Loewenberg & Hinch 1996; Zinchenko & Davis 2000; Lindbo & Tornberg 2010; Zhao *et al.* 2010). Finally, § 2.4 gives some details about how we model oscillating bubbles and § 2.5 outlines the numerical implementation of our method. Symbols are defined and explained on their first use, but are also listed in appendix A as a quick reference.

2.1. System description

2.1.1. Periodicity and the unit cell

We mostly consider flows in 3-D periodic systems. To this end, we introduce a triclinic unit cell $\Gamma \subset \mathbb{R}^3$ that is spanned by the basis $\{\mathbf{a}^{(1)}, \mathbf{a}^{(2)}, \mathbf{a}^{(3)}\}$ as shown in figure 1(a). The three basis vectors $\mathbf{a}^{(i)} \in \mathbb{R}^3$, $i = 1, 2, 3$, define a right-handed coordinate system. In the most general case they are not required to be of unit length or orthogonal and might depend on time, although the latter will not be explicitly considered here. Nevertheless, even static but skewed bases can be useful in practice, for example to model so-called deterministic lateral displacement devices (Huang *et al.* 2004; Krüger, Holmes & Coveney 2014; Zhang *et al.* 2015). The surface $\partial\Gamma$ of the unit cell is not included in the open set Γ . We will denote the volume by V_Γ .

To cast the concept of periodicity into mathematical terms, we introduce by

$$\mathbf{X}^{(\alpha)} := \alpha_1 \mathbf{a}^{(1)} + \alpha_2 \mathbf{a}^{(2)} + \alpha_3 \mathbf{a}^{(3)} \tag{2.2}$$

some grid vector with some grid index $\alpha \in \mathbb{Z}^3$. The unit cell Γ is assumed to be replicated infinitely throughout space by displacing it with all possible grid vectors.

We will show in appendix B that actually any of these boxes with any origin can be chosen as Γ . Furthermore, a general function $f: \mathbb{R}^3 \rightarrow \mathbb{R}$ is said to be periodic if it satisfies

$$f(\mathbf{x} + \mathbf{X}^{(\alpha)}) = f(\mathbf{x}) \quad \forall \mathbf{x} \in \mathbb{R}^3 \text{ and } \forall \alpha \in \mathbb{Z}^3. \quad (2.3)$$

The reciprocal (Fourier) unit cell is spanned by the reciprocal basis vectors $\mathbf{b}^{(j)} \in \mathbb{R}^3$, $j = 1, 2, 3$, defined by $\mathbf{a}^{(i)} \cdot \mathbf{b}^{(j)} = 2\pi\delta_{ij}$. Some general Fourier grid vector is then denoted by

$$\mathbf{k}^{(\kappa)} := \kappa_1 \mathbf{b}^{(1)} + \kappa_2 \mathbf{b}^{(2)} + \kappa_3 \mathbf{b}^{(3)}, \quad (2.4)$$

with $\kappa \in \mathbb{Z}^3$.

2.1.2. System components

The general system considered in this section is depicted in figure 1(b). We introduce the ambient fluid $\Omega \subset \Gamma$ which represents the open set of the space within the unit cell Γ but outside of any immersed object. The fluid is assumed to have a constant dynamic viscosity μ and is governed by the usual Stokes equation and incompressibility condition. Furthermore, we have N_O objects $O_k \subset \Gamma$, $k = 1, \dots, N_O$ in the unit cell as further detailed below. For now we assume that all of them are completely located within Γ and relax this requirement later on (which is required for dynamic simulations of dense suspensions, see appendix B). No object shall overlap with or contain any other object. The 2-D surfaces of the objects embedded in 3-D space will be denoted by the symbol ‘ ∂ ’, e.g. ∂O_k . We also assign a velocity $\mathbf{u}(\mathbf{x})$ to each point $\mathbf{x} \in \bar{\Gamma}$, where the bar represents the closure of the set.

Regarding the immersed objects, we consider three different types. First, deformable particles that can be used to mimic ‘capsule-like’ entities (such as vesicles, drops or red blood cells). The i th capsule will be denoted by the open set $C_k \subset \Gamma$ with $k = 1, \dots, N_C$, where N_C are the number of capsules. Their inside is filled with some Stokesian fluid that has a dynamic viscosity of $\mu\lambda_{C_k}$, where $\lambda_{C_k} > 0$ is the viscosity ratio between the inner and outer fluids. Their volume is conserved and as such the net flux Q_{C_k} into or out of the capsules is zero. Deformations are governed by the jump of the traction $\Delta \mathbf{f}$ across their surfaces ∂C_k . This traction jump is calculated from an appropriate constitutive law that determines the actual object properties. The velocity across the interfaces is assumed to be continuous.

Second, $N_{\mathcal{W}}$ non-closed objects \mathcal{W}_k , $k = 1, \dots, N_{\mathcal{W}}$, may exist that can be used to model deformable (fixed traction jump) or rigid (prescribed velocity) walls. Note that we set $\mathcal{W}_k = \partial \mathcal{W}_k$, i.e. these objects do not have some ‘inside’. The velocity across the walls is assumed to be continuous.

Third, we introduce our novel ingredient, N_B bubble-like objects \mathcal{B}_k , $k = 1, \dots, N_B$ whose volumes are allowed to change. Contrary to capsules their inside is filled with some compressible fluid such as air that has a much lower viscosity than the ambient fluid. Therefore, the detailed flow field inside the bubbles will not be considered and, instead of the Stokes equations, the essential model assumption for this inner fluid is simply

$$\nabla \cdot \mathbf{u}(\mathbf{x}) = c_k, \quad \mathbf{x} \in \mathcal{B}_k, \quad k = 1, \dots, N_B. \quad (2.5)$$

Here, c_k are some prescribed constants, meaning that the particles expand or contract homogeneously over their whole interior and that any inhomogeneities such as eddies are considered to vanish instantaneously. But note that c_k may depend on the time allowing for oscillating bubbles. As shown below (2.31), c_k is related to the net flux $Q_{\mathcal{B}_k}$ into or out of the bubble by $c_k = Q_{\mathcal{B}_k}/V_{\mathcal{B}_k}$, where $V_{\mathcal{B}_k}$ is the k th bubble’s volume. Moreover, the surface deformation of the bubbles is governed by the prescribed traction at the outside of the surfaces, as further elaborated in § 2.4.

For convenience, some arbitrary object of any type will be denoted by O_k . We further define $N_O := N_C + N_B + N_W$ as well as $O := \mathcal{C} \cup \mathcal{B} \cup \mathcal{W}$ where $\mathcal{C}/\mathcal{B}/\mathcal{W}$ mean the unions of all capsules/bubbles/walls. All in all, we have $\Gamma = \Omega \cup \bar{O}$. Furthermore, unit normal vectors are denoted by the symbol \mathbf{n} . We choose the convention that the normal vector of every capsule and bubble points into Ω . The normal vector of walls may point in any of the two possible directions. The normal vector on $\partial\Gamma$ shall point into Ω .

2.2. Deriving the boundary integral equation with volume-changing objects

2.2.1. The general boundary integral equation

In order to introduce the required notation and equations for later on, we start from the standard Stokes and continuity equations for flows at low Reynolds numbers which corresponds to the typical situation encountered in the microcirculation (Misbah 2012; Freund 2014):

$$-\nabla P(\mathbf{x}) + \mu \nabla^2 \mathbf{u}(\mathbf{x}) = 0, \tag{2.6a}$$

$$\nabla \cdot \mathbf{u}(\mathbf{x}) = 0, \tag{2.6b}$$

for $\mathbf{x} \in \Omega$. Here, P is the pressure, ∇^2 the usual 3-D Laplace operator and \mathbf{u} the fluid velocity. The inside of capsules is governed by analogous expressions, but with a different viscosity in general. Body forces such as gravity will be neglected, but can be easily incorporated via an effective pressure (Pozrikidis 1992, equation (1.2.9)).

Next, we introduce the traction \mathbf{f} acting on the surface ∂O_k of some object O_k via

$$\mathbf{f}_i(\mathbf{x}) := \sigma_{ij}(\mathbf{x})n_j(\mathbf{x}), \quad \mathbf{x} \in \partial O_k, \quad i = 1, 2, 3, \tag{2.7}$$

where the fluid stress tensor is defined by

$$\sigma_{ij} := -P\delta_{ij} + \mu \left(\frac{\partial u_i}{\partial x_j} + \frac{\partial u_j}{\partial x_i} \right), \quad \mathbf{x} \in \Omega, \quad i, j = 1, 2, 3. \tag{2.8}$$

Summation over repeated Cartesian components is implied throughout this work. One needs to take the limit of the stress tensor onto the surface for the evaluation of (2.7). This limit can be taken from both sides, leading to the traction on the outside (\mathbf{f}^+ , limit from Ω onto the surface) and the inside (\mathbf{f}^- , defined with the outer normal vector) of a closed object's surface. The difference is the traction jump

$$\Delta \mathbf{f}(\mathbf{x}) := \mathbf{f}^+(\mathbf{x}) - \mathbf{f}^-(\mathbf{x}), \quad \mathbf{x} \in \partial O_k, \tag{2.9}$$

which is the major quantity coupling the flow with the surface mechanics. For a wall, $\Delta \mathbf{f}$ is the difference of the tractions on its two sides.

Equations (2.6) can be efficiently and accurately solved via the boundary integral method (Pozrikidis 1992, 2001; Freund 2014). Assuming that all objects are located within the unit cell Γ (for objects crossing the unit cell boundary, see appendix B), one can derive the boundary integral (BI) equation (compare Pozrikidis 1992, chap. 2.3, pp. 37 and 143)

$$\begin{aligned} u_j(\mathbf{x}_0) = & -\frac{1}{8\pi\mu} \sum_{q=1}^{N_O} (\mathcal{N}_{\partial O_q} \mathbf{F})_j(\mathbf{x}_0) + \frac{1}{8\pi} \sum_{q=1}^{N_O} (1 - \lambda_{O_q}) (\mathcal{K}_{\partial O_q} \mathbf{u})_j(\mathbf{x}_0) \\ & - \frac{1}{8\pi\mu} (\mathcal{N}_{\partial \Gamma} \mathbf{f})_j(\mathbf{x}_0) + \frac{1}{8\pi} (\mathcal{K}_{\partial \Gamma} \mathbf{u})_j(\mathbf{x}_0), \quad \mathbf{x}_0 \in \Omega, \quad j = 1, 2, 3. \end{aligned} \tag{2.10}$$

Note that the evaluation point \mathbf{x}_0 is in the ambient fluid and not within any object or on any surface. The single-layer integral (or single-layer potential) over some surface S is defined as

$$(\mathcal{N}_S \mathbf{f})_j(\mathbf{x}_0) := \int_S f_i(\mathbf{x}) G_{ij}(\mathbf{x}, \mathbf{x}_0) \, dS(\mathbf{x}), \quad j = 1, 2, 3, \tag{2.11}$$

and the double-layer integral is

$$(\mathcal{K}_S \mathbf{u})_j(\mathbf{x}_0) := \int_S u_i(\mathbf{x}) T_{ijl}(\mathbf{x}, \mathbf{x}_0) n_l(\mathbf{x}) \, dS(\mathbf{x}), \quad j = 1, 2, 3. \tag{2.12}$$

These integrals exist for $\mathbf{x}_0 \in \mathbb{R}^3$, notably in the improper sense if $\mathbf{x}_0 \in S$ or if \mathbf{x}_0 is on some periodic image of S (Kress 2014, chap. 6). The improper double-layer integral is in this case sometimes also denoted as a principal value integral (Pozrikidis 1992, p. 27).

\mathbf{F} is a ‘unified traction’ which represents either the traction \mathbf{f}^+ on the outside in case of the bubbles, or the traction jump $\Delta \mathbf{f}$ in the case of the capsules and the walls. For notational convenience we have abbreviated $\mathbf{f} := \mathbf{f}^+$ in the last line of (2.10). Moreover, an ‘effective’ viscosity ratio is defined as

$$\lambda_{O_q} := \begin{cases} \lambda_{C_q} & \text{if } O_q \text{ is a capsule } C_q, \\ 1 & \text{if } O_q \text{ is a wall } \mathcal{W}_q, \\ 0 & \text{if } O_q \text{ is a bubble } \mathcal{B}_q, \end{cases} \quad \text{for } q = 1, \dots, N_O. \tag{2.13}$$

Thus, if $\lambda_{O_q} = 1$, the corresponding terms in the second sum are always absent (regardless of the value of $\mathcal{K}_{\partial O_q} \mathbf{u}$).

The wall contributions in (2.10) can be derived by considering as a starting point an object with a finite thickness. Taking the limit as the thickness tends to zero, integrals that previously went over the distinct opposing sides of the wall now go over essentially the same surface, except that the integrands are still evaluated on their respective sides. The normal vectors on these two sides are perfectly antiparallel. Additionally using the continuity of the velocity, one finds that the double-layer integral drops out (represented by $\lambda_{\mathcal{W}} = 1$). Furthermore, for the single-layer integral we have $\int_{\partial \mathcal{W}^+ \cup \partial \mathcal{W}^-} f_i^+ G_{ij} \, dS = \int_{\partial \mathcal{W}^+} (f_i^+ - f_i^-) G_{ij} \, dS \equiv \int_{\partial \mathcal{W}} \Delta f_i G_{ij} \, dS$ where $\partial \mathcal{W}^\pm$ denotes the two sides of the zero-thickness wall, and (2.9) was used to introduce the traction jump (Pozrikidis 1992, p. 37). The integration $\int_{\partial \mathcal{W}}$ goes over only one side of the wall. Walls spanning through the whole domain Γ can be introduced by a similar limiting procedure.

Note that the BI equation (2.10) is actually valid for any Green’s functions, no matter if periodic or not. However, in order to be able to compute anything in practice, they should follow the general symmetries of the system. As we want to implement a periodic domain, we will next introduce the appropriate expressions.

2.2.2. Appropriate Green’s functions for a 3-D periodic domain

Green’s functions G_{ij} and p_j for the velocity and pressure, respectively, are obtained by solving the singularly forced Stokes equation. It is possible to derive specialized Green’s functions such as for singly (Pozrikidis 1996) or doubly (Pozrikidis 1996; Greengard & Kropinski 2004; Cortez & Hoffmann 2014) periodic domains or with incorporated stationary walls (Blake 1971; Liron & Mochon 1976; Staben, Zinchenko

& Davis 2003; Janssen & Anderson 2008). However, we want to be able to apply our method for general channel geometries, and therefore employ the standard Green’s functions for a 3-D periodic domain. According to Hasimoto (1959) and Pozrikidis (1996), they are given by

$$G_{ij}(\mathbf{x}, \mathbf{x}_0) = \langle G_{ij} \rangle_\Gamma + \frac{8\pi}{V_\Gamma} \sum_{\kappa \neq 0} \frac{1}{|\mathbf{k}^{(\kappa)}|^2} \left(\delta_{ij} - \frac{k_i^{(\kappa)} k_j^{(\kappa)}}{|\mathbf{k}^{(\kappa)}|^2} \right) e^{-i\mathbf{k}^{(\kappa)} \cdot (\mathbf{x} - \mathbf{x}_0)}, \quad (2.14)$$

$$p_j(\mathbf{x}, \mathbf{x}_0) = \frac{8\pi}{V_\Gamma} x_j + \frac{8\pi}{V_\Gamma} i \sum_{\kappa \neq 0} \frac{k_j^{(\kappa)}}{|\mathbf{k}^{(\kappa)}|^2} e^{-i\mathbf{k}^{(\kappa)} \cdot (\mathbf{x} - \mathbf{x}_0)}, \quad (2.15)$$

with $\mathbf{x} \in \mathbb{R}^3 \setminus \{\mathbf{x}_0\}$, $i, j = 1, 2, 3$

for the velocity (G_{ij}) and the pressure (p_j), respectively. $\mathbf{x}_0 \in \bar{\Gamma}$ is arbitrary but fixed. The sums go over all possible Fourier grid vectors $\mathbf{k}^{(\kappa)}$ as defined in (2.4) with $\kappa \in \mathbb{Z}^3 \setminus \{\mathbf{0}\}$, and i is the imaginary unit. G_{ij} satisfies the incompressibility condition,

$$\frac{\partial G_{ij}(\mathbf{x}, \mathbf{x}_0)}{\partial x_i} = 0, \quad \mathbf{x} \in \mathbb{R}^3, \quad i, j = 1, 2, 3. \quad (2.16)$$

Furthermore, $\langle G_{ij} \rangle_\Gamma := (1/V_\Gamma) \int_\Gamma G_{ij}(\mathbf{x}, \mathbf{x}_0) d\mathbf{x}^3$ is independent of \mathbf{x}_0 and constitutes a free parameter representing an imposed average net flow for the Green’s function system. We choose the coordinate system such that it is zero (Zinchenko & Davis 2000):

$$\langle G_{ij} \rangle_\Gamma = 0, \quad i, j = 1, 2, 3. \quad (2.17)$$

Note that the full system can nevertheless have an imposed flow which will be introduced in § 2.2.4 via double-layer integrals over the unit cell boundary.

Combining both of the above equations (via Pozrikidis 1992, equation (2.1.8)), the stresslet is found to be

$$T_{ijl}(\mathbf{x}, \mathbf{x}_0) = -\frac{8\pi}{V_\Gamma} x_j \delta_{il} + \check{T}_{ijl}(\mathbf{x}, \mathbf{x}_0), \quad \mathbf{x} \in \mathbb{R}^3 \setminus \{\mathbf{x}_0\}, \quad i, j, l = 1, 2, 3. \quad (2.18)$$

T_{ijl} contains a linear (non-periodic) part, whereas the periodic part is

$$\check{T}_{ijl}(\mathbf{x}, \mathbf{x}_0) := -\frac{8\pi}{V_\Gamma} i \sum_{\kappa \neq 0} \left(\frac{k_j^{(\kappa)} \delta_{il} + k_l^{(\kappa)} \delta_{ij} + k_i^{(\kappa)} \delta_{lj}}{|\mathbf{k}^{(\kappa)}|^2} - 2 \frac{k_i^{(\kappa)} k_j^{(\kappa)} k_l^{(\kappa)}}{|\mathbf{k}^{(\kappa)}|^4} \right) e^{-i\mathbf{k}^{(\kappa)} \cdot (\mathbf{x} - \mathbf{x}_0)}. \quad (2.19)$$

The periodicity holds for both arguments, as well as for the Stokeslet:

$$G_{ij}(\mathbf{x}, \mathbf{x}_0) = G_{ij}(\mathbf{x} + \mathbf{X}^{(\alpha)}, \mathbf{x}_0 + \mathbf{X}^{(\alpha')}), \quad (2.20a)$$

$$\check{T}_{ijl}(\mathbf{x}, \mathbf{x}_0) = \check{T}_{ijl}(\mathbf{x} + \mathbf{X}^{(\alpha)}, \mathbf{x}_0 + \mathbf{X}^{(\alpha')}) \quad \forall \alpha, \alpha' \in \mathbb{Z}^3, \quad i, j, l = 1, 2, 3. \quad (2.20b)$$

This also implies that \mathbf{x}_0 can actually be located within almost the whole space $\mathbb{R}^3 \setminus \{\mathbf{x}\}$.

Equations (2.14) and (2.18) are the Green’s functions used below. The above given forms, however, are not computable in practice due to their slow convergence. Dramatic speedups are achieved by using the Ewald decomposition (Hasimoto 1959). The final formulas are given by Zhao *et al.* (2010).

We will additionally need two general relations. Hence, let O be some object with a closed surface ∂O , and let $\{O^{(\alpha)}\}$ be the set of O that is offset with all possible periodic grid vectors $\mathbf{X}^{(\alpha)}$ from (2.2). Then, for some proper Green's functions:

$$\oint_{\partial O} T_{ijl}(\mathbf{x}_0, \mathbf{x}) n_j(\mathbf{x}) \, dS(\mathbf{x}) = \delta_{il} \begin{cases} 8\pi & \text{if } \mathbf{x}_0 \in \{O^{(\alpha)}\}, \\ 4\pi & \text{if } \mathbf{x}_0 \in \{\partial O^{(\alpha)}\} \\ 0 & \text{otherwise,} \end{cases} \quad \text{for } \mathbf{x}_0 \in \mathbb{R}^3, \tag{2.21}$$

(Pozrikidis 1992, equation (3.2.7)),

$$\oint_{\partial O} n_i(\mathbf{x}) G_{ij}(\mathbf{x}, \mathbf{x}_0) \, dS(\mathbf{x}) = \oint_{\partial O} G_{ji}(\mathbf{x}, \mathbf{x}_0) n_i(\mathbf{x}) \, dS(\mathbf{x}) = 0, \quad \mathbf{x}_0 \in \mathbb{R}^3, \tag{2.22}$$

(Pozrikidis 1992, equations (2.1.4) and (3.1.3)).

2.2.3. Boundary conditions for a 3-D periodic domain

As we wish to simulate a 3-D periodic domain with the BI equation (2.10), we stipulate as a boundary condition that the velocity \mathbf{u} shall be periodic, i.e.

$$\mathbf{u}(\mathbf{x} + \mathbf{X}^{(\alpha)}) = \mathbf{u}(\mathbf{x}) \quad \forall \mathbf{x} \in \mathbb{R}^3 \text{ and } \forall \alpha \in \mathbb{Z}^3. \tag{2.23}$$

Note that in principle \mathbf{u} may contain a linear component, as long as the arrangement of the objects and their images retain a triclinic periodicity. This could be used to simulate an overall linear shear flow (Phan-Thien, Tran-Cong & Graham 1991; Pozrikidis 1993, 1999; Li, Zhou & Pozrikidis 1995; Loewenberg & Hinch 1996). However, this also usually implies that the basis vectors $\mathbf{a}^{(i)}$ of the unit cell have to be time-dependent, leading to additional problems for longer simulation times (Blawdziewicz 2007, p. 221).

As for the pressure Green's function from (2.15), it is possible to have a non-zero pressure gradient over the unit cell that drives a certain average flow $\langle \mathbf{u} \rangle_\Gamma$. Hence, we can decompose the pressure as $P(\mathbf{x}) = \langle \nabla P \rangle_\Gamma \cdot \mathbf{x} + \check{P}(\mathbf{x})$ for $\mathbf{x} \in \mathbb{R}^3$ where \check{P} denotes the periodic part, and

$$\langle \bullet \rangle_\Gamma := \frac{1}{V_\Gamma} \int_\Gamma \bullet \, d\mathbf{x}^3 \tag{2.24}$$

is the average over the whole unit cell. Using (2.8) and (2.7), we find for the traction (also compare Zick & Homsy 1982, equation (2.23))

$$f_i(\mathbf{x}) = -\langle \nabla P \rangle_\Gamma \cdot \mathbf{x} n_i(\mathbf{x}) + \check{f}_i(\mathbf{x}), \quad i = 1, 2, 3, \tag{2.25}$$

where \check{f} denotes the periodic part.

We finally remark that the BI equation (2.10) can be used with any Green's function to simulate a periodic domain, provided that the periodicity condition (2.23) is enforced. Using the periodic Green's functions from (2.14) and (2.18) is merely a convenient choice since the integrals over $\partial \Gamma$ then yield simple expressions, as shown next.

2.2.4. Computing the integrals over the unit cell's surface for a periodic domain

Single-layer integral. With the help of the decomposition (2.25), the periodicity of the involved quantities (due to (2.20a) and (2.23)) and the divergence theorem together with (2.17) and (2.16), one can show (Zick & Homsy 1982)

$$(\mathcal{N}_{\partial \Gamma} \mathbf{f})_j(\mathbf{x}_0) = 0, \quad \mathbf{x}_0 \in \Omega, \quad j = 1, 2, 3. \tag{2.26}$$

Double-layer integral. It is tempting to assume that the double-layer integral $\mathcal{K}_{\partial\Gamma}\mathbf{u}$ over the unit cell surface $\partial\Gamma$ is also zero. This, however, will turn out to be wrong if a net flow is imposed and/or if volume-changing objects are included. The latter will lead to an additional novel contribution to the equations. Following Zick & Homsy (1982), the first step for the evaluation is to use the decomposition (2.18). The integral term containing \tilde{T}_{ijl} vanishes due to periodicity (compare (2.23) and (2.20b), and note that normal vectors on opposing sides of $\partial\Gamma$ are antiparallel). The other term is treated by adding and subtracting integrals over the objects, resulting in

$$(\mathcal{K}_{\partial\Gamma}\mathbf{u})_j(\mathbf{x}_0) = -\frac{8\pi}{V_\Gamma} \left[\oint_{\partial\Omega} x_j u_i(\mathbf{x}) n_i(\mathbf{x}) \, dS(\mathbf{x}) - \oint_{\partial\mathcal{C} \cup \partial\mathcal{B}} x_j u_i(\mathbf{x}) n_i(\mathbf{x}) \, dS(\mathbf{x}) \right]. \quad (2.27)$$

Integrals over walls give zero contributions since the velocity \mathbf{u} is continuous across their surface, but the normal vectors on opposite sides have different signs. Using the continuity of the normal velocity across the interfaces and applying the divergence theorem while watching out for the normal vector convention (always into the ambient fluid Ω), one obtains

$$(\mathcal{K}_{\partial\Gamma}\mathbf{u})_j(\mathbf{x}_0) = -\frac{8\pi}{V_\Gamma} \left[-\int_\Omega u_j(\mathbf{x}) \, dx^3 - \int_{\mathcal{C} \cup \mathcal{B}} u_j(\mathbf{x}) \, dx^3 - \int_{\Omega \cup \mathcal{C}} x_j \nabla \cdot \mathbf{u}(\mathbf{x}) \, dx^3 - \int_{\mathcal{B}} x_j \nabla \cdot \mathbf{u}(\mathbf{x}) \, dx^3 \right]. \quad (2.28)$$

The integrals in the first line can be combined to $\int_\Gamma \mathbf{u} \, dx^3 = V_\Gamma \langle \mathbf{u} \rangle_\Gamma$, with the average defined in (2.24) (walls are nullsets). Moreover, the divergence of the velocity vanishes in Ω and the capsules \mathcal{C} because of (2.6b) (Stokesian fluids). Furthermore, the last term is absent in existing formulations without volume-changing objects, but here it is non-zero in general and therefore requires special attention.

A more usable form of this last term may be obtained by using the model from (2.5). For a particular bubble \mathcal{B}_k , $k = 1, \dots, N_\mathcal{B}$, we immediately find

$$\int_{\mathcal{B}_k} x_j \nabla \cdot \mathbf{u}(\mathbf{x}) \, dx^3 = c_k V_{\mathcal{B}_k} \chi_j^{(\mathcal{B}_k)}, \quad j = 1, 2, 3, \quad (2.29)$$

where we have defined the geometric centroid

$$\chi^{(\mathcal{B}_k)} := \frac{1}{V_{\mathcal{B}_k}} \int_{\mathcal{B}_k} \mathbf{x} \, dx^3. \quad (2.30)$$

$V_{\mathcal{B}_k}$ is the bubble volume. We obtain a connection between c_k to the more intuitive flux $Q_{\mathcal{B}_k}$ out of or into a bubble by computing

$$Q_{\mathcal{B}_k} := \oint_{\partial\mathcal{B}_k} u_i n_i \, dS = \int_{\mathcal{B}_k} \nabla \cdot \mathbf{u} \, dx^3 = c_k V_{\mathcal{B}_k}. \quad (2.31)$$

Putting it all together, the double-layer integral over $\partial\Gamma$ hence becomes

$$(\mathcal{K}_{\partial\Gamma}\mathbf{u})_j(\mathbf{x}_0) = 8\pi \langle u_j \rangle_\Gamma + \frac{8\pi}{V_\Gamma} \sum_{k=1}^{N_\mathcal{B}} Q_{\mathcal{B}_k} \chi_j^{(\mathcal{B}_k)}, \quad \mathbf{x}_0 \in \Omega, \quad j = 1, 2, 3. \quad (2.32)$$

Similar to $\langle G_{ij} \rangle_\Gamma$ for the Green's function from (2.14), the average velocity $\langle u_j \rangle_\Gamma$ is a free parameter that can be used to drive a flow through the system (Zhao *et al.* 2010). Since the flux $Q_{\mathcal{B}_k}$ is also a prescribed input parameter, and the centroid of an object can be easily computed (see e.g. Zhang & Chen 2001), we have therefore obtained an expression of the BI equation that is actually usable in practice.

2.2.5. The full boundary integral equation and some remarks

The BI equation (2.10) thus becomes

$$u_j(\mathbf{x}_0) = \langle u_j \rangle_\Gamma - \frac{1}{8\pi\mu} \sum_{q=1}^{N_o} (\mathcal{N}_{\partial O_q} \mathbf{F})_j(\mathbf{x}_0) + \frac{1}{8\pi} \sum_{q=1}^{N_o} (1 - \lambda_{O_q}) (\mathcal{K}_{\partial O_q} \mathbf{u})_j(\mathbf{x}_0) + \frac{1}{V_\Gamma} \sum_{k=1}^{N_B} Q_{B_k} \chi_j^{(B_k)}, \quad \mathbf{x}_0 \in \Omega, \quad j = 1, 2, 3, \tag{2.33}$$

with the novel bubble term in the last line. The single- as well as the double-layer integrals must be evaluated with the appropriate Green’s functions from (2.14) and (2.18), respectively.

We first remark that (2.33) reduces to the case of the infinite system for $V_\Gamma \rightarrow \infty$ (i.e. $1/V_\Gamma = 0$), as the flux terms vanish and the Green’s functions converge to the well-known expressions for an infinite system, i.e. (Pozrikidis 1992)

$$G_{ij}(\mathbf{x}, \mathbf{x}_0) = \frac{\delta_{ij}}{|\hat{\mathbf{x}}|} + \frac{\hat{x}_i \hat{x}_j}{|\hat{\mathbf{x}}|^3}, \quad \mathbf{x}, \mathbf{x}_0 \in \mathbb{R}^3 \setminus \{\mathbf{x} = \mathbf{x}_0\}, \quad i, j = 1, 2, 3 \tag{2.34a}$$

for the Stokeslet, and

$$T_{ijl}(\mathbf{x}, \mathbf{x}_0) = -6 \frac{\hat{x}_i \hat{x}_j \hat{x}_l}{|\hat{\mathbf{x}}|^5}, \quad \mathbf{x}, \mathbf{x}_0 \in \mathbb{R}^3 \setminus \{\mathbf{x} = \mathbf{x}_0\}, \quad i, j, l = 1, 2, 3 \tag{2.34b}$$

for the stresslet, where $\hat{\mathbf{x}} := \mathbf{x} - \mathbf{x}_0$.

Second, the imposed average flow $\langle u_j \rangle_\Gamma$ can be interpreted as the flow that would prevail in the absence of any objects, and is the most convenient quantity to prescribe a certain flow. A relationship to the corresponding pressure gradient is easily established (Zhao *et al.* 2010, equation (8)).

Third, the prescribed fluxes for the bubbles cannot be chosen arbitrarily. To see this, consider on the one hand

$$\oint_{\partial\Gamma} u_i n_i \, dS = 0, \tag{2.35}$$

where we used once again the periodicity of the velocity \mathbf{u} and the opposite signs of the normal vector \mathbf{n} on opposing sides of the unit cell surface $\partial\Gamma$. On the other hand,

$$\oint_{\partial\Gamma} u_i n_i \, dS = \oint_{\partial\Omega} u_i n_i \, dS - \oint_{\partial\mathcal{C} \cup \partial B} u_i n_i \, dS = - \sum_{k=1}^{N_B} Q_{B_k}, \tag{2.36}$$

where the divergence theorem and the incompressibility of the velocity in Ω and \mathcal{C} together with the definition of the flux have been employed. Combining these two equations, we find

$$\sum_{k=1}^{N_B} Q_{B_k} = 0. \tag{2.37}$$

Hence, the fluxes must be chosen such that the total flux is zero, i.e. that the outer fluid volume is conserved. This implies that at least two bubbles are required that oscillate out of phase for the periodic system. Furthermore, if the ambient fluid domain Ω is not simply connected (imagine a tube separating the unit cell Γ into an

inner and an outer domain), the fluxes must be chosen such that the volume within the respective domains is conserved.

Fourth, the initial assumption that all objects are completely located within the unit cell can be relaxed. Surface integrals can be evaluated continuously over the objects' surfaces even if these surfaces cross the boundary of the unit cell, as is common in simulations of dense suspensions. This property is usually silently assumed in the literature, although it is *a priori* unclear if it holds due to the linear part in the stresslet (2.18) and the non-periodic centroid term in (2.33). With volume-changing objects it actually follows from the non-trivial interplay between the integrals over the unit cell's surface $\partial\Gamma$ and the centroid term. We prove this result explicitly in appendix B.

2.3. Fredholm integral equation

The BI equation (2.33) can be used to compute the flow velocity everywhere within the ambient fluid Ω if the tractions/traction-jumps, the velocities and the fluxes are known. However, we usually prescribe either the tractions/traction-jumps or the velocities, while the other quantity is unknown. The basic idea to obtain a determining equation is to use (2.33) and move the evaluation point \mathbf{x}_0 onto the surface of the objects. We thereby obtain a so-called Fredholm integral equation which can be solved for the unknown variables. Section 2.3.1 summarizes the result of this standard procedure. The subsequent sections are devoted to ensuring and proving the uniqueness of the solution. This cannot be taken for granted if bubbles are included. But even without bubbles it has so far not yet been rigorously proved in periodic systems.

2.3.1. Basic equation

We now assume that all objects have surfaces of Lyapunov type (i.e. they are 'smooth': see Kress (2014), p. 96, for more details). If corners or edges within the surfaces existed, the results would change: see e.g. Pozrikidis (1992, p. 37) and Kress (2014, chap. 2.5). For smooth objects the single-layer potential is continuous (Kohr & Pop 2004, chap. 3.4.4) if \mathbf{x}_0 is moved across the surface and the double-layer potential makes a jump (Pozrikidis 1992, equation (2.3.12)). Following these two references, we obtain the Fredholm boundary integral (FBI) equation as

$$\begin{aligned}
 u_j(\mathbf{x}_0) = & \frac{2}{1 + \lambda_{O_k}} \left[\langle u_j \rangle_\Gamma - \frac{1}{8\pi\mu} \sum_{q=1}^{N_o} (\mathcal{N}_{\partial O_q} \mathbf{F})_j(\mathbf{x}_0) \right. \\
 & \left. + \frac{1}{8\pi} \sum_{q=1}^{N_o} (1 - \lambda_{O_q}) (\mathcal{K}_{\partial O_q} \mathbf{u})_j(\mathbf{x}_0) + \frac{1}{V_\Gamma} \sum_{q=1}^{N_B} \mathcal{Q}_{B_q} \chi_j^{(B_q)} \right], \\
 & \mathbf{x}_0 \in \partial O_k, \quad k = 1, \dots, N_o, \quad j = 1, 2, 3.
 \end{aligned}
 \tag{2.38}$$

Note that the evaluation point \mathbf{x}_0 is located directly on the surfaces of the objects. The single- as well as the double-layer integrals exist as improper integrals (Kress 2014, chap. 6). Equation (2.38) corresponds to the first two lines in (2.1). The missing two terms will be introduced in § 2.3.3 to ensure uniqueness of the solution.

The above FBI equation can in principle be used to find the unknown quantity – if the solution were unique in all cases. In our application presented in § 3, we prescribe the traction/traction-jump \mathbf{F} on all objects (also on walls for efficiency reasons). This

leads to a so-called Fredholm equation of the second kind that is amenable to the Fredholm theory. As will be analysed and fixed below, equation (2.38) has multiple solutions if bubbles are included. Without bubbles, the solution is unique, as will also be shown below.

On the other hand, prescribing the velocities on all objects leads to a Fredholm equation of the first kind which has various unfavourable properties: the solution is in general not unique, the condition number grows with resolution (compare Karrila & Kim 1989, p. 127, and Marin, Gustavsson & Tornberg 2012) and no general mathematical theory exists. These are the reasons why alternative approaches for such problem statements have been invented, e.g. the completed double-layer boundary integral method (Karrila & Kim 1989; Kohr & Pop 2004; Zhao *et al.* 2012).

Finally, prescribing the velocities on some objects and the tractions on others yields a mixed type equation. Similar to the first type, no general theory exists and at least parts of the system have ‘difficult’ properties.

2.3.2. Fredholm theory and the non-uniqueness of solution

Henceforth, we consider the case when (2.38) is a Fredholm integral equation of the second kind, i.e. when all velocities are unknown. In order to apply the Fredholm theory, we need to introduce the homogeneous version of (2.38),

$$h_j(\mathbf{x}_0) = \frac{1}{4\pi} \frac{1}{1 + \lambda_{O_k}} \sum_{q=1}^{N_o} (1 - \lambda_{O_q}) \oint_{\partial O_q} h_i(\mathbf{x}) T_{ijl}(\mathbf{x}, \mathbf{x}_0) n_l(\mathbf{x}) \, dS(\mathbf{x}),$$

$$\mathbf{x}_0 \in \partial O_k, \quad k = 1, \dots, N_o, \quad j = 1, 2, 3, \tag{2.39}$$

where \mathbf{h} denotes an eigensolution to the eigenvalue 1. Note again that the double-layer integral is meant to be absent for $\lambda_{O_q} = 1$ objects, especially walls. The corresponding adjoint equation (Pozrikidis 1992, p. 106, and Kress 2014) is given by

$$a_j(\mathbf{x}_0) = \frac{1 - \lambda_{O_k}}{4\pi} M_j[\mathbf{a}](\mathbf{x}_0), \quad \mathbf{x}_0 \in \partial O_k, \quad k = 1, \dots, N_o, \quad j = 1, 2, 3, \tag{2.40}$$

with the eigensolution \mathbf{a} and the abbreviation

$$M_j[\mathbf{a}](\mathbf{x}_0) := \sum_{q=1}^{N_o} \frac{1}{1 + \lambda_{O_q}} n_l(\mathbf{x}_0) \oint_{\partial O_q} a_i(\mathbf{x}) T_{jil}(\mathbf{x}_0, \mathbf{x}) \, dS(\mathbf{x}). \tag{2.41}$$

The integral kernels and their adjoints are weakly singular (see Kress 2014, p. 31 and theorem 4.12, Pozrikidis 1992, pp. 36 and 113, as well as Karrila & Kim 1989, p. 137). This means that all occurring integral operators are compact (Kress 2014, theorem 2.30), and that the eigensolutions of the homogeneous and adjoint equations are continuous (see Kress 2014, p. 58).

For walls (i.e. open objects) we adopt the convention that closed surface integrals \oint go over both sides. Due to the continuity of the eigensolutions, however, they provide no contribution. Alternatively, as in the derivation of the BI equation, one can also revert back to walls with finite thickness and take the limit afterwards. The formulas in the following have to be interpreted in the same way. Notice that in the adjoint equation integrals over objects appear which actually have $\lambda_{O_q} = 1$.

The compactness of the integral operators also implies that the Fredholm theory can be used to make precise statements about uniqueness and existence of solutions (see Pozrikidis 1992, p. 114, and Kress 2014, p. 55f.). For the present purpose the major theorem can be written as follows.

THEOREM 1 (Fredholm alternative).

- (i) The homogeneous and adjoint equations (2.39) and (2.40) have the same finite number of eigensolutions.
- (ii) If the homogeneous equation (2.39) has only the trivial solution $\mathbf{h} \equiv 0$, then the full equation (2.38) has exactly one solution (existence and uniqueness).
- (iii) If the homogeneous equation (2.39) has a non-trivial solution, then the full equation (2.38) has solutions if and only if all eigensolutions \mathbf{a} of the adjoint equation (2.40) satisfy

$$\sum_{k=1}^{N_o} \oint_{\partial O_k} \mathbf{R}_j(\mathbf{x}) a_j(\mathbf{x}) \, dS(\mathbf{x}) = 0, \quad k = 1, \dots, N_o. \tag{2.42}$$

Here, \mathbf{R} contains all fully known terms (i.e. terms that are missing in the homogeneous equation).

To arrive at uniqueness and existence statements therefore requires us to know all solutions of the adjoint equation. In the case of (2.47), the solutions are

$$\mathbf{a}^{(m)}(\mathbf{x}_0) = \begin{cases} \mathbf{n}(\mathbf{x}_0) & \text{if } \mathbf{x}_0 \in \partial \mathcal{B}_m, \\ 0 & \text{otherwise,} \end{cases} \quad m = 1, \dots, N_B, \quad \mathbf{x}_0 \in \partial O. \tag{2.43}$$

That these are indeed solutions can be easily shown with the help of (2.21). To show that they are the only solutions requires a somewhat longer procedure, similar to §2.3.4 (we skip it as it is not of any major interest here). Thus, the homogeneous equation (2.39) also has N_B solutions. Furthermore, we have $R_j(\mathbf{x}_0) = 2/(1 + \lambda_{O_k})[\langle u_j \rangle_\Gamma - (1/(8\pi\mu)) \sum_{q=1}^{N_o} (\mathcal{N}_{\partial O_q} \mathbf{F})_j(\mathbf{x}_0) + (1/V_\Gamma) \sum_{q=1}^{N_B} Q_{\mathcal{B}_q} \chi_j^{(\mathcal{B}_q)}]$, and all solutions $\mathbf{a}^{(m)}$ satisfy condition (2.42) due to equation (2.22). Hence, by virtue of the Fredholm alternative, the FBI equation (2.38) has more than one solution if bubbles are included.

2.3.3. Ensuring uniqueness: the full equation

Equation (2.38) does not have a unique solution because the flux of the bubbles is not determined by the equation. To remove this ambiguity, we introduce additional terms into equation (2.38) in such a way that the solution of the new equation is unique and simultaneously also a solution of the old equation (2.38). In analogy to Nie *et al.* (2002), the modified equation is then given by (2.1), which is repeated here for convenience:

$$\begin{aligned} u_j(\mathbf{x}_0) = & \frac{2}{1 + \lambda_{O_k}} \left[\langle u_j \rangle_\Gamma - \frac{1}{8\pi\mu} \sum_{q=1}^{N_o} (\mathcal{N}_{\partial O_q} \mathbf{F})_j(\mathbf{x}_0) \right. \\ & \left. + \frac{1}{8\pi} \sum_{q=1}^{N_o} (1 - \lambda_{O_q}) (\mathcal{K}_{\partial O_q} \mathbf{u})_j(\mathbf{x}_0) + \frac{1}{V_\Gamma} \sum_{q=1}^{N_B} Q_{\mathcal{B}_q} \chi_j^{(\mathcal{B}_q)} \right] \\ & - \frac{1 - \lambda_{O_k}}{1 + \lambda_{O_k}} z_j^{(k)}(\mathbf{x}_0) \left[\oint_{\partial O_k} u_l(\mathbf{x}) n_l(\mathbf{x}) \, dS(\mathbf{x}) - Q_{O_k} \right], \\ & \mathbf{x}_0 \in \partial O_k, \quad k = 1, \dots, N_o, \quad j = 1, 2, 3. \end{aligned} \tag{2.44}$$

This is the central equation that is solved in our VCO-BIM. It is a direct method as the solution \mathbf{u} is the physical velocity rather than an auxiliary field. The fact that (2.44) has exactly one solution will be proved below and constitutes a central result of the present work; $\mathbf{z}^{(k)}$ can be chosen arbitrarily, as long as the restriction

$$\oint_{\partial O_k} z_j^{(k)}(\mathbf{x}) n_j(\mathbf{x}) \, dS(\mathbf{x}) = 1, \quad k = 1, \dots, N_O \tag{2.45}$$

is satisfied. A convenient choice is

$$\mathbf{z}^{(k)}(\mathbf{x}) = \mathbf{n}(\mathbf{x})/S_{O_k}, \quad \mathbf{x} \in \partial O_k, \quad k = 1, \dots, N_O, \tag{2.46}$$

where S_{O_k} is the surface area of the k th object. Furthermore, Q_{O_k} is the prescribed flux of object O_k , which must be zero for all entities except the bubbles.

The integral term in the last line of (2.44) can be interpreted as part of the so-called Wielandt deflation procedure (Kim & Karrila 1991) for objects with viscosity ratios $\lambda_{O_k} > 0$. This method is sometimes used to accelerate the convergence rate of iterative solution algorithms (Zinchenko, Rother & Davis 1997; Zinchenko & Davis 2000), but is otherwise optional for $\lambda_{O_k} > 0$. Choosing not to use it amounts to setting $\mathbf{z}^{(k)} = 0$ (in which case condition (2.45) must be disregarded). For bubbles ($\lambda_{O_k} = 0$) that oscillate ($Q_{O_k} \neq 0$), however, an additional new term including the surface flux Q_{O_k} needs to be taken into account. Note that the last line is an essential ingredient to ensure uniqueness of the solution for bubbles (with and without volume changes), contrary to the usual situation found in the literature. We also remark that the FBI equation remains valid in an infinite system ($\Gamma \rightarrow \mathbb{R}^3$) similar to the BI equation from § 2.2.5.

The solution of the patched equation (2.44) is still a solution of the old equation (2.38). This can be shown by multiplying (2.44) with the normal vector n_j , summing over j and integrating over some object's surface ∂O_k . Using relations (2.21), (2.22) and (2.45) gives $\oint_{\partial O_k} u_i n_i \, dS = Q_{O_k}$, meaning that the flux out of or into the object matches with the prescribed value Q_{O_k} , as expected. Moreover, substituting it back into (2.44) recovers the original equation (2.38).

Despite the patch, equation (2.44) is still a Fredholm integral equation of the second kind for the velocities on all objects if \mathbf{F} is given. In order to apply the Fredholm theory, we need to introduce again the adjoint of the homogeneous equation, namely

$$a_j(\mathbf{x}_0) = \frac{1 - \lambda_{O_k}}{4\pi} M_j[\mathbf{a}](\mathbf{x}_0) - \frac{1 - \lambda_{O_k}}{1 + \lambda_{O_k}} n_j(\mathbf{x}_0) \oint_{\partial O_k} z_l^{(k)}(\mathbf{x}) a_l(\mathbf{x}) \, dS(\mathbf{x}), \tag{2.47}$$

$$\mathbf{x}_0 \in \partial O_k, \quad k = 1, \dots, N_O, \quad j = 1, 2, 3,$$

with the abbreviation M_j from (2.41); \mathbf{a} denotes again the eigensolutions to the eigenvalue 1.

The goal now is to prove that (2.47) has only the obvious solution $\mathbf{a} = 0$. Theorem 1 then implies that the actual FBI equation (2.44) has exactly one solution. Unfortunately, the procedure used by Pozrikidis (1992, p. 116f.) cannot be adapted for the proof in the periodic system because the artificial flow that he introduces is a source field. This works in infinite domains where the fluid can escape to infinity, but violates the conservation of the outer fluid volume in periodic domains (even if all objects were volume conserving). We keep the proof rather general, as none has been published before for the periodic system to the best of our knowledge.

2.3.4. Proof of existence and uniqueness of the solution

As a start, we assume that there is at least one non-trivial solution \mathbf{a} of the adjoint equation (2.47). We then define an artificial velocity field similar to Odqvist (1930, §4) by

$$A_j(\mathbf{x}_0) := \sum_{q=1}^{N_o} \frac{1}{1 + \lambda_{O_q}} \oint_{\partial O_q} a_i(\mathbf{x}) G_{ij}(\mathbf{x}, \mathbf{x}_0) \, dS(\mathbf{x}), \quad \mathbf{x}_0 \in \mathbb{R}^3, \quad j = 1, 2, 3. \quad (2.48)$$

This field has a few special properties. First of all, \mathbf{A} is defined within the whole space \mathbb{R}^3 because it inherits the domain from the periodic Stokeslet and because such a single-layer integral exists in the improper sense if \mathbf{x}_0 is located on any surface. Moreover, because the eigensolutions \mathbf{a} of the adjoint equation are continuous as explained above, \mathbf{A} is continuous as \mathbf{x}_0 crosses any object surface ∂O (Kohr & Pop 2004, chap. 3.4.4). The field is also periodic due to (2.20a), and we have

$$\nabla \cdot \mathbf{A}(\mathbf{x}_0) = 0, \quad \mathbf{x}_0 \in \mathbb{R}^3 \quad (2.49)$$

due to equation (2.16) and

$$\langle \mathbf{A} \rangle_\Gamma = 0 \quad (2.50)$$

because of (2.17).

Furthermore, if we define the associated pressure as

$$P^A(\mathbf{x}_0) := \mu \sum_{q=1}^{N_o} \frac{1}{1 + \lambda_{O_q}} \oint_{\partial O_q} a_i(\mathbf{x}) p_i(\mathbf{x}_0, \mathbf{x}) \, dS(\mathbf{x}), \quad (2.51)$$

with the Green’s function \mathbf{p} for the pressure from (2.15), one can show with the help of the singular Stokes equation (Pozrikidis 1996, equation (2.2)) as well as (2.14) and (2.15) that the Stokes equation with \mathbf{A} is satisfied everywhere but on the surfaces, i.e.

$$-\nabla P^A(\mathbf{x}) + \mu \nabla^2 \mathbf{A}(\mathbf{x}) = 0, \quad \mathbf{x} \in \mathbb{R}^3 \setminus \partial\{O^{(\alpha)}\}. \quad (2.52)$$

$\{O^{(\alpha)}\}$ denotes the objects and all of their periodic images. The Stokes equation can alternatively be written as

$$\frac{\partial \sigma_{ij}^A(\mathbf{x})}{\partial x_i} = 0, \quad \mathbf{x} \in \mathbb{R}^3 \setminus \partial\{O^{(\alpha)}\}, \quad j = 1, 2, 3, \quad (2.53)$$

where the stress tensor is given by $\sigma_{ij}^A := -P^A \delta_{ij} + \mu(\partial A_i / \partial x_j + \partial A_j / \partial x_i)$. Continuing, the traction (cf. (2.7)) associated with \mathbf{A} at the outside ($\mathbf{f}^{A,+}$) and inside surface ($\mathbf{f}^{A,-}$, normal vector to the outside) of some object O_k can be expressed as (compare Kohr & Pop 2004, equation (3.4.61), and Odqvist 1930, equation (2.15))

$$\mathbf{f}_j^{A,+}(\mathbf{x}_0) = -\frac{4\pi\mu}{1 + \lambda_{O_k}} a_j(\mathbf{x}_0) + \mu M_j[\mathbf{a}](\mathbf{x}_0), \quad (2.54a)$$

$$\mathbf{f}_j^{A,-}(\mathbf{x}_0) = +\frac{4\pi\mu}{1 + \lambda_{O_k}} a_j(\mathbf{x}_0) + \mu M_j[\mathbf{a}](\mathbf{x}_0), \quad (2.54b)$$

$$\mathbf{x}_0 \in \partial O_k, \quad k = 1, \dots, N_o, \quad j = 1, 2, 3,$$

where M_j was defined in (2.41). Solving equations (2.54) for \mathbf{a} and \mathbf{M} leads to

$$a_j(\mathbf{x}_0) = -\frac{1 + \lambda_{O_k}}{8\pi\mu} [f_j^{A,+}(\mathbf{x}_0) - f_j^{A,-}(\mathbf{x}_0)], \tag{2.55a}$$

$$M_j[\mathbf{a}](\mathbf{x}_0) = \frac{1}{2\mu} [f_j^{A,+}(\mathbf{x}_0) + f_j^{A,-}(\mathbf{x}_0)], \tag{2.55b}$$

$$\mathbf{x}_0 \in \partial O_k, \quad k = 1, \dots, N_O, \quad j = 1, 2, 3.$$

The last required property of the artificial field \mathbf{A} is the energy conservation. Following Pozrikidis (1992, chap. 1.5) and using (2.49) and (2.52), we can derive

$$\sum_{k=1}^{N_O} \oint_{\partial O_k} f_j^{A,+}(\mathbf{x}) A_j(\mathbf{x}) \, dS(\mathbf{x}) + \oint_{\partial \Gamma} f_j^{A,+}(\mathbf{x}) A_j(\mathbf{x}) \, dS(\mathbf{x}) = -2\mu \int_{\Omega} \sum_{i,j=1}^3 [E_{ij}^A(\mathbf{x})]^2 \, dx^3. \tag{2.56}$$

The strain rate tensor is defined as

$$E_{ij}^A(\mathbf{x}) := \frac{1}{2} \left(\frac{\partial A_i(\mathbf{x})}{\partial x_j} + \frac{\partial A_j(\mathbf{x})}{\partial x_i} \right), \quad \mathbf{x} \in \mathbb{R}^3 \setminus \partial\{O^{(\alpha)}\}, \quad i, j = 1, 2, 3. \tag{2.57}$$

The integral over the unit cell’s surface $\partial \Gamma$ is simply zero. This follows similar to the derivation of the double-layer integral in § 2.2.4 because \mathbf{A} is periodic, $f^{A,+}$ contains at most a linear component (due to the definition of the traction, equation (2.7), the pressure, equation (2.51) and the linear term in the pressure Green’s function, equation (2.15)), \mathbf{A} is incompressible according to (2.49) and because the average flow is zero as given by (2.50). Furthermore, a similar equation can be derived for the inside of the objects since \mathbf{A} is defined everywhere. In the end, we obtain

$$\sum_{k=1}^{N_O} \oint_{\partial O_k} f_j^{A,+}(\mathbf{x}) A_j(\mathbf{x}) \, dS(\mathbf{x}) = -2\mu \int_{\Omega} \sum_{i,j=1}^3 [E_{ij}^A(\mathbf{x})]^2 \, dx^3 \leq 0, \tag{2.58a}$$

and

$$\oint_{\partial O_k} f_j^{A,-}(\mathbf{x}) A_j(\mathbf{x}) \, dS(\mathbf{x}) = 2\mu \int_{O_k} \sum_{i,j=1}^3 [E_{ij}^A(\mathbf{x})]^2 \, dx^3 \geq 0, \quad k = 1, \dots, N_O. \tag{2.58b}$$

The inequalities follow because the viscosity μ is >0 and the integrals contain kernels that are obviously greater or equal to zero.

With all required properties of the artificial field \mathbf{A} established, we now proceed to show that the adjoint equation (2.47) does not have any non-trivial solution \mathbf{a} . We will do this by a *reductio ad absurdum* argument. Hence, assume that there is at least one non-trivial solution denoted by \mathbf{a} . Following Odqvist (1930, § 4), we begin by substituting (2.55) into the adjoint (2.47), leading to

$$f_j^{A,+}(\mathbf{x}_0) = \lambda_{O_k} \left[f_j^{A,-}(\mathbf{x}_0) + \frac{8\pi\mu}{1 + \lambda_{O_k}} n_j(\mathbf{x}_0) \oint_{\partial O_k} z_l^{(k)}(\mathbf{x}) a_l(\mathbf{x}) \, dS(\mathbf{x}) \right], \tag{2.59}$$

$$\mathbf{x}_0 \in \partial O_k, \quad k = 1, \dots, N_O, \quad j = 1, 2, 3.$$

We now multiply with A_j , sum over j and integrate over the surface of all objects. The contribution from the second term is simply zero because we can use (2.48) and write

$$\begin{aligned} & \oint_{\partial O_k} A_j(\mathbf{x}_0) n_j(\mathbf{x}_0) \, dS(\mathbf{x}_0) \\ &= \sum_{q=1}^{N_O} \frac{1}{1 + \lambda_{O_q}} \oint_{\partial O_q} a_i(\mathbf{x}) \underbrace{\left[\oint_{\partial O_k} G_{ij}(\mathbf{x}, \mathbf{x}_0) n_j(\mathbf{x}_0) \, dS(\mathbf{x}_0) \right]}_{=0 \text{ because of equation (2.22)}} \, dS(\mathbf{x}) = 0. \end{aligned} \quad (2.60)$$

Thus we find

$$0 \geq \sum_{k=1}^{N_O} \oint_{\partial O_k} f_j^{A,+}(\mathbf{x}) A_j(\mathbf{x}) \, dS(\mathbf{x}) = \sum_{k=1}^{N_O} \lambda_{O_k} \oint_{\partial O_k} f_j^{A,-}(\mathbf{x}) A_j(\mathbf{x}) \, dS(\mathbf{x}) \geq 0. \quad (2.61)$$

The inequality signs follow from the energy conservation (2.58) and (2.13). Both inequality signs together imply

$$\sum_{k=1}^{N_O} \oint_{\partial O_k} f_j^{A,+}(\mathbf{x}) A_j(\mathbf{x}) \, dS(\mathbf{x}) = 0, \quad (2.62)$$

and due to (2.58a) we thus have $E_{ij}^A(\mathbf{x}) = 0$ for all $\mathbf{x} \in \Omega$ and $i, j = 1, 2, 3$. This in turn means that \mathbf{A} can only represent rigid-body motion within Ω (Pozrikidis 1992, chap. 1.5), i.e.

$$\mathbf{A}(\mathbf{x}) = \mathbf{U}^\Omega + \boldsymbol{\omega}^\Omega \times \mathbf{x}, \quad \mathbf{x} \in \Omega. \quad (2.63)$$

\mathbf{U}^Ω and $\boldsymbol{\omega}^\Omega$ are constants that do not depend on \mathbf{x} . The symbol ‘ \times ’ denotes the cross-product. Furthermore, using the periodicity of \mathbf{A} , we immediately find $\boldsymbol{\omega}^\Omega = 0$.

Next, we recall that \mathbf{A} is continuous across the objects’ surfaces, i.e. $\mathbf{A}|_{\partial O} = \mathbf{A}|_\Omega = \mathbf{U}^\Omega$, to derive

$$\sum_{k=1}^{N_O} \oint_{\partial O_k} f_j^{A,-}(\mathbf{x}) A_j(\mathbf{x}) \, dS(\mathbf{x}) = U_i^\Omega \sum_{k=1}^{N_O} \int_{O_k} \frac{\partial \sigma_{ji}^A(\mathbf{x})}{\partial x_j} \, dx^3 = 0. \quad (2.64)$$

Here we used the definition of the traction from (2.7), the divergence theorem, the symmetry of the stress tensor and finally the Stokes equation (2.53). Summing expression (2.58b) over all objects, using (2.64) and that the integral arguments on the right-hand side of (2.58b) are positive, we find $E_{ij}^A(\mathbf{x}) = 0$ for all $\mathbf{x} \in O_k$, $k = 1, \dots, N_O$ and $i, j = 1, 2, 3$. Hence, \mathbf{A} must also represent rigid-body motion within every object:

$$\mathbf{A}(\mathbf{x}) = \mathbf{U}^{(k)} + \boldsymbol{\omega}^{(k)} \times \mathbf{x}, \quad \mathbf{x} \in O_k, \quad k = 1, \dots, N_O. \quad (2.65)$$

The $2N_O$ constants $\mathbf{U}^{(k)}$ and $\boldsymbol{\omega}^{(k)}$ could in principle be different for each k . But because of the continuity of \mathbf{A} across ∂O_k we have $\mathbf{U}^{(k)} = \mathbf{U}^\Omega$ and $\boldsymbol{\omega}^{(k)} = 0$ for all $k = 1, \dots, N_O$. All in all, we derived the explicit expression

$$\mathbf{A}(\mathbf{x}) = \mathbf{U}^\Omega = \text{const.}, \quad \mathbf{x} \in \mathbb{R}^3 \quad (2.66)$$

for the artificial field \mathbf{A} .

Next, we exploit the Stokes equation (2.52) which immediately leads to $\nabla P^A(\mathbf{x}) = 0$ for $\mathbf{x} \in \mathbb{R}^3 \setminus \partial\{O^{(\omega)}\}$. The pressure associated with \mathbf{A} is thus a simple constant in every connected set, which we will write as

$$P^A(\mathbf{x}) = \begin{cases} -C_\Omega & \text{if } \mathbf{x} \in \Omega, \\ -C_k & \text{if } \mathbf{x} \in O_k, \quad k = 1, \dots, N_O, \end{cases} \quad \text{with } \mathbf{x} \in \Gamma \setminus \partial O. \tag{2.67}$$

Only the values within the unit cell will be needed (the pressures within the periodic images might be different at first). The stress tensor is thus

$$\sigma_{ij}^A(\mathbf{x}) = \begin{cases} C_\Omega \delta_{ij} & \text{if } \mathbf{x} \in \Omega, \\ C_k \delta_{ij} & \text{if } \mathbf{x} \in O_k, \quad k = 1, \dots, N_O, \end{cases} \quad \text{with } \mathbf{x} \in \Gamma \setminus \partial O. \tag{2.68}$$

Taking the limit onto the surfaces from the outside and inside and multiplying them with the outer normal vector gives the tractions $f^{A,+}$ and $f^{A,-}$. By substituting them into (2.55a) we obtain

$$a_j(\mathbf{x}) = \tilde{C}_k n_j(\mathbf{x}), \quad \mathbf{x} \in \partial O_k, \quad k = 1, \dots, N_O, \quad j = 1, 2, 3, \tag{2.69}$$

with the constants $\tilde{C}_k := -((1 + \lambda_{O_k}) / (8\pi\mu))(C_\Omega - C_k)$ for $k = 1, \dots, N_O$. This result is somewhat remarkable: every solution to the adjoint equation (2.47) must be of the form given by (2.69). It also means that the global linear dependence of the pressure that appears in (2.51) via the Green’s function drops out, which is consistent with expression (2.67).

Now, the initial assumption was that there is a non-trivial solution to the adjoint equation. Since all solutions are of the above form (2.69), there must exist one $k' \in \{1, \dots, N_O\}$ with $\tilde{C}_{k'} \neq 0$. We thus substitute it into (2.47) for $\mathbf{x}_0 \in \partial O_{k'}$, and with the help of (2.21) arrive at

$$1 = \frac{1 - \lambda_{O_{k'}}}{1 + \lambda_{O_{k'}}} \left(1 - \oint_{\partial O_{k'}} z_l^{(k')}(\mathbf{x}) n_l(\mathbf{x}) \, dS(\mathbf{x}) \right). \tag{2.70}$$

The Wielandt deflation term can be active ($z^{(k')} \neq 0$) or inactive ($z^{(k')} = 0$) for a particular object. If it is active, condition (2.45) and $\lambda_{O_{k'}} \geq 0$ immediately lead to the contradiction $1 = 0$. On the other hand, if the term is inactive, equation (2.70) can only be satisfied for $\lambda_{O_{k'}} = 0$. But this means that by definition $O_{k'}$ is a bubble, where we demanded that the Wielandt term is always active. Thus we also get a contradiction. This means that our initial assumption (that there is a non-trivial solution to the adjoint equation) must have been wrong, i.e. (2.47) only has the solution $\mathbf{a} \equiv 0$.

To complete the proof, we use the Fredholm alternative from Theorem 1. The homogeneous equation therefore also has only the trivial solution, and consequently the full FBI equation (2.38) has exactly one solution (existence and uniqueness). This holds as long as the Wielandt term exists for objects O_k with $\lambda_{O_k} = 0$. Note that for $\lambda_{O_k} > 0$ the Wielandt term does not matter concerning uniqueness of the solution, but may be used to accelerate the numerical convergence as remarked before. We also mention that the above procedure carries over to other systems and Green’s functions such as for an infinite domain without any essential changes.

2.4. Bubble model details

2.4.1. The traction and the constitutive law

As stated in § 2.2 we prescribe a certain outer traction \mathbf{f}^+ on the surface of the bubbles. This is necessary because the introduction of the traction jump $\Delta\mathbf{f}$ (as is done for capsules) in the BI equation would require the application of the Stokes equation at the inside (compare § 2.2.1 and Pozrikidis 1992, pp. 37 and 143) which is not possible because the inside is a compressible fluid with very low viscosity. Due to this very low viscosity, however, we can neglect the shear stress acting on the inside surface of the bubbles and only the inner pressure $P_{\mathcal{B}_k}$ will be of relevance. Hence, the outer traction is expressible as (Youngren & Acrivos 1976; Power 1992)

$$\mathbf{f}^+(\mathbf{x}) \approx \Delta\mathbf{f}(\mathbf{x}) - P_{\mathcal{B}_k}\mathbf{n}(\mathbf{x}), \quad \mathbf{x} \in \partial\mathcal{B}_k, \quad k = 1, \dots, N_{\mathcal{B}}. \quad (2.71)$$

Note that the minus before the pressure comes from the fact that \mathbf{f}^+ represents the force exerted by the fluid on the membrane, and not *vice versa*. The traction jump $\Delta\mathbf{f}$ must be determined by some constitutive law for the interface, such as the ordinary Young–Laplace equation

$$\Delta\mathbf{f}(\mathbf{x}) = 2\gamma_{\mathcal{B}_k}H(\mathbf{x})\mathbf{n}(\mathbf{x}), \quad \mathbf{x} \in \partial\mathcal{B}_k, \quad k = 1, \dots, N_{\mathcal{B}}. \quad (2.72)$$

H is the mean curvature, taken to be positive for a sphere. This equation is valid for a spatially constant surface tension $\gamma_{\mathcal{B}_k}$, i.e. for interfaces between two immiscible substances. Additional surfactants can lead to a position dependence and non-zero tangential components (Pozrikidis 2001).

2.4.2. Imposing bubble volume changes

We can now prescribe a certain traction jump and an (in general time-dependent) internal pressure to model an oscillating bubble. The traction can then be computed via (2.71) and substituted into the FBI equation (2.1). This should work fine in principle. However, after the substitution we observe that the $P_{\mathcal{B}_k}\mathbf{n}$ term simply drops out due to (2.22), leaving us unable to enforce a certain pressure and thus any volume changes. This deficiency of the FBI equation is because of the fact that the single-layer potential is incapable of producing any flow with sinks or sources (Pozrikidis 1992, chap. 4.1). This in turn originates from the incompressibility (2.16) of the flow produced by the Stokeslet.

Rather than prescribing a certain internal pressure we therefore prescribe a certain flux $Q_{\mathcal{B}_k}$. This is easily implemented as the flux appears explicitly in the patched FBI equation (2.1). For the purpose of solving (2.1) we then set $\mathbf{f}^+ = \Delta\mathbf{f}$.

2.5. Numerical implementation

Our volume-changing object boundary integral method (VCO-BIM) solves the FBI equation (2.1) numerically. For this, we discretize the surfaces of all objects with flat triangles. Dynamic refinement and coarsening via Rivara’s longest-edge bisection algorithm (Rivara 1984) is employed (see the supplementary information available at <https://doi.org/10.1017/jfm.2017.836> for some examples). Object centroids and volumes are calculated as explained by Zhang & Chen (2001). Integrals are computed with a standard Gaussian quadrature (Cowper 1973), where quantities at points within the triangles are obtained from their nodal values via linear interpolation (Pozrikidis 1992). Surface integrals where the Green’s functions are singular are treated in polar

coordinates in the case of the single-layer integrals (Pozrikidis 1995), and by adapting the usual surface subtraction scheme for the double-layer integrals (Pozrikidis 2001, equation (8.8)). In both cases the Green’s functions of the infinite domain from (2.34) are used to eliminate the singularities (Loewenberg & Hinch 1996; Zinchenko & Davis 2000) since they are faster to calculate than their periodic counterparts and coincide with them for $\mathbf{x} \approx \mathbf{x}_0$. Nearly singular behaviour (occurring when objects come near to each other) is additionally removed for the double-layer potentials (Loewenberg & Hinch 1996). After discretization, equation (2.1) becomes a linear system that we solve with GMRES (Saad & Schultz 1986), bypassing the need to explicitly construct the system’s matrix. We remark that BiCGSTAB (van der Vorst 1992) was found to be slower in most cases.

The computation of the discretized integral equation with the periodic Green’s functions from (2.14) and (2.18) is accelerated by two different means. First of all, the Ewald decomposition by Hasimoto (1959) is used to split the expressions into fast converging real and Fourier space parts, also see Lindbo & Tornberg (2010). The final expressions are given by Zhao *et al.* (2010, chap. 5.1). Second, we employ the smooth particle mesh Ewald method (SPME) to further accelerate the computation of the Fourier parts via fast Fourier transforms (Saintillan, Darve & Shaqfeh 2005).

The time evolution of the objects is obtained by solving the kinematic condition

$$\frac{d\mathbf{x}}{dt} = \mathbf{u}(\mathbf{x}), \quad \mathbf{x} \in \partial O \tag{2.73}$$

for each mesh node by some standard explicit ordinary differential equation (ODE) integrator, such as Runge–Kutta or the adaptive Bogacki–Shampine (Bogacki & Shampine 1989) and Cash–Karp methods (Cash & Karp 1990). Unfortunately, the average volume of the objects would slowly shrink with time due to unavoidable discretization errors. To counter this, we employ two different strategies. First, we use the discretized version of the no-flux condition $\oint \mathbf{u} \cdot \mathbf{n} dS = 0$ for objects with zero flux. This equation effectively represents a hyperplane. We then rotate the solution vector onto this hyperplane. This procedure is similar to Farutin, Biben & Misbah (2014, equation (43)). Second, to eliminate the volume drift completely, we additionally employ the rescaling method as explained by Farutin *et al.* (2014, equation (63)).

Bending forces for capsule-like objects follow the Canham–Helfrich model (Canham 1970; Helfrich 1973). Various numerical implementations are explained in the article by Guckenberger *et al.* (2016) and reviewed by Guckenberger & Gekle (2017). Shear and area dilatation elasticity of cells and capsules is implemented as detailed by Krüger (2012) and Guckenberger *et al.* (2016). Large distortions of the mesh are prevented automatically in this case as the forces depend explicitly on the triangle deformations. Bubble surfaces, on the other hand, do not feature in-plane tensions. This results in their mesh becoming inhomogeneous very quickly, leading to numerical instabilities. To prevent this, we observe that the nodes need to follow the fluid velocity only in the normal vector direction since any tangential displacement leaves the bubble shape unchanged. Thus, an artificial tangential displacement of

$$\delta x_{i,\alpha}^{(a)} = \zeta \sum_{j=1}^3 (\delta_{ij} - n_{i,\alpha} n_{j,\alpha}) \frac{\sum_b (x_{j,\alpha}^{(b)} - x_{j,\alpha}^{(a)}) w_\alpha^{ab}}{\sum_b w_\alpha^{ab}}, \quad i = 1, 2, 3 \tag{2.74}$$

can be applied after every time step without modifying the physical behaviour. We apply this formula in an iterative process, indicated by the Greek subscript α .

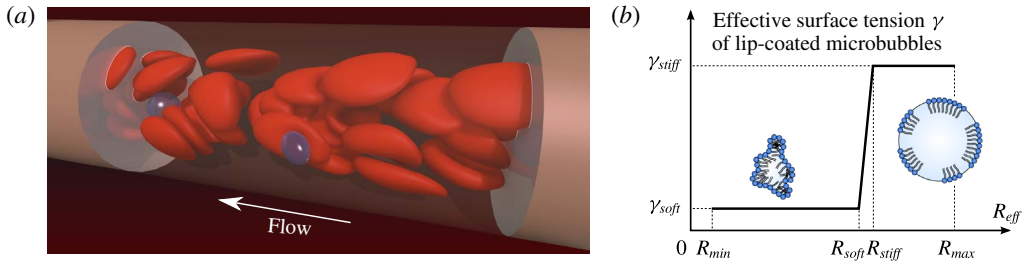


FIGURE 2. (Colour online) Simulation set-up. (a) Snapshot of the large simulation containing 30 red blood cells and two microbubbles. Periodic boundary conditions are used, i.e. the left and right non-translucent cylinders are periodic images of the centre one which has a length of $48 \mu\text{m}$ in this case. (b) Sketch of Marmottant *et al.*'s model for lipid-coated microbubbles (Marmottant *et al.* 2005; Overvelde *et al.* 2010). The effective surface tension γ is a function of the effective radius which varies between R_{min} and R_{max} during an ultrasound period. The bubble is in the soft buckled state for $R_{eff} \leq R_{soft}$ and in the stiff ruptured state for $R_{eff} > R_{stiff}$, as indicated by the two inset sketches.

The superscripts a and b denote different nodes, the Latin subscript indicates a certain Cartesian component and the sums go over the first ring of neighbours b of node a . The parameter $\zeta = 0.3$ controls the stiffness of the scheme. The iteration stops once the maximal displacement falls below a predefined threshold. Finally, the weights are chosen as $w_{\alpha}^{ab} = A_{\alpha}^{ab} / |\mathbf{x}_{\alpha}^{(b)} - \mathbf{x}_{\alpha}^{(a)}|$, where the sum of the areas A_{α}^{ab} of the two triangles containing nodes a and b tends to homogenize the triangle areas, and the denominator tries to keep possibly applied refinement local to where it had been applied. A similar approach has been used by Farutin *et al.* (2014, equation (59)).

We tested our code extensively by comparing the integrals with analytically known values (compare Farutin *et al.* 2014, § 8.3), as well as by studying usual benchmark systems such as the deformation of a capsule in an infinite shear flow (Guckenberger *et al.* 2016). The code was also successfully applied to the diffusion of particles near elastic membranes (Daddi-Moussa-Ider, Guckenberger & Gekle 2016a,b; Daddi-Moussa-Ider & Gekle 2016, 2017; Daddi-Moussa-Ider, Lisicki & Gekle 2017a,b) and was used to compare with experimental obtained shapes of red blood cells in microchannel flows (Quint *et al.* 2017). Further verifications can be found in the supplementary information. We parallelized our code with OpenMP and MPI, and we use explicit SIMD vectorization via the Vc library (Kretz & Lindenstruth 2012) in some core parts.

3. Ultrasound-triggered margination of microbubbles

We now use our VCO-BIM as introduced in the previous section to investigate the behaviour of ultrasound contrast agents (lipid-coated microbubbles) in microcapillary blood flow. Our numerical simulations consist of two ultrasound contrast agents and several red blood cells within a cylindrical blood vessel as depicted in figure 2(a). The lipid coating of the microbubbles leads to a radius-dependent effective surface tension which will be modelled as detailed in § 3.1. Red blood cells and the remaining ingredients are described in § 3.2. Our central result, namely the occurrence of ultrasound-triggered margination (UTM) is given in § 3.3.

3.1. Lipid-coated microbubbles

3.1.1. Surface forces

The coating of microbubbles leads to deviations from the simple coupling between bubble volume and external pressure expected from the expansion/compression of an ideal gas (Marmottant *et al.* 2005; de Jong *et al.* 2007; Frinking *et al.* 2010; Overvelde *et al.* 2010; Doinikov & Bouakaz 2011; Sijl *et al.* 2011). There are various models available for varying types of surface coatings that produce such nonlinear responses (e.g. Sarkar *et al.* 2005; Faez *et al.* 2013). One that incorporates the special properties of phospholipid-coated bubbles (i.e. the size-dependent state of the coating) was presented by Marmottant *et al.* (2005), providing a suitable description for their behaviour (Frinking *et al.* 2010; Overvelde *et al.* 2010; Doinikov & Bouakaz 2011; Sijl *et al.* 2011; Faez *et al.* 2013; Kooiman *et al.* 2014). The major ingredient is the introduction of an effective surface tension that depends nonlinearly on the bubble's size. Such a size dependence is the most important aspect of the model for the purpose of margination. Hence, a more elaborate surface model including surface viscosity (e.g. Paul *et al.* 2010) is not required here. The relation which we employ can be divided into three major regions (Marmottant *et al.* 2005; Overvelde *et al.* 2010) as illustrated in figure 2(b).

- (i) In the high compression regime, the area available per lipid molecule is smaller than its extent, leading to pronounced buckling as observed by ultrahigh-speed imaging (Sijl *et al.* 2011). This is modelled by an effective surface tension of $\gamma_{soft} \approx 0$ below an effective radius R_{soft} (Overvelde *et al.* 2010). The bubble is highly deformable in this state (Marmottant *et al.* 2005; Rychak *et al.* 2006).
- (ii) With increasing radius, a very narrow elastic regime occurs, extending up to a maximal radius R_{stiff} .
- (iii) Above R_{stiff} the shell ruptures, leaving floating rafts of lipids on the surface (Borden *et al.* 2005; Marmottant *et al.* 2005). This leads to the very high surface tension γ_{stiff} of a direct air–water interface.

Due to the smallness of the second regime (Overvelde *et al.* 2010), we set in the following $R_{soft} = R_{stiff}$ such that the effective surface tension in our case can be written as

$$\gamma(R_{eff}) = \begin{cases} \gamma_{soft} & \text{if } R_{eff} \leq R_{soft}, \\ \gamma_{stiff} & \text{if } R_{eff} > R_{soft}, \end{cases} \quad (3.1)$$

where $R_{eff} := \sqrt[3]{3V/(4\pi)}$ is the instantaneous effective radius and V the bubble volume. The traction jump then follows from the Young–Laplace equation (2.72).

The equilibrium radius R_0 , i.e. the radius assumed when no ultrasound is present, can be located at different positions relative to the transition radius R_{soft} depending on the process of bubble preparation. Most importantly, it was shown that they can be created in the buckled state ($R_0 \leq R_{soft}$) (Borden *et al.* 2005; Rychak *et al.* 2006; Frinking *et al.* 2010) as desired for safe transport by default within the blood vessels (Lindner *et al.* 2002).

3.1.2. Modelling the effect of an acoustic source

Because we are interested in the margination behaviour, the exact form of the oscillations is expected to be irrelevant. We therefore prescribe the flux of the i th bubble as $Q_i(t) = A_i \sin(2\pi ft)$ to model the effect of an external acoustic source. Here,

t is the time, A_i the flux amplitude and f the frequency. This results in a volume oscillation of

$$V_i(t) = V_i^{(0)} + A_i/(2\pi f)[1 - \cos(2\pi ft)] \quad (3.2)$$

for the i th bubble, with $V_i^{(0)}$ being the initial volume at $t=0$. To conserve the total outer fluid volume as required by (2.37), both bubbles are set to oscillate out of phase, i.e. $A_1 = -A_2$. Although not being entirely realistic, it is mandated on a very fundamental level by the periodic boundary conditions and the incompressibility of the ambient fluid. We do not expect that this small restriction affects the validity of the presented conclusions since (i) bubble–bubble interactions are strongly shielded by the RBCs and (ii) margination hinges upon the stiffness variations of the individual bubbles and is therefore independent of the phase of the oscillations.

Continuing, we emphasize that we impose only the instantaneous bubble volume and not a spherical shape. Hence, the bubbles are still deformable, a property which is crucial for the hydrodynamic interaction with the RBCs.

The most important quantity in the present context is the ratio of the stiff to soft duration which we denominate as $\delta = T_+/T_-$. Here, T_+ is the time spent in the stiff state (i.e. $R_{eff} > R_{soft}$) and T_- the time in the soft state ($R_{eff} \leq R_{soft}$). Since margination would trivially be expected for $\delta \gg 1$, we concentrate on $0 \leq \delta \leq 1$ in the present study, in agreement with experiments (Marmottant *et al.* 2005; de Jong *et al.* 2007; Overvelde *et al.* 2010; Sijl *et al.* 2011). We remark that δ does not depend on the frequency f .

3.1.3. Bubble parameters

In our simulations we set the surface tensions in the soft and stiff state to $\gamma_{soft} = 0.5\kappa_S$ and $\gamma_{stiff} = 10\kappa_S$, respectively. κ_S is the shear modulus of the red blood cells (see below). These choices suitably describe the stiffness of the bubbles relative to RBCs regarding margination while at the same time ensuring numerical stability. Realistic values of $\gamma_{stiff} = 7 \times 10^{-2} \text{ N m}^{-1}$ and $\gamma_{soft} \approx 0$ (Overvelde *et al.* 2010; Sijl *et al.* 2011) would lead to a numerically very stiff problem and consequently require extremely small time steps. The supplementary information (henceforth SI) shows that $\gamma_{soft} = 0.1\kappa_S$ and $\gamma_{stiff} = 25\kappa_S$ do not change the results significantly. Furthermore, we fix $R_{min} = 1.7 \mu\text{m}$ and $R_0 = R_{soft} = 2 \mu\text{m}$ which are typical values for microbubbles (Borden *et al.* 2005; Overvelde *et al.* 2010; Kooiman *et al.* 2014) (using $R_0 = 1 \mu\text{m}$ leaves the results qualitatively unchanged: see the SI). Taking δ as the major control parameter, R_{max} and the amplitudes A_i are uniquely determined via the prescribed volume oscillation law (3.2). Assuming an ideal gas within the bubbles and an atmospheric pressure of 100 kPa, a value of $\delta = 1$ then corresponds to an acoustic pressure amplitude of approximately $P_A \approx 45 \text{ kPa}$, in agreement with experimentally used values (Overvelde *et al.* 2010).

In most current applications, ultrasound pressure amplitudes and frequencies are in the kilo-pascal and mega-hertz range, respectively (Kooiman *et al.* 2014; Lammertink *et al.* 2015). Such values lead to strong primary and secondary radiation forces (Rychak, Klibanov & Hossack 2005; Johnson *et al.* 2016) making the bubbles agglomerate in a small spot on the vessel wall opposite to the ultrasound transducer (Dayton *et al.* 1999; Rychak *et al.* 2007; Kilroy *et al.* 2014). This strong localization is highly undesirable for drug delivery applications where a uniform bubble distribution over the entire vessel wall is required. In contrast, we will show below that ultrasound-triggered margination is able to reliably achieve an isotropic distribution if the ultrasound parameters are chosen such that radiation forces become

subdominant. For $P_A \approx 45$ kPa we therefore keep the acoustic frequency at $f = 1$ kHz in the following. The magnitude of the primary radiation force is then typically of the order of $|\mathbf{F}_{rad}| \approx 10^{-15}$ N, meaning that it plays only a secondary role as shown explicitly in the SI. We consequently neglect it in what follows. In order to exploit UTM also at higher frequencies, one can reduce P_A as exemplified in the SI where we consider $f \leq 10$ kHz for $P_A \approx 6$ kPa.

3.2. Blood flow in capillaries

3.2.1. Blood flow constituents

We model the blood flow by explicitly resolving the red blood cells and treating the surrounding blood plasma as a Newtonian fluid (Chien *et al.* 1966). For our simulations we use mostly 15 RBCs that are distributed randomly within the blood vessel if not noted otherwise. Each RBC has an initial large radius of $R_{RBC} = 4$ μm (Evans & Fung 1972; Freund 2014). Continuing, the RBC shear elasticity is modelled via Skalak's constitutive energy (Skalak *et al.* 1973) with a shear modulus of $\kappa_S = 5 \times 10^{-6}$ N m⁻¹ (Yoon *et al.* 2008; Freund 2014) and the typical discocyte shape as the reference geometry. This model also includes an area dilatation modulus that is set to $\kappa_A = 10\kappa_S$. Furthermore, we additionally introduce an extra surface dilatation energy $E_a = (\kappa_a/2)(S - S_0)^2/S_0$ (Krüger 2012) with the corresponding area dilatation modulus $\kappa_a = 10\kappa_S$, the instantaneous surface area S and the reference surface area S_0 . This leads to area deviations of typically $\lesssim 4\%$. Moreover, bending forces are modelled according to the Canham–Helfrich law (Canham 1970; Helfrich 1973; Guckenberger & Gekle 2017) with a bending modulus of $\kappa_B = 2 \times 10^{-19}$ N m (Park *et al.* 2010; Freund 2014) and the spontaneous curvature set to zero. For numerical efficiency we employ the usual approximation that inner and outer viscosities are equal (Krüger 2012; Zhao *et al.* 2012; Freund 2014; Kumar *et al.* 2014), i.e. the viscosity ratio is $\lambda_{RBC} = 1$. As a result, any double-layer integrals over the RBC surfaces vanish, and Wielandt deflation terms cannot appear for RBCs (compare § 2.3.3). Nevertheless, both are still present for the bubbles.

The periodic vessel has a length of usually 24 μm and a radius of $R_{Vessel} = 11$ μm . Together with the 15 RBCs this results in a haematocrit of approximately 16%, a typical value encountered in capillaries (Klitzman & Duling 1979; House & Lipowsky 1987). The larger simulation from figure 2(a) as well as higher haematocrit values lead to the same results which are presented below and in the SI. Furthermore, one possibility for the boundary condition of the vessel wall would be to set its velocity to zero. This, however, leads to a mixed-type Fredholm integral equation. As explained in § 2.3.1, no general mathematical theory exists and this type can be rather performance intensive although it might work in practice. We therefore follow Freund (2007) and fix the wall's nodes \mathbf{x}_i via springs to their original position $\mathbf{x}_i^{(0)}$, leading to a traction jump of $\Delta \mathbf{f} = \kappa_W(\mathbf{x}_i - \mathbf{x}_i^{(0)})$, where $\kappa_W = 6.25 \times 10^6$ N m⁻³ is the spring constant. Increasing κ_W by a factor of 5 does not change results qualitatively as shown in the SI. Thus we end up with a Fredholm integral equation of the second kind having exactly one solution as proved in § 2.3.4.

3.2.2. Hydrodynamics

We use our VCO-BIM for 3-D periodic domains as presented in § 2 to solve the Stokes equation. The core of this method is (2.1) which we solve for an imposed average flow chosen such that the maximal flow velocity in the middle of the vessel is roughly $u_{max} \approx 4.7$ mm s⁻¹, if not noted otherwise. This value matches with physiological flow velocities in capillaries and arterioles (Popel & Johnson 2005).

The Stokes equation is a good approximation if the Reynolds numbers are much smaller than unity. For the translational motion we find for our system $Re_T = 2R_{RBC}u_{max}\rho/\mu \approx 0.03 \ll 1$, where $\mu = 1.2 \times 10^{-3} \text{ kg (s m)}^{-1}$ is the dynamic viscosity of blood plasma (Skalak, Ozkaya & Skalak 1989) and $\rho \approx 10^3 \text{ kg m}^{-3}$ its density. A different Reynolds number can be defined based on the radial oscillations as $Re_R = (2R_0)^2 \rho f / \mu$. For $f \leq 10 \text{ kHz}$ (as used in the SI) this results in $Re_R < 0.07 \ll 1$. We thus conclude that the Stokes equation can faithfully capture the considered RBC and bubble interactions.

3.2.3. Numerical procedure

The general methodology of our numerical implementation was already explained in § 2.5. Here we only mention the remaining aspects that are specific to the present application. The triangle count for the blood vessel is 630 for the 24 μm long channel. Rivara's longest-edge bisection algorithm (Rivara 1984) is used to refine high curvature and close contact regions for the dynamic objects. Hence, the number of triangles varies over time with typical averages of approximately 1500 for the bubbles and 780 for the RBCs. See the SI for some illustrations. Artificial overlapping between the objects within the channel is further suppressed by the introduction of a short-range repulsive potential $E_{Rep}(r_{ij}) = [b/(r_{ij} - l_m)]\exp[l_c/(r_{ij} - l_c)]$ (Noguchi & Gompper 2005; McWhirter, Noguchi & Gompper 2009) with r_{ij} denoting the distance between two nodes (vertices), l_m being the minimal possible distance and l_c the distance where the potential smoothly drops to zero. We choose $l_m = 0.01R_{RBC}$ and $l_c = 0.125R_{RBC}$, the latter being of the order of the typical edge length of the initial bubble meshes.

The traction jump on the RBCs for the elasticity and dilatation contributions is computed by differentiating the energies with respect to the mesh vertices, as explained by Krüger (2012) and Guckenberger *et al.* (2016, § 4.2). The repulsive potential is handled in the same way. Bending forces (for the RBCs) and the mean curvature (required for the bubbles, cf. (2.72)) are obtained via Method C as given by Guckenberger *et al.* (2016). Despite being less precise than some alternative methods described in that work, it proved to be more stable than the others.

SPME errors for the computation of the Green's functions are kept below $\lesssim 0.01\%$. Increasing the precision by one order of magnitude did not change the results (see the SI). The Gaussian quadrature rules for the integrals use 7 Gauss points per triangle for the bubbles and the blood vessel and 4 points for the RBCs. We solve the integral equation via GMRES with a residuum of max. 10^{-4} . Furthermore, the time evolution from (2.73) is obtained by the adaptive Bogacki–Shampine method (Bogacki & Shampine 1989) with the relative tolerance fixed to 10^{-5} and the absolute tolerance set to $10^{-4}R_{RBC}$ (Press *et al.* 2007). We use the volume rescaling approach for bubbles and RBCs and additionally the hyperplane method for RBCs to handle any artificial volume drift as explained in § 2.5. No special mesh control scheme was necessary for the vessel and the RBCs due to the nature of the prescribed forces, but for bubbles we use (2.74) where the iteration stops once the maximal displacement falls below $10^{-4}R_{RBC}$. Typical simulation times are in the 1–2 weeks regime on a recent 20 core Intel system.

3.3. Results and discussion

3.3.1. Microbubbles with constant surface tensions

In order to illustrate the general effect of margination, we first consider the case when the microbubbles are prepared once in the soft state and once in the stiff state.

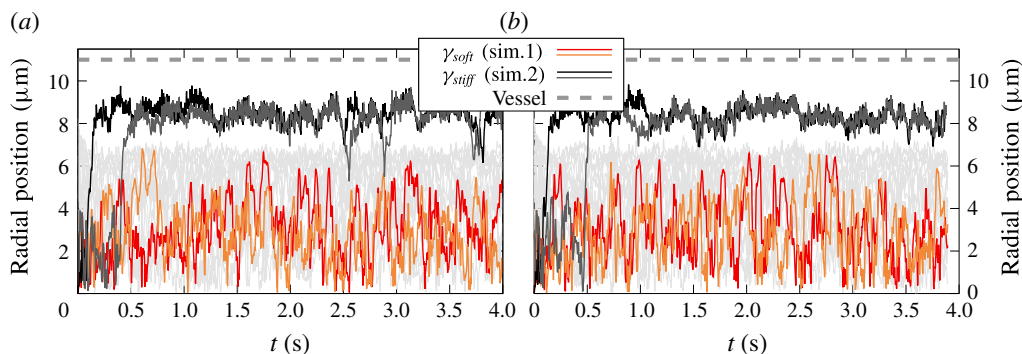


FIGURE 3. (Colour online) Margination behaviour of purely soft and purely stiff non-oscillating (a) and oscillating (b) microbubbles. $\gamma = \text{const.}$ in all cases. We depict the radial positions of the centroids of two bubbles with constant effective surface tensions in blood flow as a function of time. The surface tensions are set to $\gamma = \gamma_{\text{soft}} = 0.5\kappa_S$ (red/orange) and $\gamma = \gamma_{\text{stiff}} = 10\kappa_S$ (black/grey). For (b), bubbles oscillate with a frequency of $f = 1$ kHz, leading to a variation of R_{eff} between $1.7 \mu\text{m}$ and $2.075 \mu\text{m}$. Curves for different γ constitute independent simulations. The red blood cells, shown as light grey lines, illustrate the cell-free layer between $7 \mu\text{m}$ and the wall. The vessel radius is $11 \mu\text{m}$, the haematocrit is fixed to 16% and the maximal flow velocity is $u_{\text{max}} \approx 4.7 \text{ mm s}^{-1}$. The soft bubbles ($\gamma = \gamma_{\text{soft}}$) remain in the centre, whereas the stiff bubbles ($\gamma = \gamma_{\text{stiff}}$) show margination.

Figure 3(a) shows two simulations without any volume oscillations. The case $\gamma = \gamma_{\text{soft}}$ corresponds to coated bubbles that are always in the soft state. Thus, they have a deformability comparable to the RBCs and remain in the centre of the blood stream together with the erythrocytes. On the other hand, setting $\gamma = \gamma_{\text{stiff}}$ models pure bubbles that are much stiffer than the RBCs. Hence, they quickly migrate isotropically to the vessel wall. Similar observations are made in figure 3(b) for bubbles oscillating with a frequency of $f = 1$ kHz while keeping the effective surface tension constant. These results demonstrate that the volume oscillations by themselves do not strongly affect particle migration for the presently chosen parameters.

3.3.2. Lipid-coated microbubbles with radius-dependent surface tension

To demonstrate ultrasound-triggered margination, we consider two lipid-coated bubbles whose shells are modelled with an effective surface tension as described by (3.1) and that are prepared in the soft state ($\delta = 1$, $R_{\text{eff}} = R_{\text{soft}}$). Figure 4(a) depicts the bubbles' radial trajectories from a simulation where initially no ultrasound is applied. The bubbles are preferably located in the RBC rich core, in agreement with figure 3(a) and experimental observations (Lindner *et al.* 2002). This allows for secure travel through the vascular system. Once the volume oscillations are activated after around 4.0 s to model an ultrasound source, the bubbles oscillate periodically in stiffness due to the lipid coating that is modelled according to (3.1). This is in contrast to figure 3 where the surface tension remains constant. Most importantly, we observe fast migration towards the vessel wall within less than one second (see the SI for a movie). This time frame corresponds to a travelled distance of less than 4 mm, highlighting the rapidity of the effect. The cause of the fast margination is the lipid shell: as discussed in the previous section, the coating leads to a stiffening during the high-pressure state of the ultrasound signal and a corresponding softening

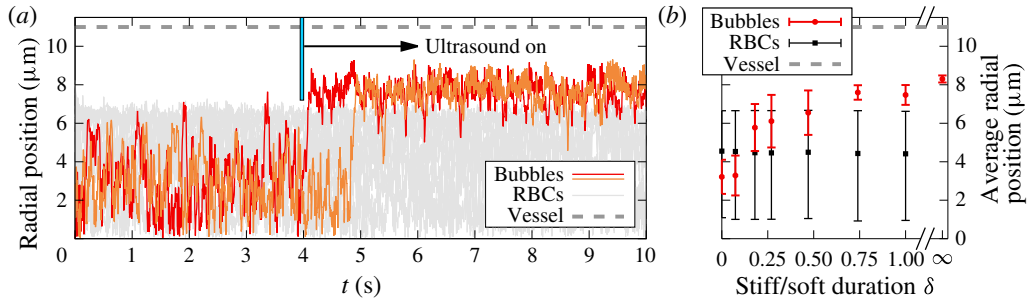


FIGURE 4. (Colour online) Ultrasound-triggered margination. (a) Radial positions of the centroids of two microbubbles coated with lipids, modelled according to Marmottant *et al.*'s law (Marmottant *et al.* 2005; Overvelde *et al.* 2010). Since the ultrasound is off at the beginning, the bubbles are soft and thus remain in the vessel interior (effective radius $R_{eff} = 2 \mu\text{m}$). When the oscillations are switched on at ≈ 4 s, ultrasound-triggered margination leads to rapid migration to the vessel wall. Here, $\delta = 1$, i.e. the bubbles are stiff for the first half of the ultrasound period and soft during the second with their effective surface tension varying in the range $\gamma \in [0.5; 10]\kappa_S$. The effective radii alternate between $1.7 \mu\text{m}$ and $2.23 \mu\text{m}$ in each period. See the SI for a movie. (b) Average radial positions of the oscillating bubbles and the RBCs for several different values of δ . The rightmost point corresponds to the limit $\delta \rightarrow \infty$ (i.e. always stiff) from figure 3(b). Error bars are determined as explained in the main text and the SI.

during the low-pressure state (Marmottant *et al.* 2005; Overvelde *et al.* 2010). As figure 4(a) clearly demonstrates, the overall behaviour is dominated by the stiff stage, as will be further analysed below.

We continue to demonstrate the robustness of ultrasound-triggered margination by considering microbubbles that are very soft in equilibrium. The bubbles then spend a much longer portion of the ultrasound period in the soft than in the stiff state ($\delta < 1$). Figure 4(b) depicts the results. The error bars are determined by considering first the minimal and maximal centroid position of all RBCs/bubbles as a function of time for $t > 1$ s or after definite margination, second a subsequent temporal average and third a weighted average over simulations with different starting configurations. This is similar to the procedure by Müller, Fedosov & Gompper (2014) and is explained in more details in the SI. Figure 4(b) shows that the bubbles are still preferably located at the outside of the RBC rich core for $\delta < 1$, even for ratios as low as $\delta \approx 0.2$. The margination is completely suppressed only at small values such as $\delta \approx 0.1$ where the soft time is around 10 times longer than the stiff time. The results from the SI for $P_A = 6$ kPa show a transition at $\delta \approx 0.3$ indicating that the precise location of the transition depends on the details of the system set-up but nevertheless happens for $\delta \ll 1$. Thus we can conclude that reliable margination is observed if the soft time is at most three times larger than the time in the stiff state ($\delta \gtrsim 0.3$).

The effect that small values of δ are sufficient to trigger ultrasound-triggered margination can be understood qualitatively. During the soft state, shearing by the flow and collisions with red blood cells cause deformations of the bubbles. Both are comparably slow processes. During the subsequent stiff stage, however, a high surface tension forces the deformed object back to a spherical shape much more quickly. More quantitatively, the typical relaxation time towards the spherical rest shape in the stiff state can be estimated as $\tau_{stiff} = 2R_{stiff}\mu/\gamma_{stiff} \approx 0.1$ ms. On the other hand, the time required by the flow to deform the bubble away from the

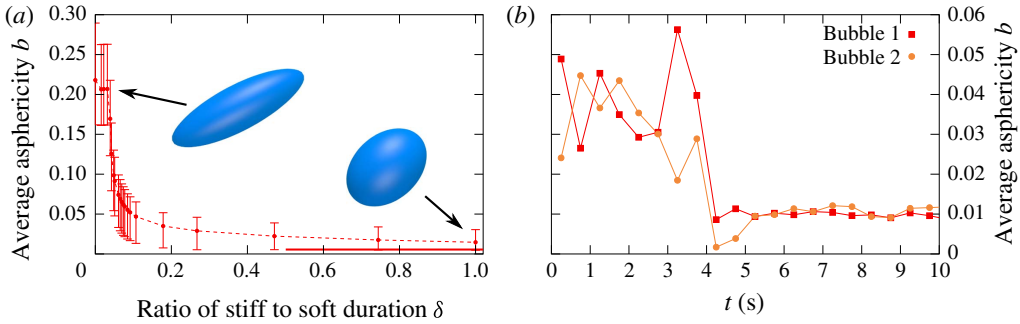


FIGURE 5. (Colour online) Average asphericities of oscillating lipid-coated microbubbles. (a) The left figure shows the result for a single microbubble in an infinite shear flow with shear rate $s = 544 \text{ s}^{-1}$ as a function of δ . At $\delta \approx 0.05$ the deformation increases sharply while for $\delta > 0.1$ almost no deformation is seen. The limiting value $\delta \rightarrow \infty$ is shown as a red solid line at the bottom. The surface tension varies in $\gamma \in [0.5; 10] \kappa_S$ and the oscillation frequency is $f = 1 \text{ kHz}$. Error bars indicate the minimal and maximal asphericities during one ultrasound period. The two inset snapshots show the bubbles with their maximal deformation for $\delta = 0.032$ (left inset) and $\delta = 1$ (right inset). (b) Asphericity of the bubbles from figure 4(a) averaged over consecutive time intervals of 0.5 s.

spherical shape in the soft state can be estimated by assuming a simple Poiseuille profile with the centre flow velocity $u_{max} = 4.7 \text{ mm s}^{-1}$. This leads to a shear rate of $s \approx 544 \text{ s}^{-1}$ if the bubble is positioned one diameter ($2R_{soft}$) away from the wall. Hence, $\tau_{deform} = 1/s \approx 1.8 \text{ ms}$, which is approximately one order of magnitude larger than the relaxation time scale τ_{stiff} in the stiff state. This explains why the latter dominates the margination behaviour. We remark that the ratio $\tau_{stiff}/\tau_{deform}$ is formally equivalent to the capillary number $Ca = 2R_{stiff}s\mu/\gamma_{stiff}$ for the bubbles in the stiff state, i.e. Ca determines their behaviour while being stiff. The interpretation of the ratio $\tau_{stiff}/\tau_{deform}$, however, is fundamentally different here, as it makes a comparison between the two different states rather than making a statement about only one state.

The above argument can be explicitly confirmed by considering an oscillating microbubble in a simple linear shear flow in an infinite domain simulated with VCO-BIM ($V_T \rightarrow \infty$, compare § 2.2.5). As a measure of deformation, we extract the asphericity $b := [(\lambda_1 - \lambda_2)^2 + (\lambda_2 - \lambda_3)^2 + (\lambda_3 - \lambda_1)^2] / (2R_g^4)$ from the shape, where $R_g^2 := \lambda_1 + \lambda_2 + \lambda_3$ is the squared radius of gyration and λ_1 , λ_2 and λ_3 are the eigenvalues of the gyration tensor (Fedosov *et al.* 2011). For reference, the discocyte equilibrium shape of an RBC leads to $b \approx 0.15$. Figure 5(a) shows that the bubble remains almost spherical for δ values as low as 0.1, meaning that the bubble is stiff only during $\approx 9\%$ of the ultrasound period. Only below a rather sharp threshold at $\delta \approx 0.05$ the bubble behaves akin to a truly soft object exhibiting strong deformation. Note that this value matches well with the ratio $\tau_{stiff}/\tau_{deform} \approx 0.056$, and reasonably well with the bubbles' transition from the inner core to the outside in figure 4(b). Furthermore, the value $b \approx 0.015$ at $\delta = 1$ approximately agrees with the asphericity observed for the simulation in figure 4(a) after the ultrasound was switched on, as depicted in figure 5(b).

3.3.3. Further investigations

Pure margination is an isotropic effect: there is no preferred initial migration direction nor a preferred position close to the wall. We exemplify this in figure 6

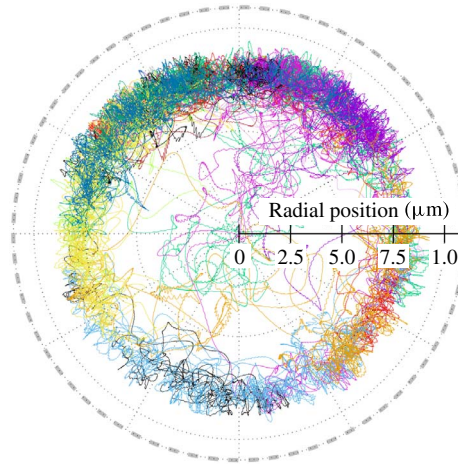


FIGURE 6. (Colour online) Polar plot of several bubble trajectories (i.e. as viewed from the outlet). The figure shows the $\delta = 0.74$ and $\delta = 1$ simulations used for figure 4(b), representing different system realizations. Trajectories only shown for $t > 1$ s or after definite margination. Rare short-lived migration events to the inside occur. Each bubble in each simulation is shown in a different colour. The outer grey dashed line depicts the vessel radius.

where we show the trajectories of migrated bubbles from several simulations representing different system realizations. Obviously, no specific accumulation point exists. This is in contrast to migration induced by buoyancy or radiation forces at much higher frequencies (Dayton *et al.* 1999; Rychak *et al.* 2007; Kilroy *et al.* 2014; Johnson *et al.* 2016). Note that the inclusion of radiation forces for the chosen parameters leaves the qualitative results unchanged, as described in detail in the SI. The major influence on figure 6 comes therefore from the initial conditions and the length of the simulations.

Figure 7(a) shows that increasing the frequency from $f = 1$ kHz to 10 kHz leaves the qualitative results for the radial position unchanged when radiation forces are neglected. Most interestingly, however, the asphericity is approximately reduced by half in the case of the faster oscillations (figure 7b). The reason is that for 10 kHz less time within one period is available to deform the bubbles before the stiff state takes over, as suggested by the above time scale estimates. This strongly indicates that higher frequencies reinforce the effect that small values of δ are sufficient to obtain ultrasound-triggered margination. Even more, this serves as a hint that the effect of UTM, which has been overlooked so far, might have provided a noticeable contribution to the effectiveness of microbubbles for targeted drug delivery observed in recent *in vivo* and clinical studies that used higher frequencies (Lammertink *et al.* 2015; Kotopoulos *et al.* 2016).

Continuing, we demonstrate that UTM intrinsically hinges on the presence of the red blood cells. If they are removed, the result in figure 8(a) is obtained, showing clearly that oscillating lipid-coated microbubbles move towards the centre of the channel for $\delta = 1$. This is in notable contrast to figure 4(a), where rapid margination for the same set of parameters is observed. Hence, neglecting the influence of the red blood cells in *in vitro* experiments can easily lead to conclusions that no longer hold for the *in vivo* case. On the other hand, with a finite haematocrit, margination

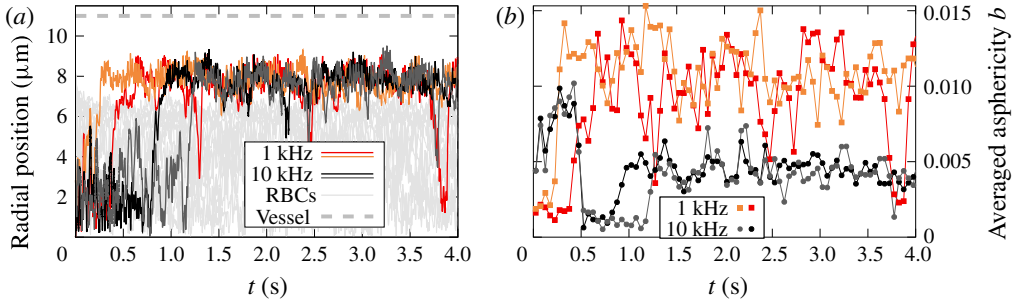


FIGURE 7. (Colour online) Influence of frequency: behaviour of two oscillating lipid-coated microbubbles for $\delta = 1$ and a haematocrit of 16%, once for a frequency of $f = 1$ kHz and once for 10 kHz (two distinct simulations); $u_{max} \approx 4.7$ mm s⁻¹. (a) Radial positions of the centroids. The red blood cells are shown in light grey. (b) Corresponding microbubble asphericities averaged over consecutive time intervals of 50 ms.

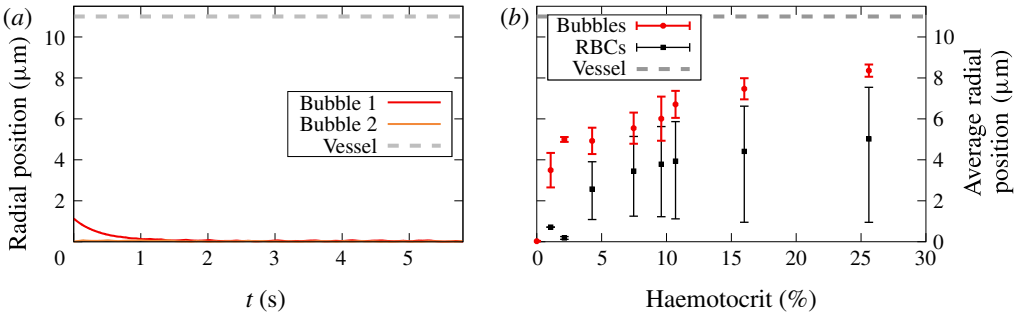


FIGURE 8. (Colour online) Influence of haematocrit: (a) only bubbles (haematocrit = 0); (b) average radial position for $\delta = 1$ as a function of haematocrit. Values and error bars extracted from several simulations as in figure 4(b).

is always observed in the sense that the RBCs are located at the interior and the bubbles form an outer layer (figure 8b). The position of this outer layer depends on the size of the RBC-rich inner region which grows when more RBCs are present (Müller *et al.* 2014), with the average radial position being reminiscent of a pitchfork bifurcation. The reason is that the RBCs migrate to the centre and push the bubbles to the outside because the latter are seen as stiffer on average as already described above.

Moreover, we depict in figure 9 the influence of the flow velocity. Margination still occurs in all cases, but higher velocities tend to decrease the radial position of the margined bubbles. The effect, however, is comparably small. The upper horizontal axis displays a corresponding effective non-dimensional shear rate defined here by

$$s^* := \frac{u_{max}}{2R_{Vessel}} \frac{\mu D_{RBC}^3}{\kappa_B}, \tag{3.3}$$

with an effective RBC diameter $D_{RBC} := \sqrt{A_{RBC}/\pi}$ and the RBC surface $A_{RBC} \approx 137 \mu\text{m}^2$. This definition is similar to the one by Müller *et al.* (2014) except that we use the maximal instead of the average flow velocity. Hence, we find qualitative

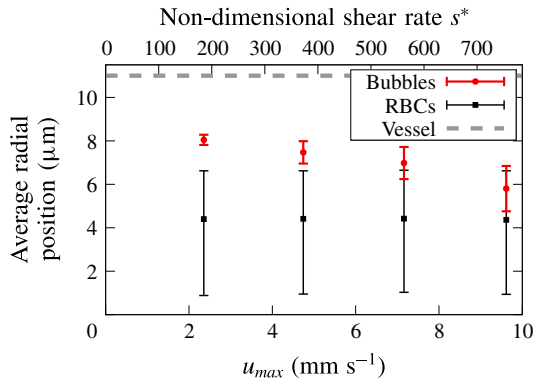


FIGURE 9. (Colour online) Influence of the velocity for $\delta = 1$ and a haematocrit of 16%: average radial position as a function of the flow velocity. Values and error bars extracted from several simulations as in figure 4(b).

agreement with their results for spherical rigid particles (compare figure 3a in Müller *et al.* 2014): margination is only a little affected by the shear rate if it is high enough.

Finally, we note that the effect of UTM does not change significantly if the effective surface tension in the soft state is decreased to $\gamma_{soft} = 0.1\kappa_S$ or the stiff tension is increased to $\gamma_{stiff} = 25\kappa_S$, if the size of the bubbles is halved to $R_0 = 1 \mu\text{m}$, if the initial particle distribution is varied or if the simulation box length is doubled as shown in the SI. Moreover, the average of the nodal velocity of the vessel wall (§ 3.2.1) after a short initial startup phase is $\lesssim 0.08u_{max}$ and the nodes move less than $0.1R_{RBC}$, indicating that the spring wall suitably replaces a completely stationary wall. Nevertheless, we also show in the SI that the results do not change if the vessel wall is made five times stiffer.

4. Conclusion

In the first part of our work we developed an extended boundary integral method to simulate volume-changing objects such as microbubbles in a 3-D periodic domain (VCO-BIM). In contrast to all other commonly used ‘capsule-like’ objects (vesicles, cells, drops), these bubbles contain a compressible gas with very low viscosity. As a consequence their volume can change as a function of time. This behaviour leads to two additional terms in the boundary integral equations which arise from (i) integrals over the unit cell and (ii) ensuring uniqueness of the solution. We showed that the latter, which can be seen as part of a Wielandt deflation procedure, is optional for capsule-like objects with a finite inner viscosity but becomes a necessary ingredient for bubbles. To this end, we proved that the resulting Fredholm integral equation has exactly one solution for an arbitrary number of bubbles and capsule-like entities with arbitrary viscosity ratios. Although periodic boundary integral methods for cells and capsules have been amply used in the past, such a proof has so far not appeared in the literature. The proof can be easily adapted for the case of other Green’s functions, e.g. in infinite domains.

In the second part we used our method to show that lipid-coated microbubbles possess unique and highly desirable properties which are not found for other drug delivery agents. During transport from the injection site to the target organ, with no ultrasound present, the bubbles behave as soft objects akin to red blood cells,

travelling near the centre of blood vessels. Application of a localized ultrasound at the target region then causes the bubbles to alternate between a soft and a stiff state. This leads to their isotropic margination towards the vessel wall within less than one second in the presence of red blood cells. Surprisingly, margination even happens when the time spent in the stiff state is more than three times smaller than the time in the soft state. We explain this observation by the fact that the effective surface tension (leading to a spherical shape during the stiff stage) acts on much shorter time scales than the surrounding flow (which deforms the bubble during the soft stage). This, together with the presented studies regarding frequency, haematocrit and flow velocity indicates that ultrasound-triggered margination is a robust effect. Given that it leads to a uniform bubble distribution on the vessel wall while other targeting mechanisms such as radiation forces often cause large inhomogeneities, the effect identified here might open a promising route to design novel drug delivery systems in the future.

Acknowledgements

Funding from the Volkswagen Foundation, funding and support from the KONWIHR network and computing time granted by the Leibniz-Rechenzentrum on SuperMUC are gratefully acknowledged by A.G. and S.G. A.G. additionally thanks the Elitenetzwerk Bayern (ENB), Macromolecular Science, for their support.

Supplementary information

Supplementary information (SI) is available at <https://doi.org/10.1017/jfm.2017.836>.

Appendix A. List of important symbols

For the reader's convenience, we provide in table 1 a short overview of the important symbols used in § 2 together with their point of definition.

Appendix B. Objects overlapping with the unit cell boundary

Section 2 assumed that all objects are completely located within the unit cell Γ . However, satisfying this condition is impossible for dense suspensions even for a single time step, and because flowing objects regularly leave and enter Γ during the course of dynamic simulations. Moreover, it is much more convenient to carry out integrations over the full surfaces of objects (i.e. including parts that lie partially outside of Γ), as otherwise the meshes would need to be split. The possibility of doing this is often assumed in the literature. Yet, due to the centroids that appear explicitly in the BI and FBI equations (2.33) and (2.1), respectively, and the linear term in the stresslet (2.18) it is not clear *a priori* whether this is indeed possible since these parts contain striking non-periodicities. Here we explicitly show that the equations nevertheless hold if applied correctly.

B.1. The boundary integral equation with cut objects

We consider a system with overlapping objects as sketched in figure 10. The outer boundary of Ω is thus not formed by $\partial\Gamma$ but rather by $\partial\tilde{\Gamma}$, A and B . The usual derivation of the BI equation starts with integrating the reciprocal identity over Ω (e.g. Pozrikidis 1992, chap. 2.3). Subsequent use of the divergence theorem then

Symbol	Meaning
O_k	The k th object (of any type), § 2.1.2.
B_k	The k th bubble, § 2.1.2.
C_k	The k th capsule-like entity (a capsule, vesicle, red blood cell, ...), § 2.1.2.
W_k	The k th wall (walls do not have any inside), § 2.1.2.
N_O	The total number of objects, § 2.1.2.
N_B, N_C, N_W	The number of bubbles, capsules and walls, § 2.1.2.
Ω	The ambient fluid (the set outside of any object), § 2.1.2.
Γ	The unit cell, § 2.1.1.
∂O_k	The surface of object O_k , § 2.1.2.
V_{O_k}, V_Γ	The volume of the k th object and of the unit cell Γ , § 2.1.1.
$\mathbf{a}^{(1)}, \mathbf{a}^{(2)}, \mathbf{a}^{(3)}$	The three base vectors spanning the unit cell Γ , § 2.1.1.
$\mathbf{X}^{(\alpha)}$	A periodic grid vector in the real space with grid index $\alpha \in \mathbb{Z}^3$, equation (2.2).
$\mathbf{b}^{(1)}, \mathbf{b}^{(2)}, \mathbf{b}^{(3)}$	The reciprocal base vectors, § 2.1.1.
$\mathbf{k}^{(\kappa)}$	A periodic grid vector in the reciprocal space with grid index $\kappa \in \mathbb{Z}^3$, equation (2.4).
\mathbf{u}	The velocity, § 2.1.2.
\mathbf{x}	A generic point, often also the integration variable.
\mathbf{x}_0	The evaluation point, § 2.2.
\mathbf{n}	The outside normalized normal vector, § 2.1.2.
P	The pressure, equation (2.6).
μ	The viscosity of the ambient fluid Ω , § 2.1.2.
σ_{ij}	The stress tensor, equation (2.8).
t	The time.
λ_C	The viscosity ratio of capsule C , § 2.1.2.
λ_O	The effective viscosity ratio of object O , equation (2.13).
$\mathbf{f}, \mathbf{f}^+, \mathbf{f}^-$	The traction (general, outside and inside), equation (2.7).
$\tilde{\mathbf{f}}$	The periodic part of the traction, equation (2.25).
$\Delta \mathbf{f}$	The traction jump, equation (2.9).
\mathbf{F}	The ‘unified traction’ (\mathbf{f}^+ or $\Delta \mathbf{f}$), § 2.2.1.
$(\mathcal{N}_{\partial O_q} \mathbf{F})$	The single-layer integral over the surface ∂O_q , equation (2.11).
$(\mathcal{K}_{\partial O_q} \mathbf{u})$	The double-layer integral over the surface ∂O_q , equation (2.12).
G_{ij}	The Green’s function for the single-layer integral (Stokeslet), equation (2.14).
T_{ijl}	The Green’s function of the double-layer integral (stresslet), equation (2.18).
\tilde{T}_{ijl}	The periodic part of T_{ijl} , equation (2.18).
c_k	The prescribed velocity divergence of the bubbles, equations (2.5) and (2.31).
Q_{O_k}	The flux out of or into the object O_k , equation (2.31).
$\chi_j^{(O_k)}, \boldsymbol{\chi}^{(O_k)}$	The geometric centroid of object O_k , equation (2.30).
$z_j^{(k)}$	The Wielandt deflation prefactor, equation (2.46).
$\langle \bullet \rangle_\Gamma$	The volume average over the whole unit cell Γ , equation (2.24).
h_j	An eigensolution to the homogeneous version of the BI equation, equation (2.39).
a_j	Eigensolutions to the adjoint of the homogeneous equation, equation (2.40).
$M_j[\mathbf{a}]$	Most of the right-hand side of the adjoint equation, equation (2.41).
R_j	Collection of the terms missing in the homogeneous equation, equation (2.42).

TABLE 1. List of important symbols used throughout the text.

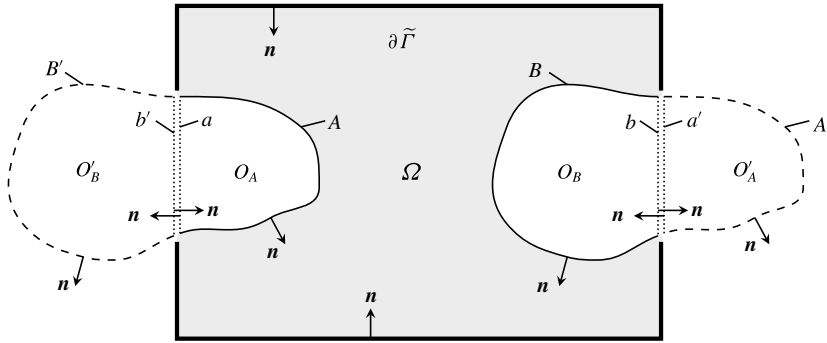


FIGURE 10. Overlapping of objects with the unit cell boundary $\partial\Gamma = \partial\tilde{\Gamma} \cup a' \cup b'$. Primed quantities lie outside of the unit cell (except a' and b' which form portions of $\partial\Gamma$). A single object $O_B \cup O_A$ is shown. This object has a periodic image $O_B \cup O_A'$. Furthermore, both are cut at the same place into two parts as they overlap with $\partial\Gamma$. The four closed sets are O_B' , O_A , O_B and O_A' . The corresponding surfaces without the cut faces are B' , A , B and A' . For the left object, the cut faces (dotted) are a and b' , where both lie on $\partial\Gamma$ and are identical except that their normal vectors point in opposite directions; i.e. there is no gap between a and b' . Similar for its right image (but with b and a'). Moreover, there is no real gap between $\partial\tilde{\Gamma}$ and the objects. $\partial\Omega$ in this figure is given by $\partial\Omega = \partial\tilde{\Gamma} \cup A \cup B$; in the general case $\partial\Omega$ also contains the full surfaces of objects completely located within the unit cell.

explicitly introduces the boundaries of Ω . In § 2.2.1 the outer boundary was simply $\partial\Gamma$ as all objects were located within Γ , but here it is given by $\partial\tilde{\Gamma} \cup A \cup B$. This leads to

$$u_j(\mathbf{x}_0) = \dots - \frac{1}{8\pi\mu} (\mathcal{N}_{A \cup B} \mathbf{f}^+)_j(\mathbf{x}_0) + \frac{1}{8\pi} (\mathcal{K}_{A \cup B} \mathbf{u})_j(\mathbf{x}_0) - \frac{1}{8\pi\mu} (\mathcal{N}_{\partial\tilde{\Gamma}} \mathbf{f}^+)_j(\mathbf{x}_0) + \frac{1}{8\pi} (\mathcal{K}_{\partial\tilde{\Gamma}} \mathbf{u})_j(\mathbf{x}_0), \quad \mathbf{x}_0 \in \Omega, \quad j = 1, 2, 3. \quad (\text{B } 1)$$

We will use the notation introduced in figure 10 from now on and only deal explicitly with one object and its periodic image (as also seen in this figure). Additional objects that lie partially outside of the unit cell result in analogous terms. Objects that lie completely within Γ do not require special treatment here. Both types of omitted terms will be indicated by an ellipsis to shorten notation.

The first goal now is to recover integrals over the full unit cell surface $\partial\Gamma$ instead of only over $\partial\tilde{\Gamma}$ in (B 1). For this we exploit $\int_a + \int_{b'} = 0$ and $\int_b + \int_{a'} = 0$ for the single- or double-layer kernels. This holds since a and b' (and b and a') denote the same surface but with antiparallel normal vectors (again, see figure 10). a' , b' and $\partial\tilde{\Gamma}$ can be combined to $\partial\Gamma$, and the remaining sets form the surfaces of the closed sets O_A and O_B . Thus, equation (B 1) becomes

$$u_j(\mathbf{x}_0) = -\frac{1}{8\pi\mu} (\mathcal{N}_{\partial O_A \cup \partial O_B} \mathbf{f}^+)_j(\mathbf{x}_0) + \frac{1}{8\pi} (\mathcal{K}_{\partial O_A \cup \partial O_B} \mathbf{u})_j(\mathbf{x}_0) + \dots - \frac{1}{8\pi\mu} (\mathcal{N}_{\partial\Gamma} \mathbf{f}^+)_j(\mathbf{x}_0) + \frac{1}{8\pi} (\mathcal{K}_{\partial\Gamma} \mathbf{u})_j(\mathbf{x}_0), \quad \mathbf{x}_0 \in \Omega, \quad j = 1, 2, 3. \quad (\text{B } 2)$$

If O_A and O_B are parts of a capsule filled with a Stokesian fluid, the reciprocal identity also holds for their insides. Integrating it over their volumes, using the divergence theorem and adding the result to the above equation (compare Pozrikidis 1992, pp. 37 and 143) recovers the form of (2.10) that includes the viscosity ratios and the traction jumps, but now with separate terms for each object part:

$$\begin{aligned}
 u_j(\mathbf{x}_0) = & -\frac{1}{8\pi\mu}(\mathcal{N}_{\partial O_A \cup \partial O_B} \mathbf{F})_j(\mathbf{x}_0) + \frac{1 - \lambda_{O_A \cup O_B}}{8\pi}(\mathcal{K}_{\partial O_A \cup \partial O_B} \mathbf{u})_j(\mathbf{x}_0) + \dots \\
 & -\frac{1}{8\pi\mu}(\mathcal{N}_{\partial \Gamma} \mathbf{f})_j(\mathbf{x}_0) + \frac{1}{8\pi}(\mathcal{K}_{\partial \Gamma} \mathbf{u})_j(\mathbf{x}_0), \quad \mathbf{x}_0 \in \Omega, \quad j = 1, 2, 3. \quad (\text{B } 3)
 \end{aligned}$$

Here $\lambda_{O_A \cup O_B} := \lambda_{O_A} \equiv \lambda_{O_B}$ denotes the effective viscosity ratio of the two object parts, and $\mathbf{f} := \mathbf{f}^+$. Hence, the original equation (2.10) remains valid if (i) only the surface parts located within Γ are taken into account, and (ii) the surfaces of the cuts lying on $\partial \Gamma$ are added.

The next goal is to check if the unconnected set $O_A \cup O_B$ in equation (B 3) can be replaced with the actual connected object $O_A \cup O'_B$ without changing the result. We additionally have to see if the equation is invariant under translation of the evaluation point \mathbf{x}_0 by some periodic grid vector $\mathbf{X}^{(\alpha)}$. This has to be done separately for the single- and double-layer integrals. Moreover, we do this for some arbitrary point $\mathbf{x}_0 \in \Gamma$ because both integral types are always well defined and we need it for the FBI equation.

B.2. The single-layer potentials

First consider the single-layer integral for the outer traction $\mathbf{f} := \mathbf{f}^+$ over $\partial O'_B$ for some general evaluation point $\mathbf{x}_0 \in \Gamma$ and an arbitrary grid vector $\mathbf{X}^{(\alpha')}$ (cf. § 2.1.1). Outer tractions only appear for bubbles which always have closed surfaces (capsule-like objects and walls possess traction jumps instead). Furthermore, the object O'_B is offset by construction from O_B by some particular grid vector $\mathbf{X}^{(\alpha)}$. Hence, we compute

$$\begin{aligned}
 (\mathcal{N}_{\partial O'_B} \mathbf{f})_j(\mathbf{x}_0 + \mathbf{X}^{(\alpha')}) &= \oint_{\partial O'_B} f_i(\mathbf{x}) G_{ij}(\mathbf{x}, \mathbf{x}_0 + \mathbf{X}^{(\alpha')}) dS(\mathbf{x}) \\
 &= \oint_{\partial O_B} f_i(\mathbf{x} + \mathbf{X}^{(\alpha)}) G_{ij}(\mathbf{x} + \mathbf{X}^{(\alpha)}, \mathbf{x}_0 + \mathbf{X}^{(\alpha')}) dS(\mathbf{x}) \\
 &= -\langle \nabla P \rangle_\Gamma \cdot \mathbf{X}^{(\alpha)} \oint_{\partial O_B} n_i(\mathbf{x}) G_{ij}(\mathbf{x}, \mathbf{x}_0) dS(\mathbf{x}) + (\mathcal{N}_{\partial O'_B} \mathbf{f})_j(\mathbf{x}_0) \\
 &= (\mathcal{N}_{\partial O_B} \mathbf{f})_j(\mathbf{x}_0). \quad (\text{B } 4)
 \end{aligned}$$

We made a simple substitution from the first to the second line. From the second to the third line, we used the periodicity of the Green's function G_{ij} , equation (2.20a), as well as relation (2.25). The last line follows because of (2.22).

If an object requires the traction jump $\Delta \mathbf{f}$ (capsules, walls) and is possibly open, an analogous result holds because $\Delta \mathbf{f} = \mathbf{f}^+ - \mathbf{f}^- = \check{\mathbf{f}}^+ - \check{\mathbf{f}}^-$ is periodic as the linear terms from equation (2.25) drop out. Adding the O_A contribution, we have

$$(\mathcal{N}_{\partial O_A \cup \partial O'_B} \mathbf{F})(\mathbf{x}_0 + \mathbf{X}^{(\alpha')}) = (\mathcal{N}_{\partial O_A \cup \partial O_B} \mathbf{F})(\mathbf{x}_0), \quad \mathbf{x}_0 \in \Gamma, \quad \forall \alpha' \in \mathbb{Z}^3. \quad (\text{B } 5)$$

Thus, we find for some general object that the single-layer integrals are invariant under any possible periodic translations. Moreover, the single-layer integral over $\partial\Gamma$ appearing in (B 3) simply vanishes for an arbitrary evaluation point $\mathbf{x}_0 \in \mathbb{R}^3$ as in § 2.2.4.

B.3. The double-layer potentials

As for the single-layer potential, consider $\mathbf{x}_0 \in \Gamma$ and an arbitrary grid vector $\mathbf{X}^{(\alpha')}$. Note that open objects (walls) do not require this integral (due to $\lambda_{\mathcal{V}} = 1$) and will therefore not be considered. Then,

$$\begin{aligned} (\mathcal{K}_{\partial O'_B} \mathbf{u})_j(\mathbf{x}_0 + \mathbf{X}^{(\alpha')}) &= \oint_{\partial O'_B} u_i(\mathbf{x}) T_{ijl}(\mathbf{x}, \mathbf{x}_0 + \mathbf{X}^{(\alpha')}) n_l(\mathbf{x}) \, dS(\mathbf{x}) \\ &= \oint_{\partial O_B} u_i(\mathbf{x}) T_{ijl}(\mathbf{x} + \mathbf{X}^{(\alpha)}, \mathbf{x}_0 + \mathbf{X}^{(\alpha')}) n_l(\mathbf{x}) \, dS(\mathbf{x}) \\ &= -\frac{8\pi}{V_\Gamma} X_j^{(\alpha)} \oint_{\partial O_B} u_i n_i \, dS + (\mathcal{K}_{\partial O_B} \mathbf{u})_j(\mathbf{x}_0), \end{aligned} \tag{B 6}$$

where a simple substitution was performed again, and the periodicity of the velocity (2.23), the normal vector and the second argument of the stresslet from (2.18) was used. The first argument of the stresslet contributes the linear part. After using the divergence theorem and adding the O_A term, we obtain for $\mathbf{x}_0 \in \Gamma$

$$(\mathcal{K}_{\partial O_A \cup \partial O_B} \mathbf{u})_j(\mathbf{x}_0) = \frac{8\pi}{V_\Gamma} X_j^{(\alpha)} \int_{O_B} \nabla \cdot \mathbf{u} \, dx^3 + (\mathcal{K}_{\partial O_A \cup \partial O_B} \mathbf{u})_j(\mathbf{x}_0 + \mathbf{X}^{(\alpha')}). \tag{B 7}$$

Hence, the double-layer integral is invariant under periodic offsets $\mathbf{X}^{(\alpha')}$ regarding the evaluation point \mathbf{x}_0 , but not under periodic translations of some object when its flux is non-zero. At first sight this would mean that bubbles cause major troubles and somewhat destroy the formalism for practical purposes as offsetting them leads to an additional term.

However, the BI equation additionally contains a double-layer integral over $\partial\Gamma$. This integral also depends on the objects via the velocity. We will see that the interplay between this integral and the double-layer integrals for the objects will recover the invariance. Thus, consider

$$(\mathcal{K}_{\partial\Gamma} \mathbf{u})_j(\mathbf{x}_0 + \mathbf{X}^{(\alpha')}) = -\frac{8\pi}{V_\Gamma} \oint_{\partial\Gamma} x_j u_i(\mathbf{x}) n_i(\mathbf{x}) \, dS(\mathbf{x}), \quad \mathbf{x}_0 \in \Gamma. \tag{B 8}$$

Note that the periodic contribution of the stresslet vanishes as in § 2.2.4, and that periodic offsets of \mathbf{x}_0 leave the equation unchanged, compare expression (2.18). Splitting up $\partial\Gamma$ and exploiting that b and a' (and a' and b) denote the same surfaces but with antiparallel normal vectors, we have $\oint_{\partial\Gamma} = \oint_{\partial\bar{\Gamma}} - \int_a - \int_b$ (with the same integrands as above). Next, we add a zero by inserting $0 = \int_A + \int_B - \int_A - \int_B + \dots$, and then use $\oint_{\partial\Omega} = \oint_{\partial\bar{\Gamma}} + \int_A + \int_B + \dots$, where the ellipsis contains analogous terms for other objects. We also have $\int_A + \int_a = \oint_{\partial O_A}$ and $\int_B + \int_b = \oint_{\partial O_B}$. With this we find

$$\begin{aligned} (\mathcal{K}_{\partial\Gamma} \mathbf{u})_j(\mathbf{x}_0 + \mathbf{X}^{(\alpha')}) &= -\frac{8\pi}{V_\Gamma} \left[\oint_{\partial\Omega} x_j u_i n_i \, dS \right. \\ &\quad \left. - \oint_{\partial O_A} x_j u_i n_i \, dS - \oint_{\partial O_B} x_j u_i n_i \, dS \right] + \dots, \quad \mathbf{x}_0 \in \Gamma. \end{aligned} \tag{B 9}$$

Applying the divergence theorem as in § 2.2.4 together with (2.6b) yields

$$\begin{aligned}
 (\mathcal{K}_{\partial\Gamma}\mathbf{u})_j(\mathbf{x}_0 + \mathbf{X}^{(\alpha')}) &= 8\pi\langle u_j \rangle_\Gamma \\
 &+ \frac{8\pi}{V_\Gamma} \left[\int_{O_A} x_j \nabla \cdot \mathbf{u} \, dx^3 + \int_{O_B} x_j \nabla \cdot \mathbf{u} \, dx^3 \right] + \dots, \\
 \mathbf{x}_0 \in \Gamma, \quad j &= 1, 2, 3.
 \end{aligned}
 \tag{B 10}$$

The appearance of the average flow is consistent with the results from § 2.2.4. The two integrals vanish for capsules, i.e. just like in (B 7) and as for the single-layer potential they do not cause any trouble. Thus, we will now concentrate on the special case of bubbles.

To this end, consider the combined double-layer potentials for the bubbles and the unit cell. Define the double-layer parts from (B 3) as

$$\text{DL}_j(\mathbf{x}_0) := (\mathcal{K}_{\partial O_A \cup \partial O_B} \mathbf{u})_j(\mathbf{x}_0) + (\mathcal{K}_{\partial\Gamma} \mathbf{u})_j(\mathbf{x}_0) + \dots, \quad \mathbf{x}_0 \in \Gamma, \quad j = 1, 2, 3, \tag{B 11}$$

where $\lambda_{O_A \cup O_B} = 0$ for bubbles has been used. By virtue of (B 7) and (B 10) we have

$$\text{DL}_j(\mathbf{x}_0 + \mathbf{X}^{(\alpha')}) = \text{DL}_j(\mathbf{x}_0), \quad \mathbf{x}_0 \in \Gamma, \quad j = 1, 2, 3 \tag{B 12}$$

and

$$\begin{aligned}
 \text{DL}_j(\mathbf{x}_0) &= (\mathcal{K}_{\partial O_A \cup \partial O'_B} \mathbf{u})_j(\mathbf{x}_0) + \frac{8\pi}{V_\Gamma} \left[\int_{O_A} x_j \nabla \cdot \mathbf{u} \, dx^3 \right. \\
 &\quad \left. + \int_{O_B} (x_j + X_j^{(\alpha)}) \nabla \cdot \mathbf{u}(\mathbf{x}) \, dx^3 \right] + \dots, \quad \mathbf{x}_0 \in \Gamma,
 \end{aligned}
 \tag{B 13}$$

where $\langle \mathbf{u} \rangle_\Gamma$ is hidden in the ellipsis. Using the periodicity of the velocity from (2.23), we find that the last integral is identical to $\int_{O'_B} x_j \nabla \cdot \mathbf{u}(\mathbf{x}) \, dx^3$. Thus,

$$\text{DL}_j(\mathbf{x}_0) = (\mathcal{K}_{\partial O_A \cup \partial O'_B} \mathbf{u})_j(\mathbf{x}_0) + \frac{8\pi}{V_\Gamma} \int_{O_A \cup O'_B} x_j \nabla \cdot \mathbf{u}(\mathbf{x}) \, dx^3 + \dots, \quad \mathbf{x}_0 \in \Gamma, \quad j = 1, 2, 3 \tag{B 14}$$

or by means of (2.29) and (2.31)

$$\text{DL}_j(\mathbf{x}_0) = (\mathcal{K}_{\partial O_A \cup \partial O'_B} \mathbf{u})_j(\mathbf{x}_0) + \frac{8\pi}{V_\Gamma} Q_{O_A \cup O'_B} \chi_j^{(O_A \cup O'_B)} + \dots, \quad \mathbf{x}_0 \in \Gamma, \quad j = 1, 2, 3. \tag{B 15}$$

Here $\chi^{(O_A \cup O'_B)}$ is the centroid of the combined object parts O_A and O'_B (i.e. the centroid of the non-split object), and $Q_{O_A \cup O'_B}$ the prescribed flux.

B.4. Putting it all together

Given the above results, the BI equation (B 3) for split bubbles is thus

$$\begin{aligned}
 u_j(\mathbf{x}_0) &= -\frac{1}{8\pi\mu} (\mathcal{N}_{\partial O_A \cup \partial O'_B} \mathbf{F})_j(\mathbf{x}_0) + \frac{1}{8\pi} (\mathcal{K}_{\partial O_A \cup \partial O'_B} \mathbf{u})_j(\mathbf{x}_0) \\
 &+ \frac{8\pi}{V_\Gamma} Q_{O_A \cup O'_B} \chi_j^{(O_A \cup O'_B)} + \dots, \quad \mathbf{x}_0 \in \Omega, \quad j = 1, 2, 3.
 \end{aligned}
 \tag{B 16}$$

If we did not move around the objects with the help of periodicity, equation (B 10) would have led to the equivalent expression

$$u_j(\mathbf{x}_0) = -\frac{1}{8\pi\mu}(\mathcal{N}_{\partial O_A \cup \partial O_B} \mathbf{F})_j(\mathbf{x}_0) + \frac{1}{8\pi}(\mathcal{K}_{\partial O_A \cup \partial O_B} \mathbf{u})_j(\mathbf{x}_0) + \frac{8\pi}{V_\Gamma}[\mathcal{Q}_{O_A} \chi_j^{(O_A)} + \mathcal{Q}_{O_B} \chi_j^{(O_B)}] + \dots, \quad \mathbf{x}_0 \in \Omega, \quad j = 1, 2, 3. \quad (\text{B } 17)$$

Comparing these two equations, we can draw the following conclusion regarding the original BI equation (2.33). If some bubble overlaps with the unit cell's boundary, we can either split it up and use the two unconnected parts (O_A and O_B) on the opposite sides of the unit cell separately, including different centroids (B 17). Or, more conveniently and intuitively, we can simply integrate over the surface of the whole connected bubble $O_A \cup O_B$ including the parts that lie outside of Γ and use its actual centroid (B 16). This is highly desirable for the numerical implementation because we only have to deal with whole objects and no splitting of the meshes is required. It also shows that the choice of the unit cell's position in the 3-D Cartesian coordinate system does not matter.

We further note that the non-zero contributions from the double-layer integrals over $\partial\Gamma$ containing the centroids are crucial to obtain invariance for bubbles, and hence the above results are non-trivial. If they were missing (by assuming $\mathcal{K}_{\partial\Gamma} \mathbf{u} = 0$), equation (B 7) would have introduced an additional position-dependent term. This would lead to changes in the flow field if a bubble is moved by a periodic grid vector – which is clearly unphysical.

For objects other than bubbles, the fluxes are missing and additional viscosity ratios appear. Nevertheless, the above statement (that we can simply choose the whole objects) remains true because the individual single- and double-layer integrals are invariant under periodic translations for objects with zero flux (compare (B 7), (B 10) and § B.2).

Analogous conclusions can be drawn for the FBI equation (2.1) which in the end is evaluated by our numerical code. First, §§ B.2 and B.3 considered a general evaluation point $\mathbf{x}_0 \in \Gamma$ and thus remain valid if \mathbf{x}_0 is located on the surface of some object. We additionally saw that the integrals are invariant if \mathbf{x}_0 is moved by some periodic grid vector $\mathbf{X}^{(a')}$, allowing \mathbf{x}_0 to be on the parts of surfaces that lie outside of Γ . Second, the imposed flow as well as the Wielandt deflation term are periodic due to (2.46). Third, the proof from § 2.3.4 is largely independent of the position of the objects. Where integrals over $\partial\Gamma$ occur (e.g. in the energy conservation statements), they can be reconstructed from $\partial\tilde{\Gamma}$ in the same way as was done for (B 2), leaving the procedure unchanged. Replacing the object parts with the whole objects therefore does not affect the proof in § 2.3.

REFERENCES

- AARTS, P. A., VAN DEN BROEK, S. A., PRINS, G. W., KUIKEN, G. D., SIXMA, J. J. & HEETHAAR, R. M. 1988 Blood platelets are concentrated near the wall and red blood cells, in the center in flowing blood. *Arterioscler. Thromb. Vasc. Biol.* **8** (6), 819–824.
- BÄCHER, C., SCHRACK, L. & GEKLE, S. 2017 Clustering of microscopic particles in constricted blood flow. *Phys. Rev. Fluids* **2** (1), 013102.
- BLAKE, J. R. 1971 A note on the image system for a Stokeslet in a no-slip boundary. *Math. Proc. Camb. Phil. Soc.* **70** (2), 303–310.
- BLAWZDZIEWICZ, J. 2007 Boundary integral methods for Stokes flows. In *Computational Methods for Multiphase Flow* (ed. P. Andrea & T. Grotar), pp. 193–236. Cambridge University Press.

- BOGACKI, P. & SHAMPINE, L. F. 1989 A 3(2) pair of Runge–Kutta formulas. *Appl. Maths Lett.* **2** (4), 321–325.
- BORDEN, M. A., KRUSE, D. E., CASKEY, C. F., ZHAO, S., DAYTON, P. A. & FERRARA, K. W. 2005 Influence of lipid shell physicochemical properties on ultrasound-induced microbubble destruction. *IEEE Trans. Ultrason. Ferroelectr. Freq. Control* **52** (11), 1992–2002.
- CANHAM, P. B. 1970 The minimum energy of bending as a possible explanation of the biconcave shape of the human red blood cell. *J. Theor. Biol.* **26** (1), 61–81.
- CASH, J. R. & KARP, A. H. 1990 A variable order Runge–Kutta method for initial value problems with rapidly varying right-hand sides. *ACM Trans. Math. Softw.* **16** (3), 201–222.
- CHIEN, S., USAMI, S., TAYLOR, H. M., LUNDBERG, J. L. & GREGERSEN, M. I. 1966 Effects of hematocrit and plasma proteins on human blood rheology at low shear rates. *J. Appl. Phys.* **21** (1), 81–87.
- CORTEZ, R. & HOFFMANN, F. 2014 A fast numerical method for computing doubly-periodic regularized Stokes flow in 3D. *J. Comput. Phys.* **258**, 1–14.
- COUTURE, O., FOLEY, J., KASSELL, N. F., LARRAT, B. & AUBRY, J.-F. 2014 Review of ultrasound mediated drug delivery for cancer treatment: updates from pre-clinical studies. *Transl. Cancer Res.* **3** (5), 494–511.
- COWPER, G. R. 1973 Gaussian quadrature formulas for triangles. *Intl J. Numer. Meth. Engng* **7** (3), 405–408.
- DADDI-MOUSSA-IDER, A. & GEKLE, S. 2016 Hydrodynamic interaction between particles near elastic interfaces. *J. Chem. Phys.* **145** (1), 014905.
- DADDI-MOUSSA-IDER, A. & GEKLE, S. 2017 Hydrodynamic mobility of a solid particle near a spherical elastic membrane: axisymmetric motion. *Phys. Rev. E* **95** (1), 013108.
- DADDI-MOUSSA-IDER, A., GUCKENBERGER, A. & GEKLE, S. 2016a Long-lived anomalous thermal diffusion induced by elastic cell membranes on nearby particles. *Phys. Rev. E* **93** (1), 012612.
- DADDI-MOUSSA-IDER, A., GUCKENBERGER, A. & GEKLE, S. 2016b Particle mobility between two planar elastic membranes: Brownian motion and membrane deformation. *Phys. Fluids* **28** (7), 071903.
- DADDI-MOUSSA-IDER, A., LISICKI, M. & GEKLE, S. 2017a Hydrodynamic mobility of a solid particle near a spherical elastic membrane. Part II. Asymmetric motion. *Phys. Rev. E* **95** (5), 053117.
- DADDI-MOUSSA-IDER, A., LISICKI, M. & GEKLE, S. 2017b Mobility of an axisymmetric particle near an elastic interface. *J. Fluid Mech.* **811**, 210–233.
- D'APOLITO, R., TOMAIUOLO, G., TARABALLI, F., MINARDI, S., KIRUI, D., LIU, X., CEVENINI, A., PALOMBA, R., FERRARI, M., SALVATORE, F. *et al.* 2015 Red blood cells affect the margination of microparticles in synthetic microcapillaries and intravital microcirculation as a function of their size and shape. *J. Control. Release* **217**, 263–272.
- DAYTON, P., KLIBANOV, A., BRANDENBURGER, G. & FERRARA, K. 1999 Acoustic radiation force *in vivo*: a mechanism to assist targeting of microbubbles. *Ultrasound Med. Biol.* **25** (8), 1195–1201.
- DOINIKOV, A. A. & BOUAKAZ, A. 2011 Review of shell models for contrast agent microbubbles. *IEEE Trans. Ultrason. Ferroelectr. Freq. Control* **58** (5), 981–993.
- EVANS, E. & FUNG, Y.-C. 1972 Improved measurements of the erythrocyte geometry. *Microvasc. Res.* **4** (4), 335–347.
- FAEZ, T., EMMER, M., KOOIMAN, K., VERSLUIS, M., VAN DER STEEN, A. F. W. & DE JONG, N. 2013 20 years of ultrasound contrast agent modeling. *IEEE Trans. Ultrason. Ferroelectr. Freq. Control* **60** (1), 7–20.
- FAN, X.-J., PHAN-THIEN, N. & ZHENG, R. 1998 Completed double layer boundary element method for periodic suspensions. *Z. angew. Math. Phys.* **49** (2), 167–193.
- FARUTIN, A., BIBEN, T. & MISBAH, C. 2014 3D numerical simulations of vesicle and inextensible capsule dynamics. *J. Comput. Phys.* **275**, 539–568.
- FARUTIN, A. & MISBAH, C. 2013 Analytical and numerical study of three main migration laws for vesicles under flow. *Phys. Rev. Lett.* **110** (10).

- FEDOSOV, D. A. & GOMPPER, G. 2014 White blood cell margination in microcirculation. *Soft Matt.* **10** (17), 2961–2970.
- FEDOSOV, D. A., PAN, W., CASWELL, B., GOMPPER, G. & KARNIADAKIS, G. E. 2011 Predicting human blood viscosity in silico. *Proc. Natl Acad. Sci. USA* **108** (29), 11772–11777.
- FERRARA, K., POLLARD, R. & BORDEN, M. 2007 Ultrasound microbubble contrast agents: fundamentals and application to gene and drug delivery. *Annu. Rev. Biomed. Engng* **9** (1), 415–447.
- FITZGIBBON, S., SPANN, A. P., QI, Q. M. & SHAQFEH, E. S. G. 2015 *In vitro* measurement of particle margination in the microchannel flow: effect of varying hematocrit. *Biophys. J.* **108** (10), 2601–2608.
- FREUND, J. B. 2007 Leukocyte margination in a model microvessel. *Phys. Fluids* **19** (2), 023301.
- FREUND, J. B. 2013 The flow of red blood cells through a narrow spleen-like slit. *Phys. Fluids* **25** (11), 110807.
- FREUND, J. B. 2014 Numerical simulation of flowing blood cells. *Annu. Rev. Fluid Mech.* **46** (1), 67–95.
- FREUND, J. B. & ORESCANIN, M. M. 2011 Cellular flow in a small blood vessel. *J. Fluid Mech.* **671**, 466–490.
- FREUND, J. B. & SHAPIRO, B. 2012 Transport of particles by magnetic forces and cellular blood flow in a model microvessel. *Phys. Fluids* **24** (5), 051904.
- FREUND, J. B. & VERMOT, J. 2014 The wall-stress footprint of blood cells flowing in microvessels. *Biophys. J.* **106** (3), 752–762.
- FRINKING, P. J. A., GAUD, E., BROCHOT, J. & ARDITI, M. 2010 Subharmonic scattering of phospholipid-shell microbubbles at low acoustic pressure amplitudes. *IEEE Trans. Ultrason. Ferroelectr. Freq. Control* **57** (8), 1762–1771.
- GEKLE, S. 2016 Strongly accelerated margination of active particles in blood flow. *Biophys. J.* **110** (2), 514–520.
- GREENGARD, L. & KROPINSKI, M. C. 2004 Integral equation methods for Stokes flow in doubly-periodic domains. *J. Engng Maths* **48** (2), 157–170.
- GUCKENBERGER, A. & GEKLE, S. 2017 Theory and algorithms to compute Helfrich bending forces: a review. *J. Phys.: Condens. Matter* **29** (20), 203001.
- GUCKENBERGER, A., SCHRAML, M. P., CHEN, P. G., LEONETTI, M. & GEKLE, S. 2016 On the bending algorithms for soft objects in flows. *Comput. Phys. Commun.* **207**, 1–23.
- HASIMOTO, H. 1959 On the periodic fundamental solutions of the Stokes equations and their application to viscous flow past a cubic array of spheres. *J. Fluid Mech.* **5** (2), 317–328.
- HELFRICH, W. 1973 Elastic properties of lipid bilayers: theory and possible experiments. *Z. Naturforsch. C* **28** (11–12), 693–703.
- HERNÁNDEZ-ORTIZ, J. P., DE PABLO, J. J. & GRAHAM, M. D. 2007 Fast computation of many-particle hydrodynamic and electrostatic interactions in a confined geometry. *Phys. Rev. Lett.* **98** (14), 140602.
- HOUSE, S. D. & LIPOWSKY, H. H. 1987 Microvascular hematocrit and red cell flux in rat cremaster muscle. *Am. J. Phys.* **252** (1), H211–H222.
- HUANG, L. R., COX, E. C., AUSTIN, R. H. & STURM, J. C. 2004 Continuous particle separation through deterministic lateral displacement. *Science* **304** (5673), 987–990.
- JANSSEN, P. J. A. & ANDERSON, P. D. 2008 A boundary-integral model for drop deformation between two parallel plates with non-unit viscosity ratio drops. *J. Comput. Phys.* **227** (20), 8807–8819.
- JOHNSON, K. A., VORMOHR, H. R., DOINIKOV, A. A., BOUAKAZ, A., SHIELDS, C. W., LÓPEZ, G. P. & DAYTON, P. A. 2016 Experimental verification of theoretical equations for acoustic radiation force on compressible spherical particles in traveling waves. *Phys. Rev. E* **93** (5), 053109.
- DE JONG, N., EMMER, M., CHIN, C. T., BOUAKAZ, A., MASTIK, F., LOHSE, D. & VERSLUIS, M. 2007 ‘Compression-only’ behavior of phospholipid-coated contrast bubbles. *Ultrasound Med. Biol.* **33** (4), 653–656.

- KARRILA, S. J. & KIM, S. 1989 Integral equations of the second kind for Stokes flow: direct solution for physical variables and removal of inherent accuracy limitations. *Chem. Engng Commun.* **82** (1), 123–161.
- KATANOV, D., GOMPPER, G. & FEDOSOV, D. A. 2015 Microvascular blood flow resistance: role of red blood cell migration and dispersion. *Microvasc. Res.* **99**, 57–66.
- KILROY, J. P., KLIBANOV, A. L., WAMHOFF, B. R., BOWLES, D. K. & HOSSACK, J. A. 2014 Localized *in vivo* model drug delivery with intravascular ultrasound and microbubbles. *Ultrasound Med. Biol.* **40** (10), 2458–2467.
- KIM, S. & KARRILA, S. J. 1991 *Microhydrodynamics: Principles and Selected Applications*. Butterworth–Heinemann.
- KLIBANOV, A. L. 2002 Ultrasound contrast agents: development of the field and current status. In *Topics in Current Chemistry* (ed. K. Werner), vol. 222, pp. 73–106. Springer.
- AF KLINTEBERG, L. & TORNBERG, A.-K. 2014 Fast Ewald summation for Stokesian particle suspensions. *Intl J. Numer. Meth. Fluids* **76** (10), 669–698.
- AF KLINTEBERG, L. & TORNBERG, A.-K. 2016 A fast integral equation method for solid particles in viscous flow using quadrature by expansion. *J. Comput. Phys.* **326**, 420–445.
- KLITZMAN, B. & DULING, B. R. 1979 Microvascular hematocrit and red cell flow in resting and contracting striated muscle. *Am. J. Phys.* **237** (4), H481–H490.
- KOHR, M. & POP, I. 2004 *Viscous Incompressible Flow for Low Reynolds Numbers*, Advances in Boundary Elements, vol. 16. WIT Press.
- KOOIMAN, K., VOS, H. J., VERSLUIS, M. & DE JONG, N. 2014 Acoustic behavior of microbubbles and implications for drug delivery. *Adv. Drug Deliv. Rev.* **72**, 28–48.
- KOTOPOULIS, S., DIMCEVSKI, G., CORMACK, E. M., POSTEMA, M., GJERTSEN, B. T. & GILJA, O. H. 2016 Ultrasound- and microbubble-enhanced chemotherapy for treating pancreatic cancer: a phase I clinical trial. *J. Acoust. Soc. Am.* **139** (4), 2092–2092.
- KRESS, R. 2014 *Linear Integral Equations*, 3rd edn. Applied Mathematical Sciences, vol. 82. Springer.
- KRETZ, M. & LINDENSTRUTH, V. 2012 Vc: a C++ library for explicit vectorization. *Softw. Pract. Exp.* **42** (11), 1409–1430.
- KRÜGER, T. 2012 *Computer Simulation Study of Collective Phenomena in Dense Suspensions of Red Blood Cells Under Shear*. Vieweg and Teubner.
- KRÜGER, T., HOLMES, D. & COVENEY, P. V. 2014 Deformability-based red blood cell separation in deterministic lateral displacement devices: a simulation study. *Biomicrofluidics* **8** (5).
- KUMAR, A. & GRAHAM, M. D. 2011 Segregation by membrane rigidity in flowing binary suspensions of elastic capsules. *Phys. Rev. E* **84** (6), 066316.
- KUMAR, A. & GRAHAM, M. D. 2012 Accelerated boundary integral method for multiphase flow in non-periodic geometries. *J. Comput. Phys.* **231** (20), 6682–6713.
- KUMAR, A., HENRÍQUEZ RIVERA, R. G. & GRAHAM, M. D. 2014 Flow-induced segregation in confined multicomponent suspensions: effects of particle size and rigidity. *J. Fluid Mech.* **738**, 423–462.
- LADYZHENSKAYA, O. A. 1969 *The Mathematical Theory of Viscous Incompressible Flow*, 2nd edn. Gordon & Breach.
- LAMMERTINK, B. H. A., BOS, C., DECKERS, R., STORM, G., MOONEN, C. T. W. & ESCOFFRE, J.-M. 2015 Sonochemotherapy: from bench to bedside. *Front. Pharmacol.* **6** (138).
- LI, X., ZHOU, H. & POZRIKIDIS, C. 1995 A numerical study of the shearing motion of emulsions and foams. *J. Fluid Mech.* **286**, 379–404.
- LINDBO, D. & TORNBERG, A.-K. 2010 Spectrally accurate fast summation for periodic Stokes potentials. *J. Comput. Phys.* **229** (23), 8994–9010.
- LINDNER, J. R. 2004 Microbubbles in medical imaging: current applications and future directions. *Natl Rev. Drug Discov.* **3** (6), 527–533.
- LINDNER, J. R., SONG, J., JAYAWEERA, A. R., SKLENAR, J. & KAUL, S. 2002 Microvascular rheology of definity microbubbles after intra-arterial and intravenous administration. *J. Am. Soc. Echocardiogr.* **15** (5), 396–403.

- LIRON, N. & MOCHON, S. 1976 Stokes flow for a Stokeslet between two parallel flat plates. *J. Engng Maths* **10** (4), 287–303.
- LOEWENBERG, M. & HINCH, E. J. 1996 Numerical simulation of a concentrated emulsion in shear flow. *J. Fluid Mech.* **321**, 395–419.
- MARIN, O., GUSTAVSSON, K. & TORNERG, A.-K. 2012 A highly accurate boundary treatment for confined Stokes flow. *Comput. Fluids* **66**, 215–230.
- MARMOTTANT, P., VAN DER MEER, S., EMMER, M., VERSLUIS, M., DE JONG, N., HILGENFELDT, S. & LOHSE, D. 2005 A model for large amplitude oscillations of coated bubbles accounting for buckling and rupture. *J. Acoust. Soc. Am.* **118** (6), 3499–3505.
- MCWHIRTER, J. L., NOGUCHI, H. & GOMPPER, G. 2009 Flow-induced clustering and alignment of vesicles and red blood cells in microcapillaries. *Proc. Natl Acad. Sci. USA* **106** (15), 6039–6043.
- MEHRABADI, M., KU, D. N. & AIDUN, C. K. 2016 Effects of shear rate, confinement, and particle parameters on margination in blood flow. *Phys. Rev. E* **93** (2), 023109.
- MISBAH, C. 2012 Vesicles, capsules and red blood cells under flow. *J. Phys.: Conf. Ser.* **392**, 012005.
- MUKHERJEE, S. & SARKAR, K. 2013 Effects of matrix viscoelasticity on the lateral migration of a deformable drop in a wall-bounded shear. *J. Fluid Mech.* **727**, 318–345.
- MUKHERJEE, S. & SARKAR, K. 2014 Lateral migration of a viscoelastic drop in a Newtonian fluid in a shear flow near a wall. *Phys. Fluids* **26** (10), 103102.
- MÜLLER, K., FEDOSOV, D. A. & GOMPPER, G. 2014 Margination of micro- and nano-particles in blood flow and its effect on drug delivery. *Sci. Rep.* **4**, 4871.
- MÜLLER, K., FEDOSOV, D. A. & GOMPPER, G. 2015 Smoothed dissipative particle dynamics with angular momentum conservation. *J. Comput. Phys.* **281**, 301–315.
- MÜLLER, K., FEDOSOV, D. A. & GOMPPER, G. 2016 Understanding particle margination in blood flow: a step toward optimized drug delivery systems. *Med. Engng Phys.* **38** (1), 2–10.
- NAMDEE, K., THOMPSON, A. J., CHAROENPHOL, P. & ENIOLA-ADEFESO, O. 2013 Margination propensity of vascular-targeted spheres from blood flow in a microfluidic model of human microvessels. *Langmuir* **29** (8), 2530–2535.
- NIE, Q., TANVEER, S., DUPONT, T. F. & LI, X. 2002 Singularity formation in free-surface Stokes flows. In *Recent Advances in Numerical Methods for Partial Differential Equations and Applications* (ed. F. Xiaobing & T. P. Schulze), Contemporary Mathematics, vol. 306, pp. 147–165. AMS.
- NOGUCHI, H. & GOMPPER, G. 2005 Dynamics of fluid vesicles in shear flow: effect of membrane viscosity and thermal fluctuations. *Phys. Rev. E* **72** (1), 011901.
- ODQVIST, F. K. G. 1930 Über die Randwertaufgaben der Hydrodynamik zäher Flüssigkeiten. *Math. Z.* **32** (1), 329–375.
- OVERVELDE, M., GARBIN, V., SIJL, J., DOLLET, B., DE JONG, N., LOHSE, D. & VERSLUIS, M. 2010 Nonlinear shell behavior of phospholipid-coated microbubbles. *Ultrasound Med. Biol.* **36** (12), 2080–2092.
- OWEN, J., GROVE, P., RADEMEYER, P. & STRIDE, E. 2014 The influence of blood on targeted microbubbles. *J. R. Soc. Interface* **11** (100), 20140622.
- PARK, Y., BEST, C. A., BADIZADEGAN, K., DASARI, R. R., FELD, M. S., KURIABOVA, T., HENLE, M. L., LEVINE, A. J. & POPESCU, G. 2010 Measurement of red blood cell mechanics during morphological changes. *Proc. Natl Acad. Sci. USA* **107** (15), 6731–6736.
- PAUL, S., KATIYAR, A., SARKAR, K., CHATTERJEE, D., SHI, W. T. & FORSBERG, F. 2010 Material characterization of the encapsulation of an ultrasound contrast microbubble and its subharmonic response: strain-softening interfacial elasticity model. *J. Acoust. Soc. Am.* **127** (6), 3846–3857.
- PHAN-THIEN, N., TRAN-CONG, T. & GRAHAM, A. L. 1991 Shear flow of periodic arrays of particle clusters: a boundary-element method. *J. Fluid Mech.* **228**, 275–293.
- POPEL, A. S. & JOHNSON, P. C. 2005 Microcirculation and hemorheology. *Annu. Rev. Fluid Mech.* **37** (1), 43–69.
- POWER, H. 1992 The low Reynolds number deformation of a gas bubble in shear flow: a general approach via integral equations. *Engng Anal. Bound. Elem.* **9** (1), 31–37.

- POWER, H. 1996 A second kind integral equation formulation for the low Reynolds number interaction between a solid particle and a viscous drop. *J. Engng Maths* **30** (1–2), 225–237.
- POWER, H. & MIRANDA, G. 1987 Second kind integral equation formulation of Stokes' flows past a particle of arbitrary shape. *SIAM J. Appl. Maths* **47** (4), 689–698.
- POWER, H. & DE POWER, B. F. 1992 The completed second kind boundary integral equation method for the deformation of a gas bubble due to low Reynolds number flow. In *Boundary Element Technology VII* (ed. C. A. Brebbia & M. S. Ingber), pp. 193–210. Springer.
- POZRIKIDIS, C. 1992 *Boundary Integral and Singularity Methods for Linearized Viscous Flow*, Cambridge Texts in Applied Mathematics, vol. 8. Cambridge University Press.
- POZRIKIDIS, C. 1993 On the transient motion of ordered suspensions of liquid drops. *J. Fluid Mech.* **246**, 301–320.
- POZRIKIDIS, C. 1995 Finite deformation of liquid capsules enclosed by elastic membranes in simple shear flow. *J. Fluid Mech.* **297**, 123–152.
- POZRIKIDIS, C. 1996 Computation of periodic Green's functions of Stokes flow. *J. Engng Maths* **30** (1–2), 79–96.
- POZRIKIDIS, C. 1999 A spectral-element method for particulate Stokes flow. *J. Comput. Phys.* **156** (2), 360–381.
- POZRIKIDIS, C. 2001 Interfacial dynamics for Stokes flow. *J. Comput. Phys.* **169** (2), 250–301.
- PRANAY, P., ANEKAL, S. G., HERNANDEZ-ORTIZ, J. P. & GRAHAM, M. D. 2010 Pair collisions of fluid-filled elastic capsules in shear flow: effects of membrane properties and polymer additives. *Phys. Fluids* **22** (12), 123103.
- PRESS, W. H., TEUKOLSKY, S. A., VETTERLING, W. T. & FLANNERY, B. P. 2007 *Numerical Recipes: The Art of Scientific Computing*, 3rd edn. Cambridge University Press.
- QI, Q. M. & SHAQFEH, E. S. G. 2017 Theory to predict particle migration and margination in the pressure-driven channel flow of blood. *Phys. Rev. Fluids* **2** (9), 093102.
- QUINT, S., CHRIST, A. F., GUCKENBERGER, A., HIMBERT, S., KAESTNER, L., GEKLE, S. & WAGNER, C. 2017 3D tomography of cells in micro-channels. *Appl. Phys. Lett.* **111** (10), 103701.
- RIVARA, M. C. 1984 Algorithms for refining triangular grids suitable for adaptive and multigrid techniques. *Intl J. Numer. Meth. Engng* **20** (4), 745–756.
- RYCHAK, J. J., KLIBANOV, A. L. & HOSSACK, J. A. 2005 Acoustic radiation force enhances targeted delivery of ultrasound contrast microbubbles: *in vitro* verification. *IEEE Trans. Ultrason. Ferroelectr. Freq. Control* **52** (3), 421–433.
- RYCHAK, J. J., KLIBANOV, A. L., LEY, K. F. & HOSSACK, J. A. 2007 Enhanced targeting of ultrasound contrast agents using acoustic radiation force. *Ultrasound Med. Biol.* **33** (7), 1132–1139.
- RYCHAK, J. J., LINDNER, J. R., LEY, K. & KLIBANOV, A. L. 2006 Deformable gas-filled microbubbles targeted to P-selectin. *J. Control. Release* **114** (3), 288–299.
- SAAD, Y. & SCHULTZ, M. 1986 GMRES: a generalized minimal residual algorithm for solving nonsymmetric linear systems. *SIAM J. Sci. Stat. Comput.* **7** (3), 856–869.
- SAINTILLAN, D., DARVE, E. & SHAQFEH, E. S. G. 2005 A smooth particle-mesh Ewald algorithm for Stokes suspension simulations: the sedimentation of fibers. *Phys. Fluids* **17** (3), 033301.
- SARKAR, K., SHI, W. T., CHATTERJEE, D. & FORSBERG, F. 2005 Characterization of ultrasound contrast microbubbles using *in vitro* experiments and viscous and viscoelastic interface models for encapsulation. *J. Acoust. Soc. Am.* **118** (1), 539–550.
- SIJL, J., OVERVELDE, M., DOLLET, B., GARBIN, V., DE JONG, N., LOHSE, D. & VERSLUIS, M. 2011 'Compression-only' behavior: a second-order nonlinear response of ultrasound contrast agent microbubbles. *J. Acoust. Soc. Am.* **129** (4), 1729–1739.
- SINGH, R. K., LI, X. & SARKAR, K. 2014 Lateral migration of a capsule in plane shear near a wall. *J. Fluid Mech.* **739**, 421–443.
- SINHA, K. & GRAHAM, M. D. 2015 Dynamics of a single red blood cell in simple shear flow. *Phys. Rev. E* **92** (4), 042710.
- SINHA, K. & GRAHAM, M. D. 2016 Shape-mediated margination and demargination in flowing multicomponent suspensions of deformable capsules. *Soft Matt.* **12** (6), 1683–1700.

- SKALAK, R., OZKAYA, N. & SKALAK, T. C. 1989 Biofluid mechanics. *Annu. Rev. Fluid Mech.* **21** (1), 167–200.
- SKALAK, R., TOZEREN, A., ZARDA, R. P. & CHIEN, S. 1973 Strain energy function of red blood cell membranes. *Biophys. J.* **13** (3), 245–264.
- SMART, J. R. & LEIGHTON, D. T. 1991 Measurement of the drift of a droplet due to the presence of a plane. *Phys. Fluids Fluid Dyn.* **3** (1), 21–28.
- SPANN, A. P., CAMPBELL, J. E., FITZGIBBON, S. R., RODRIGUEZ, A., CAP, A. P., BLACKBOURNE, L. H. & SHAQFEH, E. S. G. 2016 The effect of hematocrit on platelet adhesion: experiments and simulations. *Biophys. J.* **111** (3), 577–588.
- STABEN, M. E., ZINCHENKO, A. Z. & DAVIS, R. H. 2003 Motion of a particle between two parallel plane walls in low-Reynolds-number Poiseuille flow. *Phys. Fluids* **15** (6), 1711–1733.
- UNGER, E., PORTER, T., LINDNER, J. & GRAYBURN, P. 2014 Cardiovascular drug delivery with ultrasound and microbubbles. *Adv. Drug Deliv. Rev.* **72**, 110–126.
- UNNIKRISHNAN, S. & KLIBANOV, A. L. 2012 Microbubbles as ultrasound contrast agents for molecular imaging: preparation and application. *Am. J. Roentgenol.* **199** (2), 292–299.
- VAHIDKHAH, K. & BAGCHI, P. 2015 Microparticle shape effects on margination, near-wall dynamics and adhesion in a three-dimensional simulation of red blood cell suspension. *Soft Matt.* **11** (11), 2097–2109.
- VAN DER VORST, H. 1992 Bi-CGSTAB: a fast and smoothly converging variant of Bi-CG for the solution of nonsymmetric linear systems. *SIAM J. Sci. Stat. Comput.* **13** (2), 631–644.
- WANG, W., DIACOVO, T. G., CHEN, J., FREUND, J. B. & KING, M. R. 2013 Simulation of platelet, thrombus and erythrocyte hydrodynamic interactions in a 3D arteriole with *in vivo* comparison. *PLoS ONE* **8** (10), e76949.
- YOON, Y.-Z., KOTAR, J., YOON, G. & CICUTA, P. 2008 The nonlinear mechanical response of the red blood cell. *Phys. Biol.* **5** (3), 036007.
- YOUNGREN, G. K. & ACRIVOS, A. 1975 Stokes flow past a particle of arbitrary shape: a numerical method of solution. *J. Fluid Mech.* **69** (2), 377–403.
- YOUNGREN, G. K. & ACRIVOS, A. 1976 On the shape of a gas bubble in a viscous extensional flow. *J. Fluid Mech.* **76** (3), 433–442.
- ZHANG, C. & CHEN, T. 2001 Efficient feature extraction for 2D/3D objects in mesh representation. In *Proceedings ICIP 2001*, vol. 3, pp. 935–938. IEEE Signal Processing Society.
- ZHANG, Z., HENRY, E., GOMPPER, G. & FEDOSOV, D. A. 2015 Behavior of rigid and deformable particles in deterministic lateral displacement devices with different post shapes. *J. Chem. Phys.* **143** (24), 243145.
- ZHAO, H., ISFAHANI, A. H. G., OLSON, L. N. & FREUND, J. B. 2010 A spectral boundary integral method for flowing blood cells. *J. Comput. Phys.* **229** (10), 3726–3744.
- ZHAO, H. & SHAQFEH, E. S. G. 2011 Shear-induced platelet margination in a microchannel. *Phys. Rev. E* **83** (6).
- ZHAO, H., SHAQFEH, E. S. G. & NARSIMHAN, V. 2012 Shear-induced particle migration and margination in a cellular suspension. *Phys. Fluids* **24** (1), 011902.
- ZHAO, X., LI, J., JIANG, X., KARPEEV, D., HEINONEN, O., SMITH, B., HERNANDEZ-ORTIZ, J. P. & DE PABLO, J. J. 2017 Parallel O(N) Stokes' solver towards scalable Brownian dynamics of hydrodynamically interacting objects in general geometries. *J. Chem. Phys.* **146** (24), 244114.
- ZHU, L., RABAULT, J. & BRANDT, L. 2015 The dynamics of a capsule in a wall-bounded oscillating shear flow. *Phys. Fluids* **27** (7), 071902.
- ZICK, A. A. & HOMSIS, G. M. 1982 Stokes flow through periodic arrays of spheres. *J. Fluid Mech.* **115**, 13–26.
- ZINCHENKO, A. Z. & DAVIS, R. H. 2000 An efficient algorithm for hydrodynamical interaction of many deformable drops. *J. Comput. Phys.* **157** (2), 539–587.
- ZINCHENKO, A. Z., ROTHER, M. A. & DAVIS, R. H. 1997 A novel boundary-integral algorithm for viscous interaction of deformable drops. *Phys. Fluids* **9** (6), 1493–1511.

Supplementary information for “A boundary integral method with volume-changing objects for ultrasound-triggered margination of microbubbles”

Achim Guckenberg^{*}, Stephan Gekle^{*}

Dated: November 14, 2017

Contents

S1 Determination of error bars and average RBC/bubble positions	1
S2 Results with included radiation force	2
S2.1 Method	2
S2.2 Results for $P_A = 45$ kPa	2
S2.3 Results for $P_A = 6$ kPa	3
S3 Parameter robustness	4
S4 Code verification	6
S5 Dynamic mesh refinement	8

S1 Determination of error bars and average RBC/bubble positions

The error bars and average positions in the figures (such as fig. 4 (b)) are determined via the following steps:

- 1) We take the minimum, maximum and arithmetic mean of the centroids of *all* RBCs or bubbles in the system in each time step for $t > 1$ s or after definite margination. This gives three graphs as a function of time, once for the set of all RBCs and once for the set of the two bubbles. See figure [S1](#) for an illustration.
- 2) These time series are then averaged to obtain a mean minimal, maximal and average centroid position. See the straight horizontal lines in figure [S1](#).
- 3) This is then done for all simulations with the same set of parameters. Each of the resulting six values per simulation (three for the RBCs and three for the bubbles) are then averaged over the different simulations with the considered durations as weights. This gives the final minimal, maximal and average values which are then depicted as error bars and points, respectively.

Note that this procedure is similar to the one from reference [\[1\]](#).

^{*}Biofluid Simulation and Modeling, Fachbereich Physik, Universität Bayreuth, Bayreuth

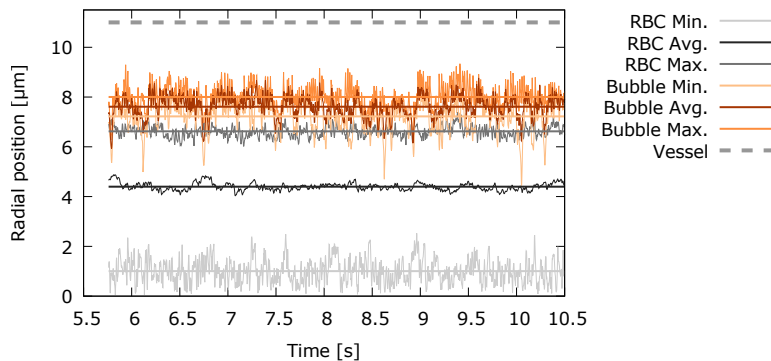


Figure S1: Illustration of the first two steps to obtain the error bars and average object positions, exemplified via the simulation from figure 4 (a) from the main text. The jagged lines show the minimal, maximal and average positions of the centroids as a function of time. The straight lines depict the corresponding temporal averages.

S2 Results with included radiation force

As explained in the main text, bubbles under the influence of ultrasound experience so-called radiation forces [2–4]. The primary radiation force \mathbf{F}_{rad} pushes them usually away from the sound source, while the secondary radiation force tends to attract the bubbles towards each other. They have been neglected in the main text. We include the primary radiation force here explicitly in order to show that it plays only a minor role for the parameters from the main text (which have been intentionally chosen such that *isotropic* margination dominates). The remaining system setup is identical to the standard one from section 3.2, if not noted otherwise.

S2.1 Method

The primary radiation force is given by [5]

$$\mathbf{F}_{\text{rad}} = -\langle V(t)\nabla P(t) \rangle_t, \quad (1)$$

where $V(t)$ is the bubble volume and the pressure gradient is computed from

$$\nabla P = -\mathbf{k}P_A \cos(2\pi f t) \quad (2)$$

with the wavevector $\mathbf{k} = 2\pi f / c \hat{\mathbf{e}}_z$ of the incoming acoustic wave in the positive z -direction which is perpendicular to the vessel's axis. f is the acoustic frequency and P_A the prescribed pressure amplitude. The angular brackets indicate the temporal average. The time evolution of the bubble volume is obtained by solving the modified Rayleigh-Plesset equation given by reference [6, eq. (3)] for a single bubble numerically. Thus, the primary radiation force is computed under the assumption of negligible deformation and an infinite ambient fluid reservoir.

We solve the Rayleigh-Plesset equation in MATLAB, where we include a certain pressure amplitude P_A , a surface dilatational viscosity of 1.5×10^{-8} kg/s, a plasma density of $\rho = 10^3$ kg/m³, a polytropic gas exponent of $\kappa = 1.095$ and the speed of sound $c = 1480$ m/s [6]. We solve it for at least 16 periods with a relative tolerance of 10^{-12} and an absolute tolerance of $10^{-12}R_0$ using the ode45 integrator. To prevent numerical artifacts, a small finite elastic compression modulus [6] of typically $\chi = 0.002$ N/m is included (we checked that the results are insensitive to the exact value of χ). The remaining two parameters that need to be specified are the radii R_0 and R_{soft} . The solution then provides us with the constant force \mathbf{F}_{rad} , which is converted to a traction jump as explained by reference [7, sec. 2.3]. Otherwise, the numerical procedure is identical to the one from the main text where radiation forces are not included.

S2.2 Results for $P_A = 45$ kPa

As an example, setting $P_A = 45$ kPa, $f = 1$ kHz and $R_0 = R_{\text{soft}} = 2$ μm as in the main text leads to $|\mathbf{F}_{\text{rad}}| \approx 1.2 \times 10^{-15}$ N. Examining again the case of two bubbles without RBCs in figure S2 (a), we find that contrary to figure 8 (a) from the main manuscript some outward migration occurs. Nevertheless, the final radial position is halved compared to full margination as observed when RBCs are included (see any graphic with RBCs, e.g.

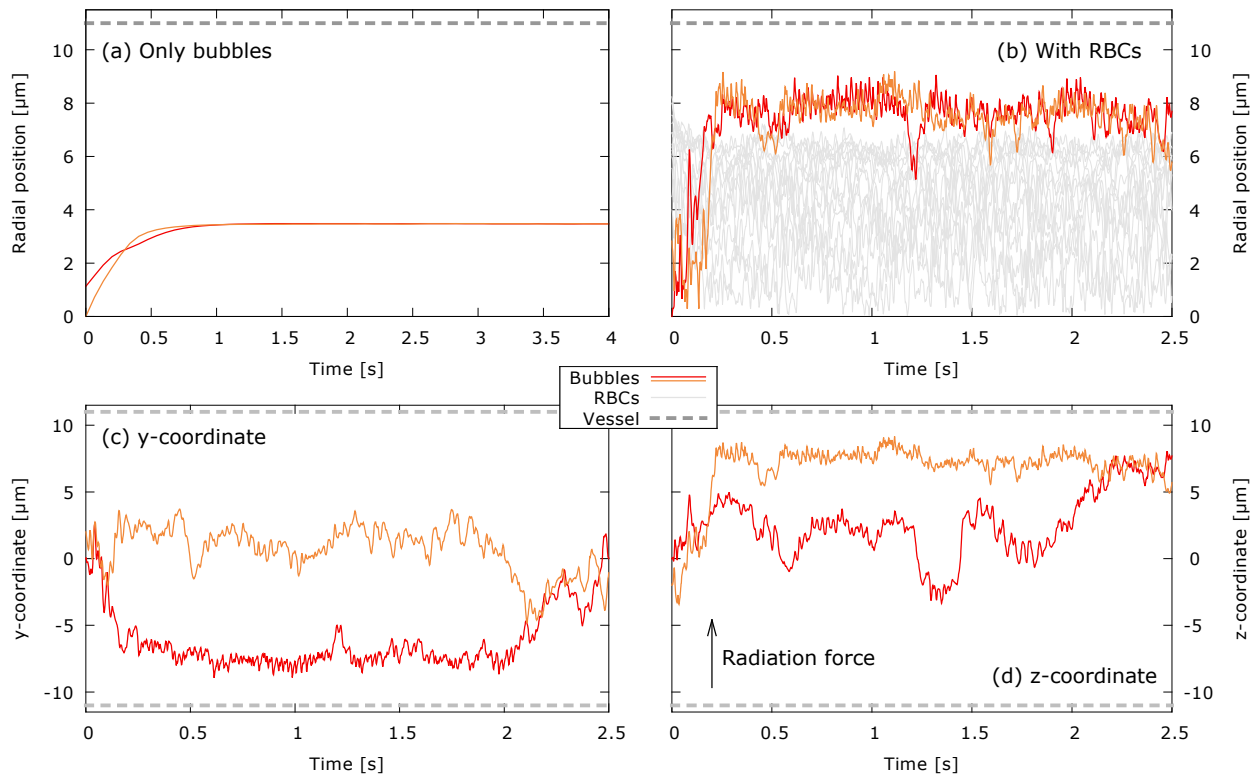


Figure S2: Radial positions of the centroids of two oscillating microbubbles ($f = 1$ kHz, $R_{\text{eff}} \in [1.7; 2.23]$ μm) that are coated with lipid molecules ($\gamma \in [0.5; 10]$ κs) for $\delta = 1$. Primary radiation force for 45 kPa included in the positive z -direction ($|\mathbf{F}_{\text{rad}}| \approx 1.2 \times 10^{-15}$ N). (a) Without red blood cells. (b) With red blood cells (hematocrit: 16%). (c) and (d) The y - and z -coordinates of the two bubbles from (b).

figure S2 (b)). This indicates that margination due to the interactions with the RBCs is the dominating factor for the outward migration.

Including RBCs as well as the primary radiation force \mathbf{F}_{rad} in the positive z -direction leads to figure S2 (b). Obviously, UTM still occurs. If this would be primarily due to the radiation force, one would expect that the bubbles are pushed in the direction of the force, i.e. in the positive z -direction. However, as figures S2 (c) and (d) show, the initial margination of one bubble is in the negative y -direction and thus perpendicular to \mathbf{F}_{rad} .

Both examples highlight that the primary radiation force plays only a secondary role for $P_A = 45$ kPa and $f = 1$ kHz. For $f = 10$ kHz, however, we find $|\mathbf{F}_{\text{rad}}| \approx 10^{-13}$ N, a value which leads to a dominating influence of the radiation force. As this goes hand in hand with the undesired one-sided agglomeration away from the ultrasound source, we thus propose to reduce the pressure amplitude at higher frequencies in order to exploit the isotropy of UTM. Corresponding results will be considered next.

S2.3 Results for $P_A = 6$ kPa

Reducing the pressure amplitude to $P_A = 6$ kPa, we find for $f = 1$ kHz and $R_0 = R_{\text{soft}} = 2$ μm a value of $|\mathbf{F}_{\text{rad}}| \approx 1.5 \times 10^{-17}$ N. For the $P_A = 6$ kPa simulations we also extract the minimal and maximal radial excursions (R_{min} and R_{max} , respectively) and thus the flux amplitudes A_i from the solution of the Rayleigh-Plesset equation.

Without RBCs, the bubbles once again migrate to the channel center as displayed in figure S3 (a), showing that a radiation force of $|\mathbf{F}_{\text{rad}}| \approx 1.5 \times 10^{-17}$ N is indeed negligible. This is further confirmed in figure S3 (b), where RBCs are included but the effective surface tension during the oscillations is held constant: The soft bubbles remain in the center as expected. The same figure also shows (see the stiff bubbles) that the smaller pressure amplitude and thus the smaller radial excursions compared to the main manuscript do not affect the margination behavior.

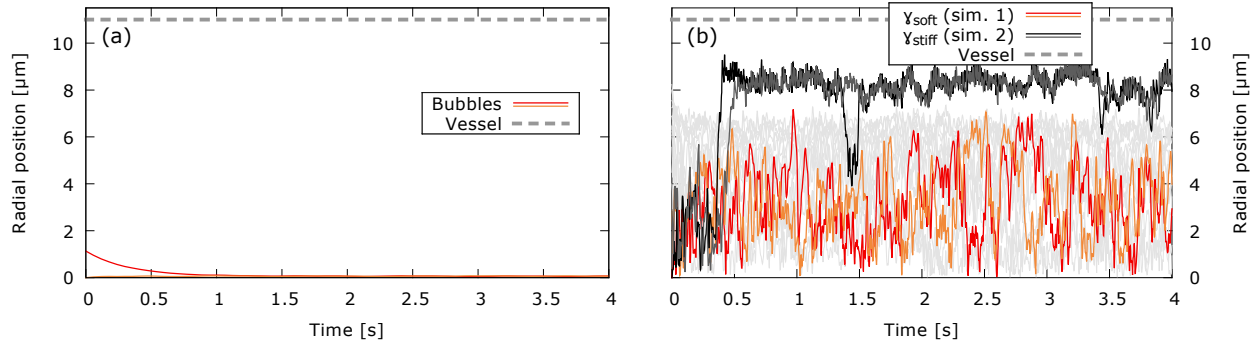


Figure S3: Radial positions of the centroids of two oscillating microbubbles ($f = 1$ kHz, $R_{\text{eff}} \in [1.96; 2.03]$ μm , $P_A = 6$ kPa). Primary radiation force included ($|F_{\text{rad}}| \approx 1.5 \times 10^{-17}$ N). (a) Without red blood cells. Lipid-coated microbubbles, i.e. $\gamma \in [0.5; 10]\kappa_S$ with $\delta = 1$. (b) Margination behavior of purely soft and purely stiff oscillating microbubbles *with* RBCs. Two distinct simulations: The constant surface tensions are $\gamma = \gamma_{\text{soft}} = 0.5\kappa_S$ (red/orange) and $\gamma = \gamma_{\text{stiff}} = 10\kappa_S$ (black/gray). The hematocrit is fixed to 16%. The soft bubbles ($\gamma = \gamma_{\text{soft}}$) remain in the center, whereas the stiff bubbles ($\gamma = \gamma_{\text{stiff}}$) show margination.

We further study this case in figure S4 (a) where we show the analogous result to figure 4 (a) from the main text. After switching on the oscillations, rapid migration within less than one second is observed. The transition in figure S4 (b) roughly corresponds to figure 4 (b); some slight differences are observed as the realized trajectories are different. Moreover, figure S5 highlights that the margination is still isotropic (i.e. similar to figure 6 from the

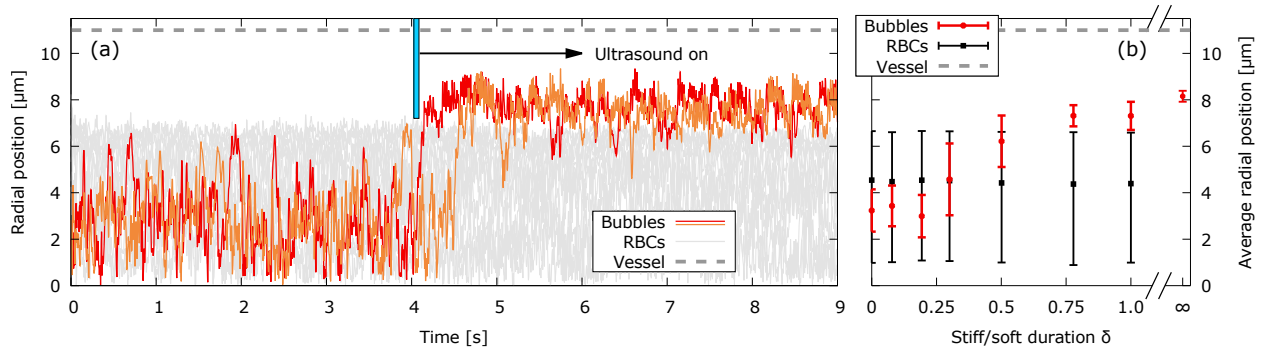


Figure S4: Ultrasound-triggered margination. Primary radiation force included for oscillating bubbles ($f = 1$ kHz, $P_A = 6$ kPa). (a) Radial positions of the centroids of two microbubbles coated with lipids. When the acoustic pressure is switched on at ≈ 4 s, ultrasound-triggered margination leads to rapid migration to the vessel wall. Here, $\delta = 1$, i.e. the bubbles are stiff for the first half of the ultrasound period and soft during the second one with their effective surface tension varying in the range $\gamma \in [0.5; 10]\kappa_S$. The effective radii alternate between 1.96 μm and 2.03 μm . The primary radiation force is $|F_{\text{rad}}| \approx 1.5 \times 10^{-17}$ N. (b) Average radial positions of the oscillating bubbles and RBCs for several different values of δ . Note that the rightmost point corresponds to the limit $\delta \rightarrow \infty$ (i.e. always stiff). The primary radiation force varies only slightly with δ ($|F_{\text{rad}}| \approx 1.5 - 1.6 \times 10^{-17}$ N). The determination of the error bars is explained in section S1.

main text), despite the inclusion of the radiation force.

Increasing the frequency from $f = 1$ kHz to 10 kHz at $P_A = 6$ kPa while the primary radiation force is included leaves the qualitative results for the radial position unchanged but approximately halves the average asphericity, as depicted in figure S6. This matches with the observations from the main manuscript where no radiation forces were considered (figure 7).

S3 Parameter robustness

Ultrasound-triggered margination is a robust effect. Figures S7 and S8 show that reducing the effective surface tension in the soft state to $\gamma_{\text{soft}} = 0.1\kappa_S$, increasing the stiff state tension to $\gamma_{\text{stiff}} = 25\kappa_S$, or changing numerical parameters such as the precision of the solver, the initial position or the length of the periodic vessel does not

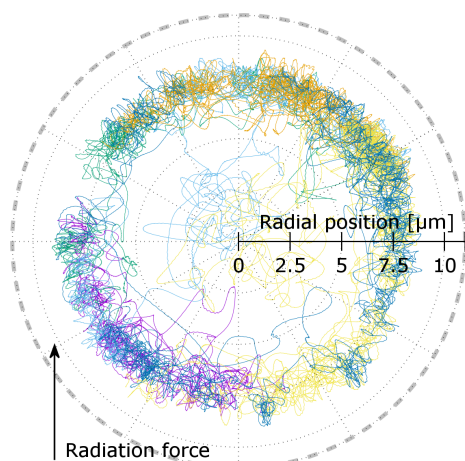


Figure S5: Polar plot of several bubble trajectories (i.e. as viewed from the outlet). The figure shows the $\delta \approx 0.78$ and $\delta = 1$ simulations used for figure S4 (b), representing different system realizations. Hence, the primary radiation force is included (for $f = 1\text{ kHz}$ and $P_A = 6\text{ kPa}$; direction indicated by the arrow). Trajectories only shown for $t > 1\text{ s}$ or after definite margination. Rare short-lived migration events to the inside occur. Each bubble in each simulation is shown in a different color. The outer gray dashed line depicts the vessel radius.

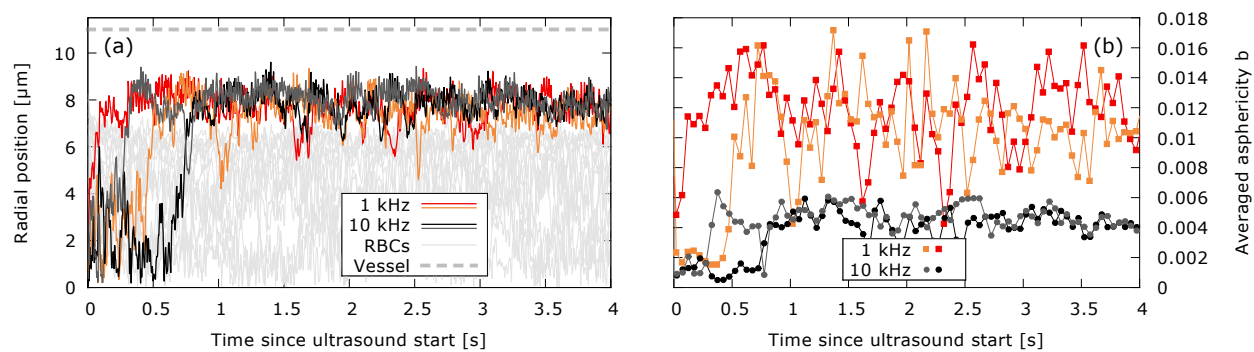


Figure S6: Behavior of two oscillating lipid coated microbubbles for $\delta = 1$ with red blood cells, once for a frequency of $f = 1\text{ kHz}$ and once for 10 kHz (two distinct simulations; the $f = 1\text{ kHz}$ curve is the simulation from figure S4 (a), but shown only from the beginning of the oscillations). The primary radiation force for 6 kPa is included ($|F_{\text{rad}}| \approx 1.5 \times 10^{-17}\text{ N}$ for 1 kHz and $|F_{\text{rad}}| \approx 1.6 \times 10^{-15}\text{ N}$ for 10 kHz). (a) Radial positions of the centroids. The red blood cells are shown in light gray. (b) Corresponding microbubble asphericities averaged over consecutive time intervals of 50 ms .

affect the overall results qualitatively (i.e. margination on average is still observed). Furthermore, halving the bubbles' equilibrium radius or making the vessel wall stiffer does not lead to significant changes either (fig. S8). Note that depending on the exact history, short lived migrations toward the vessel center can occur sometimes, which are nevertheless again followed by rapid movement to the vessel walls.

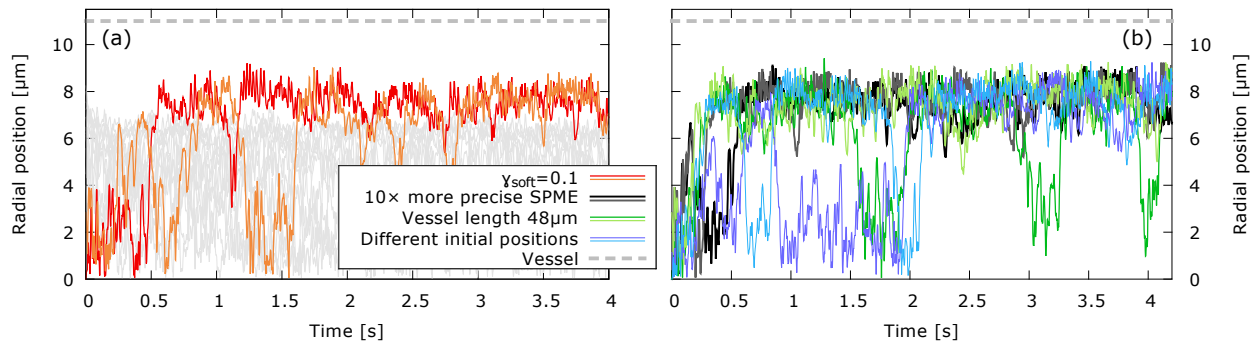


Figure S7: Radial positions of the centroids of two oscillating lipid coated microbubbles ($f = 1$ kHz, $P_A = 45$ kPa) for $\delta = 1$ with red blood cells. Radiation forces *not* included. (a) The surface tension in the soft state is reduced to $\gamma_{\text{soft}} = 0.1\kappa_S$, retaining the effect of margination without qualitative changes (red/orange). The gray lines indicate the red blood cells. (b) Three different simulations for $\gamma_{\text{soft}} = 0.5\kappa_S$: One with more precise SPME parameters (cutoff errors below $\lesssim 0.001\%$, i.e. one order of magnitude smaller than usual; also see section 2.5 in the main manuscript; black/gray lines), one with the larger system from figure 2 (a) from the main text (vessel length $48\mu\text{m}$ and hematocrit 16%; dark/light green), and one with different initial positions for all particles compared to the remaining simulations (RBCs initialized in regular arrays; purple/blue). Red blood cells omitted for clarity.

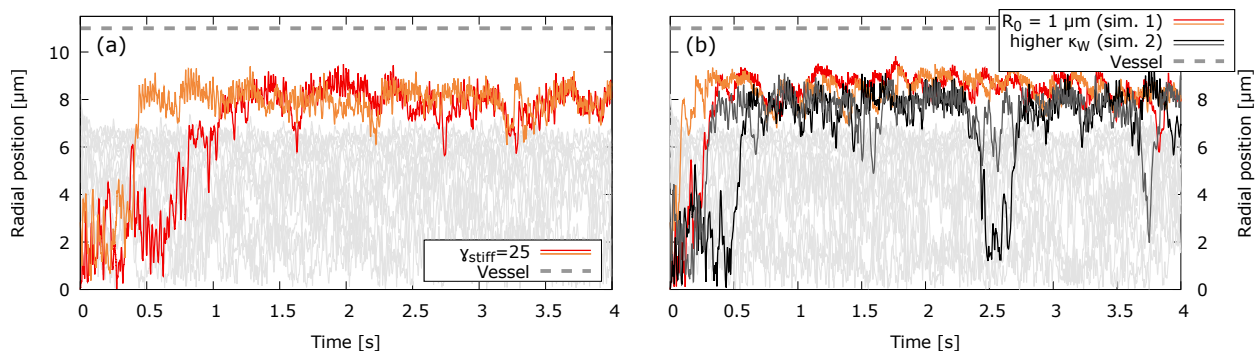


Figure S8: Behavior of two oscillating lipid coated microbubbles for $\delta = 1$, $f = 1$ kHz and $P_A = 6$ kPa with red blood cells. The primary radiation force is included ($F_{\text{rad}} \approx 1.5 \times 10^{-17}$ N). (a) The surface tension in the stiff state is increased to $\gamma_{\text{stiff}} = 25\kappa_S$. (b) Two simulations, once for bubbles of half the usual size ($R_0 = 1\mu\text{m}$) and once for a five times stiffer vessel wall ($\kappa_{\text{Wall}} = 31.25 \times 10^6$ N/m³). The qualitative results remain unchanged in all cases.

S4 Code verification

We performed extensive testing of our code to ensure correctness of both the chosen algorithms as well as of the implementation itself. For example, we compared the results of the single- and double-layer integrals for both the infinite and the periodic Green's functions with analytically known values (similar to ref. [8]). The red blood cell model was validated by considering, amongst others, the deformation of a capsule in an infinite shear flow, as published in reference [7] and further explored below, as well as by comparing with analytical calculations for a diffusing particle near elastic membranes [9–14]. We also used the code to compute the shapes assumed by red blood cells in microchannels [?].

For further verifications we consider a single bubble in an extensional flow in figure S9. More precisely, the flow is solved with VCO-BIM in an infinite domain ($V_T \rightarrow \infty$) as explained in the main text with the imposed

flow set to $\mathbf{u}^\infty(\mathbf{x}) = s(2x, -y, -z)$, where s is the shear rate (for infinite domains, more general imposed flows $\mathbf{u}^\infty(\mathbf{x})$ are possible instead of only a constant flow $\langle \mathbf{u} \rangle_T$ [15]). The bubble starts with 5120 triangles and is refined as needed [16]. Moreover, the mean curvature is computed via Method C from ref. [7] and the mesh stabilization routine from equation (2.72) from the main text is employed. The proper dimensionless parameter is the capillary number $Ca = s\mu R/\gamma$, where μ is the dynamic viscosity of the ambient fluid, R the initial bubble radius and γ the surface tension. For comparison with the literature, we extract the Taylor deformation parameter $D = (a - c)/(a + c)$. The length of the largest half-axis a and of the smallest half-axis c of the deformed object are computed from an ellipsoid with the same inertia tensor [17, 18]. Figure S9 (a) shows a cut through the bubble in the $z = 0$ plane in the stationary state and compares it with the shapes found by Youngren and Acrivos using an axisymmetric boundary integral method [19]. Furthermore, figure S9 (b) depicts the stationary value for the deformation parameter D as a function of the capillary number. We compare it with the numerical results of Youngren and Acrivos [19] and with the analytical $\mathcal{O}(Ca^2)$ theory of Barthès-Biesel and Acrivos [20]. In both cases very good agreement is observed. We also note that the deformation in the $Ca = 0.1$ case corresponds to an asphericity of around 0.295, which is larger than any values observed for the full setup from the main text. Hence we conclude that we obtain correct behavior within the relevant deformation range.

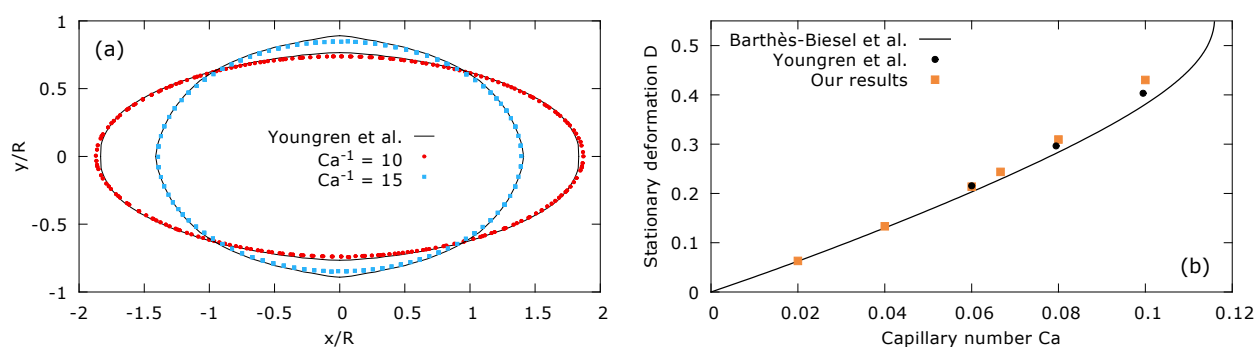


Figure S9: Verification of the bubble in an infinite extensional flow. (a) Cut through the stationary 3D shape of the bubble in the $z = 0$ plane for two different capillary numbers. The black lines depict the results obtained by Youngren and Acrivos using an axisymmetric boundary integral method [19]. (b) Stationary Taylor deformation parameter D as a function of the capillary number. The black dots depict the result by Youngren and Acrivos [19], the orange squares our results. Furthermore, we show the analytical theory of Barthès-Biesel and Acrivos as a black line [20]. Note that it quickly diverges contrary to numerical evidence [19]. Hence, its validity appears to be limited to $Ca \lesssim 0.06$ where excellent agreement is found.

In reference [7] we treated the case of a capsule in an infinite shear flow, and found very good matching with the literature (figures 12 and 17 therein). For the *periodic* system we show a similar result in figure S10. Namely, we place two flat walls with a distance $h = 19R$ in a cubic unit cell with side lengths $20R$ together with an initially spherical capsule of radius R . We implement the shear flow by prescribing the velocities $\mathbf{u} = (\pm sh/2, 0, 0)$ at the walls, whereas the top (bottom) sign corresponds to the top (bottom) wall and s is the shear rate. The capsule is endowed not only with some shear elasticity modeled according to the neo-Hookean law (shear modulus κ_S [7]), but also with some bending rigidity following the Canham-Helfrich law [21–23] (bending modulus κ_B , Method C from ref. [7], flat reference state). We set the inner viscosity to be identical to the dynamic viscosity μ of the ambient fluid. Hence, two dimensionless parameters are relevant: The capillary number $Ca = s\mu R/\kappa_S$ and the reduced bending modulus $\hat{\kappa}_B = \kappa_B/(R^2\kappa_S)$. As before, we extract the Taylor deformation parameter D . See reference [7] for further details and section 3.2 in the main text for the remaining parameters. Varying the distance between the walls does not change the results significantly compared to $h = 19R$. We therefore effectively mimic an infinite system and comparisons with results from unbounded flows are appropriate. However, the keypoint here is that we use the very same SPME code that is also employed for the simulations in the main paper, and thereby further validate the implementation. Numerical parameters include 1280 triangles for the capsule (which is well converged [7] and roughly corresponds to the maximal resolution used for the red blood cells in the margination simulations) and 800 triangles per wall. The SPME error is $\lesssim 0.01\%$ (similar to the main simulations). Obviously, figure S10 shows that our results compare very favorably with data extracted from Tsubota [24], proving that our code works as intended.

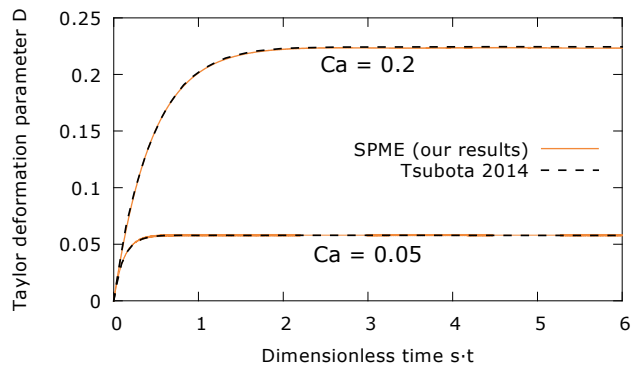


Figure S10: Deformation of a single spherical capsule (endowed with shear elasticity and bending rigidity) in a periodic system for two different capillary numbers Ca , compared to results from reference [24] (“model H” therein). We set $\hat{\kappa}_B = 2/15$. Since the wall distance h is chosen sufficiently large, the data matches very well although the values from the literature were obtained for a capsule in an infinite (rather than a periodic) system.

S5 Dynamic mesh refinement

As outlined in the main text, we employ Rivara’s longest-edge bisection algorithm [16] in order to refine the triangular meshes locally when objects come close to each other and at high curvature regions. Lower resolutions are sufficient for the other regions, i.e. we coarsen the previously refined areas again in this case. Example snapshots are shown in figure S11.

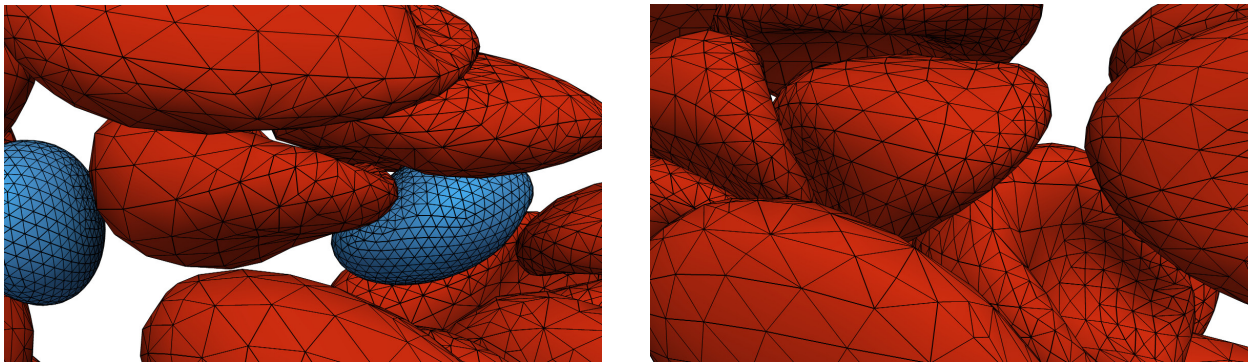


Figure S11: Example snapshots from the simulations, highlighting the dynamic mesh refinement due to close contact and high curvature regions.

References

- [1] K. Müller, D. A. Fedosov, and G. Gompper, “Margination of micro- and nano-particles in blood flow and its effect on drug delivery,” *Sci. Rep.* **4**, 4871 (2014).
- [2] P. Dayton, A. Klibanov, G. Brandenburger, and K. Ferrara, “Acoustic radiation force in vivo: A mechanism to assist targeting of microbubbles,” *Ultrasound Med. Biol.* **25**, 1195 (1999).
- [3] J. J. Rychak, A. L. Klibanov, K. F. Ley, and J. A. Hossack, “Enhanced Targeting of Ultrasound Contrast Agents Using Acoustic Radiation Force,” *Ultrasound. Med. Biol.* **33**, 1132 (2007).
- [4] K. A. Johnson, H. R. Vormohr, A. A. Doinikov, A. Bouakaz, C. W. Shields, G. P. López, and P. A. Dayton, “Experimental verification of theoretical equations for acoustic radiation force on compressible spherical particles in traveling waves,” *Phys. Rev. E* **93**, 053109 (2016).
- [5] A. Prosperetti, “Bubble phenomena in sound fields: Part two,” *Ultrasonics* **22**, 115 (1984).

- [6] P. Marmottant, S. van der Meer, M. Emmer, M. Versluis, N. de Jong, S. Hilgenfeldt, and D. Lohse, “A model for large amplitude oscillations of coated bubbles accounting for buckling and rupture,” *J. Acoust. Soc. Am.* **118**, 3499 (2005).
- [7] A. Guckenberg, M. P. Schraml, P. G. Chen, M. Leonetti, and S. Gekle, “On the bending algorithms for soft objects in flows,” *Comput. Phys. Comm.* **207**, 1 (2016).
- [8] A. Farutin, T. Biben, and C. Misbah, “3D numerical simulations of vesicle and inextensible capsule dynamics,” *J. Comput. Phys.* **275**, 539 (2014).
- [9] A. Daddi-Moussa-Ider, A. Guckenberg, and S. Gekle, “Long-lived anomalous thermal diffusion induced by elastic cell membranes on nearby particles,” *Phys. Rev. E* **93**, 012612 (2016).
- [10] A. Daddi-Moussa-Ider, A. Guckenberg, and S. Gekle, “Particle mobility between two planar elastic membranes: Brownian motion and membrane deformation,” *Phys. Fluids* **28**, 071903 (2016).
- [11] A. Daddi-Moussa-Ider and S. Gekle, “Hydrodynamic interaction between particles near elastic interfaces,” *J. Chem. Phys.* **145**, 014905 (2016).
- [12] A. Daddi-Moussa-Ider, M. Lisicki, and S. Gekle, “Mobility of an axisymmetric particle near an elastic interface,” *J. Fluid Mech.* **811**, 210 (2017).
- [13] A. Daddi-Moussa-Ider and S. Gekle, “Hydrodynamic mobility of a solid particle near a spherical elastic membrane: Axisymmetric motion,” *Phys. Rev. E* **95**, 013108 (2017).
- [14] A. Daddi-Moussa-Ider, M. Lisicki, and S. Gekle, “Hydrodynamic mobility of a solid particle near a spherical elastic membrane. II. Asymmetric motion,” *Phys. Rev. E* **95**, 053117 (2017).
- [15] C. Pozrikidis, “Interfacial Dynamics for Stokes Flow,” *J. Comput. Phys.* **169**, 250 (2001).
- [16] M. C. Rivara, “Algorithms for refining triangular grids suitable for adaptive and multigrid techniques,” *Int. J. Numer. Methods Eng.* **20**, 745 (1984).
- [17] T. Krüger, F. Varnik, and D. Raabe, “Efficient and accurate simulations of deformable particles immersed in a fluid using a combined immersed boundary lattice Boltzmann finite element method,” *Comput. Math. Appl.* **61**, 3485 (2011).
- [18] S. Ramanujan and C. Pozrikidis, “Deformation of liquid capsules enclosed by elastic membranes in simple shear flow: Large deformations and the effect of fluid viscosities,” *J. Fluid Mech.* **361**, 117 (1998).
- [19] G. K. Youngren and A. Acrivos, “On the shape of a gas bubble in a viscous extensional flow,” *J. Fluid Mech.* **76**, 433 (1976).
- [20] D. Barthès-Biesel and A. Acrivos, “Deformation and burst of a liquid droplet freely suspended in a linear shear field,” *J. Fluid Mech.* **61**, 1 (1973).
- [21] P. B. Canham, “The minimum energy of bending as a possible explanation of the biconcave shape of the human red blood cell,” *J. Theor. Biol.* **26**, 61 (1970).
- [22] W. Helfrich, “Elastic Properties of Lipid Bilayers: Theory and Possible Experiments,” *Z. Naturforsch. C* **28**, 693 (1973).
- [23] A. Guckenberg and S. Gekle, “Theory and algorithms to compute Helfrich bending forces: A review,” *J. Phys. Condens. Matter* **29**, 203001 (2017).
- [24] K.-i. Tsubota, “Short note on the bending models for a membrane in capsule mechanics: Comparison between continuum and discrete models,” *J. Comput. Phys.* **277**, 320 (2014).

Publication 4

3D tomography of cells in micro-channels

by

S. Quint, A. F. Christ, A. Guckenberger, S. Himbert, L. Kaestner,
S. Gekle and C. Wagner

Applied Physics Letters **111** (10), 103701 (2017)

DOI: [10.1063/1.4986392](https://doi.org/10.1063/1.4986392)

Reproduced with permission from AIP Publishing.



3D tomography of cells in micro-channels

S. Quint,^{1,a)} A. F. Christ,¹ A. Guckenberger,² S. Himbert,¹ L. Kaestner,^{1,3} S. Gekle,² and C. Wagner^{1,4}

¹Department of Experimental Physics, Saarland University, Campus E2.6, 66123 Saarbrücken, Germany

²Biofluid Simulation and Modeling, Department of Physics, University of Bayreuth, Universitätsstraße 30, 95440 Bayreuth, Germany

³Theoretical Medicine and Biosciences, Campus University Hospital, Saarland University, Building 61.4, 66421 Homburg, Germany

⁴Physics and Materials Science Research Unit, University of Luxembourg, Luxembourg, Luxembourg

(Received 5 June 2017; accepted 19 July 2017; published online 5 September 2017)

We combine confocal imaging, microfluidics, and image analysis to record 3D-images of cells in flow. This enables us to recover the full 3D representation of several hundred living cells per minute. Whereas 3D confocal imaging has thus far been limited to steady specimens, we overcome this restriction and present a method to access the 3D shape of moving objects. The key of our principle is a tilted arrangement of the micro-channel with respect to the focal plane of the microscope. This forces cells to traverse the focal plane in an inclined manner. As a consequence, individual layers of passing cells are recorded, which can then be assembled to obtain the volumetric representation. The full 3D information allows for a detailed comparison with theoretical and numerical predictions unfeasible with, e.g., 2D imaging. Our technique is exemplified by studying flowing red blood cells in a micro-channel reflecting the conditions prevailing in the microvasculature. We observe two very different types of shapes: “croissants” and “slippers.” Additionally, we perform 3D numerical simulations of our experiment to confirm the observations. Since 3D confocal imaging of cells in flow has not yet been realized, we see high potential in the field of flow cytometry where cell classification thus far mostly relies on 1D scattering and fluorescence signals. *Published by AIP Publishing.* [<http://dx.doi.org/10.1063/1.4986392>]

The optical detection and classification of biological cells are usually performed by two complementary approaches. On the one hand, optical microscopy is suitable for small sample amounts and steady specimens such as tissue slices. Many techniques exist that allow us to reveal textures at high resolutions on the sub- μm scale. For example, detailed 3D images of resting bio-particles such as red blood cells (RBCs) can be produced with confocal microscopes by scanning the z -axis of the objective in subsequent steps.^{1–4} This technique also allows us to highlight special structures by activating specifically dyed regions of interest. However, even with fast spinning Nipkow disks, the recording of moving objects such as cells in flow is highly challenging. Constraints mainly arise from the limited scanning performance of the mechanical actuators of microscopes. On the other hand, flow cytometry targets bio-particles suspended in flowing liquids and allows for high-throughput classification of objects.^{5,6} Statistical information based on a few measurement parameters (fluorescence emission and scattering signals) finally serves to discriminate between different cell populations.

Obtaining the 3D shape of individual cells in flow has thus far been restricted to special circumstances such as when the cell performs a full rotation in the microscope’s field of view.⁷ However, being able to analyze individual cells under general flow conditions is a very important task as it can give answers to basic questions concerning the physical properties of the cell membrane (elastic moduli, stress-free shape, etc.) or the preferred shape in various

environments. Understanding the detailed behavior of individual cells also serves as a first step towards an in-depth comprehension of multi-particle interactions or even dense suspensions.^{4,8,9}

Here, we introduce a flow cytometry technique based on confocal imaging to record the *three-dimensional* shape of *flowing* cells in a micro-channel. The basic idea is to not actuate the objective or sample stage but rather to tilt the channel such that successive frames record different slices of the object moving through the focal plane of the confocal microscope (Fig. 1). Depending on the cell velocity, about one hundred layers of a single cell can be recorded and then assembled to obtain a full 3D reconstruction. The acquisition speed is only limited by the rotation speed of the employed Nipkow disk and the frame rate of the used camera.

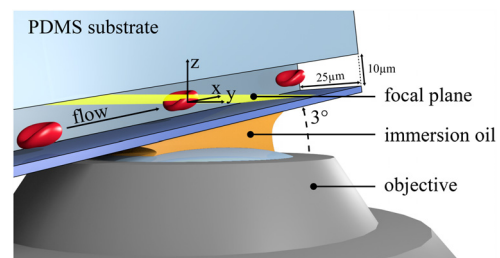


FIG. 1. Sketch of the used setup. With a tilted stage, we incline our micro-channels with respect to the focal plane (yellow) of the objective such that we can take advantage of the objective’s full field of view. Cells traverse the focal plane sectional-wise and a stack of image slices is recorded to recover the full 3D representation. Since movement of mechanical stages is not necessary, frame rates up to 600 frames per second (FPS) can be realized. The used channel has a cross-section of $25\ \mu\text{m} \times 10\ \mu\text{m}$ (width \times height) and is tilted by an angle of $\approx 3^\circ$.

^{a)}Stephan.Quint@physik.uni-saarland.de

Typically, a throughput of several hundred cells per minute can be handled and reconstructed by our technique. We exemplify our technique by considering the shapes of single human red blood cells (RBCs) in channel-sizes comparable to the structures found in the microvasculature. The attained shapes are of high importance for the macroscopic properties such as the pronounced shear thinning of blood. Yet, current research on this topic was so far limited to 2D imaging methods^{10–18} where the shapes are not always clearly identifiable,¹² 3D imaging of “frozen” cells where the method of freezing might influence the form,^{4,19} and 2D^{20–26} as well as 3D^{27–34} simulations. Our method allows for the full 3D capturing of moving bio-particles in micro-sized channels, which has so far been impossible (Fig. 2). We found two very different shapes of RBCs in the experiments: a croissant-like and a slipper-like shape. These observations are confirmed by 3D numerical simulations.

Our 3D imaging technique enables us to access the full 3D information at frame rates comparable to 2D approaches. In contrast to common z -scanning methods, we use a micro-fluidic channel which is tilted by a small angle with respect to the focal plane of a confocal microscope (Fig. 1). This arrangement forces cells to pass the focal plane in an inclined manner and the acquisition of cross-sectional images (slices) of cells becomes possible without objective or stage motion. Due to their velocity, cells pass the field of view in the x -direction while the z -axis is automatically scanned in subsequent frames. In a post-processing step, the cell contour is then cropped from individual pictures and the volumetric representation assembled. Data acquisition is performed at a maximum rate of 600 frames per second (FPS), which facilitates capturing cells at velocities up to 1.5 mm/s. This mostly covers the physically relevant range of blood in the microvascular system. Limitations mainly arise from the maximum rotation speed of the Nipkow disks and the frame rate of the used camera.

Special care is required when choosing the objective. Since channels are tilted, sufficient working distance of the objective is mandatory for mechanical reasons. Specifically if channels with heights $>10\ \mu\text{m}$ are used, the tilt angle must be increased to fully capture the cross-section of the channel by the field of view. However, this can easily lead to mechanical collision of the channel substrate and the objective housing. For our experiments, we found an inclination angle of approximately 3° to be sufficient to fully take advantage of the available field of view ($225\ \mu\text{m} \times 225\ \mu\text{m}$). Measurements are taken at a distance of $\approx 50\ \text{mm}$ away from the channel inlet. Our micro-fluidic channels are fabricated in a standard soft-lithography process and are made of polydimethylsiloxane (PDMS) based substrates attached to glass slides. The channel cross-section corresponds to $25\ \mu\text{m} \times 10\ \mu\text{m}$ (width \times height). For our experiments, cells are stained with Cell-MaskTM Red which is excited at 647 nm. Using a standard protocol for staining, this dye very homogeneously attaches to the cell membrane and cross-sectional images clearly show the cell outlines (Fig. 3). Achieving high selectivity between different slices, a $60\times$ oil immersion objective at high numerical aperture ($\text{NA} = 1.2$) is used for confocal imaging. Aiming to characterize single cells, highly diluted RBC concentrations are used (approximately $10\ \mu\text{l}$ blood suspended in 1 ml phosphate buffered saline (PBS)). Within the buffer solution, the viscosity contrast (ratio of inner and outer viscosity of cells) corresponds to $\lambda \approx 5$, which is in accordance with physiological conditions.³⁵

Confocal cross-sectional imaging is performed with a spinning micro-lens enhanced Nipkow disk. Rotating at $4000\ \text{min}^{-1} \approx 67\ \text{s}^{-1}$ and equipped with multiple micro-lens sections, the disk allows for a nominal frame rate of 200 FPS. Since the camera exhibits an acquisition speed of 600 FPS, images are taken three times faster than the maximum rate specified for the disk. This results in noticeable dark areas from the micro-lens array that can be seen at

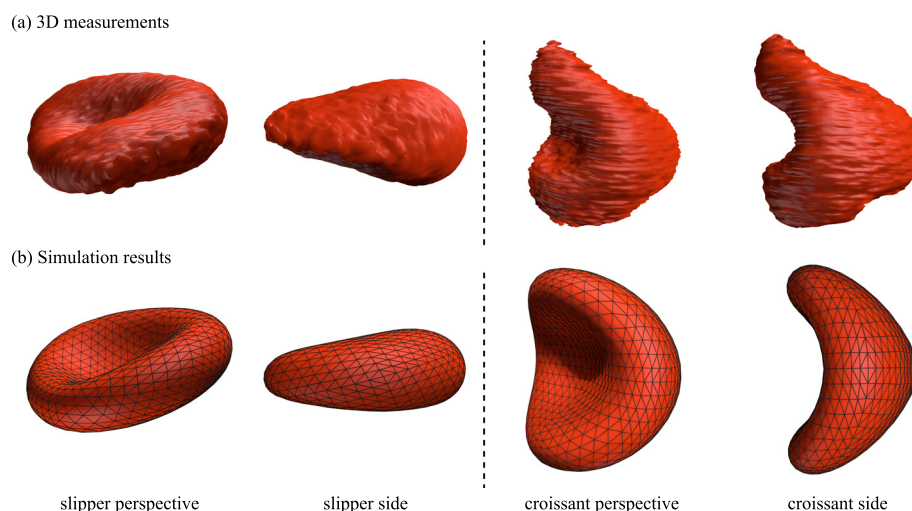


FIG. 2. 3D reconstruction of moving RBCs in micro-fluidic flow (top row). The channel dimension corresponds to $25\ \mu\text{m} \times 10\ \mu\text{m}$ (width \times height). 3D assemblies are made up of about 250 cross-sectional images and show two possible RBC configurations at the same applied pressure drop: a slipper at $\approx 330\ \mu\text{m/s}$ and a croissant at $\approx 370\ \mu\text{m/s}$ (the difference in cell velocity results from a different vertical cell position). A perspective as well as a side view of the slipper and the croissant shapes are illustrated. Pictures are rotated to give a proper impression on the cell geometry. However, since the rotation of cells relative to the flow is different, slices course from front to back in the case of the slipper shape and from top to bottom for the croissant. Simulations of the respective cell shapes (bottom row) are generated using the periodic boundary integral method (see text). Giving a better impression on the volumetric representation, we refer the reader to our [supplementary material](#) videos.

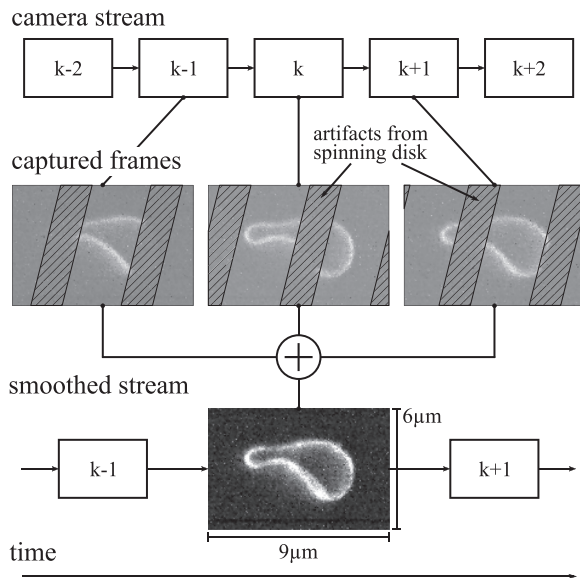


FIG. 3. Post-processing of subsequent velocity corrected image frames (“camera stream”) taken at discrete time-steps k . Artifacts from confocal imaging can exemplarily be seen for three subsequent cross-sectional images (“captured frames”). Areas (hatched) which are not excited by the light source and not seen by the camera remain dark and the observed cell reveals missing parts. Therefore, the superposition of three subsequent images is continuously built to get the full representation of the cell for each time-step (“smoothed stream”). As a side-effect, this procedure additionally improves the signal-to-noise ratio by a factor of ≈ 1.7 and therefore enhances the image contrast.

individual image frames taken at a maximum of 600 FPS (Fig. 3) and mainly concerns the illumination as well as the fluorescence detection at certain image areas. For overcoming these disturbances, two obvious approaches exist. First, the camera could be synchronized with the rotating disk. Doing so, an overall sample rate of 200 FPS would result which limits the observable velocity range of passing cells. Second, the camera can be decoupled from the disk, runs at maximum acquisition speed, and records complete as well as fractional cell images (preferred method). Due to this oversampling, more information content on cells or fraction of cells can be gathered. However, for reconstructing a clean 3D representation of each cell, partial images must be supplemented by complete frames. This can be done by taking bundles of three subsequent cross-sectional slices which are continuously summarized to obtain the full representation of the cell membrane. Besides the effect that dark areas from confocal imaging are smoothed out, an improved signal-to-noise-ratio (factor ≈ 1.7) is obtained, which enhances the image contrast.

Moreover, due to cell motion, the spatial shift of cell signals between subsequent frames must be determined for correct volumetric recovery. To access this shift, the cell velocity has to be measured. This is achieved by calculating the center of mass of individual cells for each time-step (frame) to obtain a position (pixel) vs. time diagram that is linearly fitted. Taking the magnification into account, the slope of this fit represents the cell velocity. Finally, a velocity corrected stack of cross-sectional cell images is obtained, which is then assembled to get the full 3D representation.

At equilibrium, shape assembly errors may only be due to statistical rotational or translational fluctuations caused by Brownian motion. Giving the reader a rough estimation on

diffusion processes, spherical particles of similar volume serve as a placeholder in the following calculation. Assuming a velocity of $350 \mu\text{m/s}$, cells take $\tau = 660 \text{ ms}$ to pass the field of view ($225 \mu\text{m}$). With a radius of $R = 4 \mu\text{m}$ and dynamic viscosity $\eta = 1 \text{ mPa s}$ of the medium, the root mean-square angular deviation during the interaction corresponds to $\sqrt{\langle \Theta^2 \rangle} = 0.057 \text{ rad} = 3.25^\circ$. Moreover, the translational root mean square displacement amounts to $\sqrt{\langle x^2 \rangle} = 0.26 \mu\text{m}$. Consequently, the rotational diffusion accounts for less than 1% of a full rotation. Translational diffusion corresponds to $\approx 6.5\%$ of the object size during its time of flight. Both diffusion processes may lead to slight displacements when the cross-sectional image slices are assembled. Fortunately, the main features of cell geometries are maintained and clear pictures evolve in practice. Thus, our measuring approach is in principle not affected by Brownian motion.

Figure 2 (top row) shows typical 3D measurements for RBCs within a Poiseuille flow, comprising a slipper and a croissant shape as also observed in previous experiments^{10,11,13,14,19} and simulations^{20–22,24,27,31} (see the [supplementary material](#) for movies). The slipper has a somewhat lower velocity ($\approx 330 \mu\text{m/s}$) than the croissant ($\approx 370 \mu\text{m/s}$), despite being driven by the same pressure drop, because it is slightly off-centered. This is in agreement with previous 2D simulations.²⁴ Note that the croissant shape is similar to a parachute. But where the latter is perfectly rotationally symmetric around its axis, the croissant has only two symmetry planes. This is due to the rectangular form of the channel.

In addition to our experiments, we perform numerical simulations to confirm these shapes theoretically by using the periodic boundary integral method.³⁶ As it is based on the Stokes equation, the Reynolds number must be small in order to faithfully capture the dynamics. For the present case, it can be estimated to be $\text{Re} = D_{\text{RBC}} u \rho / \mu < 10^{-2}$, with the equilibrium diameter of the red blood cell $D_{\text{RBC}} \approx 8 \mu\text{m}$, the velocity $u \approx 370 \mu\text{m/s}$, the density $\rho \approx 10^3 \text{ kg/m}^3$, and the dynamic viscosity $\mu \approx 10^{-3} \text{ kg/(s m)}$. The simulated channel has the same cross-section ($25 \mu\text{m} \times 10 \mu\text{m}$) as in the experiments and a length of $60 \mu\text{m}$. A single red blood cell is started in the equilibrium discocyte state and axis-aligned with the channel axis. The viscosity at the inside is chosen to be 5 times higher than at the outside ($\lambda = 5$). For further details, we refer the reader to our recent publications^{36–38} and the [supplementary material](#). Depending on the starting position, either an off-centered and slower slipper or a centered and faster croissant can be observed (see the [supplementary material](#) for movies). They compare favorably with the experimentally obtained forms as shown at the bottom of Fig. 2. Note that the croissant shape is found to be metastable for the present parameters, i.e., it switches to a slipper shape after several seconds. This also suggests that the croissant as seen in the experiments might be of transient nature. However, further studies are needed to confirm this observation. Moreover, the slipper was found to exhibit pronounced tank-treading in accordance with previous publications.^{24,31}

Summarizing, we developed a tomography based 3D imaging technique for moving bio-particles in micro-fluidic flow. Our approach will enable a large set of practically relevant application scenarios which have hitherto been

inaccessible to the confocal (or any other) 3D imaging technique. The key of our approach is a tilted channel that allows objects to traverse the field of view in an inclined manner. At sufficient frame rates, a number of cross-sectional images are taken, which are then assembled to obtain the full 3D representation of bio-particles. This method enables us to characterize the shape of flowing cells, exemplified herein by using human RBCs. With 3D tomography, we are able to confirm or refute theoretical and numerical predictions of cell shapes and can therefore provide more detailed information on cell-intrinsic parameters. In addition to our experimental technique, we performed numerical simulations of RBCs in the same environment as in the experiments. Employing the periodic boundary integral method, we found good agreement with the experimental results. Our approach could be utilized for diagnostics, e.g., to identify shape-related anomalies such as sickle-cell anemia. This makes micro-fluidic based 3D tomography a possible supplement or even replacement for flow cytometers in specific use-cases.

See [supplementary material](#) for a detailed description of the numerical simulation methods used as well as for videos of our results.

Funding from the Volkswagen Foundation and computing time granted by the Leibniz-Rechenzentrum on SuperMUC are gratefully acknowledged by A. Guckenberger and S. Gekle. S. Quint, A. F. Christ, S. Himbert, and C. Wagner kindly acknowledge the support and funding of the “Deutsch-Französische-Hochschule” (DFH). Funding from the European Framework “Horizon 2020” under Grant Agreement No. 675115 (RELEVANCE) is received by C. Wagner and L. Kaestner.

¹K. Khairy, J. Foo, and J. Howard, *Cell. Mol. Bioeng.* **1**, 173 (2008).

²A. Sakashita, N. Urakami, P. Zihlerl, and M. Imai, *Soft Matter* **8**, 8569 (2012).

³T. Kim, R. Zhou, M. Mir, S. D. Babacan, P. S. Carney, L. L. Goddard, and G. Popescu, *Nat. Photonics* **8**, 256 (2014).

⁴L. Lanotte, J. Mauer, S. Mendez, D. A. Fedosov, J.-M. Fromental, V. Claveria, F. Nicoud, G. Gompper, and M. Abkarian, *Proc. Natl. Acad. Sci.* **113**, 13289 (2016).

⁵H. M. Shapiro, *Practical Flow Cytometry*, 4th ed. (Wiley-Liss, New York, 2003).

⁶O. Otto, P. Rosendahl, A. Mietke, S. Golfier, C. Herold, D. Klaue, S. Girardo, S. Pagliara, A. Ekpenyong, A. Jacobi, M. Wobus, N. Töpfner, U.

F. Keyser, J. Mansfeld, E. Fischer-Friedrich, and J. Guck, *Nat. Methods* **12**, 199 (2015).

⁷F. Merola, P. Memmolo, L. Miccio, R. Savoia, M. Mugnano, A. Fontana, G. D’Ippolito, A. Sardo, A. Iolascon, A. Gambale, and P. Ferraro, *Light: Sci. Appl.* **6**, e16241 (2017).

⁸A. M. Forsyth, J. Wan, P. D. Owrutsky, M. Abkarian, and H. A. Stone, *Proc. Natl. Acad. Sci.* **108**, 10986 (2011).

⁹T. Krüger, M. Gross, D. Raabe, and F. Varnik, *Soft Matter* **9**, 9008 (2013).

¹⁰M. Abkarian, M. Faivre, R. Horton, K. Smistrup, C. A. Best-Popescu, and H. A. Stone, *Biomed. Mater.* **3**, 034011 (2008).

¹¹G. Tomaiuolo, M. Simeone, V. Martinelli, B. Rotoli, and S. Guido, *Soft Matter* **5**, 3736 (2009).

¹²G. Couplier, A. Farutin, C. Minetti, T. Podgorski, and C. Misbah, *Phys. Rev. Lett.* **108**, 178106 (2012).

¹³L. Lanotte, G. Tomaiuolo, C. Misbah, L. Bureau, and S. Guido, *Biomechanics* **8**, 014104 (2014).

¹⁴G. Prado, A. Farutin, C. Misbah, and L. Bureau, *Biophys. J.* **108**, 2126 (2015).

¹⁵G. Tomaiuolo, L. Lanotte, R. D’Apolito, A. Cassinese, and S. Guido, *Med. Eng. Phys.* **38**, 11 (2016).

¹⁶V. Claveria, O. Aouane, M. Thiébaud, M. Abkarian, G. Couplier, C. Misbah, T. John, and C. Wagner, *Soft Matter* **12**, 8235 (2016).

¹⁷J. Dupire, M. Socol, and A. Viallat, *Proc. Natl. Acad. Sci.* **109**, 20808 (2012).

¹⁸H. Basu, A. K. Dharmadhikari, J. A. Dharmadhikari, S. Sharma, and D. Mathur, *Biophys. J.* **101**, 1604 (2011).

¹⁹P. Gaegtgens, C. Dührssen, and K. H. Albrecht, *Blood Cells* **6**, 799 (1980).

²⁰T. W. Secomb, B. Styp-Rekowska, and A. R. Pries, *Ann. Biomed. Eng.* **35**, 755 (2007).

²¹B. Kaoui, G. Biros, and C. Misbah, *Phys. Rev. Lett.* **103**, 188101 (2009).

²²B. Kaoui, N. Tahiri, T. Biben, H. Ez-Zahraouy, A. Benyoussef, G. Biros, and C. Misbah, *Phys. Rev. E* **84**, 041906 (2011).

²³C. Misbah, *J. Phys.: Conf. Ser.* **392**, 012005 (2012).

²⁴N. Tahiri, T. Biben, H. Ez-Zahraouy, A. Benyoussef, and C. Misbah, *Microvasc. Res.* **85**, 40 (2013).

²⁵O. Aouane, M. Thiébaud, A. Benyoussef, C. Wagner, and C. Misbah, *Phys. Rev. E* **90**, 033011 (2014).

²⁶G. R. Lázaro, A. Hernández-Machado, and I. Pagonabarraga, *Soft Matter* **10**, 7195 (2014).

²⁷H. Noguchi and G. Gompper, *Proc. Natl. Acad. Sci.* **102**, 14159 (2005).

²⁸L. V. Pivkin and G. E. Karniadakis, *Phys. Rev. Lett.* **101**, 118105 (2008).

²⁹J. L. McWhirter, H. Noguchi, and G. Gompper, *Soft Matter* **7**, 10967 (2011).

³⁰X. Li, P. M. Vlahovska, and G. E. Karniadakis, *Soft Matter* **9**, 28 (2013).

³¹D. A. Fedosov, M. Peltomäki, and G. Gompper, *Soft Matter* **10**, 4258 (2014).

³²K. Sinha and M. D. Graham, *Phys. Rev. E* **92**, 042710 (2015).

³³J. B. Freund, *Annu. Rev. Fluid Mech.* **46**, 67 (2014).

³⁴D. Cordasco and P. Bagchi, *Phys. Fluids* **29**, 041901 (2017).

³⁵G. R. Cokelet and H. J. Meiselman, *Science* **162**, 275 (1968).

³⁶A. Guckenberger and S. Gekle, preprint [arXiv:1608.05196](https://arxiv.org/abs/1608.05196) [physics] (2017).

³⁷A. Guckenberger, M. P. Schraml, P. G. Chen, M. Leonetti, and S. Gekle, *Comput. Phys. Commun.* **207**, 1 (2016).

³⁸A. Guckenberger and S. Gekle, *J. Phys.: Condens. Matter* **29**, 203001 (2017).

Supplementary information for “3D tomography of cells in micro-channels”

S. Quint,* A. F. Christ,* A. Guckenberger,† S. Himbert,* L. Kaestner*,‡ S. Gekle,† C. Wagner*

Dated: June 2, 2017

S1 Numerical method

S1.1 The boundary integral method

We use the boundary integral method (BIM) [1] with periodic boundary conditions [2, 3] to perform our numerical simulations. An essential property of this method is that only integrals over the surface of the objects appear (due to the linearity of the underlying Stokes equation), making a discretization of the fluid volume unnecessary. Two objects are required in the present case: One red blood cell (RBC) and one rectangular channel. Flat triangles are used for the surface discretization in all cases.

The RBC is discretized with 2048 triangles. The ratio of the viscosities at the inside and outside is set to $\lambda = 5$ which is the typical physiological value of healthy red blood cells [4, 5]. Furthermore, the in-plane elasticity of the RBC is modeled with the Skalak law [6] with a shear modulus of $\kappa_S = 5 \times 10^{-6}$ N/m and an area dilatation modulus of $\kappa_A = 100\kappa_S$. The reference state is taken to be the typical equilibrium shape [7, 8] of the RBC. Using e.g. an oblate spheroid as the reference state will cause only minor changes to the results for $\lambda = 5$ as shown by Cordasco *et al.* [9]. Moreover, the bending resistance follows from the Helfrich model [10, 11] with a bending modulus of $\kappa_B = 3 \times 10^{-19}$ N m and the spontaneous curvature set to zero. Computing the bending forces is actually non-trivial because a fourth order derivative of the surface is required. We use Method C from refs. [11, 12] for this purpose. For a comparison with other algorithms we also refer the reader to these two publications.

The channel itself has a width of $25 \mu\text{m}$, a height of $10 \mu\text{m}$ and a length of $60 \mu\text{m}$. It is modeled with 4374 flat triangles. To prevent numerical problems, its corners are “rounded” (compare figure S1). Furthermore, prescribing a velocity of zero on the surface would result in a numerically very stiff system. For efficiency we therefore adapt the approach from refs. [2, 5] and fix the nodes with springs to their original positions. The corresponding spring constant is set to the high value of $\kappa_W = 1.875 \times 10^7$ N/m³ to ensure negligible influence on the results.

The boundary integral equation is computed by a combination of the standard Gaussian quadrature [13] (7 Gauss points per triangle) with appropriate singularity removal procedures [2]. Evaluation of the Green’s functions are accelerated by the smooth particle mesh Ewald method [3, 14] (errors are kept below 5×10^{-5}). This results in a linear system that is solved via GMRES [15] (residuum $\leq 10^{-4}$). We employ the adaptive Bogacki-Shampine method [16] to integrate the system in time with an absolute tolerance of $10^{-5}R_{\text{RBC}}$, where R_{RBC} is the initial large radius of the RBC (see below). Changes in the total RBC surface area are usually below 0.1% due to the high value of κ_A . The volume is kept constant as in reference [2] by a combined hyperplane and rescaling method. Further implementation details together with validation results can be found in our previous publications [2, 11, 12, 17].

*Saarland University, Department of Experimental Physics

†University of Bayreuth, Department of Physics, Biofluid Simulation and Modeling

‡Saarland University, Theoretical Medicine and Biosciences

S1.2 Initial condition

The RBC is initially in the typical equilibrium shape [7, 8] with a large radius of $R_{\text{RBC}} = 4 \mu\text{m}$ (compare figure S1). Its initial axis is aligned with the channel's axis. The initial position perpendicular to the symmetry axis, however, is varied: Moving the cell along the long side of the channel's cross-section favors slippers, whereas an initial offset along the short side produces (metastable) croissants.

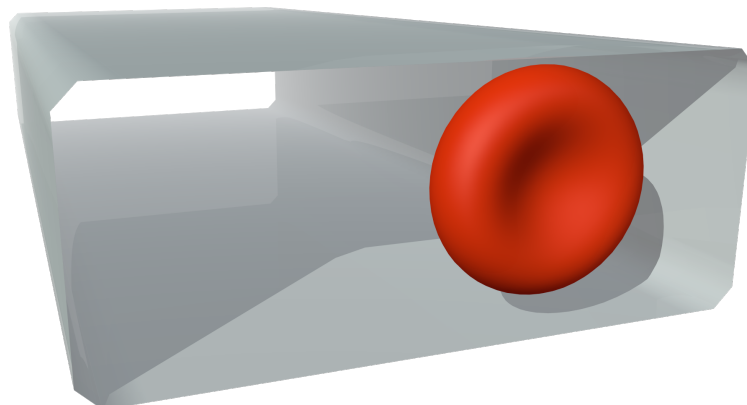


Figure S1: Numerical setup: A single red blood cell flows in a rectangular channel. The initial shape is the typical discocyte shape axis-aligned with the channel axis, and offset from the channel center.

References

- [1] C. Pozrikidis, *Boundary Integral and Singularity Methods for Linearized Viscous Flow*, Cambridge Texts in Applied Mathematics No. 8 (Cambridge University Press, New York, 1992).
- [2] A. Guckenberger and S. Gekle, "A boundary integral method with volume-changing objects for ultrasound-triggered margination of microbubbles," arXiv:1608.05196 [physics] (2017), [arXiv:1608.05196 \[physics\]](https://arxiv.org/abs/1608.05196)
- [3] H. Zhao, A. H. Isfahani, L. N. Olson, and J. B. Freund, "A spectral boundary integral method for flowing blood cells," *Journal of Computational Physics* **229**, 3726 (2010).
- [4] G. R. Cokelet and H. J. Meiselman, "Rheological Comparison of Hemoglobin Solutions and Erythrocyte Suspensions," *Science* **162**, 275 (1968).
- [5] J. B. Freund, "Leukocyte margination in a model microvessel," *Physics of Fluids* **19**, 023301 (2007).
- [6] R. Skalak, A. Tozeren, R. P. Zarda, and S. Chien, "Strain Energy Function of Red Blood Cell Membranes," *Biophysical Journal* **13**, 245 (1973).
- [7] E. Evans and Y.-C. Fung, "Improved measurements of the erythrocyte geometry," *Microvascular Research* **4**, 335 (1972).
- [8] D.-V. Le, "Subdivision elements for large deformation of liquid capsules enclosed by thin shells," *Computer Methods in Applied Mechanics and Engineering* **199**, 2622 (2010).
- [9] D. Cordasco, A. Yazdani, and P. Bagchi, "Comparison of erythrocyte dynamics in shear flow under different stress-free configurations," *Physics of Fluids* **26**, 041902 (2014).
- [10] W. Helfrich, "Elastic Properties of Lipid Bilayers: Theory and Possible Experiments," *Zeitschrift für Naturforschung. Teil C: Biochemie, Biophysik, Biologie, Virologie* **28**, 693 (1973).

- [11] A. Guckenberger and S. Gekle, “Theory and algorithms to compute Helfrich bending forces: A review,” [Journal of Physics: Condensed Matter](#) **29**, 203001 (2017).
- [12] A. Guckenberger, M. P. Schraml, P. G. Chen, M. Leonetti, and S. Gekle, “On the bending algorithms for soft objects in flows,” [Computer Physics Communications](#) **207**, 1 (2016).
- [13] G. R. Cowper, “Gaussian quadrature formulas for triangles,” [International Journal for Numerical Methods in Engineering](#) **7**, 405 (1973).
- [14] D. Saintillan, E. Darve, and E. S. G. Shaqfeh, “A smooth particle-mesh Ewald algorithm for Stokes suspension simulations: The sedimentation of fibers,” [Physics of Fluids](#) **17**, 033301 (2005).
- [15] Y. Saad and M. Schultz, “GMRES: A Generalized Minimal Residual Algorithm for Solving Nonsymmetric Linear Systems,” [SIAM Journal on Scientific and Statistical Computing](#) **7**, 856 (1986).
- [16] P. Bogacki and L. F. Shampine, “A 3(2) pair of Runge - Kutta formulas,” [Applied Mathematics Letters](#) **2**, 321 (1989).
- [17] A. Daddi-Moussa-Ider, A. Guckenberger, and S. Gekle, “Long-lived anomalous thermal diffusion induced by elastic cell membranes on nearby particles,” [Physical Review E](#) **93**, 012612 (2016).

Publication 5

Numerical-experimental observation of shape bistability of red blood cells flowing in a microchannel

by

A. Guckenberger, A. Kihm, T. John, C. Wagner and S. Gekle

Soft Matter **14** (11), pp. 2032–2043 (2018)

DOI: [10.1039/C7SM02272G](https://doi.org/10.1039/C7SM02272G)

Reproduced with permission from the Royal Society of Chemistry.



Cite this: *Soft Matter*, 2018, 14, 2032

Numerical–experimental observation of shape bistability of red blood cells flowing in a microchannel†

Achim Guckenbergler,^{‡*a} Alexander Kihm,^{‡b} Thomas John,^b Christian Wagner^{‡§bc} and Stephan Gekle^{‡§a}

Red blood cells flowing through capillaries assume a wide variety of different shapes owing to their high deformability. Predicting the realized shapes is a complex field as they are determined by the intricate interplay between the flow conditions and the membrane mechanics. In this work we construct the shape phase diagram of a single red blood cell with a physiological viscosity ratio flowing in a microchannel. We use both experimental *in vitro* measurements as well as 3D numerical simulations to complement the respective other one. Numerically, we have easy control over the initial starting configuration and natural access to the full 3D shape. With this information we obtain the phase diagram as a function of initial position, starting shape and cell velocity. Experimentally, we measure the occurrence frequency of the different shapes as a function of the cell velocity to construct the experimental diagram which is in good agreement with the numerical observations. Two different major shapes are found, namely croissants and slippers. Notably, both shapes show coexistence at low ($<1 \text{ mm s}^{-1}$) and high velocities ($>3 \text{ mm s}^{-1}$) while in-between only croissants are stable. This pronounced bistability indicates that RBC shapes are not only determined by system parameters such as flow velocity or channel size, but also strongly depend on the initial conditions.

Received 17th November 2017,
Accepted 10th February 2018

DOI: 10.1039/c7sm02272g

rsc.li/soft-matter-journal

1 Introduction

Red blood cells (RBCs) are the major constituent of mammalian blood and therefore determine the majority of its flow properties. One of the most amazing features of RBCs is their deformability, allowing them to squeeze through channels with diameters much smaller than their own equilibrium size.^{1–3} Another consequence of their deformability is the wide range of stationary and non-stationary shapes assumed by the RBCs in microchannel flows with dimensions similar to or slightly larger than the RBC equilibrium radius.^{4–6} Understanding and being able to predict these shapes is of high importance

for a variety of reasons. From a fundamental point of view, it serves as the foundation in a bottom-up approach to understand the properties of red blood cell suspensions which are chiefly determined by single particle behavior.^{7–13} From an applied perspective, a series of recent investigations have devised promising approaches for sorting cells based on their mechanical properties either in lateral displacement devices¹⁴ or using high-speed video microscopy.¹⁵ Finally, knowledge of the precise cell shape is also essential for accurately measuring geometric properties of cells.¹⁶

The most frequently observed shapes of RBCs in microchannel flows are the so-called “croissant” and “slipper” shapes. Examples are depicted in Fig. 1. Some researchers refer to croissants also as parachutes, although here we prefer the term croissant since our shapes are not perfectly rotationally symmetric (similar to the ones found by Farutin and Misbah¹⁷). Probably one of the earliest experimental studies on isolated red blood cells in flow was performed by Gaehtgens *et al.*,¹⁸ where slippers as well as parachutes have been found depending on the diameter of the cylindrical channel. Suzuki *et al.*¹⁹ presented an *in vivo* phase diagram of parachutes and slippers as a function of velocity and confinement. Slippers dominated at smaller diameters and higher velocities. Secomb *et al.*²⁰ compared experiments with 2D simulations in cylindrical

^a Biofluid Simulation and Modeling, Theoretische Physik, Universität Bayreuth, Germany. E-mail: achim.guckenbergler@uni-bayreuth.de; Tel: +49 921 55 4472

^b Experimental Physics, Saarland University, Saarbrücken, 66123, Germany

^c Physics and Materials Science Research Unit, University of Luxembourg, Luxembourg

† Electronic supplementary information (ESI) available: One PDF containing further details regarding setups, analysis methodology and additional experimental data such as the original photographs of the cells; one excel sheet containing the raw data from Fig. 4; five videos showing the various shapes observed in the numerical simulations; and one PDF with short descriptions of the videos. See DOI: 10.1039/c7sm02272g

‡ A. Guckenbergler and A. Kihm contributed equally to this work.

§ S. Gekle and C. Wagner contributed equally to this work.

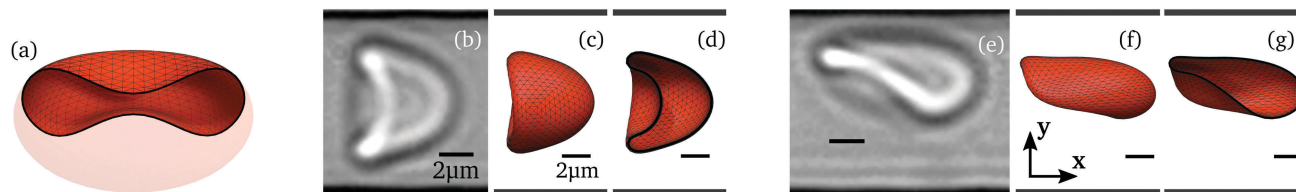


Fig. 1 Typical RBC shapes from simulations and experiments. (a) The typical discocyte shape employed in some of the simulations as the starting shape. Half of it was made transparent for illustration purposes. Its horizontal diameter is $8\ \mu\text{m}$. (b) A typical croissant observed in the experiments when applying a pressure drop of 100 mbar (cell velocity $0.98 \pm 0.07\ \text{mm s}^{-1}$). (c) A croissant with a velocity of $\approx 1.1\ \text{mm s}^{-1}$ obtained from the numerical simulations. (d) The cross-section of the croissant from (c). (e) A slipper from the experiments at 500 mbar (cell velocity $5.16 \pm 0.11\ \text{mm s}^{-1}$). (f) A typical slipper from the simulations with a cell velocity of $\approx 5.2\ \text{mm s}^{-1}$. (g) The cross-section of the slipper from (f). The black lines on the shapes from the simulations depict the mesh. The bottom and top black lines in all figures are the walls ($L_y \approx 12\ \mu\text{m}$ apart), while the small black lines are scale bars of length $2\ \mu\text{m}$. The flow is in the positive x -direction (except in figure (a) where no flow exists).

channels of $8\ \mu\text{m}$ diameter for a cell velocity of approximately $1.25\ \text{mm s}^{-1}$. Furthermore, two other publications^{21,22} considered the flow of RBCs at very low viscosity ratios of $\lambda \lesssim 0.27$. They presented a phase diagram showing parachutes and slippers, where the velocity was varied in the very high regime of 10 to $170\ \text{mm s}^{-1}$. Tomaiuolo *et al.*²³ found parachutes at smaller and slippers at higher velocities in cylindrical channels of $10\ \mu\text{m}$ diameter. A subsequent study²⁴ as well as Prado *et al.*²⁶ considered the transient during start-up of the flow. Cluitmans *et al.*²⁶ detected croissants at lower ($\lesssim 5\ \text{mm s}^{-1}$) and slippers at higher velocities ($\gtrsim 10\ \text{mm s}^{-1}$) in rectangular channels with widths $\leq 10\ \mu\text{m}$. Moreover, Quint *et al.*²⁷ found a stable slipper and a metastable croissant at the same set of parameters in a wider channel of $25\ \mu\text{m} \times 10\ \mu\text{m}$. Other publications presenting experiments in channel flow also touch the subject of RBC shapes but focus on other aspects such as the methodology,^{28–35} dense suspensions and cell interactions^{18,22,35–42} or use vastly larger channel diameters.^{13,43}

Numerical simulations and semi-analytical calculations of isolated particles in microchannels mostly studied axisymmetric RBCs^{44–46} or 2D vesicles.^{5,6,47–52} The numerical work by Aouane *et al.*,⁵ for example, identified a large amount of dynamics including deterministic chaos. The first full 3D simulation of a single cell with a realistic RBC model (but with a ratio of inner to outer viscosity of $\lambda = 1$) was conducted by Noguchi and Gompper⁵³ who used a cylindrical tube with a diameter of $9.2\ \mu\text{m}$. They found the typical discocyte shape below and parachutes above a critical velocity which depends on the elastic parameters. A subsequent study by the same group additionally explored this threshold as a function of confinement.⁵⁴ Moreover, Fedosov *et al.*⁴ presented very detailed phase-diagrams where the velocity and confinement was varied for three different sets of elastic moduli and a viscosity ratio of $\lambda = 1$. They observed four distinct regions where snaking, tumbling, slippers and parachutes occurred. Recently, Ye *et al.*⁵⁵ considered the shapes of an RBC with $\lambda = 1$ in rectangular microchannels (with width $10\ \mu\text{m}$ and aspect ratios 1 to 2) for the three cell velocities 4, 20 and $100\ \text{mm s}^{-1}$ and observation times up to $\approx 0.03\ \text{s}$. Snapshots after this short initial transient showed parachutes or slightly slipper-like shapes.

Bistability, *i.e.* the observation of two different stable shapes depending on the initial condition but at otherwise identical system parameters, was barely considered so far. It was

observed for simpler situations such as close-to-spherical vesicles in unbounded Poiseuille flow analytically⁵⁶ and numerically¹⁷ or near a single wall,⁵⁷ for a 2D RBC model in bounded Poiseuille flow,²⁰ for the initial transient of a red blood cell in a rectangular channel⁵⁵ or for simple shear flows.^{13,58–60} No systematic experimental investigations exist for cells flowing in microchannels. Moreover, the 3D simulations and experimental investigations that were mentioned above and that consider the RBC shapes in microchannels in more detail all used a viscosity ratio of $\lambda \leq 1$, although analytical and numerical computations showed that choosing a physiologically more realistic value of $\lambda \approx 5$ ⁶¹ can significantly affect RBC dynamics.^{6,17,50,56}

Here we present a detailed systematic experimental-numerical study on the steady-state shape of isolated red blood cells in a rectangular microchannel. We use the physiological viscosity ratio of $\lambda = 5$ appropriate for healthy human red blood cells in the microcirculation.⁶¹ The initial position is varied in the simulations directly, while experimentally we determine it *via* measurements at the channel entrance. Our central finding is that the initial starting position of the RBC has a decisive influence on the final steady-state shape of the red blood cell.

We begin by outlining our experimental and numerical methods in Section 2. Afterwards, the results from our experiments (Section 3) and simulations (Section 4) are presented, while Section 5 is dedicated to their detailed comparison. Finally, we conclude our work in Section 6.

2 Methods

2.1 Experimental setup

The sample preparation and experimental setup is mostly identical to the one used recently by Clavería *et al.*³⁶ In short, human red blood cells were obtained from healthy donors by needle-prick and used within three hours. After appropriate preparation,³⁶ they are suspended in a phosphate buffered saline (PBS) and bovine serum albumin solution which has a viscosity of approximately $1\ \text{mPa s}$. The viscosity ratio of the cells is therefore $\lambda \approx 5$.²⁷ This value corresponds to the typical physiological value of healthy red blood cells in blood plasma.⁶¹ The RBCs are pumped at room temperature through

rectangular, PDMS-based channels by a high-precision pressure device (Elveflow OB 1, MK II) with pressure drops ranging from 20 to 1000 mbar. The channels have a cross-section width of $L_y = (11.9 \pm 0.3) \mu\text{m}$ and a height of $L_z = (9.7 \pm 0.3) \mu\text{m}$ without any applied pressure drop and are thus similar to the vessel diameters found in the microvascular system.^{62,63} Their length is approximately $L_x = 40 \text{ mm}$. We use rectangular rather than cylindrical channels since they are easier to manufacture, are therefore prevalent in lab-on-a-chip devices^{63,64} and have the merit that cells are not rotated randomly around their axis due to the missing rotational symmetry. The latter property greatly simplifies the microscopic observation and analysis of the RBCs.

The hematocrit (volume percentage of RBCs) in the reservoir before the inlet is always $\lesssim 1.0\%$, *i.e.* very low. Nevertheless, we find cells flowing in clusters as well as single cells. For the present work we have analyzed only the latter. To this end, previous experimental and theoretical results showed that the hydrodynamic interaction in a linear channel decays exponentially, and becomes negligible if the inter-particle distance is more than twice the channel width.^{54,65,66} Considering that our channel has the dimensions $\approx 12 \mu\text{m} \times 10 \mu\text{m}$, cells can be considered as being single for distances $\gtrsim 25 \mu\text{m}$. We only used cells that were at least $40 \mu\text{m}$ apart from other entities.

We perform measurements at two locations along the channel, namely at the entrance ($x = 0 \text{ mm}$) and at $x = 10 \text{ mm}$ downstream. Clavería *et al.*³⁶ showed that only minor differences occur between measurements at $x = 2 \text{ mm}$ and $x = 10 \text{ mm}$, *i.e.* the cells are well converged at the latter position. This position is also consistent with other references^{18,22,26} and our simulations as explained in the ESI.† Vessel lengths in-between bifurcations in the microvascular system are less than 1 mm , *i.e.* much shorter.⁶⁷ Nevertheless, this is not necessarily true for *in vitro* experiments or lab-on-a-chip devices, and the long-time behavior also holds information about the general intrinsic properties. The flowing RBCs are recorded by an inverted bright-field microscope (Nikon TE 2000-S) with an oil-immersion objective (Nikon CFI Plan Fluor 60 \times , NA = 1.25) and a high-resolution camera (Fastec HiSpec 2G) at a frame rate of 400 frames per second. The camera is aligned along the z -direction so that the photographs show the cells in the x - y -plane (compare Fig. 2). Hence, determination of the z -position is not possible, but also not absolutely necessary as our simulations always show a z -position of nearly 0 (see Section 5). We analyze the recorded image sequence with a custom MATLAB script that detects each projected cell shape and the corresponding 2D center of mass position. It additionally tracks the cell position over the image sequence to obtain the individual cell velocity. Considering the optical setup, we assume an uncertainty in the position measurements of $\pm s_p$ with $s_p = 0.1 \mu\text{m}$. The cell shapes are classified by hand.

2.2 Simulation setup

The numerical simulations mimic our experimental setup as far as possible. Hence, we place a single red blood cell in a rectangular channel as shown in Fig. 2. The channel has a

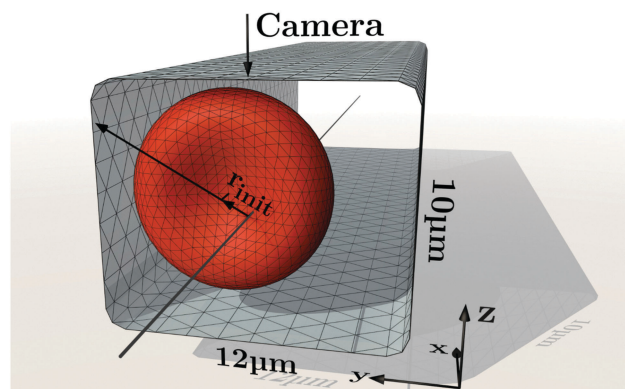


Fig. 2 Simulation setup: a single red blood cell is placed in a rectangular channel of width $L_y = 12 \mu\text{m}$ and height $L_z = 10 \mu\text{m}$. Periodic boundary conditions are employed. Initially, the centroid of the cell is offset from the center axis along the left black arrow by a distance r_{init} . The depicted RBC illustrates the discocyte starting shape, although other shapes have been used, too, as explained in the main text and the ESI.† Furthermore, the black lines on the surfaces illustrate the employed meshes. The arrow at the top shows the view from the camera in the experiments (*i.e.* onto the x - y -plane) and the flow is in the positive x -direction.

cross-section of width $L_y = 12 \mu\text{m}$ and height $L_z = 10 \mu\text{m}$. Periodic boundary conditions are assumed in the x -direction with a periodicity of $L_x = 42.7 \mu\text{m}$, in agreement with above estimates for the decay of hydrodynamic interactions.

We vary the initial y - z -position (relative to the channel center) of the RBC's centroid along the line $z_{\text{init}} = 5y_{\text{init}}/9$, which almost corresponds to the channel diagonal. The corresponding initial radial position is thus simply given by $r_{\text{init}} = \sqrt{y_{\text{init}}^2 + z_{\text{init}}^2}$. Apart from the initial position, we also vary the initial shape. The first employed shape is the typical discocyte equilibrium shape,^{68,69} as depicted in Fig. 1(a), where the RBC axis is aligned with the channel axis (as shown in Fig. 2). The second and third starting shapes are a croissant and slipper, whose geometries are obtained from two simulations that start with a discocyte. They are further detailed in the ESI.†

Cell velocities are extracted by considering the difference of the centroids between successive time steps. During the simulation, we monitor several quantities such as the radial, y - and z -positions, the RBC asphericity and the cell velocity as well as the full 3D shape to determine when the steady state has been fully reached. The assumed shapes are classified manually by considering the 3D geometry and the graphs of the cell position, velocity and asphericity, similar to ref. 4. For example, slippers are off-centered and show periodic oscillations in the graphs, while croissants are centered and have a static shape (also compare the ESI.†).

Regarding the actual modeling of the constituents, the RBC is filled with a Newtonian fluid with a dynamic viscosity μ_{RBC} , whereas the ambient flow is a Newtonian fluid with the dynamic viscosity $\mu = 1.2 \text{ mPa s}$ of blood plasma.^{70–72} We set the viscosity ratio $\lambda = \mu_{\text{RBC}}/\mu$ to a value of 5 in all simulations. The surface area of the RBC is set to $140 \mu\text{m}^2$ and the volume is set to $100 \mu\text{m}^3$ (see *e.g.* ref. 71 and 73), leading to a large radius of $R_{\text{RBC}} = 4 \mu\text{m}$ when the cell is in the typical discocyte

equilibrium shape (Fig. 1(a)). The mechanics of the infinitely thin membrane are governed by Skalak's law^{74,75} for the in-plane elasticity with a shear modulus of $\kappa_S = 5 \times 10^{-6} \text{ N m}^{-1}$ ^{76,77} and an area dilatation modulus of $\kappa_A = 100\kappa_S$. This value for κ_A ensures that the area changes remain below 2% in all cases. We take the reference state for the Skalak model to be the typical discocyte shape.^{68,69} The membrane is additionally endowed with some bending resistance which is modeled according to the Canham–Helfrich law,^{78–80} where the bending modulus is fixed to $\kappa_B = 3 \times 10^{-19} \text{ N m}$.^{77,81} The spontaneous curvature is set to zero.

We use 2048 flat triangles to discretize the RBC in our numerical implementation. The forces are computed as described by Guckenberger *et al.*,⁸² with Method C therein being used for the bending contribution. An unavoidable artificial volume drift of the cell is countered by adjusting the velocity to obey the no-flux condition and by a subsequent rescaling of the object.^{83,84} Moreover, the channel is represented by 2166 flat triangles. The corners are rounded to prevent numerical problems (compare Fig. 2). Rather than prescribing a zero velocity at the channel walls, we use a penalty method for efficiency reasons with a spring constant of $\kappa_W = 1.9 \times 10^7 \text{ N m}^{-3}$.^{6,84} Increasing the triangle counts and the box length L_x did not change the results significantly.

The Reynolds number in the considered system is defined as $Re = 2R_{\text{RBC}}u_{\text{max}}\rho/\mu$. For a velocity of $u_{\text{max}} \leq 10 \text{ mm s}^{-1}$ and the density $\rho \approx 10^3 \text{ kg m}^{-3}$ of the ambient and inner liquid we therefore have $Re < 0.1$. Hence, the flow can be appropriately described using the Stokes equation. This allows us to employ the boundary integral method (BIM)⁸⁵ for 3D periodic systems.^{84,86} Note that this method requires to prescribe a certain average flow through the whole unit cell instead of a pressure drop within the channel. The latter is unfortunately not easily accessible. We therefore compare with experiments by means of cell velocities. Continuing, the integrals are computed by a standard Gaussian quadrature with 7 points per triangle in conjunction with linear interpolation of nodal quantities and appropriate singularity removal for the single- and double-layer potentials.⁸⁴ Furthermore, we use the smooth particle mesh Ewald (SPME) method⁸⁷ to accelerate the computation of the periodic Green's functions; cutoff errors are kept below 5×10^{-5} . The resulting linear system is solved *via* GMRES⁸⁸ up to a residuum of 10^{-5} , and the kinematic condition is integrated in time using the adaptive Bogacki–Shampine algorithm⁸⁹ with the absolute tolerance set to $10^{-5}R_{\text{RBC}}$. When the run-times are normalized to a two-socket system with 28 cores, each simulation took 1 to 29 days, with an average of around 5 days. The phase diagrams below are formed by 329 of such simulations in total. Further details on the numerical method as well as verifications of the implementation can be found in our previous publications.^{27,82,84,90}

3 Experimental results

We classify cells in the experiments either as croissants, slippers or “other” not uniquely identifiable or completely

different shapes. Typical slipper and croissant shapes are shown in the photographs (b and e) of Fig. 1. See the ESI† for a collection of all images.

To systematically investigate the occurrence of the different shapes, we vary the imposed pressure drops from 20 to 1000 mbar. The corresponding cell velocities range from 0.14 mm s^{-1} to 10.6 mm s^{-1} , covering the whole physiological range in microchannels.^{62,91,92} We consider the cells 10 mm away from the channel entrance where most of the cells reached a steady state.³⁶ Fig. 3(a) depicts the fraction of observed shapes as a function of the measured cell velocities, constituting our central result from the experiments. This distribution was obtained by considering typically more than 100 cells per imposed pressure drop. The average velocities were computed by averaging over all cells at a certain pressure drop, with the horizontal error bars showing the corresponding standard deviations σ_u in cell velocity. Not all velocities are the same because croissants and slippers have different velocities at otherwise identical flow conditions,²⁷ and because of the natural variations of cell properties such as elasticity and size, as also noted by Tomaiuolo *et al.*²³ See the ESI† for more details. Considering Fig. 3(a), high velocities obviously favor slippers while croissants are the most prominent for medium velocities. A pronounced peak exists from around 1 to 2 mm s^{-1} . Very small velocities produce mostly shapes that fall outside our simple two-state classification.

Fig. 3(b) illustrates the corresponding estimated probability density function of the center of mass y -position of the cells at the various pressure drops. This estimate was obtained from the measured y -positions by using the kernel density estimator as implemented in MATLAB R2017a (ksdensity) with a support of $[-6,6] \mu\text{m}$ and otherwise default settings. Thus, croissants and “others” occurring at lower velocities are centered in the channel, while slippers occurring at high velocities show a pronounced off-centered position. The assumed shapes therefore imply a certain y -position within the channel with slippers being off-centered and croissants centered. This is confirmed when analyzing the offset distribution separately for each shape class as shown in the ESI.†

From Fig. 3(a) it is tempting to conclude that the flow velocity is the major parameter that determines the RBC shape, with low velocities favoring centered and high velocities favoring off-centered flow positions. However, looking at the cell positions near the channel entrance (Fig. 4) we find that already upon entering the channel RBCs are not homogeneously distributed. At low velocities we observe a clear bias towards a centered initial position, with the distribution becoming approximately homogeneous only at the highest measured velocities. These experimental observations allow two distinct parameters as the reason for the dominance of the slipper shapes at high velocities: either the higher flow velocity itself or the more off-centered entry into the channel. To disentangle these two possibilities we now present numerical simulations whose geometry directly corresponds to the experimental setup.

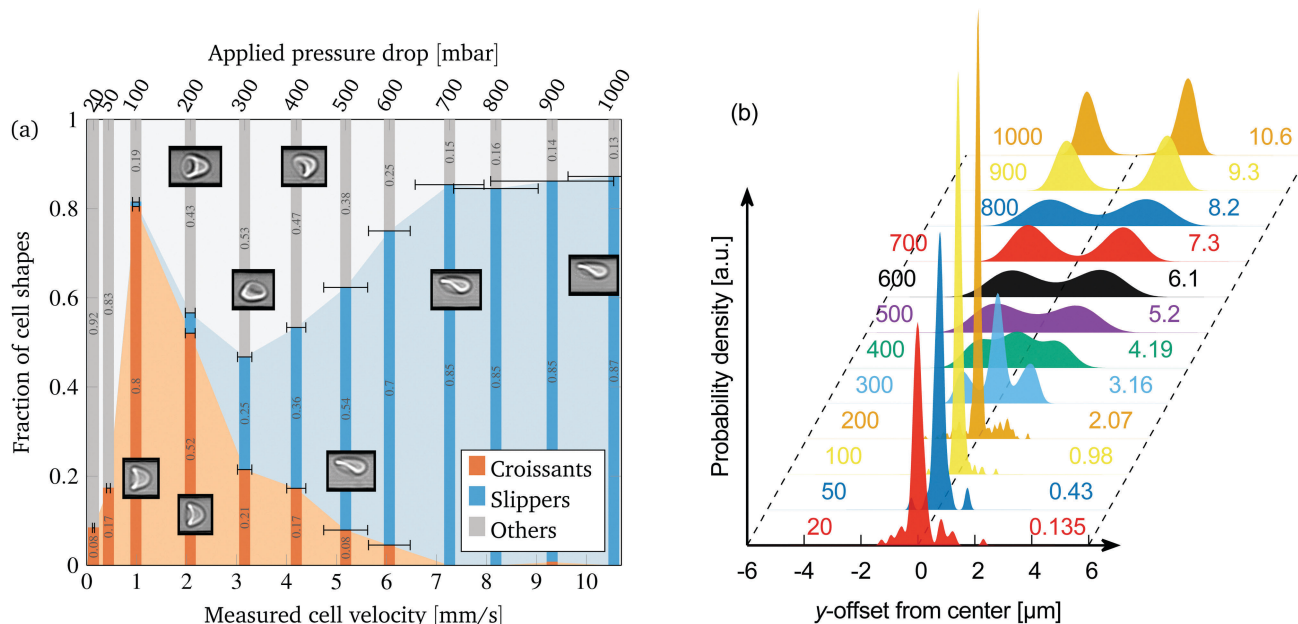


Fig. 3 Experimental results: (a) fraction of observed cell shapes as a function of the applied pressure drop (top axis) and mean cell velocity (bottom axis). The horizontal error bars depict the standard deviation of the measured cell velocities for each applied pressure drop. The shaded background is a guide to the eye. Furthermore, the insets show examples of experimental images (see the ESI† for a collection of all photographs). (b) Estimated probability density function of the RBCs' center-of-mass y -position within the channel for various pressure drops (indicated as numbers on the left in millibar) for all shapes combined. The corresponding measured mean cell velocities are depicted on the right in mm s^{-1} . We show the separated contributions of each shape to the distribution in the ESI†. The area under the curves is normalized to one. The dashed lines illustrate the wall positions. Both figures are for the position 10 mm downstream from the channel entrance.

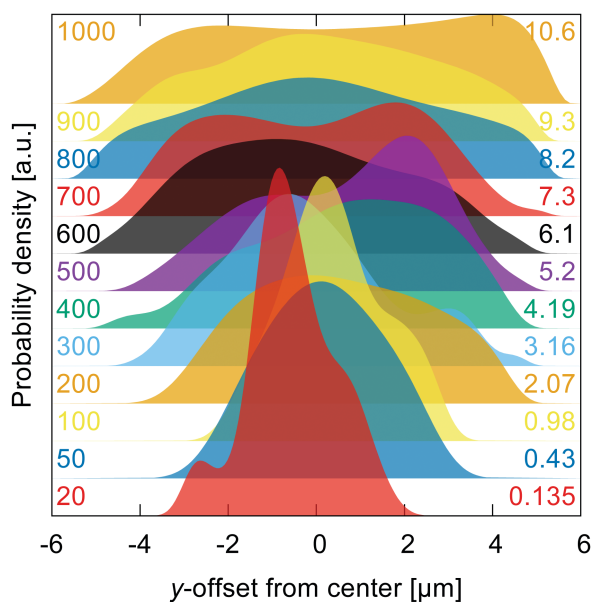


Fig. 4 Experimental results: estimated probability density function of the cells' center-of-mass y -position at the channel entrance (position $x = 0$ mm). The pressure drops increase from the bottom (20 mbar) to the top (1000 mbar) with the numbers on the left side indicating the corresponding value in millibar. We display the respective measured mean cell velocities in mm s^{-1} on the right side. The area under the curves is normalized to one. The curves are offset in the vertical direction for illustration purpose.

4 Numerical results

We numerically study the behavior of a single RBC in a rectangular microchannel by varying the imposed flow velocity, the initial shape and the initial offset r_{init} from the centerline of the tube (see Section 2.2). After starting the flow, we wait until the RBC reaches the steady state where the shape as well as the radial position does no longer change, or alternatively until periodic motion is observed.

In the majority of cases, we observe two different states: a croissant shape (which moves as a rigid body, Fig. 1(c)) and a slipper shape (Fig. 1(f)). The latter exhibits tank-treading (TT) and oscillatory contractions similar to the slippers seen by Fedosov *et al.*⁴ (see the ESI† for a movie and the insets in Fig. 5). Tank-treading refers to the motion of the membrane around a (more or less) static shape. Note that perfectly axisymmetric parachutes are suppressed by the rectangular channel flow, contrary to the situation for cylindrical tubes⁴ or unbounded Poiseuille flows.¹⁷

To start the systematic study, we take a red blood cell that is initially in the typical discocyte shape with its rotation axis aligned along the tube's axis (*cf.* Fig. 2). We then vary the radial offset r_{init} from the center line as described in Section 2.2 and record the final radial position as well as the shape. The mean of the radial position is extracted by a temporal average once the cell is in the steady state (see the ESI† for more details). Fig. 5 shows the result for a cell velocity of $\approx 6.5 \text{ mm s}^{-1}$. A single sharp transition

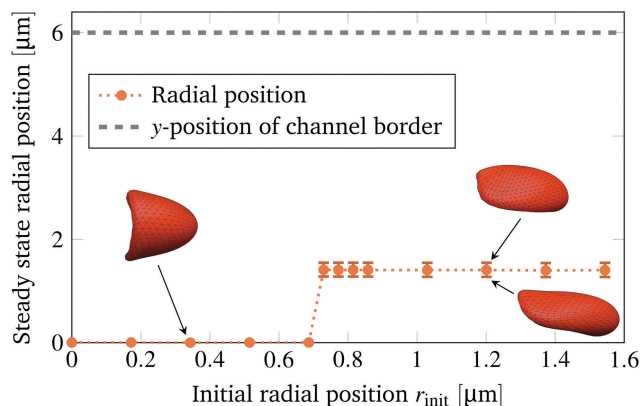


Fig. 5 Simulation results: averaged radial position in the steady state as a function of the initial radial offset for a cell velocity of $\approx 6.5 \text{ mm s}^{-1}$. The RBC starts in the typical discocyte shape with its rotation axis aligned with the tube's axis (Fig. 2). The dotted line is a guide to the eye. Half of the channel's extent along the y -direction (width) is shown as a dashed line at the top. The extent in the z -direction (height) is of less significance here since the steady states are always almost centered in the z -direction. Furthermore, the radial position for the converged slippers oscillates around a mean value and their shapes show periodic "contractions" as indicated by the vertical error bars and the right two insets, respectively.

at $r_{\text{init}} \approx 0.7 \text{ μm}$ from centered croissants to off-centered slippers is observed. The final position of the slippers is mostly offset only along the wider width of the channel (y -direction), but not along the smaller height (z -direction). Due to the transition we find pronounced bistability: the result is significantly determined by the initial condition and two different shapes (croissant and slipper) coexist. This is consistent with the 2D simulations by Secomb *et al.*²⁰ and Tahiri *et al.*⁶ It also agrees qualitatively with observations by Farutin and Misbah for 3D simulations of vesicles in unbounded Poiseuille flow.¹⁷

To study the bistability in more detail, we vary the imposed flow velocity as well as the initial offset r_{init} and characterize the behavior in the steady state. This yields the shape phase diagram depicted in Fig. 6(a). The cell velocity is extracted in the steady state *via* a temporal average. For slippers the velocity varies periodically (similar to the radial position): the minimum and maximum in one period is indicated by the horizontal error bars. Overall, the mean cell velocity u ranges from 0.132 mm s^{-1} to 10.4 mm s^{-1} , matching with the experimentally covered range. The corresponding shear capillary number $Ca_S := \mu u / \kappa_S$ varies therefore in the interval $Ca_S \in [0.0317, 2.50]$, while the bending capillary number $Ca_B := \mu u R_{\text{RBC}}^2 / \kappa_B$ lies in the range $Ca_B \in [8.45, 666]$. The reddish area illustrates the approximated region where croissants exist. Furthermore, there is a maximal initial offset r_{init} above which overlapping with the vessel wall would occur.

The shape phase diagram in Fig. 6(a) (together with (b and c) explained below) constitutes our main result from the simulations. Starting near the channel center (in the reddish region) results in croissants, whereas higher initial offsets lead to slippers. The transition is found to be sharp, and depends significantly on the velocity. Croissants are the only stable steady state in a small region ranging from around 2 to 3 mm s^{-1} , independently of the initial radial position. Smaller and larger velocities tend to favor slippers. Stable croissants do not appear below 0.25 mm s^{-1} .

While the final shape is recognizable often early on, some small changes can still occur before the cell completely reaches the steady state. In the case of the slippers, the final perfectly periodic state is usually reached after roughly 2 s to 10 s . Relative to a typical flow timescale of $\tau := R_{\text{RBC}}/u$ (where u is the mean cell velocity), it is typically reached after 1τ to 500τ . In contrast, the final croissant state is in some cases achieved only after more than 30 s (*i.e.* $> 10^4\tau$), possibly after an intermediate

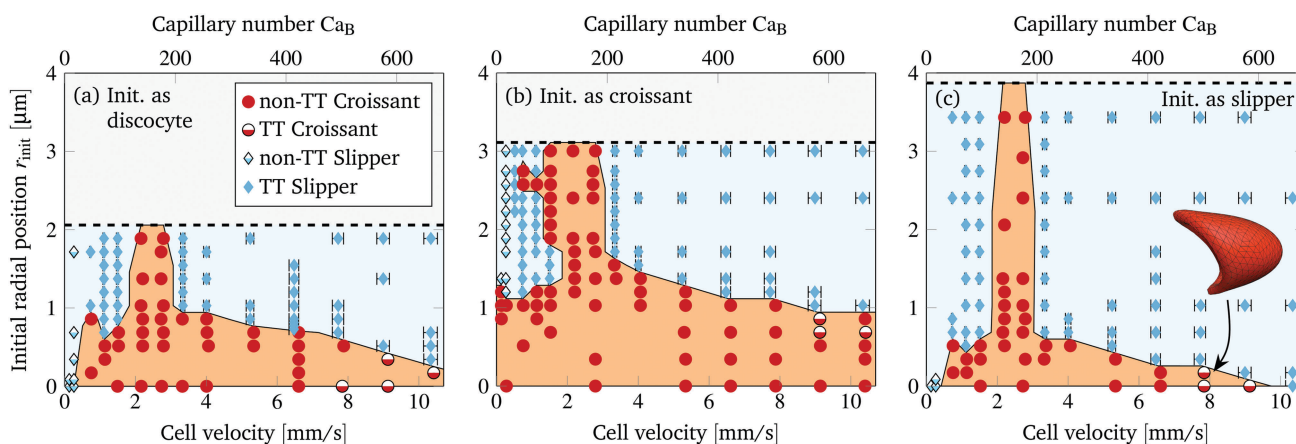


Fig. 6 Simulation results: shapes obtained when varying the initial offset r_{init} and the velocity. Each symbol corresponds to one simulation. The lower horizontal axis shows the average cell velocity in the steady state, while horizontal error bars depict the minimal and maximal velocities in one period (variations for croissants nearly zero and thus not visible). The upper dashed line represents the maximal initial offset: above this offset, the cell would overlap with the wall. The other lines and the colored areas are guides to the eye and illustrate the different regions in the phase diagram. Each figure corresponds to a different initial shape, namely (a) to the typical discocyte shape, (b) to a croissant and (c) to a slipper. These shapes are shown in Fig. 1(a) and in the ESI.† The inset in the last figure depicts an example of a tank-treading croissant. Fig. 5 corresponds to the vertical column at $\approx 6.5 \text{ mm s}^{-1}$ in sub-figure (a).

slipper state that can last several seconds (see Fig. S7 and the movie in the ESI†). Hence, shapes observed in the simulations much earlier than one second can often turn out to be transient, contrary to the interpretation of Ye *et al.*⁵⁵ but in agreement with Prado *et al.*²⁵

Considering our results in Fig. 6(a) in more detail, we find that two different types of croissants and slippers are possible. On the one hand, at very low velocities ($\lesssim 0.7$ mm s⁻¹) the slippers no longer exhibit tank-treading motion of the membrane and instead show tumbling behavior: the cell rotates around the *z*-axis while approximately preserving its shape (similar to a rigid-body, see the ESI† for a movie). The difference compared to the tumbling motion observed by Fedosov *et al.*⁴ is that the cell still exhibits a clear slipper-like instead of a proper discocyte shape. Hence, we classify this mode still as slipper. On the other hand, at very high velocities ($\gtrsim 7$ mm s⁻¹) slightly asymmetric shapes strongly reminiscent of croissants with a distinct tank-treading motion can sometimes be observed (see the inset in Fig. 6(c) for an example). As the shape itself is very close to a croissant, we will nevertheless consider it to be a croissant below.

A natural question that occurs in light of the profound bistability is the influence of other initial shapes on the result. To this end, we consider a typical croissant as well as a typical slipper as the starting shape. Both were obtained from previous simulations that started with the discocyte form and are characterized in the ESI.† We once again construct the shape phase diagram as before and display the results in Fig. 6(b) and (c). Note that the different starting shapes admit a larger initial radial position r_{init} of the

centroid. In short, starting with a croissant favors croissants in the steady state (the reddish area is larger than in Fig. 6(a)). For slippers it is the other way around: starting with a slipper tends to produce more slippers (reddish area smaller than in Fig. 6(a)). Despite this, the croissant-only region from around 2 to 3 mm s⁻¹ still exists unscathed. Overall, only two qualitative differences occur between the phase diagrams of different initial shapes, both at lower velocity when starting with the croissant shape (Fig. 6(b)): first, stable croissants emerge at very low velocities ($\lesssim 0.7$ mm s⁻¹) and second, the croissant-only peak exhibits a “protrusion” into the slipper space. This observation suggests that slippers and croissants can be stable below 2 mm s⁻¹ for most r_{init} values. It is further confirmed by simulations that start with differently rotated discocytes in the ESI.†

Another interesting aspect concerns the radial positions of the centroids in the final steady states. The average values are obtained by computing the temporal average in the steady state first for each simulation, and then combining the results for identical shapes *via* a weighted arithmetic mean. We use the observation time in the steady state as the weight. This procedure leads to Fig. 7(a). Obviously, the final radial positions are independent of the initial starting shape, *i.e.* a particular steady state shape at a certain velocity is always located at the same position. Furthermore, non-tank-treading croissants are always almost centered, with only minor deviations away from zero. These slight deviations in the range from 2 to 4 mm s⁻¹ are mainly due to some croissants exhibiting minuscule periodic shape deformations. Moreover, the centroids of tank-treading croissants occurring at velocities $\gtrsim 8$ mm s⁻¹ are located near

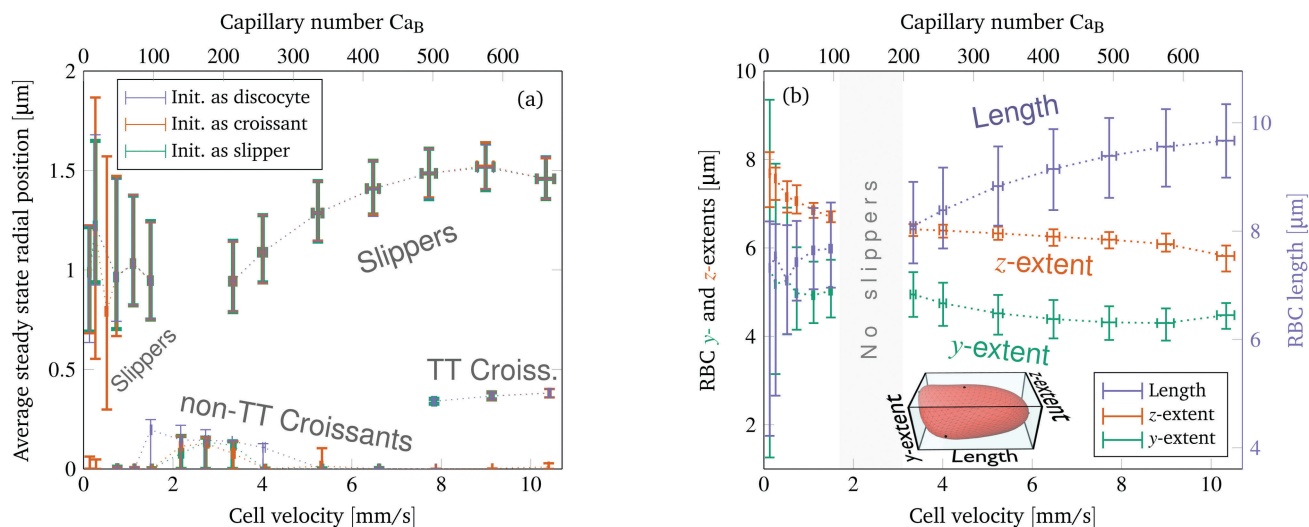


Fig. 7 Simulation results: (a) average radial positions of the steady states from Fig. 6 as a function of cell velocity for the three different starting shapes. The lower curves are for steady states forming non-TT croissants and TT croissants, the upper curves are for (TT and non-TT) slippers. Note that the data points coincide for different starting configurations, showing that the initial shape does not influence the final radial position. We show on the vertical axis the weighted temporal mean of the radial centroid position of RBCs that assume the same shapes. The vertical error bars depict the total minimal and maximal position, while the horizontal error bars show the total minimal and maximal cell velocities (in each period of the steady states, respectively). (b) Extents of the slipper shapes from figure (a) in the flow (*x*-)direction (length) and along the other two axes, as illustrated by the inset showing the channel-aligned bounding box around a slipper. The vertical error bars depict the minimum and maximum extents during the periodic contractions, while the horizontal error bars are the same as in (a).

but not directly in the center. Their slight off-centered position is a result of their asymmetry.

In contrast to croissants, slippers are located 0.8 to 1.5 μm away from the channel's axis. The minimum position is attained for velocities near the border of the croissant-only region in the phase diagram (at around 2 and 3 mm s^{-1} , compare Fig. 6). Above, the off-center position increases and seems to converge to a value of around 1.5 μm . The reason for this increase is that slippers become more elongated and thinner at higher velocities (up to a certain degree), as shown in Fig. 7(b) and also observed in previous experiments.²³ Thus, they effectively become thinner in the radial direction and their centroids can move closer to the wall. We note that the distance between the wall and the upper side of the slipper approximately remains the same for all velocities. This also hints at that the “optimal” off-center position for the slippers is more than 1.5 μm away from the center, and that this particular value is due to the smallness of the channel.

5 Comparison between experiments and simulations

5.1 Comparison of shapes

Considering Fig. 1, the croissants obtained from simulations and experiments look very similar, although the experimental shapes appear to be somewhat larger. The reason is diffraction: the “true” cell border lies in the bright and not within the dark rim. However, the slippers appear to look qualitatively different. This is due to the high magnification and numerical aperture of the objective which results in a small depth of field of around 1 μm . Cell borders above and below the middle plane are therefore blurred out and become invisible while the mid-plane cut becomes dominant. Thus, for comparison we should use the middle cross-section of the numerically obtained shapes. Here we find good agreement (compare Fig. 1(g) with Fig. 1(e)).

5.2 Comparison of the phase diagrams

A qualitative comparison between the phase diagrams of steady states from the experiments (Fig. 3(a)) and the simulations (Fig. 6) shows a striking resemblance: both exhibit a distinct peak in the number of croissants at lower velocities (1 to 3 mm s^{-1}) at the expense of the number of slippers. The latter dominate the picture at high velocities ($> 7 \text{ mm s}^{-1}$). At intermediate velocities both shapes coexist and can therefore be observed simultaneously in the measurements. Moreover, the simulations at very low velocities showed croissants only if the initial RBC was already prepared in that state, meaning that in the experiments this shape is highly unexpected. Indeed, we were not able to clearly classify most of the observed shapes in that regime as either croissants or slippers.

Obtaining a direct quantitative comparison requires a translation of the numerical threshold in Fig. 6 (which is in terms of the initial offset) into a prediction regarding the fraction of shapes, because the experimental diagram is in terms of the observed fraction of shapes. This is done by counting the

fraction of croissants entering the channel with an offset below the numerical threshold. This fraction corresponds directly to the predicted fraction of croissant shapes. More precisely, we first define r_{trans} as the initial radial offset which separates croissants from slippers in the simulations by using the black line in Fig. 6. An exception is the small croissant-only region (*i.e.* the interval of the topmost horizontal line in Fig. 6) where we take $r_{\text{trans}} \rightarrow \infty$. This is consistent with our interpretation that only croissants exist in this particular interval. One r_{trans} is computed for each experimental cell velocity from Fig. 3(a). Second, each radial position r_{trans} is projected onto the y -axis to give y_{trans} (see Section 2.2) because only the y -offset is known from experiments. Third, from the experimental offset distribution at the channel entrance (Fig. 4) we can then estimate the fraction of cells ϕ that enter the channel with an offset below y_{trans} . Accordingly, the simulations predict a fraction ϕ of croissants in the steady state. The value of ϕ can thus be directly compared with the experimental phase diagram from Fig. 3(a). This is done once for every starting configuration employed in the simulations.

Fig. 8 shows this key result of our contribution, *i.e.* the predicted fraction of croissants ϕ as a function of the cell velocity for each starting shape. The vertical error bars depict the uncertainty in the prediction, whose computation is explained in the ESI.† They are comparably large in the croissant-only region because the experimental velocities lie very near its sharp boundary. The horizontal error bars illustrate the standard deviation σ_u of the experimentally measured cell velocities. Clearly, we find very good agreement between the prediction from the simulation and the experimental observation when considering the slipper starting shape (Fig. 8(c)). Starting with a discocyte or croissant leads to slightly more pronounced deviations (Fig. 8(a) and (b)), but still a satisfactory semi-quantitative agreement is maintained. This suggests the intuitive conclusion that the starting shapes in the experiment are closer to the rather asymmetric slippers than to the highly symmetric discocytes or croissants. Indeed, as explicitly shown in the ESI,† we only observe non-classifiable and rather asymmetric “other” shapes at the channel entrance.

As mentioned in the introduction, experimental investigations with more detailed shape studies are rather scarce. A comparison of the phase diagrams with the experimental literature is therefore limited to rough qualitative statements. Tomaiuolo *et al.*²³ found croissants and “others” for a cell velocity of 1.1 mm s^{-1} using $\lambda \approx 5$ in a cylindrical tube with diameter 10 μm . This is in agreement with our results. At 36 mm s^{-1} , slippers but also croissants have been observed. Since we cannot reach velocities that high, we can neither confirm nor refute the occurrence of the latter. Extrapolation of Fig. 8 is dangerous since the Reynolds number at 36 mm s^{-1} is around $\text{Re} \approx 0.24$ and thus inertia effects might have noticeable contributions.^{93,94} Continuing, Cluitmans *et al.*²⁶ found croissants and tumbling “others” at 1.1 mm s^{-1} and slippers at 13.6 mm s^{-1} in rectangular channels of 10 μm and 7 μm widths and a height of 10 μm , which is consistent with our results. The experimental phase diagram presented in ref. 22 and 21 also agrees with our results insofar that slippers occur at higher

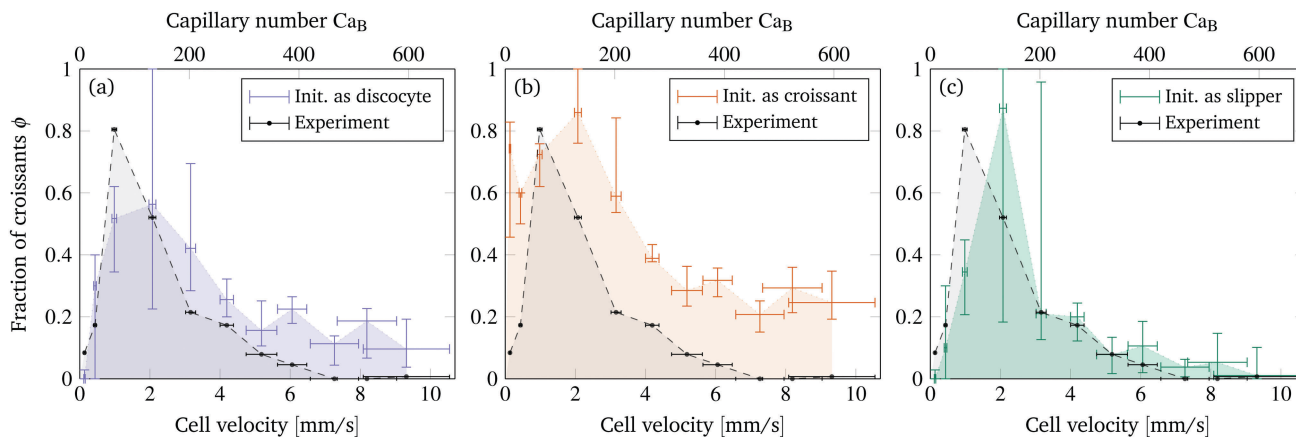


Fig. 8 Fraction of croissants ϕ predicted by the simulations, once for each starting configuration employed in the simulations: (a) simulations started with the typical discocyte, (b) with the croissant and (c) with the slipper shape. To allow for a direct comparison, we included the experimental results from Fig. 3(a) in each diagram (black dashed line). The horizontal error bars depict the standard deviation σ_u of the measured cell velocities (as in Fig. 3(a)), while the vertical error bars show the uncertainty in the prediction as explained in the ESI.† The lines and shaded areas serve as guides to the eye. See the main text for further details.

and croissants at lower velocities. Yet, the considered velocities were higher than 10 mm s^{-1} and the viscosity ratio was $\lambda \lesssim 0.27$, *i.e.* much lower. Furthermore, Fig. 3 in ref. 19 (*in vivo* experiments) also showed coexistence of croissants and slippers for velocities $\lesssim 1 \text{ mm s}^{-1}$ and only croissants in the range $1\text{--}2 \text{ mm s}^{-1}$, matching approximately with our results.

Regarding previous numerical studies, Fedosov *et al.*⁴ performed detailed 3D numerical simulations in cylindrical channels for $\lambda = 1$. Taking a diameter of $10 \mu\text{m}$ (translating into a confinement value of $\chi = 0.65$ in their work), they varied the average velocity from around 0.05 mm s^{-1} to 0.7 mm s^{-1} . They observed a transition from snaking, to tumbling, to tank-treading slippers and finally to parachutes (which are very similar to croissants). In our simulations we found tumbling and tank-treading slippers at velocities of the order of 0.1 mm s^{-1} , and an increasing frequency of croissants above. This matches at least qualitatively with Fedosov *et al.*'s results. However, they did not vary the initial condition.

5.3 Comparison of cell positions

Next, we compare the preferred position of the cells in the steady state. The simulations predict a centered positioning of croissants (Fig. 7(a)), *i.e.* both the y - and the z -offsets are nearly zero. This matches with Fig. 3(b) where a very sharp peak at the channel center is found for the pressure drops within the croissant-peak region.

For slippers, the simulations showed an increase of the radial position of up to around $1.5 \mu\text{m}$ (Fig. 7(a)). Considering the y - and z -coordinates separately in Fig. 9, we see that $z \approx 0$ and the major offset happens in the y -direction. This is rather fortunate as the y -offset is also easily accessible in the experiments, contrary to the z -offset. As can be seen in the measured y -distribution (Fig. 3(b)), we have two off-centered peaks for slippers. Taking the distribution function for only the slippers, we extract the positions y_1 and y_r of the two peaks. Exploiting the $\pm y$ -symmetry of the channel, the off-centered position is

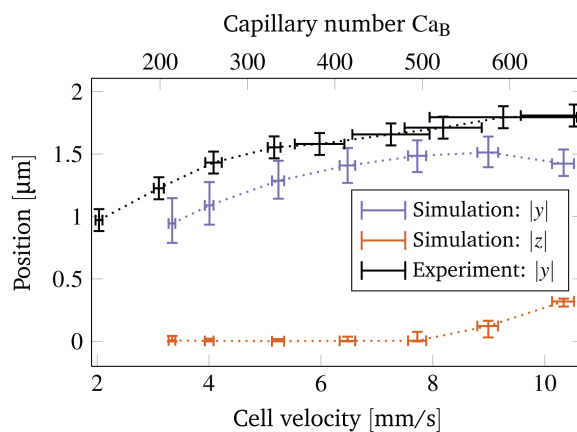


Fig. 9 Comparison between the centroid positions from the simulations (absolute values of the y - and z -coordinates) and experiments (absolute value of the y -coordinate) for cells that have a TT-slipper shape in the steady state. Error bars for the simulations as in Fig. 7(a). The horizontal error bars for the experimental data depict the standard deviation σ_u of the cell velocities, while the vertical error bars represent the estimated uncertainty in the position determination.

then computed as $(y_r - y_1)/2$, *i.e.* in essence as the average of the two peak distances to the central minimum. Fig. 9 compares these values with the numerical results: the behavior is the same (an increase with velocity) and the predicted values show only a small systematic deviation of around $\approx 0.3 \mu\text{m}$, *i.e.* of less than 4% of the RBC diameter $2R_{\text{RBC}}$. A possible reason is that the optically recorded boundaries of the RBC and the channel walls are somewhat blurry (compare the experimental images in Fig. 1).

5.4 Implications of the comparison

There has been quite some debate in the literature if the croissant (or parachute) shapes observed *via* light microscopy are indeed what they appear to be. Gaegtgens *et al.*¹⁸ (Fig. 4 therein), for example, solidified the flowing RBCs with

glutaraldehyde and found that the croissant-like shapes were actually slipper-like. Skalak and Branemark³⁸ pointed out that such shapes can also be “edge-on” discocytes with a flattened back. Ultimately, to uniquely identify the forms one needs some method to record the full 3D geometry of the flowing cells (*e.g.* as in ref. 16, 27, 33 and 95–99). This is unfortunately very hard to implement in the present experimental setup. However, this missing information is complemented here by the numerical simulations which are in good agreement with the experiments and thus our interpretation of the shapes as croissants should be correct.

The good agreement furthermore implies that our red blood cell model and simulation method is fully appropriate for describing the flow of RBCs in a straight microchannel. More sophisticated methods including *e.g.* thermal fluctuations or surface viscosity^{4,25,53,54,100,101} are, at least for the present geometry, not required. For croissants this is intuitive since membrane movement such as tank-treading is absent, for the tank-treading slippers it is somewhat less obvious.

6 Summary & conclusion

To summarize, we have performed *in vitro* experiments and 3D simulations of healthy red blood cells flowing in a microchannel. The viscosity ratio was approximately 5 and the flow velocities ranged from around 0.1 mm s⁻¹ to 10 mm s⁻¹ in both methodologies, corresponding to the typical conditions prevailing in the microvascular system. We found that both the flow velocity as well as the initial starting configuration (shape and offset from channel center) have a major impact on the final steady state of the cells. Using three different starting shapes (discocyte, croissant and slipper), we constructed the corresponding phase diagrams *via* simulations. In most cases the cells assumed one out of two different forms: either a centered croissant or an off-centered slipper. Interestingly, for most velocities bistability, *i.e.* a dependence of the final shape on the initial condition, was observed. Only in a small range of velocities (at around ≈ 1 mm s⁻¹) was the final shape found to be always a croissant. The experimental diagram showed very good agreement with the numerical result, especially when considering the simulations that used the rather asymmetric slipper as starting shape.

We thus conclude that the employed numerical RBC model can sensibly describe the cell behavior in the presented setup. Moreover, since we used physiological viscosity ratios and flow velocities, we speculate that croissants and slippers can occur in the microvasculature at the same set of system parameters not just as transients but rather that both are states which are intrinsically assumed by the cells. Our results are important for applications where the cells should be in a specific state (*e.g.* in lab-on-a-chip devices) and allow for a comprehensive validation of numerical models.

Conflicts of interest

There are no conflicts to declare.

Acknowledgements

Funding from the Volkswagen Foundation and computing time granted by the Leibniz-Rechenzentrum on SuperMUC are gratefully acknowledged by A. Guckenberger and S. Gekle. A. Kihm, T. John and C. Wagner kindly acknowledge the support and funding of the “Deutsch-Französische-Hochschule” (DFH) DFDK “Living Fluids”.

References

- 1 J. B. Freund, *Phys. Fluids*, 2013, **25**, 110807.
- 2 J. Picot, P. A. Ndour, S. D. Lefevre, W. El Nemer, H. Tawfik, J. Galimand, L. Da Costa, J.-A. Ribeil, M. de Montalembert, V. Brousse, B. Le Pioufle, P. Buffet, C. Le Van Kim and O. Français, *Am. J. Hematol.*, 2015, **90**, 339–345.
- 3 S. Salehyar and Q. Zhu, *Soft Matter*, 2016, **12**, 3156–3164.
- 4 D. A. Fedosov, M. Peltomäki and G. Gompper, *Soft Matter*, 2014, **10**, 4258–4267.
- 5 O. Aouane, M. Thiébaud, A. Benyoussef, C. Wagner and C. Misbah, *Phys. Rev. E: Stat., Nonlinear, Soft Matter Phys.*, 2014, **90**, 033011.
- 6 N. Tahiri, T. Biben, H. Ez-Zahraouy, A. Benyoussef and C. Misbah, *Microvasc. Res.*, 2013, **85**, 40–45.
- 7 G. Danker and C. Misbah, *Phys. Rev. Lett.*, 2007, **98**, 088104.
- 8 V. Vitkova, M.-A. Mader, B. Polack, C. Misbah and T. Podgorski, *Biophys. J.*, 2008, **95**, L33–L35.
- 9 D. A. Fedosov, W. Pan, B. Caswell, G. Gompper and G. E. Karniadakis, *Proc. Natl. Acad. Sci. U. S. A.*, 2011, **108**, 11772–11777.
- 10 T. Krüger, M. Gross, D. Raabe and F. Varnik, *Soft Matter*, 2013, **9**, 9008–9015.
- 11 M. Thiébaud, Z. Shen, J. Harting and C. Misbah, *Phys. Rev. Lett.*, 2014, **112**, 238304.
- 12 D. Katanov, G. Gompper and D. A. Fedosov, *Microvasc. Res.*, 2015, **99**, 57–66.
- 13 L. Lanotte, J. Mauer, S. Mendez, D. A. Fedosov, J.-M. Fromental, V. Claveria, F. Nicoud, G. Gompper and M. Abkarian, *Proc. Natl. Acad. Sci. U. S. A.*, 2016, **113**, 13289–13294.
- 14 E. Henry, S. H. Holm, Z. Zhang, J. P. Beech, J. O. Tegenfeldt, D. A. Fedosov and G. Gompper, *Sci. Rep.*, 2016, **6**, 34375.
- 15 O. Otto, P. Rosendahl, A. Mietke, S. Golfier, C. Herold, D. Klaue, S. Girardo, S. Pagliara, A. Ekpenyong, A. Jacobi, M. Wobus, N. Töpfner, U. F. Keyser, J. Mansfeld, E. Fischer-Friedrich and J. Guck, *Nat. Methods*, 2015, **12**, 199–202.
- 16 F. Merola, P. Memmolo, L. Miccio, R. Savoia, M. Mugnano, A. Fontana, G. D'Ippolito, A. Sardo, A. Iolascon, A. Gambale and P. Ferraro, *Light: Sci. Appl.*, 2017, **6**, e16241.
- 17 A. Farutin and C. Misbah, *Phys. Rev. E: Stat., Nonlinear, Soft Matter Phys.*, 2014, **89**, 042709.
- 18 P. Gaegtgens, C. Dührssen and K. H. Albrecht, *Blood Cells*, 1980, **6**, 799–817.
- 19 Y. Suzuki, N. Tateishi, M. Soutani and N. Maeda, *Microcirculation*, 1996, **3**, 49–57.
- 20 T. W. Secomb, B. Styp-Rekowska and A. R. Pries, *Ann. Biomed. Eng.*, 2007, **35**, 755–765.

- 21 M. Faivre, PhD thesis, Université Joseph-Fourier – Grenoble I, Grenoble, 2006.
- 22 M. Abkarian, M. Faivre, R. Horton, K. Smistrup, C. A. Best-Popescu and H. A. Stone, *Biomed. Mater.*, 2008, **3**, 034011.
- 23 G. Tomaiuolo, M. Simeone, V. Martinelli, B. Rotoli and S. Guido, *Soft Matter*, 2009, **5**, 3736–3740.
- 24 G. Tomaiuolo and S. Guido, *Microvasc. Res.*, 2011, **82**, 35–41.
- 25 G. Prado, A. Farutin, C. Misbah and L. Bureau, *Biophys. J.*, 2015, **108**, 2126–2136.
- 26 J. C. A. Cluitmans, V. Chokkalingam, A. M. Janssen, R. Brock, W. T. S. Huck and G. J. C. G. M. Bosman, *BioMed Res. Int.*, 2014, e764268.
- 27 S. Quint, A. F. Christ, A. Guckenberger, S. Himbert, L. Kaestner, S. Gekle and C. Wagner, *Appl. Phys. Lett.*, 2017, **111**, 103701.
- 28 R. M. Hochmuth, R. N. Marple and S. P. Suter, *Microvasc. Res.*, 1970, **2**, 409–419.
- 29 V. Seshadri, R. M. Hochmuth, P. A. Croce and S. P. Suter, *Microvasc. Res.*, 1970, **2**, 434–442.
- 30 V. P. Zharov, E. I. Galanzha, Y. Menyaev and V. V. Tuchin, *J. Biomed. Opt.*, 2006, **11**, 054034.
- 31 G. Tomaiuolo, V. Preziosi, M. Simeone, S. Guido, R. Ciancia, V. Martinelli, C. Rinaldi and B. Rotoli, *Ann. Ist. Super. Sanita*, 2007, **43**, 186–192.
- 32 S. Guido and G. Tomaiuolo, *C. R. Phys.*, 2009, **10**, 751–763.
- 33 S. S. Gorthi and E. Schonbrun, *Opt. Lett.*, 2012, **37**, 707–709.
- 34 L. Lanotte, G. Tomaiuolo, C. Misbah, L. Bureau and S. Guido, *Biomicrofluidics*, 2014, **8**, 014104.
- 35 G. Tomaiuolo, L. Lanotte, R. D'Apolito, A. Cassinese and S. Guido, *Med. Eng. Phys.*, 2016, **38**, 11–16.
- 36 V. Clavera, O. Aouane, M. Thiébaud, M. Abkarian, G. Couplier, C. Misbah, T. John and C. Wagner, *Soft Matter*, 2016, **12**, 8235–8245.
- 37 M. M. Guest, T. P. Bond, R. G. Cooper and J. R. Derrick, *Science*, 1963, **142**, 1319–1321.
- 38 R. Skalak and P. I. Branemark, *Science*, 1969, **164**, 717–719.
- 39 K. Kubota, J. Tamura, T. Shirakura, M. K. Imura, K. Y. Amanaka, T. Isozaki and I. Nishio, *Br. J. Haematol.*, 1996, **94**, 266–272.
- 40 G. Tomaiuolo, L. Lanotte, G. Ghigliotti, C. Misbah and S. Guido, *Phys. Fluids*, 2012, **24**, 1–8.
- 41 C. Wagner, P. Steffen and S. Svetina, *C. R. Phys.*, 2013, **14**, 459–469.
- 42 M. Brust, O. Aouane, M. Thiébaud, D. Flormann, C. Verdier, L. Kaestner, M. W. Laschke, H. Selmi, A. Benyoussef, T. Podgorski, G. Couplier, C. Misbah and C. Wagner, *Sci. Rep.*, 2014, **4**, 4348.
- 43 H. L. Goldsmith and J. Marlow, *Proc. R. Soc. London, Ser. B*, 1972, **182**, 351–384.
- 44 T. W. Secomb, R. Skalak, N. Özkaya and J. F. Gross, *J. Fluid Mech.*, 1986, **163**, 405–423.
- 45 T. W. Secomb, *Microvasc. Res.*, 1987, **34**, 46–58.
- 46 T. W. Secomb, R. Hsu and A. R. Pries, *Am. J. Physiol.: Heart Circ. Physiol.*, 2001, **281**, H629–H636.
- 47 T. W. Secomb and R. Skalak, *Microvasc. Res.*, 1982, **24**, 194–203.
- 48 B. Kaoui, G. Biroos and C. Misbah, *Phys. Rev. Lett.*, 2009, **103**, 188101.
- 49 B. Kaoui, N. Tahiri, T. Biben, H. Ez-Zahraouy, A. Benyoussef, G. Biroos and C. Misbah, *Phys. Rev. E: Stat., Nonlinear, Soft Matter Phys.*, 2011, **84**, 041906.
- 50 B. Kaoui, T. Krüger and J. Harting, *Soft Matter*, 2012, **8**, 9246–9252.
- 51 L. Shi, T.-W. Pan and R. Glowinski, *Phys. Rev. E: Stat., Nonlinear, Soft Matter Phys.*, 2012, **85**, 016307.
- 52 G. R. Lázaro, A. Hernández-Machado and I. Pagonabarraga, *Soft Matter*, 2014, **10**, 7195–7206.
- 53 H. Noguchi and G. Gompper, *Proc. Natl. Acad. Sci. U. S. A.*, 2005, **102**, 14159–14164.
- 54 J. L. McWhirter, H. Noguchi and G. Gompper, *Soft Matter*, 2011, **7**, 10967–10977.
- 55 T. Ye, H. Shi, L. Peng and Y. Li, *J. Appl. Phys.*, 2017, **122**, 084701.
- 56 G. Danker, P. M. Vlahovska and C. Misbah, *Phys. Rev. Lett.*, 2009, **102**, 148102.
- 57 B. Kaoui, G. Couplier, C. Misbah and T. Podgorski, *Houille Blanche*, 2009, 112–119.
- 58 D. Cordasco, A. Yazdani and P. Bagchi, *Phys. Fluids*, 2014, **26**, 041902.
- 59 Z. Peng, A. Mashayekh and Q. Zhu, *J. Fluid Mech.*, 2014, **742**, 96–118.
- 60 K. Sinha and M. D. Graham, *Phys. Rev. E: Stat., Nonlinear, Soft Matter Phys.*, 2015, **92**, 042710.
- 61 G. R. Cokelet and H. J. Meiselman, *Science*, 1968, **162**, 275–277.
- 62 A. S. Popel and P. C. Johnson, *Annu. Rev. Fluid Mech.*, 2005, **37**, 43–69.
- 63 B. Sebastian and P. S. Dittrich, *Annu. Rev. Fluid Mech.*, 2018, **50**, 483–504.
- 64 M. Toner and D. Irimia, *Annu. Rev. Biomed. Eng.*, 2005, **7**, 77–103.
- 65 B. Cui, H. Diamant and B. Lin, *Phys. Rev. Lett.*, 2002, **89**, 188302.
- 66 H. Diamant, *J. Phys. Soc. Jpn.*, 2009, **78**, 041002.
- 67 A. Koller, B. Dawant, A. Liu, A. S. Popel and P. C. Johnson, *Am. J. Physiol.: Heart Circ. Physiol.*, 1987, **253**, H154–H164.
- 68 E. Evans and Y.-C. Fung, *Microvasc. Res.*, 1972, **4**, 335–347.
- 69 D.-V. Le, *Comput. Methods Appl. Mech. Eng.*, 2010, **199**, 2622–2632.
- 70 S. Chien, S. Usami, H. M. Taylor, J. L. Lundberg and M. I. Gregersen, *J. Appl. Physiol.*, 1966, **21**, 81–87.
- 71 R. Skalak, N. Ozkaya and T. C. Skalak, *Annu. Rev. Fluid Mech.*, 1989, **21**, 167–200.
- 72 T. W. Secomb, *Annu. Rev. Fluid Mech.*, 2017, **49**, 443–461.
- 73 Y. Kim, H. Shim, K. Kim, H. Park, S. Jang and Y. Park, *Sci. Rep.*, 2014, **4**, 6659.
- 74 R. Skalak, A. Tozeren, R. P. Zarda and S. Chien, *Biophys. J.*, 1973, **13**, 245–264.
- 75 T. Krüger, F. Varnik and D. Raabe, *Comput. Math. Appl.*, 2011, **61**, 3485–3505.
- 76 Y.-Z. Yoon, J. Kotar, G. Yoon and P. Cicuta, *Phys. Biol.*, 2008, **5**, 036007.
- 77 J. B. Freund, *Annu. Rev. Fluid Mech.*, 2014, **46**, 67–95.

- 78 P. B. Canham, *J. Theor. Biol.*, 1970, **26**, 61–81.
- 79 W. Helfrich, *Z. Naturforsch., C: J. Biosci.*, 1973, **28**, 693–703.
- 80 A. Guckenberger and S. Gekle, *J. Phys.: Condens. Matter*, 2017, **29**, 203001.
- 81 Y. Park, C. A. Best, K. Badizadegan, R. R. Dasari, M. S. Feld, T. Kuriabova, M. L. Henle, A. J. Levine and G. Popescu, *Proc. Natl. Acad. Sci. U. S. A.*, 2010, **107**, 6731–6736.
- 82 A. Guckenberger, M. P. Schraml, P. G. Chen, M. Leonetti and S. Gekle, *Comput. Phys. Commun.*, 2016, **207**, 1–23.
- 83 A. Farutin, T. Biben and C. Misbah, *J. Comput. Phys.*, 2014, **275**, 539–568.
- 84 A. Guckenberger and S. Gekle, *J. Fluid Mech.*, 2018, **836**, 952–997.
- 85 C. Pozrikidis, *J. Comput. Phys.*, 2001, **169**, 250–301.
- 86 H. Zhao, A. H. Isfahani, L. N. Olson and J. B. Freund, *J. Comput. Phys.*, 2010, **229**, 3726–3744.
- 87 D. Saintillan, E. Darve and E. S. G. Shaqfeh, *Phys. Fluids*, 2005, **17**, 033301.
- 88 Y. Saad and M. Schultz, *SIAM J. Sci. Stat. Comput.*, 1986, **7**, 856–869.
- 89 P. Bogacki and L. F. Shampine, *Appl. Math. Lett.*, 1989, **2**, 321–325.
- 90 A. Daddi-Moussa-Ider, A. Guckenberger and S. Gekle, *Phys. Rev. E*, 2016, **93**, 012612.
- 91 A. R. Pries, T. W. Secomb and P. Gaehtgens, *Am. J. Physiol.: Heart Circ. Physiol.*, 1995, **269**, H1713–H1722.
- 92 O. Baskurt, B. Neu and H. Meiselman, *Red Blood Cell Aggregation*, CRC Press, 2011.
- 93 B. Kaoui and J. Harting, *Rheol. Acta*, 2016, **55**, 465–475.
- 94 C. Schaaf and H. Stark, *Soft Matter*, 2017, **13**, 3544–3555.
- 95 N. C. Pégard and J. W. Fleischer, *J. Biomed. Opt.*, 2013, **18**, 040503.
- 96 N. C. Pégard, M. L. Toth, M. Driscoll and J. W. Fleischer, *Lab Chip*, 2014, **14**, 4447–4450.
- 97 V. K. Jagannadh, M. D. Mackenzie, P. Pal, A. K. Kar and S. S. Gorthi, *Opt. Express*, 2016, **24**, 22144–22158.
- 98 K. Kim, K. Choe, I. Park, P. Kim and Y. Park, *Sci. Rep.*, 2016, **6**, 33084.
- 99 C. K. Rasmi, S. Padmanabhan, K. Shirlekar, K. Rajan, R. Manjithaya, V. Singh and P. P. Mondal, *Appl. Phys. Lett.*, 2017, **111**, 243702.
- 100 G. Tomaiuolo, M. Barra, V. Preziosi, A. Cassinese, B. Rotoli and S. Guido, *Lab Chip*, 2011, **11**, 449–454.
- 101 A. Yazdani and P. Bagchi, *J. Fluid Mech.*, 2013, **718**, 569–595.

Supplementary information for “Numerical-experimental observation of shape bistability of red blood cells flowing in a microchannel”

Achim Guckenberger^a, Alexander Kihm^b, Thomas John^b, Christian Wagner^{b,c}, Stephan Geckle^a

Dated: January 22, 2018

Contents

S1 About the initial condition	1
S1.1 Croissant and slipper initial shapes	1
S1.2 Starting with rotated discocytes	2
S2 Time evolution and steady state details	4
S3 About the error bars in the prediction	5
S4 Supplementary information for the experiments	7
S4.1 Inlet in the experimental setup	7
S4.2 Additional experimental data	8
S5 References	10
S6 Raw experimental images at $x = 10$ mm	11
S7 Raw experimental images at $x = 0$ mm	16

S1 About the initial condition

S1.1 Croissant and slipper initial shapes

Figure S1 shows the employed red blood cell (RBC) shapes when the initial shape is taken to be a croissant or slipper. These shapes were obtained from previous simulations where we started with the typical discocyte shape¹ whose axis was aligned with the channel's axis (see figure 2 in the main text). On the one hand, the croissant shape was extracted from a converged simulation where the initial radial offset was $0.17\ \mu\text{m}$ and the steady state cell velocity was $6.61\ \text{mm/s}$. The ellipsoidal rim of the croissant has a diameter ranging from $6.0\ \mu\text{m}$ to $6.6\ \mu\text{m}$. Moreover, the total length of the cell (rim to tip) is $6.7\ \mu\text{m}$, while the distance from the dent to the tip is $4.4\ \mu\text{m}$. On the other hand, the slipper was retrieved from a simulation with an initial radial offset of $0.86\ \mu\text{m}$, with the average cell velocity in the steady state being $6.48\ \text{mm/s}$. The slipper has a total length of $9.7\ \mu\text{m}$, a height (y -extent) of $4.0\ \mu\text{m}$ and a width (z -extent) of $6.2\ \mu\text{m}$. We chose a frame in the middle of the periodic contraction/expansion of the cell. Hence, these two shapes correspond to two simulations from figure 5 in the main text. The slightly different velocities come from the fact that at otherwise identical flow

^aBiofluid Simulation and Modeling, Fachbereich Physik, Universität Bayreuth, Bayreuth

^bExperimental Physics, Saarland University, 66123, Saarbrücken, Germany

^cPhysics and Materials Science Research Unit, University of Luxembourg, Luxembourg, Luxembourg

¹For the formula of the typical discocyte shape see references [1, 2].

parameters croissants are faster than slippers as the first are centered while the second are off-centered (and thus see a lower flow velocity) [3].

Figure S2 depicts the corresponding simulation setups, which are identical to the one from the main text except for the different RBC shape. Especially note that the initial radial offset r_{init} of the centroid is along the same line. We always use the same croissant or slipper shape, regardless of the value of r_{init} .

The slipper and croissant shapes represent the “extreme” cases, as the steady state consists of slippers and croissants and thus by starting with the respective shape one expects to “manipulate” the cells into these particular shapes. The discocyte shape represents the equilibrium shape assumed by RBCs without external forces and is thus another natural starting point.

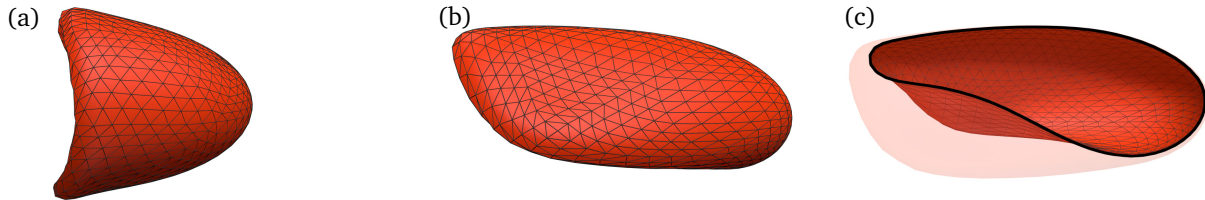


Figure S1: Employed initial shapes in the simulations when starting as a (a) croissant or (b) slipper. Figure (c) shows the cross-section of the slipper from (b). The black lines on the surfaces represent the used mesh.

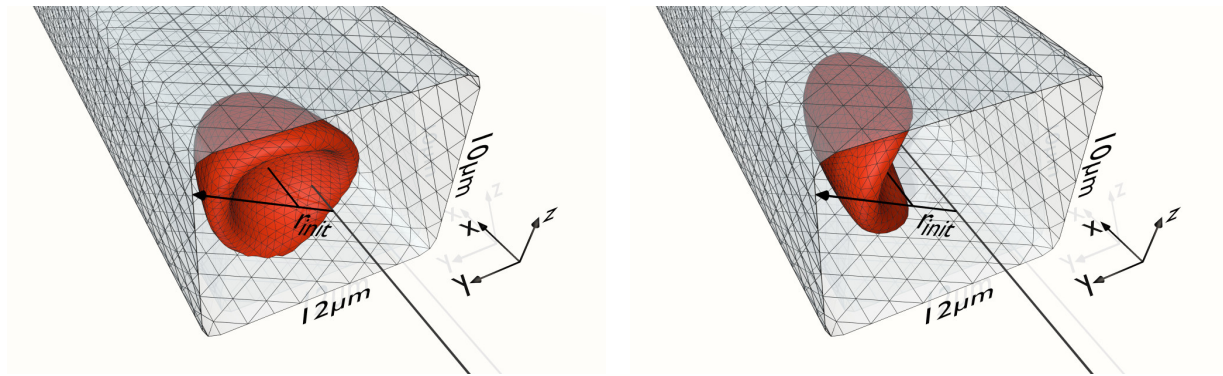


Figure S2: The simulation setups when starting with a croissant (left) or a slipper shape (right), similar to figure 2 from the main text. The cell shapes are the ones from figure S1.

S1.2 Starting with rotated discocytes

When we start with the discocyte shape in the main text, it is axis-aligned with the channel’s axis (x -axis; see figure 2 in the main text). A natural question that occurs is thus how the results change if the rotation is varied. We therefore present in figure S3 phase diagrams when the symmetry axis of the initial discocyte is aligned with the y -axis (a) or z -axis (b).

Compared to the results from the main text, we observe that many more of the final shapes are croissants, even for high initial radial positions r_{init} that resulted in slippers for our main starting shapes (croissant, slipper, x -aligned discocyte). Considering the time evolution of the radial position (exemplified in figure S4), we find that the rotated discocytes are quickly pushed into the center of the channel before sufficient deformations can occur that would induce a slipper as the final state. In other words, the initial transient of these initial shapes happens to favor croissants. A more detailed analysis of this behavior and the underlying reason will be left for future research.

Some of the experimental recordings at the channel entrance (see section S7) appear to be somewhat similar to z -aligned discocytes. However, as we almost only find croissants in the steady state for this particular starting shape in the simulations (figure S3(b)), contrary to the actually observed domination of slippers in the steady state in the experiments (figure 3(a) in the main text), it is likely that many of these cells at the channel entrance

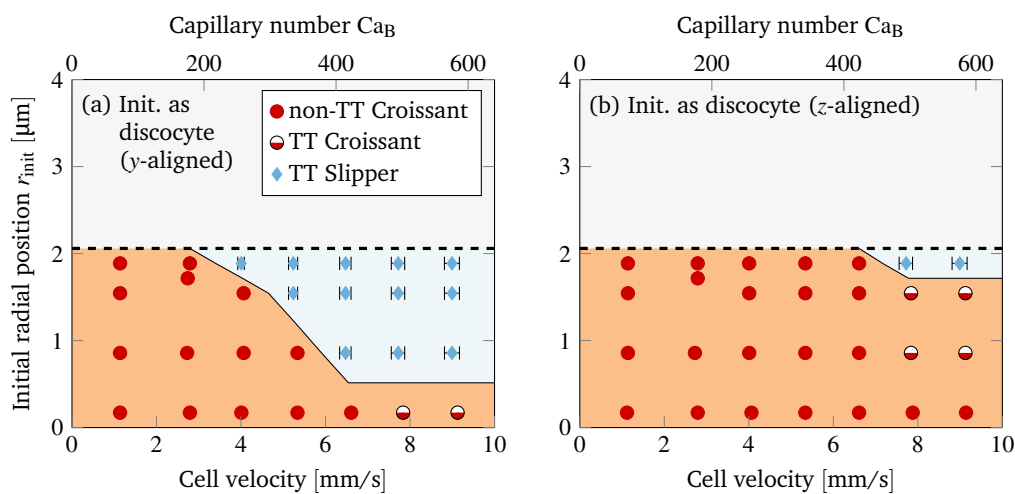


Figure S3: Phase diagrams obtained from the simulations when starting with the typical discocyte shape which is aligned with (a) the y-axis and (b) the z-axis. Figure elements as in figure 6 in the main text.

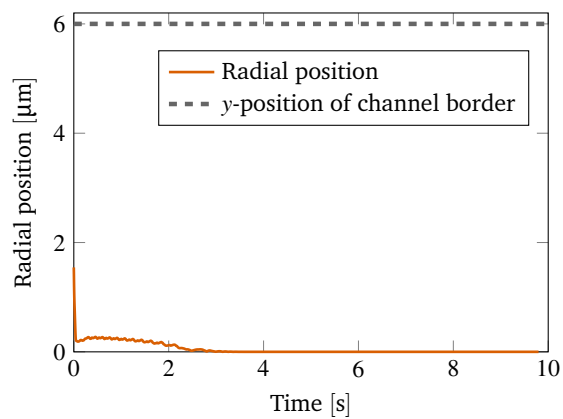


Figure S4: Radial position of an RBC started in the typical discocyte shape that is aligned along the z-axis with a radial offset of $r_{init} \approx 1.54 \mu\text{m}$. It has a cell velocity of approximately 6.61 mm/s in the steady state. The initial transient quickly pushes the cell to the center of the channel, where it becomes a croissant.

are actually not discocytes but rather deformed shapes, such as slippers viewed from the top or “edge-on” discocytes [4].

S2 Time evolution and steady state details

As noted in the main text and shown in the TTSlipper supplementary video, the tank-treading (TT) slipper exhibits oscillatory contractions. These result in periodic variations of the radial position and the cell velocity, as exemplified in figure S5. This figure also illustrates how we extract the average, minimal and maximal values after reaching the steady state. The simulation results from the main text depict the average values as the main data points and the minimal and maximal values via error bars. Note that we do the same for the other shapes, although the resulting error bars are too small to be seen in the figures.

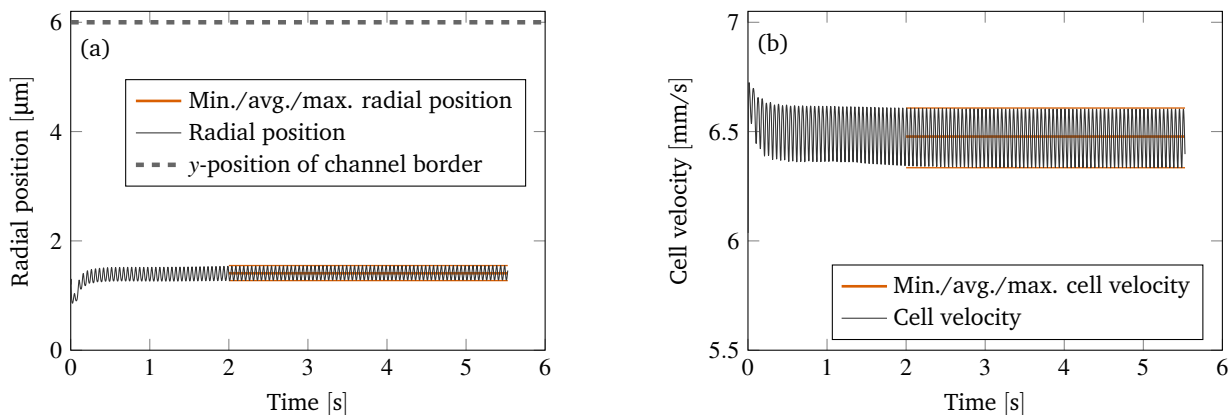


Figure S5: Time evolution of (a) the radial position and (b) the cell velocity for a slipper shape. The data is for the numerical simulation with $r_{\text{init}} = 1.2 \mu\text{m}$ from figure 5 in the main text. The orange lines show from bottom to top the minimum, average and maximum values that are extracted in the steady state, which is taken to begin at 2 s in this particular example.

Furthermore, reaching the steady state often takes a few seconds. Convergence into the croissant shape usually takes longer than reaching a steady slipper state. This is illustrated in figure S6(a) where we show for each simulation from figure 6 in the main text the approximated time t_{steady} until the steady state is reached. This time t_{steady} is the duration measured from the start of the simulations until the position, shape, velocity and asphericity (a measure of deformation [5]) of the cells no longer change or become periodic. Figure S6(b) shows the same times non-dimensionalized with a typical flow timescale $\tau := R_{\text{RBC}}/u$, where u is the mean cell velocity.

The longest times are observed when the velocity lies in the croissant-only range. An example for such a case is displayed in figure S7: For around eight seconds, the cell is in an almost periodic slipper state before moving to the center and becoming a croissant. However, after another four seconds some membrane rotation occurs, i.e. the RBC dimples (which are special points due to the discocyte reference state) move to a slightly different location. This results in a short lived and slightly off-centered position. After a total time of around 14 s the cell is in the final croissant state, with no movement occurring anymore. See the video LongCroissant for an illustration.

Regarding a more quantitative measure for the steady state: Within a time frame spanning several oscillations or a time frame of 1000τ measured from the beginning of the steady state (t_{steady}), the changes are approximately

- below 2% for the radial position (even below 0.2% for $u > 0.8 \text{ mm/s}$; relative to R_{RBC}),
- below 1% for the cell velocity (even below 0.1% for $u > 0.8 \text{ mm/s}$; relative to the average cell velocity u) and
- below 1% for the asphericity (relative to the average asphericity).

For periodic motion, the maxima/minima within the time frame are considered.

It is important to note that the times reported here are the times until the cell shapes have entirely converged. The rough cell shape (TT/non-TT croissant or TT/non-TT slipper) are usually apparent much earlier. For

example, in figures S5 the slipper can be recognized even before 1 s, while the perfectly periodic state is reached only after 2 s. Another example is figure S7, where we find a croissant already at approximately 9 s, and only minor differences occur compared to the fully converged state at 14 s. Considering the times until the rough cell shape is apparent together with the cell velocities, we find that in the overwhelming majority of cases the cells have traveled for less than 10 mm before the rough cell shape is attained. This is in agreement with our choice of measurement position in the experiments (10 mm away from the channel entrance).

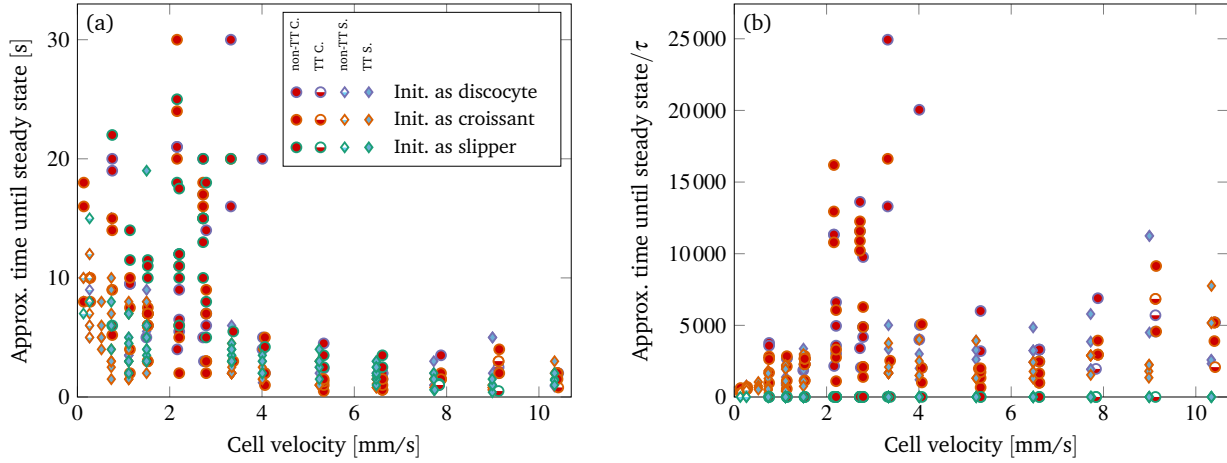


Figure S6: Estimates of the time t_{steady} it takes for the cells to reach the steady state. Figure (a) depicts this time in seconds, while figure (b) shows the time non-dimensionalized with a typical flow timescale τ . The images show the results for all simulations from the three diagrams from figure 6 in the main text, where the cell was initialized as x -aligned discocyte, croissant and slipper, respectively. These three initial shapes are indicated by the purple, orange and green borders around the symbols (see the three rows in the legend). The final steady state shapes (non-tank-treading croissant, tank-treading croissant, non-tank-treading slipper and tank-treading slipper) are represented by the same symbols as in the main text (compare the four columns in the legend).

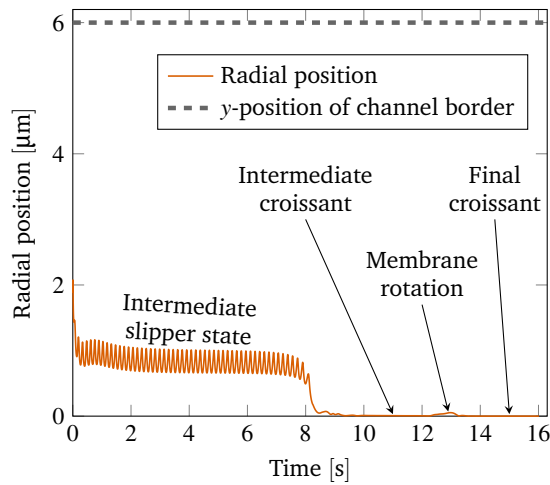


Figure S7: Time evolution of the radial position of a cell which is initially in the x -aligned discocyte state with $r_{\text{init}} \approx 1.89 \mu\text{m}$ and has an average velocity of $\approx 2.79 \text{ mm/s}$ in the steady state (i.e. it lies in the croissant-only region). The steady state begins at around 14 s. See the movie `LongCroissant` for a 3D visualization.

S3 About the error bars in the prediction

The determination of the vertical error bars in the comparison between experiments and simulations (figure 8 in the main text) consists of several steps that will be described in the following. To this end, consider figure S8. This figure shows exemplarily the numerical phase diagram when the starting shape is the x -aligned discocyte, i.e. the symbols that indicate the steady states are identical to figure 6(a) from the main text. The middle gray line represents the position of the approximated transition threshold r_{trans} between croissants and slippers, which was obtained by averaging the values from the adjacent simulation symbols.

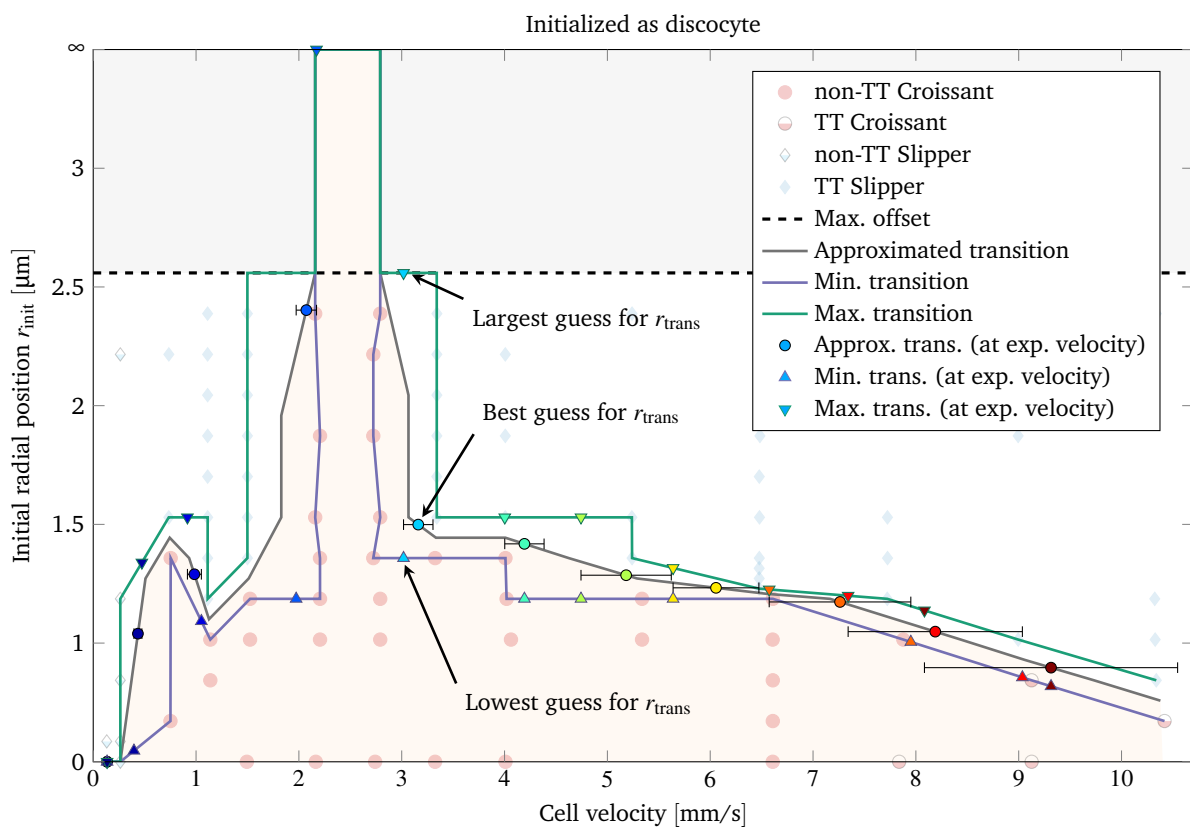


Figure S8: Numerical phase diagram from figure 6(a) from the main text for the x -aligned discocyte starting shape. The nearly transparent shape symbols and the maximal offset are identical to figure 6(a). The violet, gray and green lines depict the minimal, average and maximal position, respectively, of the transition threshold r_{trans} between croissants and slippers. These lines are evaluated at the experimental velocities u and $u \pm \sigma_u$, giving the circular and triangular symbols. Each triple of these symbols that shares the same color corresponds to one particular experimental velocity and shows the lowest, best and largest guess for r_{trans} . This is exemplified via the three labels and arrows for $u \pm \sigma_u = (3.16 \pm 0.14)$ mm/s which corresponds to a pressure drop of $\Delta P = 300$ mbar. The horizontal error bars depict σ_u . Also note that in the croissant-only region we take $r_{\text{trans}} \rightarrow \infty$, as indicated by the ∞ symbol on the top left.

The first step in the determination of the vertical error bars is to compute a lower and upper bound for the transition threshold. We do this by drawing a line through the highest croissant and lowest slipper symbols. This leads to the lower violet and upper green lines in figure S8. Thus, these two lines represent the uncertainty of the transition, which is a result of the finite distance between the simulations.

An exception in the construction of the three lines occurs in the region where the simulations predict only croissants. Due to the particular starting shape, there is a maximal initial offset. Experimentally, however, it is of course possible that the cells at the channel entrance have a larger offset (i.e. one that lies above the black dashed line in figure S8). Since the results from the simulations indicate that only croissants really exist in this region (regardless of the initial shape and offset), we take $r_{\text{trans}} \rightarrow \infty$. That way we predict a value of 1 for the fraction of croissants.

Second, we need to evaluate the transition lines at the experimental velocities. However, the measured velocities have not only an average u but also a certain standard deviation σ_u . σ_u is taken as the uncertainty in the velocity here. Evaluating the middle gray line at the average velocity u results in the “best guess for r_{trans} ” (the circular symbols in figure S8). This value is then directly converted into the predicted fraction of croissants ϕ as described in the main text (via conversion to y_{trans} and the measured offset distribution at the channel entrance). For the vertical error bars, we evaluate the three numerical transition lines (lower, middle and upper, i.e. violet, gray and green) at the three velocities u , $u - \sigma_u$ and $u + \sigma_u$, leading to nine values for r_{trans} . The ones that will yield the lowest and largest fraction of croissants are shown as triangular symbols in figure S8 (the “lowest guess for r_{trans} ” and the “largest guess for r_{trans} ”).

Third, the predicted fractions of croissants are computed from the offset distribution at the channel entrance for each of these nine r_{trans} values (as described in the main text), and additionally for $r_{\text{trans}} \pm s_p$. This takes into account the uncertainty in the offset distribution due to the uncertainty s_p in the position measurement. As a result, we now have 27 predictions.

Fourth, we search for the minimum (ϕ_{min}) and maximum (ϕ_{max}) of these 27 values. ϕ_{min} and ϕ_{max} are then interpreted as the uncertainty in the prediction. The vertical error bars in figure 8 from the main text therefore depict ϕ_{min} and ϕ_{max} .

All of this is performed not only for the phase diagram with the discocyte, but also for the ones with the croissant and slipper starting shapes. In case of the croissant starting shape, r_{trans} is not a proper function due to the protrusions, i.e. we find several transition offsets for certain velocities (compare figure 6(b) in the main text). Hence, the simple “counting of cells that enter with an offset below r_{trans} ” to form the prediction becomes a “counting of cells that enter with offsets in the intervals formed by the numerical transition offsets”. As an example, if a certain velocity leads to transitions at r_1 , r_2 and r_3 (such that the simulations yield croissants in the two intervals $[0, r_1]$ and $[r_2, r_3]$), then we count how many cells enter the channel with offsets that lie in these two intervals (after their projection on the y -axis). The computation of the uncertainty is adapted accordingly.

S4 Supplementary information for the experiments

S4.1 Inlet in the experimental setup

Figure S9 depicts part of the inlet reservoir and the start of the channels. The whole chip is made of PDMS. The total reservoir is rectangular with a length of 4 mm and a width of 1 mm. Multiple channels are connected to this reservoir, having a width of $L_y \approx 12 \mu\text{m}$ and a height of $L_z \approx 10 \mu\text{m}$. Using our microscope, we record several channels simultaneously to increase the throughput.

To connect the reservoir with our high-precision pressure device, we pinch a hole into the PDMS substrate. Its diameter is approximately 1 mm, matching with the diameter of the connected tube. In the example in figure S9 the flow together with the RBCs is coming from the top. The RBCs then flow into the channels since the outlet is at the end of them. The outlet reservoir looks similar. Also note that the distribution of the RBCs before the channel entrances is without significance for the present work since we record the actual state directly beyond the entrance, effectively *defining* it as the initial condition in the experiments (see below for the shapes and figure 4 in the main text).

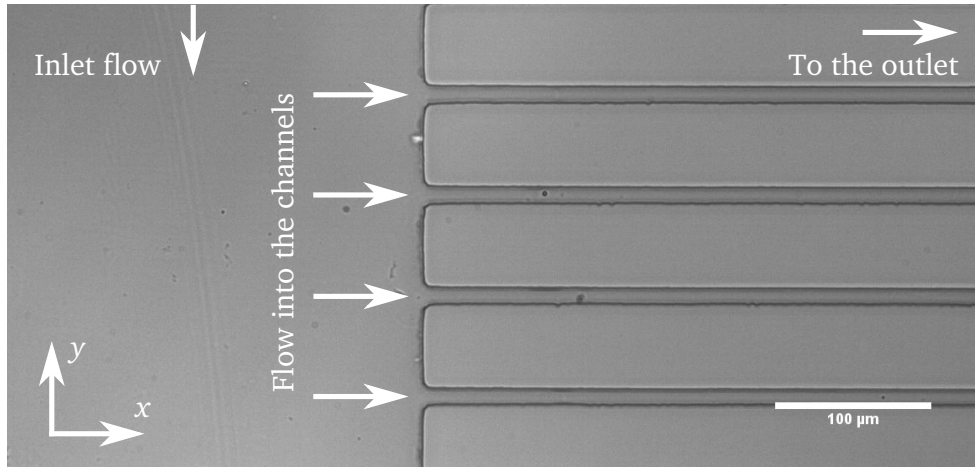


Figure S9: Part of the channel inlet used in the experiments. Top-view, i.e. gravity is going into the image plane (z -direction). Note that the total length of the channels is $L_x \approx 40$ mm, i.e. only the entry part is shown here.

S4.2 Additional experimental data

We depict in figure S10 the measured cell velocities for each applied pressure drop ΔP . The data shows the result when the averaging goes over all cells regardless of their shape (“All”), and also for the three shape classes separately. Obviously, the cell velocities are roughly proportional to ΔP . However, croissants tend to be a bit faster than slippers because croissants are located in the high-velocity center of the channel while slippers are off-centered (see the main text). This is in agreement with previous publications [3, 6].

Table S1 lists the corresponding raw data, as well as the number of cells that were taken into account. It additionally shows the number of cells at the channel entrance. The raw images from the experiments are included in sections S6 and S7 below.

Furthermore, we list in an extra Excel sheet (SI_rawYPos_pos0.xls) the raw y -positions of the cells at the channel entrance. This data makes it possible to compare one’s own simulation results with our experiments (as we did in figure 8 in the main text).

Moreover, figure S11 depicts the experimental y -offset distributions separated into the contributions from the three different shapes (croissants, slippers and “others”) at position $x = 10$ mm in the channel. This figure complements figure 3(b) from the main text where all three shapes have been considered together.

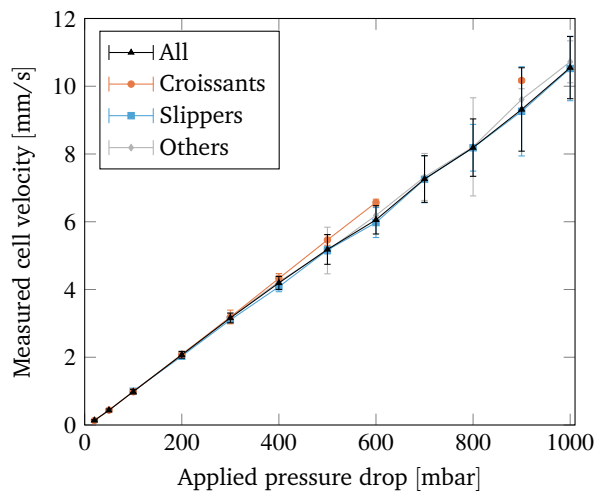


Figure S10: Measured average cell velocities for each applied pressure drop for the three different shape classes and once for all shapes together (“All”). The vertical error bars depict the standard deviation σ_u . Measurements were performed at position $x = 10$ mm in the channel. The corresponding raw data is listed in table S1. The lines are guides for the eyes.

ΔP [mbar]	N_0^{all}	N_{10}^{all}	N_{10}^{Crois}	N_{10}^{Slipper}	N_{10}^{Other}	u_{10}^{all} [mm/s]	u_{10}^{Crois} [mm/s]	u_{10}^{Slipper} [mm/s]	u_{10}^{Other} [mm/s]
20	35	107	9	0	98	0.135 ± 0.021	0.132 ± 0.020		0.135 ± 0.021
50	10	52	9	0	43	0.43 ± 0.04	0.440 ± 0.005		0.43 ± 0.04
100	29	205	165	2	38	0.98 ± 0.07	0.98 ± 0.07	0.996 ± 0.002	0.99 ± 0.04
200	71	484	252	22	210	2.07 ± 0.10	2.09 ± 0.08	2.03 ± 0.06	2.06 ± 0.12
300	95	475	102	120	253	3.16 ± 0.14	3.19 ± 0.20	3.10 ± 0.09	3.18 ± 0.13
400	90	463	80	167	216	4.19 ± 0.19	4.33 ± 0.14	4.08 ± 0.15	4.23 ± 0.19
500	179	215	17	117	81	5.2 ± 0.4	5.46 ± 0.16	5.16 ± 0.11	5.2 ± 0.7
600	151	176	8	124	44	6.1 ± 0.4	6.57 ± 0.10	6.0 ± 0.4	6.19 ± 0.25
700	159	123	0	105	18	7.3 ± 0.7		7.3 ± 0.7	7.3 ± 0.7
800	75	200	0	169	31	8.2 ± 0.8		8.2 ± 0.7	8.21 ± 1.40
900	187	282	2	241	39	9.3 ± 1.2	10.17 ± 0.06	9.3 ± 1.3	9.6 ± 0.3
1000	141	305	0	266	39	10.6 ± 0.9		10.5 ± 1.0	10.7 ± 0.6

Table S1: Experimental data: The table lists for each applied pressure drop ΔP the total number of analyzed cells N_0^{all} at position $x = 0$ mm in the channel and the total number of analyzed cells N_{10}^{all} at position $x = 10$ mm. For the latter we also show the number of croissants, slippers and “others”, together with the measured velocities u_{10} . The uncertainties are the standard deviation. The subscripts “0” and “10” in the heading specify the x -position in the channel (0 mm or 10 mm).

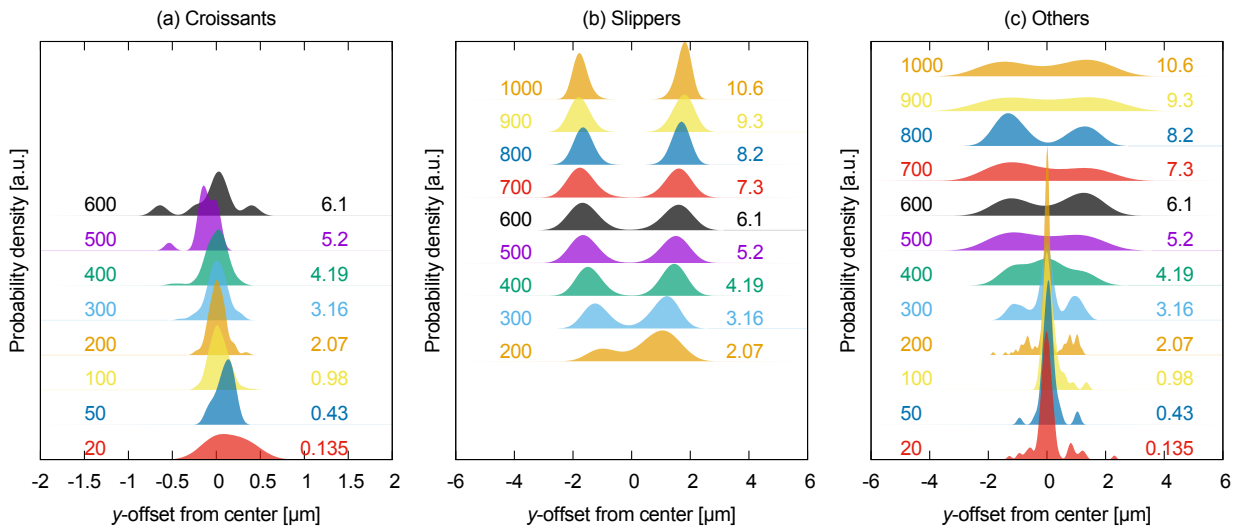
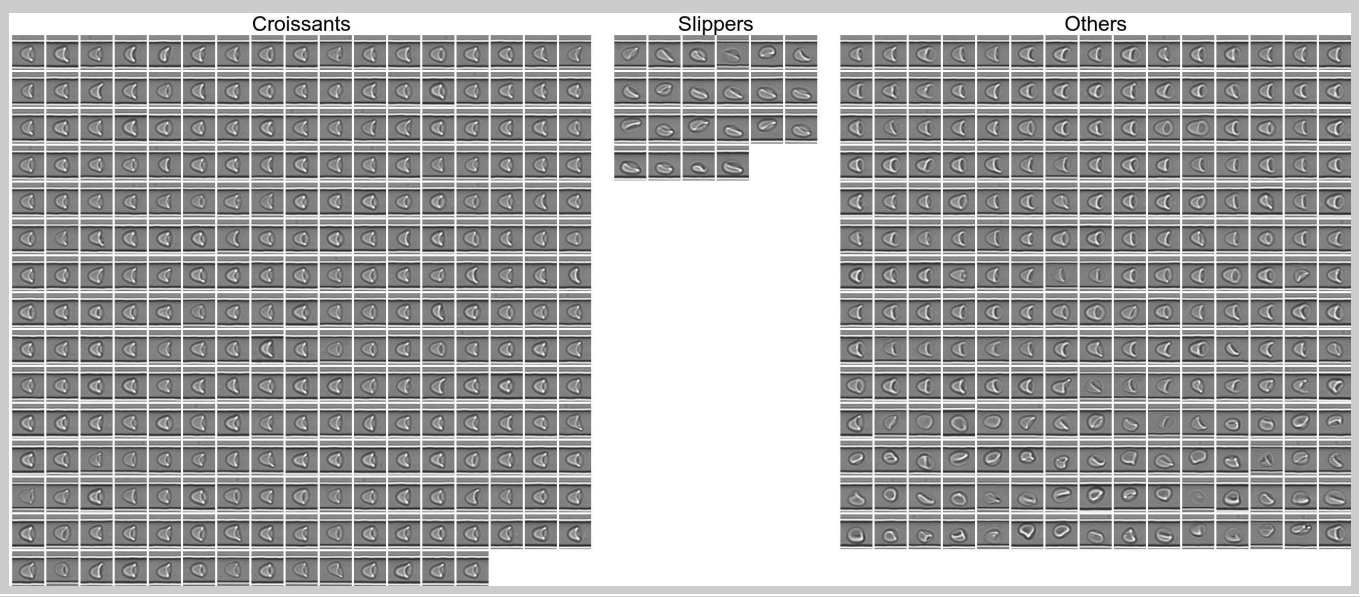


Figure S11: Estimated probability density functions for the experimental y -offset distributions at position $x = 10$ mm in the channel for (a) the croissant, (b) the slipper and (c) the “other” shapes. The result for all three shapes combined was shown in figure 3(b) in the main text. The area below each curve is normalized to 1, and they are offset in the vertical direction for illustration purposes. The applied pressure drop is indicated on the left side of the figures in millibars, while the corresponding mean cell velocity is shown on the right side in mm/s. Also note the different scale of the horizontal axis in the first figure.

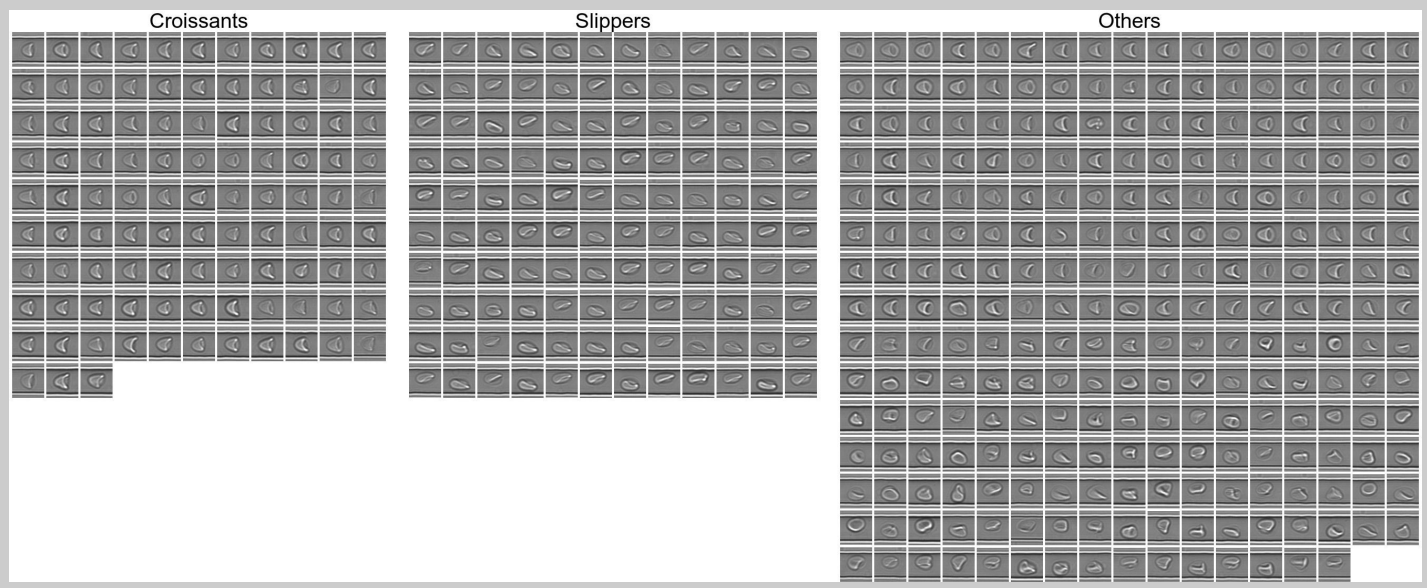
S5 References

- [1] E. Evans and Y.-C. Fung, “Improved measurements of the erythrocyte geometry,” *Microvasc. Res.* **4**, 335 (1972).
- [2] D.-V. Le, “Subdivision elements for large deformation of liquid capsules enclosed by thin shells,” *Comput. Methods Appl. Mech. Eng.* **199**, 2622 (2010).
- [3] S. Quint, A. F. Christ, A. Guckenberger, S. Himbert, L. Kaestner, S. Gekle, and C. Wagner, “3D tomography of cells in micro-channels,” *Appl. Phys. Lett.* **111**, 103701 (2017).
- [4] R. Skalak and P. I. Branemark, “Deformation of Red Blood Cells in Capillaries,” *Science* **164**, 717 (1969).
- [5] D. A. Fedosov, M. Peltomäki, and G. Gompper, “Deformation and dynamics of red blood cells in flow through cylindrical microchannels,” *Soft Matter* **10**, 4258 (2014).
- [6] G. Tomaiuolo, M. Simeone, V. Martinelli, B. Rotoli, and S. Guido, “Red blood cell deformation in microconfined flow,” *Soft Matter* **5**, 3736 (2009).

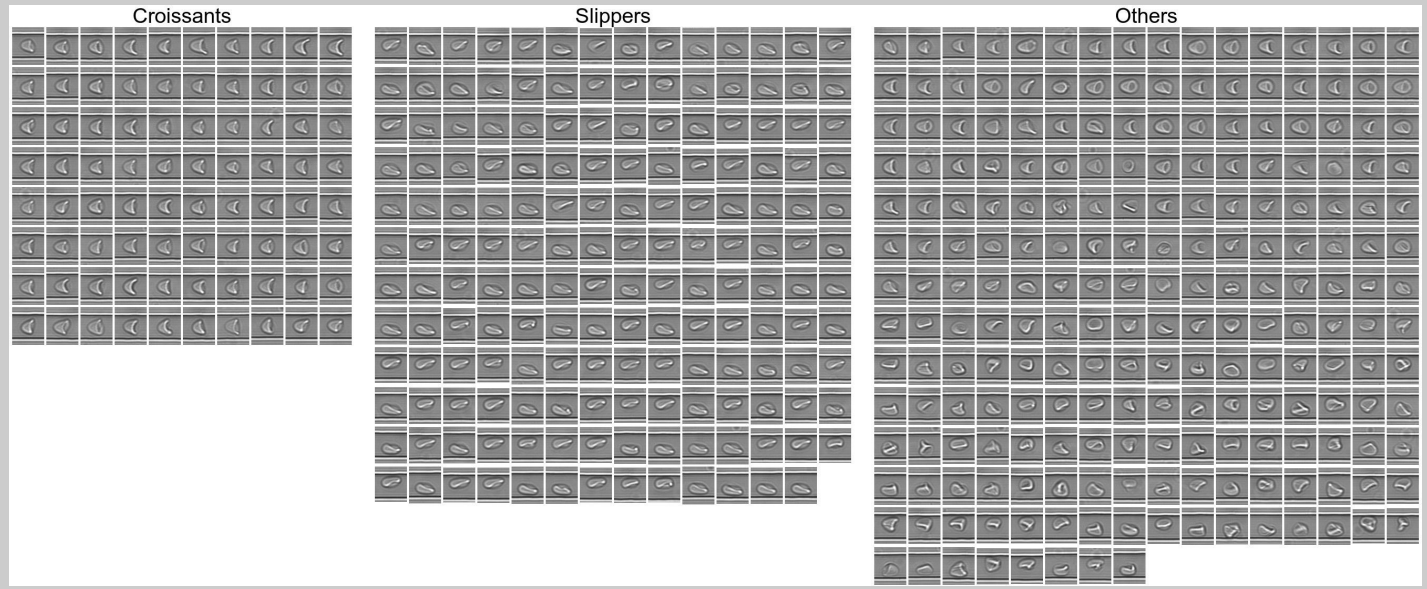
$\Delta P = 200 \text{ mbar}, x = 10 \text{ mm}$



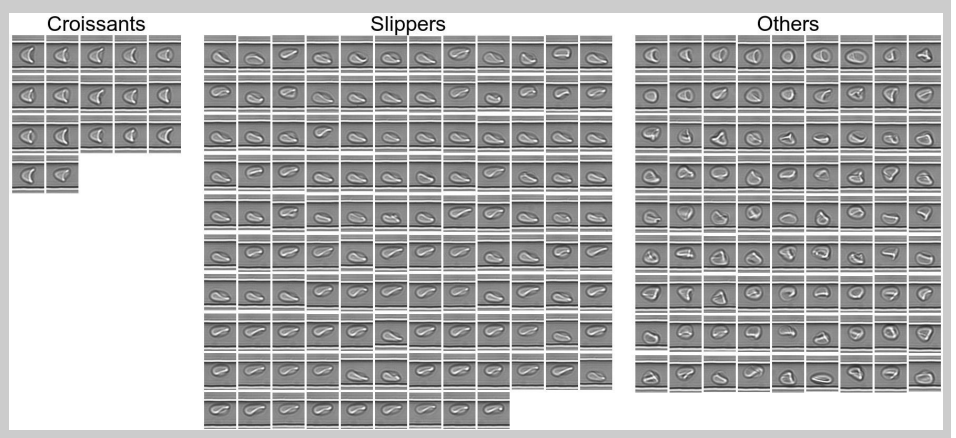
$\Delta P = 300 \text{ mbar}, x = 10 \text{ mm}$



$\Delta P = 400 \text{ mbar}, x = 10 \text{ mm}$



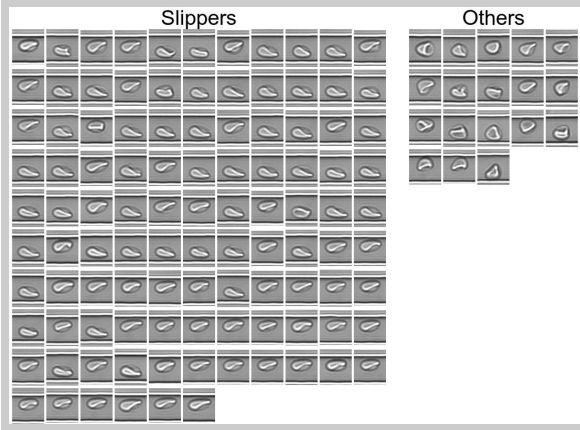
$\Delta P = 500 \text{ mbar}, x = 10 \text{ mm}$



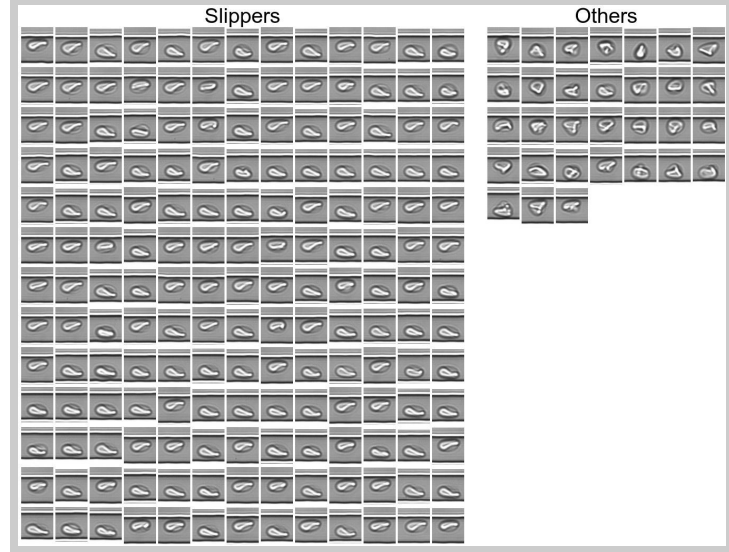
$\Delta P = 600 \text{ mbar}, x = 10 \text{ mm}$



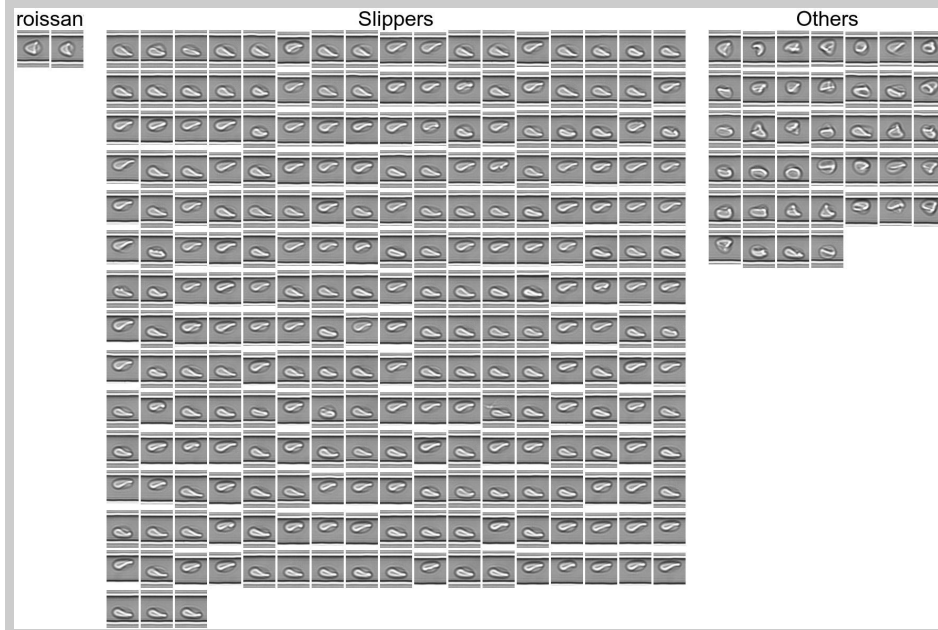
$\Delta P = 700 \text{ mbar}, x = 10 \text{ mm}$



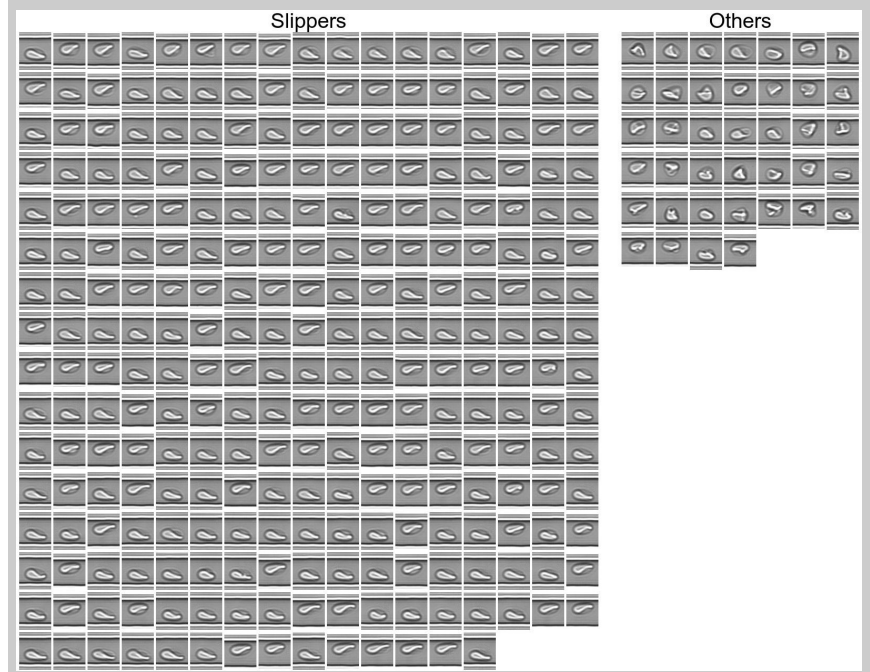
$\Delta P = 800 \text{ mbar}, x = 10 \text{ mm}$



$\Delta P = 900 \text{ mbar}, x = 10 \text{ mm}$



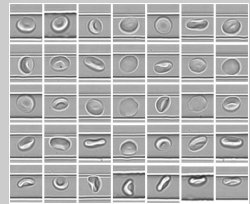
$\Delta P = 1000 \text{ mbar}, x = 10 \text{ mm}$



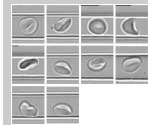
S7 Raw experimental images at $x = 0$ mm

Note: The images in the individual collections are ordered from centered to off-centered.

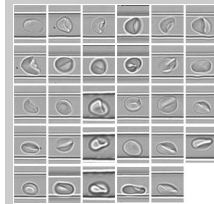
$\Delta P = 20$ mbar, $x = 0$ mm



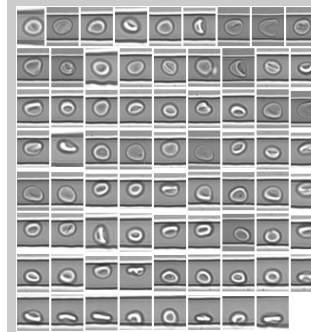
$\Delta P = 50$ mbar, $x = 0$ mm



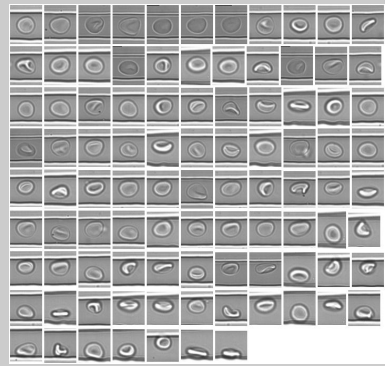
$\Delta P = 100$ mbar, $x = 0$ mm



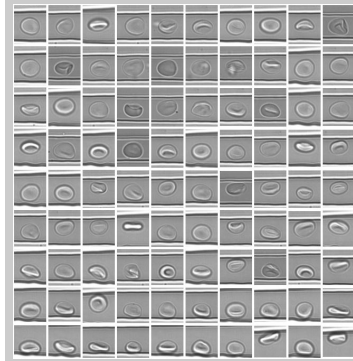
$\Delta P = 200$ mbar, $x = 0$ mm



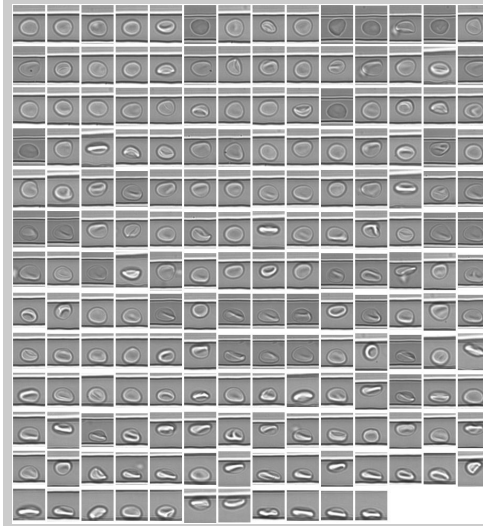
$\Delta P = 300$ mbar, $x = 0$ mm



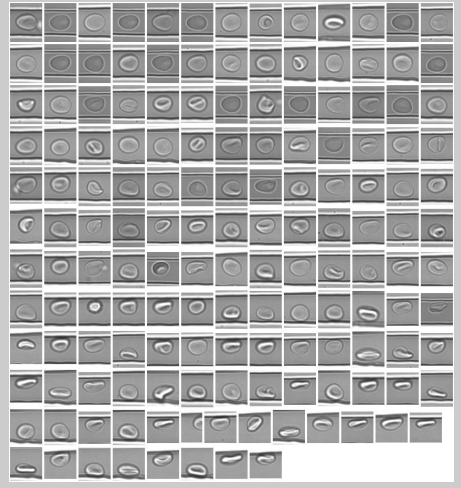
$\Delta P = 400$ mbar, $x = 0$ mm



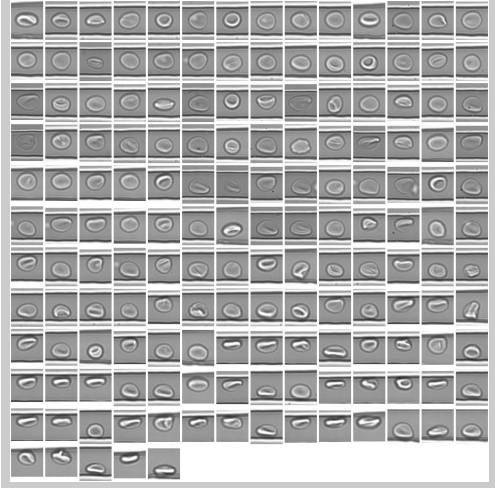
$\Delta P = 500$ mbar, $x = 0$ mm



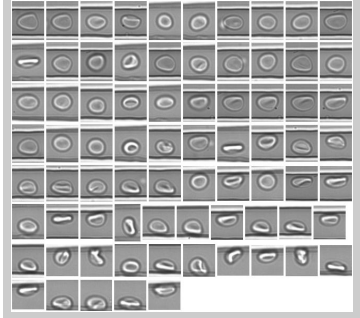
$\Delta P = 600 \text{ mbar}, x = 0 \text{ mm}$



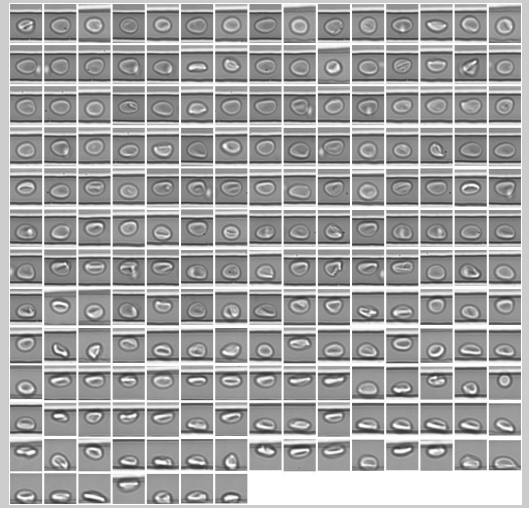
$\Delta P = 700 \text{ mbar}, x = 0 \text{ mm}$



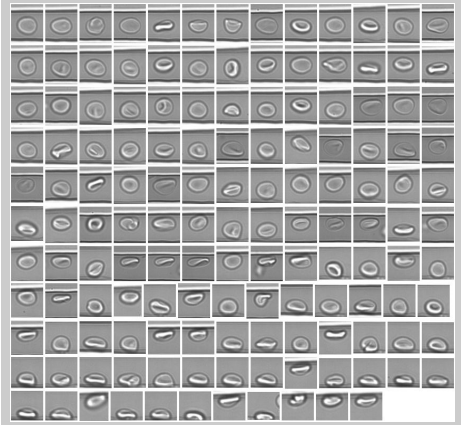
$\Delta P = 800 \text{ mbar}, x = 0 \text{ mm}$



$\Delta P = 900 \text{ mbar}, x = 0 \text{ mm}$



$\Delta P = 1000 \text{ mbar}, x = 0 \text{ mm}$



Erklärung

Hiermit versichere ich an Eides statt, dass ich die vorliegende Arbeit selbstständig verfasst und keine anderen als die von mir angegebenen Quellen und Hilfsmittel verwendet habe. Weiterhin erkläre ich, dass ich die Hilfe von gewerblichen Promotionsberatern bzw. -vermittlern oder ähnlichen Dienstleistern weder bisher in Anspruch genommen habe, noch künftig in Anspruch nehmen werde. Zusätzlich erkläre ich hiermit, dass ich keinerlei frühere Promotionsversuche unternommen habe. Die Arbeit wurde nicht bereits in gleicher oder vergleichbarer Form zur Erlangung eines akademischen Grades eingereicht.

Bayreuth, den

Achim Guckenberger